Experimental Study and Numerical Modelling of Intra-Array Interactions and Extra-Array Effects of Wave Energy Converter Arrays

Experimentele studie en numerieke modellering van intra-array-interacties en extra-array-effecten van golfenergieconvertorparken

Vasiliki Stratigaki

Promotor: prof. dr. ir. M. Vantorre
Proefschrift ingediend tot het behalen van de graad van
Doctor in de Ingenieurswetenschappen: Bouwkunde

Vakgroep Civiele Techniek
Voorzitter: prof. dr. ir. P. Troch
Faculteit Ingenieurswetenschappen en Architectuur
Academiejaar 2013 - 2014

UNIVERSITEIT GENT

ISBN 978-90-8578-681-8
NUR 956, 961
Wettelijk depot: D/2014/10.500/27

Universiteit Gent
Faculteit Ingenieurswetenschappen en Architectuur
Vakgroep Civiele Techniek
Afdeling Weg- en Waterbouwkunde

Supervisor:

Prof. dr. ir. M. Vantorre

Research institute:

Ghent University
Faculty of Engineering and Architecture

Department of Civil Engineering
Coastal Engineering Division
Technologiepark 904
B-9052 Zwijnaarde, Belgium

Tel.: +32-9-264.54.89
Fax.: +32-9-264.58.37

Research funded by a PhD grant of the Research Foundation Flanders, Belgium (FWO - Fonds Wetenschappelijk Onderzoek).

Experiments for the development and construction of the physical models funded by the Research Foundation Flanders, Belgium (FWO - Fonds Wetenschappelijk Onderzoek) - Contract no. FWO-KAN-1523712N.

Experiments in the large-scale facility of DHI have been supported by European Community's Seventh Framework Programme through the grant to the budget of the Integrating Activity HYDRALAB IV within the Transnational Access Activities, Contract no. 261520.

Acknowledgements

At the end of this research part, I would like to thank the following persons for their contribution in completing this PhD research.

Professor Peter Troch (Head of the Research Group of Coastal Engineering, Ghent University (UGent)), as coordinator of the WEC array experiments at DHI ("WECwakes" project), performed within the framework of the EU FP7 HYDRALAB IV Programme, and as supervisor of the FWO-KAN-project for the construction of the 25 WEC units. I thank him, for introducing me into the topic of renewable (wave) energy research performed within his group, and for sharing his expertise in the topic of WEC array effects, in numerical wave propagation models and in experimental modelling on wave-structure interaction.

Professor Marc Vantorre (Maritime Technology Division, UGent) for his support on theoretical issues on the point absorber theory. Also for his advice on the development of the prototype WEC unit during the testing at the large wave flume of Flanders Hydraulics Research (FHR). Finally, I thank him for offering his expertise in point absorber WECs and for reviewing and recommending improvements for my PhD manuscript.

Em. Professor Ronny Verhoeven (Hydraulics Laboratory, UGent) for his technical support, together with Professor Tom De Mulder, for making means and technical staff available for the construction of structural elements of the WEC units at the Hydraulics Laboratory of Ghent University. I also thank Em. Prof. Ronny Verhoeven for the educational and pleasant cooperation during the past four years.

The "WECwakes" consortium composed of European partners: Dr. Tim Stallard (School of Mechanical Aerospace and Civil Engineering, University of Manchester, UK); Dr. David Forehand (Institute for Energy Systems, School of Engineering, The University of Edinburgh, UK); Assoc. Prof. Jens Peter Kofoed (Wave Energy Research Group, Department of Civil Engineering, Aalborg University, Denmark); Dr. Matt Folley (School of Planning, Architecture & Civil Engineering, Queen's University Belfast, Northern Ireland / QML, UK); Dr. Michel Benoit (Saint-Venant Laboratory for Hydraulics, EDF-Recherche et Développement, Laboratoire Saint-Venant (EDF R&D, CETMEF, Ecole des Ponts ParisTech), France); Dr. Aurélien Babarit (Ocean Energy and Ocean Waves Group, Ecole Centrale de Nantes, LHEAA Lab - CNRS: Hydrodynamics, Energetics, Atmospheric Environment, France) and Jens Kirkegaard (Ports and Offshore Technology, DHI, Hørsholm, Denmark), for their contribution to the design and conduct of the WEC array experiments.

Moreover, the staff from UGent, QML, FHR and DHI and the researchers from all partners institutions involved with the conduct of the WEC array experiments, are acknowledged for their technical support. Especially, I would like to thank Dr. David Forehand, Dr. Tim Stallard and Assoc. Prof. Jens Peter Kofoed for their significant contribution to the preparation of publications.

Moreover, I would like to acknowledge the following infrastructure managers, for providing experimental facilities and software for this PhD research:

- Wave flume / workshop / MILDwave software of Coastal Engineering group, Ghent University: Prof. Peter Troch;
- Shallow Water Wave basin / workshop of DHI: Jens Kirkegaard;
- WAMIT software: Prof. Marc Vantorre (Ghent University); Dr. David Forehand (The University of Edinburgh);
- Tensile testing machine of Ghent University: Dr. Ives De Baere;
- Workshop of Hydraulics Laboratory, Ghent University: Em. Professor Ronny Verhoeven, Prof. Tom De Mulder;
- Wave basin of Queen's Marine Laboratory (QML) of the Queen's University Belfast: Dr. Björn Elsäßer and Dr. Matt Folley;
- Wave flume of Flanders Hydraulics Research: Toon Verwaest and Prof. Marc Vantorre.

From Ghent University, I would like to thank my colleagues and thesis students, and especially Herman, Tom, David, Lieselot, Pieter, Sam, Dave and Stefaan for their significant technical support, for our fluent and pleasant cooperation, and for their presence during the experimental testing, both at home (wave flumes of UGent and FHR) and abroad (wave basins of QML and DHI). Also, for the administrative tasks, I would like to thank Ludo, Ellen and Lien.

Last but not least, I thank my parents Chrysanthi and Konstantinos Stratigakis for being my most loyal supporters throughout all my studies and choices till now. I would also like to thank my family and friends: Ine, Vincent, Philippos, Maria, Nikos, Aliki, Evi, Diane, Herman, Hans, Mayette, Milou and Nick.

Finally, a special *thanks* and appreciation to my husband Peter for his constant support, for his positive approach to difficult moments and for *everything* that helped me to get to this day.

Vasiliki Stratigaki

Ghent, April 2014

Nederlandse samenvatting

–Summary in Dutch–

Duurzame en hernieuwbare energiebronnen hebben heel wat belangstelling opgewekt tijdens de voorbije decennia, ten gevolge van de toenemende vraag naar energie, de krimpende reserves aan fossiele brandstoffen en de klimaatverandering. De noodzaak om de uitstoot van broeikasgassen te verminderen heeft geleid tot maatregelen die worden genomen op Europees niveau, maar ook op nationaal niveau door de lidstaten, zodat de EU erin zou slagen te voldoen aan de doelstellingen van het Protocol van Kyoto en de "20/20/20" doelstellingen.

Energie uit windgolven is één van de zich intensief ontwikkelende hernieuwbare energiebronnen met een groot potentieel. Energie uit windgolven kan worden geoogst door het installeren van GolfEnergieConvertoren (verder afgekort als *GECs*) op zee, dit zijn toestellen die de kinetische en/of potentiële energie van golven omzetten in elektriciteit. Er zijn al vele concepten van GECs ontwikkeld, voornamelijk te onderscheiden op basis van het omzettingsprincipe, in (i) het type van de oscillerende waterkolom en de golf-geactiveerde lichamen, die oscilleren bij invallende golfwerking en (ii) het type van golfoverslagtoestellen, die de overslaande golven opvangen in een reservoir boven de zeespiegel om een hoogteverschil te creëren.

Om een aanzienlijke hoeveelheid energie te kunnen oogsten op een bepaalde locatie, en om de commerciële exploitatie van golfenergie mogelijk te maken, zal de installatie van grote aantallen GECs (b.v. tientallen GECs tegelijk) vereist zijn. De GECs zullen moeten gerangschikt worden in een array (of een *matrix* of *park*), gebruikmakend van een bepaalde geometrische indeling. De energieproductie van de array kan evenwel kleiner of groter zijn dan de som van de energieproducties gegenereerd door het equivalente aantal individuele GECs, als een resultaat van de hydrodynamische interacties tussen de GECs in een array (dit zijn zogenaamde *intra–array interacties*). Bovendien wordt, als gevolg van het grote aantal GECs in een array, traditioneel een afname van de golfhoogte waargenomen, zowel in numerieke als in schaalmodel experimenten van kleine GEC arrays. Deze afname van de golfhoogte wordt meestal waargenomen tussen de plaats van de geïnstalleerde GEC array en een verder afwaarts gelegen locatie (ten opzichte van de golfrichting), b.v. de kustlijn (dit zijn zogenaamde *extra–array-effecten*). Deze wijzigingen in het golfveld kunnen een invloed hebben op naburige activiteiten op

zee, alsook op andere mariene (energie) projecten, kust–ecosystemen en zelfs op de kustlijn en de randvoorwaarden voor de kustverdediging.

Daarom is een diepgaand inzicht nodig in deze *GEC array effecten*, die samengesteld zijn uit de *intra–array interacties* tussen GECs in een golfenergiepark en de *extra–array-effecten* op het milieu. Met dit inzicht kan de optimale geometrische configuratie van de GEC array bepaald worden, kunnen optredende wijzigingen in golfcondities gekwantificeerd worden, en kunnen finaal de energiekosten aanzienlijk worden verminderd.

Er zijn al verschillende numerieke studies op zowel kleine als grotere GEC arrays uitgevoerd, en deze hebben al een eerste inzicht verschaft in de grootte en omvang van de GEC interacties voor geïdealiseerde condities en configuraties. Er is evenwel slechts een zeer beperkte validatie van deze numerieke modellen uitgevoerd op basis van resultaten verkregen via fysische schaalmodellen van GEC arrays. Er zijn slechts een paar literatuurvermeldingen hiervan, die bovendien gebruik maken van doorgaans minder dan 12 GECs, terwijl er geen gepubliceerde gegevens beschikbaar zijn met betrekking tot de fysische modellering van GEC array effecten gecombineerd met gelijktijdige metingen van de GEC respons.

Op basis hiervan wordt een duidelijke kennislacune in de literatuur vastgesteld, alsook de nood ervaren voor het uitvoeren van grootschalige experimenten van GEC arrays. Dergelijke experimentele gegevens zijn essentieel voor de beoordeling van de juistheid van de gebruikte numerieke modellen, voor hun validatie, en voor hun verdere ontwikkeling en verbetering. Er is ook nood aan nauwkeurige metingen van de respons van individuele GECs, van de energieopbrengst van een GEC array, en van de ruimtelijke variatie van golfcondities in de nabijheid van de array, om het inzicht in de fundamentele processen die golfcondities beïnvloeden op- en afwaarts van GEC arrays te verbeteren. Bovendien zijn de resultaten van het testen van diverse geometrische configuraties van GEC arrays nodig voor het optimaliseren van de array lay-outs voor echte praktijktoepassingen.

Anderzijds vormt het grote aantal verschillende GEC concepten, ontwikkeld in de afgelopen decennia (onlangs ingeschat op ongeveer een 150tal), een belemmering voor het testen van GEC arrays, aangezien GEC concepten zeer vaak gebaseerd zijn op complexe operationele en structurele principes, of zelfs gecompliceerde geometrieën. Daarbij neigen GEC ontwikkelaars zich doorgaans vooral te richten op de ontwikkeling en optimalisatie van een enig prototype toestel, waardoor een GEC concept niet tot het stadium van de GEC array testen (met verschillende operationele toestellen) raakt. Daarnaast zijn structurele details en testgegevens van deze GEC concepten dikwijls privé en vertrouwelijk, waardoor de oorzaken van falen of succes van een GEC concept niet toegankelijk zijn voor de onderzoeksgemeenschap. Tenslotte, zoals meestal het geval is tijdens een strikt gedefinieerde en vrij korte financieringsperiode, is het economisch (vanwege de hoge bouwkosten) en praktisch (moeilijk te vervaardigen) niet haalbaar om een GEC concept in een groot aantal te

vervaardigen binnen de voorziene periode van onderzoeksfinanciering, om experimentele testen uit te voeren met grote GEC arrays. Desalniettemin zullen GECs in grote aantallen dienen geïnstalleerd te worden om een levensvatbare vermogensoutput te waarborgen.

GEC array effecten worden ook intensief numeriek gemodelleerd. Ten gevolge van de wisselwerking tussen oscillerende GECs en het invallende golfveld, worden extra golfvelden gegenereerd: het geradieerde en het gediffracteerde golfveld rond elke GEC, die samen met het invallende golfveld het verstoorde golfveld rond de GECs vormen. Verschillende numerieke methoden worden gebruikt om deze golfvelden rond de GECs te beschrijven en analyseren. Voor het onderzoek naar golf-structuur (golf-GEC) interacties, golfenergieabsorptie en intra–array interacties, zijn de meest gebruikte en meest geschikte modellen gebaseerd op de randelementenmethode (Boundary Element Method, BEM) voor het oplossen van de potentiaalstroming formulering (b.v. WAMIT, Aquaplus, enz.), of gebaseerd op de Navier–Stokes vergelijkingen (b.v. CFD modellen). Voor het onderzoek naar extra–array-effecten van GEC arrays in grote gebieden, zijn golfvoortplantingsmodellen het meest geschikt en gewoonlijk toegepast (MILDwave, SWAN, MIKE21, enz.). Al deze modellen lijden echter aan een gemeenschappelijk probleem: ze kunnen niet gebruikt worden om tegelijkertijd zowel intra–array interacties als extra–array-effecten te modelleren omwille van de volgende beperkingen: (a) modellen gebaseerd op de BEM methode voor potentiaalstroming of op de Navier–Stokes vergelijkingen lijden aan een hoge computationele kost, wanneer deze de energie-absorptie en de gerelateerde wijzigingen in het golfveld simuleren voor grote GEC arrays, waardoor deze modellen doorgaans gebruikt worden voor arrays met minder dan 12 GECs; (b) het gebruik van golfvoortplantingsmodellen maakt de simulatie van extra–array-effecten mogelijk. Grote GEC arrays in grote domeinen worden gemodelleerd met een redelijke computationele kost. Hierdoor kunnen de veranderingen in het golfveld en de daarmee samenhangende milieueffecten bestudeerd worden op grotere regionale schaal. De GECs worden echter tot op heden slechts benaderend gesimuleerd met behulp van geparameteriseerde energie"*putten*" (Eng.:"*sinks*") en empirisch afgestemde energieabsorptie-coëfficiënten, waardoor deze werkwijze slechts gedeeltelijk de onderliggende fysica beschrijft, wat aanleiding kan geven tot foutieve modelconclusies.

Gezien de bovengenoemde tekortkomingen van de huidige stand van de techniek, heeft dit doctoraatsonderzoek zich gericht op GEC arrays of golfenergieconvertorparken. De kerntaak bestond erin om experimenten uit te voeren met grote golfenergieconvertorparken. Een uitgebreide databank is opgesteld voor het gedetailleerde onderzoek naar GEC array effecten. Bovendien zijn, door de analyse van de verkregen metingen, intra-array-interacties en extra-array-effecten gekwantificeerd voor een ganse reeks van geometrische configuraties van GEC arrays. Vooraleer deze experimenten uit te voeren, is een relatief eenvoudig GEC

toestel ontwikkeld, speciaal voor deze GEC array testen. Het ontwikkelde GEC toestel is op voorhand –zowel experimenteel als numeriek– in detail gemodelleerd, om de beste performantie te garanderen. Daarnaast is een methodologie ontwikkeld voor de numerieke modellering van de golfveldwijzigingen ten gevolge van de energie-extractie van de GEC (array) uit de golven. Een methode van gekoppelde numerieke modellering is ontwikkeld voor de gecombineerde simulatie van intra-array-interacties en extra-array-effecten van GEC (arrays).

Derhalve zijn de belangrijkste resultaten van dit doctoraatsonderzoek: (a) de opmaak van de eerste "grote GEC array" databank; (b) GEC array effecten zijn gekwantificeerd voor een ganse reeks van geometrische configuraties van GEC arrays en kenmerken van het invallende golfveld, (c) een GEC toestel voor het testen van arrays, representatief voor het type "*point absorber*" GEC, is ontwikkeld en geconstrueerd in grote aantallen (26 in totaal), (d) een numerieke methodologie is ontwikkeld voor de simulatie van zowel intra-array-interacties als extra-array-effecten van GEC (arrays). Dit doctoraatsmanuscript is opgebouwd uit drie delen, die deze resultaten (a-d) verder in detail beschrijven.

In het **eerste deel** van dit doctoraatsonderzoek wordt **het ontwerp, de ontwikkeling en de evaluatie van het GEC toestel** gepresenteerd. Het doel van de ontwikkeling van deze GEC was niet om een nieuw GEC concept in de sector van de golfenergie te introduceren, maar om een GEC te creëren die zeer efficiënt de experimentele én numerieke modellering van grote GEC arrays ondersteunt en faciliteert. Het GEC toestel heeft om die reden een generieke geometrie, gebaseerd op het "*point absorber*" type (GEC type (i)), aangezien de golfenergie sector momenteel gedomineerd wordt door het type "*point absorber*" GECs.

Het ontwikkelde GEC toestel beoogt in zijn ontwerp een aantal belangrijke vereisten te verenigen, die nodig zijn voor de reproductie in grote aantallen en voor de gemakkelijke herpositionering van de GECs in de golfgoot en –tank, zodat alternatieve geometrische configuraties van GEC arrays handig te realiseren zijn. Ten eerste, is het ontwikkelde GEC toestel robuust; is het gemakkelijk te bedienen en economisch, praktisch, eenvoudig en haalbaar te vervaardigen, gekoppeld aan lage bouwkosten voor identieke GEC toestellen. Ten tweede, is het GEC toestel voldoende groot om meetbare respons en energie-extractie te realiseren bij het geteste invallende golfveld. Het GEC toestel is ontworpen om de daadwerkelijke invloed van een GEC op het golfklimaat te simuleren op basis van een eenvoudig concept van energiewinning uit de invallende golven. Dit kenmerk leidt tot meetbare veranderingen in het golfveld en maakt daarom de kwantificering van extra-array-effecten zeer goed mogelijk. Ten derde, is het GEC toestel eenvoudig te modelleren, zowel analytisch als numeriek, aangezien het aantal vrijheidsgraden, die gemodelleerd worden in een responsmodel van de gehele GEC array, beperkt zijn (nl. gelijk aan het aantal GEC toestellen binnen een array). Dit wordt gerealiseerd door het ontwerpen van een één-graad-van-vrijheid (1-DOF) GEC toestel, en

bijvoorbeeld geen 6-DOF (of minder) GEC toestel, wat zou leiden tot een hoge complexiteit van de numerieke en analytische behandeling van de gehele GEC array, evenredig aan het aantal vrijheidsgraden van de array. Daarnaast heeft de GEC een geïdealiseerde en eenvoudige boei geometrie met rechte zijden ter hoogte van het wateroppervlak.

Het ontwikkelde GEC toestel is eerst grondig getest in, in totaal, twee golfgoten en twee golftanks om aan de gestelde vereisten te voldoen. Dankzij zijn eenvoudige ontwerp konden met het ontwikkelde GEC toestel 36 verschillende GEC (array) configuraties getest worden. Een lineaire analyse van de GEC respons is uitgevoerd met behulp van WAMIT naast de experimentele testen, teneinde de prestaties van het GEC toestel te evalueren. Vier reeksen van experimenten zijn uitgevoerd, met inbegrip van droog-testen van de GEC lager, evaluatie van het GEC ondersteuningssysteem, respons van een individueel GEC toestel onder golfaanval, en respons van tot vier GEC toestellen die samen een kleine array vormen. Experimentele evaluatie van de GEC toestellen is uitgevoerd met behulp van een trekproef machine en een golfgoot aan de Universiteit Gent, in België, de golftank van Queen's Marine Laboratory van Queen's University in Belfast (UK), en de golfgoot (grootschalige faciliteit) van het Waterbouwkundig Laboratorium in België. Het voorgestelde GEC toestel heeft hierbij aangetoond dat aan de vereisten voor grote array experimenten voldaan is, alsmede aan de vereisten voor de reproductie van identieke GEC toestellen in grote aantallen.

Het **tweede deel** van dit doctoraatsonderzoek focust op de **numerieke modellering van de resulterende golfvelden rond oscillerende golfenergieconvertoren**, met de bedoeling om GEC (array) effecten te bestuderen. In dit doctoraatsonderzoek wordt een generieke koppelingsmethodologie ontwikkeld, om de twee eerder genoemde methodes te combineren; (a) de methode van de solvers voor golf-structuur interactie, gebruikt om intra-array-effecten te modelleren, die fysisch correct de golfenergieabsorptie en de resulterende golfvelden gegenereerd door oscillerende GECs of GEC arrays modelleren, en (b) de methode van golfvoortplantingsmodellen, gebruikt om extra-array-effecten te modelleren, die het effect van GEC arrays op het golfveld en de kustlijn kunnen modelleren. Bovendien wordt een golfgeneratietechniek in een golfvoortplantingsmodel voorgesteld voor het genereren van het verstoorde golfveld dat geïnduceerd wordt door een oscillerende GEC. Een golfgeneratiecirkel wordt gebruikt, geplaatst rondom de GEC, en waarop voorgeschreven interne golfrandvoorwaarden als input worden opgelegd, die aangeleverd zijn door een golf-structuur interactie solver. Belangrijk is op te merken dat beide, zowel de gepresenteerde koppelingsmethodologie als de golfgeneratietechniek, generiek zijn: (i) de koppeling kan worden gerealiseerd tussen om het even welke golf-structuur interactie solver en golfvoortplantingsmodel, (ii) het betreft om het even welke oscillerende/drijvende constructie, b.v. oscillerende waterkolommen/GECs,

drijvende golfbrekers, platformen, enz. De voorgestelde koppelingsmethodiek wordt geverifieerd op basis van het gebruik van de in dit werk ontwikkelde dompende (Eng.: "*heaving*") GEC. In deze testcase wordt de koppeling tussen de golf-structuur interactie solver, WAMIT, en het tijdsdomein golfvoortplantingsmodel, MILDwave, gerealiseerd. De resultaten van de gediffracteerde, geradiëerde en verstoorde golfvelden rond de GEC onder invallende golfwerking, verkregen met behulp van de gepresenteerde koppelingsmethodologie, zijn geverifieerd met de resultaten verkregen met de golf-structuur solver, en tonen zeer goede overeenkomst. Tenslotte worden de voordelen besproken van de voorgestelde koppelingsmethodologie om drijvende lichamen te modelleren in een tijdsdomein golfvoortplantingsmodel.

Het **derde deel** van dit doctoraatsonderzoek richt zich op het uitvoeren van **fysische grootschalige modelproeven van GEC arrays samengesteld uit een groot aantal GECs**. Deze experimenten zijn zowel voorbereid als uitgevoerd binnen dit doctoraatsonderzoek, en maken deel uit van het onderzoeksproject "WECwakes", gefinancierd door het EU FP7 Hydralab IV programma. Ten eerste is een testprogramma opgesteld op basis van een literatuurstudie over onderzoek met GEC arrays. Op deze manier zijn de belangrijke bepalende parameters geïdentificeerd voor het uitvoeren van GEC array testen, zoals b.v. de geometrische configuraties van de array, de tussenafstand tussen de GECs, kenmerken van het invallende golfveld, enz. Vervolgens zijn de experimentele tests uitgevoerd in de ondiep water golftank van DHI (Hørsholm, Denemarken) in de periode januari-februari 2013. GEC arrays opgebouwd uit maximaal 25 identieke GECs zijn getest, op basis van het generieke dompende GEC toestel ontwikkeld binnen dit doctoraatsonderzoek.

Deze experimentele set-up van 25 individuele GEC toestellen in een array lay-out, geplaatst in een grote golftank, is op dit moment de grootste opstelling van zijn soort, wereldwijd, voor het bestuderen van de belangrijke impact van de GEC-array effecten op energieabsorptie en golfcondities .

Als belangrijk resultaat, levert het uitvoeren van de experimentele testen zoals gerealiseerd binnen dit doctoraatsonderzoek, een uitgebreide niet-vertrouwelijke databank voor "*point absorber*" GECs. Ten eerste zijn voor het eerst gegevens van grote GEC arrays betreffende de fysische modellering van intra-array-interacties en extra-array-effecten verkregen, in combinatie met gelijktijdige metingen van GEC respons, golf-geïnduceerde krachten op de GECs en golfcondities. Ten tweede omvat de verkregen databank een groot bereik aan parametervariaties zoals: de geometrische configuratie van de array, het aantal GECs, de laterale en de longitudinale afstand (hart op hart) afstand tussen de GECs, de beweging van de GEC (afname van de beweging, vaste GECs dia als "obstakels" functioneren, vrije respons of gedempte beweging van GECs met wisselende demping), golfcondities (variërende golfperiode, golfhoogtes, golfaanval hoeken) en golftypes (regelmatig, polychromatisch, onregelmatig langkruinig en kortkruinig met verschillende

spreidingsparameters). Ten derde is deze databank niet alleen toepasselijk voor GEC arrays, maar ook voor drijvende constructies/platforms, stationaire cilinders onder golfaanval, enz. De hier verkregen metingen kunnen worden gebruikt voor het onderzoeken van bijvoorbeeld golfimpact op cilinders en de aanpassingen van het golfveld eromheen. Als een vierde voordeel van de verkregen databank wordt de niet-confidentialiteit vermeld. De gegevens zijn toegankelijk voor de onderzoeksgemeenschap, zoals bepaald in de Hydralab regels. Ten slotte zullen de metingen verkregen uit deze experimentele testen zeer nuttig zijn om een groot scala aan numerieke modellen te valideren en uit te breiden, die gebruikt worden om de respons, de energieabsorptie en de wijzigingen in het golfveld als gevolg van het oscilleren van de GECs te modelleren. Validatie van deze modellen zal optimalisering van de geometrische opstelling van GEC arrays voor reële toepassingen mogelijk maken, en zal zodoende de energiekost van golfenergiesystemen reduceren.

Een andere verwezenlijking op basis van de opgestelde GEC array databank, is de data-analyse ervan zoals uitgevoerd in dit doctoraatsonderzoek. De resultaten verkregen door het uitvoeren van de GEC array experimenten, hebben geleid tot een eerste reeks van generieke richtlijnen voor GEC array ontwerp. Deze richtlijnen kunnen worden gebruikt door golfenergie projectontwikkelaars voor het optimale ontwerp van GEC arrays zowel met betrekking tot hun energieabsorptie, als hun impact op het milieu. Deze aanbevelingen zijn gebaseerd op een literatuur studie van numeriek en experimenteel onderzoek, én op de resultaten met betrekking tot de constructieve en destructieve invloed van intra-array-effecten op het totale opgenomen vermogen van de geteste GEC array configuraties. Bovendien zijn deze richtlijnen gebaseerd op verkregen resultaten voor golfdissipatie (dus extra-array-effecten) achter de geteste GEC arrays, zoals b.v. de grote arrays van 25 GECs, zowel in rechtlijnige als versprongen lay-out, en is het aangetoond dat deze significante gevolgen kan hebben op de resulterende golfveld achter de GEC array.

English summary

Sustainable and renewable energy resources have gained interest the past decades, as a result of the increasing energy demand, the shrinking fossil fuel reserves and the climate change. The need to reduce greenhouse gas emissions has led to measures that are being taken at European level, as well as by Member States at national level, so that the EU succeeds in meeting its targets under the Kyoto Protocol and the "20/20/20" objectives.

Ocean wave energy is one of the intensively developing renewable energy resources with great potential. Energy from ocean waves can be utilized by installing Wave Energy Converters (abbreviated as *WECs*) in the sea, which are devices that convert the kinetic and/or potential energy of waves into electricity. Many concepts of WECs have already been developed, mainly distinguished based on the conversion principle, in (i) oscillating water columns and wave-activated bodies, which oscillate under incident waves, and (ii) overtopping devices, which capture the overtopped waves in a basin above sea level that creates a hydraulic head.

Most importantly, in order to extract a considerable amount of energy at a specific site location, and to make the commercial exploitation of wave energy possible, installation of large numbers of WECs (e.g. tens of WECs simultaneously) will be required. The WECs will have to be arranged in an array (or a *farm* or *park*) using a particular geometric layout. However, power production of the array may be smaller or larger than the sum of the power produced by the equivalent number of individual WECs, due to hydrodynamic interactions between the WECs within an array (so-called *intra-array interactions* or *park effect*). Moreover, as a result of the large number of WECs within an array, usually wave height attenuation is observed numerically and in scale model experiments with small WEC arrays. This wave height dissipation is observed mostly between the WEC array installation site and a downwave location, e.g. the shoreline (so-called *extra-array effects*). These wave field modifications can influence neighbouring activities in the sea, other marine (energy) projects, coastal eco-systems and even the coastline and the coastal defence conditions and parameters.

Therefore, an accurate understanding is required of the *WEC array effects*, which consist of the *intra-array interactions* between WECs in a wave farm and the *extra-array effects* on the environment. With this understanding, the optimal geometric layout of the WEC array can be determined, changes to wave conditions can be quantified and ultimately the cost of energy will be reduced significantly.

Several numerical studies on both small and large WEC arrays have already been performed, and have provided a first insight into the magnitude and extent of WEC interactions for idealized conditions and configurations. However, there has been very limited validation of these numerical models using physical scale models of WEC arrays; only a few are reported in the literature using typically less than 12 WECs, while no published data are available concerning the physical modelling of WEC array effects combined with simultaneous measurements of WEC response.

Therefore, there is a clear **knowledge gap** in the literature and need for large scale experiments on WEC arrays. Such experimental data are essential for the evaluation of the accuracy of the used numerical tools, their verification, as well as for their further development and improvement. Accurate measurements of individual WEC response, WEC array power output and spatial variation of wave conditions in the vicinity of the array are required to improve understanding of the fundamental processes influencing wave conditions down- and up-wave of wave energy converter arrays. Moreover, results from testing various WEC array geometric configurations are necessary for the optimization of the array lay-outs for real applications.

On the other hand, the large number of different WEC concepts developed during the past decades (very recently estimated around 150), becomes prohibitive for WEC array testing, as, very often, WEC concepts are based on complex operating and structural principles, or even complicated geometries. Most importantly, WEC developers tend to focus on the development and optimization of single prototype devices, and, therefore, WEC concepts do not reach the stage of WEC array testing. In addition, structural details and testing data of these WEC concepts are private and confidential. As a result, the reasons of failure or success of a WEC concept are not accessible to the research community. Finally, as usually the case is within a well-defined and rather short funding period, it is economically (due to high construction cost) and practically (difficult to manufacture) not feasible to produce a WEC concept in large numbers within a normal research funding period, in order to perform tests with large WEC arrays. However, WECs will have to be installed in large numbers to ensure viable power output.

WEC array effects are also intensively numerically modeled. As a result of the interaction between oscillating WECs and the incident wave field, additional wave fields are generated: the radiated and the diffracted wave field around each WEC, which together with the incident wave field compose the perturbed wave field around the WECs. Several numerical methods are employed to analyse these wave fields around WECs; for investigating wave-structure (wave-WEC) interactions, wave energy absorption and intra-array interactions, the commonly used and most suitable models are based on Boundary Element Methods (BEMs) for solving the potential flow formulation (e.g. WAMIT, Aquaplus, etc.), or models based on the Navier-Stokes equations (e.g. CFD models). For investigating extra-array effects of

WEC arrays in large areas, wave propagation models are most suitable and commonly employed (MILDwave, SWAN, MIKE21, etc.). However, all these models suffer from a common problem; they cannot be used to model simultaneously, both intra-array interactions and extra-array effects due to limitations: (a) models based on the BEM approach of potential flow theory or on the approach of Navier-Stokes equations suffer from a high computational cost, when simulating power absorption and the wave field alteration due to large WEC arrays and are used typically for less than 10 WECs; (b) the approach of wave propagation models enables simulation of extra-array effects. Large WEC arrays installed in large domains are modeled at a reasonable computational cost. As a result, the changes in wave field and the associated environmental impacts can be studied at regional scale. However, the WECs are approximated up to now by using parameterized energy sinks and empirically tuned energy absorption coefficients, and therefore this method only partially addresses the underlying physics, which can lead to erroneous model conclusions.

Taking into account the above mentioned shortcomings of the present state of the art, this PhD research has focused on WEC arrays. The main deliverable was to perform experiments with large wave energy converter arrays. A comprehensive database for the detailed investigation of WEC array effects has been created. Moreover, through the analysis of the obtained measurements, intra-array interactions and extra-array effects have been quantified for a range of WEC array geometric configurations. Before performing these experiments, the development of a simple WEC unit has been achieved, specially designed for WEC array testing. The developed WEC unit has been experimentally and numerically modeled in detail, in advance, to ensure high performance. In addition, a methodology has been developed for the numerical modelling of the wave field modifications as a result of energy extraction from the waves by WEC (arrays). A coupled numerical modelling has been developed for the combined simulation of intra-array interactions and extra-array effects of WEC (arrays).

Therefore, the key results of this PhD research are: (a) the first large model WEC array testing database; (b) WEC array effects have been quantified for a range of WEC array geometric configurations and sea state characteristics; (c) a WEC for array testing, representative of point absorber type WEC concepts, has been developed and constructed in large numbers; (d) a numerical methodology to tackle both intra-array interactions and extra-array effects of WEC (arrays) has been established. This PhD manuscript has three parts dealing with these deliverables (a-d).

In the **first part** of this PhD research, the **design, development and evaluation of the WEC** unit is presented. The objective of developing this WEC was not to introduce a new WEC concept in the wave energy sector, but to create a WEC that efficiently supports and facilitates experimental and numerical modelling of large

WEC arrays. The WEC unit has, therefore, a generic geometry based on the point absorber type (WEC type (i)), as the wave energy sector is currently dominated by point absorber type WECs.

The developed WEC unit aimed at a number of key requirements, necessary for its reproduction in large numbers and for the easy repositioning of the WECs within the wave basin/flume to allow alternative WEC array geometric configurations. Firstly, the developed WEC is robust; it is easy to operate and, economically and practically, straightforward and feasible to manufacture, since it facilitates low cost construction of identical WEC units. Secondly, the WEC unit is sufficiently large to develop measurable response and energy extraction for the tested incident wave conditions. The WEC has been designed to simulate the real impact of a WEC on the wave climate, by using a simple concept of energy extraction from the incoming waves. This characteristic results in measurable changes to the wave field and, therefore, facilitates the quantification of extra-array effects. Thirdly, the WEC is straightforward to be modelled analytically and numerically in a response model, since the number of degrees of freedom of the entire WEC array is limited (equal to the number of WEC units within an array). This has been achieved by designing a single-degree-of-freedom (DOF) WEC unit, and e.g. not a 6-DOF (or less) WEC unit, which would result in high complexity of the numerical and analytical treatment of the entire WEC array, proportional to the total number of DOFs of the array. In addition, the WEC has an idealised and simple WEC buoy geometry with vertical sides at the water plane.

The developed WEC unit has been first thoroughly tested in two wave flumes and two wave basins, in total, to satisfy the necessary requirements. Due to its simple design, the developed WEC unit allowed experiments of 36 different WEC (array) configurations. Linear analysis of the WEC response using WAMIT, as well as experimental testing have been conducted, with the aim to evaluate the performance of the WEC unit. Four series of experiments have been performed, including mechanical testing of the WEC shaft bearings, evaluation of the WEC support system, response of an individual WEC unit under waves and response of up to four WEC units forming a small array. Experimental evaluation of the WEC units is conducted using the tensile test machine and the wave flume at Ghent University, in Belgium, the wave basin of the Queen's Marine Laboratory of the Queen's University of Belfast (UK), and the wave flume (large-scale facility) of Flanders Hydraulics Research, in Belgium. The proposed WEC unit has been shown to satisfy the performance requirements for large array experiments, as well as the feasibility requirements for the reproduction of identical WEC units in large numbers.

The **second part** of this PhD research focuses on the **numerical modelling of the resulting wave fields around oscillating wave energy converters**, with the intention to study WEC (array) effects. In this PhD research, a generic coupling methodology has been established, to combine the two approaches mentioned

previously; (a) the approach of wave-structure interaction solvers used for investigating intra-array effects, which model physically correct wave energy absorption and the resulting wave fields induced by oscillating WECs or WEC arrays, and (b) the approach of wave propagation models used for predicting extra-array effects, which can model the effect of WEC arrays on the wave field and the shoreline. In addition, a wave generation technique is presented, for generating the perturbed wave field induced by an oscillating WEC, in a wave propagation model. A wave generation circle is used, surrounding the WEC, on which prescribed internal boundary wave conditions are inserted as input, provided by a wave-structure interaction solver. Most importantly, both, the presented coupling methodology and wave generation technique are generic: (i) the coupling can be realized between any wave-structure solver and wave propagation model, (ii) they apply to any oscillating/floating structure, e.g. oscillating water columns/WECs, floating breakwaters, platforms, etc. The proposed coupling methodology has been verified, by employing the heaving WEC developed within this PhD research. In this test case, coupling between the wave-structure interaction solver, WAMIT, and the time domain wave propagation model, MILDwave, has been realized. The results obtained for the diffracted, radiated and perturbed wave field around the WEC under incident waves using the presented coupling methodology are verified against the results obtained from the wave-structure model, showing very good agreement. Finally, the benefits of the presented coupling methodology to model floating bodies in a phase resolving wave propagation model are discussed.

The **third part** of this PhD research focusses on the conduct of **physical large-scale modelling of large WEC arrays** (large numbers of WECs tested in a large-scale facility). These experiments have been prepared and carried out within this PhD research and are part of the research project "WECwakes", funded by the EU FP7 HYDRALAB IV programme. Firstly, a testing programme has been designed based on a literature study of research with WEC arrays. In this way, the important varying parameters have been identified for WEC array testing, e.g. array geometric configurations, spacing between the WECs, sea states characteristics, etc. Secondly, the experimental testing has been carried out in the Shallow Water Wave basin of DHI (Hørsholm, Denmark) during the period January-February 2013. WEC arrays composed of up to 25 identical WEC units have been tested, based on the generic heaving WEC unit developed within this PhD research.

This experimental set-up of 25 individual WEC units in an array layout, placed in a large wave basin, is at present the largest set-up of its kind, worldwide, studying the important impacts of WEC array effects on power absorption and wave conditions.

Most importantly, this experimental testing performed within this PhD research, resulted in a comprehensive non-confidential database for point absorber type WECs. Firstly, for the first time, data from large WEC arrays concerning the

physical modelling of intra-array interactions and extra-array effects, combined with simultaneous measurements of WEC response, wave induced forces on the WECs and of the wave conditions, have been obtained. Secondly, the obtained database comprises a wide range of parameter variations such as: the array geometric configuration, the WEC number, the lateral and longitudinal (centre-to-centre) spacing between the WECs, the WECs' motion (decay motion, stationary WECs, "free" response or damped motion of WECs with varying damping), wave conditions (varying wave period, wave heights, wave attack angles) and wave types (regular, polychromatic, irregular long- and short-crested with varying spreading parameters). Thirdly, this database is applicable not only to WEC arrays but also to floating structures/platforms, stationary cylinders under wave action, etc.. The here obtained measurements can be used for investigating e.g. wave impact on the cylinders and wave field modifications around them. As a fourth advantage of the obtained database, its non-confidentiality is identified. The data is accessible to the research community as specified under the HYDRALAB rules. Finally, the measurements obtained from these experimental tests will be very useful to validate and extend a large range of numerical models used to model response, power absorption and wave field modifications due to oscillating WECs. Validation of such models will enable optimization of the geometrical layout of WEC arrays for real applications and will therefore enable reduction of the cost of energy from wave energy systems.

Another achievement based on the acquired WEC array database, is the data analysis performed in this PhD research. The obtained results by the WEC array experiments, have resulted in a first set of generic guidelines for WEC array design. These guidelines can be used by wave energy project developers for optimal design of WEC arrays regarding their power absorption, as well as their impact on the environment. These recommendations are based both on a literature study of numerical and experimental research, and on the results concerning constructive or destructive influence of intra-array effects on the overall power absorption of the tested WEC array configurations. Moreover, these guidelines are based on the obtained results for wave dissipation (thus extra-array effects) downwave of the tested WEC arrays, as e.g. the large arrays of 25 WECs, both in rectilinear and staggered lay-out, are shown to have significant effect on the resulting wave field downwave of the WEC array.

Table of contents

List of abbreviations

AEP	Annual Energy Production
AWACS	Active Wave Absorption Control System
BEM	Boundary Element Method
CERC	Coastal Engineering Research Center
CFD	Computational Fluid Dynamics
DHI	formerly known as "Dansk Hydraulisk Institut" (EN: "Danish Hydraulic Institute")
DOF	Degree Of Freedom
FHR	Flanders Hydraulics Research
FWO	Research Foundation Flanders
GA	Genetic Algorithm
JONSWAP	Joint North Sea Wave Project
LCW	Long-Crested Waves
LVDT	Linear Variable Differential Transformer
PI	Parabolic Intersection
PTFE	PolyTetraFluoroEthylene (commonly known as "*Teflon*")
PTO	Power Take-Off
PUR	PolyURethane
PVC	PolyVinylChloride
QML	Queen’s Marine Laboratory
RAO	Response Amplitude Operator
S1-S6	Cross Sections (1-6)
SCW	Short-Crested Waves

UGent	Universiteit Gent
WEC	Wave Energy Converter
WG	Wave Gauge
2-D	two dimensional
3-D	three dimensional

List of symbols

a	(m)	Wave amplitude of numerical input wave (in MILDwave or WAMIT)
a_{0r}	(m)	Target wave amplitude for regular waves
a_m	(m)	Measured wave amplitude
a_M	(m)	Wave amplitude calculated using MILDwave
$a_{r,M}$	(m)	Wave amplitude on a radius, $r > r_C$ calculated using MILDwave
a_W	(m)	Wave amplitude calculated using WAMIT
$a_{r,W}$	(m)	Wave amplitude on a radius, $r > r_C$ calculated using WAMIT
a_w	(m)	Wave amplitude
A_w	(m^2)	Water-plane area of the WEC buoy (= πR^2)
b_c	(kg/s)	Critical damping coefficient
b_d	(kg/s)	Damping coefficient
b_{ext}	(kg/s)	External damping coefficient
b_{hyd}	(kg/s)	Hydrodynamic damping coefficient (heave mode)
C	(m/s)	Phase celerity
C_e	(m/s)	Energy velocity
C_g	(m/s)	Group velocity
$\bar{C}$	(m/s)	Phase celerity corresponding to the carrier wave frequency for irregular waves, $\bar{f}$
$\overline{C_g}$	(m/s)	Group velocity corresponding to the carrier wave frequency for irregular waves, $\bar{f}$
d_{buoy}	(m)	WEC buoy draft
d_w	(m)	Water depth

dx	(mm)	Spring compression increment
D	(m)	Diameter of the WEC buoy
f	(Hz)	Wave frequency
$\bar{f}$	(Hz)	Carrier wave frequency for irregular waves
f_n	(Hz)	Natural frequency of the WEC
f_p	(Hz)	Peak wave frequency of irregular waves
F	(N)	Force
F_{arch}	(N)	Archimedes force
$F_{av,surge}$	(N)	Average wave induced surge force
$F_{bearings}$	(N)	Vertical frictional force due to the WEC shaft bearings
F_{damp}	(N)	Damping force
$F_{damp,A}$	(N)	Amplitude of the damping force
$F_{damp,tot}$	(N)	Total damping force
F_{ex}	(N)	Exciting force (heave mode)
F_{fric}	(N)	Frictional force (Coulomb friction)
F_g	(N)	Gravity force
F_{heave}	(N)	Heave force
F_n	(N)	Force on a spring with fully compressed length
F_N	(N)	Normal force
F_{PTO}	(N)	External damping force exerted by the PTO-system
$F_{PTO,A}$	(N)	Amplitude of the external damping force exerted by the PTO-system
F_{rad}	(N)	Radiation force
F_{res}	(N)	Restoring force

$F_{springs}$	(N)	Total force exerted by the springs of the PTO-system
$F_{springs,i}$	(N)	Force exerted by the i spring of the PTO-system
F_{surge}	(N)	Wave induced surge force
$F_{surge,MAX}$	(N)	Amplitude of wave induced surge force
$F_{surge,meas}$	(N)	Measured wave induced surge force
$F_{surge,filt}$	(N)	Filtered wave induced surge force
$F_{surge,filt,MAX}$	(N)	Maximum filtered wave induced surge force
g	(m/s^2)	Acceleration due to gravity (g = 9.81 m/s^2)
h_{buoy}	(m)	Total height of the WEC buoy
H	(m)	Wave height
H_{0i}	(m)	Target wave height for irregular waves
H_{0r}	(m)	Target wave height for regular waves
H_i	(m)	Incident wave height
H_{m0}	(m)	Significant wave height based on spectral density
$H_{m0,GB}$	(m)	Significant wave height based on spectral density at the wave generation boundary
H_m	(m)	Measured wave height
$\overline{H_m}$	(m)	Mean measured wave height
H_r	(m)	The wave height on a circle with radius, r, larger than the radius of the wave generation circle, r_C (thus $r > r_C$)
H_{rc}	(m)	Wave height on the wave generation circle with radius, r_C
H_s	(m)	Significant wave height
H_{target}	(m)	Target wave height
H_{total}	(m)	Total wave height
k	(kg/s^2)	Hydrostatic restoring coefficient or stiffness

k_{ext}	(kg/s^2)	External hydrostatic restoring coefficient or stiffness (from additional stiffness term)
k_{spring}	(N/mm)	Spring stiffness coefficient
k_t	(m)	Typical dimension of a WEC
k_w	(m^{-1})	Wave number
K_d	(-)	Disturbance coefficient
K_R	(-)	Wave reflection coefficient
K_T	(-)	Wave transmission coefficient
$\overline{k_w}$	(m^{-1})	Wave number corresponding to the carrier wave frequency for irregular waves, $\bar{f}$
l	(m)	Longitudinal spacing between WECs
L	(m)	Wavelength
L_0	(mm)	Natural (uncompressed) length of each of the springs of the PTO-system of the WEC unit (L_0 = 80.50 mm)
L_n	(mm)	Fully compressed length of each of the springs of the PTO-system of the WEC unit (L_n = 20.60 mm)
L_p	(m)	Wavelength for peak wave period, T_p
l_d	(m)	Length of computational domain
m	(kg)	Mass of the WEC buoy
m_α	(kg)	Added mass
m_{sup}	(kg)	Supplementary mass
N	(-)	Number of WECs in an array
P	(W)	Net power absorption
$P_{0,tot}$	(W)	Total power absorbed by an isolated WEC
P_{av}	(W)	Avearge net power absorption
$P_{av,bearings}$	(W)	Time-averaged power absorption due to the WEC shaft bearings
$P_{av,PTO}$	(W)	Time-averaged power absorption of the power take-off system

$P_{av,tot}$	(W)	Time-averaged total power absorption
$P_{av,tot,OPT}$	(W)	Optimum time-averaged power absorption of a WEC unit
$P_{bearings}$	(W)	Instantaneous power absorption due to the WEC shaft bearings
$P_{i,tot}$	(W)	Total power absorbed by the i WEC in an array
P_m	(W)	Measured net power absorption of a WEC
P_{PTO}	(W)	Instantaneous power absorption by the power take-off system
$P_{PTO,MAX}$	(W)	Maximum value of the instantaneous power absorption by the power take-off system
P_{tot}	(W)	Instantaneous total power absorption
$P_{tot,MAX}$	(W)	Maximum value of the instantaneous total power absorption
P_{wave}	(W/m)	Wave energy flux (wave power) per unit length of wave crest
q	(-)	Ratio $a_{r,M}/\, a_{r,W}$
q_0	(m)	Initial position of the WEC buoy in a decay test
$\dot{q}_0$	(m/s)	Initial velocity of the WEC buoy in a decay test
$\bar{q}$-factor	(-)	WEC array interaction factor
r	(m)	Radius of a circle larger than the wave generation circle of radius, r_C (thus $r > r_C$)
r_c	(m)	Radius of the wave generation circle with centre of co-ordinates (x_C, y_C)
R^2	(-)	Determination coefficient
s	(-)	Directional spreading parameter
S	(-)	Absorption coefficient
$S(f)$	($m^2 \cdot s$)	Frequency spectrum
$S_D(f)$	($m^2 \cdot s$)	Frequency spectrum of the diffracted wave field
$S_{JONSWAP}(f)$	($m^2 \cdot s$)	JONSWAP frequency spectrum
$S_P(f)$	($m^2 \cdot s$)	Frequency spectrum of the perturbed wave field

$S_T(f)$	($m^2 \cdot s$)	Frequency spectrum of the target (or else the "theoretical") wave field
$S_U(f)$	($m^2 \cdot s$)	Frequency spectrum of the recorded undisturbed wave field
t	(s)	Time
T	(s)	Wave period
T_m	(N.m)	Mechanical torque
T_n	(s)	Natural period of the WEC unit
$T_{n,WAMIT}$	(s)	Theoretically derived value of the natural period of the WEC unit, using WAMIT
T_p	(s)	Peak wave period
U_{10}	(m/s)	Wind speed relative to the ocean surface (at 10.0 m height)
V_{subm}	(m^3)	Instantaneous submerged WEC buoy volume
w	(m)	Lateral spacing between WECs
w_d	(m)	Width of computational domain
w_s	(m)	Width of the square hole in the buoy that the shaft passes through
x_A	(m)	Amplitude of lateral displacement
x_C	(m)	x-co-ordinate of centre of circle
X_1	(m)	Amplitude of the first oscillation of the WEC buoy in a decay test
X_n	(m)	Amplitude of the n^{th} oscillation of the WEC buoy in a decay test
y_A	(m)	Amplitude of longitudinal displacement
$y_{A,MAX}$	(m)	Maximum amplitude of longitudinal displacement
y_C	(m)	y-co-ordinate of centre of circle
z	(m)	Time varying heave displacement of the WEC buoy
z_A	(m)	Amplitude of the WEC buoy heave displacement
z_{Af}	(m)	Amplitude of the WEC buoy heave displacement ("free" response)

z_e	(m)	The envelope of the WEC buoy oscillations in a "free" decay test
z_m	(m)	Measured heave displacement of the WEC buoy
$\dot{z}$	(m/s)	The time derivative of the time varying heave displacement of the WEC buoy or heave velocity of the WEC buoy
$\dot{z}_{av}$	(m/s)	Average value of the time derivative of the time varying heave displacement of the WEC buoy or heave velocity of the WEC buoy
$\dot{z}_A$	(m/s)	The amplitude of the time derivative of $z(t), \dot{z}(t)$
$\dot{z}_{A,MAX}$	(m/s)	The maximum amplitude of the time derivative of $z(t), \dot{z}(t)$
β_f	(rad)	Phase angle of the "free" response of the WEC buoy
γ	(-)	Peak enhancement factor
Δb	(rad)	Angle interval
Δt	(s)	Time step
Δx	(m)	Grid cell size in x-direction
Δy	(m)	Grid cell size in y-direction
$\Delta\varphi$	(rad)	Phase shift between the radiated and the diffracted wave
ζ_d	(-)	Damping factor
η	(m)	Surface elevation
η^*	(m)	Additional surface elevation
θ	(°)	Wave propagation angle
Λ	(-)	Logarithmic decrement of underdamped mechanical oscillator
μ	(-)	Coefficient of friction
μ_d	(-)	Dynamic coefficient of friction
μ_s	(-)	Static coefficient of friction
ρ_w	(kg/m^3)	Water density(for sea water, ρ_w = 1026 kg/m^3)

σ	(-)	Spectral width parameter
φ	(rad)	Phase shift
ϕ	(m^2/s)	Velocity potential
ω	(rad/s)	Angular wave frequency
ω_d	(rad/s)	Damped natural frequency of the WEC buoy
ω_n	(rad/s)	Angular natural frequency of the WEC buoy
$\bar{\omega}$	(rad/s)	Angular wave frequency corresponding to the carrier wave frequency for irregular waves, $\bar{f}$
∇	(-)	Horizontal gradient operator

List of Publications

o Articles in journals included in the ISI Web of Science

A1-Articles

1. Stratigaki, V., Troch, P., Stallard, T., Forehand, D., Kofoed, J.P., Folley, M., Benoit, M., Babarit, A., Kirkegaard, J. *Wave basin experiments with large wave energy converter arrays to study interactions between the converters and effects on other users in the sea and the coastal area*. Energies, *7*, 701-734. doi:10.3390/en7020701, 2014.

2. Stratigaki, V., Troch, P., Forehand, D., Stallard, T.. *A fundamental coupling methodology for the combined modelling of near and far field effects of oscillating wave energy converters*. Submitted for publication in Coastal Engineering, 2014.

3. Stratigaki, V., Troch, P., Stallard, T., Forehand, D., Folley, M., Vantorre, M., Kofoed, J.P., Babarit, A., Benoit, M.. *Development of heaving wave energy converters for large-scale WEC array experiments: design, development, theoretical-numerical–experimental study and evaluation of the WEC*. Submitted for publication in Renewable Energy, 2014.

4. Koftis, T., Prinos, P., Stratigaki, V.. *Wave damping over artificial Posidonia Oceanica meadow: A large-scale experimental study*, Coastal Engineering, Volume 73, Pages 71-83, http://dx.doi.org/10.1016/j.coastaleng.2012.10.007, 2013, ISSN 0378-3839.

5. Manca, E., Caceres, I., Alsina, J., Stratigaki, V., Townend, I. and Amos, C.L. *Wave energy and wave-induced flow reduction by full-scale model Posidonia oceanica seagrass*. Continental Shelf Research, doi:10.1016/j.csr.2012.10.008, 2012.

6. Stratigaki, V., Manca, E., Prinos, P., Losada, I.J., Lara, J.L., Sclavo, M., Amos, C.L., Cáceres, I., Sánchez-Arcilla, A.. *Large-scale experiments on wave propagation over Posidonia oceanica*, Journal of Hydraulic Research, 49:sup1, 31-43, doi:10.1080/00221686.2011.583388, 2011.

P1-Articles

7. Folley, M., Babarit, A., O' Boyle, L., Child, B., Forehand, D., Silverthorne, K., Spinneken, J., Stratigaki, V., Troch, P.. *A review of numerical modelling of wave energy converter arrays*. doi:10.1115/OMAE2012-83807, pp. 535-545; Volume 7: Ocean Renewable Energy; ASME 2012 31st International Conference on Ocean, Offshore & Arctic Engineering (OMAE2012), July 1–6, Rio de Janeiro, Brazil, 2012.

8. Stratigaki, V., Troch, P., Baelus, L., and Keppens, Y.. *Introducing wave regeneration by wind in a mild-slope wave propagation model, MILDwave, to investigate the wake effects in the lee of a farm of wave energy converters*. doi:10.1115/OMAE2011-49347; pp. 429-436, Volume 5: Ocean Renewable Energy, ASME 2011 30th International Conference on Ocean, Offshore & Arctic Engineering (OMAE2011), June 19–24, Rotterdam, The Netherlands, 2011.

o Editor in Books (B3-Books)

9. *Book of Proceedings of the 4th International Conference on the Application of Physical Modelling to Port and Coastal Protection - Coastlab12*. Department of Civil Engineering, Ghent University, Ghent, Belgium, September 17-20, 2012. Troch, P.; Stratigaki, V.; De Roo, S. (Ed.) (2013). Ghent University/IAHR, ISBN 978-9-09-027444-7. 879 pp.

10. *Book of Abstracts of the 4th International Conference on the Application of Physical Modelling to Port and Coastal Protection - Coastlab12*. Department of Civil Engineering, Ghent University, Ghent, Belgium, September 17-20, 2012. Troch, P.; Stratigaki, V.; De Roo, S. (Ed.) (2012). Ghent University/IAHR. ISBN 978-90-382-2008-6. 292 pp.

o Articles in national journals (A4-Articles)

11. Troch, P., Stratigaki, V.. *Van vijandige golven vrienden maken*, Tijdschrift Universiteit Gent-juli 2012, 26ste jaargang | nr. **6** | nr. 219 | P409859, p.14-15 (in Dutch), 2012.

12. Troch, P., Stratigaki, V.. *Optimalisatie van de lay-out van een park golfenergieconvertoren via numerieke modellering van zogeffecten*, Het Ingenieursblad. 80(5). p.53-57 (in Dutch), 2011.

o Articles in conference proceedings (C1-Articles)

13. Stratigaki, V., Troch, P., Stallard, T., Forehand, D., Folley, M., Kofoed, J.P., Babarit, A., Benoit, M.. *Modelling of wave attenuation induced by multi-purpose floating structures*. Accepted for publication in the Proceedings of the 34th International Conference on Coastal Engineering (ICCE 2014), Seoul, Korea, 15-20 June, 2014.

14. Stratigaki, V., P., Troch, D. Forehand, T. Stallard, J.P. Kofoed, M. Folley, M. Benoit, A. Babarit, D. Gallach Sánchez, L. De Bosscher, P. Rauwoens, B. Elsässer, P. Lamont-Kane, P. McCallum, C. McNatt, E. Angelelli, A. Percher, E. Carpentero Moreno, S. Bellew, E. Dombre, F. Charrayre, M. Vantorre, J. Kirkegaard, S. Carstensen. *Physical modelling of large wave energy converter arrays in a large-scale wave basin: the WECwakes project*, Submitted for publication in the Proceedings of the HYDRALAB IV Joint Transnational Access User Meeting, 2-4 July, Lisbon, Portugal, 2014.

15. Stratigaki, V., Troch, P., Stallard, T., Forehand, D., Kofoed, J.P., Folley, M., Benoit, M., Babarit, A., Vantorre, M., Kirkegaard, J.. *Large scale experiments with point absorber type wave energy converters: the WECwakes database*. Accepted for publication in the Proceedings of the 5th International Conference on the Application of Physical Modelling to Port and Coastal Protection - Coastlab14; Varna, Bulgaria, 29 September – 02 October, 2014.

16. Troch, P., Stratigaki, V., Stallard, T., Forehand, D., Folley, M., Kofoed, J.P., Benoit, M., Babarit, A., Vantorre, M., Kirkegaard, J. *An overview of the WECwakes project: physical modelling of an array of 25 wave energy converters*. In the Proceedings of the 3rd IAHR Europe Congress, Porto, Portugal 14-16 April 2014.

17. Troch, P., V. Stratigaki, T. Stallard, J.P. Kofoed, D. Forehand, M. Folley, M. Benoit, A. Babarit, D. Gallach Sánchez, L. De Bosscher, P. Rauwoens, B. Elsässer, P. Lamont-Kane, P. McCallum, C. McNatt, E. Angelelli, A. Percher, E. Carpentero Moreno, S. Bellew, E. Dombre, F. Charrayre, M. Vantorre, J. Kirkegaard, S. Carstensen. *Large scale physical modelling of an array of 25 wave energy converters in the WECwakes project*, In the Proceedings of the 10th European Wave

and Tidal Energy Conference Series (EWTEC), Aalborg, Denmark, 2-5 September 2013.

18. Stratigaki, V., Troch, P., Stallard, T., Forehand, D., Folley, M., Vantorre, M., Kofoed, J.P., Babarit, A., Benoit, M.. *Development of a point absorber Wave Energy Converter for investigation of array wake effects in large scale experiments*. In the Proceedings of the 4th International Coastlab12 Conference, Ghent, Belgium, 2013.

19. Stratigaki, V., Troch, P., Stallard, T., Kofoed, J.P., Benoit, M., Mattarollo, G., Babarit, A., Forehand, D., Folley, M.. *Large scale experiments on farms of heaving buoys for investigation of wake dimensions, near-field and far-field effects*. In the Proceedings of the International Conference on Coastal Engineering 2012, Santander, Spain, 2012.

20. Stratigaki, V., Troch, P., Margheritini, L., and Kofoed, J.P.. *Estimation of wave conditions along a new SSG breakwater for the hanstholm harbour using the numerical model MILDwave*. In the Proceedings of the 22nd International Ocean and Polar Engineering Conference (ISOPE-2012), Rhodes, Greece, 2012.

21. Margheritini, L., Stratigaki, V., Troch, P.. *Geometry optimization of an Overtopping Wave Energy Device implemented into the new breakwater of the Hanstholm Port Expansion.* In the Proceedings of the 22nd International Ocean and Polar Engineering Conference (ISOPE-2012), Rhodes, Greece, 2012.

22. Margheritini, L., Frigaard, P., Stratigaki, V.. *Characterization of wave climate at hanstholm location with focus on the ratio between average and extreme wave heights*. In the Proceedings of the European Wave and Tidal Energy Conference, Southampton, UK, 2011.

23. Manca E., Stratigaki V., Prinos P.. *Large scale experiments on spectral wave propagation over Posidonia oceanica seagrass.* In the Proceedings of the 6th International Symposium on Environmental Hydraulics, 23-25 June 2010– Athens, Greece, 2010.

24. Frigaard, P., Lykke Andersen, T., Ramirez, J.R., Sorensen, S.P., Martinelli, L., Lamberti, A., Troch, P., De Vos, L., Kisacik, D., Stratigaki, V., Q. Zou, K. Monk, J. Vandamme, M. Linhardt Damsgaard, H. Gravesen. *Loads on entrance platforms for offshore wind turbines*, In the Proceedings of the HYDRALAB III Joint Transnational Access User Meeting, 2-4 February, Hannover, Germany, 2010.

25. Prinos P., Stratigaki V., Manca E., Losada I., Lopez Lara J., Sclavo M., Caceres I., Sanchez-Archilla A.. *Wave Propagation Over Posidonia Oceanica: Large Scale Experiments.* In the Proceedings of the HYDRALAB III Joint Transnational Access User Meeting, 2-4 February, Hannover, Germany, 2010.

26. Stratigaki, V., Vanneste, D., Troch, P., Gysens, S., and Willems, M.. *Numerical modelling of wave penetration in Ostend Harbour*. In the Proceedings of the International Conference on Coastal Engineering, No. 32(2010), Shanghai, China. Paper #790: waves.42. Retrieved from http://journals.tdl.org/ICCE/, 2010.

27. Stratigaki, V., Manca, E., and Prinos, P., Losada I., Lara J., Sclavo M., Caceres I., Sanchez-Arcilla A.. *Large scale experiments on wave propagation over Posidonia oceanica*, In the Proceedings of the 33rd IAHR congress, Vancouver, Canada, 9-14 August, 2009.

28. Stratigaki, V., Manca, E., and Prinos, P.. *Effects of Posidonia Oceanica Meadow on Wave Propagation: Large-Scale Experiments.* In the Proceedings of the 4th SCACR International Short Conference on Applied Coastal Research, Barcelona, Spain, 15-17 June 2009.

29. Stratigaki, V., Prinos, P.. *Wave Propagation over vegetation.* In the Proceedings of the 4th Panhellenic Conference for Management and Improval of Coastal Zones, NTUA, Mytilini, Greece, 2008.

o Abstracts in conference books of abstracts and symposia (C3)

30. Stratigaki, V. and Troch, P., *Wave basin experiments with large wave energy converter arrays*, SET5Y – Sustainable Energy Technologies Symposium – Ghent University, Ghent, Belgium, 28th January 2014.

31. Stratigaki, V., Troch, P., Malherbe, B., Fordeyn, J.. *Flanders Bays: Estimation of the wave climate along the Flemish bays using the numerical model MILDwave*, Book of Abstracts of the 4th International Coastlab12 Conference, Ghent, Belgium, 2012.

32. Stratigaki, V., Troch, P., Vantorre, M., Folley, M.. *Development of a point absorber Wave Energy Converter for investigation of wake effects and wave energy*

absorption. Book of Abstracts of the 4th International Coastlab12 Conference, Ghent, Belgium, 2012.

33. Stratigaki, V., Troch, P., Stallard, T., Kofoed, J.P., Benoit, M., Mattarollo, G., Babarit, A., Forehand, D., Folley, M.. *Large scale experiments on farms of heaving buoys for investigation of wake dimensions, near-field and far-field effects.* Book of Abstracts of the International Conference on Coastal Engineering 2012, Santander, Spain, 2012.

34. Stratigaki, V., Vanneste, D., Troch, P., Gysens, S., and Willems, M.. *Numerical modelling of wave penetration in Ostend Harbour*. Book of Abstracts of the International Conference on Coastal Engineering, No. 32(2010), Shanghai, China, 2010.

35. Stratigaki, V., Manca, E., and Prinos, P.. *Effects of Posidonia Oceanica Meadow on Wave Propagation: Large-Scale Experiments*. Book of Abstracts of the 4th SCACR International Short Conference on Applied Coastal Research, Barcelona, Spain, 15-17 June 2009.

36. Stratigaki, V., Troch, P.. *Large scale experiments on farms of heaving wave energy converters.* Book of Abstracts of the VLIZ Young Scientists' Day; KHBO, Brugge, 24 February, 2012.

37. Stratigaki, V., Troch, P., and Degroote, J.. *Numerical modelling of wake effects of a farm of Wave Energy Converters: computational performance evaluation.* Book of Abstracts of the 5th International Conference on Advanced COmputational Methods in ENgineering (ACOMEN 2011), Liège, Belgium, 14-17 November 2011.

38. Baelus, L., Keppens, Y., Stratigaki, V., Troch, P.. *Numerieke modellering van de golfgroei door wind in de zogzone van een park van golfenergieconvertoren m.b.v. het golfvoortplantingsmodel MILDwave.* Book of Abstracts of the VLIZ Young Marine Scientists' Day.SSN 1377-0950, pp. 114-120, site Oud Sint-Jan, Brugge, (in Dutch), 25 February 2011.

39. Stratigaki, V., Troch, P., Baelus, L., Keppens, Y.. *Study of wave regeneration by wind in the lee of a farm of wave energy converters using the mild-slope wave propagation model, MILDwave.* Book of Abstracts of the VLIZ Young Marine Scientists' Day, SSN 1377-0950, pp. 84-85, site Oud Sint-Jan, Brugge, 25 February 2011.

40. Stratigaki, V., Manca, E., and Troch, P.. *Large scale experimental investigation on waves-vegetation interaction.* SSN 1377-0950, pp. 82-83, Book of Abstracts of the VLIZ Young Marine Scientists' Day, site Oud Sint-Jan, Brugge, 25 February 2011.

41. Manca E., Stratigaki V., Prinos P., Amos C.L.. *Full scale experiments on the effect of Posidonia oceanica seagrass on waves and wave-induced flows.* Book of Abstracts of the 6th Young Coastal Scientists and Engineers, London, UK, 29-30 March 2010.

42. Manca E., Stratigaki V., Prinos P., Caceres I., Alsina J., Amos C.. *The first application of full scale Posidonia seagrass mimics to investigate wave flow and energy dissipation.* Book of Abstracts of the HYDRALAB III Workshop for Young Researchers in Hannover, Hannover, Germany, 4 February 2010.

43. Stratigaki, V. and Troch, P.. *Numerical modelling of near-field and far-field wake effects of a farm of wave energy converters.* Book of Abstracts of the UGent-FirW Doctoraatssymposium 10e, pp.176-177, 2009.

44. Stratigaki, V. and Troch, P.. *Numerical modelling of near-field and far-field wake effects of a farm of wave energy converters.* Book of Abstracts of the 10th VLIZ Young Scientists' Day, Vol. 43, pp.131-132, Oostende, Belgium, 26-27 November 2009.

45. Stratigaki, V., Manca, E., and Prinos, P.. *Large Scale Experimental Investigation On Waves-Posidonia Oceanica Interaction*, Book of Abstracts of the 10th VLIZ Young Scientists' Day, Vol. 43, pp.129-130, Oostende, Belgium, 26-27 November 2009.

46. E. Manca, Caceres I., Alsina J., Stratigaki V., Prinos P., Losada I., Sclavo M.,Amos C. and Sanchez-Arcilla A.. *Effects of a Posidonia seagrass meadow on waves: Flume experiments at full scale.* Book of Abstracts Mediterranean Seagrass Workshop 09, Hvar, Croatia, 6-10 September 2009.

o Selected scientific reports (V)

47. Stratigaki, V. and Troch, P.. *Large scale experiments on wave energy converter farms to study the near-field effects between the converters and the far-field effects on other users in the coastal area: the WECwakes research project.* EU FP7 HYDRALAB IV programme (contract no. 261520), Research report, Ghent University, Ghent, 2013.

48. Stratigaki, V., and Troch, P.. *An introduction to the wave propagation model MILDwave.* Department of Civil Engineering, Ghent University, Ghent, 2012.

49. Stratigaki, V., and Troch, P.. *Zeebrugge Harbour: Numerical Simulation of Wave diffraction through the gap of the breakwaters using the mild slope wave propagation model, MILDwave*. Dept. of Civil Engineering, Ghent University, Ghent, 2011.

50. Stratigaki, V., and Troch, P.. *Design of Ostend harbour: numerical simulation of wave diffraction through the gap at Montgomery dock using the mild slope wave propagation model, MILDwave*. DBO107- 97, 43 pp. April 2010. Report for Flemish Government, Brussels, Belgium, 2010.

51. Margheritini, L., Kofoed, J.P., Stratigaki, V., and Troch, P.. *Estimation of Wave Conditions for SSG Breakwater at Hanstholm Location.* Aalborg University, Department of Civil Engineering. 78 pp. (DCE Contract Reports; 90), Aalborg, 2010.

52. Kofoed, J.P., L., Margheritini, V. Stratigaki, and P. Troch. *Estimation of Wave Conditions for SSG Breakwater at Svåheia SSG pilot site.* Aalborg University, Department of Civil Engineering. 154 pp. (DCE Contract Reports; 52), Aalborg, 2008.

53. Manca, E., Stratigaki, V., Caceres, I., Prinos, P. *Wave Propagation over Posidonia Oceanica: the WAPOC research project.* EU FP6 HYDRALAB III programme, 022441 (RII3), Research report, Barcelona, 2009.

1

Introduction

Abstract: *Renewable energy is constantly being developed to reduce the dependency on fossil fuels. Energy from ocean waves can be utilized by installing Wave Energy Converters (abbreviated as WECs) in the sea, which are devices that convert the kinetic and/or potential energy of waves into electricity. Many concepts of WECs have already been developed, mainly distinguished based on the conversion principle, in (i) oscillating water columns and wave-activated bodies, which oscillate under incident waves, and (ii) overtopping devices, which capture the overtopped waves in a basin above sea level that creates a hydraulic head. In order to extract a considerable amount of energy at a specific site location, the installation of large numbers of WECs will be required, arranged using specific geometric configuration. In this chapter, an overview of typically performed research on wave-activated bodies and WEC arrays is provided, since this PhD dissertation deals with arrays of this WEC type. In contrast to the large body of numerical simulations of WEC arrays and the physical modelling of individual WECs or pairs of WECs, very few experimental studies are publically available which deal with only small WEC arrays. There is, therefore, a lack of physical modelling studies on large WEC arrays and a clear need to perform such experiments, which has been dealt with within the main objective of this PhD research.*

1.1. Renewable energy

1.1.1. Role of renewable energy resources

Over the last decades, the human development has been based in an increasing consumption of energy resources to sustain all kind of human activities, from transport to industrial processes. Fossil fuels have been the main energy resources, a finite non-renewable resource that has been overexploited throughout the last decades and it is now giving signs of depletion.

As a result, renewable energy resources have gained interest in the past decades. The need to reduce greenhouse gas emissions has led to measures that are being taken at a European level, as well as by Member States at national level, so that the EU succeeds in meeting its targets under the Kyoto Protocol and the "20/20/20" objectives within the framework of low carbon economy. These targets demand a reduction in greenhouse gas emissions of 20 % compared to 1990, an amount of 20 % of the total energy consumption to come from renewable energy resources and an increase of 20 % in energy efficiency, as presented in [1].

1.1.2. Wave energy

Ocean wave energy is one of the intensively developing renewable energy resources with great potential. The global power potential represented by wave energy in the open ocean is estimated to be 10 TW [2], a quantity comparable with the world's present power consumption [3].

Energy from ocean waves can be utilized by installing Wave Energy Converters (abbreviated as *WECs*) in the sea, which are devices that convert the kinetic and/or potential energy of waves into electricity. Many concepts of WECs have already been developed, mainly distinguished based on the conversion principle, in (i) oscillating water columns and wave-activated bodies, which oscillate under incident waves, and (ii) overtopping devices, which capture the overtopped waves in a basin above sea level that creates a hydraulic head. Type (i) includes absorption and radiation, while type (ii) includes only absorption. A WEC extracts power from the waves through a mechanical part, the so called *power-take-off system* (abbreviated as *PTO-system*).

1.1.3. WEC array effects

In order to extract a considerable amount of energy at a specific site location, and to make the commercial exploitation of wave energy possible, installation of large numbers of WECs (e.g. tens of WECs simultaneously) will be required [4]. The WECs will have to be arranged in an array (or else referred to as a *farm* or *park*) using a particular geometric layout. However, power production of the array may be smaller or larger than the sum of the power produced by the equivalent number of individual WECs. This is caused by hydrodynamic interactions between the WECs within an array in the near-field (the so-called *intra-array interactions* or *park effect*). Therefore, the operational behaviour of the individual WECs of an array may have a positive (constructive) or negative (destructive) effect on the overall power absorption of the WEC array. Moreover, as a result of the large number of WECs within an array, usually wave height attenuation is observed numerically and in scale model experiments with small WEC arrays. This wave height dissipation is observed in the far-field, mostly between the WEC array installation site and a downwave location, e.g. the shoreline (the so-called *extra-array effects*). These wave field modifications can influence neighbouring activities in the sea, other marine (energy) projects, coastal eco-systems and even the coastline and the coastal defence conditions and parameters. Both the intra-array interactions and the extra-array effects will be referred to as *WEC array effects* in this PhD dissertation.

Therefore, an accurate understanding is required of both the intra-array interactions between WECs in a wave farm and the extra-array effects on the environment. With this understanding, the optimal WEC array geometric layout can be determined, changes to wave conditions can be quantified and ultimately the cost of energy will be reduced significantly, as shown in [5].

The design of a WEC array and the study of WEC array effects, require both numerical modelling and experimental testing of a physical scale model. Numerical modelling is very efficient, especially in the first design stages, but model tests in a wave basin or wave flume are necessary since the numerical methods suffer from important limitations (e.g. inability of numerical models to account for losses due to real viscous fluid effects [6] in a computationally efficient way). Numerical studies on both small and large WEC arrays have already been performed, and have provided insight into the magnitude and extent of WEC array effects for idealized conditions and configurations.

The importance of WEC array effects and of the geometric lay-out of a WEC array is illustrated here using the example of Figure 1.1. Using the wave propagation model MILDwave [7], extra-array effects have been modelled downwave of the WECs. Results are presented in terms of the disturbance coefficient K_d ($=H_{m0}/H_{m0,GB}$, with H_{m0} the local significant wave height based on the spectral density and $H_{m0,GB}$ the wave height at the wave generation boundary). Waves are

propagating from the bottom to the top of Figure 1.1, while the "white squares" simulate generic wave energy converters of the overtopping type, with a specific power absorption. The extra-array effects in the lee of the WEC array are clearly visible, indicated by areas of reduced K_d values, with contour lines of K_d values ranging between 0.65 and 1.05. When the geometric layout or the number of WECs of the WEC array changes (Figure 1.1(a–d)), the wave field downwave of the WEC array changes as well.

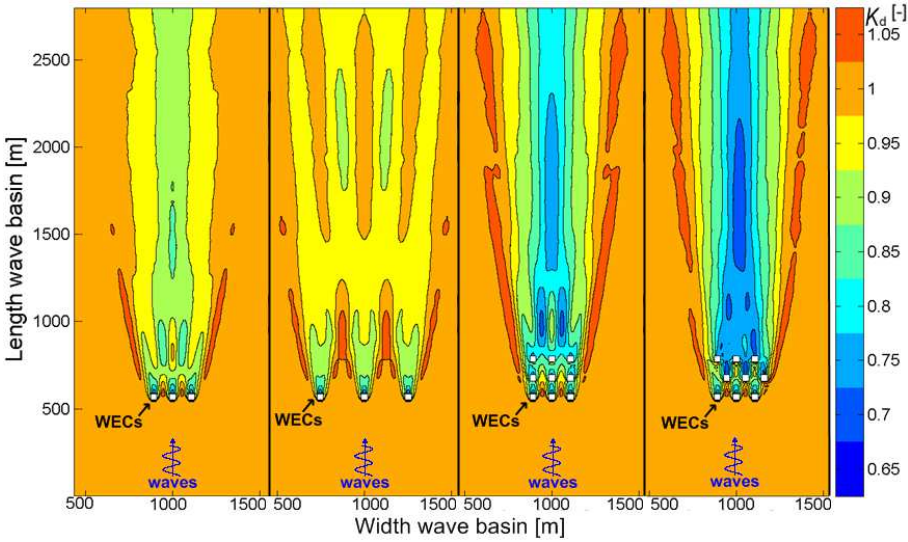

Figure 1.1. Extra-array effects downwave of WEC arrays (generic WECs of the overtopping type with a specific power absorption). Wave height reduction downwave of the WECs (for long-crested waves) is visualized by the reduction of the disturbance coefficients K_d (=H_{m0} / $H_{m0,GB}$). WEC arrays of: (a) 3 WECs; (b) three WECs with larger lateral spacing, w, between the WECs; (c) nine WECs in rectilinear lay-out; (d) nine WECs in staggered lay-out. Results are from [8].

Figures 1.1(a-b), where a row of three WECs is simulated, reveal the importance of the spacing between the WECs of an array. The resulting extra-array effects, e.g. when the lateral spacing, w, between the WECs is smaller (Figure 1.1(a)) are much different compared to the extra-array effects (here, wave field modification) downwave of an array with the same number of WECs but much larger w between the WECs (Figure 1.1(b)). Figures 1.1(c-d), where an array of nine WECs is simulated, reveal the importance of the geometric lay-out of the WECs within an array. The resulting extra-array effects, e.g. downwave of a 9-WEC rectilinear array (Figure 1.1(c)) differ compared to the extra-array effects downwave of a 9-WEC staggered array (Figure 1.1(d)).

1.2. Literature overview

In this section, a literature overview is presented, based on examples of research dealing with WECs and WEC (arrays). A presentation of indicative numerical studies concerning WEC arrays is provided, followed by an overview of physical modelling of WECs. The emphasis lies on experimental and numerical research on WEC types consisting of wave-activated bodies, since this has been the focus of this PhD work.

Conventionally, here a *row* of WECs refers to a number of devices oriented parallel to the wave crests, while a *column* of WECs refers to a number of devices parallel to the wave propagation direction.

1.2.1. Numerical modelling of WEC arrays

The hydrodynamic behavior of WECs is modeled by a wide range of numerical methods. As recently reviewed in [9] and [10], each method has its drawbacks and assets. For instance, certain models are more suitable for studying intra-array interactions in the near-field, whilst others are preferable for investigating extra-array effects in the far-field of the WEC array.

The most commonly used methods for prescribing intra-array interactions are models based on Boundary Element Methods (BEMs) for solving the potential flow formulation (e.g. Aquaplus [11], ANSYS Aqwa [12], WAMIT [13]). A shortcoming of this theory is its poor description of viscous effects, incorporated in a parameterized way. In [14] a comparison has been carried out between the application of the WAMIT (BEM) solver and a Navier-Stokes solver, to identify the essential physics which are not captured by BEM solvers: the vortex shedding (viscous effect) behind a heaving buoy, wave overtopping, and the re-entering impact of an out-of-water body. Because of its better description of the physics, the use of a Navier-Stokes solver for modelling WEC behavior is growing nowadays, e.g. [15], [16]. However, the above methods suffer dramatically from a high computational cost for large WEC arrays, while the simulated domains are limited to constant water depth.

For simulating extra-array effects, both time and frequency domain wave propagation models are generally employed. Spectral wave propagation models such as SWAN [17] and Boussinesq models such as MIKE21 [18] have both been employed to study the change of wave conditions inshore of WEC arrays. SWAN has been used to study the change of the wave climate caused by the installation of a WEC array 20 km off the north coast of Cornwall, UK [19]. An array of 5 bottom mounted, fixed WECs has been modelled by Venugopal and Smith [20] in the nonlinear Boussinesq wave model, MIKE21. Representation of large WEC arrays

within spectral models may be accomplished by using transmission and reflection coefficients [21] or subgrid models [22]. Moreover, wave height attenuation in the lee of an individual WEC and WEC arrays of various geometric layouts have been studied in ([5], [8], [23]-[25]) by using the mild-slope wave propagation model MILDwave developed by Troch ([7], [26]). A sponge layer technique is applied, by which the redistribution of wave power within and behind each WEC array is studied in detail. These models are able to simulate the effect of large WEC farms in large domains at a reasonable computational cost. As a result, the changes in wave field and the associated environmental impacts can be studied at regional scale. However, the WECs are approximated up to now by using parameterized energy sinks and sources with coefficients requiring empirical calibration. This method only partially addresses the underlying physics, which can lead to erroneous model conclusions.

In this section, a few examples of numerical simulations with WEC arrays from the literature are presented. In [27] input of hydrodynamic coefficients calculated using the BEM based code AQUADYN [28] has been used to model small WEC arrays. The impact of the spacing between two devices within a wave farm on the power absorption in deep water for both regular and irregular waves has been studied. The study presented in [27] resulted in noticeable wave interaction effects at large distances. Two different WEC arrays have been considered, composed of WECs of the same "typical dimension", k_t= 10.0 m: one composed of two heaving, semi-submerged cylinders with diameter and draft of 10.0 m and another composed of two surging, semi-submerged rectangular bodies with width and draft equal to 10.0 m, both with an idealised PTO-system. The traditional interaction factor, which is the ratio of the average power output of arrays to the total power output of the same number of individual (isolated) devices, has not been used in this study. Instead, a modified interaction factor has been introduced to study WEC array effects, defined as the ratio of the difference between the total power absorbed by the i WEC in an array, $P_{i,tot}$, minus the power absorbed by an isolated WEC, $P_{0,tot}$, divided by the maximum absorbed power by an isolated WEC, $\max_T P_{0,tot}(T)$. Based on the calculation of this modified interaction, it has been concluded in [27] that the influence of wave interactions on absorbed power decreased in regular waves with the square root of the distance resulting in an impact of 10.0 % to 15.0 % at a distance of 2000 m (i.e. 200 x k_t). The impact in irregular waves was smaller, as constructive and destructive interactions compensated each other (less than 10.0 % at 400 m, i.e. 40 x k_t). As a result, it has been suggested in [27] that wave interaction effects may be neglected for distance greater than 500 m (i.e. 50 x k_t) and should be taken into account for distance shorter than 100 m (i.e. 10 x k_t) for WECs with typical dimension, k_t = 10.0 m.

Similarly, WEC types have been studied in [29] by using the BEM model Aquaplus [11]. WEC arrays of 9, 16 and 25 devices, identical in geometry and PTO

characteristics, placed in a regular square and triangular grid, have been considered in a parametric study to assess the influence of the spacing between the WECs on the overall yearly energy production of the array (10 to 50 times the typical dimension of the WEC, k_t). Grouping the devices into arrays generally had a constructive effect; however, a square grid seemed not appropriate for surging bars as strong destructive interference occurred. It was recommended to tune the PTO of the WEC to the local wave climate, thereby maximizing the yearly energy production. By using large-banded WECs, interactions over a significant part of the wave frequency range were ensured. The negative and positive interactions, compensating each other, allowed flexibility in the positioning of the WECs.

In [30], the BEM package WAMIT [13] has been used to predict the response of a wave follower type WEC, which was not designed to resonate. The WEC geometry comprised a cylinder with a diameter of 10.0 m and a height of 2.0 m, with six degrees of freedom. Only power extraction from the heave motion has been considered. The predicted response has been used to estimate the power output, which has been maximized by adjusting the damping to one year of hourly wave spectra, measured by a buoy located 30 km off the coast of central Oregon. The passive tuning was applied for different time scales from hourly to annually. The difference in power output was only 3.0 %, indicating that the considered WEC was not significantly sensitive to the applied damping. A square array of four WECs with 100 m spacing and annually tuning has also been studied, showing that the annual power output was 5 % lower than for four isolated WECs. This study concluded that array interactions may be neglected at first order if the WECs are non-resonating and placed at a distance of 10 times the diameter from each other.

In [31], BEM hydrodynamic calculations have been carried out with the software package DIFFRACT [32] on three-member arrays, namely an array composed of heaving hemispheres, one out of surging and swaying hemispheres and another one out of a heaving hemisphere, a surging ellipsoid and a swaying elliptical cylinder. All rigid bodies underwent optimum displacements in regular waves, while the aim was to examine the influence of the wave direction. The results for the arrays with axisymmetric WECs confirmed the identity that the average of the interaction factor over all incident wave directions from 0 to 2π is equal to unity. A more fundamental result underlies this identity, namely that the maximum power an individual non-axisymmetric WEC can absorb, averaged over all directions, is the same as for an axisymmetric WEC. This has been confirmed also for a heterogeneous array. It has been indicated that the high power absorption for a specific incident wave angle must be associated with less absorption at another wave heading.

In [33], a WEC spectral model has been developed, which can be included in spectral wave models with minimal modification, an extension to frequency-domain models that can accurately simulate non-linear forces and reasonably estimate the

WEC performance. The model assumes that the dynamics can be separated into a set of statistically orthogonal frequency components, calculating the response of a WEC as the sum of the individual frequency responses. The model has been applied to a flap-type WEC with a quadratic damping term to model the effect of vortex shedding and a flap-type WEC with large amplitudes of motion to represent wave force decoupling. Both showed similar levels of accuracy compared to time-domain simulations, but being less demanding, computationally.

In [34], the total power output of a WEC array has been optimized by selecting an appropriate geometric configuration using two different methods: the Parabolic Intersection (abbreviated as *PI*) method and a Generic Algorithm (abbreviated as *GA*). An arrangement of five identical truncated circular cylinders, heaving in water of constant depth has been considered. The optimization process has been performed for regular waves with one incident wave frequency and direction, and for two different PTO arrangements (real and reactively tuned WECs). For the array of reactively tuned WECs, minimum power output has been pursued to demonstrate potential array-related losses. Regular incident waves of different frequency and direction have been applied on the resulting WEC arrays with fixed layout and PTO characteristics, resulting in suboptimal conditions. Results have been interpreted in terms of the features of the WEC array geometric configurations. In [35], irregular sea states have been applied to the aforementioned WEC array configurations, optimised for regular wave climates. The changes in power output of the WEC arrays compared to individual WECs have been found to be less significant in irregular waves than in regular waves. GA has been then employed to obtain optimal WEC array layouts for the irregular sea states.

In [36], tentative recommendations have been provided for the design of the WEC array layout for oscillating wave energy converter arrays. For small arrays of conventional WECs (less than 10 WECs of typical dimensions, k_t = 10.0 to 20.0 m) with usual layouts (regular or shifted grids with separating distance of order 100 to 200 m), it is suggested in [36] that intra-array interactions should be negligible. For larger arrays (more than 10 WECs), negative (destructive) intra-array interactions are increasingly important with increasing number of WEC rows (the lines of WECs perpendicular to the incident wave direction), as presented in [36]. Therefore, in [36] it is suggested to keep the number of WEC rows in an array as small as possible, and the spacing between the WECs as large as possible.

1.2.2. Physical modelling of individual and pairs of WECs

Individual or pairs of WECs have been widely experimentally studied, based both on complex and simple geometries, operational principles and PTO-systems.

In [37] a pair of hemispherical ended WECs (floats) has been tested, with a diameter of 15.0 cm and a draft of 17.5 cm. By using a rigid connection between the two devices, an identical response amplitude and phase could be realised. The tests have been performed in a 1.0 m wide flume with a water depth of 1.5 m. The devices have been placed at 0.25 m from the flume sides realising an array of two devices with a spacing of 6.66 times the radius along the wave crest. The "free" response amplitude and absorption have been measured for a wave period of 1.5 s. By adapting the mass and damping of the device, they were tuned to attain resonant response with the incident wave. A good agreement with the point absorber theory was found since the interaction factor increases linearly towards π as the device spacing approaches the wavelength.

In [38], tests at the University of Edinburgh have been performed at a similar time. The experiments consisted of the measurement of the interaction factor of a linear array of two to ten WECs with relatively large spacing (order of 10 x "the typical WEC dimension", thus the WEC radius). A reasonable agreement has been found with point absorber predictions, though friction on the supporting strut presented difficulties during testing.

More recent research has been performed in [39], for the evaluation of the possibility of wave energy conversion in the Belgian coastal area of the North Sea. Numerical modelling based on linear theory using Aquaplus [11], has been performed to optimise the geometry and dimensions of a heaving point absorber to obtain maximum power absorption. The results of these numerical simulations have been afterwards evaluated by physical model tests, performed in the wave flume of Flanders Hydraulics Research (Antwerp, Belgium), with 70.0 m length, 4.0 m width and 1.4 m depth. The buoy, illustrated in Figure 1.2, was connected to a steel rod that could translate vertically, guided by two axial bearings attached to a frame. In the system of Figure 1.2, a supplementary mass (see part 2 in Figure 1.2) could be added. The damping of the rotation was realised by a mechanical system, consisting of two curved elements covered by felt that could be pressed against a wheel, attached to one of the guiding pulleys (see part 3 in Figure 1.2). Based on measurements at the Belgian coast corresponding with the dominant wind direction, nine classes of significant wave height and average wave period have been considered, reaching 4.5 m and varying from 2.5 s to 6.5 s, respectively. The effect in both regular and irregular waves has been studied.

The numerical simulations resulted in a conical buoy shape, found to ensure the optimum hydrodynamic performance. In regular waves, the system was first tuned towards the incident wave field by adding an appropriate supplementary mass. However, the high velocity of the heave motion of the buoy caused undesired energy losses due to viscous effects and vortex shedding, which were not taken into account in the numerical model. The differences between the measured and calculated values decreased with increasing damping. Moreover, the incident wave period has been

varied with the supplementary mass held fixed. The corresponding power absorption showed a decrease when there is discrepancy between the natural frequency, ω_n, of the device and the angular frequency, ω, of the incident wave. In irregular waves, the mechanical damping system did not operate as desired since the damping force had a constant absolute value regardless the buoy's velocity. In small waves this caused an overdamping, while in high waves the damping was insufficient. Mistuning the device by varying the supplementary mass showed a decrease in absorbed power.

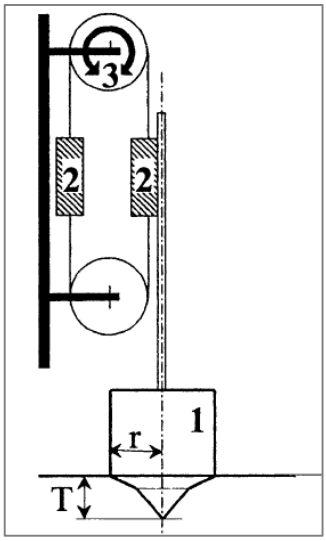

Figure 1.2. Definition sketch of the WEC tested in [39].

Validation of numerical models by using experimental results has also been performed in [40]. Experiments have been executed with the 1:12 scale model SEAREV_G1 in the wave tank of Ecole Centrale de Nantes, with dimensions 30.0 m by 50.0 m and a depth of 5.0 m. The device had the first shape of the SEAREV WEC, which consists of a closed floating buoy with a large pendulum wheel inside (see Figure 1.3), that moves relative oscillatory around a horizontal axis when waves set the device into motion. The buoy has more than one degrees of freedom. The mooring has been realised by three submerged buoys and six chain mooring lines. Regular and irregular waves with wave amplitude of 0.042 m and wave frequencies varying from 0.4 Hz to 0.65 Hz have been applied. Two numerical models have been validated: a fully linear numerical model, which assumed linearity of the behaviour of the pendulum and of the fluid, and a non-linear mechanics numerical model, in which a non-linear motion of the pendulum was considered.

In regular waves, the correspondence of the measured buoy motion and absorbed power with the fully linear theory was not satisfactory. A good agreement between the experimental results and the non-linear mechanics numerical model has been found over the whole frequency range, except between 0.52 Hz and 0.58 Hz. This discrepancy at the central range has been attributed to slamming of the buoy around the pitch natural frequency of the device, which caused energy dissipation. The numerically derived amplitude was therefore higher than the experimentally measured amplitude. Adapting the numerical model by adding empirical damping laws to model slamming ensured a good agreement with the experimental results over the whole frequency range. In irregular waves, the mean energy production was measured and compared with a linear numerical model. When the wave amplitude remained small, a good agreement was observed between the numerical and the experimental model. When waves of larger amplitude were generated, non-linear effects such as slamming and roll instabilities limited the buoy motion in the vertical plane and the energy absorption decreased. However, the numerical model did not predict these effects. Real time latching of the device by a magnetic brake has also been applied and improved the energy production in regular waves over practically the whole frequency range by a factor from 1.0 to 10.0. In irregular waves, the improvement reached values of 50.0 % to 86.0 %.

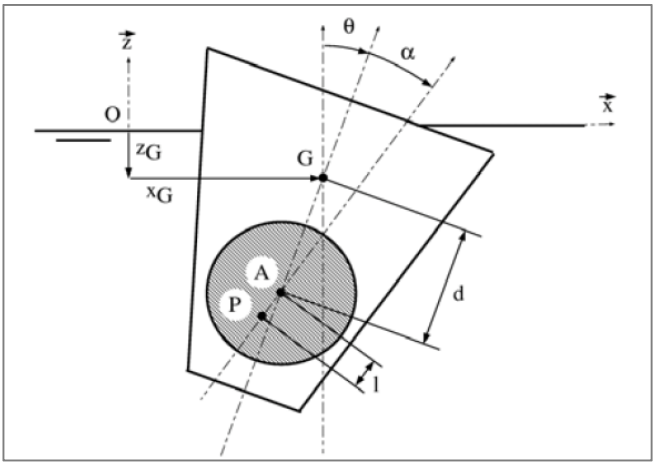

Figure 1.3. Definition sketch of the SEAREV WEC tested in [40].

In [41], the experimental research from [37] has been continued by performing tests with an individual WEC buoy taking into account slamming, stroke and force constraints. The wave flume of Flanders Hydraulic Research (Antwerp, Belgium), has been used with an operating water depth of 1.0 m. The model, of a scale 1:15.9,

consisted of a floating buoy connected to a rod, oscillating with respect to a fixed structure (illustrated in Figure 1.4). This rod was attached to a rotating belt, supported by three bearings and a pulley, connected to a rotating shaft. Two buoy shapes have been investigated: a cone and hemisphere shape, both with a cylindrical upper part and a diameter of 31.5 cm, while the draft varied from 18.90 cm over 22.05 cm to 28.35 cm by changing the mass on top of the buoy. The damping force has been realised by a mechanical brake made out of a circular element, covered by felt at the inside which could be pressed on a wheel mounted on the shaft. Regular waves with a wave height varying from 10.4 cm to 14.4 cm and a wave period varying from 1.36 s to 1.75 s have been tested. Also irregular waves have been tested: with wave height 6.2 cm and wave period 1.59 s, and with wave height 9.6 cm and wave period 1.83 s. The tested sea states are representative for the mild wave climate on the Belgian Continental Shelf.

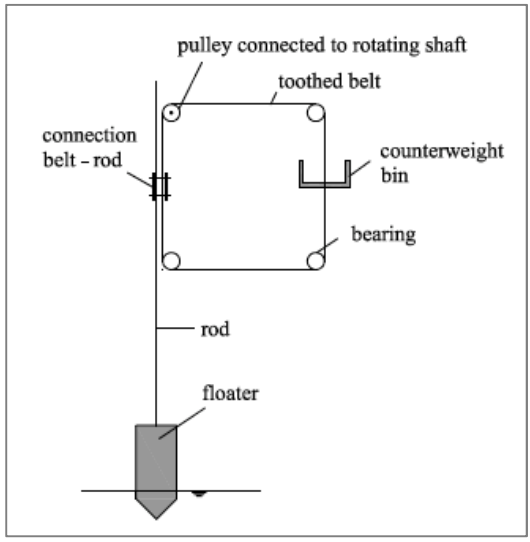

Figure 1.4. Definition sketch of the WEC tested in [41].

Comparison to measurements from the physical tests has shown good agreement with the linear point absorber theory. The hydrodynamic parameters have been derived from the BEM package WAMIT [13]. The non-negligible internal friction of the setup has been taken into account for the comparison. When the buoy operated in regular waves, relatively far from resonance, the correspondence between the calculated and measured results was very good. When the difference between the natural frequency and the frequency of the incident wave decreased, the discrepancy increased and became very large for small external damping values.

Similarly to [39], this discrepancy has been attributed to the assumptions of the linear theory: the amplitude of the vertical motion and the velocity of the tested point absorber WEC were very large near resonance, especially when the damping was low. Therefore, it could not be precisely described by a linear theory due to non-linear effects such as viscosity and a non-linear hydrostatic restoring force, not taken into account in the numerical model. The theoretical WEC buoy efficiency has been overestimated and reached values larger than 100 %, as the experiments showed maximum efficiency values of 60 %. Tests with the irregular waves have been performed with the cone-cylinder shape for suboptimal tuning. The agreement between experimental and numerical results was found to be very good, and the difference in power absorption did not exceed 20 %. In [41] it has been concluded that the linear theory can predict the point absorber behaviour in irregular waves for all frequencies when the waves and buoy motion remain small.

1.2.3. Physical modelling of small WEC arrays

Only a few studies have been performed on arrays of heaving wave energy converters. Examples illustrating arrays of up to 12 WECs are presented here.

In [42], the effect of the WEC array size and geometric configuration on the power output and the response of individual WECs (floats) have been investigated, compared to an isolated WEC. Experimental tests have been performed in the wave flume of Manchester University (5.0 m wide, 18.5 m long and 45.0 cm deep). The WECs had a hemisphere-cylinder shape with a diameter of 15 cm supported by a cable running over a pulley to a counterweight (shown in Figure 1.5). The pulley shaft was connected to a generator shaft through a freewheel clutch. A mechanical torque T_m (indicated in Figure 1.5) resisted the rotation of the flywheel, thereby applying damping on the system and extracting energy. Tethers should ensure only heave motion, however, in order to avoid large horizontal loads on the structure, surge motion has also been allowed for specific extreme wave conditions. When comparing these results to numerical simulations, attention has to be paid to the non-linear influence of the tethers and the clutch. Three configurations have been tested: an array of three WECs aligned with the direction of wave propagation, nine WECs in rectilinear arrangement and an array of three by four WECs, all with equal spacing of four times the device radius. Regular waves with a nominal amplitude of 13 mm and varying frequency have been applied. Within the array of three WECs of identical mechanical torque applied, and therefore of identical damping, the magnitude of the power generation and the wavelength, responsible for the peak absorption, changed with position in the array. The middle WEC had the largest power output peak due to circular waves radiated by the neighbouring WECs. The WEC at the rear had similar power output peak as an individual WEC, while the

mean power output over the wave frequency range was slightly increased. The front WEC had a lower mean output than the other two WECs, but quite constant over a range of wave frequencies around the peak. Within the rectilinear WEC array, the power output was symmetric about the centreline of the array, but the response of each row of three WECs differed from the aforementioned isolated column. The WEC in the centre of the front row produced the largest power and its mean power output was larger than that of the central WEC in a 3x1 array, due to the presence of the adjacent WECs. WEC response attenuation has been observed through the array: the middle and rear WECs along the centreline showed a great reduced response compared to the 3x1 array, although this was not observed for the WECs at the edges of the array configuration.

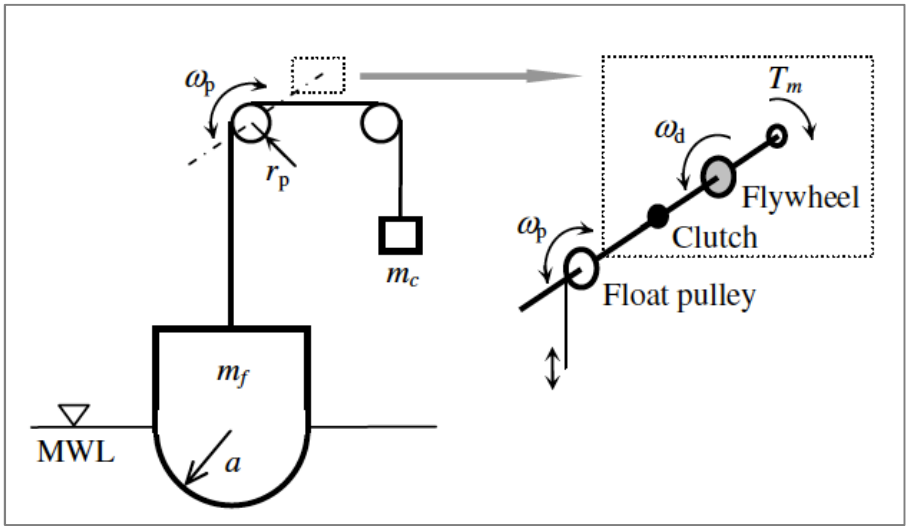

Figure 1.5. Definition sketch of the WEC tested in [42].

Compared to an individual WEC, constructive interactions occurred since the interaction factors were greater than unity for all three WECs in the front row. These factors decrease with distance through the array, resulting in destructive intra-array interactions for the WECs at the rear row. The mean interaction factor for the entire array varied with applied wave period between -25 % and +10 % of the power output from an individual WEC when the mechanical torque, T_m, had a value of 8.0 Nm. When T_m increased, the interaction factors also increased, in particular for low frequency waves. The "free" response measurements in the rectilinear array showed similar results as for the power capture: the maximum response occurred in the front row, where amplitudes of more than double the wave amplitude have been measured, and the results were symmetric about the central line of the WECs. In

longer waves, all devices oscillated with similar response amplitude, which decreased with increasing wavelength. Compared to the response of an individual WEC, the response amplitude increased in longer waves and decreased in shorter waves.

In [43], experimental measurements have been conducted of the power absorbed by a two-dimensional rectilinear array of twelve heaving devices (4x3) in both regular and irregular waves, in a 5.0 m wide wave flume. The devices were cable supported, axisymmetric WECs (floats), held in equilibrium by a counterweight over a pulley. The WECs have been placed with a centre-to-centre spacing equal to four times the WEC radius (shown in Figure 1.6). Regular and irregular waves with amplitudes varying from 0.0075 m to 0.032 m with frequencies ranging from 0.5 Hz to 1.63 Hz were generated.

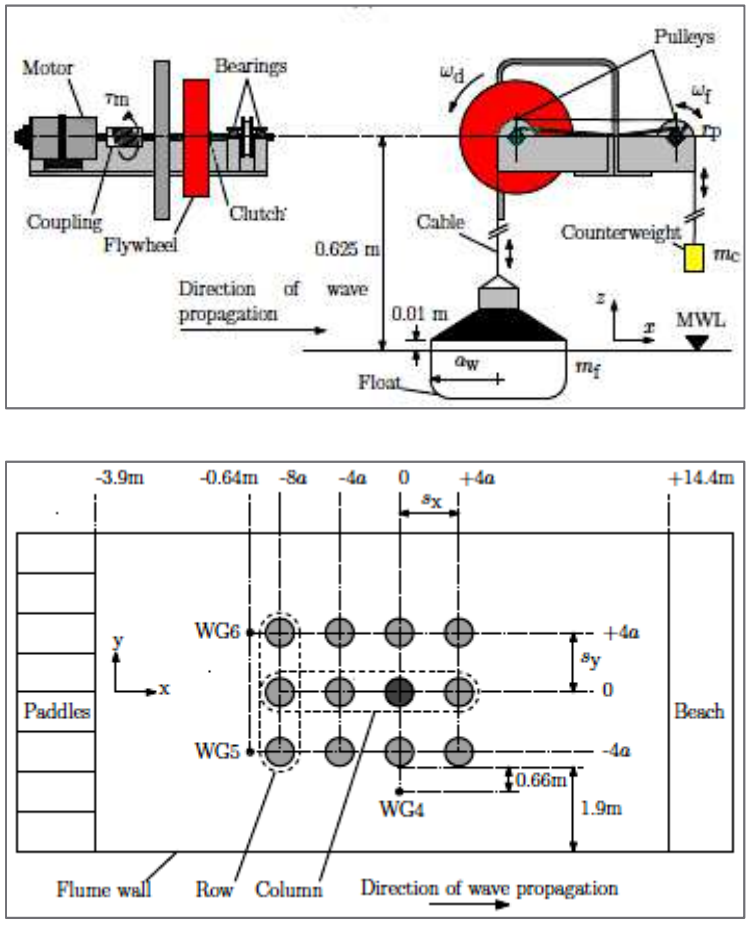

Figure 1.6. Experimental setup used in [43]. Top: Definition sketch of the WEC – Bottom: wave flume experimental arrangement. The WEC diameter is 0.15 m.

The *capture width* has been estimated in [43] and is defined to be the width of the wave front containing the same available power as the useful power captured by the WEC in the same wave climate. For WEC rows under regular waves, average values of the *capture width* indicated that this width was similar for all WEC rows at low wave frequencies. However, for higher wave frequencies, this similarity between the WEC row behaviour disappeared and the non-similarity increased with wave frequency. Similar agreement has also been found for all WEC columns at low wave frequencies, but again at higher wave frequencies, differences have been observed. The central WEC column had lower average capture widths, possibly due to destructive intra-array interactions caused by radiated waves from the WECs located in the outer columns. The power absorbed by the WEC array has also been compared to that of an individual WEC, located at the centreline of the wave flume. In general, the row and column averaged interaction factors were close to unity across the wave frequency range. The natural frequency of each WEC (1.2 Hz) was high, compared to the tested range of wave frequencies. The same tests have been, therefore, performed using twelve WECs with a lower natural frequency (0.9 Hz), resulting in larger WEC array averaged interaction factors. For low wave frequencies, the ranking of absorbed power per WEC row was dependent on the incident wave frequency. For higher wave frequencies, power output attenuation has been observed. Less power was absorbed by WEC rows further away from the paddles and this attenuation across the WEC array became more pronounced with increasing wave frequency. The central column of WECs produced on average, less power than the outer columns. The calculated interaction factors thus, appeared to vary with both incident wave conditions and device location within the array. In irregular waves, all central WECs produced less power than the outer ones on the same WEC row, while the average power from the outer columns showed good agreement for all applied wave frequencies. The interaction factors associated with the lower significant wave height were higher, and consequently the destructive intra-array interactions increased with wave height. The ratio of the power absorbed in irregular waves to the power absorbed in regular waves declined with increasing peak wave frequency. This ratio was found to be almost consistently higher for the case of an individual WEC, than for the case of the WEC array.

In [44], measurements of the free response amplitude have been recorded, from rectilinear 5x1 WEC arrays composed of tuned hemispherical WECs (floats) with a spacing equal to four times the WEC radius. The tests have been performed in a 5.0 m wide wave flume, with shallow draft heaving WECs of diameter 0.15 m, supported by a pulley and counterweight (see Figure 1.7). Small scale monochromatic waves with a wave amplitude of 0.013 m and wave frequencies varying from 0.75 to 1.75 Hz have been applied. The incident wave angle was 0° (head sea) and 90° (beam sea).

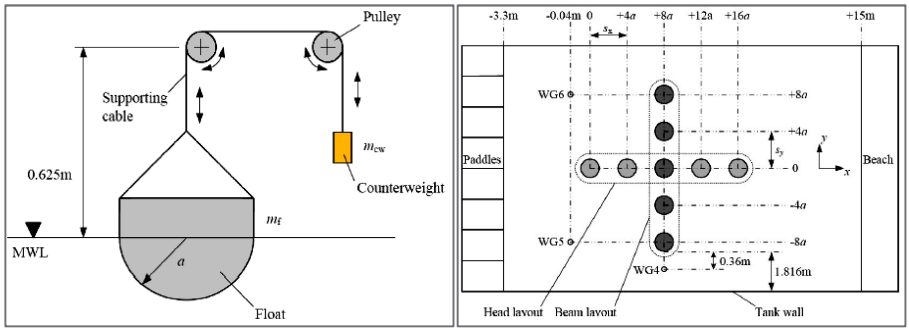

Figure 1.7. Experimental setup used in [44]. left: Definition sketch of the WEC – right: wave flume experimental arrangement.

Significant intra-array interactions have been observed for the tested WECs, since the mean response amplitude was greater than for an individual WEC, for incident wave period larger than the natural period of the WEC. Within a head sea, the WEC response was asymmetric. Response attenuation has also been observed, e.g. for a wave frequency of 1.44 Hz for which the response of the front float has been found to be three times the response of the WEC at the rear. The experimental measurements have been compared to numerical predictions, derived from WAMIT [13], by considering small-amplitude assumptions. The agreement between numerical and experimental results was good, except for the cases where the incident wave amplitude became too large. The small-amplitude assumptions on which the numerical model is based, are then no longer valid. At low wave frequencies, the measured WEC responses were higher than predicted. This discrepancy can be attributed to the reduced waterline area for amplitudes larger than the WEC radius, which has not been considered in the numerical predictions.

Alteration of the wave characteristics due to the presence of a WEC array has been quantified in [45]. Experiments have been performed in the wave flume of Manchester University. Heaving point absorber WECs have been tested, based on the principle of the Manchester Bobber [46]. Each device is composed of a WEC (float) with a diameter of 15.0 cm and a mass of 1.8 kg diameter float whose motion drives a generator, partially supported by a counterweight of 0.4 kg. The vertical motion of the WEC was translated into the rotation of a flywheel via a pulley and a clutch. A friction-compensated dynamometer has been employed to model the generator, by applying a load specified to represent full-scale power outputs of 300 kW and 600 kW per WEC, corresponding to normal operating conditions. Two WEC array configurations have been investigated: a single row of 5 WECs (5x1) and a double row of 5 WECs (5x2), WEC spacing equal to four times the WEC radius. Irregular waves with a significant wave height of 2.7 m and a peak period of 10.7 s, at full scale, have been applied. Water surface elevations have been measured

both before the deployment of the WEC arrays (in an empty wave flume) and with the WEC arrays at place, using a network of three wave gauges installed up- and downwave of the WEC array (Figure 1.8).

Measurements have shown attenuation of the significant wave height across the array for all tested cases, with a maximum reduction of 14.0 % in the case of the 5x2 array. The largest wave height reduction has been found across the centreline of the WEC array due to the symmetric positioning of the wave gauge. The magnitude of wave height dissipation varied with the number of installed WECs and the rated power of the WECs. The latter had a non-linear influence on the wave height attenuation. For a 5x1 array, the wave attenuation was smaller with increased rated power, corresponding to a larger energy extraction despite the smaller wave height modification. In [45], this has been attributed to the higher reduction of the WEC motion, resulting in a smaller amplitude of the radiated waves. For a 5x2 array, wave height measurements at the centreline and one side of the array, showed a larger dissipation of the significant wave height with increasing rated power. The rest of the wave gauges registered decrease of this dissipation. The spectral density variation across a 5x2 WEC array has also been measured, with power extraction of 600 kW. The presence of the WECs caused a slight reduction of the wave energy, measured by the upwave wave gauges near the peak wave frequency, as well as an increase over other wave frequency ranges. In [45] this has been thus related to the radiated waves sent out by the WECs and the reflection of the incident waves from the WEC. The wave gauges downwave showed that the WEC array caused changes in the wave spectrum that were frequency dependent. In two distinct regions, the energy reduction was highest: near the peak wave frequency of 0.1 Hz of the irregular waves and near the natural frequency of 0.15 Hz of the WECs.

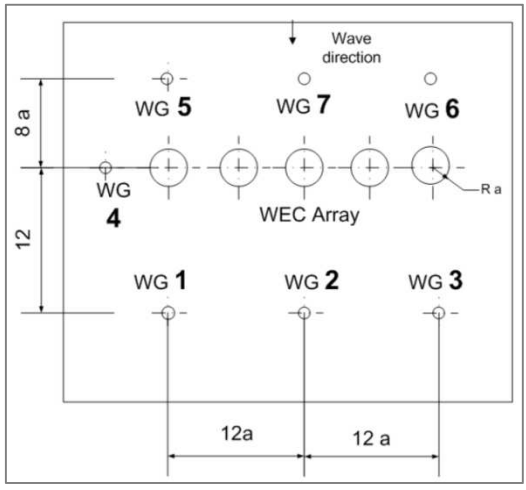

Figure 1.8. Experimental arrangement used in [45].

1.2.4. Small WEC arrays tested at sea

A number of wave energy converters formed by heaving multi-point absorbers have been tested under real sea conditions. This type of WEC consists of a number of oscillating bodies installed close to each other, for economical and practical reasons, and supported from a common structure. Wave energy converters such as Wavestar [47], FO³ ([48], [49]) and the Manchester Bobber [46] are considered as heaving multi-point absorbers.

In 2009, the large-scale test (1:2 scale) and demonstration Wavestar WEC has been installed by Roshage pier near Hanstholm, at the Western coast of Denmark. The prototype has two floats with a diameter of 5.0 m placed on one side (shown in Figure 1.9) and has been installed at a water depth of approximately 6.0 m with a nominal power of 110 kW, as presented in [47]. The maximum allowed wave height for operation is 6.0 m. When higher waves occur, the jacking sections at the end of the main tube, lift this tube along the four legs of the structure, up to the storm protection level (see Figure 1.9, left).

The Wavestar full commercial WEC design consists of two rows of 10 round floats with a diameter of 5.0 m attached to a bridge structure, secured to the sea bed by the use of steel piles, cast into concrete foundations (see Figure 1.10). All moving parts are therefore above normal sea water level. The device is installed with the structural bridge, which supports the floats, directed towards the dominant wave direction. The floats oscillate driven by the incoming waves. The Wave star WEC has been designed to be installed at water depths of 10.0 to 20.0 m and has a nominal power of 600 kW. The power production depends on the wave climate, the control strategy, the period of the year, etc., as presented in [47].

The FO^3 WEC [49] has 12 to 21 heaving egg-cylindrical floaters, connected to a large square rig, made out of lightweight composite material with a side of 36.0 m (see Figure 1.11, left). The vertical motion of the cylinders caused by the incoming waves, is converted to rotational motion of a hydraulic motor which drives a generator. A first model on a 1:20 scale was built at the Marintek/Sintef laboratories in Trondheim (Norway). The promising results obtained by this experimental testing, lead to the construction of the Buldra, a model of a 1:3 scale —12.0 m x 12.0 m, 8.0 m high— (see Figure 1.11, right) [48]. The European funded SEEWEC project has assisted in the further development of the FO^3 WEC, which resulted in an optimized WEC design. This WEC (known as the "B1") consists of an individual point absorber WEC, moored directly to the seabed instead of attached to a platform (see Figure 1.12) [49].

Figure 1.9. Wave star prototype. Left: Storm protection mode. Right: Normal operation mode [47].

Figure 1.10. Artist impression of a commercial Wave star [47].

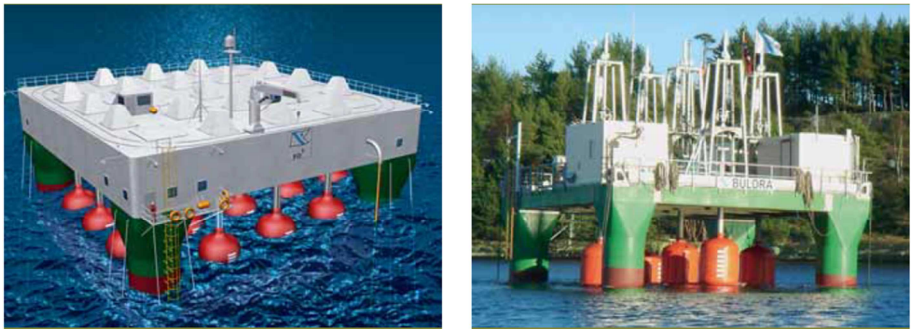

Figure 1.11. Left: FO^3 WEC platform concept. Right: Buldra as a 1:3 scale research platform ([48], [49]).

Figure 1.12. B1 full prototype at sea [49].

The Manchester Bobber WEC has been designed at Manchester University [46]. It is a flotation WEC that generates power from waves coming from any direction. It can be installed at 20.0 m-60.0 m water depth, which allows a minimal visual impact onshore. The Manchester Bobber can include 25-50 individual floats with a hemispherical base (each float rated at 500kW), that heave independently and generate electricity [46]. The floats are connected to a platform, which contains all mechanical and electrical components and is placed at a sufficient height above sea level (see Figure 1.13). Only the floats are in contact with water, which results in easier maintenance. Two scale models of the Manchester Bobber have been constructed: a 1:100 scale model in 2004; and a 1:10 scale model in 2005, while both have been tested with positive results obtained. The robust nature of the system

and its simplicity are great advantages in comparison with other wave energy converters.

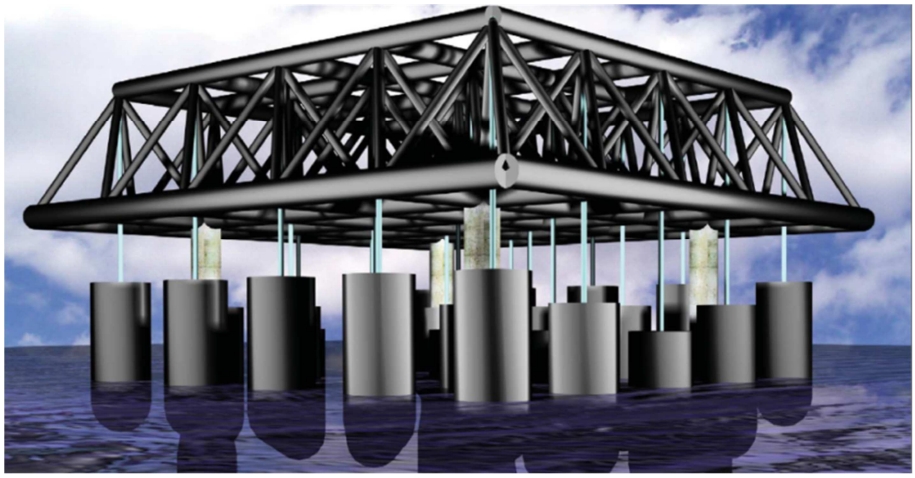

Figure 1.13. Manchester Bobber [46].

1.3. Literature knowledge gaps

In the previous, an overview has been presented of research performed to study WEC arrays numerically and experimentally, as well as laboratory tests with individual WECs or pairs of WECs. Regarding the design of the optimal configuration of a WEC array to obtain maximum power production and its numerical study, a generic numerical tool for the combined accurate prediction of intra-array interactions and extra-array effects is still missing. In addition, there has been very limited validation of the previously mentioned numerical models, using only small physical scale models of WEC arrays, which have been presented in the previous sections.

Moreover, in contrast to the large quantity of numerical simulations of WEC arrays and the large body of experimental work concerning individual WECs, there is limited published data concerning either the response of such WECs located in arrays, or the corresponding wave field changes. Data from large WEC arrays concerning the physical modelling of intra-array interactions and extra-array effects, combined with simultaneous measurements of WEC response, wave induced forces on the WECs and of the wave conditions, are not reported in literature.

Such data are, however, essential for evaluation of the accuracy of the used numerical tools, their validation, as well as for their further development and improvement. Accurate measurements of individual WEC response, WEC array power output and spatial variation of wave conditions in the vicinity of the array are

required to improve understanding of the fundamental processes influencing wave conditions down- and up-wave of wave energy converter arrays. Moreover, results from testing various WEC array geometric configurations will lead to the optimization of the array lay-outs for real applications.

However, in order to realise such experiments, a WEC based on simple operating principles and easy to construct in large numbers, should be available. This WEC should be generic and representative of a large number of existing WEC concepts, to ensure large applicability of the generated WEC array database.

1.4. Objectives

Taking into account the previously mentioned shortcomings of the present state of the art, this PhD research is focusing on wave energy converter arrays.

The **main objective of this PhD research** is to improve the understanding of *intra-array interactions* and *extra-array effects* of WEC arrays. By using experimental and numerical modelling, this PhD research aims to deal with fundamental underlying questions on WEC array design: identifying the optimal and most effective geometric configurations of WEC arrays for power production as a result of intra-array interactions, and quantifying the related environmental impact (extra-array effects). In order to achieve the main objective, the following specific objectives are defined, illustrated in the flow chart of Figure 1.14.

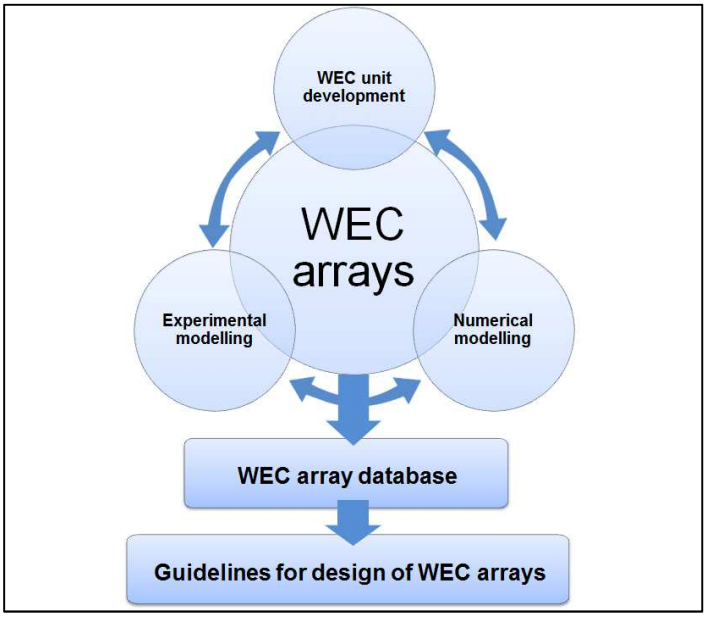

Figure 1.14. Objectives of this PhD research.

1.4.1. Objective 1: Design, development and evaluation of an individual wave energy converter, suitable for experiments with large WEC arrays.

In order to study WEC arrays experimentally, first a WEC unit suitable for this testing should be developed. The objective of developing this WEC is not to introduce a new WEC concept in the wave energy sector, but to create a WEC that efficiently supports and facilitates experimental and numerical modelling of large WEC arrays. This first objective is dealt with in the first part of this PhD dissertation.

In order to achieve this objective, the following research methodology and tasks have been adopted:

o Selecting a WEC based on operating principles, representative of a large number of existing WEC concepts in the wave energy sector. The selection of such a WEC type is important for the applicability of the WEC array database, which is the main deliverable of this PhD research.

o A number of key requirements should be identified, necessary for the WEC's reproduction in large numbers and for the easy repositioning of the WECs within the wave basin/flume to allow alternative WEC array geometric configurations.

The developed WEC should be robust, easy to operate and, economically and practically straightforward and feasible to manufacture. Therefore a WEC had to be designed, that facilitates low cost construction of a large number of identical WEC units. Secondly, the WEC unit should be sufficiently large to develop measurable response and energy extraction for the tested incident wave conditions. The WEC should be able to simulate the real impact of a WEC on the wave climate, by using a simple concept of energy extraction from the incoming waves. This characteristic results in measurable changes to the wave field and, therefore, the WEC facilitates the quantification of extra-array effects. Thirdly, the WEC should be straightforward to be modelled analytically and numerically, by keeping e.g. the total number of degrees of freedom of the entire WEC array limited, which results in simple response model of the array. In addition, the WEC should have a generic and simple WEC buoy geometry, for its straightforward analytical and numerical treatment.

o After finalizing the first design of the WEC unit, funding should be sought and requested for access to a large-scale experimental facility, able to accommodate at least 25 WECs for WEC array testing. The wave basin should be sufficiently wide to allow measurement the extra-array effects. At the same time, the wave basin should be shallow to allow easy access for repositioning of the WEC units, in order to test a large number of different WEC array geometric configurations. This was realized through an EU FP7 HYDRALAB IV programme project proposal, submitted together with other 6 EU partners and coordinated by Ghent University.

o After finalizing the first design of the WEC unit, funding should be sought and requested for the construction of the first prototype model and of a larger number of identical WECs. This was realized through an FWO-KAN project proposal.

o Once the geometry and PTO principle has been selected, and before WEC array testing, the performance of the WEC unit should be evaluated, through detailed experimental testing and numerical analysis to predict the WEC response. The WEC response, stability and correct performance under incident waves, the instrumentation mounted on the WEC should be investigated in detail to satisfy the performance requirements for large array experiments, as well as the feasibility requirements for the reproduction of identical WEC units in large numbers.

o After evaluation, optimization and finalizing the geometry and the mechanical parts of the developed individual WEC unit, identical WECs should be constructed for WEC array testing.

1.4.2. Objective 2: Numerical modelling of the wave field around a heaving wave energy converter.

A second objective of this PhD work is to establish a coupling methodology to tackle both intra-array interactions and extra-array effects of WEC (arrays), simultaneously. The numerical study of the resulting wave fields around the developed heaving WEC (from Objective 1), as well as the details of the developed methodology, are presented in the second part of this PhD dissertation.

This coupling methodology should combine:

i. the advantages of the approach of wave-structure interaction solvers, which accurately formulate and efficiently resolve the physical processes in wave energy absorption;

ii. and, the benefits of the approach of wave propagation models, which efficiently resolve the propagation and transformation of waves over large distances, including bathymetric variability over the WEC farm area and wave transformation processes when approaching the coastline.

In order to achieve this objective, the following research tasks have been adopted:

o The development of a wave generation technique, to generate the perturbed or radiated wave field induced by an oscillating WEC in a wave propagation model.

The WEC has been implemented using prescribed internal boundary wave conditions, on a wave generation circle which surrounds the WEC location.

o The coupling methodology should be generic, in order to achieve wide applicability, so that it can be used for combining any wave-structure interaction solver and wave model.

o The implementation of the coupling methodology in the wave propagation model, MILDwave [7] as a first application of the modelling methodology.

o The verification of the developed coupling methodology by using a test case based on the developed WEC unit during Objective 1.

1.4.3. Objective 3: Physical modelling of large WEC arrays

The main and final objective of this PhD research is to improve the understanding of *WEC array effects* by: (a) creating the first large WEC array database; (b) analysing the obtained results to quantify WEC array effects for a range of WEC array geometric configurations and sea state characteristics; and (c) generating a first series of guidelines for WEC array design based on experimental measurements. These objectives are presented in the third part of this PhD dissertation.

In order to achieve this objective, the following research tasks have been adopted:

o Before the conduct of experiments with large WEC arrays, the set-up of the WEC array testing programme has been prepared, based on numerical predictions of WEC array effects found in the literature. Based on this literature research, sea state characteristics and WEC array geometric configurations have been selected for the test programme.

o Preparation of 25 identical WEC units, with the accompanying instrumentation. After the construction of the WEC models, quality tests should be performed to assure identical characteristics and performance.

o Conduct of large-scale experiments with various large WEC arrays composed of up to 25 WECs, in the wave basin of DHI (Denmark).

o Establishment of a comprehensive WEC array database for heaving WECs in which wave elevations, WEC response and wave induced surge forces on the WECs have been simultaneously measured. The experimental database should comprise a wide range of parameter variations such as: the array geometric configuration, the WEC number, the lateral and longitudinal (centre-to-centre) spacing between the WECs, the WECs' motion (decay motion, stationary WECs, "free" response or

damped motion of WECs with varying damping), wave conditions (varying wave period, wave heights, wave attack angles) and wave types (regular, polychromatic, irregular long- and short-crested with varying spreading parameters).

o Analysis of the obtained results from the WEC array testing, including the development of a methodology both for the data analysis and for the results' presentation.

o Generation of a first set of guidelines for WEC array design, to be used by wave energy project developers for optimal design of WEC arrays regarding their power absorption, as well as their impact on the environment for real wave energy applications.

1.5. Outline

This PhD dissertation is divided into three parts:

A first part deals with the design, development and evaluation of a WEC specially for WEC array experiments. The WEC unit is developed specially for experiments to study WEC array effects. In Chapter 2, the design of the WEC unit is presented, including detailed description of its structural and mechanical parts. The principle of the PTO-system is presented, as well as its structural elements. The theoretical operating principles of the point absorber type WEC unit are presented, as well as numerical predictions of the WEC response and power output, performed using hydrodynamic parameters obtained from WAMIT. Experimental evaluation of the WEC units is conducted using the tensile test machine and the wave flume at Ghent University, in Belgium, the wave basin of the Queen's Marine Laboratory of the Queen's University of Belfast (UK), and the wave flume (large-scale facility) of Flanders Hydraulics Research, in Belgium. Finally, the most important results of the experimental testing are provided. Experimental measurements of the WEC response have also been compared to numerical predictions of the WEC response obtained using WAMIT. Then, a summary is presented of the conclusions and the design specifications of the WEC unit, which enable tests with WEC arrays, composed of large numbers of WECs.

The second part of this PhD dissertation is on the numerical modelling of the resulting wave fields around oscillating wave energy converters, with the intention to study WEC (array) effects. The details of the presented coupling methodology are provided in Chapter 3 with clear illustrations of the step-by-step procedure. Two schemes are presented for modelling the resulting wave field due to interaction of a WEC with waves: (i) for a generic coupling between any wave-structure interaction solver and any wave propagation model, and, (ii) a scheme for coupling between the two selected models, for the case of an individual heaving WEC. In addition, the technique used to model WEC arrays by using the presented coupling methodology is shown. Chapter 3 provides information on the selected wave propagation model (MILDwave) in which the coupling methodology has been implemented. Here, the details of the developed wave generation technique on a wave generation circle are presented. Furthermore, this part includes all the details of the implementation of the proposed coupling methodology for the modeled test case of the developed heaving WEC, described in the first part of this dissertation. The diffracted, radiated and perturbed wave field around the WEC are modeled, using the selected wave-structure interaction model. This simulation provides the prescribed internal boundary wave conditions on the wave generation circle used for the proposed coupling methodology, in order to generate the radiated wave field around the WEC. Furthermore, by using the proposed coupling methodology, the diffracted, radiated and perturbed wave field around the WEC are modeled in the selected wave

propagation model. Finally, verification results are provided, of the proposed coupling methodology against the wave fields around the WEC simulated by the selected wave-structure solver. The agreement between the results from the proposed coupling methodology and those obtained by the wave-structure solver is evaluated and discussed, first for the diffracted and radiated wave field separately, and then for the perturbed wave field around the WEC. At the end of Chapter 3, a summary of the obtained conclusions from the verification results is presented, including a discussion on the potential of the proposed coupling methodology and its benefits.

The third part of this PhD dissertation focusses on the WEC array experiments performed to study experimentally intra-array interactions and extra-array effects caused by large WEC arrays. An introduction to the testing programme objectives is presented in Chapter 4. A detailed overview of the design and execution procedure of the experiments and of the WECwakes database is given. In Chapter 4, experimental results are presented, for the power absorption of individual WECs and the tested WEC arrays. Moreover, data analysis referring to the incident wave conditions generated during the testing programme, the effect of WEC support structures on the wave field and the wave field modification caused by the tested WEC arrays of different configuration is presented. A summary of the presented findings and the characteristics of the WECwakes database are presented in Chapter 4.

In Chapter 5, a first set of generic guidelines for WEC array design, based both on the obtained experimental results and on a literature study, is presented. In Chapter 6, general conclusions and recommendations for further research on WEC array modelling are formulated.

Six appendices are included at the end of the dissertation. Appendix A provides an overview of the solution scheme and the applications of the wave propagation model MILDwave, as well as the implementation of wave regeneration by wind performed within this PhD research. Appendices B-F provide more detailed information $_{on}$ the WEC array database obtained during this PhD work; the lay-out of the force gauges, a summary of the tested sea states, sketches of the tested geometric WEC (array) configurations, a summary of the PTO-system settings of the tested WEC (array) configurations and a plan view of the experimental arrangement in the Shallow Water Wave basin of DHI, are presented.

1.6. References

[1] European Commission, Europe 2020, http://ec.europa.eu/europe2020, Accessed March **2013**.

[2] Panicker, N. N. *Power resource estimate of ocean surface waves*. Ocean Engineering, 3(6), 429–439. doi:10.1016/0029-8018(76)90016-0, **1976**.

[3] Falnes, Johannes. *A review of wave-energy extraction*. Marine Structures, 20(4), 185–201. doi:10.1016/j.marstruc.2007.09.001, **2007**.

[4] Falnes, J.. *Teaching on ocean-wave-energy conversion.* Proceedings of wave energy for the new millennium, Fourth European wave energy conference, Aalborg University, Denmark, **2000**.

[5] Beels, C., Troch, P., Kofoed, J.P., Frigaard, P., Vindahl Kringelum, J., Carsten Kromann, P., Heyman Donovan, M., De Rouck, J., De Backer, G., *A methodology for production and cost assessment of a farm of wave energy converters.* Renewable Energy.36(12), 3402-3416, **2010**.

[6] Falcão, A.F.0. *Wave energy utilization: A review of the technologies.* Renewable and Sustainable Energy Reviews 14, 3, 899-918, **2010**.

[7] Troch, P.. *MILDwave – A numerical model for propagation and transformation of linear water waves.* Internal Report, Department of Civil Engineering, Ghent University, **1998**.

[8] Troch, P., Beels, C., De Rouck, J., De Backer, G.. *Wake effects behind a farm of wave energy converters for irregular long-crested and short-crested waves.* Proceedings of the International Conference on Coastal Engineering, No. 32 (**2010**), Shanghai, China. Paper #: waves.22. Retrieved from http://journals.tdl.org/ICCE/.

[9] Li, Y., Yu, Y.-H.. *A synthesis of numerical methods for modelling wave energy converter point absorbers.* Renewable & Sustainable Energy Reviews. 16.6, 4352-4364, **2012**.

[10] Folley, M., Babarit, A., O' Boyle, L., Child, B., Forehand, D., Silverthorne, K., Spinneken, J., Stratigaki, V., Troch, P.. *A review of numerical modelling of wave energy converter arrays*. Proceedings of the 31st International Conference on Offshore Mechanics & Arctic Engineering, Rio de Janeiro, Brazil, **2012**.

[11] Delhommeau G.. *Le problème de diffraction radiation et de résistance de vagues : étude théorique et résolution numérique par la méthode des singularités*, Thèse Ecole Nationale Supérieure de Mécanique, Nantes, **1987**.

[12] ANSYS Aqwa, Product features, http://www.ansys.com, Accessed March **2013**.

[13] WAMIT version 7.0 user manual. [Online]. Available: http://www.wamit.com/. Accessed March **2013**.

[14] Yu, Y.-H., Li, Y.. *Reynolds-Averaged Navier-Stokes simulation of the heave performance of a two-body floating-point absorber wave energy system.* Computers & Fluids, 73, 104-114, **2013**.

[15] Agamloh, E.B., Wallace, A.K., von Jouanne, A.. *Application of fluid-structure interaction simulation of an ocean wave energy extraction device.* Renewable Energy. 33(4), 748-757, **2008**.

[16] Finnegan,W., Goggins, J.. *Numerical simulation of linear water waves and wave–structure interaction.* Ocean Eng. 43, 23-31, **2012**.

[17] N. Booij, I.J.G. Haagsma, L.H. Holthuijsen, A.T.M.M. Kieftenburg, R.C. Ris, A.J. van der Westhuysen, M. Zijlema, *SWAN cycle III version 40.51AB User Manual,* **2007**.

[18] P.A. Madsen, O.R. Sørensen. *A new form of the Boussinesq equations with improved linear dispersion characteristics.* Part 2: A slowly-varying Bathymetry. Coastal Eng. 18(1992), 183-204, **1992**.

[19] Millar, D.L., H.C.M. Smith, and D.E. Reeve. *Modelling analysis of the sensitivity of shoreline change to a wave farm.* Ocean Engin., 34, 884-901, **2006**.

[20] V. Venugopal, G.H. Smith. *Wave climate investigation for an array of wave power devices.* Proceedings of the 7th European Wave and Tidal Energy Conference, Porto, **2007**.

[21] Alexandre, A., T. Stallard, and P.K.Stansby. *Transformation of Wave Spectra across a Line of Wave Devices.* Proceedings of the 8th European Wave and Tidal Energy Conference, Uppsala, Sweden, **2009**.

[22] Silverthorne, K. and Folley, M.. *A new numerical representation of wave energy converters in a spectral wave model.* 9th European Wave and Tidal Energy Conference, Southampton, UK, **2011**.

[23] Beels, C., Troch, P., De Backer, G., Vantorre, M., De Rouck, J.. *Numerical implementation and sensitivity analysis of a wave energy converter in a time-dependent mild-slope equation model.* Coastal Engineering, 57(5), 471-492, **2010**.

[24] Beels, C., Troch, P., De Visch, K., Kofoed, J.P., De Backer, G.. *Application of the time-dependent mild-slope equations for the simulation of wake effects in the lee of a farm of Wave Dragon wave energy converters.* Renewable Energy. 35, 1644-1661, **2010**.

[25] Stratigaki, V., Troch, P., Baelus, L., and Keppens, Y.. *Introducing wave regeneration by wind in a mild-slope wave propagation model, MILDwave, to*

investigate the wake effects in the lee of a farm of wave energy converters. Proceedings of the ASME 2011 30th International Conference on Ocean, Offshore and Arctic Engineering (OMAE 2011). Rotterdam, The Netherlands, **2011**.

[26] Stratigaki, V., Troch, P.. *An introduction to the wave propagation model MILDwave.* Department of Civil Engineering, Ghent University, **2012**.

[27] Babarit, A.. *Impact of long separating distances on the energy production of two interacting wave energy converters.* Ocean Engineering, 37, 718–729. doi:10.1016/j.oceaneng.2010.02.002, **2010**.

[28] AQUADYN. http://www.scisoftware.com, Accessed November **2013**.

[29] Borgarino, B., Babarit, A., & Ferrant, P.. *Impact of wave interactions effects on energy absorption in large arrays of wave energy converters.* Ocean Engineering, 41, 79–88. doi:10.1016/j.oceaneng.2011.12.025, **2012**.

[30] Oskamp, J. A., & Özkan-Haller, H. T.. *Power calculations for a passively tuned point absorber wave energy converter on the Oregon coast.* Renewable Energy, 45, 72–77. doi:10.1016/j.renene.2012.02.004, **2012.**

[31] Wolgamot, H.A., Taylor,P.H. & Eatock Taylor, R.. *The interaction factor and directionality in wave energy arrays.* Ocean Engineering 47, 65 73, **2012.**

[32] DIFFRACT. http://www.mmresearch.com/diffract/diffract.htm, Accessed January **2014**.

[33] Folley, M. & Whittaker, T.. *Spectral modelling of wave energy converters.* Ocean Engineering 57, 892 897, **2010**.

[34] Child, B. F. M., & Venugopal, V.. *Optimal configurations of wave energy device arrays.* doi:10.1016/j.oceaneng.2010.06.010, Ocean Engineering, 37(16), 1402–1417, **2010**.

[35] Child, Benjamin F. M.. *On the configuration of arrays of floating wave energy converters.* PhD thesis, The University of Edinburgh, **2011**.

[36] Babarit, A.. *On the park effect in arrays of oscillating wave energy converters.* Renewable Energy. 58, 68-78, **2013**.

[37] Budal, K., Falnes, J., Kyllingstad, A., & Oltedal, G. P. of F. S. on W. E. U.. *Experiments with point absorbers.* Proceedings of First Symposium on Wave Energy Utilization (pp. 253–282), **1979**.

[38] Count, B.M. & Jefferys, E.R.. *Wave power, the primary interface.* Proceedings of the 13th Symp. Naval Hydrodynamics 8, 1 10, **1980**.

[39] Vantorre, M., Banasiak, R., & Verhoeven, R.. *Modelling of hydraulic performance and wave energy extraction by a point absorber in heave.* Applied Ocean Research, 26(1-2), 61–72. doi:10.1016/j.apor.2004.08.002, **2004**.

[40] Durand, M., Babarit, A., Pettinotti, B., Quillard, O., Toularastel, J. & Clément, A.. *Experimental validation of the performances of the SEAREV wave energy converter with real time latching control.* Proceedings of the 7th European Wave & Tidal Energy conference, Portugal, **2007**.

[41] De Backer, G.. *Hydrodynamic design optimization of wave energy converters consisting of heaving point absorbers.* Ph.D. Thesis, Ghent University, **2009**.

[42] Stallard, T., Stansby, P.K. & Williamson, A.. *An experimental study of closely spaced point absorber arrays.* Proceedings of the 18th International Offshore & Polar Engineering Conference, Canada, **2008**.

[43] Weller, S., Stallard, T. & Stansby, P.K.. *Experimental measurements of irregular wave interaction factors in closely spaced arrays.* Proceedings of the 8th European Wave & Tidal Energy Conference, Sweden, **2009**.

[44] Thomas, S., Weller, S. & T. Stallard. *Comparison of numerical and experimental results for the response of heaving floats within an array.* Proceedings of the 2nd International Conference on Ocean Energy, France, **2008**.

[45] Alexandre, A., Stallard, T., and Stansby, P. K.. *Transformation of Wave Spectra across a Line of Wave Devices.* Proceedings of the 8th European Wave and Tidal Energy Conference (pp. 943–951). Uppsala, Sweden, **2009**.

[46] Katofsky, R.. *Ocean energy: technology basics.* Renewable Energy Focus, (May/June 2008), 34–36, **2008**.

[47] Kramer, M., Marquis, L. & Frigaard, P.. *Performance Evaluation of the Wavestar Prototype.* Proceedings of the 9th European Wave and Tidal Conference, Southampton University, UK, **2011**.

[48] Leirbukt, A., & Tubaas, P.. *A wave of renewable energy.* ABB Review, 3, 29–31, **2006**.

[49] SEEWEC Project. (2005). Sustainable Economically Efficient Wave Energy Converter; SES6-CT2005-019969. Retrieved from http://www.seewec.org/, Accessed May **2013**

2

Development of a heaving wave energy converter for WEC array experiments

Abstract: *In this chapter, an overview is presented of the design, development and evaluation of a wave energy converter that is suitable for experiments with large WEC arrays. The objective of developing this WEC was not to introduce a new WEC concept in the wave energy sector, but to create a WEC that efficiently supports and facilitates experimental and numerical modelling of large WEC arrays. The design specifications are based on the need to efficiently calibrate and operate at least 25 WECs simultaneously, with the intention to study WEC array effects within the main deliverable of this PhD research. WEC array effects consist of intra-array interactions between WECs in a wave farm and extra-array effects on their environment.*

The developed WEC unit comprises a hemispherical ended cylindrical buoy of diameter, D, and draft, d_{buoy}, 0.315 m, with overall height 0.600 m. The WEC buoy is constrained to heave along a vertical square-section WEC supporting shaft, through PTFE-bearings. A generic WEC design has been developed, in order to create a widely applicable WEC array database that can be employed for inter-comparison of numerical models.

Linear analysis of the WEC response using WAMIT and experimental testing have been conducted, with the aim to evaluate the performance of the WEC unit. The present chapter focuses on the design and the development of the WEC unit, as well as its underlying theoretical and numerical study using WAMIT. The WEC unit is designed based on feasibility requirements for usage in large numbers, within WEC arrays of various array geometric configurations.

Furthermore, the evaluation of the developed WEC unit is presented in this chapter, realised by performing experimental studies. Four series of experiments have been performed, including mechanical dry and wet testing of the WEC shaft bearings, evaluation of the WEC support system, response of an individual WEC unit under waves and response of up to four WEC units forming a small array. The proposed WEC unit is shown to satisfy the performance requirements for large array experiments, as well as the feasibility requirements for the reproduction of identical WECs in large numbers.

The research presented in this chapter has, finally, resulted in the construction of 25 identical WEC units which have been used intensively for WEC array testing. Through this WEC array testing, detailed experimental data has been obtained for the understanding of WEC array effects caused by the response and power absorption of WECs in various array geometric configurations.

2.1. Introduction

2.1.1. Problem statement: lack of WEC array experiments due to complexity of existing WEC concepts

The large number of different WEC concepts developed during the past decades, is representative for the research intensity and great interest in wave energy. The number of different WEC concepts has been very recently estimated around 150 [1], at different stages of development. These WEC concepts operate using very different principles, while the wave energy sector is presently dominated by point absorber type WECs (~46%), followed by oscillating wave surge converter type WECs (~16%) and oscillating water column type WECs (~15%) [1].

WEC developers have mainly focused on the experimental testing of typically 1-12 WECs and pilot site installations of individual wave devices. However, the need for design of WEC array installations becomes more and more obvious through numerical studies [2]. As shown by numerical simulations ([3]-[6]), in order to extract a considerable amount of wave power from wind waves, large numbers of WECs will have to be arranged in arrays using a specific geometric configuration. However, power production of such arrays will be affected by WEC array affects, described in the introductory part of this PhD dissertation, e.g. hydrodynamic WEC-WEC interactions, which consist of intra-array interactions between WECs in a wave farm and extra-array effects on their environment.

Nevertheless, WEC concepts are very often based on complex operating and structural principles, or even complicated geometries. Moreover, in most of the cases, structural details and testing data of these WEC concepts are private and confidential. As a result, the reasons of failure or success of a certain WEC concept are not accessible to the research community. Most importantly, as is usually the case within a well-defined and rather short funding period, it is economically (due to high construction cost) and practically (difficult to manufacture) not feasible to produce the developed WEC concept in large numbers, in order to perform tests with large WEC arrays.

Consequently, the combination of the large number of different WEC concepts, confidentiality of the underlying development information, high WEC structural and operational complexity and high manufacture costs, result in severe feasibility restrictions for reproduction and testing of a WEC concept in large numbers, within large WEC arrays.

Therefore, in order to obtain insight into the important WEC array effects, fundamental research based on simple principles is necessary, by starting e.g. from testing generic WECs in array formations. Once an individual generic WEC proves

to operate properly, it can be further reproduced in large numbers to be used for WEC array testing. Finally, the results from such testing can be extrapolated to WEC concepts based on similar operating principles.

2.1.2. Physical modelling of individual WECs or pairs of WECs

Individual or pairs of WECs have been widely experimentally studied, while nowadays a small number of single prototypes of WECs are being tested at sea. In 1979, Budal et al. [7] reported measurements of the "free" response amplitude and absorption of a (rigidly connected) pair of hemispherical ended floats with a diameter of 0.15 m. The device mass and damping were specified to attain a resonant response with the incident wave and good agreement was observed with the point absorber theory. At a similar time, a series of tests was conducted by Count and Jeffreys [8] at the University of Edinburgh. Measurements of the interaction factor of a linear array of both two and ten WECs at different spacings were in reasonable agreement with point absorber predictions.

In the eighties, Vantorre [9] performed numerical and experimental tests on a 2-body point absorber system. In 2004, Vantorre et al. [10] compared numerical (using Aquaplus [11]) and experimental results of the hydrodynamic performance of a heaving point absorber, followed by tests on a single buoy by De Backer [12]. At the Ecole Centrale de Nantes the SEAREV WEC has been extensively studied both numerically and experimentally. Validations of (non)linear models are presented in [13] - [15]. In 2008, Payne et al. [16] compared BEM simulations of the sloped IPS buoy with experimental tests, carried out in the Edinburgh Curved Tank.

2.1.3. Physical and numerical modelling of WEC arrays

In contrast to the large quantity of numerical simulations of WEC arrays and the large body of experimental work concerning individual WECs or pairs of WECs, there is limited published data concerning either the response of such WECs located in arrays or of the corresponding wave field changes. To mention a few, experimental measurements of the response and power output of arrays of up to 12 closely spaced heaving floats have been reported by Stallard et al. [17] for regular waves and Weller et al. [18] for irregular waves. Thomas et al. [19] compared experimental measurements of the heave response of a line and row of 5 heaving WECs to response predictions from WAMIT [20], observing reasonable agreement. Within the UK Supergen Marine and the EU Hydralab III programmes, tests have

been conducted of a WEC array of five oscillating water column WECs interconnected by mooring lines [21].

2.1.4. Design of a WEC unit to perform experiments with large WEC arrays

Recently, as one of the main deliverables of this PhD research, experiments have been performed in the Shallow Water Wave basin of DHI (Denmark) on large arrays of point absorber type WECs. These experiments are part of the research project "WECwakes" [22], [23], funded by the EU-FP7-HYDRALAB-IV programme. WEC array effects have been studied for a range of WEC array geometric configurations and wave conditions. The experimental set-up has been designed to simulate the real impact of WEC arrays on the wave climate by using a simple concept of energy extraction from the incoming waves.

In this chapter, the design, development and evaluation of the WEC unit is presented, developed specially for the WEC array experiments. This WEC unit, which has been tested to satisfy the necessary requirements, has enabled tests with large WEC arrays. The presented here WEC unit resulted in the creation of a comprehensive non-confidential database (the created database is accessible to the research community as specified under the HYDRALAB rules) and allowed large scale experiments by testing 28 different WEC (array) configurations in the wave basin of DHI. The WEC unit is generic and is based on simple operating principles (both response and PTO-system).

It has to be noted that the developed WEC unit and especially its PTO-system do not represent a new WEC concept. The PTO-system, for instance, has been designed only to simulate and realize power extraction from the waves and not to represent a new PTO principle.

The design of the WEC unit is based on the point absorber principle. The WEC unit is composed of a buoy, designed to heave along a vertical shaft only, and can thus be modeled as a single degree of freedom (abbreviated as *DOF*) system. Energy absorption through the WEC's PTO-system, is modelled by realising energy dissipation through damping of the WEC's heave motion.

The WEC geometry and PTO-system principle are generic and the WEC unit can therefore be used for any study of WEC array effects of similar WECs. The developed WEC is easy to operate and feasible to manufacture in large numbers, economically and practically. Moreover, it is simple to be modelled analytically and numerically. The PTO-system simulates WEC power absorption in a simple way, both concerning operation and construction.

2.1.5. Chapter overview

This chapter details the design, development and evaluation of the individual WEC units developed specially for use in experiments with large WEC arrays.

In Section 2.2, the design of the WEC unit is presented, including detailed description of its structural and mechanical parts. The principle of the PTO-system is presented, as well as its structural elements. In Section 2.3, the theoretical operating principles of the point absorber type WEC unit are presented, as well as numerical predictions of the WEC response and power output, performed using hydrodynamic parameters obtained from WAMIT. In Section 2.4, a description is provided of the experimental evaluation procedures (aims and characteristics of the experimental testing). The experimental evaluation of the WEC units has been conducted using the tensile test machine and the wave flume at Ghent University, in Belgium (hereafter UGent), the wave basin of the Queen's Marine Laboratory (hereafter QML) of the Queen's University of Belfast, in the UK, and the wave flume (large-scale facility) of Flanders Hydraulics Research, in Belgium (hereafter FHR). Section 2.5 provides details on the four experimental set-ups employed. Finally in Section 2.6, the most important results of the experimental testing are presented. In addition, experimental measurements of the WEC response have been compared to numerical predictions of the WEC response obtained using WAMIT. Finally, in Section 2.7, a summary is presented of the conclusions and the design specifications of the WEC unit, which has enabled tests with large WEC arrays.

2.2. Design of the WEC unit

2.2.1. Design requirements of the WEC unit

The main objective of this PhD research is to study wave field modifications in the vicinity of arrays formed by both small numbers of wave energy converters (e.g. less than 10 WECs) and by larger numbers (more than 10 WECs, as defined by Child et al. [24]). First, the necessary design requirements of the individual WEC units have been identified within this PhD research, to facilitate large scale-experiments. These design requirements are as follows:

1. The WEC unit should be efficient and straightforward to manufacture, in order to facilitate low cost construction of at least 25 identical WEC units (based on the maximum WEC number tested within this PhD work, simultaneously).

2. The WEC unit should be simple to represent in numerical models:

- The number of degrees of freedom of a response model of the WEC unit is preferably limited to the number of WEC units in an array. Therefore a single DOF WEC unit has been selected.
- Idealised and simple WEC buoy geometry with vertical sides at the water plane.

3. The WEC unit should have a simple support system and PTO-system, in order to ensure repeatable operation of each WEC unit:

- PTO damping force, F_{PTO}, should allow straightforward representation in a range of models. In the developed WEC unit, F_{PTO} is proportional to the force applied by linear springs.
- Measurement of the wave induced surge force on the WEC, F_{surge}, should be simple in order to quantify non-PTO loads.

4. The WEC unit should have sufficient dimensions to develop measurable response and energy extraction under the tested wave conditions. For the developed WEC unit in particular, measurements of the time varying heave displacement of the WEC, $z(t)$, and of F_{surge}, are necessary to quantify energy extraction from the waves by the WEC mechanical system.

5. An easy/practical system is required to reposition individual WECs within the wave basin/flume to allow the study of alternative WEC array geometric configurations, particularly with varying WEC number and WEC spacing.

6. The use of a generic WEC design (a buoy) and of a simple mooring/support structure is important to develop a widely applicable WEC array database that can be employed for inter-comparison of numerical models.

Based on these requirements, the developed WEC unit comprises a simple design composed of a hemispherical ended cylindrical buoy (point absorber type WEC), a vertical supporting shaft, a bottom base and a PTO-system. A point absorber typically consists of a float with horizontal dimensions that are small compared to the incident wavelengths. Through the PTO-system, power is extracted from the waves by the WEC unit. The WEC buoy is constrained to heave only, by PTFE bearings running on a square section supporting vertical shaft, and can thus be modeled as a single DOF system. PTFE stands for *Polytetrafluoroethylene* material, commonly known as "*Teflon*". The supporting shaft is bottom mounted to a heavy steel base plate, and at the same time, fixed to adjacent structures at the top (a metal frame). The PTO-system comprises two blocks made of PTFE. These PTFE-blocks are pressed against the WEC shaft by using linear springs, normal to the wave direction. Power developed by the PTO-system is therefore proportional to the friction between PTFE and steel and a normal force, proportional to the spring

compression increment, dx. In addition, power will be absorbed by the PTFE bearings along the vertical WEC shaft, again through friction, as a function of the wave induced surge force, F_{surge}, on the WEC buoy.

2.2.2. Structural and mechanical design

A freely floating body in ocean waves has generally six degrees of freedom: 3 translational modes (surge, sway and heave) and 3 rotational modes (roll, pitch and yaw) as illustrated in Figure 2.1. The xy-plane of the right-handed coordinate system is the horizontal plane, parallel to the still water surface. The z-axis is positive in the upward direction and coincides with the axis of symmetry of the floating body (here the WEC), while the origin point corresponds to the undisturbed free surface. The y-direction is parallel to the wave propagation direction and is positive in the same direction of the wave propagation.

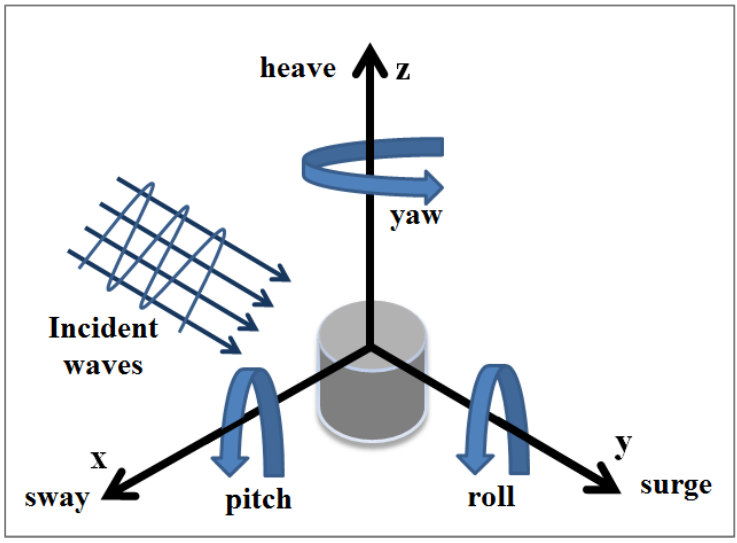

Figure 2.1. Six degrees of freedom (6-DOF) of a freely floating structure in ocean waves.

The developed WEC unit has been designed as a 1-DOF system, where only heave motion along its vertical shaft is allowed. The WEC unit comprises three main parts, illustrated in Figure 2.2: (a) a hemispherical ended cylindrical buoy of diameter, D = 31.5 cm, and draft, d_{buoy} = 31.5 cm and overall height h_{buoy}= 60.0 cm (detail in Figure 2.3), (b) a vertical steel shaft of 40 mm square section with a

gravity metal base, and (c) a PTO-system based on friction brakes comprising PTFE-blocks and 4 linear springs (detail in Figure 2.4). The dry mass of the buoy is m = 20.490 kg and the natural period, by decay test and response measurement in regular waves, is T_n = 1.176 s. The top part of the buoy is a horizontal PVC (*Polyvinylchloride* material) cover, on which the PTO-system is installed and a potentiometer is connected for the measurement of the WEC's heave displacement.

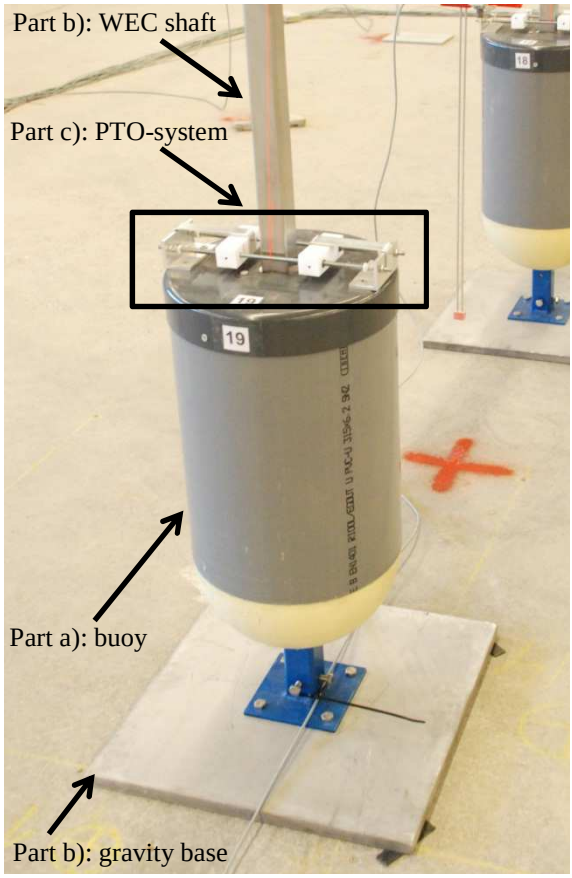

Figure 2.2. The parts of an individual wave energy converter illustrating geometry, bearings and power take off system.

Regarding WEC part (a), shown in Figure 2.3, the buoy has a hemispherical bottom and a cylindrical PVC prefabricated vertical body. The hemispherical bottom is made out of *Polyurethane* (PUR) cast in a mould (Figure 2.3, right). The movement of the buoy in the horizontal plane (sway motion in the x-direction direction), due to the margin between the WEC shaft and the shaft bearing, is

prevented by two PTFE-bearings at the top and bottom of the buoy (Figure 2.3, left). PTFE is selected for its low friction coefficient, μ, on steel, which limits the vertical frictional force due to the shaft bearings, $F_{bearings}$.

With regard to WEC part (b), the buoy heaves along a vertical, square, hollow stainless steel shaft with a cross-section of 4.0 cm x 4.0 cm. The shaft passes through a slightly larger shaft bearing inside the WEC (Figure 2.3, left), which extends over the total height of the buoy, h_{buoy}, to avoid water infiltration. The square form of the vertical shaft hinders rotation of the buoy around the shaft (yaw motion around the z-direction shown in Figure 2.1). The vertical WEC shaft is anchored in a gravity metal base installed at the wave flume/basin bottom. At the same time the WEC shaft is fixed at the top, on beams that span over the WEC (array). The metal base has dimensions 50.0 cm x 50.0 cm, a thickness of 2.0 cm and weighs 45.0 kg.

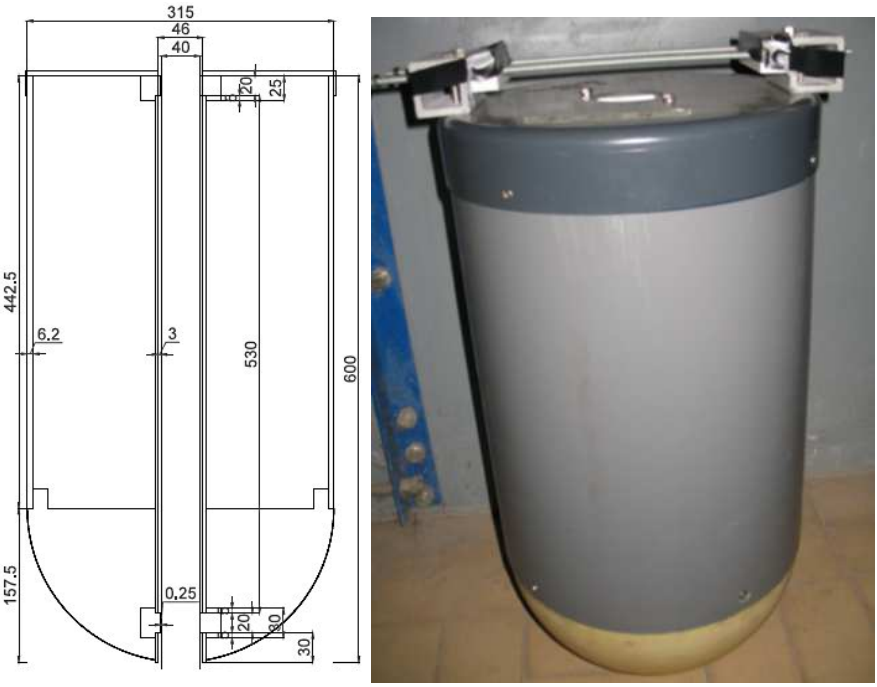

Figure 2.3. Details of the WEC part (a): left (dimensions in mm): Cross section showing the 2 PTFE-bearings at the top and at the bottom (20-25 mm thick). The WEC shaft passes through a shaft bearing along the entire length of the buoy; right: Front view showing the lower hemispherical PUR part, the cylindrical vertical PVC part and the top PVC cover.

WEC part (c) - the PTO-system – is installed on the PVC cover of the buoy (Figure 2.4). The working principle of the PTO-system is presented in detail in Section 2.2.3.

2.2.3. Principle of the PTO-system of the WEC unit

The power take-off system of the WEC unit is based on the principle of a mechanical friction brake by applying damping on the WEC buoy's heave motion. Energy is extracted from the waves through the PTO-system and is dissipated by friction, as the WEC buoy heaves along the WEC shaft under incident waves. The PTO-system consists of 4 compression springs, installed symmetrically along a WEC diameter (2 springs at each side of the WEC, as shown in Figure 2.4).

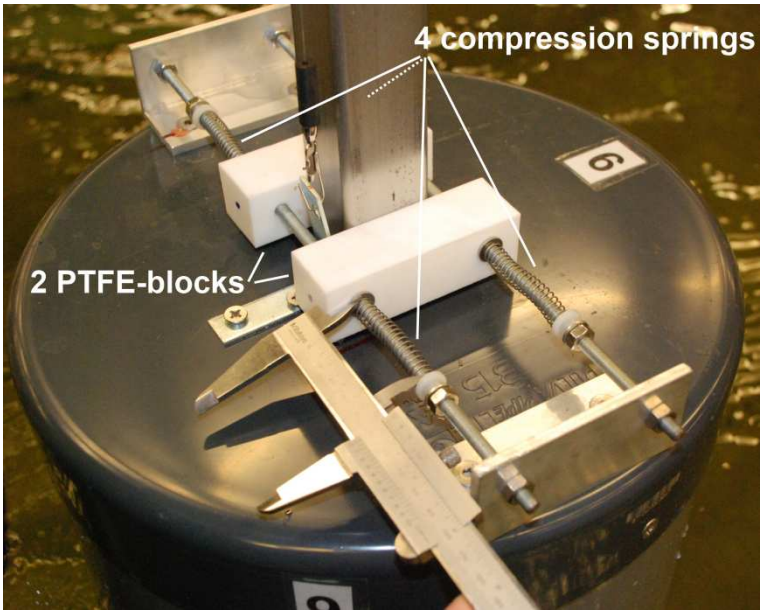

Figure 2.4. View from the top, showing the PTO-system of the WEC, mounted at the top PVC cover of the WEC buoy.

The springs exert a normal force, F_N, on the two PTFE-blocks of the PTO-system, installed symmetrically along a WEC diameter. The PTFE-blocks are pressed against the vertical WEC shaft, passing through the entire length of the WEC buoy, increasing friction, which causes damping of the amplitude of the WEC buoy heave displacement, z_A. To simulate a situation without the PTO-system

connected, separating metal elements are placed between the PTFE-blocks and the WEC shaft, keeping them from contacting each other. The external damping force, F_{damp}, is exerted by the PTO-system only. Therefore, F_{damp} is represented by the power take-off force, F_{PTO}, and is proportional to $F_{springs}$, which is the normal force, F_N, exerted by the springs of the PTO-system.

Therefore, by adjusting the compression increment of the springs, dx, F_{PTO} is modified. The springs are placed in parallel, so that the total spring force, $F_{springs}$, is equal to the sum of the individual spring forces, $F_{springs,i}$.

$$F_{springs} = 4\ dx\ k_{spring} \tag{2.1}$$

where k_{spring} is the spring stiffness coefficient.

The employed compression springs have the characteristics shown in Figure 2.5. As described in Section 2.6.4.3, F_{PTO} has been tuned experimentally to achieve optimum average power absorption, $P_{av,tot,OPT}$, and varies for each of the tested wave conditions.

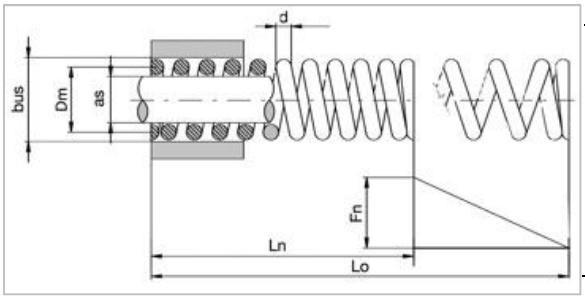

d	0.63	mm
$\boldsymbol{D_m}$	8.00	mm
$\boldsymbol{L_0}$	80.50	mm
$\boldsymbol{L_n}$	20.60	mm
Axis	6.80	mm
Bus	9.40	mm
$\boldsymbol{F_n}$	8.33	N
$\boldsymbol{k_{spring}}$	0.14	N/mm

F_n = force with fully compressed spring length (N)
k_{spring} = spring stiffness (N/mm)

Figure 2.5. Characteristics of the compression springs used for the PTO-system of the developed WEC unit.

2.2.4. Frictional forces responsible for power absorption by the WEC unit

Both F_{PTO} and the vertical frictional force due to the shaft bearings, $F_{bearings}$, are the forces taken into account for the calculation of the total power absorption of the WEC unit, $P_{av,tot}$. Therefore, it is important to know the exact characteristics of those two forces acting on the WEC buoy.

In general, the frictional force, F_{fric}, arises between solid surfaces, when these are pressed against each other. Friction characteristics of the PTO-system have been investigated experimentally during testing of the WEC unit in the tensile machine (see Section 2.5.1). The damping force, F_{damp}, represented by F_{PTO}, is a block signal with constant magnitude during the experiment, $F_{damp,A}$. A minus sign is added in Eq. (2.2) as F_{damp} has an opposite sign with reference to the buoy velocity. The WEC buoy velocity is expressed by $\dot{z}(t)$ which denotes the time derivative of the time varying heave displacement of the WEC buoy, $z(t)$.

$$F_{damp}(t) = F_{damp,A} \text{ sign } \left(\dot{z}(t)\right) \tag{2.2}$$

In general, the magnitude of a frictional force, F_{fric}, is derived from the product of the dimensionless coefficient of friction, μ, and the normal force, F_N.

$$F_{fric} = -\mu F_N \text{sign } \left(\dot{z}(t)\right) \tag{2.3}$$

where μ is the coefficient of friction.

The frictional force, F_{fric}, is parallel to the contact surface, in a direction opposite to the velocity.

By replacing F_{damp} by F_{PTO} in Eq. (2.2), also F_{PTO} is expressed as a block signal with the $F_{springs}$ (from Eq. (2.1)) magnitude as amplitude and an opposite sign compared to $\dot{z}(t)$. The resultant vertical frictional PTO force, F_{PTO}, can be modelled to a reasonable accuracy using Coulomb damping [25] as:

$$F_{PTO}(t) = -\mu F_N \text{sign } \left(\dot{z}(t)\right) \tag{2.4}$$

In the case of F_{PTO}, F_N of Eq. (2.4) is replaced by $F_{springs}$ in Eq. (2.5):

$$F_{PTO}(t) = -\mu F_{springs} \text{ sign } \left(\dot{z}(t)\right) \tag{2.5}$$

where μ is the coefficient of friction, F_N is the normal force developed by the friction brakes, and $\dot{z}(t)$ denotes the time derivative of the time varying heave displacement of the WEC buoy, $z(t)$.

In addition to F_{PTO} acting on the WEC buoy, there is also $F_{bearings}$. $F_{bearings}$ is expressed similarly to the damping force, F_{damp} of Eq. (2.2) using Coulomb damping, but this time F_N is taken to be the absolute value of the surge force, F_{surge}:

$$F_{bearings}(t) = -\mu \, abs\left(F_{surge}(t)\right) \text{ sign } \left(\dot{z}(t)\right) \tag{2.6}$$

2.3. Predicted performance of the WEC unit

2.3.1. Theoretical point absorber response with and without linear damping

The behavior of a heaving point absorber can be compared to that of a mechanical oscillator, composed of a mass-spring-damper system with one DOF, subjected to an external force in the direction of the DOF. More details can be found in the literature, e.g. [26]; [27].

As, the point absorber type WEC considered here, is restricted to heave motion only, the equation of motion for the WEC buoy is obtained using linear theory under the assumption of small buoy motions:

$$m\frac{d^2z(t)}{dt^2} = F_{ex} + F_{rad} + F_{res} + F_{PTO} \tag{2.7}$$

where m is the mass of the WEC buoy and $z(t)$ is the time varying buoy heave displacement from its equilibrium position. F_{ex} is the exciting wave force due to incident waves, which equals the sum of (i) the Froude-Krylov force and (ii) the diffraction force. The first component of F_{ex} - (i) - is the force experienced by the heaving WEC buoy as if there was no disturbance of the incident wave field by the WEC. The second component of F_{ex}- (ii) - is linked to the diffraction problem: when the WEC buoy is held stationary, diffraction of the incident wave field is caused in front of and in the lee of the buoy.

$F_{rad}$is the radiation force due to the WEC buoy heave motion. It is associated with the radiation problem, concerning the hydrodynamic pressure field that arises when a buoy is forced to move in a harmonic oscillation in initially still water. It can be decomposed into two terms as shown in Eq. (2.8), which applies to cases of harmonic oscillation of the buoy with the frequency, ω, under regular waves:

$$F_{rad} = -m_\alpha(\omega)\frac{d^2z(t)}{dt^2} - b_{hyd}(\omega)\frac{dz(t)}{dt} \tag{2.8}$$

where $m_\alpha(\omega)$ is the added mass and $b_{hyd}(\omega)$ is the added damping.

F_{res} from Eq. (2.7) is the hydrostatic restoring force and is equal to the Archimedes force, F_{arch}, minus the gravity force, F_g:

$$F_{res} = F_{arch} - F_g = \rho_w V_{subm}(t)g - mg = -kz(t) \tag{2.9}$$

where ρ_w is the water density, $V_{subm}(t)$ is the instantaneous submerged buoy volume and g is the acceleration due to gravity. The linear spring constant or hydrostatic restoring coefficient k is expressed as:

$$k = \rho_w g A_w = \rho_w g \left(\frac{\pi D^2}{4} - w_s^2 \right) \tag{2.10}$$

where A_w, D and w_s are the water-plane area, the diameter of the WEC buoy and the width of the square hole where the WEC shaft passes through, respectively.

F_{PTO} from Eq. (2.7) is the force applied to the buoy by the PTO-system. In its simplest form, this force is modeled by a pure linear damping term $-b_{ext}\dot{z}(t)$, where b_{ext} is the damping coefficient and $\dot{z}(t)$ the time derivative of $z(t)$. However, an additional stiffness term $-k_{ext}z(t)$ and an additional inertia term $(-m_{sup}(d^2z(t)/d^2t))$, where m_{sup} is the supplementary mass) can also be added to allow reactive or phase control. By using such an approach, the natural angular frequency of the buoy, ω_n, can be tuned to the principal angular frequency, ω, of the incident waves. Phase control is not considered within this PhD research.

By substituting Equations (2.8) and (2.9) for F_{rad} and F_{res} into Eq. (2.7) and by rearranging, the following form of the equation of motion is obtained for a harmonically moving buoy with ω:

$$\begin{aligned} \big(m + m_\alpha(\omega)\big) \frac{d^2z(t)}{dt^2} + b_{hyd}(\omega) \frac{dz\,(t)}{dt} + kz(t) \\ = F_{ex}(\omega, t) + F_{PTO} \end{aligned} \tag{2.11}$$

All the parameters, except F_{PTO}, are dependent on the buoy geometry, while m_α, b_{hyd} and F_{ex} also depend on the angular frequency of the incident wave, ω, and F_{ex} is directly proportional to the wave amplitude, a_w.

It should be noted that Eq. (2.11) is solved for the steady-state oscillatory response of the WEC buoy subject to an incident sinusoidal wave of angular frequency ω, or an external sinusoidal force of frequency ω in no waves (the latter being the radiation problem). That is, Eq. (2.11) is essentially the frequency-domain (as opposed to time-domain) equation of motion.

The frequency-domain panel method WAMIT [20] has been used first to obtain the hydrodynamic coefficients $m_\alpha(\omega)$, $b_{hyd}(\omega)$, k (expressed as in Eq. (2.8) and (2.10)) and $F_{ex}(\omega, t)$, and then to solve Eq. (2.11) for the time varying WEC buoy heave displacement (or else *WEC response*), $z(t)$.

In Figure 2.6, curves (a) and (b) show the predicted (undamped, i.e. F_{PTO} = 0) amplitude of the WEC buoy heave displacement, z_A, which has been normalized by the unit amplitude of the incident wave, a_w, (z_A / a_w, termed the response amplitude operator (abbreviated as *RAO*)). RAO is plotted against the incident angular wave frequency, ω, for two different water depths, d_w = 0.61 m and d_w = 0.70 m,

respectively. The RAO reaches a maximum at resonance, when the incident wave frequency ω is approximately equal to the natural frequency of the WEC buoy, ω_n (or in wave periods: when wave period $T \approx T_n$, where T_n is the natural period of the WEC). For higher wave frequencies, ω (i.e. $\omega > \omega_n$, or else, for shorter wave periods with $T < T_n$, RAO approaches zero. This is because the WEC is not able to follow the excitation, since the exciting force, F_{ex}, varies too rapidly compared to ω_n. For lower wave frequencies, ω, (i.e. $\omega < \omega_n$, or else for longer wave periods, with $T > T_n$), RAO approaches the asymptote RAO = 1 and the WEC buoy just moves with the waves.

In Figure 2.6, curves (c) and (d) show the predicted (damped, i.e. $F_{PTO} = -b_{ext}\dot{z}(t)$) RAO, plotted against the incident wave frequency, ω, for two different water depths, d_w = 0.61 m and d_w = 0.70 m, respectively. In WAMIT, the damping coefficient, b_{ext}, is taken to be constant and has the same value for both water depths. This selected value of b_{ext} is 6.5 kg/s, close to the optimum b_{ext} value (for maximum power production) at the resonance frequencies for both water depths. Note how the RAOs are reduced in the damped cases compared to the undamped cases.

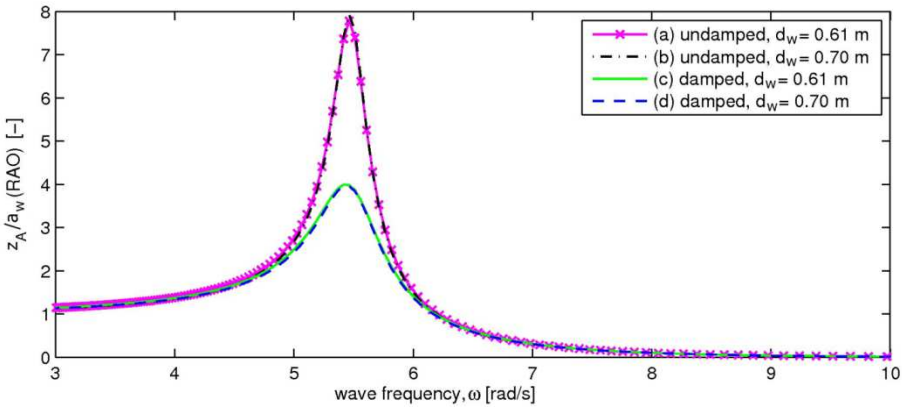

Figure 2.6. Numerically obtained amplitude of the buoy heave displacement, z_A, per unit wave amplitude, a_w, (z_A/a_w termed as RAO) as a function of the incident angular wave frequency, ω, for both the undamped and damped cases, and for water depths, d_w = 0.61 m and d_w = 0.70 m. For the damped cases, b_{ext} = 6.5 kg/s [28].

Figure 2.7 shows the corresponding predicted average power outputs P_{av} for the two damped WEC responses presented in Figure 2.6. The amplitude of the incident wave, a_w = 0.05 m, and P_{av} is calculated using Eq. (2.12):

$$P_{av} = \frac{\omega^2 {a_W}^2 {z_A}^2 b_{ext}}{2} \tag{2.12}$$

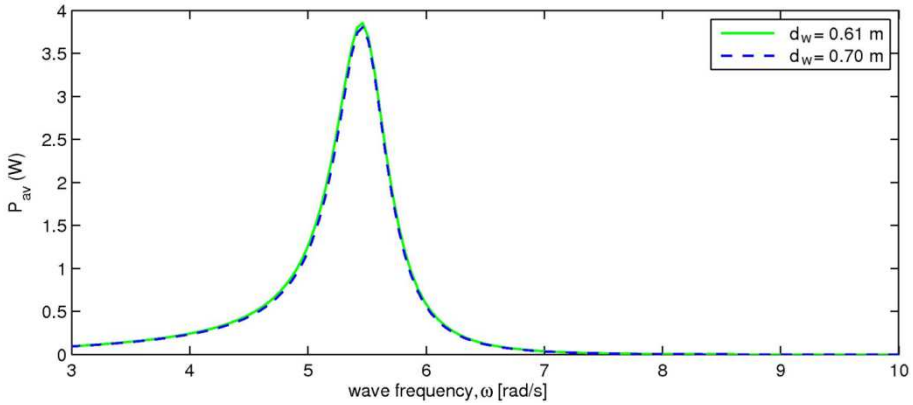

Figure 2.7. Numerically obtained average power absorption P_{av} as a function of the incident angular wave frequency, ω, for water depths, d_w = 0.61 m (solid line) and d_w = 0.70 m (dashed line), and for an incident wave amplitude, a_w = 0.05 m (b_{ext} = 6.5 kg/s) [28].

In both Figures 2.6 and 2.7, the results for the two different water depths (d_w = 0.70 m and 0.61 m) are almost exactly the same. WAMIT is a linear code and it solves for the problem around the equilibrium position of the WEC buoy, i.e. it solves for small oscillations of the buoy. Therefore, in the limit of small incident wave amplitude (and small wave steepness) WAMIT provides almost the exact result. That is, for small incident wave amplitudes, the WEC buoy response amplitude would be almost the same for both water depths, also at resonance (the RAOs reach approximately the same maximum values).

However, when the amplitude of the incident wave is large, then the RAOs would predict a large response amplitude of the WEC buoy. In this case, the motion of the WEC buoy will be influenced by the wave basin bottom. However, a large response amplitude of the WEC buoy is nonlinear and does not take into account nonlinear effects, such as viscous damping etc. Hence the WAMIT solution would not be valid for the case of large response amplitude of the WEC buoy, and thus for large amplitudes of the incident waves.

2.3.2. Linear natural frequency of the WEC unit

The predicted linear natural frequency, ω_n, of the WEC unit can be obtained from WAMIT results, by finding the ω which satisfies Eq. (2.13):

$$\omega = \sqrt{\frac{k}{m + m_\alpha(\omega)}} \tag{2.13}$$

where it should be noted that m_α is a function of ω, as well. For example, this could be achieved by finding the ω which minimizes $abs\big(\omega(m + m_\alpha(\omega) - k/\omega)\big)$. To obtain an estimate from experiments, of the natural frequency of the buoy, ω_n, a "free" decay test (termed as "*free*" because no damping is applied) can be performed. This "free" decay problem can be approximately modeled by Eq. (2.11) with no wave excitation term and no PTO force (i.e. F_{ex} = F_{PTO} = 0). The WEC response, $z(t)$, of the resulting under-damped, homogeneous system has the following solution:

$$z(t) = z_{Af}\exp(-\zeta_d\omega_n t)\sin\big(\omega_d t + \beta_f\big) \tag{2.14}$$

which represents an exponentially decaying oscillation. As seen later in this chapter, the damped natural frequency, ω_d, and the damping parameter, ζ_d, have been determined using experimental measurements. Once these parameters have been determined, a good estimate for the linear natural frequency, ω_n, can be obtained, as ω_d and ω_n are related by Eq. (2.15):

$$\omega_n = \frac{\omega_d}{\sqrt{1 - {\zeta_d}^2}} \tag{2.15}$$

However, it should be pointed out that the use of the homogeneous version of Eq. (2.11) to solve the "free" decay response is not exactly correct. This is because this problem is a transient problem, and as a result its solution comes from solving the time-domain equation of motion. The time-domain equation of motion is obtained by taking the inverse Fourier transform of the frequency-domain equation of motion and it has the following form:

$$\begin{aligned}\big(m + m_\alpha(\infty)\big)\frac{d^2z(t)}{dt^2} + \int_0^t k_{rad}(\tau - t)\,\dot{z}(\tau)\,dt + kz(t) \\ = F_{ex}(t) + F_{PTO}(t)\end{aligned} \tag{2.16}$$

where $m_\alpha(\infty)$ is the added mass at infinite frequency and $k_{rad}(t)$ is the radiation impulse response function. During the evaluation of the WEC unit within this PhD research, frequency-domain modelling has been used for the WEC unit.

2.3.3. Realistic numerical modelling of the frictional forces acting on the WEC buoy

Modelling the $F_{PTO}$and $F_{bearings}$ by using a linear damping term such as $-b_{ext}\dot{z}(t)$ (Section 2.3.1) is not ideal for the friction based PTO-system presented here. Instead, a far more accurate approach would be to use a Coulomb damping model based on Eqs. (2.4) and (2.6), to model F_{PTO} and $F_{bearings}$, respectively.

For a sinusoidal incident wave, F_{surge} of Eq. (2.6), is also sinusoidal and can be predicted by WAMIT. Figure 2.8 shows the surge force, $F_{surge}(t)$ and the heave force, which is the excitation force as predicted by WAMIT ($F_{ex}(t)$), for an incident sinusoidal wave with period T = 1.100 s and water depth of d_w = 0.61 m. Both forces have been normalised by the amplitude of the heave force. Therefore Figure 2.8, shows how much greater the surge force is than the heave force. In Figure 2.8, the free surface elevation at the WEC buoy is also indicated, normalised by its amplitude. In this way, the phase difference is illustrated, between the surge force, $F_{surge}(t)$, the heave force $F_{ex}(t)$ and the wave elevation, $\eta(t)$.

Since F_{PTO} and $F_{bearings}$, modeled using Eqs. (2.4) and (2.6), respectively, are nonlinear forces, it is not possible to use them in a frequency-domain analysis. Instead, they must be added to the time-domain equation of motion (Eq. (2.16)) and numerical solutions sought for that equation. However, here, only frequency-domain modelling is used for the WEC unit.

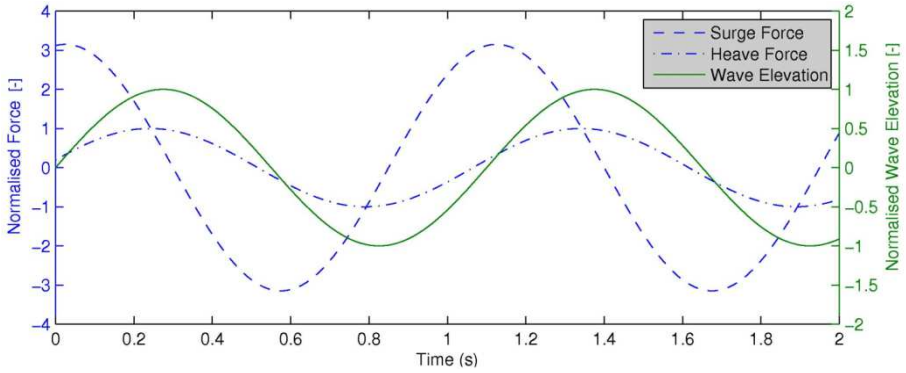

Figure 2.8. Numerically predicted surge force, F_{surge}, (dashed line) and heave force, F_{ex}, (dashed-dotted line) on the WEC unit, as a function of time for an incident sinusoidal wave with period T = 1.100 s, wave amplitude a_w = 0.05 m and water depth d_w = 0.61 m. Both forces are normalised by the amplitude of the heave force. The corresponding wave elevation at the buoy, normalised by its amplitude, is also shown (solid line) for comparison between the relative phases of the forces and the wave elevation [28].

2.4. Evaluation of the WEC unit

2.4.1. Deployment methodology of the WEC unit(s)

Since the developed WEC unit is intended for use in large WEC array configurations, the ease of rearranging multiple WEC units in the wave flume/basin is a crucial factor, influencing the time to setup each array geometric configuration. The ability to add or remove WECs in an array in a very short time is advantageous, since the granted testing period had a fixed start and end date.

Moreover, to provide sufficient rigidity of the supporting WEC shaft, it is necessary to fix the WEC shaft at both ends (at the metal base, at the bottom part, and the top, on a metal frame). As a result, adding or removing a complete WEC unit from an array configuration is not straightforward. Therefore, an approach has been developed to deal with these time and installation issues; all slender WEC support shafts remained in place throughout the entire testing period. The "unused" WEC units are then held stationary above the water surface. In this way, by using a specific stencil of the WEC shafts, a large number of different WEC arrays can be considered in short time. For instance, a column of four WECs at longitudinal spacing between the WECs, $l = 5D$ (where D is the WEC buoy diameter), requires a stencil of four WEC support shafts at $l = 5D$. By holding the WECs stationary above the water surface, the same support structure can be employed e.g. to test pairs of WECs at l equal to $5D$, $10D$ and $15D$ and columns of two to four WEC units.

Conventionally, here a "column" of WECs refers to a number of devices oriented perpendicular to the wave generator (i.e. parallel to the wave propagation direction, $\theta = 0°$).

2.4.2. Experimental testing aims and characteristics

Experiments to evaluate the designed WEC unit have been conducted in four phases:

1. Phase 1: Friction evaluation of the WEC unit by mechanical (dry and wet) testing, conducted using an electromechanical tensile testing machine of UGent.

2. Phase 2: Evaluation of the WEC support system and the instrumentation of the WEC unit, conducted in the wave flume at UGent.

3. Phase 3: Measurement of the WEC response, $z(t)$, conducted in the 3-D wave basin of QML.

4. Phase 4: Measurement of F_{surge} on the WEC unit to estimate power absorption by the WEC. During these experiments, a first small array of 4 WEC units has been tested. This experimental research has been conducted in the wide FHR wave flume.

Flume tests at UGent and at FHR have been conducted in water depth, d_w = 0.70 m equal to the design water depth used during the large WEC array experiments in the DHI wave basin. The water depth, d_w = 0.61 m, used in the QML basin imposes a limit on the WEC response amplitude, $z(t)$ (d_w = 0.61 m is the maximum operational water depth of the QML wave basin). However, for the wave conditions considered, this would only impede the WEC buoy motion at resonance under large incident wave amplitudes (see comment in Section 2.3). The UGent wave flume, with a width of approximately $3D$, is considered to be narrow for testing the WEC unit, and as a result, reflection of radiated waves from the flume side walls may magnify or inhibit WEC response. Therefore, WEC response measurements have been obtained in the wider experimental facilities, of QML and FHR, with a width of 15.0 m and 4.0 m, respectively. For the experiments performed in QML and FHR, the waves radiated from the heaving WEC(s) located at the centerline of the wave flume/basin are expected to be of negligible amplitude when reflected back onto the WEC unit.

2.5. Experimental arrangements employed for the development and evaluation of the WEC units

2.5.1. Mechanical testing of the WEC unit

It is important to quantify friction characteristics, and the corresponding frictional forces acting on the WEC buoy, for two components of the WEC unit: (a) the PTO-system, and (b) the WEC shaft bearings, as seen in Section 2.2.4. Physical tests have been conducted to determine the non-lubricated (*dry*) and lubricated (*wet*) static, μ_s, and dynamic, μ_d, coefficient of friction between PTFE and steel. The WEC unit has been mounted to an electromechanical INSTRON 5800R tensile testing machine with a FastTrack 8800 digital controller at UGent (Department of Materials Science and Engineering), shown in Figure 2.9.

Figure 2.9. Front view of the WEC buoy in the experimental setup of the electromechanical tensile testing machine during tests at Ghent University, Belgium.

The tests have shown that the difference is negligible, between the static and dynamic frictional forces, F_{fric}, exerted by the steel surface of the WEC shaft on the PTFE surface of the PTFE-blocks (from the PTO-system shown in Figure 2.4). The value of μ was found to be strongly dependent on the environment conditions (i.e. temperature and humidity). Nevertheless, the value range found for the friction coefficient, μ, is representative of the friction characteristics between PTFE and industrial (non highly polished) steel sliding interfaces [29]. Finally, a coefficient of friction μ = 0.17 is found to provide reasonable agreement between measurement and prediction of WEC response amplitude and mean power absorption over a range of PTO spring compression increments, dx.

2.5.2. Experiments to measure the wave induced surge force on the WEC unit and the WEC response

Throughout this experimental research to evaluate the developed WEC unit, the wave induced force on the WEC unit(s) and the WEC response have been measured under regular and irregular long-crested waves (Table 2.1), for a range of wave heights, H/H_{m0}, and wave periods, T/T_p. Tests have also been performed with wave period equal to the resonance period of the WEC unit, T_n.

Table 2.1. Summary of target sea state characteristics for regular and irregular (defined by JONSWAP spectra) long-crested waves.

Wave period T/T_p (s)	**Wave frequency f/f_p (Hz)**	**Wave angular frequency ω/ω_p (rad/s)**	**Wave height H/H_{m0} (m)**		
0.800	1.250	7.854	0.050	0.074	0.100
1.000	1.000	6.283	0.050	0.074	0.100
1.050	0.952	5.984	0.050	0.074	0.100
1.100	0.909	5.712	0.050	0.074	0.100
T_n	f_n	ω_n	0.050	0.074	0.100
1.200	0.833	5.236	0.050	0.074	0.100
1.250	0.800	5.027	0.050	0.074	0.100
1.300	0.769	4.833	0.050	0.074	0.100
1.500	0.667	4.189	0.050	0.074	0.100

Several measurements have been taken during those tests. Firstly, wave elevation time series ($\eta(t)$) have been recorded, with the WEC unit(s) held stationary above the water surface, to measure the undisturbed wave field.

Furthermore, the diffracted wave field has been measured in front of, at the sides and in the lee of the WEC unit(s). For these measurements the WEC buoy is held stationary at mean draft, d_{buoy}.

The "free" WEC response, $z(t)$, has also been measured under incident waves. In this case, the external damping force exerted by the PTO-system only is zero (F_{PTO} = 0), while the vertical frictional force due to the shaft bearings, $F_{bearings}$, is non-zero.

Finally, the damped WEC response, $z(t)$, has been recorded for non-zero both F_{PTO} and $F_{bearings}$.

2.5.2.1. Individual WEC unit evaluation: wave flume of UGent

A first series of experiments has been carried out in the wave flume of Ghent University [30] for an individual WEC unit. These experiments aimed at the evaluation of the rigidity and stability of the WEC supporting shaft. As part of this testing, the horizontal displacement of the top part of the WEC shaft has been measured using an optical technique. The UGent wave flume, illustrated in Figure 2.10, is 1.0 m wide and 30.0 m long. The experimental arrangement employed, is shown in Figure 2.11.

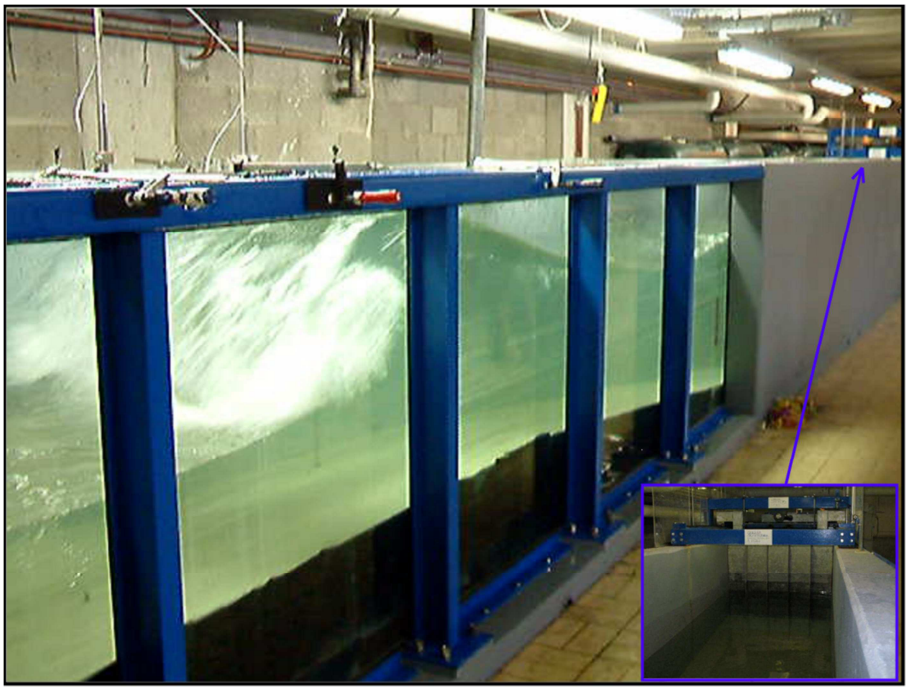

Figure 2.10. Front view of the wave paddle (down-right) and side view of the wave flume of Ghent University, Belgium.

Moreover, alternative techniques have been evaluated, for measuring the time varying WEC buoy heave displacement, $z(t)$. Within this investigation, the accuracy obtained by a camera (optical measurement technique), a potentiometer (draw wire sensor for linear displacement) and an LVDT (linear variable differential transformer) has been evaluated. For the final selection of a technique to measure $z(t)$, the combination of "*measurement accuracy - specifications of the target WEC array testing – feasibility aspects – low cost*", have been taken into account. The consideration of all these aspects is necessary, since a large number of heave displacements have to be measured simultaneously, during WEC array tests.

The WEC unit is installed at a distance of 11.60 m from the front side of the wave paddle. At the shoreward end of the wave flume, a wave absorbing gravel beach has been constructed. Two active wave absorption sensors (denoted as AWA1 and AWA2) have been installed immediately downwave of the wave paddle and are part of the active absorption system. Furthermore, 7 wave gauges (abbreviated as *WGs*) have been installed along the length of the wave flume, forming two arrays of 3 WGs used for wave reflection analysis [31], in front of the WEC unit (WGs 1-2-3) and in front of the wave absorbing beach (WGs 5-6-7), respectively. At the leeward side of the WEC unit, WG4 has been installed for registering wave field changes.

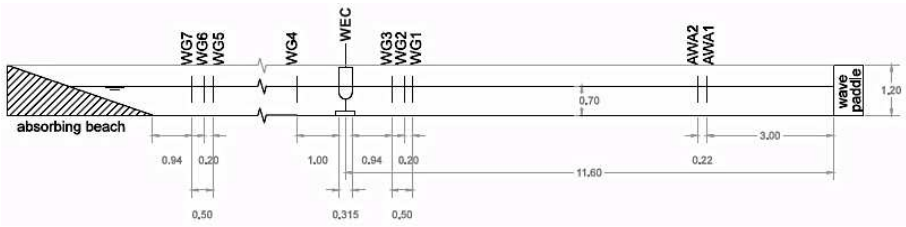

Figure 2.11. Longitudinal cross section of the wave flume of UGent, showing the experimental arrangement used for testing an individual WEC unit (all dimensions are in m).

2.5.2.2. Individual WEC unit response: wave basin of QML

Tests using similar wave conditions as in the UGent wave flume have been performed in the wave basin of Queen's University Belfast for an individual WEC unit. The first objective of this testing was to investigate the variation of $z(t)$, with the wave frequency, f. In this way, the accuracy of the WEC model (i.e. repeatability of WEC response) has been evaluated by using potentiometer measurements of $z(t)$. Furthermore, these experiments aimed at the tuning of the PTO-system, in order to maximize PTO power output in specified wave conditions.

During the testing at QML, only the frictional force applied through the PTO-system has been taken into account.

The QML wave basin is 15.0 m wide and 17.0 m long. Waves are generated along one side of the wave basin by a 12 m wide bank of 24 wave paddles (shown in Figure 2.12). Each paddle is 0.60 m high and 0.50 m wide and can move independently. The experimental arrangement used in QML is shown in Figure 2.13, with a detail shown in Figure 2.14. The water depth is uniform (d_w = 0.61 m) over a 5.25 m long bottom and subsequently slopes at 1:24 to a wave absorbing beach with water depth, d_w = 0.20 m. The beach is constructed by folded geo-textile material, to minimise longitudinal wave reflection. Absorption of directional and transverse waves is provided by means of gravel slopes. Any overtopping waves spill into the trough running along the sides of the wave basin behind the gravel slopes. The WEC shaft is located 3.08 m from the paddles at the centreline of the wave basin (Figure 2.14, left). Measurements of $z(t)$ have been taken using a potentiometer. Wave elevation time series, $\eta(t)$, have been recorded at specific locations around the WEC unit by using a network of 10 resistive WGs. Two arrays of 3 WGs arranged according to [31], have been used to collect data for wave reflection analysis at the seaward and shoreward side of the WEC unit. Moreover, 2 pairs of WGs are installed at the right and left side of the WEC (Figure 2.14).

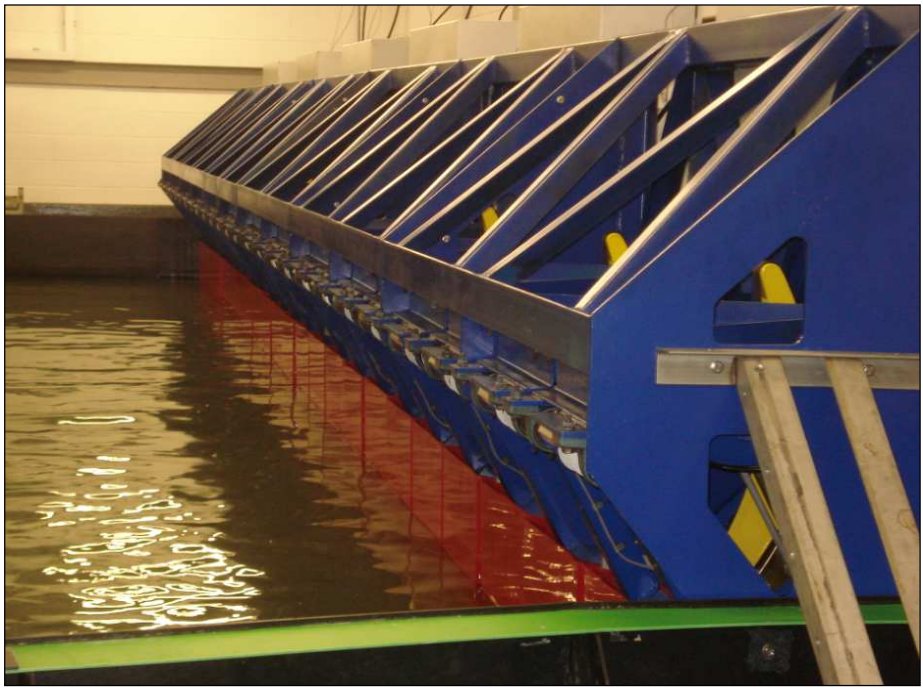

Figure 2.12. Side view of the wave paddles in the basin of Queen's University Belfast, UK.

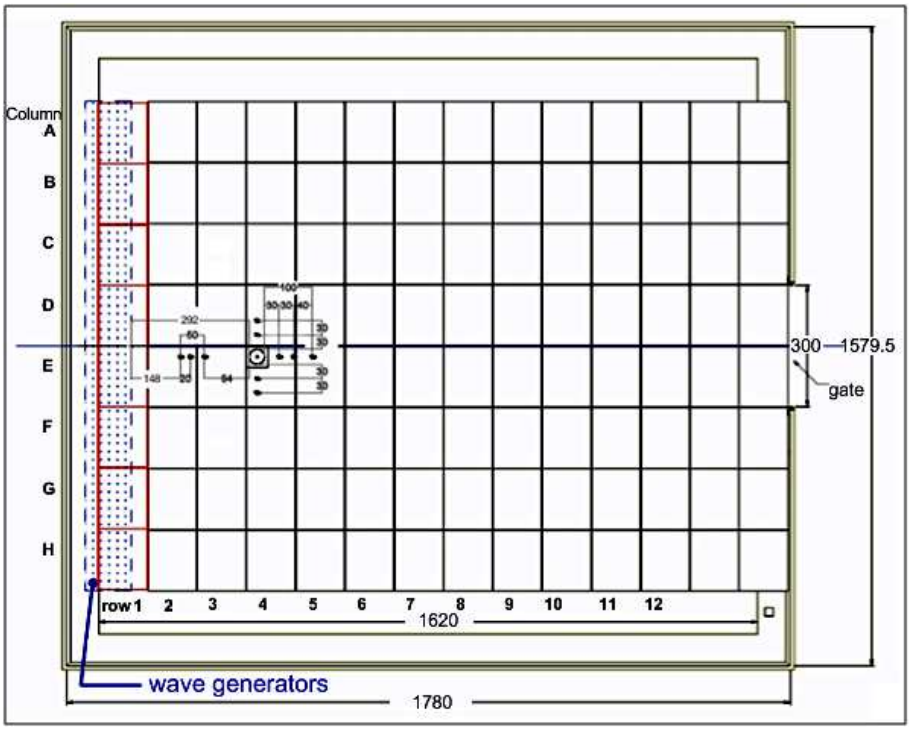

Figure 2.13. Plan view of the experimental setup employed in the wave basin of QML for testing an individual WEC unit (dimensions in cm).

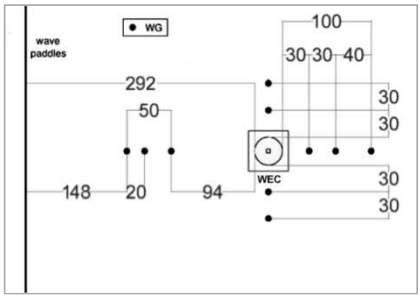

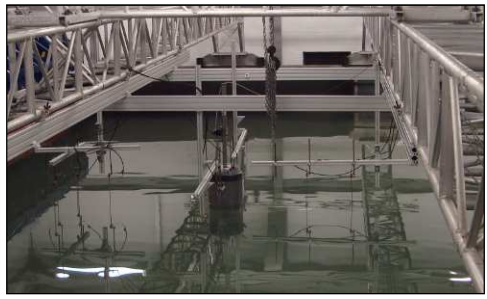

Figure 2.14. Sketch (left) and image (right) of the experimental arrangement used in QML. Waves are generated at the left side and propagate from left to the right, towards the WEC unit.

2.5.2.3. WEC response of an array composed of four WEC units: wave flume of FHR

The main objective of these experiments is to tune in detail the PTO-system for the selected wave conditions. The tuning is performed by aiming at optimum average power absorption, $P_{av,tot,OPT}$, of the WEC unit (illustrated in Figure 2.7). Both the frictional force applied through the PTO-system, F_{PTO}, and the WEC shaft bearing frictional force, $F_{bearings}$, have been taken into account during the tests at FHR for the tuning of the PTO-system.

Surge force, F_{surge}, measurements have been obtained when WEC-WEC interactions take place (intra-array interactions), using load cells. These tests have been performed for varying longitudinal spacing between the WECs, l, and number of WECs in a single array column. Moreover, both time varying WEC heave displacement, $z(t)$, and wave elevation time series, $\eta(t)$, have been recorded.

A summary of the tested WEC (array) geometric configurations is shown in Table 2.2.

Table 2.2. Summary of tested WEC (array) geometric configurations in FHR.

Geometric WEC (array) configurations	**Longitudinal spacing between WECs, l (m)**
1 WEC	-
2-WEC Column	5D
	10D
	15D
3-WEC Column	5D
4-WEC Column	5D

where D = 0.315 m, is the WEC buoy diameter.

The experiments have been conducted in a 4.0 m wide flume with d_w = 0.70 m, illustrated in Figure 2.15. The experimental arrangement employed at FHR is illustrated in Figure 2.16. The test region comprises a flat bed of 13.25 m followed by 1:35 bed-slope over a length of 24.5 m. Waves are generated on one side of the wave flume along a 4.0 m wide wave paddle. Measurements of $\eta(t)$ are taken using a network of 15 resistive WGs. Two arrays of 3 WGs arranged according to [31], are used to collect data for reflection analysis at the seaward and shoreward side of WEC #01 (Figure 2.16). Moreover, 2 pairs of WGs are installed at the right and left side of each of WECs #01 and #02, as shown in Figure 2.16. In Figure 2.17, the installation technique is presented, employed to test a small WEC array in the FHR wave flume. The developed WEC deployment technique has been described in Section 2.4.1.

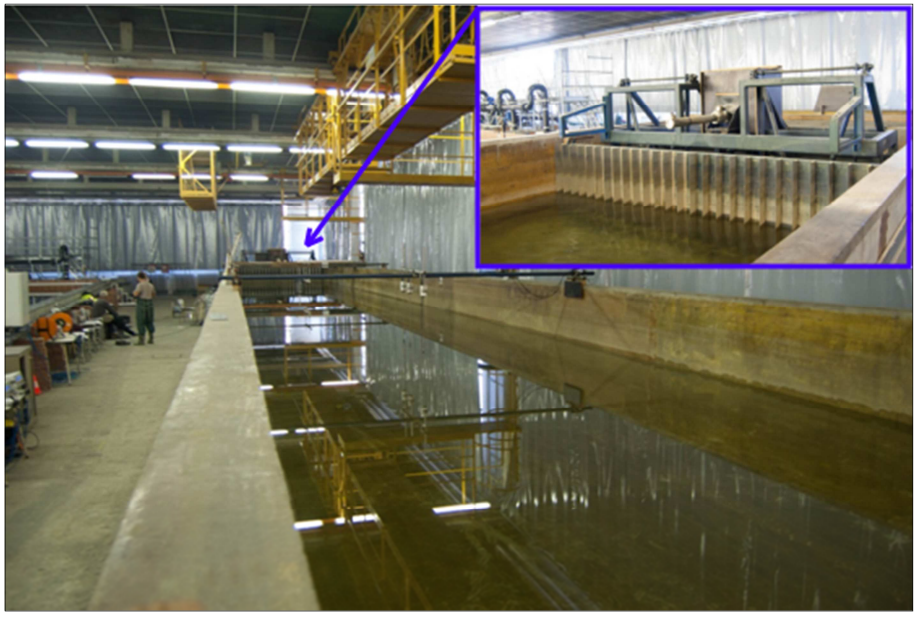

Figure 2.15. Side view of the wave paddle (upper-right) and front view of the large wave flume at Flanders Hydraulics Research, Belgium.

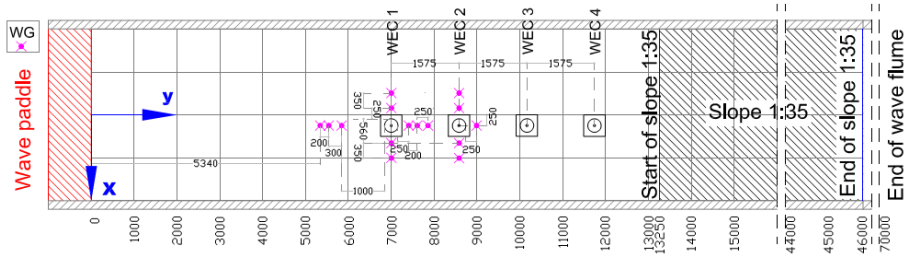

Figure 2.16. Plan view of the experimental arrangement showing the position of WEC units #01-#04 and the network of WGs used in the wave flume of FHR (dimensions in mm).

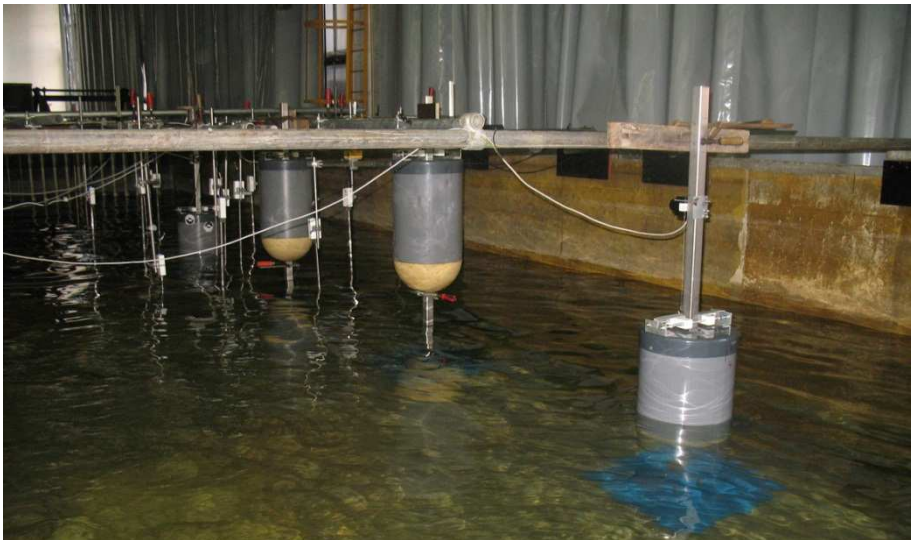

Figure 2.17. View from the flume side: an array of 4 WEC units in the wave flume of Flanders Hydraulics Research, Antwerp, Belgium. The spacing between the WEC support shafts, arranged along the direction of wave propagation, is $l = 5D$. Waves propagate towards the WECs from the rear to the front on the photo. The two WEC buoys shown in the middle of the WEC array do not interact with the waves and thus this geometric configuration represents a pair of WECs at $l = 15D$ spacing.

2.6. Main results from the experimental evaluation of the WEC units

2.6.1. Evaluation of the WEC support structure

The WEC supporting shaft should be sufficiently rigid, to ensure that the surfaces of the WEC shaft bearings and the WEC shaft, remain in contact. Moreover, the amplitude of the longitudinal, y_A, and the lateral, x_A, displacement should be limited, both for the metal base and the WEC shaft (where, y_A is parallel to the wave propagation direction). Longitudinal and lateral displacement is due to surge excitation force on the WEC unit, F_{surge}.

To confirm the rigidity of the WEC shaft, y_A has been recorded by placing a marker on the WEC shaft, at 1.50 m above the wave flume bottom (Figure 2.18). A high-resolution camera has been used for this purpose, sampling at 23.6 Hz. The video measurements have been analysed using a custom LabVIEW [32] routine. A maximum $y_{A,MAX}$ = 1.50 mm has been found when the WEC shaft is only fixed at

the bottom, while $y_{A,MAX}$ = 0.50 mm when the WEC shaft is fixed at both ends. Therefore, the latter installation technique is shown to be most suitable, allowing only very limited longitudinal displacement of the WEC shaft, y_A.

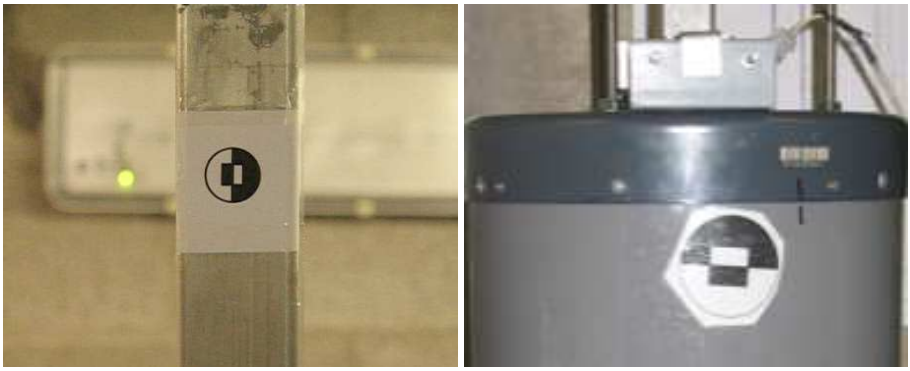

Figure 2.18. Side view of markers used for registering longitudinal displacement, y_A, of the WEC shaft (left) and the WEC buoy (right).

2.6.2. Evaluation of the measurement techniques for the WEC heave displacement

A potentiometer has been selected for recording $z(t)$, as a feasible measurement technique for use in a large number of WEC units, simultaneously. Nevertheless, since a specific measurement technique might modify the WEC buoy's behaviour, the influence of the potentiometer on the recorded $z(t)$ and of alternative instrumentation has been investigated. In Figure 2.19, results are presented of the effect of the potentiometer on the measured time varying WEC buoy heave displacement, $z(t)$. Two different techniques are shown in Figure 2.19, for given incident wave conditions: the solid line shows video camera results for $z(t)$ with the potentiometer connected to the WEC buoy, while the dotted line provides camera results for $z(t)$ without the potentiometer connected to the WEC buoy. The camera does not affect the recorded $z(t)$, since there is no contact with the WEC buoy. The acquisition frequency of the camera measurements shown in Figure 2.19 is 60 Hz. The presented results confirm that the effect of the potentiometer on the recorded $z(t)$ is small. Figure 2.20 shows an example of a comparison between the measured $z(t)$ by using a video camera and the measured $z(t)$ by using LVDT. The acquisition frequency of the camera data shown in Figure 2.20 is 23.6 Hz. The presented results confirm that the camera and the LVDT deliver almost the same accuracy of the recorded $z(t)$. Therefore, taking into account the $z(t)$ results presented in Figure 2.19 and 2.20, the effect of the potentiometer on the recorded $z(t)$ is considered to be small, compared to the $z(t)$ measurements obtained using the LVDT.

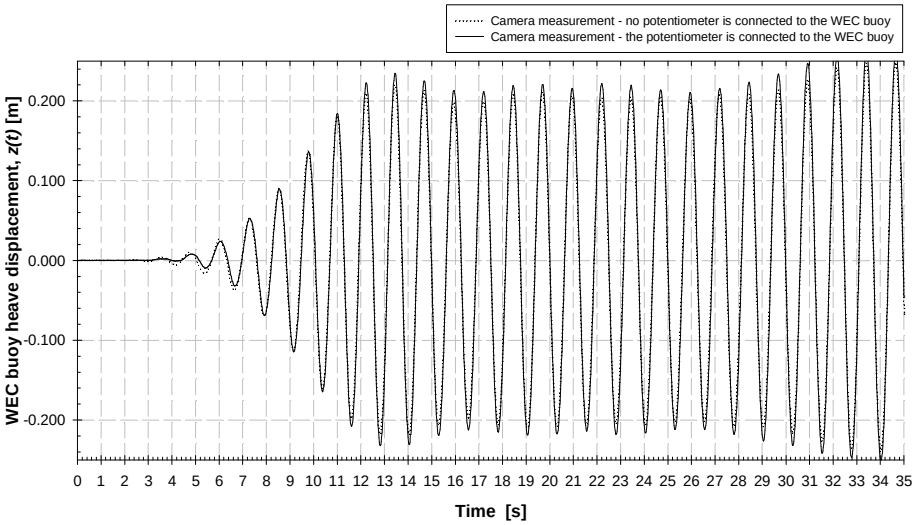

Figure 2.19. Time variation of $z(t)$, measured using video camera (acquisition frequency: 60 Hz) for 2 cases: with (solid line) and without (dotted line) the potentiometer connected to the WEC buoy. Wave conditions: H = 0.100 m – T = 1.250 s – d_w = 0.70 m [28].

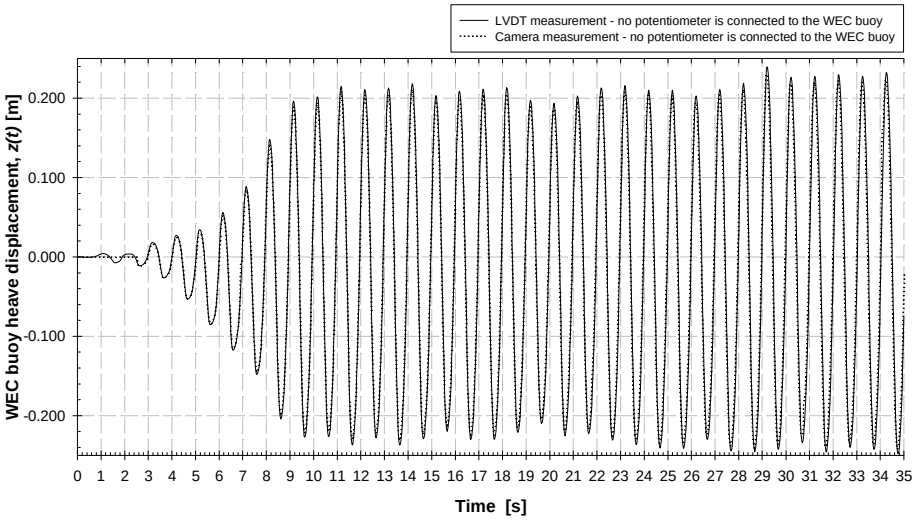

Figure 2.20. Time variation of $z(t)$, measured using high speed (acquisition frequency: 23.6 Hz) video camera (dotted line) and an LVDT (solid line). For both measurements, no potentiometer is connected to the WEC buoy. Wave conditions: H = 0.100 m – T = 1.000 s – d_w = 0.70 m [28].

These tests have shown that the effect of the selected potentiometer on the measured $z(t)$ is small. The use of an LVDT or a camera does not offer a significant advantage in the obtained precision of $z(t)$ measurements. Finally, the LVDT or the camera techniques do not offer a practically and economically feasible solution for measuring the $z(t)$ of a large number of WEC units simultaneously.

2.6.3. Free decay test of the WEC unit

A "free" decay test yields a first estimation of the hydrodynamic behaviour of the WEC unit, allowing derivation of the natural angular frequency, ω_n, and the damping factor, ζ_d (see Eqs. (2.14) - (2.15)). During a "free" decay test (i.e. no external damping force is applied through the PTO-system), the WEC buoy is released from a non-equilibrium position in otherwise quiescent water and subsequently undergoes an oscillatory response of decaying amplitude to return to its equilibrium position. The time series of the decaying buoy position (or else "*the decay curve*") has been measured using a camera and presented in Figure 2.21. From the decay curve of Figure 2.21, the damping factor, ζ_d, is obtained using Eq. (2.17):

$$\Lambda = \ln\frac{X_1}{X_2} = \frac{1}{n-1}\ln\frac{X_1}{X_n} = \frac{2\pi\zeta_d}{\sqrt{1-{\zeta_d}^2}} \tag{2.17}$$

where X_1 and X_n are the amplitudes of the first and n^{th} oscillation respectively, and Λ is the logarithmic increment. For the calculations of Table 2.3, n = 10.

The natural frequency, ω_n, is obtained from Eq. (2.15) using the ζ_d value derived from Eq. (2.17).

Other parameters which describe the underdamped system are the critical damping coefficient, b_c, (Eq. (2.18)) and the damping coefficient, b_d. These are related to the damping factor, ζ_d, by Eq. (2.19).

$$b_c = 2m\omega_n = 2\sqrt{km} \tag{2.18}$$

$$\zeta_d = \frac{b_d}{b_c} \tag{2.19}$$

The WEC unit is an underdamped system, as the damping factor, ζ_d, is smaller than unity.

Measured and calculated characteristics of the underdamped WEC unit for a decay test are given in Table 2.3. The experimentally measured characteristics have derived from a frequency domain analysis of the "free" oscillation of the WEC buoy using LabVIEW [32]. Then, using Eqs. (2.17), (2.18) and (2.19), ζ_d, b_c and b_d, have

been calculated, respsectively. The amplitude of the "free" WEC response, z_{Af}, and the phase angle, β_f, have been calculated using the angular frequencies, ω_n and ω_d, the damping factor, ζ_d, and the initial conditions of the system, namely the initial position q_0 and the initial velocity $\dot{q}_0$:

$$z_{Af} = \sqrt{q_0^2 + (\dot{q}_0 + \zeta_d \omega_n q_0)^2 \cdot \frac{1}{\omega_d^2}} \tag{2.20}$$

$$\beta_f = \arctan \frac{q_0}{\frac{1}{\omega_d} \cdot (\dot{q}_0 + \zeta_d \omega_n q_0)} \tag{2.21}$$

where in the decay test, q_0 and $\dot{q}_0$ *are* the initial position and velocity of the WEC buoy, respectively, and β_f, is the phase angle of the "free" WEC response.

Based on the damping in the system, the oscillations fade exponentially and eventually disappear after a certain time. The envelope can be described using:

$$z_e(t) = z_{Af} \cdot \exp(-\zeta_d . \omega_n . t) \tag{2.22}$$

Table 2.3. Measured and calculated characteristics of the underdamped WEC unit for a decay test in the wave flume of UGent.

Experimentally measured characteristics					
Parameter	*Value*	*Units*	*Parameter*	*Value*	*Units*
q_0	134.040	mm	z_{Af}	134.080	mm
$\dot{q}_0$	0.000	mm/s	ω_d	5.344	rad/s
X_1	126.100	mm	T_n	1.176	s
X_n	30.500	mm	f_n	0.850	Hz
Calculated characteristics					
Parameter	*Value*	*Units*	*Parameter*	*Value*	*Units*
ζ_d	0.023	-	b_c	219.6	kg/s
b_d	4.96	kg/s	β_f	-1.55	rad

Figure 2.21 shows the decayed WEC response from an initial position, q_0 = -134 mm. During the decay test, the buoy oscillates with the damped natural frequency, ω_d = 5.343 rad/s which results in a natural period, T_n = 1.176 s.

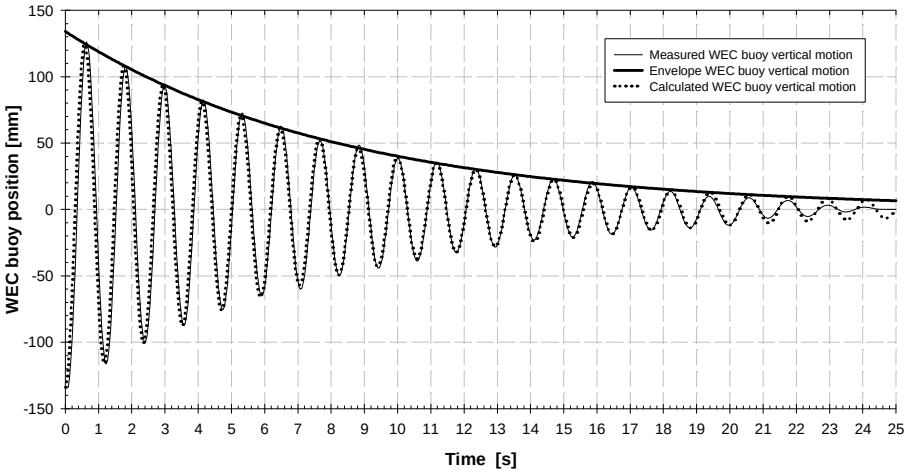

Figure 2.21. Time series of the WEC buoy position, relative to its equilibrium position during a decay test: (a) the solid oscillating line gives the time series of the decaying buoy position, as measured using a camera; (b) the dotted oscillating line shows the theoretically calculated decaying buoy position using Eq. (2.14); and, (c) the thick solid line is the theoretically calculated envelope using Eq. (2.22) [28].

The agreement between the measured T_n (= 1.176 s) and the theoretically derived value, $T_{n,WAMIT}$ = 1.143 s, is good, considering the shortcomings of the numerical model (2.9 % deviation of the numerically with regard to the experimentally derived value of T_n). A very good fit is observed between the time-history of measured response and theoretical predictions. Agreement deteriorates slightly at the end of the "free" oscillation, as the amplitude of the heave buoy displacement, $z_{A,}$ becomes small and more difficult to measure accurately with the employed instrumentation. Subsequently, this estimate of natural period T_n is used as the incident wave period, T, during the experimental testing to measure z_A, F_{surge}, and wave elevations, when the WEC unit is at resonance.

2.6.4. Response of the WEC unit under wave action

2.6.4.1. WEC buoy heave displacement

The WEC buoy heave displacement, $z(t)$, has been recorded for regular incident waves of period 1.0 s < T < 1.3 s. No external damping force, F_{PTO}, is applied on the WEC unit and so this is referred to as "free" WEC response. However, the WEC shaft bearing frictional force is non-zero. The amplitude of the WEC buoy heave displacement, z_A, is determined based on a steady-state interval. An example is given in Figure 2.22 for which a response amplitude, z_A = 13.27 cm is obtained over an interval t > 15 s. Less than 2.0 % variation of z_A has been observed between repetition of these WEC responses under regular waves.

The amplitude of the WEC heave displacement, z_A, has been measured both in the UGent wave flume (water depth, d_w = 0.70 m) and in the QML wave basin (water depth, d_w = 0.61 m). Moreover, the obtained z_A measurements have been compared to numerical predictions (Figure 2.23). No PTO force, F_{PTO} has been applied (therefore b_{ext} = 0.0), and RAO is plotted against the incident angular wave frequency, ω. The difference between the measured WEC response in the QML basin and the UGent flume is the result of a number of parameters. Firstly, the WEC shaft was fixed at both ends in QML, while the WEC shaft in the UGent wave flume was only bottom fixed. Secondly, the friction of the WEC shaft bearing had different characteristics between the different tests, due to lack of maintenance of the WEC shaft and bearings. This essential maintenance procedure has been identified as necessary only later, during the WEC evaluation experiments at the FHR wave flume. Away from resonance conditions, the magnitudes of the RAOs are similar. However, around the resonance frequency of the WEC unit, ω_n, both the z_A and the WEC buoy heave velocity, $\dot{z}(t)$, expressed as the time derivative of $z(t)$, become large. Therefore in resonance conditions, non-linear effects take place, responsible for the less good agreement between the experimental and numerical RAO results. Most importantly, the damping of the WEC's motion caused by $F_{bearings}$ has not been taken into account on the numerical model. Therefore, the discrepancy between the RAO results from the numerical and the experimental model indicates the importance of $F_{bearings}$.

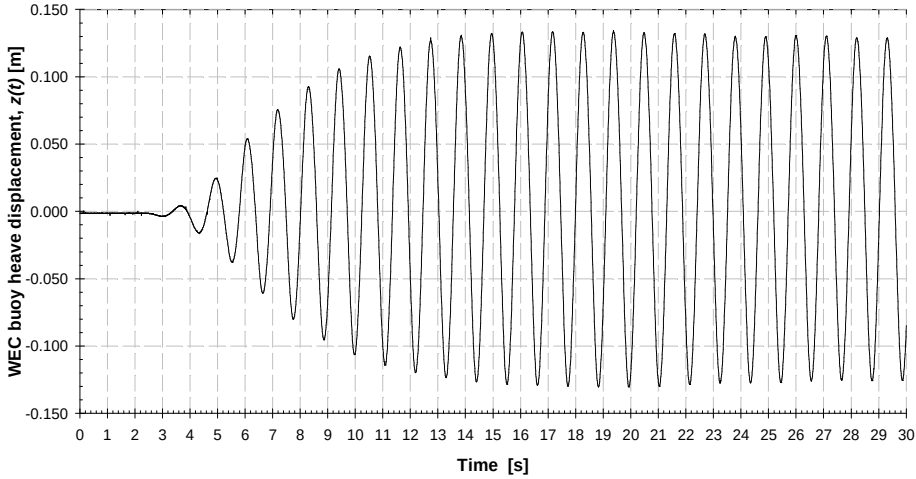

Figure 2.22. Time series of WEC buoy heave displacement, $z(t)$, for regular waves during tests in the wave basin of QML (H_i = 0.100 m – T = 1.100 s – d_w =0.61 m).

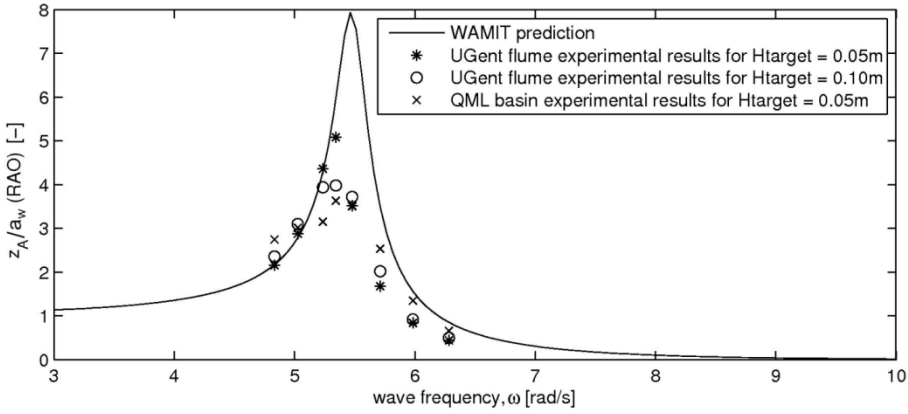

Figure 2.23. Numerically predicted and experimentally measured RAOs without external damping force, F_{PTO}, as a function of the angular wave frequency, ω. The water depth, d_w , is 0.70 m at UGent wave flume and 0.61 m at the QML wave basin and regular waves have been generated: wave height, H = 0.050 m ("*" symbols – UGent flume results; "x" symbols – QML basin results) and wave height, H = 0.100 m ("o" symbols – UGent flume results) [28].

2.6.4.2. Wave induced surge force on the WEC unit(s)

In Figure 2.24, a comparison between numerical and experimental results is presented, for the amplitude of the wave induced surge forces, $F_{surge,MAX}$, exerted on an individual WEC unit, plotted against the wave angular frequency, ω. The surge forces of Figure 2.24 have been measured for target wave height H_{target} = 0.074 m and are normalised by the recorded wave heights, H. Measurements of the total wave height, H_{total}, have been taken at the WG upwave of WEC #02, shown in Figure 2.16. The array of 3 WGs upwave of WEC #02 provides the incident wave height, H_i, by performing a reflection analysis according to [31]. For all wave periods considered (Table 2.1 for H = 0.074 m), reasonable agreement is observed between the experimental measurements and numerical predictions by WAMIT. The values of F_{surge} are calculated in WAMIT for a unit incident wave amplitude, a_w = 1.0 m. However, there is increasing disparity between measurement and prediction of F_{surge} close to the natural frequency of the WEC, ω_n. This occurs due to the large change of instantaneous immersion of the WEC buoy during a wave-cycle, which contradicts the zero-displacement amplitude assumption employed in the WAMIT analysis.

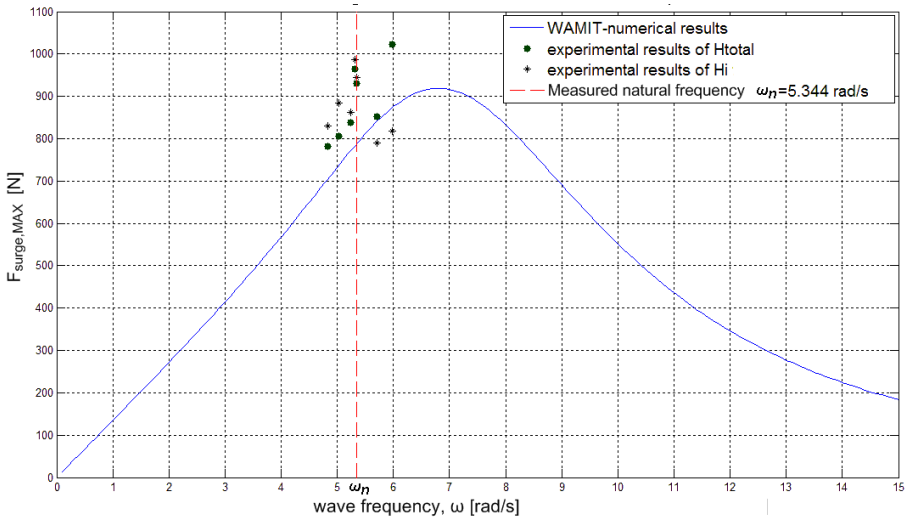

Figure 2.24. Maximum value of surge force, $F_{surge,MAX}$, for wave amplitude, a_w = 1.0 m, as a function of the angular frequency, ω, for water depth, d_w = 0.70 m and regular waves. Solid line: WAMIT numerical results; Solid circles "●": experimental results for H_{total}; Stars "*": experimental results for H_i; The vertical dashed line indicates the undamped ω_n on the horizontal graph axis, which is the experimentally derived natural frequency of the WEC [28].

In Figure 2.25, the variation of the measured surge force, F_{surge}, on WEC #02 is presented for three (array) geometric configurations: a) WEC #02 heaves as an individual WEC, b) WECs #01 and #02 heave simultaneously, and c) WECs #01, #02 and #03 heave simultaneously. No damping is applied through the PTO-system on the WEC's heave motion. A filter is applied to obtain the amplitude of F_{surge}. Differences in the measured magnitude of F_{surge} and in the shape of the F_{surge} signal on WEC #02 appear due to hydrodynamic interaction between the WECs. However, these discrepancies are a small percentage of the surge force amplitude and the phase is not substantially altered. Therefore the method described in Section 2.2.4 for calculating $F_{bearings}$ is applicable.

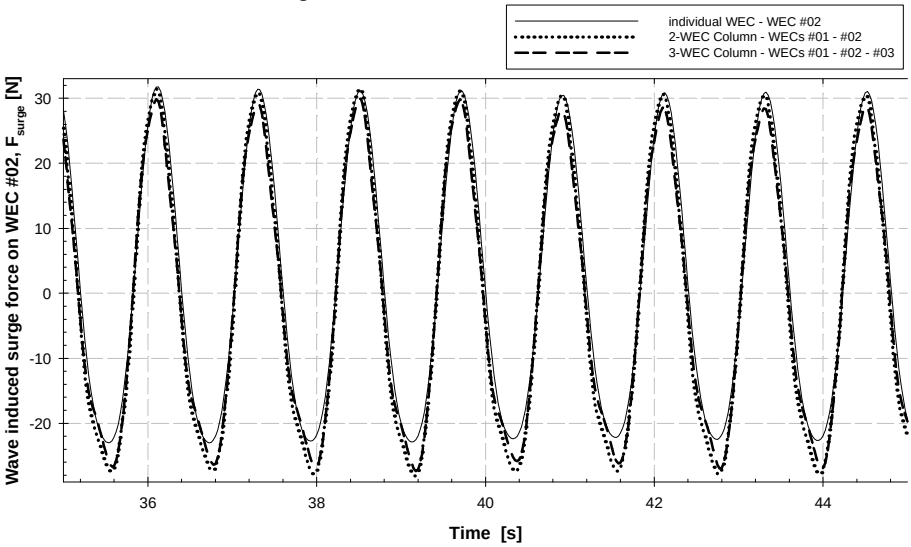

Figure 2.25. WEC-WEC interaction (intra-array interactions) expressed by the time variation of the measured filtered surge force, F_{surge}, on WEC #02 for three (array) geometric configurations: a) WEC #02 heaves as an individual WEC unit (solid line), b) WECs #01 and #02 heave simultaneously (dotted line), and c) WECs #01, #02 and #03 heave simultaneously (dashed line). No damping is applied through the PTO-system on the WECs' heave motion (H_i = 0.074 m – T = 1.176 s – d_w = 0.70 m) [28].

2.6.4.3. Calculation of the absorbed wave power by the WEC unit

This PhD research addresses the development of a WEC unit to study the effect of wave energy extraction by WEC arrays on the wave field. However, it remains important to maximise (optimize) power output for the individual WEC units in order to cause measurable wave field changes in the vicinity of WEC arrays. The

total damping force, $F_{damp,tot}$, consists of two components: F_{PTO} and $F_{bearings}$, as seen in Section 2.2.4. The net total damping force, $F_{damp,tot}$, is therefore time varying and can be expressed as:

$$\begin{aligned} F_{damp,tot}(t) = \; & F_{PTO}(t) + F_{bearings}(t) \\ & = -\mu \left(F_{springs} + \text{abs}\big(F_{surge}(t)\big)\right) \text{sign}\left(\dot{z}(t)\right) \end{aligned} \tag{2.23}$$

Thus, net power absorption, P_{tot}, is therefore obtained as:

$$\begin{aligned} P_{tot}(t) = \; & P_{PTO}(t) + P_{bearings}(t) = -\dot{z}(t)F_{PTO}(t) - \dot{z}(t)F_{bearings}(t) \\ & = -\dot{z}(t)\left(F_{PTO}(t) + F_{bearings}(t)\right) \\ & = \dot{z}(t)\mu\big(F_{springs} + \text{abs}\big(F_{surge}(t)\big)\big)\text{sign}\left(\dot{z}(t)\right) \\ & = \dot{z}(t)\mu\big(4dxk_{spring} + \text{abs}\big(F_{surge}(t)\big)\big)\text{ sign}\left(\dot{z}(t)\right) \end{aligned} \tag{2.24}$$

Experiments have been conducted to measure the time variation of surge force, F_{surge}, and $\dot{z}(t)$, for a range of spring compression increments, dx. Subsequently, by these experiments, the value of dx is obtained (and hence of F_{PTO}), required to maximise the average power output by both PTO-system and the WEC shaft bearings. F_{surge} and $\dot{z}(t)$, are out-of phase, which is also experimentally observed in Figure 2.26. The measured surge force, F_{surge}, also exhibits high frequency fluctuations indicating a small amplitude oscillation of the WEC buoy around the WEC supporting shaft. A Butterworth low-pass filter [33] is applied to obtain the amplitude of the first order component of the surge excitation force, for comparison to numerical predictions and for evaluation of time-averaged absorbed power.

The total time-averaged power, $P_{av,tot}$, absorbed by both the PTO-system and the WEC shaft bearings is obtained from the mean of Eq. (2.24) for a range of spring compression increments, dx. The resultant variation of absorbed power for an individual WEC unit is shown in Figure 2.27. Time averaged power due to the PTO-system only, $P_{av,PTO}$, increases with spring compression increment, dx. As $F_{springs}$ (and thus F_{PTO}) increases, the WEC response amplitude, z_A, and consequently the amplitude of the time derivative of $z(t)$, $\dot{z}_A$, are reduced, and therefore $P_{av,PTO}$ will reach a maximum. Time averaged power due to the WEC shaft bearings, $P_{av,bearings}$, is maximum when dx = 0, since this corresponds to maximum WEC buoy velocity, expressed by the maximum $\dot{z}_{A,MAX}$. As $F_{springs}$ (and thus F_{PTO}) increases, $\dot{z}(t)$ reduces. The phase, though, of the surge excitation force, F_{surge}, is not substantially changed and therefore $P_{av,bearings}$ reduces with dx. The total net time averaged power, $P_{av,tot}$, is the sum of $P_{av,bearings}$ and $P_{av,PTO}$ and is found to be close to maximum or optimum ($P_{av,tot,OPT}$) for a spring compression increment, dx = 30.5 mm, for the WEC unit under regular waves of H = 0.074 m and T = 1.260 s. It has to be noted, that accurate determination of the dx which results in the exact

value of $P_{av,tot,OPT}$ is not an objective of this research. Therefore in this research, dx = 30.5 mm has been selected as the spring compression increment which refers to optimum power absorption conditions, $P_{av,tot,OPT}$ from this point onwards. Moreover, it has to be noted that the WEC unit has been designed to simulate considerable energy extraction from the incoming waves, in first instance, by applying damping on the WEC motion through a PTO-system based on the friction brake principle. By the available and feasible employed means, the friction of the WEC shaft bearings made out of *Teflon* still causes damping (and therefore wave energy extraction) comparable to that realized by the PTO-system. In a commercial WEC concept, though, damping through the WEC bearings would not be desirable, which results in energy losses. However, the objective of this PhD research is to study *WEC array effects* due to wave energy extraction by WECs within arrays (using the developed heaving WEC unit in large numbers), and not the development/optimization of a new WEC concept. As a result, the objective of this PhD research is not obstructed by the damping applied on the WEC motion, both through the PTO-system and the WEC shaft bearings.

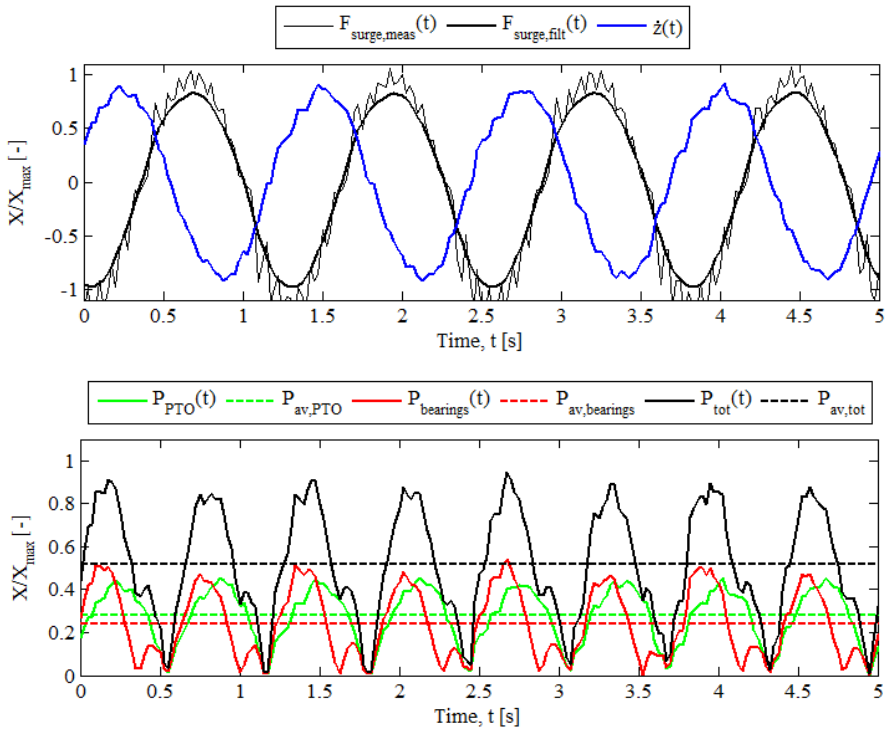

Figure 2.26. *Cont. Next Page*

Figure 2.26. *Cont.*

Figure 2.26. Time-variation of: (top) the measured surge force, $F_{surge,meas}(t)$, filtered surge force, $F_{surge,filt}$, the time derivative of time varying heave displacement of the WEC, $\dot{z}(t)$; and (bottom) resultant absorbed power due to the WEC shaft bearings, $P_{bearings}(t)$, the PTO, $P_{PTO}(t)$, and total, $P_{tot}(t)$. $F_{surge,meas}(t)$ and $F_{surge,filt}(t)$ are normalised to the amplitude of the surge force, $F_{surge,MAX}$. $P_{bearings}(t)$ and $P_{PTO}(t)$ are normalised to the amplitude of the PTO absorbed power, $P_{PTO,MAX}$. The dashed lines represent the time-averaged values, $P_{av,bearings}$ and $P_{av,PTO}$ [28]. Results are presented for an individual WEC under regular waves (H = 0.074 m, T = 1.260 s, wave angle, θ = 0º).

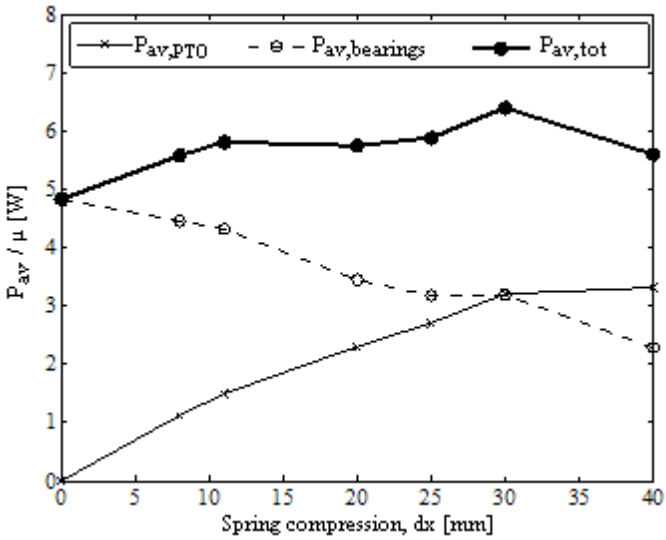

Figure 2.27. Time averaged power absorption (normalised by friction coefficient, μ) by power take off system, $P_{av,PTO}$ (solid line with "x"-symbols), by the WEC shaft bearings, $P_{av,bearings}$ (dashed line with "o"-symbols), and total, $P_{av,tot}$ (thick solid line with solid circles "●"), measured for a range of spring compression increments, dx. $P_{av,tot,OPT}$ is obtained for dx = 30.5 mm [28].

2.7. Design specifications of the WEC unit and conclusions

A WEC unit has been designed, developed and evaluated in order to be used in experimental testing of large WEC arrays, with the intention to obtain measurements for the quantification of intra-array interactions and extra-array effects. Criteria for the design of this WEC unit have been identified, with efficiency, simplicity of manufacture and calibration as key requirements. The evaluated individual WEC units satisfy the performance requirements of the target WEC array testing:

1. Due to the selected WEC construction materials, the WEC unit is straightforward to manufacture. Most importantly, the developed WEC unit facilitates low cost construction of large numbers of identical WEC units.

2. Due to the selected WEC geometry and WEC motion/operation principle, the WEC unit is simple to represent in numerical models:

- The number of degrees of freedom to be simulated in a response model of the WEC array remains limited to the number of WEC units in an array (single DOF WEC units, only).
- The geometry of the WEC buoy is idealised and simple, with vertical sides at the water plane.

3. The developed PTO-system of the WEC unit is based on the simple friction brake principle; a PTO damping force, F_{PTO}, applied through linear springs, allows straightforward representation in a range of models.

4. The developed WEC support shaft and PTO-system are simple and ensure repeatable operation for each WEC unit. By using a square, instead of circular cross-section for the WEC shaft, rotation is hindered. Furthermore, measurements of surge force, F_{surge}, can be taken, allowing quantification of non-PTO-system loads.

5. The WEC unit is sufficiently large to provide measurable WEC response and / or power output of the WEC unit. This results in measurable WEC array effects. Moreover, WEC response and power output have been validated by performing numerical simulations in WAMIT.

6. Energy extraction by the mechanical system of the WEC unit under the tested wave conditions, is easily quantified by using measurements of time varying buoy heave displacement, $z(t)$, and surge force, F_{surge}.

7. The developed WEC deployment methodology allows straightforward rearrangement of the WEC units in the wave flume/basin. By employing a WEC shafts stencil and by holding the WEC units above the water surface when not used in the WEC array, various WEC array geometric configurations can be tested. As a result, no WEC units need to be removed from the experimental arrangement, which

accelerates the testing procedure and leads to efficient use of the available testing time.

8. The selected instrumentation for $z(t)$ is sufficiently accurate and offers a practically and economically feasible solution for its use in large numbers for WEC array testing.

9. A generic WEC design has been developed, rather than a commercial WEC concept. This feature is important for developing a widely applicable WEC array database that can be employed for inter-comparison of numerical models.

The developed WEC unit is based on the point absorber type. Firstly, frequency domain analysis of the WEC response, $z(t)$, and of the average power output, $P_{av,tot}$, of the WEC unit has been conducted, using hydrodynamic parameters obtained in WAMIT. Furthermore, experimental measurements of the WEC response have been performed and compared to numerical WAMIT predictions, with the objective to evaluate the performance of the designed WEC unit. Initial evaluation of the WEC unit comprised experimental evaluation of its mechanical system and of the instrumentation. A vertical WEC supporting shaft fixed at both ends, a PTO-system based on the friction brakes principle (PTFE blocks on the WEC shaft) and heave displacement measurement by using a potentiometer have been selected for each WEC unit. Frequency domain analysis of the response, $z(t)$, and total average power output, $P_{av,tot}$, of the WEC unit have been conducted, using hydrodynamic parameters obtained in WAMIT. WEC response is in good agreement with the experimental measurements conducted in a narrow and a wide wave flume, as well as in a wide wave basin. The measured maximum value of the surge force, $F_{surge,MAX}$, is also found to be in reasonable agreement with linear predictions using WAMIT. Discrepancy between numerically and experimentally obtained $F_{surge,MAX}$ values, though, increases as the WEC response amplitude, z_A, becomes large relative to the WEC buoy draft, d_{buoy}. Calibration of the friction between the PTFE bearings and the supporting WEC shaft through a mechanical test (in both, dry and wet conditions) in combination with prediction of response amplitude and mean power absorption over a range of PTO spring compression increments, dx, indicates an average friction coefficient, μ = 0.17. This coefficient is representative of the friction between PTFE and industrial (non highly polished) steel sliding interfaces.

This result of μ, combined with measurements of F_{surge} and $z(t)$, are employed to obtain appropriate PTO-system spring compression increment, dx, which maximizes (optimizes) the total power output of the WEC unit, $P_{av,tot,OPT}$. The total energy absorption by the WEC unit is modelled by realising energy dissipation through friction based damping of the WEC's heave motion, both by the PTO-system and the WEC shaft bearings. Achieving optimum power absorption by the

WEC unit is important for the objectives of the WEC array testing, as $P_{av,tot,OPT}$ results in measurable WEC array effects due to power absorption (extraction) by the WEC units of the tested arrays.

The developed WEC unit is suitable for the WEC array experiments, for which the WEC has been specially developed, and has been therefore reproduced in multiple copies for the WEC array experiments presented in the third part of this PhD dissertation.

2.8. References

[1] K. Koca, A. Kortenhaus, H. Oumeraci, B. Zanuttigh, E. Angelelli, M. Cantu, R. Suffredini, G. Franceschi. *Recent Advances in the Development of Wave Energy Converters.* In the Proceedings of the 10th European Wave and Tidal Energy Conference Series (EWTEC), Aalborg, Denmark, 2-5 September **2013**.

[2] M. Folley, A. Babarit, L. O' Boyle, B. Child, D. Forehand, K. Silverthorne, J. Spinneken, V. Stratigaki, P. Troch. *A review of numerical modelling of wave energy converter arrays*. Proceedings of the 31st International Conference on Offshore Mechanics & Arctic Engineering, Rio de Janeiro, Brazil, **2012**.

[3] Beels, C., P. Troch, G. De Backer, M. Vantorre, & J. De Rouck. *Numerical implementation & sensitivity analysis of a wave energy converter in a time-dependent mild-slope equation model.* Coastal Engin. Vol. 57(5), pp. 471-492, **2010**.

[4] Beels, C., P. Troch, K. De Visch, J.P. Kofoed, and G. De Backer. *Application of the time-dependent mild-slope equations for the simulation of wake effects in the lee of a farm of Wave Dragon wave energy converters.* Renewable Energy, 35, pp.1644-1661, **2010**.

[5] Beels C., P. Troch, J.P. Kofoed, P. Frigaard, J. Vindahl Kringelum, P. Carsten Kromann, M. Heyman Donovan, J. De Rouck and G. De Backer. *A methodology for production and cost assessment of a farm of wave energy converters.* Renewable Energy,Vol. 36(12),p.3402-3416, **2010**.

[6] P. Troch, C. Beels, J. De Rouck, G. De Backer. *Wake effects behind a farm of wave energy converters for irregular long-crested and short-crested waves.* Proceedings of the International Conference on Coastal Engineering, No. 32 (**2010**), Shanghai, China. Paper #: waves.22. Retrieved from http://journals.tdl.org/ICCE/.

[7] K. Budal, J. Falnes, A. Kyllingstad, G. Oltedal. *Experiments with point absorbers in regular waves.* Proceedings of the 1st Symposium on Wave Energy Utilization, 253–282, Gothenburg, Sweden, **1979**.

[8] Count, B.M. and E.R. Jeffreys. *Wave power, the primary interface.* Proceedings 13th Symposium for Naval Hydrodynamics, 8, 1-10, **1980**.

[9] Vantorre M. *Third-order potential theory for determining the hydrodynamic forces on axisymmetric floating and submerged bodies in a forced periodic heave motion.* PhD thesis, Ghent University, **1985**.

[10] Vantorre M., R. Banasiak, R. Verhoeven. *Modelling of hydraulic performance and wave energy extraction by a point absorber in heave.* Applied Ocean Research; 26:61–72, **2004**.

[11] Delhommeau G. *Le problème de diffraction radiation et de résistance de vagues : étude théorique et résolution numérique par la méthode des singularités*. Thèse Ecole Nationale Supérieure de Mécanique, Nantes, **1987**.

[12] De Backer, G.. *Hydrodynamic Design Optimization of wave energy converters consisting of heaving point absorbers*. PhD thesis, Department of Civil Engineering, Ghent University, Belgium, **2009**.

[13] Durand M., A. Babarit, B. Pettinotti, O. Quillard, J. Toularastel, and A. Clement. *Experimental validation of the performances of the SEAREV wave energy converter with real time latching control.* Proceedings of the 7th European Wave and Tidal Energy Conference, Portugal, **2007**.

[14] Gilloteaux J.C., A. Babarit, G. Ducrozet, M. Durand, and A. Clement. *A nonlinear potential model to predict large-amplitude motions: application to the SEAREV wave energy converter.* Proceedings of the 26th International Conference on Offshore Mechanics & Arctic Engineering, USA, **2007**.

[15] Babarit A., H. Mouslim, A. Clement, and P. Laporte-Weywada. *On the numerical modelling of the non-linear behaviour of a wave energy converter*. Proceedings of the 28th International Conference on Offshore Mechanics & Arctic Engineering, Honolulu, Hawaii, OMAE, **2009**.

[16] Payne G., J. Taylor, T. Bruce, and P. Parkin. *Assessment of boundary-element method for modelling a free-floating sloped wave energy device.* Part 2: Exp. validation. Ocean Engineering, 35: 342–357, **2008**.

[17] T.J. Stallard, P.K. Stansby, A. Williamson. *An experimental study of closely spaced point absorber arrays*. Proceedings of the 18th International Offshore & Polar Engineering Conference, Canada, **2008**.

[18] S.D. Weller, T.J. Stallard, P.K. Stansby. *Interaction factors for a rectangular array of heaving floats in irregular waves*. IET Renewable Power Generation. 4(6), (**2010**), 628–637.

[19] S. Thomas, S. Weller, T.J. Stallard. *Float response within an array: Numerical and experimental comparison*. Proceedings of 2nd International Conference on Ocean Energy (ICOE), Brest, France, **2008**.

[20] WAMIT, User Manual. http://www.wamit.com/manual.htm. Accessed March **2013**.

[21] Ashton, I., L. Johanning, and B.Linfoot. *Measurement of the Effect of Power Absorption in the Lee of a Wave Energy Converter*. Proceedings of the 28th International Conference on Offshore Mechanics & Arctic Engineering, Honolulu, Hawaii, OMAE 2009, vol. OMAE2009-79793, **2009**.

[22] Stratigaki, V.; Troch, P.; Stallard, T.; Forehand, D.; Kofoed, J.P.; Folley, M.; Benoit, M.; Babarit, A.; Kirkegaard, J. *Wave Basin Experiments with Large Wave Energy Converter Arrays to Study Interactions between the Converters and Effects on Other Users in the Sea and the Coastal Area*. *Energies* **2014**, *7*, 701-734.

[23] Troch, P.; Stratigaki, V.; Stallard, T.; Kofoed, J.P.; Forehand, D.; Folley, M.; Benoit, M.; Babarit, A.; Gallach Sánchez, D.; De Bosscher, L.; Rauwoens, P.; Elsässer, B.; Lamont-Kane, P.; McCallum, P.; McNatt, C.; Angelelli, E.; Percher, A.; Carpentero Moreno, E.; Bellew, S.; Dombre, E.; Charrayre, F.; Vantorre, M.; Kirkegaard, J.; Carstensen, S. *Large scale physical modelling of an array of 25 wave energy converters in the WECwakes project.* In the Proceedings of the 10th European Wave and Tidal Energy Conference Series (EWTEC), Aalborg, Denmark, 2-5 September **2013**.

[24] B.F.M. Child, J. Cruz, M. Livingstone. *Development of a tool for optimising arrays of wave energy converters*. In Proceedings of the 9th European Wave and Tidal Energy Conference, Southampton, UK, **2011**.

[25] Bjarte-Larsson, T. *Friction for a floating body heaving along a fixed vertical guiding strut.* In the Proceedings 7th EWTEC, Porto, Portugal, **2007**.

[26] S. Chakrabarti, *Hydrodynamics of Offshore Structures.* WIT press, **1987**.

[27] J. Falnes. *Ocean Waves and oscillating systems, linear interactions including wave-energy extraction.* Cambridge University Press, **2002**.

[28] Stratigaki, V., Troch, P., Stallard, T., Forehand, D., Folley, M., Vantorre, M., Kofoed, J.P., Babarit, A., Benoit, M.. *Development of heaving wave energy converters for large-scale WEC array experiments: design, development, theoretical-numerical–experimental study and evaluation of the WEC.* Submitted for publication in Renewable Energy, **2014**.

[29] K. Friedrich. *Friction and wear of polymer composites*. Elsevier - Technology & Engineering, **1986**.

[30] P. Troch. *Experimentele studie en numerieke modellering van golfinteractie met stortsteengolfbrekers* – appendix E (in Dutch). PhD Thesis, Ghent University, **2000**.

[31] E.P.D. Mansard, E.R. Funke. *The measurement of incident and reflected spectra using a least square method.* Proceedings of the 17th ICCE, 154-172, **1980**.

[32] LabVIEW System Design Software, http://www.ni.com/labview/, National instruments. Accessed January **2014**.

[33] Butterworth, S.. *On the theory of filter amplifiers*. Experimental Wireless and the Wireless Engineer, vol. 7, pp. 536–541, **1930**.

3

Numerical modelling of the wave field around a heaving wave energy converter

Abstract: *This chapter focuses on the numerical modelling of the resulting wave fields around oscillating wave energy converters, with the intention to study both intra-array interactions and extra-array effects of a WEC (array). As a result of the interaction between oscillating WECs and the incident wave field, additional wave fields are generated: the radiated and the diffracted wave field around each WEC, which together with the incident wave field compose the perturbed wave field around the WECs. Several numerical methods are employed to analyse these wave fields around WECs; for investigating wave-structure (wave-WEC) interactions, wave energy absorption and intra-array interactions, the commonly used and most suitable models are based on Boundary Element Methods (BEMs) for solving the potential flow formulation (e.g. WAMIT, Aquaplus, etc.), or models based on the Navier-Stokes equations (e.g. CFD models). For investigating extra-array effects of WEC arrays in large areas, wave propagation models are most suitable and commonly employed (MILDwave, SWAN, MIKE21, etc.). However, all these models suffer from a common problem; they cannot be used to model simultaneously, both intra-array interactions and extra-array effects due to limitations: (a) models based on the BEM approach of potential flow theory or on the approach of Navier-Stokes*

equations suffer from a high computational cost, when simulating power absorption and the wave field alteration due to large WEC arrays, and are typically used for less than 10 WECs; (b) the approach of wave propagation models enables simulation of far field effects. Large WEC arrays installed in large domains are modeled at a reasonable computational cost. As a result, the changes in wave field and the associated environmental impacts can be studied at regional scale. However, the WECs are approximated up to now by using parameterized energy sinks and empirically tuned energy absorption coefficients, and therefore this method only partially addresses the underlying physics, which can lead to erroneous model conclusions.

In this chapter, a generic coupling methodology is presented, developed to combine the above two approaches; (a) the approach of wave-structure interaction solvers used for investigating intra-array interactions, which model physically correct wave energy absorption and the resulting wave fields induced by oscillating WECs or WEC arrays, and (b) the approach of wave propagation models used for predicting extra-array effects, which can model the effect of WEC arrays on the wave field and the shoreline. In addition, a wave generation technique is presented, for generating the perturbed wave field induced by an oscillating WEC, in a wave propagation model. A wave generation circle is used, surrounding the WEC, on which prescribed internal boundary wave conditions are inserted as input, provided by a wave-structure interaction solver. Most importantly, both, the presented coupling methodology and wave generation technique are generic: (i) the coupling can be realized between any wave-structure solver and wave propagation model, (ii) they apply to any oscillating/floating structure, e.g. oscillating water columns/WECs, floating breakwaters, platforms, etc. For the verification of the presented coupling methodology, a test case using the heaving WEC developed during the first part of this PhD research, for which coupling between the wave-structure interaction solver, WAMIT, and the time domain wave propagation model, MILDwave, has been realized. The results obtained for the diffracted, radiated and perturbed wave field around the WEC under incident waves using the presented coupling methodology are verified against the results obtained from the wave-structure model, showing very good agreement. Finally, the benefits of the presented coupling methodology to model floating bodies in a phase resolving wave propagation model are discussed.

3.1. Introduction

3.1.1. Wave fields around a heaving WEC

The operation of a wave energy converter is based on the principle that a WEC interacts with the incident waves and absorbs a certain amount of energy from them. In this chapter, the resulting wave fields around an oscillating WEC due to its interaction with the incident waves, are numerically modelled.

Around a stationary or oscillating wave energy converter under incident waves, additional wave fields are generated: a diffracted wave field, and in the case of an oscillating WEC, also a radiated wave field. Usually linear theory is used to model wave-structure interaction and therefore the generated wave fields can be separated by applying the superposition principle. The superposition of the (i) incident, the (ii) diffracted and the (iii) radiated wave fields is the "*perturbed wave field*" around the WEC [1].

For an incident plane wave propagating in one direction, the shape of the diffracted and radiated waves is altered and these waves propagate in every direction from the oscillating WEC, as shown in Figure 3.1. Therefore, the wave field is perturbed everywhere around the WEC.

When the WEC is assumed to be stationary, the diffracted wave field is generated, as a result of the WEC's geometry. In that case, the incident waves are partly reflected from, diffracted around and transmitted under the WEC, and no wave power is absorbed. When the WEC oscillates, an additional radiated wave field is generated. In that case, the WEC absorbs wave power (through its PTO-system) by generating a wave.

As seen in the introductory part of this PhD dissertation, in order to extract a considerable quantity of wave power from the incident waves, large numbers of WECs will have to be arranged in arrays using a particular geometrical configuration.

The wave field around an individual WEC in an array is modified in all directions due to wave-WEC interaction, as already described in Figure 3.1. In an array, additional hydrodynamic interactions take place between the WECs of the array (the intra-array interactions). These interactions between neighbouring WECs of an array are illustrated in Figure 3.2, where it is shown that the wave fields around the WECs under incident waves interfere with each other.

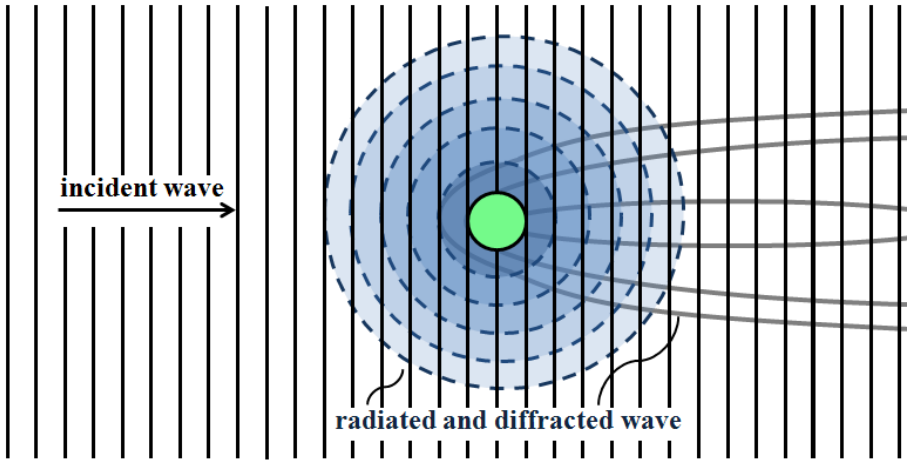

Figure 3.1. Illustration of the resulting diffracted and radiated wave field around an oscillating WEC (represented by the solid circle) under incident waves.

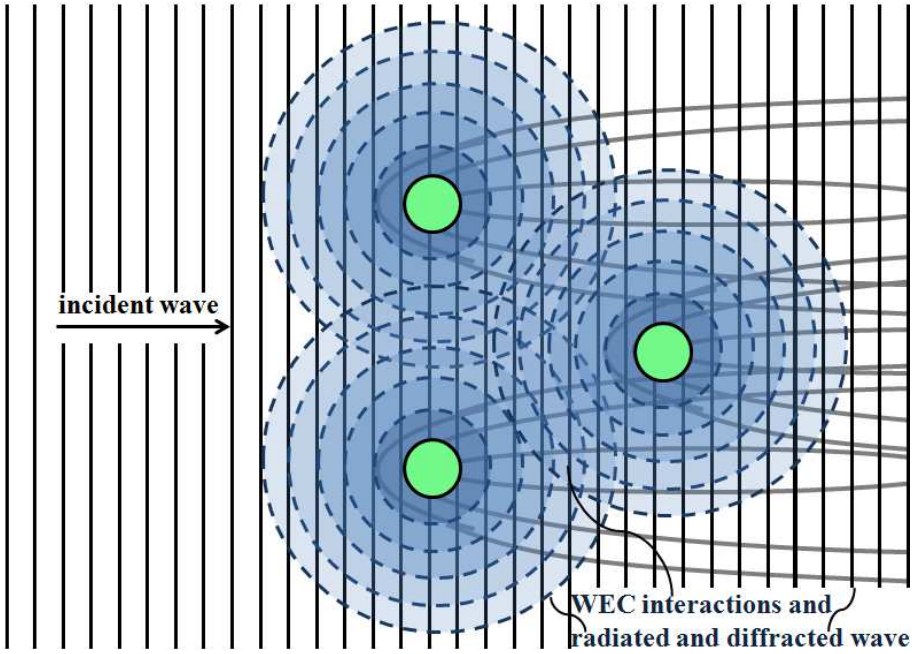

Figure 3.2. Illustration of the interactions between neighbouring oscillating WECs (represented by solid circles) in an array under incident waves.

As a result of these interactions between the WECs of an array, the overall power output of the wave farm is affected and is therefore not equal to the power output from an individual WEC times the total number of WECs. In addition, the wave field at large distances behind the WEC arrays is typically a region of reduced wave energy density and wave heights, as a result of the extra-array effects.

3.1.2. Numerical modelling of WEC (array) effects on the wave field – State of the art

A numerical methodology for the combined accurate prediction of both intra-array interactions and extra-array effects is still lacking, and is therefore the main focus of this chapter. In this chapter, a generic coupling methodology between the approach used for investigating intra-array interactions and the approach used for predicting extra-array effects, is presented.

The most commonly used models for simulating intra-array interactions and wave energy absorption by WECs, are based on the Boundary Element Method (abbreviated as *BEM*) approach of potential flow theory. These models (e.g. Aquaplus [2], ANSYS Aqwa [3], WAMIT [4]) have been used for computational domains with constant water depth and small WEC arrays (1-10 WECs) ([5] - [7]) and only for constant water depths (e.g. WAMIT). However, due to a better description of the related physics as presented in [8], the use of codes resolving the Navier-Stokes equations (e.g. Computational Fluid Dynamics (abbreviated as *CFD*) models) for modelling WECs, is growing nowadays ([9] - [11]). The BEM and the Navier-Stokes based solvers will be hereafter referred to as "*wave-structure interaction solvers*".

For simulating extra-array effects, the approach of wave propagation models is employed. Within these, a WEC is represented in a simplified way, by a porous structure that extracts a specific quantity of wave power. The simulated WEC exhibits a specific amount of reflection, transmission and absorption of the incident waves. Spectral wave propagation models, e.g. SWAN [12] and Boussinesq models, e.g. MIKE21 BW [13] have both been employed to study the change of shoreline waves due to the installation of a WEC array near a coastline (e.g. [14] - [17]). Extra-array effects in the lee of a WEC array have been studied by ([18] - [20]) by using the mild-slope wave propagation model MILDwave [21], resulting to guidelines for optimal WEC array geometric lay-outs.

All of the above mentioned models suffer, though, from a common problem; these cannot be used to model both intra-array interactions and extra-array effects, as recently reviewed in ([22], [23]).

Models based on the Boundary Element Method (BEM) approach of potential flow theory or on the approach of Navier-Stokes equations suffer from a high

computational cost, when simulating power absorption and the wave field alteration due to large WEC arrays. Simulation domains of non-constant water depth are prohibitive, which results also in restrictions on the number of the simulated WECs (typically less than 10 WECs). However, in order to investigate extra-array effects, for example to study coastal impact, much larger computational domains are required.

On the other hand, the approach of wave propagation models enables simulation of these extra-array effects. Large WEC arrays installed in large domains (several tens of kilometers) are modelled at a reasonable computational cost. As a result, the changes in wave field and the associated environmental impacts can be studied at regional scale. However, the WECs are approximated up to now by using parameterized energy sinks and empirically tuned energy absorption coefficients. This method only partially addresses the underlying physics, which may lead to erroneous model conclusions. Moreover, when it comes to the modelling of oscillating WECs, the radiated wave field induced by the WEC's motion is not considered in wave propagation models such as in ([24] - [26]).

In [22], the metrics of fundamental modelling characteristics, computational processing characteristics and usability characteristics are used for a comparative analysis of the numerical techniques most commonly employed to model WEC arrays. Based on these metrics, the suitability of each numerical technique is evaluated for various different modelling tasks, including investigation of intra-array interactions, estimation of annual energy production (abbreviated as *AEP*) and assessment of distal environmental impacts (extra-array effects).

As a result of the analysis presented in [22], models based on the BEM approach of linearized potential flow theory are suitable for modelling intra-array hydrodynamic interactions in the vicinity of large WECs in deep water, that shed minimal vortices. When localized effects such as vortex shedding (viscous effects) behind an oscillating WEC, wave overtopping and the re-entering impact of an-out-of-water body are important, the approach of Navier-Stokes solvers is the most suitable. Whilst Boussinesq/mild-slope models resolve phase, they are unlikely to accurately model the near field and the wave-WEC interaction, and so are poorly suited.

Regarding AEP, models based on the BEM approach of linearized potential flow theory, rapidly become unsuitable for that purpose as the number of WECs increases, due to the quadratic relationship between the computation effort and the number of WECs. Similarly, the approach of CFD models resolving the Navier-Stokes equations is not suitable due to high computational requirements. The Boussinesq/mild-slope and spectral models are highly suitable for the calculation of the AEP.

Concerning suitability for determining the distal environmental impact (extra-array effects): none of the BEM models are suitable because of the assumption of

constant water depth. This assumption makes them unsuitable for propagating the waves to the shoreline, where the environmental impact is typically most significant. Furthermore, the large propagation distances make CFD models poorly suited due to their high computational requirements. Boussinesq/mild-slope and spectral models are highly suitable for determining environmental impact and have been used extensively for this task in applications other than in the wave energy field.

In this chapter, a numerical coupling methodology for predicting WEC array effects is presented. This coupling methodology has been developed to combine:

i. the advantages of the approach of wave-structure interaction solvers, which accurately formulate and efficiently resolve the physical processes in wave energy absorption;

ii. and, the benefits of the approach of wave propagation models, which efficiently resolve the propagation and transformation of waves over large distances, including bathymetric variability over the WEC array area and wave transformation processes when approaching the coastline.

Moreover, a wave generation technique is presented to generate the perturbed or radiated wave field induced by an oscillating WEC in a wave propagation model. The WEC is implemented using prescribed internal boundary wave conditions, on a wave generation circle which surrounds the WEC location.

The presented coupling methodology is illustrated here by its implementation in the wave propagation model, MILDwave [21] and is verified using a test case based on the heaving WEC, developed within this PhD research in order to study experimentally WEC array effects. The coupling methodology has been verified against wave field results obtained by the wave-structure interaction solver, frequency domain code, WAMIT [4]. Therefore, the test case used to verify the proposed coupling methodology, illustrates the coupling of the BEM approach of linearized flow theory and the approach of a time domain wave propagation model.

3.1.3. Chapter overview

The details of the coupling methodology are presented in Section 3.2 with clear illustrations of the step-by-step procedure. Two schemes are presented for modelling the resulting wave field due to interaction of a WEC with waves: (i) for a generic coupling between any wave-structure interaction solver and any wave propagation model, and, (ii) a scheme for coupling between the two selected models, for the case of an individual heaving WEC. In addition, at the end of Section 3.2, the technique used to model multiple WECs or WEC arrays by using the developed coupling methodology, is presented step-by-step with the essential illustrations. Section 3.3

provides information on the selected wave propagation model (MILDwave) in which the coupling methodology has been implemented. Here, the details of the developed wave generation technique on a wave generation circle are presented. Section 3.4, starts with a brief reference to the selected model for wave-structure interaction (WAMIT). Furthermore, Section 3.4 includes all the details of the implementation of the proposed coupling methodology. First the characteristics of the modeled test case with a heaving WEC are briefly mentioned. The diffracted, radiated and perturbed wave field around the WEC are modeled, using the selected wave-structure interaction model. This simulation provides the prescribed internal boundary wave conditions on the wave generation circle used for the proposed coupling methodology, in order to generate the radiated wave field around the WEC. Furthermore, by using the proposed coupling methodology, the diffracted, radiated and perturbed wave field around the WEC are modeled in the selected wave propagation model. Section 3.5 provides the verification results of the presented coupling methodology against the wave fields around the WEC simulated by the selected wave-structure solver. The agreement between the results from the presented coupling methodology and those obtained by the wave-structure solver is evaluated and discussed, first for the diffracted and radiated wave field separately, and then for the perturbed wave field around the WEC. Finally, in Section 3.6, a summary of the obtained conclusions from the verification results is presented, including a discussion on the potential of the proposed coupling methodology and its benefits.

3.2. Description of the presented coupling methodology

3.2.1. The generic description

The presented generic coupling methodology, as illustrated in Figure 3.3, consists of three steps. Firstly, the wave propagation model is used to obtain the incident wave field at the location of the WEC (array). Secondly, the obtained incident wave field, is used as input in the wave-structure interaction solver to obtain an accurate solution of the perturbed wave field around the WEC. The resulting perturbed wave field information along a circle that surrounds the WEC, is used in the next step.

Thirdly, this perturbed wave field information is used as input in the wave propagation model. The perturbed wave field is imposed as prescribed internal boundary wave conditions on a wave generation circle which surrounds the WEC, as shown in Figure 3.4. Using the wave propagation model, the far field perturbed wave field (including the radiated and diffracted wave fields) is calculated. This is

the last step of the procedure described in Figure 3.3. In this way, the resulting extra-array effects of a WEC (array) can be further modeled using the wave propagation model, in a time efficient and accurate way, taking into account both the geometric/bathymetric characteristics and wave transformation at the installation site, and the detailed perturbed wave field around the WEC due its oscillation.

Figure 3.4 represents the numerical domain in the wave propagation model when the coupling methodology is used. Incident waves are generated along the wave generation boundary. The WEC is implemented using the wave generation circle upon which prescribed internal boundary wave conditions are imposed, for the perturbed wave field. In the area within the wave generation circle, a wave absorbing sponge layer is used to avoid disturbances of the generated wave field. The details of the proposed wave generation technique on a circle are presented in Section 3.3.3.2.

Most importantly, the proposed coupling methodology is generic:

i. any wave-structure solver or analytical expression describing the perturbed wave field (e.g. the so called Kochin function ([27] - [28])) can be used to provide the perturbed wave field used as prescribed internal boundary wave conditions. This perturbed wave field is imposed on the wave generation circle around the WEC. Models based on the Boundary Element Method (BEM) approach of potential flow theory or models based on the approach of resolving the Navier-Stokes equations (e.g. Computational Fluid Dynamics (CFD) models), are all suitable for providing detailed perturbed wave field information in the vicinity of the WEC.

ii. any wave propagation model can be used; the wave generation circle can be implemented in the numerical domain of any wave model (in both phase resolving and phase averaging models).

iii. it applies to any oscillating/floating structure; in this chapter, a heaving WEC has been selected for the verification test case, but the same methodology is applied to e.g. oscillating water columns, floating breakwaters, platforms, etc.

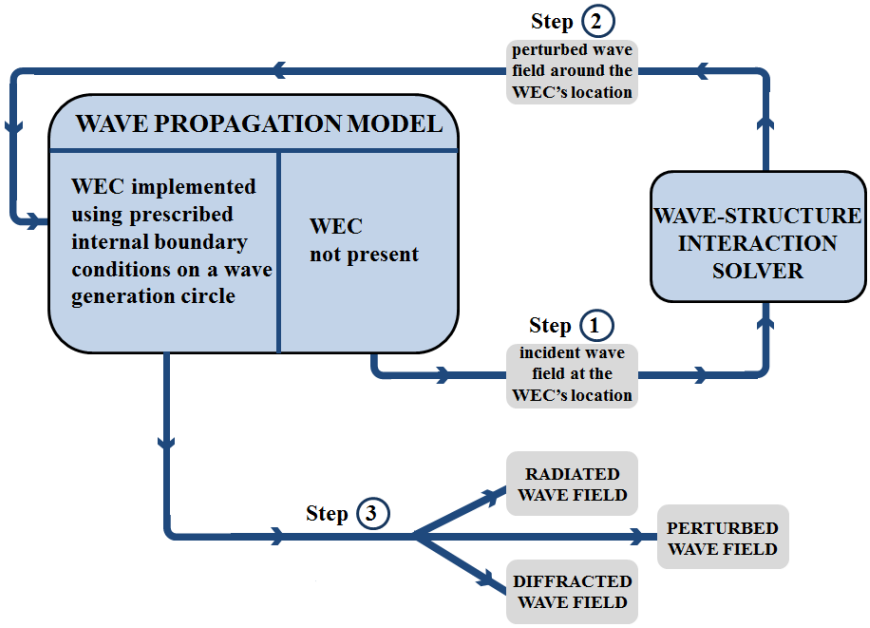

Figure 3.3. Flow chart illustrating the step-by-step procedure for realizing the presented generic coupling methodology between the approach of a wave–structure interaction solver and a wave propagation model, respectively, to predict intra-array interactions and extra-array effects of an oscillating WEC (array).

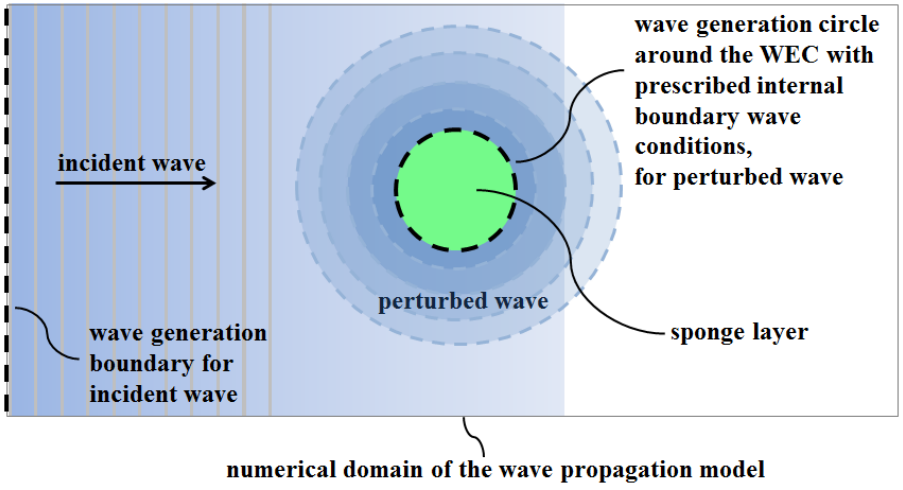

Figure 3.4. Definition sketch of the technique of the wave generation on a circle around the WEC using prescribed internal boundary wave conditions for the perturbed wave field around the WEC. The perturbed wave field around the WEC is derived from a wave-structure interaction solver. The wave generation boundary for the incident wave field is also presented.

3.2.2. A more specific description for a verification test case with an individual heaving WEC

As an example of the implementation and verification of the presented generic coupling methodology described in Section 3.2.1, a test case has been set up using wave field results obtained by a wave-structure interaction solver:

- the selected WEC for the test case, has the same geometric and operation characteristics as the single-DOF heaving WEC unit developed in the first part of this PhD research;
- the selected wave-structure interaction solver is WAMIT [4];
- the selected wave propagation model is MILDwave [21].

Therefore, the test case used to verify the presented coupling methodology, enables the coupling of the BEM approach of linearized flow theory and the approach of a time domain wave propagation model.

The step-by-step procedure for the presented generic coupling methodology, as presented in Figure 3.3, has now been adjusted to the flow chart presented in Figure 3.5. Note that the only procedure difference is that only the radiated wave field from WAMIT is further used as input (as prescribed internal boundary wave conditions along the wave generation circle) in MILDwave. This is because diffraction around the WEC is modeled intrinsically in MILDwave and therefore only the radiated wave field from WAMIT is necessary for the implementation of the proposed coupling methodology.

The definition sketch of Figure 3.6, illustrates the presented coupling methodology between WAMIT and MILDwave, to model intra-array interactions and extra-array effects around the heaving WEC. Wave amplitude, a, and phase shift, φ, for the radiated wave field around the WEC, which is derived from WAMIT, are inserted as prescribed internal boundary wave conditions along the wave generation circle imposed in MILDwave. In Figure 3.6, incident waves are generated along the wave generation line, which propagate from the left to the right. At the same time, waves are generated along the wave generation circle in the centre of the domain, simulating the radiated wave field induced by the heave movement of the WEC. The radiated waves propagate in all directions as indicated in Figure 3.6. In MILDwave, the diffracted wave field (the WEC is considered to be stationary) and the radiated wave field (the WEC heaves) are calculated separately during each time step. Consequently, each time step two wave patterns are calculated and summed up. Wave absorbing sponge layers are placed along all sides of the computational grid, as well as inside the wave generation circle. This is necessary, in order to avoid disturbances in the wave field of the effective domain (domain without sponge layers).

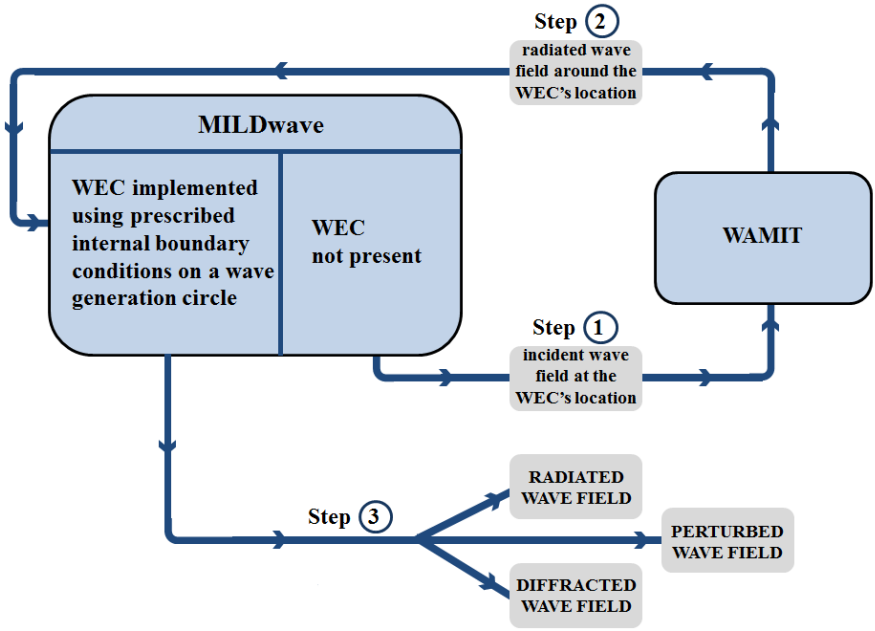

Figure 3.5. Flow chart illustrating the step-by-step procedure of the test case used for verifying the presented coupling methodology. Coupling between the BEM approach of linearized potential flow theory (WAMIT) and the approach of a time domain mild-slope wave propagation model (MILDwave) is realised to predict intra-array interactions and extra-array effects of the heaving WEC used in the test case.

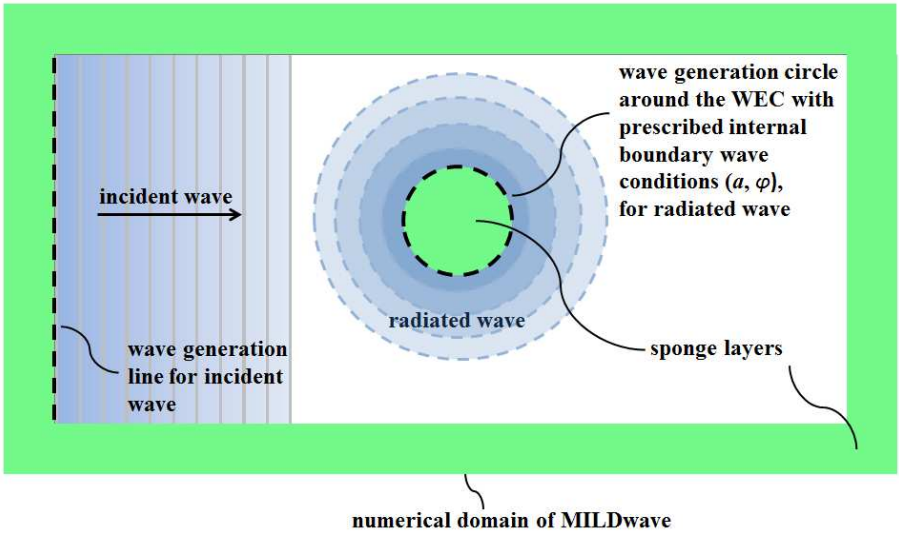

Figure 3.6. Definition sketch, referring to the employed verification test case, of the technique of the wave generation on a circle around the WEC using prescribed internal boundary wave conditions (radiated wave field around the WEC). The radiated wave field around the heaving WEC is derived from WAMIT.

It has to be noted that by using this coupling methodology, it is possible to model the resulting wave fields around WECs that can also pitch, sway, etc., and therefore not only WECs that heave. In this case, the a and φ values for the radiated wave field around the WEC which are inserted along the wave generation circle in MILDwave, are not constant as for a heaving WEC. Instead, the a and φ values differ at each one of the discretization points on the wave generation circle (with angle interval, Δb, as seen in Section 3.3.3.2) and the resulting radiated wave field may be not be axi-symmetric, as that shown in Fig. 3.6.

3.2.3. Step-by-step procedure of the presented coupling methodology to model a WEC array of oscillating WECs

After implementing an individual WEC in MILDwave (Section 3.2.2), based on the diffracted and radiated wave fields generated from WAMIT results, the implementation of more than one WEC is presented in this section. The methodology employed to simulate an array of oscillating WECs in MILDwave is discussed here, using the coupling methodology presented in Section 3.2.2. Interactions between the radiated and diffracted wave fields of all WECs are taken into account.

As presented in [29], to study a WEC array, the diffracted wave field (all WECs of the array are considered to be stationary) and the radiated wave field for each WEC (one WEC is oscillating, the other WEC(s) are stationary) are calculated separately during each time step. Consequently, if N is the number of the WECs of the array, each time step, N+1 wave fields are calculated and summed up.

The radiated wave field generated by each oscillating WEC is determined in two steps. For simplicity, the methodology is illustrated for an array (or "system") of two oscillating WECs, as shown in Figure 3.7.

First, the diffracted wave field around the WEC caused by the incident wave in MILDwave, η_i, is calculated separately, in order to determine the wave amplitude in front of each WEC.

Furthermore, the amplitude of the radiated wave, a_W, as determined for an individual oscillating WEC using WAMIT (see Section 3.2.2), is multiplied by the calculated wave amplitude (from the previous step) in front of each WEC. This results in the primary radiated wave caused by the diffracted wave, η_{rad_diff}. Note that in front of the first row of WECs of an array (in Figure 3.7, WEC 1), the incident wave is not diffracted yet. Consequently, the primary radiated wave of those WECs (in Figure 3.7, WEC 1), η_{rad_i}, is caused by the incident wave, η_i.

In a second step, the amplitude of the radiated wave of each WEC (in Figure 3.7, WEC 1), η_{rad_diff} or η_{rad_i}, on the location of the neighbouring WEC (in Figure 3.7, WEC 2) is calculated, as seen in [29].

For WEC 2, this radiated wave is another incident wave which causes secondary radiated waves; ($\eta_{rad\_rad\_i}$ or $\eta_{rad\_rad\_diff}$ with $\eta_{rad\_rad\_i}$, the radiated wave in WEC 2 caused by the primary radiated wave η_{rad_i} of WEC 1, and with $\eta_{rad\_rad\_diff}$, the radiated wave in WEC 1, caused by the primary radiated wave of WEC 2, η_{rad_diff}).

The amplitude of $\eta_{rad\_rad\_i}$ is calculated by multiplying the amplitude of the radiated wave, a_W, of an individual WEC as calculated using WAMIT (see Section 3.2.2), by the amplitude of η_{rad_i} in front of WEC 2. The amplitude of $\eta_{rad\_rad\_diff}$ is calculated by multiplying the amplitude of the radiated wave, a_W, of an individual WEC as calculated using WAMIT (see Section 3.2.2), by the amplitude of η_{rad_diff} downwave of WEC 1. However, as in most cases the amplitude of these secondary radiated waves in front of the neighbouring WECs is very small compared to that of the incident wave, these secondary radiated waves could be neglected in a first "engineering" approach [29]. Therefore, only one radiated wave, determined by the diffracted/incident wave amplitude has to be generated around each WEC, when using the proposed coupling methodology presented in Sections 3.2.1 - 3.2.2.

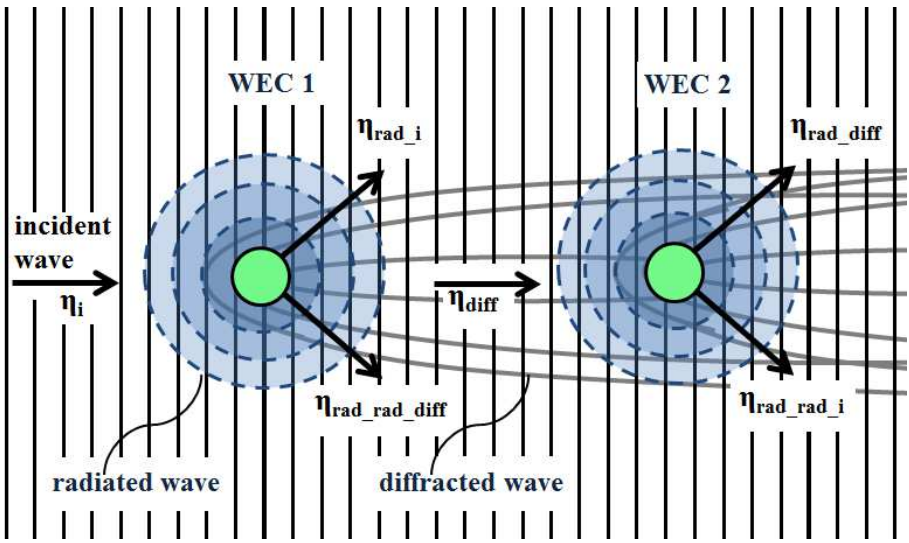

Figure 3.7. Definition sketch of wave field interaction between two oscillating WECs.

3.3. Description of the selected wave propagation model, used to simulate extra-array effects

3.3.1. The mild-slope wave propagation model, MILDwave

The phase-resolving model MILDwave [30] is a mild-slope wave propagation model developed by Troch [21]. MILDwave is able to generate linear water waves over a mildly varying bathymetry. Bathymetries can be modelled accurately, since the model has mostly been applied for fine grid cell sizes. The model calculates instantaneous surface elevations throughout the domain, with a relatively low computational and accuracy cost and with a high stability performance.

Wave transformation processes such as refraction, shoaling, reflection, transmission, diffraction can be simulated intrinsically. Also wave breaking and wave growth by wind are modelled by means of MILDwave. The model can generate regular and irregular long- and short-crested waves. Radiated wave patterns can also be modeled, as presented and verified in this chapter.

In Appendix A, information on the model applications and solution scheme are provided. Moreover, the implementation of a new physical process, i.e. wave growth by wind [31] is presented in Appendix A for a wave energy application, carried out within this PhD work.

MILDwave makes use of the hyperbolic mild-slope equations of Radder and Dingemans [32]. For regular waves, these equations are expressed by Eq. (3.1):

$$\begin{cases} \dfrac{\partial \eta}{\partial t} = B\phi - \nabla \cdot (A \nabla \phi) \\ \dfrac{\partial \phi}{\partial t} = -g\eta \end{cases} \tag{3.1}$$

where η and ϕ are respectively the surface elevation and the velocity potential at the free water surface, ∇ is the horizontal gradient operator, t is the time, g is the gravitational acceleration and the values of A and B are calculated using Eq. (3.2) and Eq. (3.3), respectively:

$$A = \frac{CC_g}{g} = \frac{1}{2k_w} \tanh(k_w d_w) \left(1 + \frac{2k_w d_w}{\sinh(2k_w d_w)} \right) \tag{3.2}$$

$$B = \frac{\omega^2 - k^2 CC_g}{g} = \frac{k_w}{2} \tanh(k_w d_w) \left(1 - \frac{2k_w d_w}{\sinh(2k_w d_w)} \right) \tag{3.3}$$

with d_w the water depth, C the phase velocity and C_g the group velocity for a wave with wave number, k_w, angular frequency, ω, wavelength, L and frequency, f. Equation (3.1) can be modified using Eq. (3.2) and Eq. (3.3), as presented in Eq. (3.4):

$$\begin{cases} \dfrac{\partial \eta}{\partial t} = \dfrac{\omega^2 - k^2 C C_g}{g}\phi - \nabla \cdot \left(\dfrac{C C_g}{g}\nabla \phi\right) \\ \dfrac{\partial \phi}{\partial t} = -g\eta \end{cases} \tag{3.4}$$

A derivation of these equations can be found in [32]. For irregular waves C, C_g, k_w and ω are replaced in Eq. (3.4) by the wave characteristics for the carrier frequency $\bar{f}$, i.e. $\bar{C}$, $\overline{C_g}$, $\overline{k_w}$and $\bar{\omega}$.

In Appendix A and [31], Equation (3.4) has been extended within this PhD research in order to account in MILDwave for depth-induced wave breaking and wave growth by wind.

3.3.2. Implementation of wave energy converters in MILDwave

In MILDwave, extra-array effects in the lee of WEC arrays and energy absorption have been extensively studied (e.g. [18] - [20], [22], [31], [33]). A sponge layer technique is applied, by which the redistribution of wave power both within and downwave of each WEC array can be studied in detail. Each combination of reflection and transmission characteristics, and consequently absorption characteristics, can be modelled for all individual WECs in an array ([18], [19]), which results in a representation of the extra-array effects in the lee of a WEC array. As presented in [29], a WEC is implemented in MILDwave as an array of cells (covering the spatial extent of the WEC) that have been assigned a given degree of absorption using the sponge layer technique. Absorption functions define the absorption coefficient S attached to each cell of the WEC in the x-direction and the y-direction (reference coordinate system is shown in Figure 3.8). By changing the values of the absorption coefficients or the number of absorbing cells, the degree of reflection and transmission, and therefore absorption of the porous structure, can be modified. When assuming a constant absorption coefficient S for all cells of the WEC, the amount of reflection, transmission and absorption are paired, as applied in [15]. To avoid this dependency, the shape of the absorption function throughout the WEC is modified, as it has been first presented by ([18], [19], [33]). This technique has been further used by [34]. This way, the degree of absorption (and consequently

transmission) of the WEC, given in the power matrix of the WEC, can be tuned for a fixed amount of reflection on the WEC as specified by the developer.

The power absorption of a WEC typically varies with wave frequency; however it is possible, using MILDwave, to represent the wave frequency dependent absorption by appropriate adjustment of the sponge layers, used to represent the wave power absorption by the WECs. In this way, the region of reduced wave energy density downwave of a WEC (array) is studied for each wave frequency component separately, as the amount of absorption of the WEC (array) in its lee, depends on the remaining energy in the considered wave frequency components. This is also the case for wave direction dependent WECs. The region of reduced wave energy density behind a WEC (array) is then not only calculated for each wave frequency component but also for each wave direction.

3.3.3. Implementation of wave generation on a circle in MILDwave

3.3.3.1. Wave generation on a line and on an arc

In MILDwave, waves are typically generated at the offshore boundary by using the source term method, i.e. by adding an additional surface elevation η^* to the calculated value on a wave generation line [35] or wave generation arc [36] for each time step.

The additional surface elevation η^* on a wave generation line for generating waves with wave direction θ in deep and shallow water, is given by Eq. (3.5) for a wave generation line parallel to the y-direction, and by Eq. (3.6) and for a wave generation line parallel to the x-direction:

$$\eta^* = 2\eta_i \frac{C_e \Delta t}{\Delta x} \cos\theta \tag{3.5}$$

$$\eta^* = 2\eta_i \frac{C_e \Delta t}{\Delta y} \cos\theta \tag{3.6}$$

with $\eta_i = a \sin(\omega t)$, the surface elevation of the incident waves (where the subscript "i" refers to incident waves, a, is the wave amplitude, ω, is the angular wave frequency and, t, is the time), C_e the energy velocity, Δt the time step, Δx and Δy the grid cell size in x- and y-direction, respectively, and θ the angle of wave propagation.

3.3.3.2. Wave generation on a circle

As presented in [29], around oscillating WECs, a radiated wave field is generated by the WEC motion. This is also valid for any floating structure (floating breakwaters, platforms), oscillating water columns, etc. In MILDwave, the generation of the radiated wave field is implemented by wave generation on a circle, based on [36]. Recently, this technique presented in [29] and extended and improved in this PhD work, has been adopted in [28] for modelling WECs in wave models. The improvements of this wave generation technique performed within this PhD work (e.g. adjustment of the employed *sponge layer function*, application of phase and wave amplitude correction at each one of the discretization cells along the wave generation circle replacing the use of constant values, improvement in the definition of *obstacle cells*, modification of the definition of Δb, etc.) have led to improvement in the accuracy of modelling the perturbed wave field around WECs by at least 17.5 %. To generate waves on a circle with centre (x_C, y_C) and radius r_C in a rectangular grid, the circle is approximated by a discrete number of grid cells (Figure 3.8). The x- and y-co-ordinates of these grid cells, in the x- and y-direction, respectively, are given by Eqs. (3.7) and (3.8) for $i \in [1, 360°/\Delta b]$. Note that iΔb = 90° represents a location behind the WEC, which is important for the case when the WEC is also under incident waves (e.g. as shown in Figure 3.6):

$$x = \left\{ floor\left[\frac{x_C + r_C \cos(i\Delta b)}{\Delta x} \right] \right\} \times \Delta x \tag{3.7}$$

$$y = \left\{ floor\left[\frac{y_C + r_C \sin(i\Delta b)}{\Delta y} \right] \right\} \times \Delta y \tag{3.8}$$

where the floor function rounds to the largest previous integer. More precisely, $floor(x) = \lfloor x \rfloor$, is the largest integer not greater than *x*.

The angle interval Δb can be approximated by *arctan* $(\Delta y / r_c)$. The additional surface elevation η^* is given by Eq. (3.9).

$$\eta^* = 2\eta_i \frac{C_e \Delta t}{\Delta x} \tag{3.9}$$

with $\eta_i = a \sin(-\omega t)$, and here $\Delta x = \Delta y$.

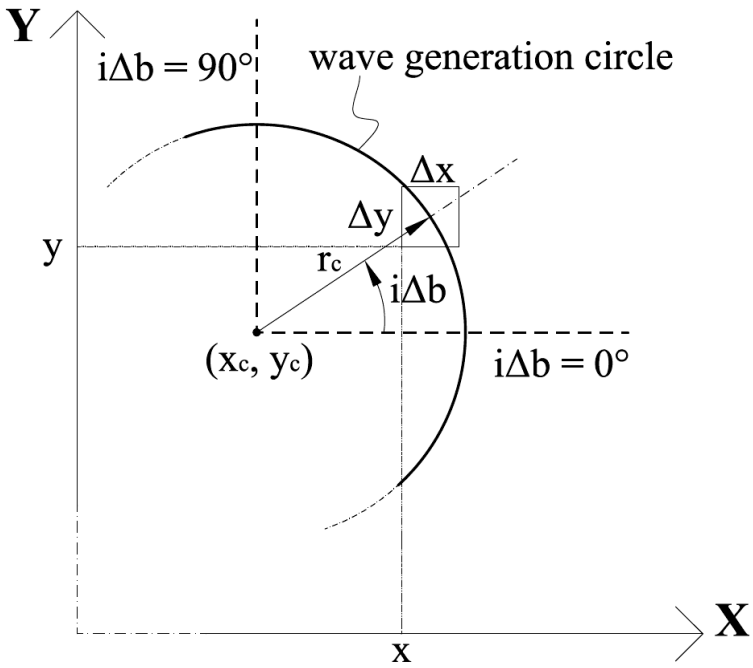

Figure 3.8. Definition sketch of wave generation on a circle.

Each grid cell on the wave generation circle is an individual wave generation source, which is affected by its neighbouring wave generation sources. To minimize the disturbances in the wave generation, a wave absorbing sponge layer is implemented in the inner part of the wave generation circle.

The wave generation on a circle is verified with the principle of conservation of energy for regular waves with H_{rc} and T, generated on a wave generation circle with radius r_C in the centre of the simulation domain (deep water conditions). The wave power on a circle with radius $r > r_C$ (where the wave height is H_r) is equal to the wave power on the wave generation circle according to the conservation of energy, as no energy sources or energy sinks are present between the two circles. The conservation of energy in deep water is expressed in Eq. (3.10).

$$\frac{1}{8}\rho_w g {H_{rc}}^2 C_g 2\pi r_c = \frac{1}{8}\rho_w g {H_r}^2 C_g 2\pi r \tag{3.10}$$

with H_r the wave height on a circle with radius $r \geq r_c$, as illustrated in the definition sketch of Figure 3.9. Equation (3.10) yields the ratio H_r / H_{rc}:

$$\frac{H_r}{H_{rc}} = \frac{\sqrt{r_c}}{\sqrt{r}} \tag{3.11}$$

The ratio H_r / H_{rc} has a starting value of 1.0 for $r = r_c$, and decreases when r increases as given by the analytical solution of Eq. (3.11). However in MILDwave, it is observed that the obtained ratio receives too high values (with e.g. a starting value for H_r / $H_{rc} \neq 1.0$) for the characteristics of the used sponge layer inside the wave generation circle, used in the study case presented in Section 3.4. Too much destructive interference occur on the wave generation circle by using the approximated value of the angle interval Δb ($arctan\ (\Delta y\ /\ r_c)$), due to mutual influences of the wave generation sources on the wave generation circle and due to the characteristics of the used sponge layer inside the wave generation circle. On the other hand, as shown later in Figure 3.14, too fine Δb results in generation of too much energy by the individual wave generation sources on the wave generation circle. Therefore an iterative approach (described in Section 3.4.4.2.2) is used to define the value of the angle interval Δb, for achieving good agreement between the analytical solution of Eq. (3.11) and the obtained numerical results.

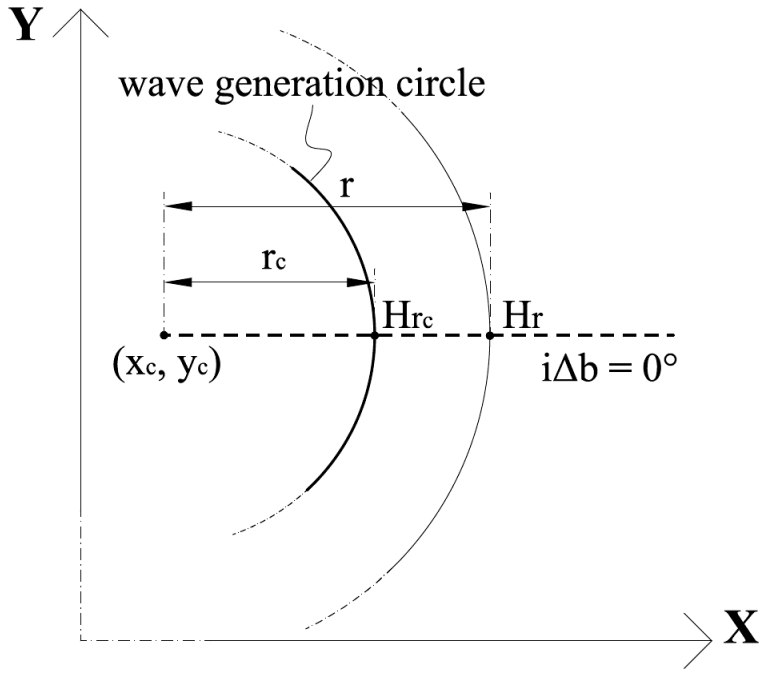

Figure 3.9. Definition sketch of the wave heights at radii r and r_c from the centre of the wave generation circle with coordinates (x_c, y_c).

3.4. Implementation of the coupling methodology for hydrodynamic modelling of a heaving WEC

3.4.1. Short description of the selected model for wave-structure interaction

To model the wave-structure interaction of an individual WEC with the incident wave field, the Boundary Element Method approach of linearized potential flow is used (WAMIT [4]). A brief description of the equations upon which the potential flow methods are based, is given e.g. in [22]. The assumptions upon which WAMIT is based, are the small amplitude of motions and small wave steepness, as well as the assumption of uniform water depth.

3.4.2. Description of the test case used to model a heaving WEC

3.4.2.1. Characteristics of the modelled WEC

In order to verify the proposed coupling methodology presented in Section 3.2, a test case has been set up. The heaving WEC developed during the first part of this PhD dissertation, has been selected for the test case. A detailed description of the WEC geometry, response and power-take off system is provided in Chapter 2. First, the hydrodynamic interaction between the modeled heaving WEC and the incident wave field is modeled using the model WAMIT. No damping is applied on the WEC through the PTO-system and therefore the results presented here refer to a freely (undamped) heaving WEC unit. Extra-array effects have been modeled using the coupling methodology implemented in MILDwave.

3.4.2.2. Modelled wave conditions

The wave diffraction and radiation wave fields generated by the modeled WEC are investigated for one set of incident regular wave conditions with wave direction θ = 90° and wave amplitude a = 0.037 m, wave period T = 1.26 s, constant water depth d_w = 0.70 m and wavelength L = 2.384 m, corresponding to studied wave conditions

during the WEC array experiments (Chapter 4) for which the developed WEC unit (Chapter 2) has been used.

3.4.2.3. Characteristics of the numerical domains

In MILDwave, a computational domain of length 26L (61.4 m) in the y-direction (parallel to the incident waves with wave direction θ = 90°) and width 30.5L (71.9 m) in the x-direction is defined (with L, the wavelength of a regular wave with T = 1.26 s). Wave absorbing sponge layers are implemented at the domain boundaries to prevent reflection inside the domain. Therefore, an effective domain (area without the sponge layers) of 49.7 m x 39.2 m (w_d x l_d) has been modeled, using grid cell size, $\Delta x = \Delta y$ = 0.018 m. All MILDwave results presented here refer to steady-state.

In WAMIT, a much smaller area of 10.0 m x 10.0 m around the WEC is modeled, using grid cell size, $\Delta x = \Delta y$ = 0.100 m for the free-surface elevation output points. In the middle of the grid cells, the wave amplitude a, and phase shift, φ, are calculated.

In order to compare the obtained MILDwave results to WAMIT results, the same area around the WEC is considered in both models (10.0 m x 10.0 m). In Section 3.5.4 the two models are compared also for a domain of extended dimensions, 49.7 m x 39.2 m (w_d x l_d).

3.4.3. Wave fields obtained by the selected model used for wave-structure interaction

In this section, the obtained wave field results, using the model WAMIT, are presented in terms of wave amplitude, a, and phase shift, φ, relative to the centre of the WEC.

3.4.3.1. Diffracted wave field in WAMIT

The resulting wave amplitude, a, is shown in Figure 3.10, when only diffraction is considered in WAMIT. In Figure 3.10, both the incident and diffracted wave fields are presented.

The WEC is implemented as a fully reflecting stationary structure, placed in the centre of the numerical domain. In Figure 3.10, a "square" of 3 x 3 cells is shown (thus an area of 0.3 m x 0.3 m) in the centre of the domain, where no WAMIT results are provided due to results' post-processing. Note, however, that the geometry used for the WAMIT calculations is indeed the actual WEC geometry and

the obtained WAMIT results do refer to the correct WEC geometry. In this area, the values of a (and φ) are set to zero. It has to be noted, that this area of zero-values in WAMIT, has slightly different dimensions and shape than the area occupied by the WEC in MILDwave (Section 3.4.4.1), where also a (and φ) are zero (in WAMIT: square area 0.3 m x 0.3 m; in MILDwave: circle area with $r = D / 2 = 0.1575$ m, where D, is the diameter of the WEC).

In Figure 3.10, the incident waves propagate from the bottom to the top. The resulting wave field around the WEC shows clearly the reflected waves in front of the WEC, as well as the locally reduced wave amplitudes in the lee of the WEC.

Also, in Figure 3.10, six lines are shown (S1 – S6) which indicate the location of cross sections used for the verification of the coupling methodology presented in Section 3.5.2.

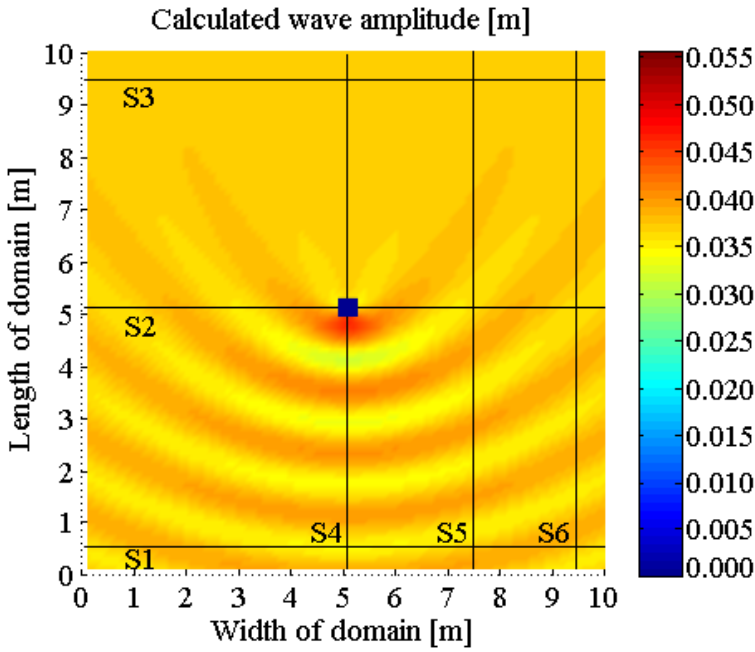

Figure 3.10. Calculated wave amplitude, a, in WAMIT, around a stationary WEC. The incident waves propagate from the bottom to the top. Both the incident and diffracted wave fields are presented [37].

3.4.3.2. Radiated wave field in WAMIT

The calculated wave amplitude, a, and phase shift, φ, relative to the motion of the WEC, are shown in Figures 3.11(a) and 3.11(b), respectively, for the radiating case.

The WEC is implemented as a heaving structure, placed in the centre of the numerical domain. The propagating incident waves are not shown in Figure 3.11.

In this case, the area where a and φ are set to zero in MILDwave, is the area occupied by the wave absorbing sponge layer inside the wave generation circle (Section 3.4.4.2.3) with r_C = 0.2 m, where r_C the radius of the wave generation circle around the WEC, instead of an area with $r = D / 2 = 0.1575$ m, where D is the diameter of the WEC, in the diffraction case of Section 3.4.3.1.

In Figure 3.11(a), the waves propagate in all directions from the source (WEC). The wave amplitude due to radiation is decreasing, further away from the WEC.

In, both, Figures 3.11(a) and 3.11(b), the contour plots of the presented results are axisymmetric, as they are caused by the heave motion of an axisymmetric cylindrical WEC.

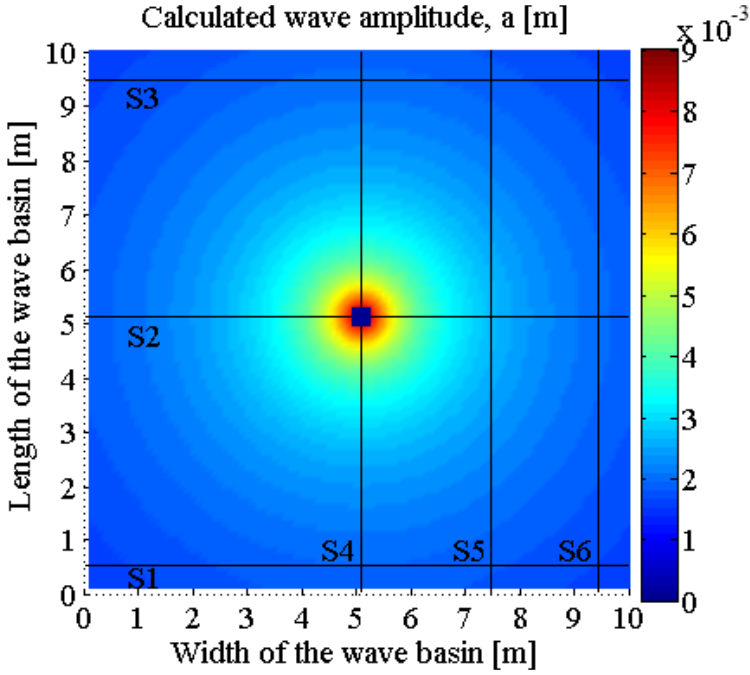

(a) wave amplitude, a.

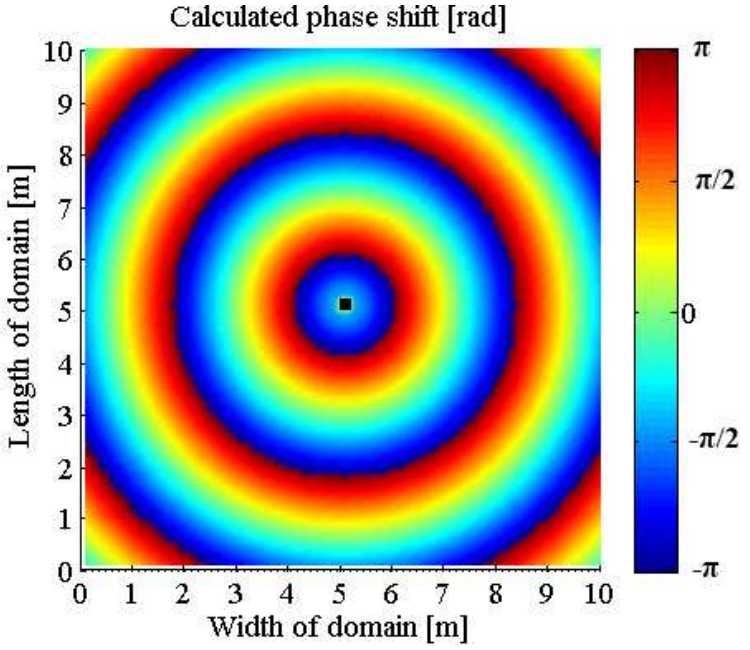

(b) Phase shift, φ.

Figure 3.11. Calculated (a) wave amplitude, a, and (b) phase shift, φ, in WAMIT, for the radiated wave field around a heaving WEC. The radiated waves propagate in all directions from the source (WEC) [37].

3.4.3.3. Perturbed wave field in WAMIT

The resulting wave amplitude, a, of the perturbed wave field, is shown in Figure 3.12, when simultaneously diffraction and radiation caused by the incident waves are considered in WAMIT.

The WEC is implemented as a fully reflecting heaving structure, placed in the centre of the numerical domain. In this case, the area where a and φ are set to zero in MILDwave, is the area occupied by the wave absorbing sponge layer inside the wave generation circle (Section 3.4.4.2.3) with r_C = 0.2 m, where r_C the radius of the wave generation circle around the WEC, similarly to radiation (Section 3.4.3.2).

In Figure 3.12, the incident waves propagate from the bottom to the top, and simultaneously, radiated waves propagate in all directions from the source (WEC). The resulting perturbed wave field around the WEC is similar to the diffracted wave field of Figure 3.10. However, in Figure 3.12, the wave amplitudes in the lee of the WEC appear to have larger variation and receive higher values. Specifically, the wave amplitudes are increased and this increase remains visible for larger distances. Moreover, the local peak of wave amplitude in front of the WEC due to wave reflection shown in Figure 3.12, is now less present compared to Figure 3.10, and a new peak is dominating in the lee of the WEC.

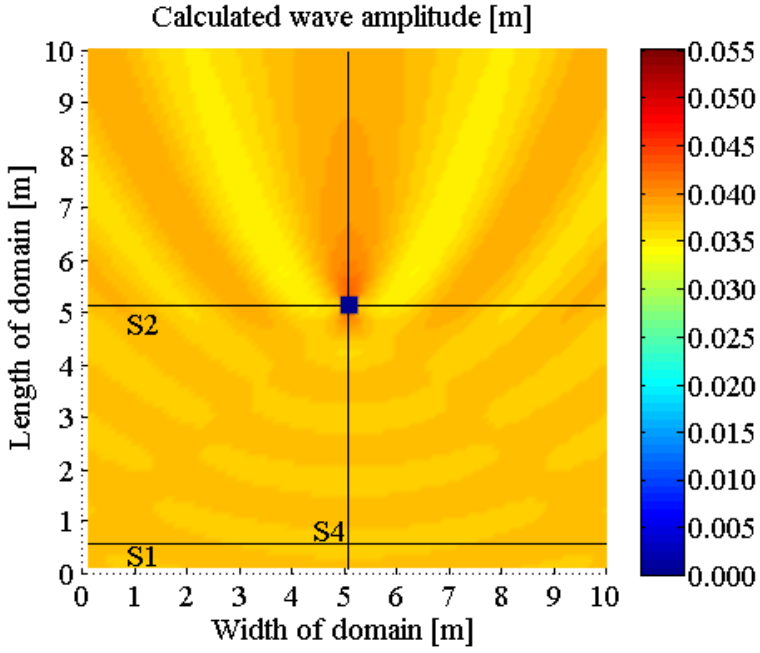

Figure 3.12. Calculated wave amplitude, a, in WAMIT, for the perturbed wave field around a heaving WEC. Incident waves propagate from the bottom to the top and radiated waves propagate in all directions from the source (WEC), simultaneously [37].

3.4.4. Step-by-step procedure in MILDwave

3.4.4.1. Diffracted wave field in MILDwave

The resulting wave amplitudes, a, are shown in Figure 3.13, when only diffraction is considered in MILDwave. Here, waves are generated only along a wave generation line (Section 3.3.3.1). In Figure 3.13, the incident waves propagate from the bottom to the top and both, the incident and diffracted wave fields are presented.

The WEC is implemented as a fully reflecting stationary structure, placed in the centre of the numerical domain. Moreover, in this test case, the WEC has been modeled for the sake of simplicity as a bottom based cylinder and therefore no wave transmission has been taken into account here. In Figure 3.13, the WEC is represented by a circle with diameter, D = 0.315 m. The values of a are zero in the grid cells occupied by the WEC.

The resulting wave field around the WEC shows clearly the reflected waves in front of the WEC, as well as the locally reduced wave amplitudes in the lee of the WEC, similarly to the wave amplitude results presented in Figure 3.10.

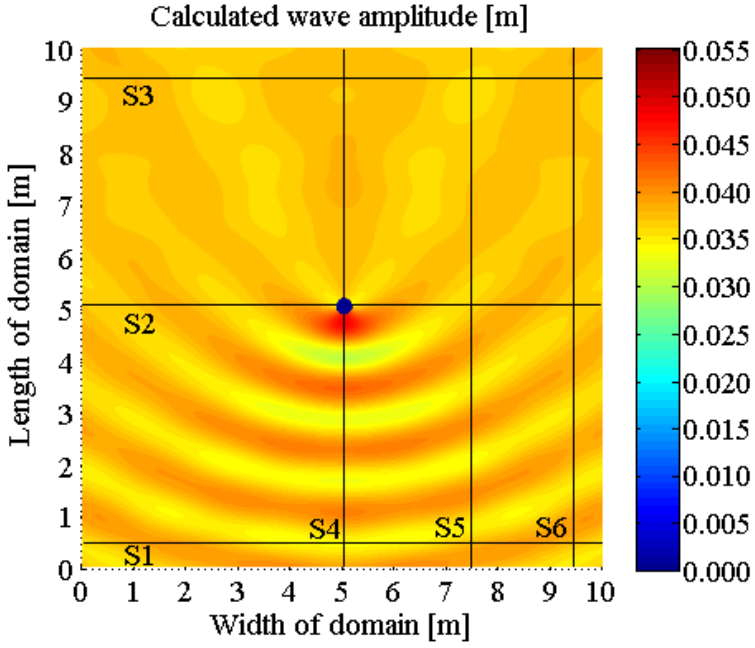

Figure 3.13. Calculated wave amplitude, a, in MILDwave, around a stationary WEC. The waves propagate from the bottom to the top and are generated along a wave generation line placed far from the here presented part of the numerical domain. Both the incident and diffracted wave fields are presented.

3.4.4.2. Wave radiation around the WEC in MILDwave, using a wave generation circle

In this section, radiated waves are generated on a wave generation circle using the wave generation technique described in Section 3.3.3.2. A wave generation circle with centre (x_C, y_C) and radius r_C = 0.20 m has been defined around the WEC, in the rectangular MILDwave simulation grid. Note that the radius of the WEC is 0.1575 m, and that the coordinates of the centre of the wave generation circle (x_C, y_C) coincide with the centre of the WEC and with the centre of the numerical domain.

3.4.4.2.1. Prescribed internal boundary wave conditions used as input on the wave generation circle

Prescribed internal boundary wave conditions are imposed on the wave generation circle which consist of wave amplitudes, a, and phase shifts, φ. These prescribed internal boundary wave conditions are derived from WAMIT output, taken from circular sections (at r_C = 0.2 m from the WEC centre) in the results of a and φ presented in Figure 3.11(a) and Figure 3.11(b), respectively.

The value of the Δb parameter, used for wave generation on a circle in MILDwave (see Section 3.3.3.2), is 2.14°. The determination of Δb, an important parameter for the correct simulation of the wave fields, is described in Section 3.4.4.2.2.

3.4.4.2.2. Iterative approach for determining the angle interval, Δb, used for wave generation on a circle

As seen in Section 3.3.3.2, an iterative approach is used to define the angle interval, Δb. Firstly, the term q is defined as the ratio $a_{r,M} / a_{r,W}$. $a_{r,M}$ and $a_{r,W}$ are the wave amplitudes of the radiated wave field on a radius r from the WEC centre, calculated using MILDwave and WAMIT, respectively. The wave amplitudes, $a_{r,M}$, are obtained by using prescribed internal boundary wave conditions on the wave generation circle with radius r_C = 0.20 m, which conditions derive from WAMIT output (see Section 3.4.4.2.1). The wave amplitudes, $a_{r,W}$, derive from the WAMIT output of wave amplitudes, a, taken from a radial section when $i\Delta b$ = 0° (see Figure 3.9 for convention of angle interval along the wave generation circle) in the results of a and φ presented in Figure 3.11(a) and Figure 3.11(b), respectively .

In Figure 3.14, the resulting q values as a function of Δb are provided, along the radial section when $i\Delta b$ = 0°. Results of q are presented on two different radii; on r

= r_c = 0.20 m on the wave generation circle, and on r = 0.40 m (2 x r_c). The target value of q ($q_{,target}$) is 1.0 and is obtained for $a_{r,M} = a_{r,W}$. A non-linear regression (power law) has been applied through the data.

The determination coefficient R^2 equals 0.9975 and 0.9934, which confirms that the regression lines (Eqs. (3.12) and (3.13), respectively) approximate well the data points on $r = r_C$ = 0.20 m and r = 0.40 m, respectively.

$$q = 1.903\ \Delta b^{-0.760} \quad , \qquad \text{on } r = r_C = 0.20 \text{ m} \tag{3.12}$$

$$q = 2.049\ \Delta b^{-0.968} \quad , \qquad \text{on } r = 0.40 \text{ m} \tag{3.13}$$

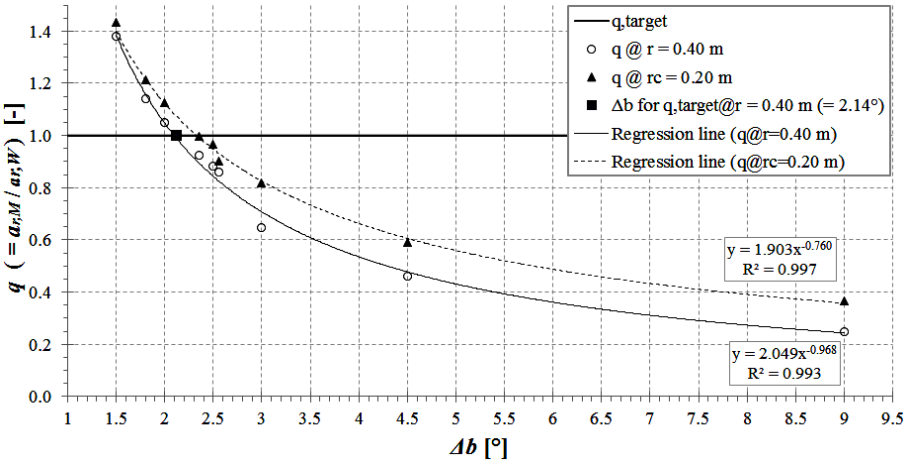

Figure 3.14. Ratio q (= $a_{r,M} / a_{r,W}$) as a function of Δb, for regular wave generation on a circle with r_C = 0.20 m. q is calculated for two radii around the WEC: $r = r_C$ = 0.20 m ("triangle"-symbols) and r = 0.40 m ("circle"-symbols). The target value of q ($q_{,target}$) is indicated at value 1.0 (thick continuous horizontal line). The resulting Δb (=2.14°) for achieving $q_{,target}$ is indicated using a "square"-symbol. The regression lines of the q-values for $r = r_C$ = 0.20 m (thin dashed line) and for r = 0.40 m (thin continuous line) are also shown.

In Figure 3.14, as Δb increases (>2.35°), q becomes too low and therefore the wave amplitudes generated in MILDwave along a wave generation circle do not reach the target wave amplitude values which are derived from WAMIT and used as input on the wave generation circle. On the other hand, very small Δb values (< 2.00°) result in the generation of too high wave amplitudes, especially in the vicinity of the wave generation circle. Nevertheless, in the following sections, the agreement

between MILDwave and WAMIT results for wave amplitudes will not be investigated on the wave generation circle, but further from the WEC and specifically at radii ≥ 0.40 m. Therefore, as shown in Figure 3.14, in order to achieve $q_{,target}$, Δb should be between 2.0° and 2.35°. It is found that Δb = 2.14°, which derives from the q values on r = 0.40 m in Figure 3.14. Consequently, Δb = 2.14° is used for generating radiated waves around the WEC, by applying the technique described in Section 3.3.3.2.

The comparison of the calculated wave amplitudes in MILDwave (a_M) when using Δb = 2.14°, against the calculated wave amplitudes in WAMIT (a_W) throughout the entire simulated domain, is presented in Section 3.5.3, in detail.

3.4.4.2.3. Radiated wave field in MILDwave

The calculated wave amplitude, a, and phase shift, φ, relative to the motion of the WEC, are shown in Figures 3.15(a) and 3.15(b), respectively. The WEC is implemented as a wave source realized by a wave generation circle with a radius (r_C = 0.20 m) slightly larger than the WEC radius (0.1575 m). Waves are generated only on a wave generation circle using the technique described in Section 3.3.3.2, while no incident waves are interacting with the WEC. The results in the circular area with radius $r < r_C$ (where r_C = 0.20 m) and (x_C, y_C) in the centre of the domain in MILDwave, are set to zero; the values within the wave generation circle have no physical meaning, as this area corresponds to a wave absorbing sponge layer.

In Figure 3.15(a), the waves propagate in all directions from the source (wave generation circle around the WEC). The wave amplitude due to radiation is decreasing, further away from the WEC. In, both Figures 3.15(a) and 3.15(b), the contour plots of the presented results are axisymmetric, as they are caused by the heave motion of an axisymmetric cylindrical WEC.

The instantaneous surface elevations at $t = 270T$ (where T is the wave period) are given in Figure 3.16 for the radiated wave field around the WEC. It is clear that the wave crests decrease further away from the wave generation circle.

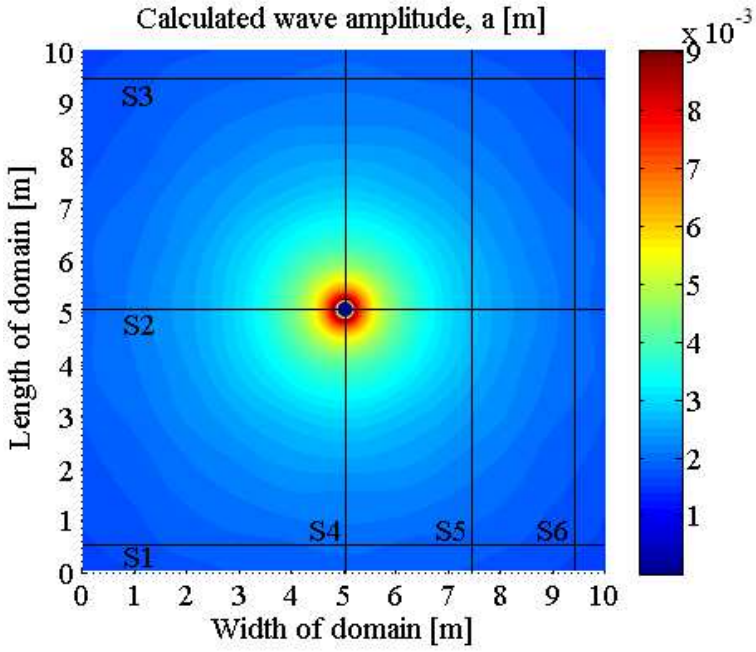

(a) Wave amplitude, a.

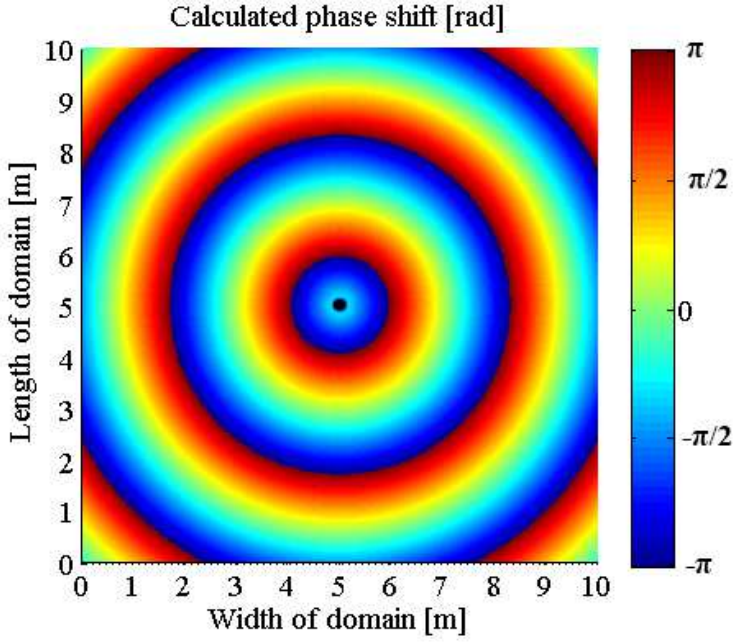

(b) Phase shift, φ.

Figure 3.15. Calculated (a) wave amplitude, a, and (b) phase shift, φ, in MILDwave, for the radiated wave field around a heaving WEC. Radiated waves propagate in all directions from the source (WEC).

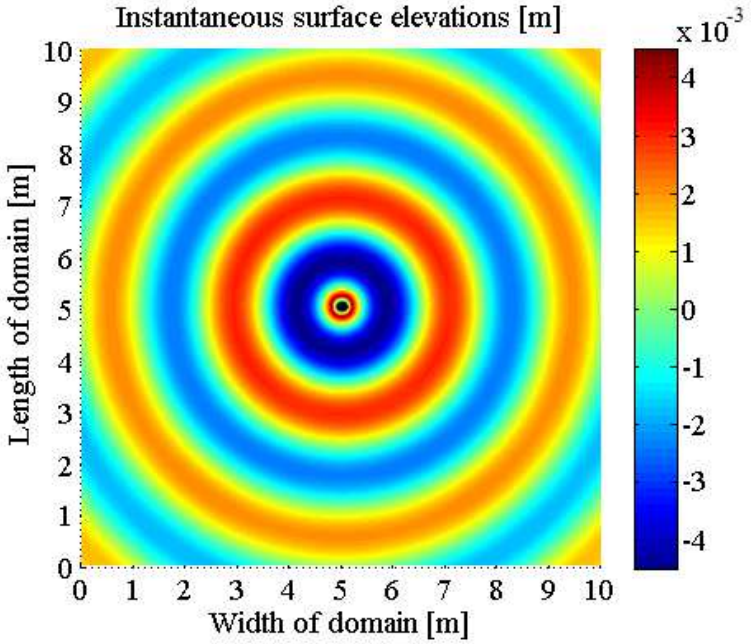

Figure 3.16. Instantaneous surface elevations at t = 270T (where T is the wave period) calculated using the coupling methodology implemented in MILDwave along a wave generation circle, for the radiated wave field around the heaving WEC. Radiated waves propagate in all directions from the source (WEC).

3.4.4.3. Perturbed wave field in MILDwave

For the calculation of the perturbed wave field in MILDwave, an additional phase shift, φ, between the radiated and diffracted wave field is obtained from the WAMIT results. A longitudinal section through the WEC is considered in the numerical domain with extended dimensions, 49.6 m x 49.6 m (w_d x l_d), at x^* = 24.8 m, taking into account only the area downwave of the WEC (Figure 3.17). In this longitudinal section the radiated and diffracted wave have the same direction of wave propagation. From Figure 3.17 it is seen that an additional phase shift, $\Delta\varphi$ = 0.53 rad (30.5°) is needed between the radiated and the diffracted wave, when modelling the perturbed wave field in MILDwave, using the here presented coupling methodology.

The resulting wave amplitude, a, of the perturbed wave field, is shown in Figure 3.18, when simultaneously diffraction and radiation caused by the incident waves are considered in MILDwave by applying the coupling methodology presented in Section 3.2.2.

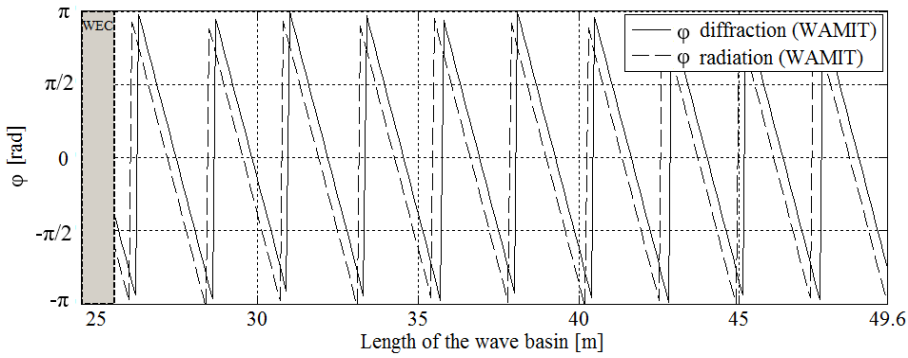

Figure 3.17. Difference between phase shift (relative to the centre of the WEC) of the radiated and diffracted wave field, as calculated using WAMIT [37].

In MILDwave, each time step, the diffracted and radiated wave field are calculated separately and afterwards the wave elevations and velocity potentials are summed up. By separating the calculation of both wave fields the diffracted wave is not disturbed by the wave absorbing sponge inside the wave generation circle. On the other hand, the radiated wave is not disturbed by the fully reflecting structure (or structure with specific absorption coefficients assigned, in another case) used for the simulation of the diffracted wave field.

The WEC is implemented as a fully reflecting structure surrounded by the wave generation circle, and is placed in the centre of the numerical domain. Here waves are simultaneously generated along a wave generation line (see Section 3.3.3.1) and on a wave generation circle (see Section 3.3.3.2), using the presented coupling methodology. Incident waves propagate in Figure 3.18 from the bottom to the top, and, simultaneously, radiated waves propagate in all directions from the source (the wave generation circle around the WEC). The results in the circular area with radius $r < r_C$ (where r_C = 0.20 m, the radius of the wave generation circle) and (x_C, y_C) in the centre of the domain in MILDwave, are set to zero; the values within the wave generation circle have no physical meaning, as this area corresponds to a wave absorbing sponge layer.

The resulting perturbed wave field around the WEC is similar to the diffracted wave field of Figure 3.13. However, in Figure 3.18, the wave amplitudes appear to have larger variation and receive higher values in the lee of the WEC. Specifically, the wave amplitudes are increased and this increase remains visible for larger distances. Moreover, the local peak of wave amplitude in front of the WEC due to wave reflection shown in Figure 3.13, is now less present compared to Figure 3.10, and a new peak is dominating in the lee.

Also, in Figure 3.18, three lines are shown (S1, S2, S4) which indicate the location of cross sections used for the verification of the proposed coupling methodology in Section 3.5.4.

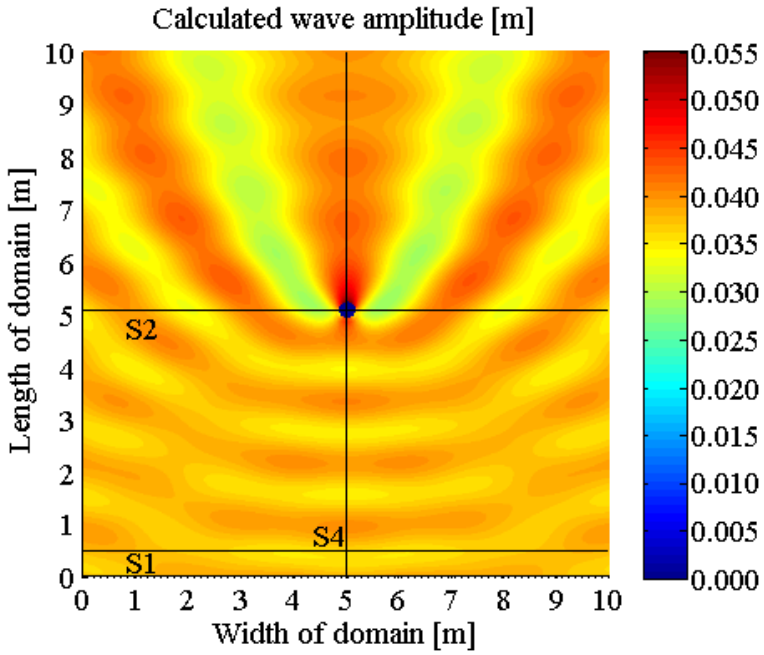

Figure 3.18. Calculated wave amplitude, a, in MILDwave, for the perturbed wave field around a heaving WEC. Incident waves, generated along a wave generation line, propagate from the bottom to the top, and radiated waves, generated along a wave generation circle, propagate in all directions from the source (WEC), simultaneously.

3.5. Verification of the coupling methodology against results by a wave-structure interaction model

3.5.1. Presentation methodology of verification results

For the verification of the obtained results using MILDwave with the presented coupling methodology implemented, the WAMIT results are used as reference. Therefore, the objective is to achieve good agreement between MILDwave and WAMIT results.

To make a detailed comparison between the employed model for the wave-structure interaction (WAMIT) and the results from the coupling methodology implemented in MILDwave, cross sections at several distances from the centre of the WEC are studied, showing the wave amplitude, a. The locations of the used cross sections for this verification (S1 - S6) are indicated e.g. on Figures 3.10, 3.11(a), 3.12, 3.13, 3.15(a) and 3.18 for the domain of 10.0 m x 10.0 m, w_d x l_d.

The results for the wave amplitude, a, have been compared at a lateral section in front of (S1), through (S2) and behind (S3) the WEC unit at respectively y^* = 0.5 m, 5.0 m and 9.5 m. Also three longitudinal sections at x^*= 5.0 m (S4) through the WEC, 7.5 m (S5) and 9.5 m (S6) at the side of the WEC are used. Moreover, similar cross sections are shown for the domain with extended dimensions (49.6 m x 39.2 m, w_d x l_d) when results of the perturbed wave field are compared.

For simplicity reasons, only (S1), (S2) and (S4) are presented for the perturbed wave field, identified as the most important cross sections. In addition, results of the obtained wave amplitudes, a, and phase shifts, φ, are compared, on a circular section around the WEC with r = 0.40 m (further from the wave generation circle, r_C = 0.20 m, used in the coupling methodology implemented in MILDwave).

The values of absolute differences of wave amplitude, a, between WAMIT and MILDwave are also shown at the end of Section 3.5.4 for the entire domain, in terms of 100 % percentages and are calculated as:

$$\left|\frac{a_M - a_W}{a_W}\right| x100\ \% \tag{3.14}$$

where a_M, the calculated wave amplitude in MILDwave and a_W, the calculated wave amplitude in WAMIT.

3.5.2. Diffracted wave field using the coupling methodology

In Figures 3.19(a-b-c), the calculated wave amplitude, a, for the incident and diffracted wave field in WAMIT and MILDwave are compared in three lateral sections (S1 – S3) as indicated on Figures 3.10 and 3.13. Figures 3.20(a-b-c) show a comparison of the calculated wave amplitude, a, obtained using WAMIT and MILDwave, for the three longitudinal sections (S4 – S6), also indicated on Figures 3.10 and 3.13.

The location of the WEC in the presented 10.0 m x 10.0 m numerical domain is also indicated. Moreover, on a circular section around the WEC with r = 0.40 m, the obtained wave amplitudes, a, and phase shifts, φ, are compared (Figure 3.21).

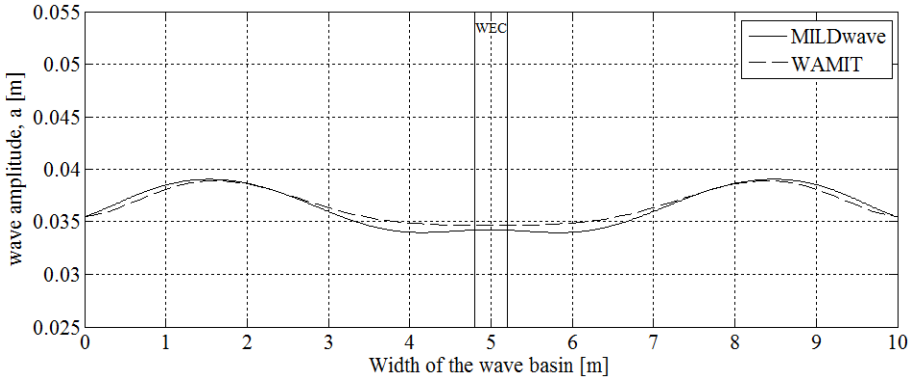

(a) Section S1.

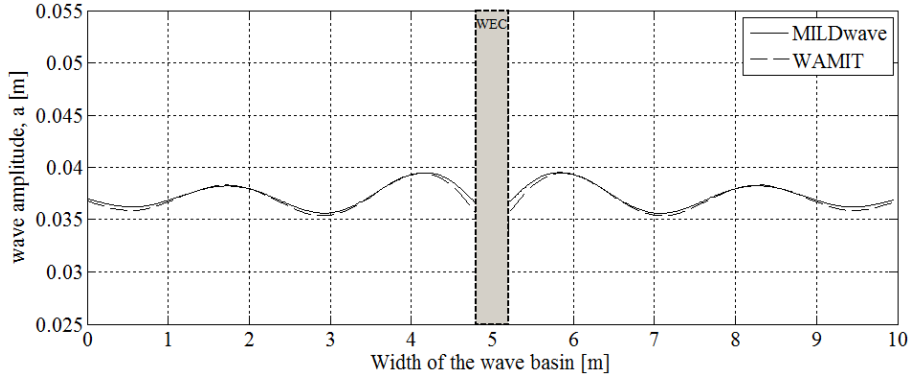

(b) Section S2.

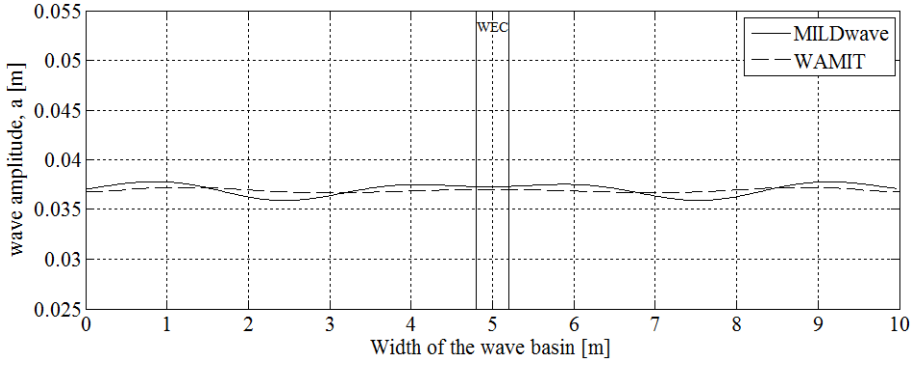

(c) Section S3.

Figure 3.19. Calculated wave amplitude, *a*, in section (a) S1, (b) S2, (c) S3 (incident and diffracted wave field).

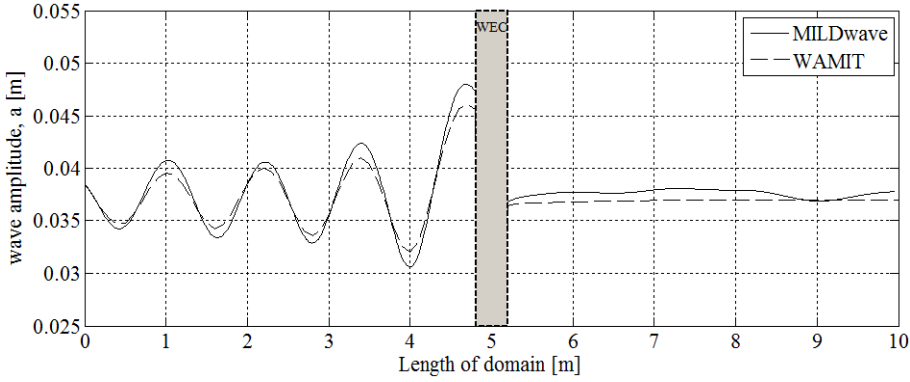

(a) Section S4.

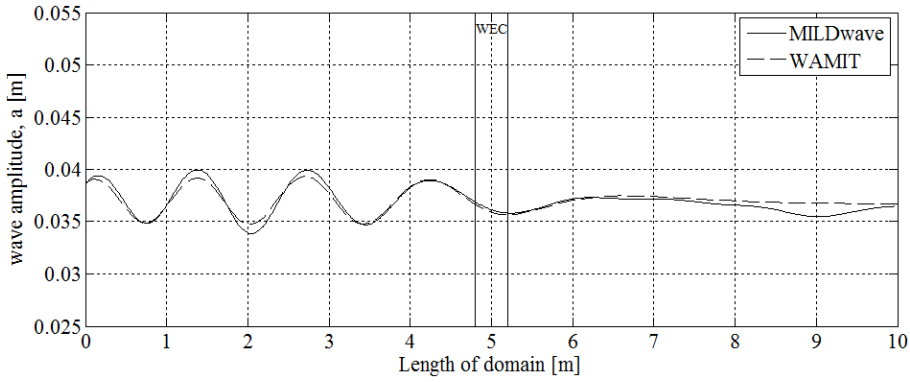

(b) Section S5.

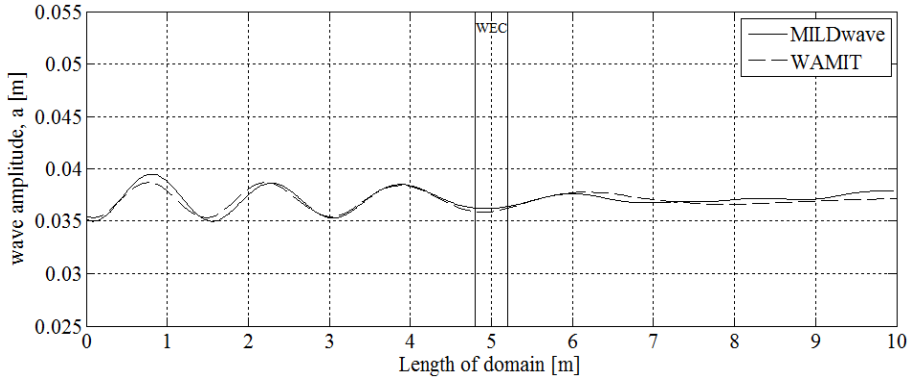

(c) Section S6.

Figure 3.20. Calculated wave amplitude, a, in section (a) S4, (b) S5, (c) S6 (incident and diffracted wave field).

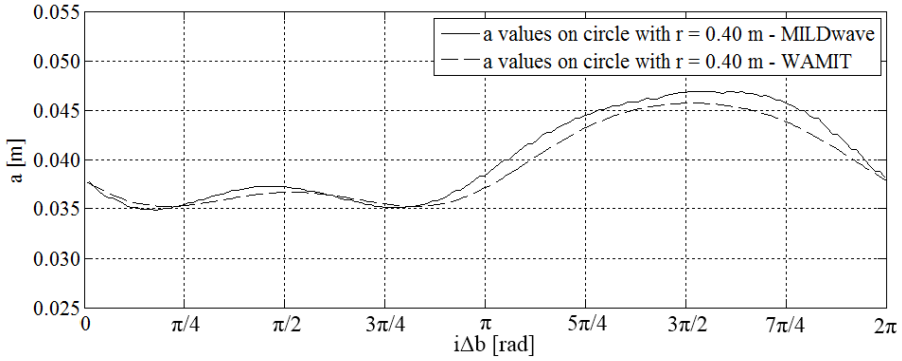

(a) wave amplitude, a.

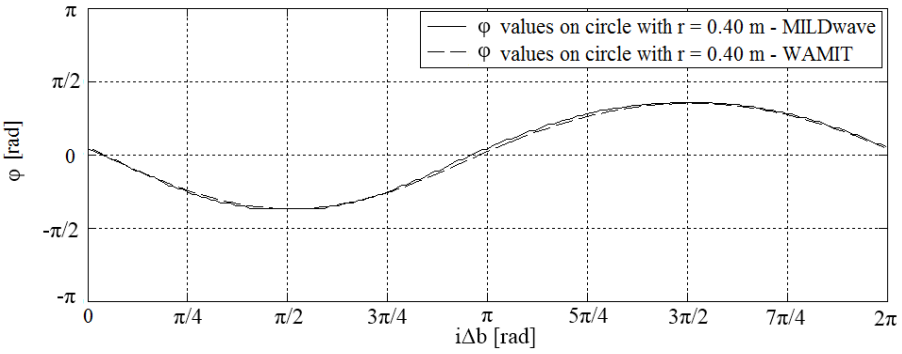

(b) phase shift, φ.

Figure 3.21. Calculated wave amplitude, a, and phase shift, φ, on a circle with centre equal to the centre of the WEC and radius, r = 0.40 m (incident and diffracted wave field).

Very good agreement is observed, while the differences between the wave amplitudes, a, calculated using WAMIT and MILDwave do not exceed 4.1 % in all cases. However, it should be noted that in this test case, the WEC in MILDwave has been modeled as a bottom based cylinder, for the sake of simplicity, and therefore no wave transmission has been taken into account here. On the other hand, the WEC in WAMIT is modeled as it actually is, (3-D) taking into account the buoy draft and wave transmission. Therefore, modelling of wave transmission in MILDwave, which is achieved by using the sponge layer technique described in Section 3.3.2, will lead to better agreement between the two numerical models, since both models are based on potential theory.

This largest difference of 4.1% is observed in S4 just in front of the WEC, showing that the modeled WEC exhibits in MILDwave higher wave reflection.

Small deviations are seen in the lee of the WEC reaching 2.9 % (section S3) and 3.6 % (section S4). In the area in front of the WEC, the largest differences are observed within the zone at the sides of the WEC (± 1.0 m) where these reach 2.6 % (S1), due to higher wave reflection by the WEC in MILDwave. Also in Figures 3.21(a-b), very good agreement is observed between the two models for the wave amplitudes and phase shifts (relative to the centre of the WEC), respectively, on a circle with r = 0.40 m.

3.5.3. Radiated wave field using the coupling methodology

In Figures 3.22(a-b-c), the calculated wave amplitude, a, for the radiated wave field in WAMIT and MILDwave are compared in three longitudinal sections (S4 - S6) as indicated on Figures 3.11(a) and 3.15(a). The three lateral sections (S1, S2, S3) are not plotted separately, for the sake of simplicity, as the radiated wave field around the axi-symmetric WEC is also axi-symmetric.

Very good agreement is observed, with the WAMIT and MILDwave results hardly being distinguished from each other. Very small deviations are seen only on the wave generation circle, in the sections through the WEC (section S2 and section S4). However, the results on the wave generation circle are not taken into account for this comparison.

The location of the WEC in the presented 10.0 m x 10.0 m numerical domain is also indicated on Figures 3.22(a-b-c).

Moreover, on a circular section around the WEC with r = 0.4 m, the obtained wave amplitudes, a, and phase shift, φ, are compared (Figures 3.23). Also those results show very good agreement, confirming the accuracy of the implemented wave generation technique in MILDwave, for generating waves on a circle.

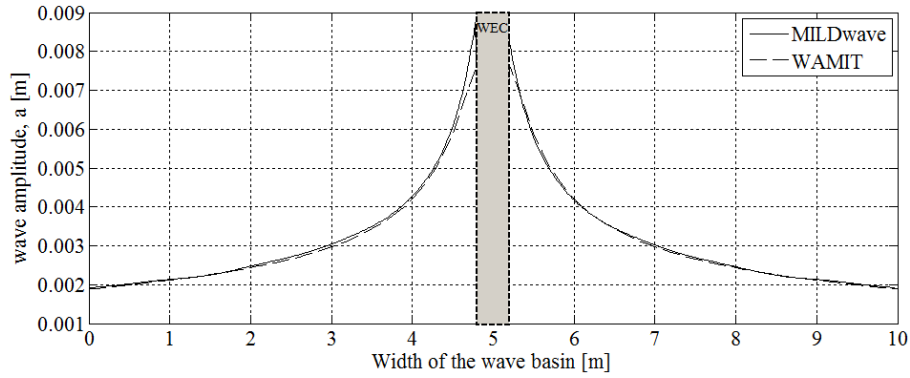

(a) Section S4 = Section S2.

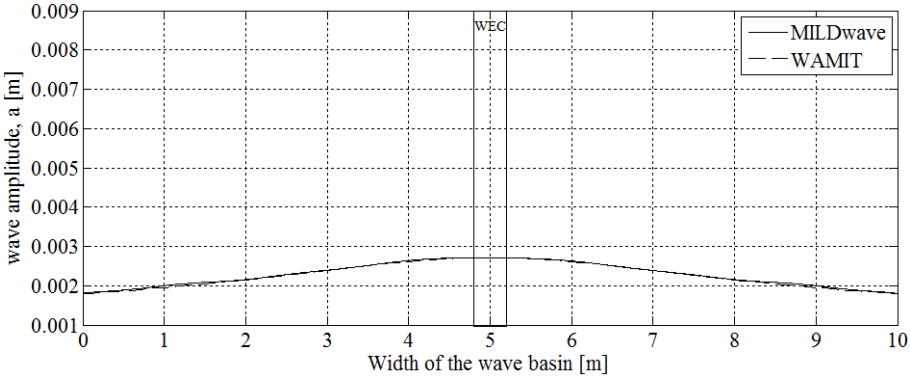

(b) Section S5.

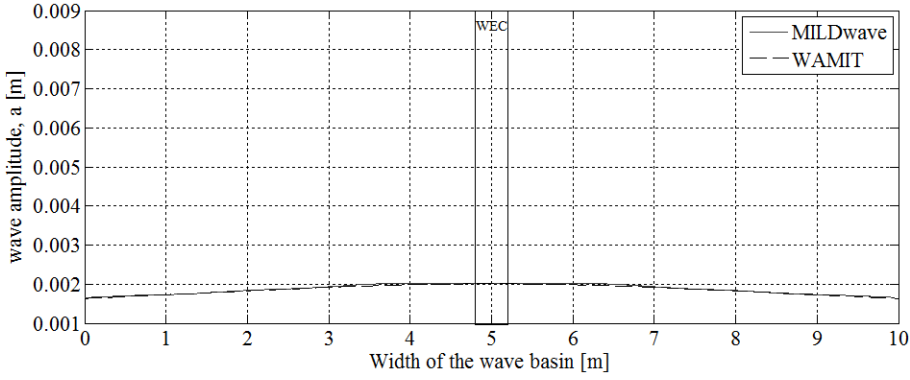

(c) Section S6 = Section S1 = Section S3.

Figure 3.22. Calculated wave amplitude, *a*, in section (a) S4 (= S2), (b) S5, (c) S6 (= S1= S3) (radiated wave field).

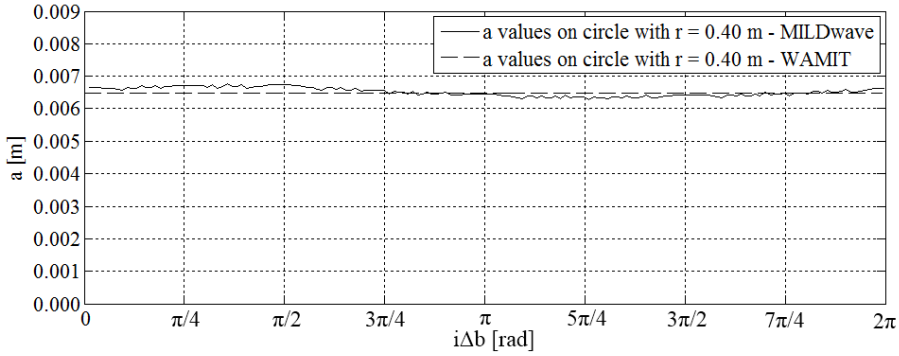

(a) wave amplitude, a.

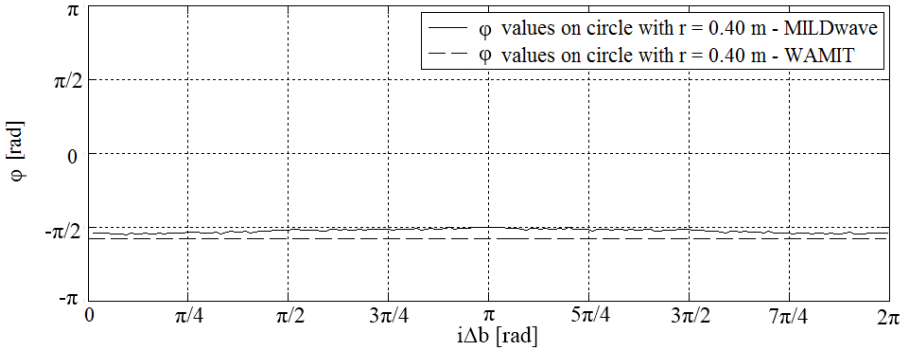

(b) phase shift, φ.

Figure 3.23. Calculated (a) wave amplitude, a, and (b) phase shift, φ, on a circle with centre equal to the WEC centre and radius, r = 0.40 m (radiated wave field).

3.5.4. Perturbed wave field using the coupling methodology

In Figures 3.24(a-b-c), the calculated wave amplitude, a, for the perturbed wave field in WAMIT and in MILDwave (with the coupling methodology implemented), are compared in two lateral sections (S1 and S2) and one longitudinal section (S4), as indicated on Figures 3.12 and 3.18.

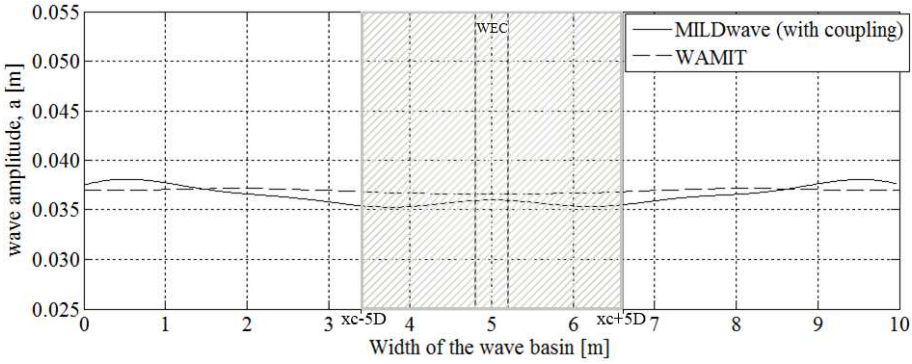

(a) Section S1.

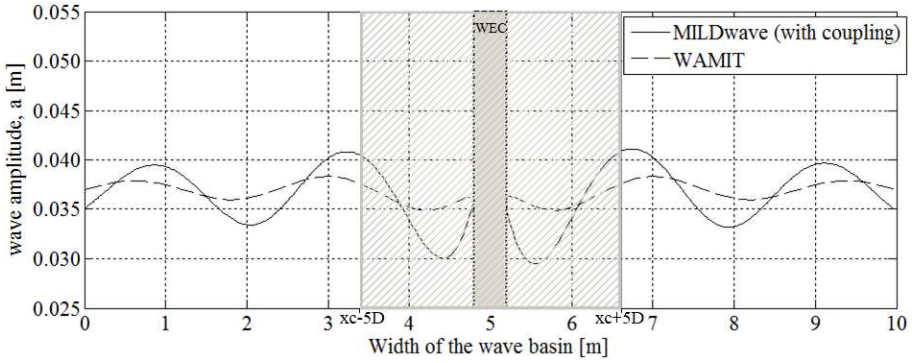

(b) Section S2.

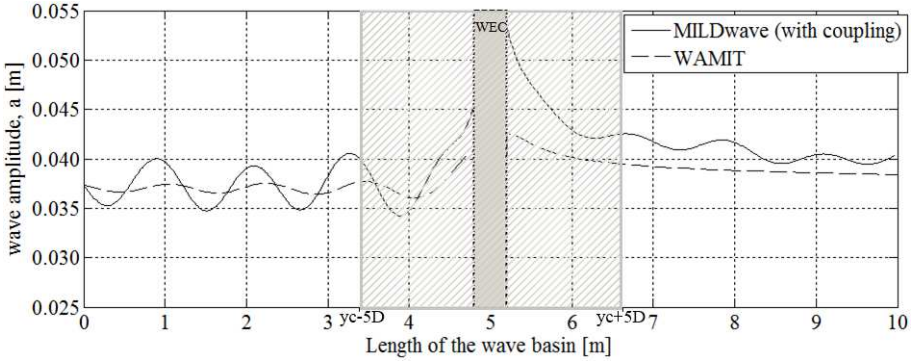

(c) Section S4.

Figure 3.24. *Cont.*

Figure 3.24. Calculated wave amplitude for the perturbed wave field, a, in section (a) S1, (b) S2, (c) S4. The hatched area around the WEC is also indicated, with radius ($x_C \pm 5D$) or ($y_C \pm 5D$), where (x_C, y_C) is the centre of the WEC and of the wave generation circle, and D is the WEC diameter. Within this area, the obtained results are of no importance.

Moreover, the two models are compared also for numerical domains with extended dimensions, 49.6 m x 39.2 m (w_d x l_d), shown in Figure 3.25 and Figure 3.26, in order to make a detailed comparison of the far-field effect of the WEC on the wave field. In Figures 3.27(a-b-c), the calculated wave amplitude, a, in WAMIT and in MILDwave (with the coupling methodology implemented), are compared in two extended lateral sections (S1' and S2') and one extended longitudinal section (S4').

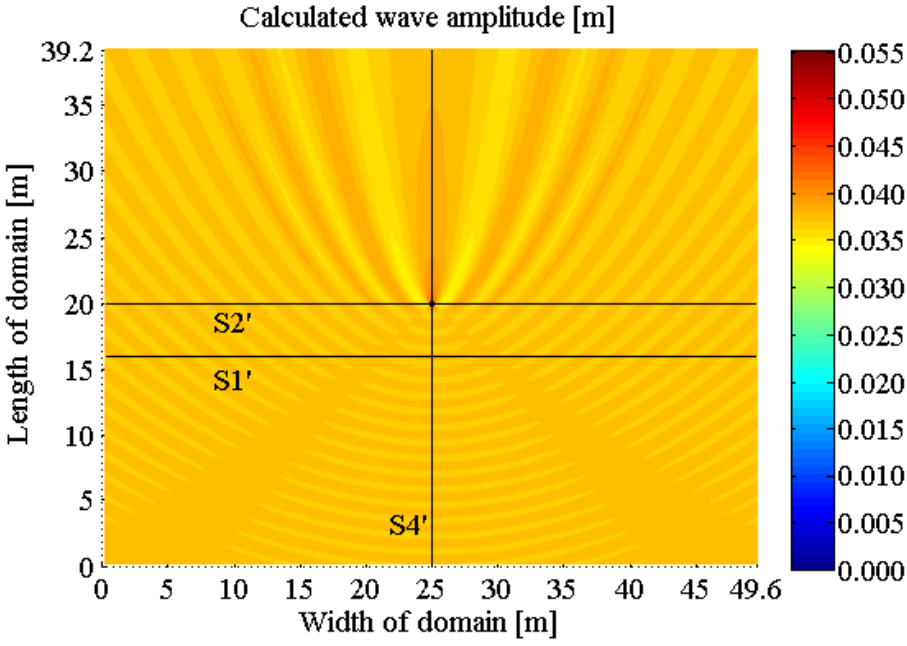

Figure 3.25. Calculated wave amplitude, a, in WAMIT, for the perturbed wave field around a heaving WEC for a domain with extended dimensions, 49.6 m x 39.2 m (w_d x l_d). Incident waves, generated along a wave generation line, propagate from the bottom to the top, and radiated waves, generated along a wave generation circle, propagate in all directions from the source (WEC), simultaneously.

The location of the WEC in the presented 10.0 m x 10.0 m and 49.6 m x 39.2 m numerical domains is also indicated. By pursuing an "engineering" approach, a near-field area around the WEC is considered, in which the MILDwave results will not be used. Based on practical considerations, this area is taken equal to the surface area of a circle with radius $5D$, conventionally used as the shortest WEC-to-WEC distance in the WEC arrays tested during part I and III of this PhD research, where $5D$ = 5 x (0.315 m) = 1.575 m and D is the WEC diameter. The hatched area shown at the sides (in S1, S2, S1', S2'), as well as upwave and downwave (in S4, S4') of the WEC, represents the area around the WEC with radius ($x_C \pm 5D$) or ($y_C \pm 5D$), where (x_C, y_C) is the centre of the WEC and of the wave generation circle. Outside the hatched area, MILDwave results will be compared to WAMIT results to evaluate the achieved accuracy of the coupling methodology, presented here. For largely spaced WEC arrays the hatched may be even larger.

Moreover, on a circular section around the WEC with r = 0.40 m, the obtained values of phase shift, φ, using MILDwave (with the coupling methodology implemented) are compared to WAMIT results for φ (Figure 3.28).

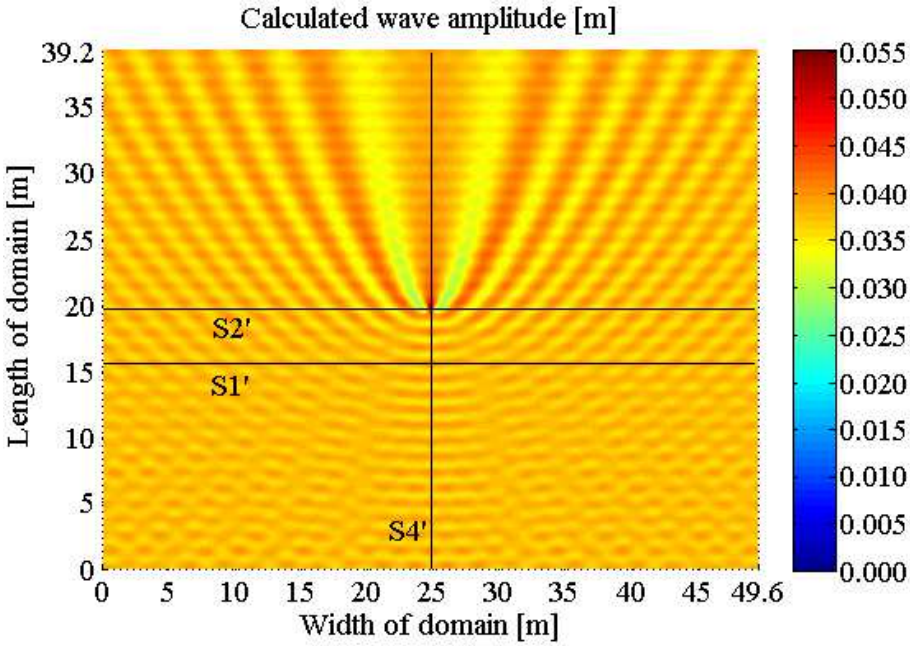

Figure 3.26. Calculated wave amplitude, a, in MILDwave (with the coupling methodology implemented), for the perturbed wave field around a heaving WEC for a domain with extended dimensions, 49.6 m x 39.2 m (w_d x l_d). Incident waves, generated along a wave generation line, propagate from the bottom to the top, and radiated waves, generated along a wave generation circle, propagate in all directions from the source (WEC), simultaneously.

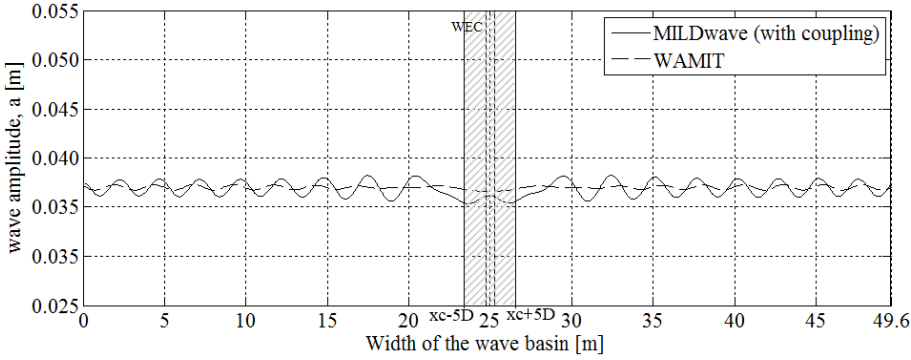

(a) Section S1'.

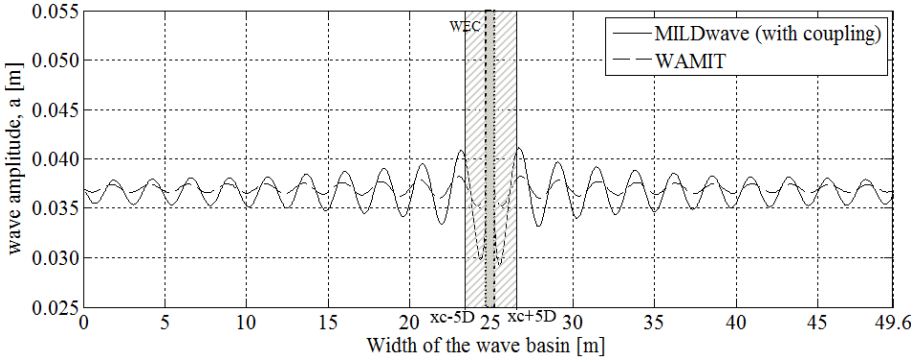

(b) Section S2'.

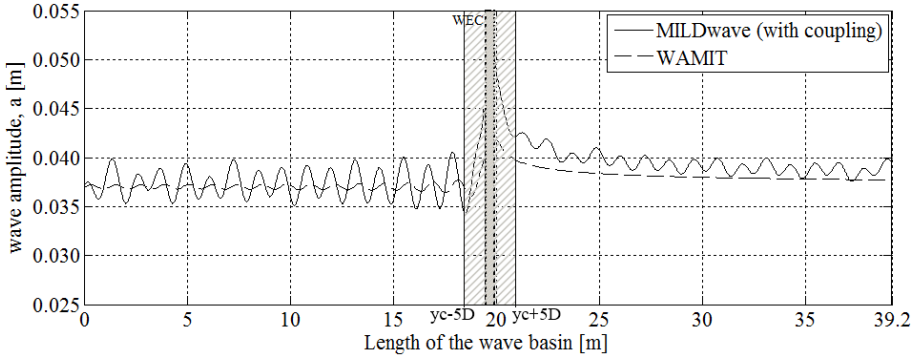

(c) Section S4'.

Figure 3.27. Calculated wave amplitude for the perturbed wave field, a, in section (a) S1', (b) S2', (c) S4'. The hatched area around the WEC is also indicated, with radius ($x_C \pm 5D$) or ($y_C \pm 5D$), where (x_C, y_C) is the centre of the WEC and of the wave generation circle, and D is the WEC diameter. Within this area, the obtained results are of no importance.

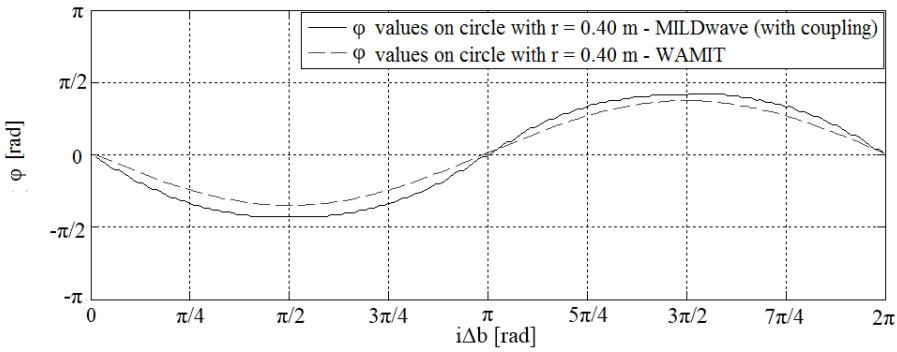

Figure 3.28. Calculated phase shift, φ, on a circle with centre equal to the centre of the WEC and radius, r = 0.40 m (perturbed wave field).

In general, a very good agreement is observed in the far-field. The differences between the wave amplitudes, a, for the perturbed wave field calculated using WAMIT and MILDwave (with the coupling methodology implemented) do not exceed in S1 3.3 %, while the largest difference at the far field (far from the WEC), as shown in S1', reduces to 1.8 % (i.e. in Figures 3.25 and 3.26, and 3.27(a) at distance x = 0.0 m and x = 49.6 m of the domain width).

In S2, the largest wave amplitude difference appears at x_C ± 0.4 m from the WEC centre and is a very localized effect. However, in this chapter only results within radii larger than r = 0.4 m from the WEC centre (x_C, y_C) are discussed. Results within radii smaller than r = 0.4 m are considered to be too close to the wave generation circle and are not taken into account in the comparisons. Moreover, this largest wave amplitude difference (at x_C ± 0.4 m) is situated within the hatched area around the WEC, with radius x_C ± 5D, where the obtained results are not used for comparison.

In S2, a little further from the WEC centre, at x_C ± 1.7 m and x_C ± 3.0 m, the wave amplitude differences reduce to 7.3 %, while the largest difference at the far-field, as shown in S2', reduces to 3.1 % (i.e. in Figures 3.25 and 3.26, and 3.27(b) at distance x^*= 0.0 m and x^* = 49.6 m of the domain width).

In S4, the largest wave amplitude difference appears in the lee of the WEC, at a distance of 0.2 m from the WEC centre and is a very localized effect. This high difference appears, though, on the wave generation circle, where the wave amplitude differences are not taken into account for this comparison. As shown in S4, in the lee of the WEC and right after 1.0 m from the WEC centre, those differences are 6.9 % (which is still within the hatched area of (y_C + 5D), so not to be used for comparison), and reduce to 0.0 % - 5.7 % in the far-field (i.e. in Figures 3.25 and 3.26, and 3.27(c) at distance x^* = 39.2 m of the domain length). In the same section S4, in front of the WEC, the largest differences appear again on the wave generation circle, which results are not taken into account in the presented comparisons. These

differences reduce to 0.8 - 7.1 % at the far-field, as shown in S4' (i.e. in Figures 3.25 and 3.26, and 3.27(b) at distance x^* = 0.0 m of the domain length).

Also in Figure 3.28, acceptable agreement is observed between the two models for the phase shifts (relative to the centre of the WEC), on a circle with r = 0.40 m. However, there are differences, especially in the lee (at $i\Delta b = \pi/2$) and at the front (at $i\Delta b = 3\pi/2$) of the WEC. These differences in the phase shifts, φ, are also responsible for the wave amplitude differences. Therefore, in case one is interested in the very near-field, the necessary phase shift correction can be applied along the wave generation circle. This will also result in higher agreement between the calculated wave amplitudes in the near-field, and therefore better estimation of the intra-array effects. Moreover, a better agreement can be achieved by modelling the wave transmission under the WEC in MILDwave, as commented in Section 3.5.2.

In order to make a detailed comparison between the two models, also the differences over the entire domains calculated using Eq. (3.14), are shown in Figure 3.29 and Figure 3.30, for the 10.0 m x 10.0 m and the 49.6 m x 39.2 m numerical domain, respectively. In this way, a clear overview is given, of the spatial variability of the wave amplitude differences in the entire domain.

Most importantly, in order to visualize the effect of these differences for the studied case, two circles have been drawn in Figure 3.29, indicating the proposed hatched area. The centres of the circles coincide with the centre of the WEC. The radius of the inner circle is equal to $5D$, and within this area, the results are not used for performance comparison between the two models. As also shown in the cross sections of Figures 3.24 and 3.27, the largest wave amplitude differences remain within this circle of radius $5D$. As a result, when a second (or third) WEC is added at a distance of $5D$ in front of and/or in the lee of the WEC shown in Figure 3.29, the largest wave amplitude differences that the new WEC(s) will experience, when the coupling methodology implemented in MILDwave is used, do not exceed 8.0 %. This wave amplitude difference of 8.0 % represents two local peaks in front of and in the lee of the WEC, as shown in detail in Figure 3.27(c). Moreover, as presented in Figure 3.29, the largest wave amplitude differences (16.5 %) appear in the lee of the WEC at ± 45°, and are spatially very limited and localized effects. Differences between 7.5 % and 15.0 % are visible at the sides of the WEC. In the largest part of the domain, and especially in front of and in the lee of the WEC, the wave amplitude differences are small (<7.5 %) which shows the good agreement between the results obtained using WAMIT and MILDwave (with the coupling methodology implemented).

In Figure 3.29, also a second circle is drawn (the outer circle). The radius of the outer circle is equal to $10D$, where D is the WEC diameter. The radius of the outer circle ($10\,D$) represents the distances between successive WECs for specific geometric WEC array layouts layouts tested during this PhD research. Most importantly, a WEC-to-WEC distance equal to $10D$ represents a typical spacing

between the WECs of an array [38]. When in a WEC array the spacing between the WECs of the array are larger than $10D$, intra-array interactions are no longer important and can be neglected as recently presented in [38]. As shown in Figure 3.29, the largest wave amplitude differences remain in an area within this circle of diameter $10D$. As a result, the coupling methodology implemented in MILDwave can be used to model WEC arrays with spacing between the WECs equal and larger than $10D$, installed e.g. in front of and/or in the lee of the WEC shown in Figure 3.29. In that case, the largest wave amplitude differences the additional successive WEC(s) will experience are small, and do not exceed the 7.5 %, while at the largest part of the domain they are even smaller than 5.0 %.

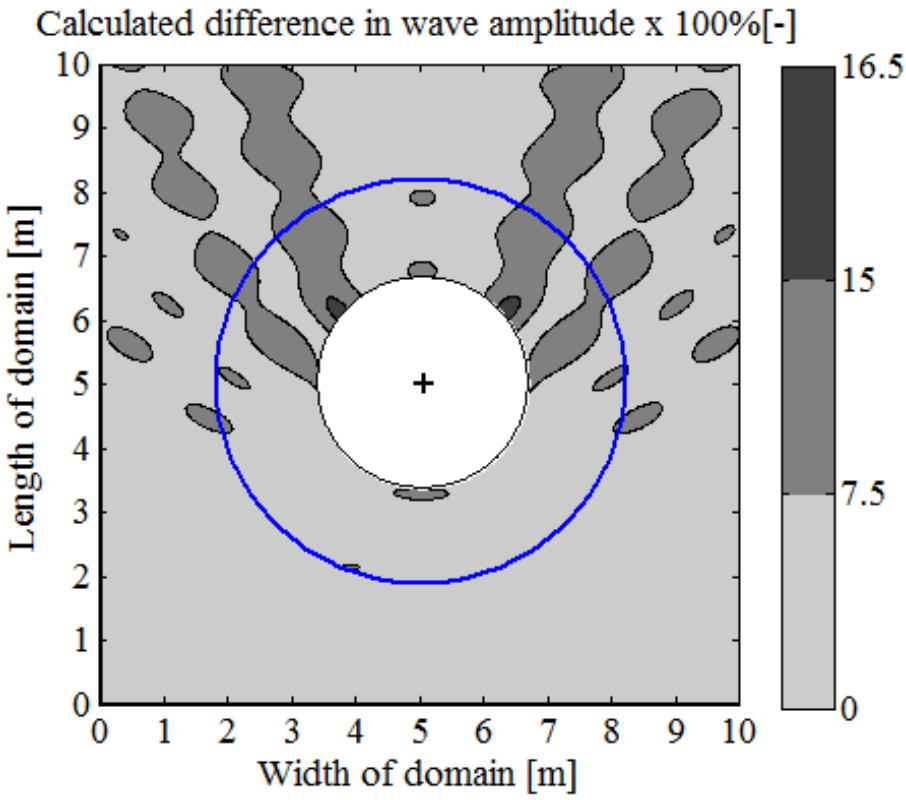

Figure 3.29. Calculated (using Eq. (3.14)) wave amplitude differences between WAMIT and MILDwave (with the coupling methodology implemented), for the perturbed wave field around a heaving WEC. A domain with dimensions, 10.0 m x 10.0 m (w_d x l_d) is shown. Light grey, grey and dark grey colour, represent areas with differences smaller than 7.5 %, between 7.5 % and 15.0 %, and max 16.5 %, respectively. The zones within the drawn inner and outer circles are indicated, with radii $5D$ and $10D$, respectively, where D is the WEC diameter. The "+"-symbol indicates the WEC centre.

In Figure 3.30, the extended domain is presented, showing the achieved accuracy for estimating extra-array effects. The drawn square represents the 10.0 m x 10.0 m (w_d x l_d) domain of Figure 3.29. Also the inner and outer circles are drawn, with radius $5D$ and $10D$, respectively, in order to indicate the location of the above discussed differences in the extended domain of 49.6 m x 39.2 m (w_d x l_d).

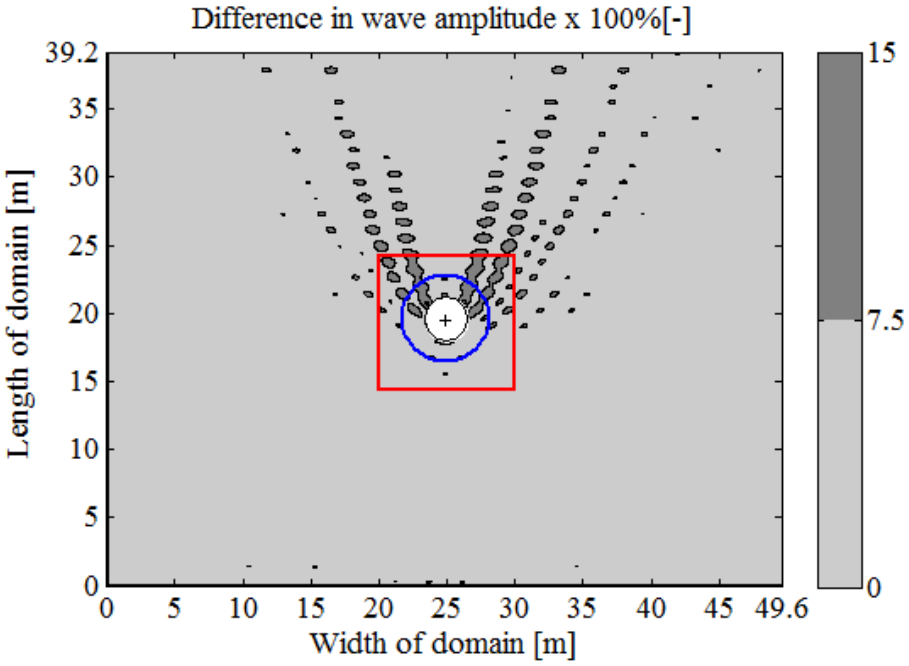

Figure 3.30. Calculated (using Eq. (3.14)) wave amplitude differences between WAMIT and MILDwave (with the coupling methodology implemented), for the perturbed wave field around a heaving WEC. An extended domain with dimensions, 49.6 m x 39.2 m (w_d x l_d) is shown. Light grey and grey colour, represent areas with differences smaller than 7.5 % and between 7.5 % and 15.0 %, respectively. The zones within the drawn inner and outer circles are indicated, with radii $5D$ and $10D$, respectively, where D is the WEC diameter. The "+"-symbol indicates the WEC centre. The drawn square indicates the limits of the 10.0 m x 10.0 m domain shown in Figure 3.29.

The largest wave amplitude differences remain in the inner circle with diameter $5D$, as well as in the 10.0 m x 10.0 m (w_d x l_d) domain. For large distances both upwave and downwave of the WEC, the differences in the wave amplitude calculated using WAMIT and MILDwave (with the coupling methodology

implemented) are small (in general < 7.5 % and at the largest part of the domain even < 5.0 %).

Therefore, the coupling methodology implemented in the wave propagation model MILDwave is suitable for modelling far-fields effects of the modeled WEC. In the largest part of the 49.6 m x 39.2 m domain, and especially in front and in the lee of the WEC and in the far-field, the wave amplitude differences are very small which confirms the good agreement between the results obtained using WAMIT and MILDwave (with the coupling methodology implemented).

3.6. Conclusions

This chapter focuses on the numerical modelling of the resulting wave fields around oscillating wave energy converters, with the intention to model both intra-array interactions in the near-field, and extra-array effects in the far-field of a WEC (array).

A generic coupling methodology is presented, which has been developed to combine (a) the approach of wave-structure interaction solvers used for investigating intra-array interactions, which can model physically correct wave energy absorption and the resulting wave fields induced by oscillating WECs or WEC arrays, and (b) the approach of wave propagation models used for predicting extra-array effects, which can model the effect of WEC arrays on the wave field and the shoreline. In addition, a wave generation technique is presented, for generating the perturbed wave field induced by an oscillating WEC, in a wave propagation model. A wave generation circle is used, surrounding the WEC, on which prescribed internal boundary wave conditions are inserted as input, provided by a wave-structure interaction solver.

Most importantly, both, the presented coupling methodology and wave generation technique are generic:

(i) any wave-structure solver can be used to provide the perturbed wave field used as the prescribed internal boundary wave conditions. This perturbed wave field is imposed on the wave generation circle around the WEC. Models based on the Boundary Element Method (BEM) approach of potential flow theory or models based on the approach of resolving the Navier-Stokes equations (e.g. Computational Fluid Dynamics (CFD) models), are all suitable for providing detailed perturbed wave field information in the vicinity of the WEC.

(ii) any wave propagation model can be used; the wave generation circle can be implemented in the numerical domain of any wave model (in both phase resolving and phase averaging models).

(iii) it applies to any oscillating/floating structure; in this chapter, the developed heaving WEC unit (Chapter 2) has been selected for a verification test case of the coupling methodology, but exactly the same methodology is applied to e.g. oscillating water columns, floating breakwaters, platforms, etc.

For the verification of the presented coupling methodology, a test case of a heaving WEC is used, for which coupling between the wave-structure interaction solver, WAMIT, and the time domain wave propagation model, MILDwave, has been realized. The results obtained for the diffracted, radiated and perturbed wave field around the WEC under incident waves using the coupling methodology, have been verified against the results obtained by the wave-structure model, WAMIT. Furthermore, MILDwave can provide results at larger distances downwave of the WEC in a time-effective way, using the actual bathymetry of the domain, which is not possible by using WAMIT.

The resulting wave amplitudes show very good agreement, when only diffraction is considered both in WAMIT and in MILDwave. For modelling the diffracted wave field around the WEC, the WEC is implemented as a fully reflecting stationary structure. In MILDwave, incident waves are generated along a wave generation line and propagate toward the WEC, located in the middle of the numerical domain.

The resulting wave amplitudes show very good agreement, when only radiation is considered both in WAMIT and in MILDwave. In MILDwave, radiated waves are generated along a wave generation circle surrounding the WEC, on which prescribed internal boundary wave conditions are inserted as input, provided by the wave-structure interaction solver, WAMIT. Therefore, the WEC has been implemented as a wave source realized by the wave generation circle with a radius (r_C = 0.20 m) slightly larger than the WEC radius (0.1575 m). In this case, the waves propagate in all directions from the source.

Finally, the resulting wave amplitudes when, simultaneously, diffraction and radiation are considered in MILDwave by applying the presented coupling methodology, are compared to WAMIT results. The resulting wave field is the perturbed wave field around the heaving WEC under incident waves.

In MILDwave, each time step, the diffracted and radiated wave field are calculated separately and afterwards the wave elevations and velocity potentials are summed up. By separating the calculation of both wave fields, the diffracted wave is not disturbed by the wave absorbing sponge inside the wave generation circle. On the other hand, the radiated wave is not disturbed by the fully reflecting structure (or structure with specific absorption coefficients assigned, in another case) used for the simulation of the diffracted wave field.

The WEC is implemented as an oscillating fully reflecting structure surrounded by the wave generation circle, and is placed in the centre of the numerical domain.

The waves are simultaneously generated along a wave generation line and on a wave generation circle, using the proposed coupling methodology.

The results obtained for the perturbed wave field using WAMIT and MILDwave (with the coupling methodology implemented) show very good agreement. The largest wave amplitude differences, appear to be very localized effects at very small distances around the WEC and on the wave generation circle. These areas, however, are not used in MILDwave for the study of WEC (array) effects. In the largest part of the 49.6 m x 39.2 m domain, and especially in front of, in the lee of the WEC and in the far-field, the wave amplitude differences are small (smaller than 7.5 % and at the largest part of the domain even smaller than 5.0 %) which shows the good agreement between the results obtained using WAMIT and MILDwave (with the coupling methodology implemented). Therefore, the coupling methodology implemented in the wave propagation model MILDwave is suitable for modelling extra-array effects of the modeled WEC.

It has been shown that the numerical coupling methodology for predicting WEC array effects presented in this chapter, can combine **(i)** the advantages of wave-structure interaction solvers, and **(ii)** the benefits of wave propagation models, yielding a cost-effective and accurate tool/methodology.

3.7. References

[1] Falnes, J.. *Principles for capture of energy from ocean waves. Phase control and optimum oscillation.* Technical report, Department of Physics, NTNU, **1997**.

[2] Delhommeau, G.. *Le problème de diffraction radiation et de résistance de vagues: étude théorique et résolution numérique par la méthode des singularités.* Thèse Ecole Nationale Supérieure de Mécanique, Nantes, **1987**.

[3] ANSYS Aqwa, Product features, http://www.ansys.com, Accessed March **2013**.

[4] WAMIT, User Manual. http://www.wamit.com/manual.htm, Accessed March **2013**.

[5] Mavrakos, S., McIver, P.. *Comparison of methods for computing hydrodynamic characteristics of arrays of wave power devices.* Applied Ocean Research, 19, 283-91, **1997**.

[6] De Backer, G., Vantorre, M., Beels, C., De Rouck, J., Frigaard, P.. *Power absorption by closely spaced point absorbers.* IET Renewable Power Generation. 4(6), 579-91, **2010**.

[7] Vicente, P.C., de O. Falcão, A.F., Gato, L.M.C., Justino, P.A.P.. *Dynamics of arrays of floating-point absorber wave energy converters with inter-body and bottom slack-mooring connections.* Applied Ocean Research. 31, 267-81, **2009**.

[8] Yu, Y.-H., Li, Y.. *Reynolds-Averaged Navier-Stokes simulation of the heave performance of a tow-body floating-point absorber wave energy system.* Computers & Fluids, **2013**.

[9] Westphalen, J., Greaves, D., Williams, C., Taylor, P., Causon, D., Mingham, C., Hu, Z., Stansby, P., B, R., Omidvar, P.. *Extreme wave loading on offshore wave energy devices using CFD: a hierarchical team approach.* Proceedings of the 8th European Wave and Tidal Energy Conference, Uppsala, Sweden, **2009**.

[10] Agamloh, E.B., Wallace, A.K., von Jouanne, A.. *Application of fluid-structure interaction simulation of an ocean wave energy extraction device.* Renewable Energy. 33(4), 748-757, **2008**.

[11] Finnegan,W., Goggins, J.. *Numerical simulation of linear water waves and wave–structure interaction.* Ocean Eng. 43, 23-31, **2012**.

[12] Booij, N., Haagsma, I.J.G., Holthuijsen, L.H., Kieftenburg, A.T.M.M., Ris, R.C., van der Westhuysen, A.J., Zijlema, M. *SWAN cycle III version 40.51AB User Manual*, **2007**.

[13] Madsen, P.A., Sørensen, O.R.. *A new form of the Boussinesq equations with improved linear dispersion characteristics. Part 2: A slowly-varying Bathymetry.* Coastal Engineering, 18, 183-204, **1992**.

[14] Millar, D.L., Smith, H.C.M., Reeve, D.E.. *Modelling analysis of the sensitivity of shoreline change to a wave farm.* Ocean Engineering. 34, 884-901, **2006**.

[15] Venugopal, V., Smith, G.H.. *Wave climate investigation for an array of wave power devices*. Proceedings of the 7th European Wave and Tidal Energy Conference (2007), Porto, **2007**.

[16] Alexandre, A., Stallard, T.J., Stansby, P.K.. *Transformation of wave spectra across a line of wave devices.* Proceedings of the 8th European Wave & Tidal Energy Conference (EWTEC), Uppsala, Sweden, **2009**.

[17] González-Santamaría, R., Zou, Q., Pan, S.. *Modelling of the impact of a wave farm on nearshore sediment transport.* Proceedings of the 33rd International Conference on Coastal Engineering (ICCE2012), Santander, Spain, **2012**.

[18] Beels, C., Troch, P., De Backer, G., Vantorre, M., De Rouck, J.. *Numerical implementation and sensitivity analysis of a wave energy converter in a time-dependent mild-slope equation model.* Coastal Engineering, 57(5), 471-492, **2010**.

[19] Beels, C., Troch, P., De Visch, K., Kofoed, J.P., De Backer, G.. *Application of the time-dependent mild-slope equations for the simulation of wake effects in the lee of a farm of Wave Dragon wave energy converters.* Renewable Energy. 35, 1644-1661, **2010.**

[20] Beels, C., Troch, P., Kofoed, J.P., Frigaard, P., Vindahl Kringelum, J., Carsten Kromann, P., Heyman Donovan, M., De Rouck, J., De Backer, G.. *A methodology for production and cost assessment of a farm of wave energy converters.* Renewable Energy.36(12), 3402-3416, **2010.**

[21] Troch, P.. *MILDwave – A numerical model for propagation and transformation of linear water waves.* Internal Report, Department of Civil Engineering, Ghent University, **1998**.

[22] Folley, M., Babarit, A., O' Boyle, L., Child, B., Forehand, D., Silverthorne, K., Spinneken, J., Stratigaki, V., Troch, P.. *A review of numerical modelling of wave energy converter arrays*. Proceedings of the 31st International Conference on Offshore Mechanics & Arctic Engineering, Rio de Janeiro, Brazil, **2012**.

[23] Li, Y., Yu, Y.-H.. *A synthesis of numerical methods for modelling wave energy converter point absorbers.* Renewable & Sustainable Energy Reviews. 16.6, 4352-4364, **2012**.

[24] Vidal, C. , Mendez, F. J., Diaz, G., Legaz, R.. *Impact of Santona WEC installation on the littoral processes.* Proceedings of the 7th European Wave and Tidal Energy Conference (EWTEC), Porto, Portugal, **2007**.

[25] Mendes, L., Palha, A., Conceicao, J.F., Brito-Melo, A., Sarmento, A.J.N.A.. *Analysis of the impact of a pilot zone for wave energy conversion offshore Portugal.* Proceedings of the 18th International Offshore and Polar Engineering Conference (ISOPE), Vancouver, British Columbia, Canada, **2008**.

[26] Le Crom, I., Brito-Melo, A., Sarmento, A.J.N.A.. *Maritime Portuguese Pilot Zone for Wave Energy Conversion: Modelling Analysis of the Impact on Surfing Conditions.* Proceedings of the 2nd International Conference on Ocean Energy (ICOE), Brest, France, **2008**.

[27] Mei, C.C., Stiassnie, M., Yue, D.K.P.. *Theory and applications of ocean surface waves. Part 1, Linear aspects.* World Scientific, Singapore, **2005**.

[28] Babarit, A., Folley, M., Charrayre, F., Peyrard, C., Benoit, M.. *On the modelling of WECs in wave models using far field coefficients.* Proceedings of EWTEC2013, Aalborg, Denmark, **2013**.

[29] Beels, C.. *Optimization of the lay-out of a farm of wave energy converters in the North Sea: analysis of wave power resources, wake effects, production and cost.* PhD dissertation, Ghent University, **2009**.

[30] Stratigaki, V., Troch, P., 2012. An introduction to the wave propagation model MILDwave. Department. of Civil Engineering, Ghent University.

[31] Stratigaki, V., Troch, P., Baelus, L., and Keppens, Y.. *Introducing wave regeneration by wind in a mild-slope wave propagation model, MILDwave, to investigate the wake effects in the lee of a farm of wave energy converters.* Proceedings of the ASME 2011 30th International Conference on Ocean, Offshore and Arctic Engineering (OMAE 2011). Rotterdam, The Netherlands, **2011**.

[32] Radder, A.C., Dingemans, M.W.. *Canonical equations for almost periodic, weakly nonlinear gravity waves.* Wave Motion, 7, 473-485, **1985**.

[33] Troch, P., Beels, C., De Rouck, J., De Backer, G.. *Wake effects behind a farm of wave energy converters for irregular long-crested and short-crested waves.* Proceedings of the International Conference on Coastal Engineering, No. 32 (**2010**), Shanghai, China. Paper #: waves.22. Retrieved from http://journals.tdl.org/ICCE/.

[34] Nørgaard, J., Q., H., Lykke Andersen, T.. *Investigation of wave height reduction behind the Wave Dragon wave energy converters and application in Santander, Spain.* To be submitted to a conference. Retrieved from: "Nørgaard, J., Q., H., 2013. Upgrade and design of coastal structures exposed to climate changes. PhD thesis, Alborg University, Denmark", **2013**.

[35] Lee, C., Suh, K.D.. *Internal generation of waves for time-dependent mildslope equations.* Coastal Engineering. 34, 35–57, **1998**.

[36] Lee, C., Yoon, S.. *Internal generation of waves on an arc in a rectangular grid system.* Coastal Engineering. 54, 357–368, **2007**.

[37] Stratigaki, V., Troch, P., Forehand, D., Stallard, T.. *A fundamental coupling methodology for the combined modelling of near and far field effects of oscillating wave energy converters*. Submitted for publication in Coastal Engineering, **2014**.

[38] Babarit, A.. *On the park effect in arrays of oscillating wave energy converters.* Renewable Energy. 58, 68-78, **2013**.

4

Physical modelling of large Wave Energy Converter arrays

Abstract: *In this chapter, a detailed description is provided of the design of experiments with WEC arrays. Tests have been performed in the Shallow Water Wave Basin of DHI (Hørsholm, Denmark), on large arrays of up to 25 heaving point absorber type Wave Energy Converters (WECs), for a range of geometric layout configurations and wave conditions. WEC response and modification of the wave field are measured to provide data for the understanding of WEC array interactions and for the evaluation of array interaction numerical models. Each WEC consists of a buoy with a diameter of 0.315 m and power take-off is modeled by realizing friction based energy dissipation through damping of the WEC's motion. Wave gauges are located within and around the WEC array. Wave conditions studied include regular, polychromatic, long- and short-crested irregular waves. A rectilinear arrangement of WEC support structures is employed such that several array configurations can be studied. In this chapter, the experimental arrangement and the obtained database are presented. Also, results are presented for power absorption by the WECs and wave height attenuation downwave of the WEC arrays. For long-crested irregular waves and in WEC arrays with large spacing or large number of WECs, intra-array interactions are constructive regarding power output of the array. For small arrays with small WEC spacing, these interactions are*

destructive. For short-crested irregular wind waves, intra-array interactions are negative for both the rectilinear and the staggered 5x5-WEC arrays. Moreover for long-crested irregular waves, up to 18.1 % and 20.8 % reduction in significant wave height is observed downwave of the 5x5-WEC rectilinear and staggered array, respectively, for the perturbed wave field. This wave height attenuation is expected to be larger, since the WEC units used for the presented WEC array experiments are not optimally controlled in irregular seas; in real wave farm applications WECs are designed to be optimally controlled to extract a great amount of power from the waves, and therefore the array will cause larger wave height dissipation downwave. When the spacing between the WECs increases, the dimensions of the zone of wave height reduction decrease downwave of the array.

4.1. Introduction

4.1.1. WEC array effects

Commercial exploitation of wave energy will require installation of large numbers of wave energy converters, arranged in an array (see Chapter 1). Power production of an array, may be smaller or larger than the sum of the power by the equivalent number of individual WECs, due to hydrodynamic intra-array interactions. The geometric configuration of the WEC array plays a significant role in these interactions, as well as in the impact of the array on its environment (extra-array effects). Therefore, with an accurate understanding of the WEC array effects, the optimal farm geometric layout can be determined and changes to wave conditions can be quantified.

4.1.2. Numerical and experimental modelling of WEC arrays

Several numerical methods have been employed to analyse the response of arrays of wave energy converters to the incident wave climate, as well as the resulting modification of wave conditions, particularly down-wave of such arrays ([1]-[5]). Reviews of available modelling approaches and their applications are discussed in [6] and [7], while a detailed overview has been provided in Chapters 1 and 3. However, to date, there has been very limited validation of these numerical models using physical scale models of WEC arrays.

In contrast to the large quantity of numerical simulations of WEC arrays and the large body of experimental work concerning individual WECs (e.g. [9], [10], [11]) or pairs of WECs (e.g. [12], [13]), there is limited published data concerning either the response of such WECs located in arrays or the corresponding wave field changes.

Only a few experimental studies of small WEC arrays have been conducted. As presented in Chapter 1, 5 to 12 WECs have been tested including response to regular waves [15], power output and response in irregular waves [16] and wave spectra changes across the array [17]. Within the UK Supergen Marine and the EU Hydralab III programmes, tests have been conducted with a WEC array of five oscillating WECs interconnected by mooring lines [18]. As part of the PerAWaT project, several studies of wave energy converter arrays have been conducted, both of idealized geometries (e.g. [19]) and scale models of WEC systems under development by private companies.

4.1.3. Need for experiments with large WEC arrays

Real wave energy applications, however, will demand the installation of arrays composed of large numbers of WECs. Therefore, there is a clear need for experiments with large WEC arrays.

Presently, no experimental studies are publicly available detailing WEC response, power output and wave field modifications due to an array. Data from large WEC arrays concerning the physical modelling of intra-array interactions and extra-array effects, combined with simultaneous measurements of WEC response, wave induced forces on the WECs and recording of the wave conditions, are not reported in literature.

Such data are essential for evaluation of the accuracy of the employed numerical tools, their validation, as well as for their further development and improvement. Accurate measurements of individual WEC response, WEC array power output and spatial variation of wave conditions in the vicinity of the array, are required to improve understanding of the fundamental processes, influencing wave conditions down- and up-wave of WEC arrays. Moreover, results from testing various WEC array geometric configurations will lead to the optimization of the array lay-outs for real applications.

4.1.4. A first database for large WEC arrays

Recently, within the main deliverable of this PhD research, and as part of the research project "WECwakes" ([20], [21]) funded by the EU FP7 HYDRALAB IV programme, WEC array experiments have been performed. Tests have been conducted in the Shallow Water Wave basin of DHI (Hørsholm, Denmark) on large arrays of point absorber type WECs (up to 25 WEC units).

A range of WEC array geometric configurations and wave conditions have been tested. The WEC unit developed within the first part of this PhD work has been reproduced in 25 identical copies. Therefore, each WEC unit is composed of a buoy, designed to heave along a vertical shaft only, and can thus be modelled as a single degree of freedom system. Energy absorption through the WECs' PTO-system is modelled by realising energy dissipation through friction based damping of the WECs' heave motion. Wave gauges have been used to measure the wave field within and around the arrays. Displacement meters are mounted on each WEC unit for the measurement of the heave displacement. On 5 WECs along the central line of the array, the wave induced surge force has been measured.

This experimental set-up of 25 WEC units in an array layout, placed in a large wave tank, is at present the largest set-up of its kind, worldwide, studying the important impacts on power absorption and wave conditions of WEC array effects.

Most importantly, the established database is comprehensive, and is applicable not only to WEC arrays but also to floating structures/platforms, stationary cylinders under wave action, etc., for understanding of e.g. wave impact on the cylinders and wave field modifications around them. The obtained WEC array database, as part of the "WECwakes" project, is accessible to the research community as specified under the HYDRALAB rules.

4.1.5. Chapter overview

An introduction to the objectives of the performed WEC array experiments is presented in Section 4.2. A detailed overview of the design and execution procedure of the experiments, as well as of the obtained WEC array database, is given in Sections 4.3-4.5. In Section 4.6, experimental results are presented, that are available to-date. Power output results (Sections 4.6.1 – 4.6.4) and wave field modification measurements (Sections 4.6.5 – 4.6.12) are presented, for various WEC array geometric configurations and for both long- and short-crested irregular waves. A summary of the presented findings and the characteristics of the obtained WEC array database are presented in Section 4.7. Detailed conclusions and discussion on the experimental results are presented in Chapter 5, where guidelines for the design of WEC arrays are presented, based on the obtained results.

4.2. Research description

4.2.1. Research objectives

From the introductory part of this PhD dissertation, it is clear that very few small scale experiments have been performed dealing with waves and WEC arrays. Therefore, the following questions have to be addressed:

i. what is the positive or negative effect on power absorption when the number of WECs in an array is increasing?

ii. what is the magnitude and the impact of the extra-array effects on other users in the sea and the coastal area?

iii. what is the extent of the region of wave field modifications downwave of the WEC arrays?

iv. what is the influence of the geometric configuration of the WECs within the array, on the extra-array effects?

v. what is the influence of the WEC number on net power absorption by an array?

vi. what is the influence of the lateral, w, and longitudinal, l, spacing between the WECs on net power absorption by an array?

The main objective of the research performed within this PhD work, is to provide insight to the above questions and therefore, to improve the understanding of WEC array effects, i.e. the change of wave conditions due to energy extraction by WEC arrays and interactions between the WECs of an array. Knowledge of both the behaviour of an individual WEC affecting its neighbours (intra-array interactions) and the effects downwave of a large array (extra-array effects), are very important in the design of WEC arrays.

In order to achieve the main objective of the third part of this PhD work, the following more detailed objectives have been defined:

- To understand the behaviour of WEC arrays under varying wave conditions;
- To determine the intra-array interactions between the WECs;
- To determine the extra-array effects: to measure and detect the dimensions of wave field changes due to WEC arrays and their impact;
- To quantify the effect on power absorption, by:
  (i) changing the lateral, w, and longitudinal, l, spacing between the WECs within an array,
  (ii) changing the number of the WECs within an array,
  (iii) modifying the WEC array geometric layout.
- To provide an experimental database for validation of numerical models, used by researchers worldwide (see [6], [7]) for wave propagation through WEC arrays and wave-WEC interaction.

4.2.2. Methodology of the experiments

Several idealised wave and wave-WEC interaction problems have been considered (diffraction, radiation and absorption) for varying WEC array configurations and wave conditions. Generic point absorber type wave energy converters have been developed for these experiments (see Chapter 2). The tested WEC arrays provide experimental data suitable for studies of the interaction between both widely and closely spaced point absorber type WEC arrays.

Regarding the wave conditions, the experiments are based on theoretical arguments for: (i) waves propagating through a WEC array, (ii) the dependence of wave transformation on geometrical and operational properties of the WECs which compose the array, and (iii) the dependence of wave transformation on the lateral, w, and longitudinal, l, spacing between the WECs. The methodology includes regular (with varying wave propagation angles), polychromatic, irregular and short-crested waves propagating through WEC arrays.

The reflection, transmission and absorption of an individual WEC unit have been firstly experimentally determined, as well as decay characteristics (no wave action). Additional WECs have been gradually added in the set-up, eventually forming WEC arrays.

The experiments have focussed on the acquisition of the following data:

1. Wave height, as primary output, around and within the WEC array.

2. Measurements of undisturbed wave field, around and within the WEC array and at the locations (centres) of the wave energy converters.

3. Measurements of diffracted wave (only) and perturbed wave field (presented in detail in Chapter 3), due to WECs under incident wave conditions. Measurements have been taken around and within the WEC array.

4. Measurements of wave field in front of the WEC arrays providing data for the incident wave field.

5. Measurements of the response of all WECs of the array (recording of the WEC heave displacement).

6. Measurements of the wave induced surge forces on the WECs used for estimating WEC array power absorption and wave impact on the WECs.

4.2.3. Preparation of the large scale experiments

A series of experiments with (i) an individual point absorber type WEC unit and (ii) small WEC arrays composed of up to 4 WEC units has been performed within the framework of the preparation of the WEC array experiments. The preparatory experiments are described in detail in Chapter 2.

After evaluation, optimization and finalizing the geometry and the mechanical parts of the developed individual WEC unit, a large number of identical WECs have been constructed at the workshop of Ghent University. Twenty-five WEC units have been prepared prior to the WEC array experiments, as well as the accompanying instrumentation, by conducting the necessary quality tests to assure identical characteristics and performance.

4.3. Experimental setup

4.3.1. Characteristics of an individual wave energy converter

The experimental arrangement has been designed to attain WEC response amplitude operator (abbreviated as *RAO*) greater than unity and a measurable power output, whilst ensuring that the system is simple to setup for multiple WEC units, as discussed in Chapter 2. Details on the WEC unit development, evaluation and experimental study for an individual WEC unit are presented in Chapter 2. In Figure 4.1, the definition sketch of the cross section of an individual WEC showing geometry, bearings and power take-off system, as well as an illustration of an individual WEC within a WEC array, are presented.

Net power absorption, P_{tot}, of each WEC unit, is obtained by Eq. (2.24) (Chapter 2). Since surge force, F_{surge}, is out of phase with the WEC velocity, $\dot{z}(t)$, power due to bearings, $P_{bearings}$, (and therefore P_{tot}, as well) vary substantially during each wave cycle, as presented in Figure 4.2. In Figure 4.2, the time-variation of the capture width ratio is presented, thus the width of the wave front containing the same available power as the useful power captured by the WEC in the same wave climate.

As shown in Section 4.6.1, results for WEC RAO and power output, show reasonable agreement between measured response for individual WECs, and power output and WEC response predicted using a linear time domain model.

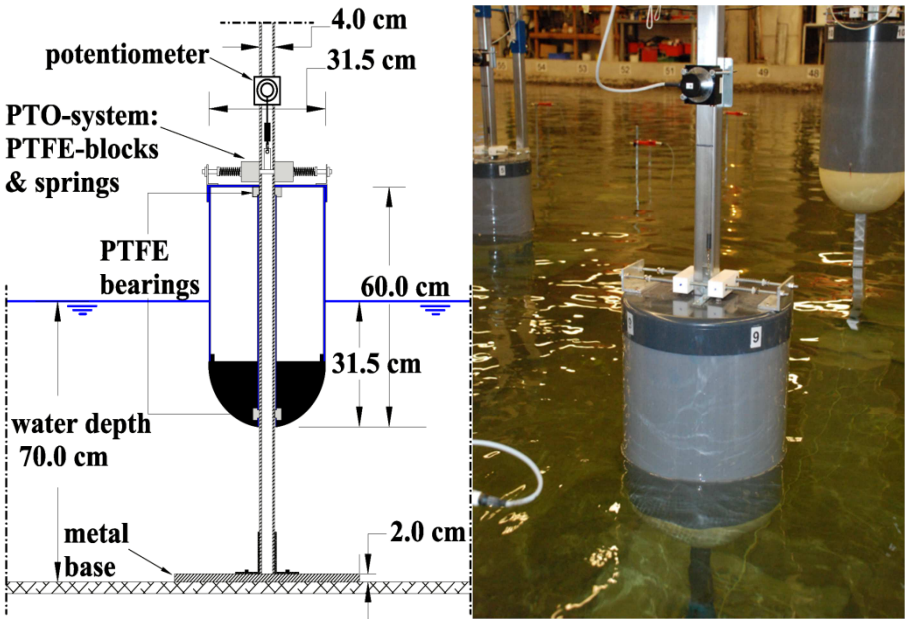

Figure 4.1. Definition sketch of the cross section of an individual WEC illustrating geometry, bearings and power take off system (left), and illustration of an individual wave energy converter within a WEC array (right).

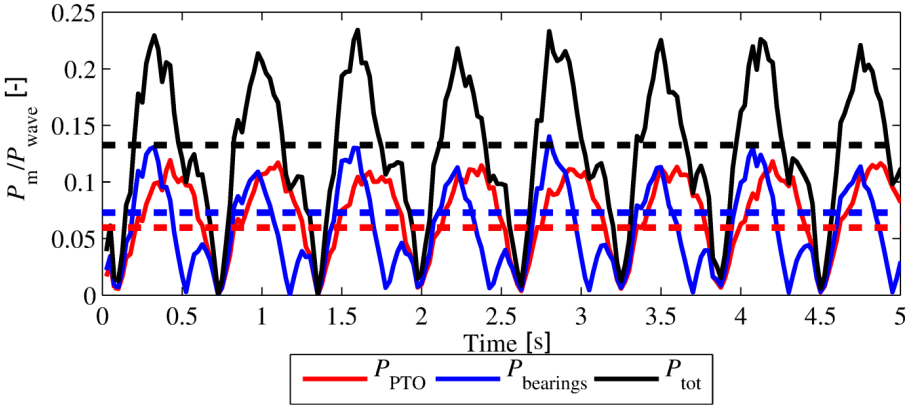

Figure 4.2. Typical measured time-variation of total power, P_{tot}, power due to constant power take off force (F_{PTO}), P_{PTO}, and power due to time-varying surge force (F_{surge}) on the bearings, $P_{bearings}$. The dashed horizontal lines represent time-averaged values [20].

4.3.2. Characteristics of the wave basin

Tests have been performed in the Shallow Water Wave Basin of DHI (Hørsholm, Denmark). An illustration of the empty wave basin (only wave gauges are present) is shown in Figure 4.3. The experimental facility is 25.0 m long and 35.0 m wide, with an overall depth of 0.8 m. Forty-four piston type wave paddles, presented in Figure 4.4, generate waves at one end of the wave basin. Each wave paddle is 1.2 m high and 0.5 m wide, and thus the total width of the wave generator is 22.0 m. The wave paddles are arranged in two segments of length 18.0 m and 4.0 m with a 20.0 cm step between the two segments. The 3-D wave generator is designed to operate at water depths, d_w, between 0.2 m and 0.8 m. The wave generator is equipped with Active Wave Absorption Control System (abbreviated as *AWACS*) in order to deal with undesired re-reflexion of waves to the wave generator, and to allow full control of the incident waves. A gravel beach with a slope of 1/5.59 has been constructed to provide energy absorption at the opposite end of the wave basin.

Figure 4.3. Shallow Water Wave basin at DHI (Hørsholm, Denmark). View from a location behind the wave generator, while taking wave height measurements using a network of resistive wave gauges in the empty wave basin (sea-states characterization: no WECs/support structures present).

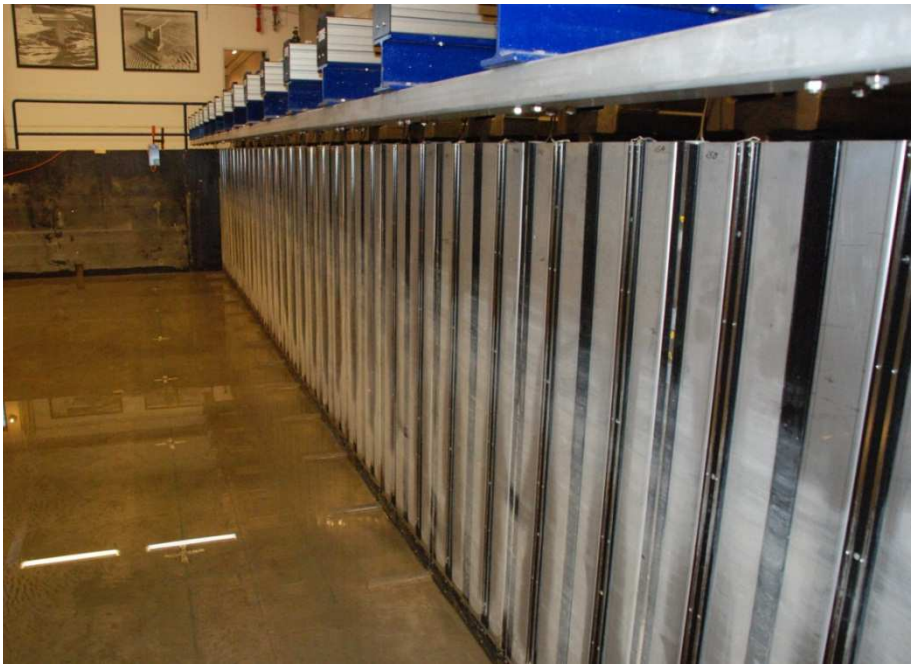

Figure 4.4. Wave generator at the Shallow Water Wave basin of DHI. View to the wave paddles from the side of the wave basin.

4.3.3. Description of the experimental arrangement

In Figure 4.5, a plan view of the general experimental arrangement in the wave basin, and the configuration comprising the 5x5-WEC rectilinear array, is presented (see also Appendix F). Also the standard locations of the wave gauges are shown. The standard lateral, w, and longitudinal, l, (centre-to-centre) spacing between the WECs, are $w = l = 5D = 1.575$ m, where D, is the WEC diameter. The complexity of the tested WEC array layouts increases gradually. The experiments start with the testing of individual WEC units at different locations within the wave basin. Furthermore, different WEC arrays have been tested, with various geometric configurations and different/increasing WEC numbers.

The wave generator has a total width of 22.0 m and thus, does not extend across the entire wave basin width of 35.0 m. Vertical guide walls have been installed in order to avoid diffraction of the generated waves to either side of the wave basin. This technique results in a larger *effective* domain within the wave basin. Moreover, it simplifies the numerical treatment of the experimental set-up, using fully reflective boundaries for simulating the guide walls. The distance between the guide walls and the outermost WECs of the 5x5-WEC array, is nearly $25D = 7.875$ m, and

so reflection of waves diffracted and radiated by the array is not expected to substantially influence the findings. The guide walls comprise plywood panels that extend 2.0 m beyond the toe of the absorbing beach, such that directional waves are not reflected back to the test region.

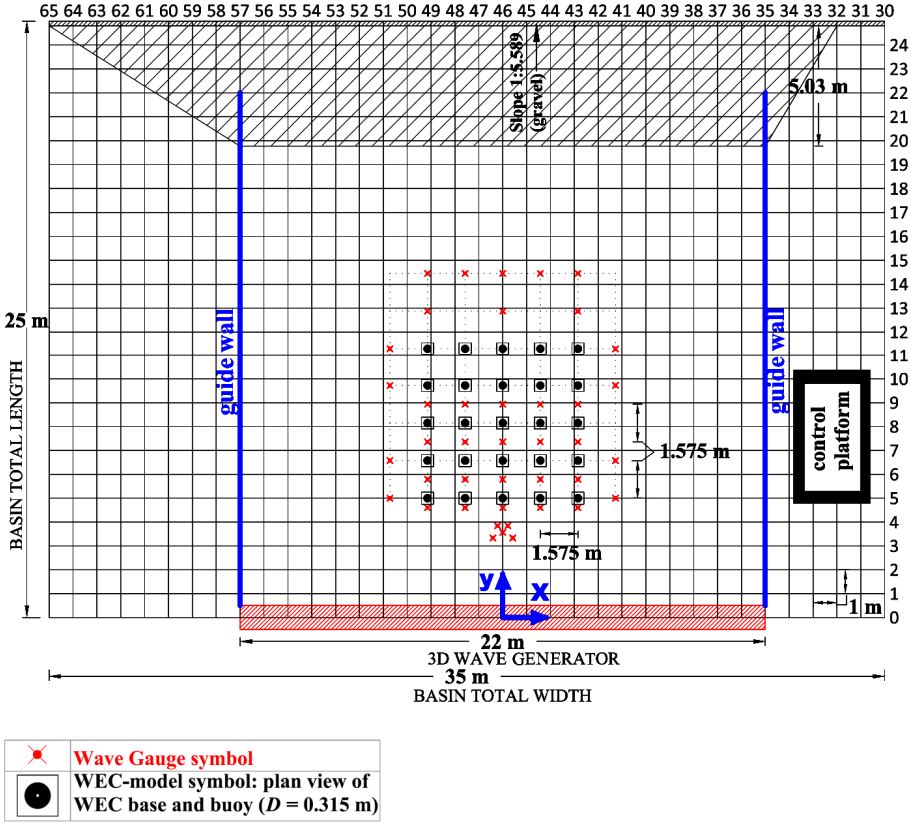

Figure 4.5. Plan view of the WECwakes experimental arrangement in the DHI wave basin and standard 5x5-WEC rectilinear array. Grid at 1.0 m increments, wave gauge arrangement (**x**) and WEC positions (●) are indicated. The hatched region along the x-axis at the bottom of the figure denotes the extent of the wave paddles, while at the opposite end, the wave absorbing beach is shown. At the sides, plywood guide walls are used. Water depth is constant, d_w = 0.70 m.

For the installation of the WEC units in the wave basin, support structures have been used comprising, (i) the WEC metal gravity bases, 2.0 cm thick, (ii) the WEC steel vertical shafts of 4.0 cm × 4.0 cm section (see Figure 4.1, left), and (iii) a connecting steel frame at the top of the WEC shafts, as shown in Figure 4.6.

Figure 4.6. Construction of WEC support structures in the wave basin of DHI.

Conventionally, here a *row* of WECs refers to a number of devices oriented parallel to the wave generator. A *column* of WECs refers to a number of devices oriented perpendicular to the wave generator (i.e. parallel to the wave propagation direction, $\theta = 0°$).

Two different layouts of these support structures (*shafts stencils*) have been constructed to install: (a) the 5x5-WEC rectilinear array (Figures 4.5 and 4.7) and all WEC (array) geometric configurations composed of less than 25 WEC units (*shafts stencil 1*), and (b) the 5x5-WEC staggered array (*shafts stencil 2*). For *shafts stencil 2*, the shafts of 2 WEC rows have been moved with an offset of $2.5D = 0.7875$ m between alternating rows of WECs (Figure 4.8).

Each of the 25 WEC units has been assigned a unique number, shown in Figures 4.7 and 4.8.

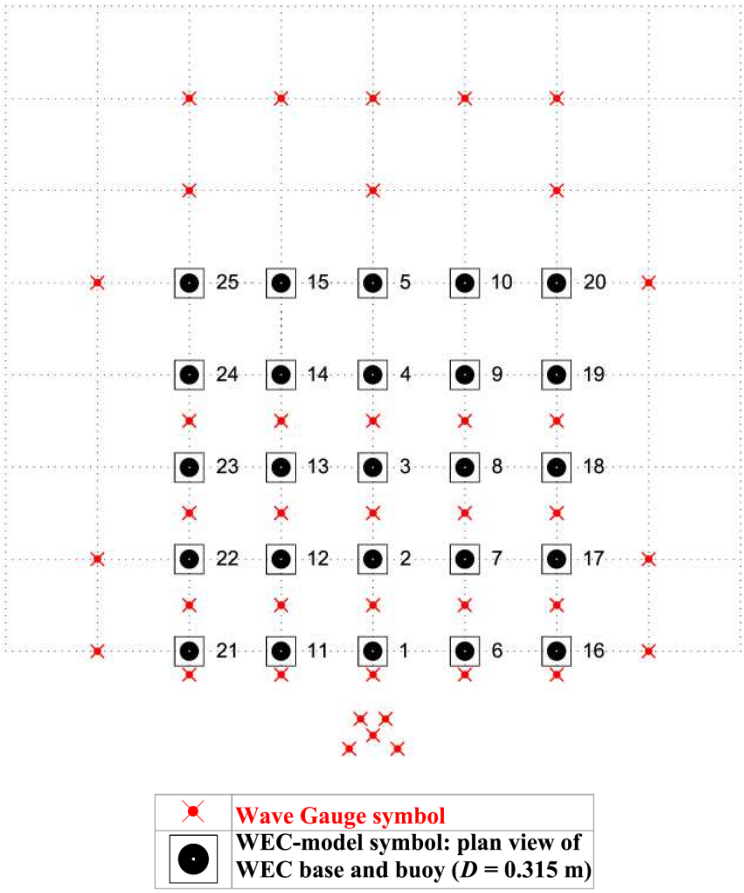

Figure 4.7. Plan view of the 5x5-WEC rectilinear array with lateral, w, and longitudinal, l, spacing between the WECs, $w = l = 5D = 1.575$ m. *Shafts stencil 1* is used for supporting the WEC units. Wave gauge arrangement (**x**) and WEC positions (●) are indicated. The squares represent the metal bases of the WECs. The unique numbering of the WECs is shown.

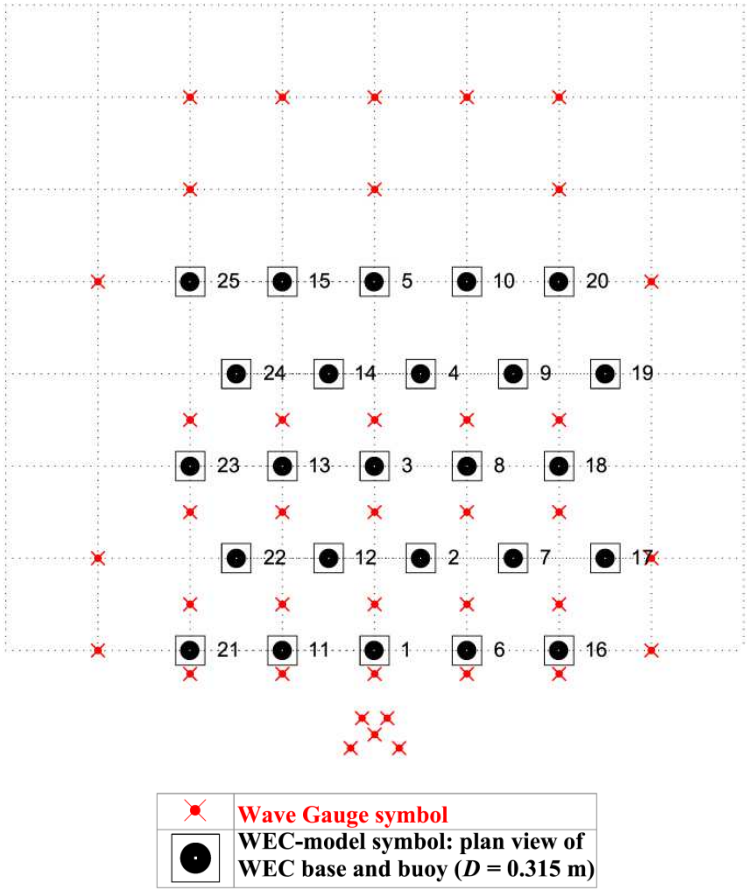

Figure 4.8. Plan view of the 5x5-WEC staggered array with lateral, w, and longitudinal, l, spacing between the WECs, $w = l = 5D = 1.575$ m. *Shafts stencil 2* is used for supporting the WEC units. Wave gauge arrangement (**x**) and WEC positions (●) are indicated. The squares represent the metal bases of the WECs. The unique numbering of the WECs is shown.

4.4. Instrumentation

4.4.1. Measured parameters

During the WEC array experiments, measurements of time series of wave elevations, WEC heave displacement and wave induced surge forces on the WEC buoys have been acquired (with acquisition frequency of 40 Hz), simultaneously (up to 76, simultaneously, measured parameters). A short overview is provided hereafter. Moreover, an example of the acquired data from one test (list of recorded parameters) showing the composition of the created database within this PhD research is presented in Appendix B.

4.4.2. Measurements of wave elevations

Resistive Wave Gauges (abbreviated as *WGs*), have been used to acquire wave elevation time series ($\eta(t)$) at specific locations throughout the wave basin. A total number of 41 WGs has been used, positioned around and at the locations of the WEC units, according to the tested WEC array geometric configurations. Moreover, a *CERC 5 wave gauge array* introduced by [22] is used upwave of the WEC arrays for estimating wave directionality and wave reflection. The distances between the WGs of the *CERC 5 wave gauge array* are presented in Appendix B.

Two *WG plans* have been used throughout the experiments: (a) *WG plan 1* (Figure 4.9) for recording the wave elevations around the WEC units, and (b) *WG plan 2* (Figure 4.10) for recording the wave elevations at all locations where WEC units have been installed and tested within all WEC array configurations. For setting up *WG plan 2*, first all WEC units and the support structures have been removed, and then the wave gauges of *WG plan 1* have been placed to the center points of the WECs. Each of the 41 WGs has been assigned a unique number as shown in Figures 4.9 and 4.10. Also, the undisturbed wave field has been recorded in an empty wave basin (without any WECs or support structures), using both *WG plans 1* and *2* (illustrated in Figure 4.3).

4.4.3. Measurements of the heave displacement of the WEC units

A potentiometer is attached to each WEC unit, for measuring time series of the heave displacement, $z(t)$. In total, 25 potentiometers have been used. The used types of potentiometers are shown in Figure 4.11. The heave displacement measurements provide information on the WEC response, as well as data for calculating power absorption of the WEC units as presented in Chapter 2. Technical information of the used types of potentiometers is available in [23].

4.4.4. Measurements of the wave induced surge force on the WEC units

The arrangement (Figure 4.12) for measuring the time varying wave induced surge force on each WEC unit, $F_{surge}(t)$, requires two load cells, attached both, at the top and at the bottom, respectively, of the WEC shaft and to an auxiliary parallel axis, in the longitudinal direction of the wave basin. To calculate F_{surge} on a WEC unit, the sum is taken of the recorded signal at the top and the bottom load cell.

F_{surge} has been measured on WECs # 01-05 (Figures 4.7 and 4.8) which are situated in the central column of the WEC array geometric configurations. In total, ten load cells have been used. In Appendix B, the layout of the force gauges is presented.

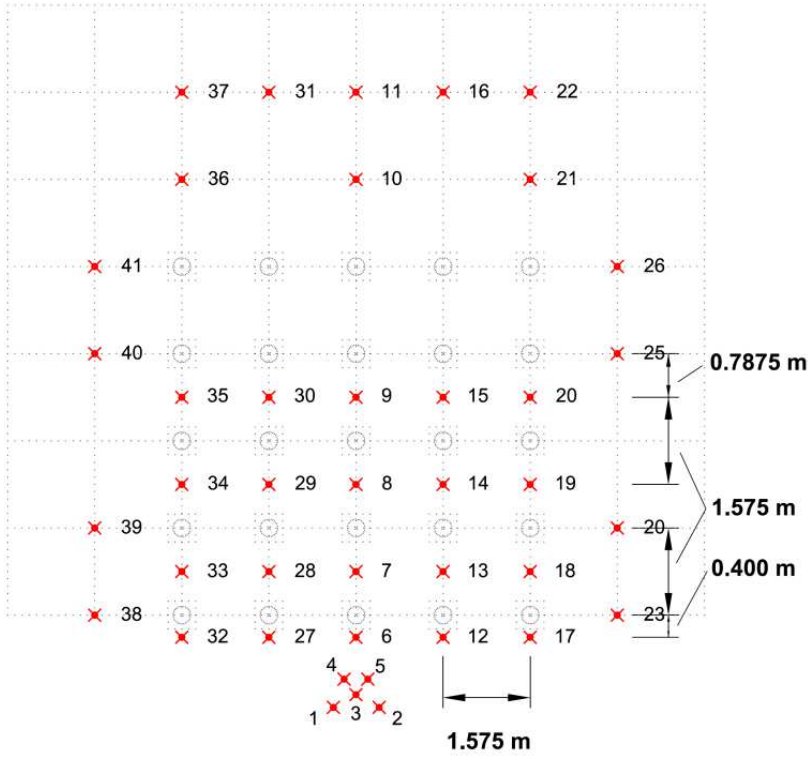

Figure 4.9. Plan view of *WG plan 1*. The arrangement of the 41 wave gauges (**x**) and 25 WEC positions (o) are indicated. The squares represent the metal bases of the WECs. The unique numbering of the WGs is shown.

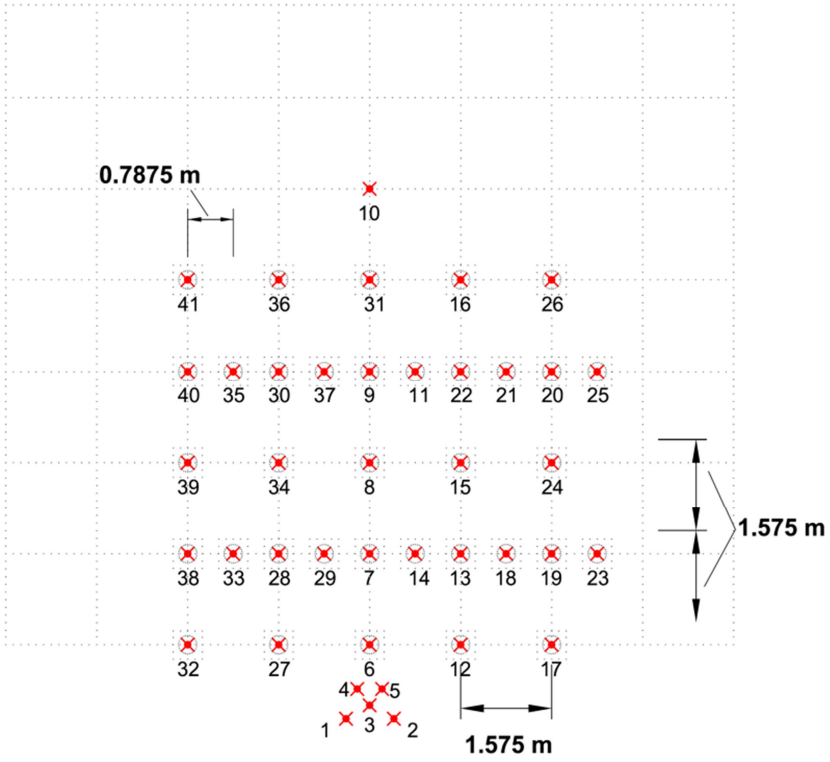

Figure 4.10. Plan view of *WG plan 2*. The arrangement of the wave gauges (**x**) is indicated, which have been moved to all locations where WECs have been installed and tested within all WEC array configurations (o). Only WGs #01 - #05 and WG #10 have remained at the same location compared to *WG plan 1*. The squares represent the metal bases of the WECs. The unique numbering of the WGs is shown.

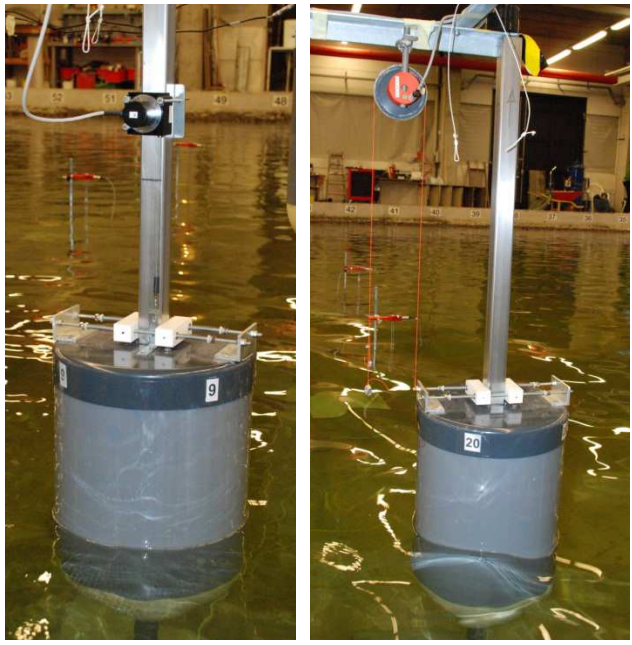

Figure 4.11. Rotary potentiometer (left) and DHI Ship Movement potentiometer (right), used for heave displacement measurements of the WEC units.

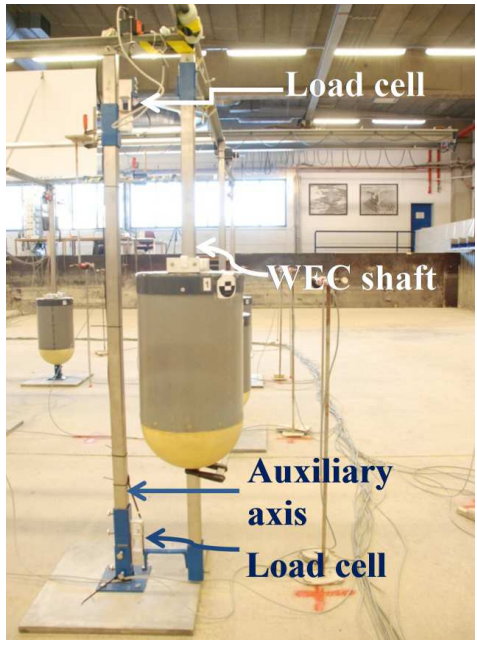

Figure 4.12. Load cells installed at the top and at the bottom of the WEC shaft, used for measurement of the wave induced surge force on the WEC units, F_{surge}.

4.5. Experimental test programme

4.5.1. Tested sea states

Four types of waves have been considered: regular, polychromatic, long-crested irregular and short-crested irregular waves. For the majority of the tests, two wave periods, T = 1.180 s and T = 1.260 s, have been tested. For the polychromatic waves, the range of T is wider, which allows the testing of a wider range of ratios between wavelength L , w and l (the array spacings), in a time efficient way. Also for irregular long-crested waves, a wider range of T_p has been tested. The wave period, $T = T_p$ = 1.180 s, corresponds to the natural period of the WEC unit, T_n (see Chapter 2). Wave period, $T = T_p$ = 1.260 s, has been selected based on the ratio between the wavelength, L, and the lateral, w, and longitudinal, l, spacings between the WECs [24]. The water depth, has been kept constant throughout the entire testing period at d_w = 0.70 m. A summary of all target sea states tested during the WEC array experiments, is provided in Appendix C.

The regular waves are defined in terms of a wave period, T, and a wave height, H. For the majority of the regular wave tests, H = 0.074 m has been used. For the regular waves, wave attack of different directions is also considered, with waves propagating from the wave paddles to the WEC arrays under different wave angles, θ = 0°, 10° and 20°. The wave paddles are operating with activated AWACS. However, additional tests have been performed for regular waves without the AWACS activated, in order to study in detail the start of the WEC heave motion. In Table 4.1, the target sea state characteristics are summarized, used to generate regular waves.

Polychromatic waves have also been considered, which consist of superimposed regular waves with different wavelengths, L. The wave period, T, and wave height, H, thus varies during the test. A polychromatic wave can be expanded as a sum of regular (monochromatic) waves. The polychromatic waves have been defined based on [24], applying a random starting phase to each wave component. Polychromatic waves have been generated with wave propagation angle, θ = 0°. The target sea state characteristics used to generate polychromatic waves are presented in Table 4.2.

The irregular waves are defined by a JONSWAP spectrum, $S_{JONSWAP}(f)$, with peak period, $T_p = T$, and, for the majority of the tests, significant wave height based on the spectral density, H_{m0} = 0.104 m, in order to achieve equivalent energy contents to the regular waves with H = 0.074 m.

Long-crested irregular waves have been generated with wave propagation angle, θ = 0°. Tests with irregular long-crested waves have been performed for a wider range of significant wave heights, H_{m0}, and peak wave periods, T_p (Table 4.3).

The short-crested irregular waves have a directional spread that is defined by the parametrical cosine power 2s model [25]. The spreading parameter, s, gives the degree of directional energy concentration. In general, the value of s depends on whether wind or swell waves are considered: s = 10 for wind waves, s = 25 for swell with short decay distance and s = 75 for swell with long decay distance [26]. Short-crested irregular waves with s = 10 (with directional spreading σ = 24°) and s = 75 (with directional spreading σ = 9°) have been considered here to represent wind and swell seas, respectively. The selection of the irregular short-crested wave conditions is based on research findings in ([1]-[2]; [27]-[28]). Short-crested irregular waves have been generated with wave propagation angle, θ = 0°, using the target sea state characteristics presented in Table 4.4.

In Table 4.5, a summary of the tested wave basin and WEC array configurations is presented, with regard to the studied wave conditions. The detailed layouts of all tested experimental arrangements are presented in Appendix D. A short description of the wave basin and the WEC array configurations is given in the first column of Table 4.5, as well as in the last column where configuration sketches can be visualized. In columns 2-5, the types of tests regarding wave conditions are listed, for each wave basin and WEC (array) geometric configuration (where *Reg.* and *Irr.* refer to *regular* and *irregular* waves, respectively, while *LCW* and *SCW* refer to *long-* and *short-crested* waves, respectively). In columns 6-7, it is indicated whether the diffracted wave field for WEC units or shafts under incident waves and whether tests for WEC decay motion have been performed for a specific WEC (array) configuration. For the tests of column 6, the WECs are held stationary at the equilibrium position (where the WEC buoy draft d_{buoy}= 31.5 m) and therefore the WECs behave as "obstacle cylinders" under wave action.

Regarding the PTO-system damping characteristics for the WEC array configurations of Table 4.5, the tests for individual WECs have been performed for damped WEC response, with varying spring compression in PTO, dx, within the range 10.5 - 50.5 mm, and for undamped WEC response ("free" WEC response with dx = 0.0 mm and F_{PTO} = 0.0 N). The 5-WEC Column tests have been performed for dx = 30.5 and 35.5 mm. The rest of the WEC array configurations have been tested using dx = 30.5 mm, which corresponds to optimum power absorption of an individual WEC as presented in Chapter 2 and Section 4.6.1. In Appendix E, a summary of the tested WEC (array) geometric configurations with regard to the applied PTO-system and WEC motion characteristics is presented.

Individual WEC units have been tested at various positions in the wave basin, to investigate the WECs' response. In total, 28 different WEC (array) geometric configurations have been tested during the WEC array experiments. Indicative illustrations of tested WEC array configurations and wave conditions during the WECwakes project are presented in Figures 4.13 - 4.16.

Table 4.1. Target sea state characteristics used to generate regular waves.

Wave height H (m)	Wave period, T (s)	Wavelength, L (m)	Wave angle, θ (°)		
0.074	1.180	2.133	0	10	20
	1.260	2.384	0	10	20

Table 4.2. Target sea state characteristics used to generate polychromatic waves (θ = 0°).

Wave height, H (m)	Wave period, T (s)	Wavelength, L (m)
0.024	0.870	1.186
0.030	1.008	1.581
0.036	1.178	2.109
0.032	1.217	2.231
0.030	1.260	2.367
0.022	1.385	2.761
0.018	1.510	3.152

Table 4.3. Target sea state characteristics used to generate irregular long-crested waves (θ = 0°).

Significant wave height, H_{m0} (m)	Peak wave period, T_p (s)	Wavelength for peak wave period, L_p (m)
0.0749	1.050	1.733
0.0816	1.100	1.890
0.1040	1.180	2.156
	1.260	2.405
	1.350	2.687
	1.500	3.154

Table 4.4. Target sea state characteristics used to generate irregular short-crested waves (θ = 0°).

Directional spreading parameter, s (-)	Significant wave height, H_{m0} (m)	Peak wave period, T_p (s)	Wavelength for peak wave period, L_p (m)
75	0.104	1.260	2.405
10	0.104	1.260	2.405

Table 4.5. Summary of the tested wave basin and WEC (array) configurations with regard to wave conditions studied (Table page 1/2).

Configu-ration	Types of tests regarding wave conditions						
	Reg. LCW	**Poly-chromatic**	**Irr. LCW**	**Irr. SCW**	**Diffracted wave field; no motion**	**WEC decay motion**	**WEC lay-out sketches**
Waves only	√	√	√	√	√ (shafts)	N/A	-
Individual WEC	√	√	√	√	√	√	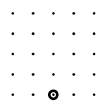
2-WEC column [A]	√	√	√	√ (spacing, l=5D)	√ (spacing, l=5D)	√	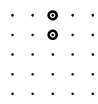
2-WEC row [B]	√	√	√	-	√ (spacing, w =5D)	-	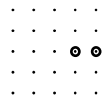
5-WEC column [C]	√	√	√	√ (middle column)	√ (middle column)	√ (middle column)	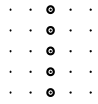
5-WEC row	√	√	√	-	-	-	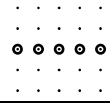
10-WEC, 2 columns	√	√	√	-	-	-	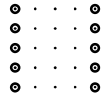
5 × 5-WEC rectilinear array	√	√	√	√	√	-	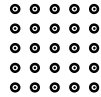
5 × 5-WEC staggered array	√	√	√	√	√	-	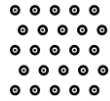

Table 4.5. *Cont.* Summary of the tested wave basin and WEC (array) configurations with regard to wave conditions studied (Table page 2/2).

Configuration	Types of tests regarding wave conditions						
	Reg. LCW	**Poly-chromatic**	**Irr. LCW**	**Irr. SCW**	**Diffracted wave field; no motion**	**WEC decay motion**	**WEC lay-out sketches**
3 × 3-WEC rectilinear 10*D*	√	√	√	√	-	-	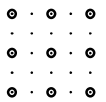
3 × 3-WEC rectilinear 5*D*	√	√	√	√	-		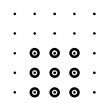
13-WEC staggered array	√	√	√	√	√	-	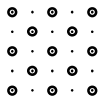

Notes:

[A]: Spacing, *l*, 5*D* to 20*D*	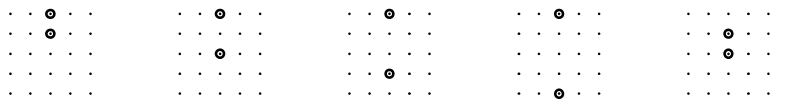
[B]: Spacing, *w*, 5*D* to 20*D*	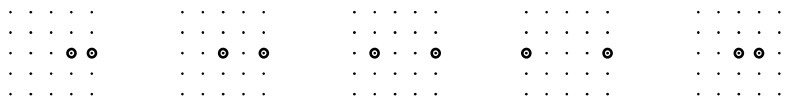
[C]: Repetition on each column	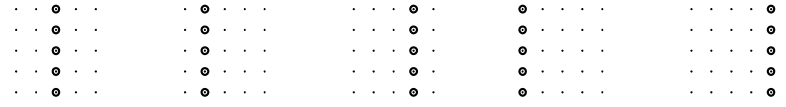

Figure 4.13. A 2-WEC column array (WECs #04 and #05) under regular waves with θ = 0°. The rest of the 23 WEC units are held stationary above the water surface. View from behind the wave absorbing beach.

Figure 4.14. Sea-state characterisation for regular waves with θ = 20°. All 25 WEC units are held stationary above the water surface. View from behind the wave generator.

Figure 4.15. A 10-WEC 2-Column array (WECs #21 - #25 and WECs #16 - #20) under regular waves with θ = 0°. The rest of the 15 WEC units are held stationary above the water surface. View from behind the wave absorbing beach.

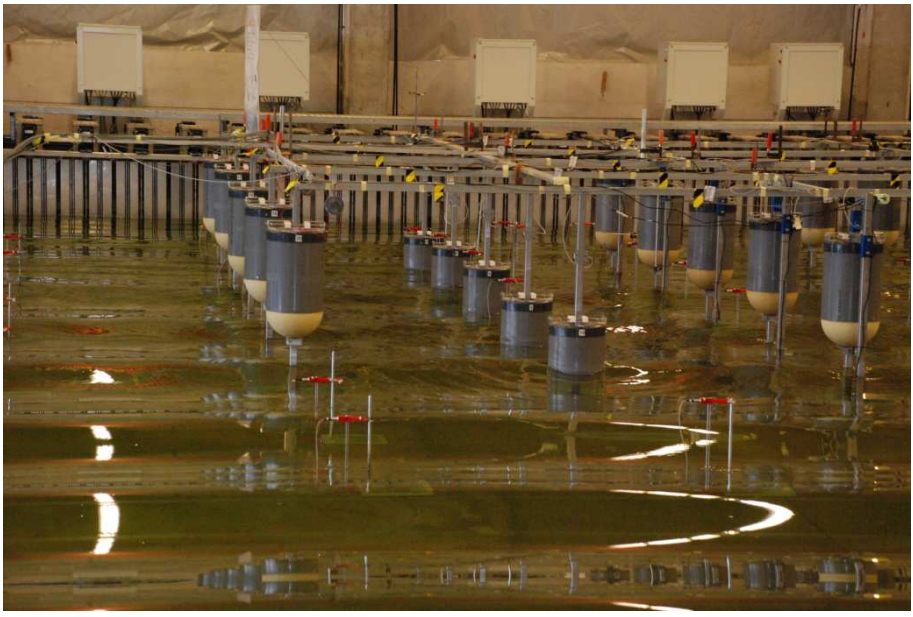

Figure 4.16. A 5-WEC column array (WECs #06 - #10) under regular waves with θ = 0°. The rest of the 20 WEC units are held stationary above the water surface. View from behind the wave absorbing beach.

4.6. Results and discussion

4.6.1. WEC Response Amplitude Operator (RAO) and power output

WEC response is measured during all tests. Since power absorption is due to a constant spring force, $F_{springs}$, and time-varying surge force, F_{surge}, WEC response is analysed employing a time-domain model [21]. The approach used follows [29] and is based on hydrodynamic coefficients obtained from the linear frequency-domain code WAMIT [30]. Frequency dependent radiation damping and added mass are subsequently converted, via approximating transfer functions, to a state-space formulation to represent the time-varying hydrodynamic damping force. Both the heave and surge excitation force are also obtained from WAMIT. Hydrodynamic parameters are obtained for a hemispherical ended float only, neglecting the WEC support structure arrangement. The mechanical constraints due to the PTO-system, F_{PTO}, and bearing friction, $F_{bearings}$, are modelled using Equations (2.5) and (2.6) from Chapter 2, respectively [21].

In Figure 4.17(a) the RAO is presented against the spring compression increments, dx, expressed by the non-dimensional amplitude of the measured or predicted heave displacement amplitude of the WEC, z_A, as the ratio to the measured wave amplitude, a_m. In Figure 4.17(b), the non-dimensional power output, expressed by the ratio, P / P_{wave} is presented against dx, where P, is the net power absorption (P_{tot} or P_{PTO} or $P_{bearings}$, as presented in Section 4.3.1), and P_{wave}, the power in the incident wave per metre width (i.e. per unit wavefront).

In Figure 4.17, measurements have been used from three experiments on different individual WEC units, as well as results from numerical predictions.

The RAO graph (Figure 4.17(a)) shows the numerically predicted RAO, the measured RAO for WEC unit #03 and the measured RAO for WEC unit #05 (sweep increasing dx and sweep decreasing dx). The shaded regions indicate ±4% variation in measured amplitudes over three repeats of the experiment.

The power graph (Figure 4.17(b)) shows the numerically predicted power due to constant power take off force (F_{PTO}), P_{PTO}, the power due to time-varying surge force (F_{surge}) on the bearings, $P_{bearings}$, and the total power due to both forces, P_{tot}. Moreover, the measured P_{PTO}, $P_{bearings}$ and P_{tot} are presented for (i) WEC unit #03 (thin solid lines with bars), (ii) WEC unit #05 and sweep increasing dx (thin dashed lines with "+"-symbols), and (iii) WEC unit #05 and sweep decreasing dx (thin dotted lines with "+"-symbols). The shaded regions indicate ±10% variation in measured powers.

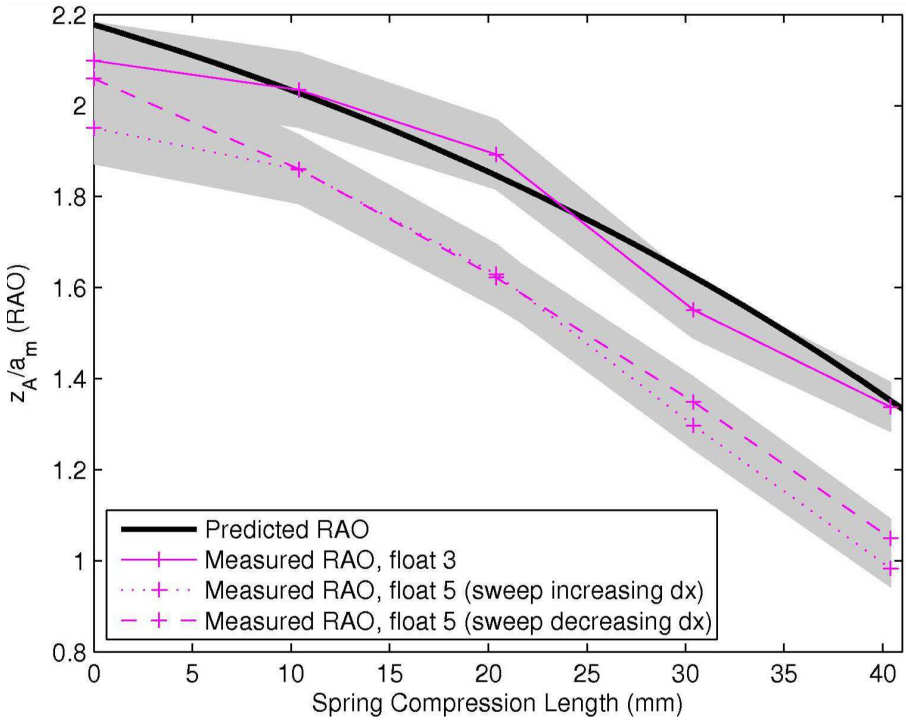

(a) WEC response (RAO) with spring compression, dx.

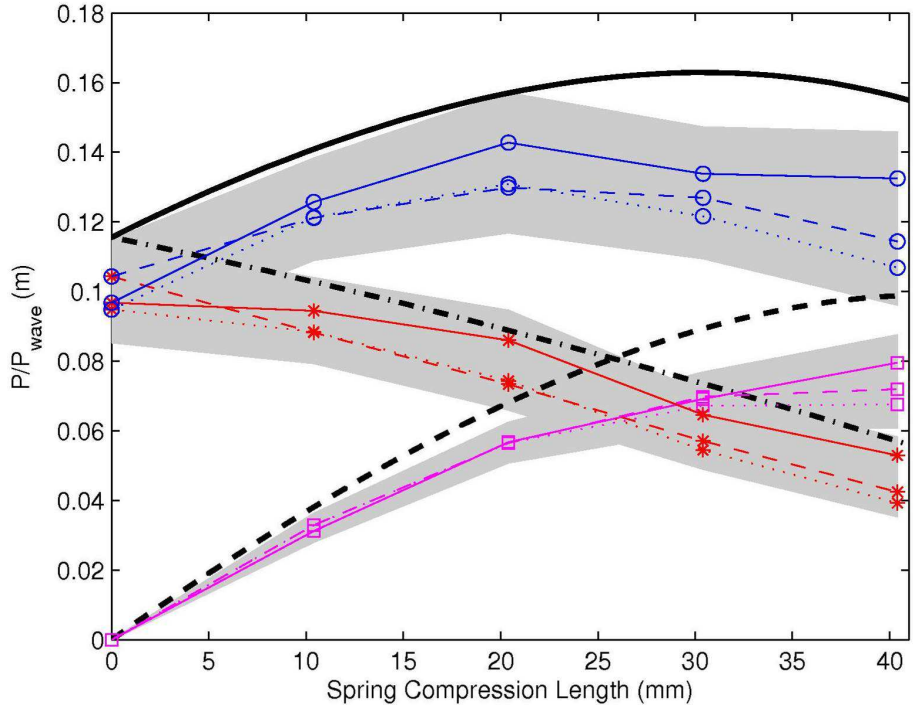

(b) Power output of the WEC unit with spring compression.

Figure 4.17. *Cont.*

Figure 4.17. RAO (a) and power output (b) with spring compression increment, dx, from three experiments on different individual WEC units and from numerical prediction. In the RAO graph (a), the shaded regions indicate ±4% variation in measured amplitudes over three repeats of experiment. For power graph (b): thick dashed line – numerically predicted P_{PTO}; thick dash-dot line – numerically predicted $P_{bearings}$; thick solid line – numerically predicted P_{tot}; thin magenta lines with squares – measured P_{PTO}; thin red lines with asterisks – measured $P_{bearings}$; thin blue lines with circles – measured P_{tot}; thin solid lines – WEC unit #03; thin dotted lines – WEC unit #05, sweep increasing dx; thin dashed lines – WEC unit #05, sweep decreasing dx. Shaded regions indicate ±10% variation in measured powers. P_{wave} is the power in the incident wave per metre width (i.e. per unit wavefront). Regular waves (H = 0.074 m, T = 1.260 s, wave angle, θ = 0º) [21].

The coefficient of friction μ = 0.17 (see Chapter 2) is found to provide reasonable agreement between measurement and numerical prediction of RAO and mean power absorption over a range of PTO-system spring compression increments, dx (Figure 4.17). The numerically predicted powers in Figure 4.17(b) also show good agreement with the measurements but again there is some discrepancy between the two WEC units considered. Note that, for this comparison, the measured response amplitudes of the WEC unit, z_m, are normalised to the wave amplitude measured at the WEC shafts location, a_m, because wave amplitude varies with location within the wave basin. Power absorption of a WEC unit within an array is expected to vary due to the time derivative of the WEC heave displacement, $\dot{z}(t)$, and surge force, $F_{surge}(t)$. For all multi-WEC tests, the same F_{PTO} is applied to each WEC unit for the test duration. For the majority of tests, a spring compression increment dx = 30.5 mm is employed since this corresponds to maximum power absorption as shown in Figure 24(b) and in Chapter 2.

Similar analysis has been performed for a column of five WEC units at longitudinal spacing, $l = 5D$, taking into account the experimentally measured response (Figure 4.18(a)) and power (Figure 4.18(b)). The response of a column of five WEC units indicates that there is greater variation of absorbed power, P_{tot}, with position than variation of response with position (Figure 4.18(a)). Compared to an individual WEC unit, the response of the front WEC unit is reduced and response of WEC units #02, #03, #04 and #05 are comparable. However, the proportion of the incident power absorbed differs by a factor of 2.25 between the front WEC unit (at Y = $0D$) and middle WEC unit (at $l = 10D$ from the front WEC unit). This spatial variation is greater than both the range of responses observed during the test and the spatial variation of measured wave amplitude, a_m.

However, from the individual isolated WEC tests (for WECs at different locations within the array) it seems that power absorption and response (and therefore the interaction factors described in Section 4.6.3) depend on the device location within the array. This conclusion, has also been found in [31] for a 4x3-WEC array of heaving WECs under irregular waves. Nevertheless, there are several similarities between the individual WECs, tested at different locations within the WEC array, e.g. regarding larger power absorption for short-crested waves for both WEC #03 and WEC #05, compared to that obtained for long-crested waves. Another similarity is that for short-crested waves, there are small variations regarding power output by the different individual WEC units (within arrays) and thus, the obtained results appear to be less location dependent. Since for WEC #03 persistently higher $F_{surge}(t)$, $\dot{z}(t)$ and $P_{tot}(t)$ are found, compared to other WECs of the central column, WEC #05 has been selected as the reference individual isolated WEC unit for the analysis in Sections 4.6.2 - 4.6.4. With regard to the coefficient of friction, μ, its value does not affect the analysis and interpretation of the obtained results, since either WEC array interaction factors (described in Section 4.6.3) or ratios of total power absorption of the arrays are used.

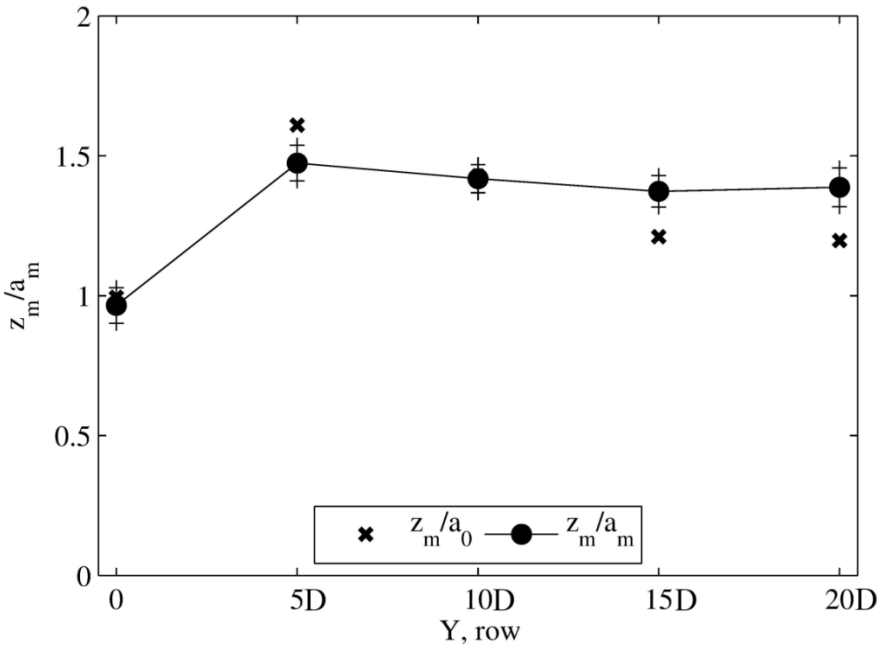

(a) Response amplitude operator (RAO) with distance along the 5-WEC column.

Figure 4.18. *Cont. Next Page*

Figure 4.18. *Cont.*

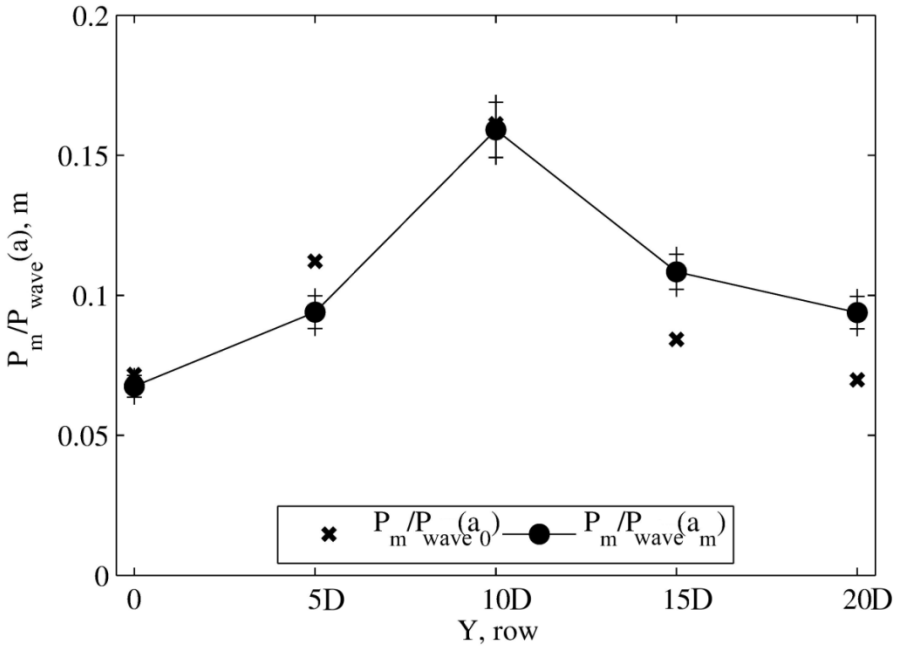

(b) Capture width ratio with distance along the 5-WEC Column.

Figure 4.18. WEC response (RAO) and capture width of five WEC units at longitudinal spacing, $l = 5D$, aligned with the wave propagation direction and averaged over 60 wave periods, T. Each point is normalised to measured wave amplitude at WEC shafts (a_m) for target regular wave amplitude (a_{0r} = 0.037 m). Error bars denote standard deviation. The wave basin length (Y, rows) is expressed in number of WEC unit diameters, D = 0.315 m. Results from [21].

4.6.2. Power absorption of an individual WEC unit

The instantaneous total power absorption, P_{tot}, has been calculated for the WEC unit situated on the central column and the last row of WECs. The selection of WEC #05 has been discussed in Section 4.6.1. All tests presented in this section, have been performed using a spring compression increment dx = 30.5 mm at the PTO-system, which corresponds to optimal power absorption of an individual WEC unit under regular waves of H = 0.074 m and T = 1.260 s. Moreover for the calculation of all power results, a coefficient of friction, μ = 0.17, has been used.

4.6.2.1. Regular waves

All results presented in this section refer to the individual WEC #05 under regular waves (H = 0.074 m, T = 1.260 s, wave angle, θ = 0º).

In Figure 4.19, plot (a) shows the normalized values of the measured surge forge, $F_{surge,meas}(t)$, the filtered surge force, $F_{surge,filt}(t)$, and the heave WEC buoy velocity, $\dot{z}(t)$. Both $F_{surge,meas}(t)$ and $F_{surge,filt}(t)$ are normalized to the maximum absolute value of filtered surge force, $F_{surge,filt,MAX}$, while $\dot{z}(t)$ is normalized to the maximum absolute value of the amplitude of the time derivative of $z(t)$, $\dot{z}_{A,MAX}$. A sinusoidal pattern is observed with a phase difference between the filtered surge force, $F_{surge,filt}(t)$, and the heave WEC buoy velocity, $\dot{z}(t)$.

In Figure 4.19, plot (b) shows the instantaneous normalized values of the total power absorption, $P_{tot}(t)$, the power absorption of the PTO-system, $P_{PTO}(t)$, and the power absorption of the WEC shaft bearings, $P_{bearings}(t)$. $P_{tot}(t)$, $P_{PTO}(t)$ and $P_{bearings}(t)$ are normalized to the maximum value of the instantaneous total power absorption, $P_{tot,MAX}$. The dashed horizontal lines represent time-averaged values. The peak values of $P_{PTO}(t)$ and $P_{bearings}(t)$ reach similar normalized values, indicating that they both have a similar contribution to the peak values of $P_{tot}(t)$ of the WEC unit under regular waves.

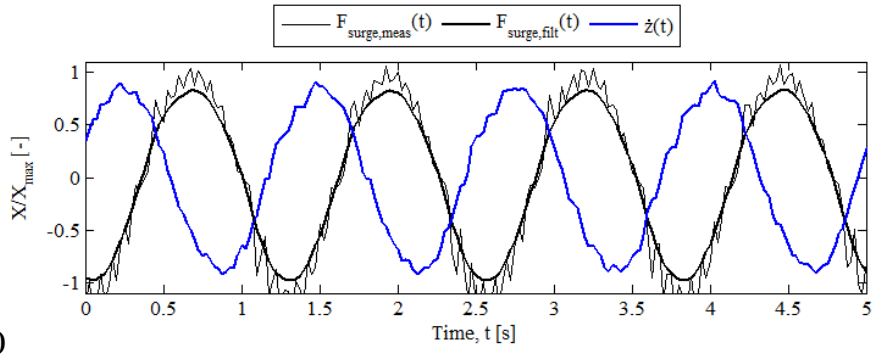

(a)

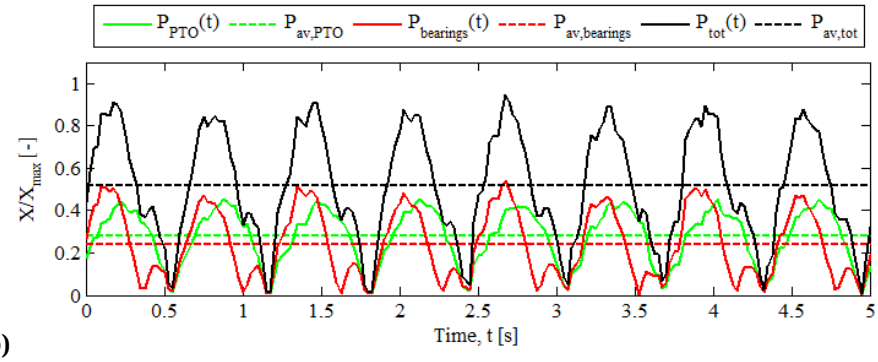

(b)

Figure 4.19. *Cont.*

Figure 4.19. Normalized values of: (a) measured surge forge, $F_{surge,meas}(t)$, filtered surge force, $F_{surge,filt}(t)$, heave WEC buoy velocity, $\dot{z}(t)$; and (b) instantaneous total power absorption, $P_{tot}(t)$, instantaneous power absorption of the PTO-system, $P_{PTO}(t)$, and instantaneous power absorption of the WEC shaft bearings, $P_{bearings}(t)$. The dashed horizontal lines represent time-averaged values. Results are presented for the individual WEC #05 under regular waves (H = 0.074 m, T = 1.260 s, wave angle, θ = 0º).

In Figure 4.20, plot (a) shows the actual values of measured surge force, $F_{surge}(t)$, and the filtered surge force, $F_{surge,filt}(t)$, while plot (b) shows $\dot{z}(t)$, the time derivative of $z(t)$. The same trend as in the normalized values of Figure 4.19 is observed. Also, the absolute average values have been calculated for the surge force and the WEC buoy velocity: $F_{av,surge}$ = 16.075 N and $\dot{z}_{av}$ = 0.134 m/s. Figure 4.20(c) shows the instantaneous absolute values of the total power absorption, $P_{tot}(t)$, the power absorption of the PTO-system, $P_{PTO}(t)$, and the power absorption of the WEC shaft bearings, $P_{bearings}(t)$, for the individual WEC #05. The dashed horizontal lines represent time-averaged values. The average value of the instantaneous total power absorption, $P_{av,tot}$, of the individual WEC #05 under regular waves (H = 0.074 m, T = 1.260 s, wave angle, θ = 0º) is 0.727 W. In Figure 4.20(c), a periodic pattern of $P_{tot}(t)$ is observed. At each oscillation, the time instant when a peak value of $P_{tot}(t)$ occurs, matches the time instant when a peak value — negative or positive— of $\dot{z}(t)$ occurs. Moreover, $\dot{z}(t)$ has greater influence on $P_{tot}(t)$ compared to $F_{surge}(t)$, as both $P_{PTO}(t)$ and $P_{bearings}(t)$ depend on $\dot{z}(t)$, while $F_{surge}(t)$ only affects $P_{bearings}(t)$. Moreover, $P_{av,PTO}$ = 0.388 W and $P_{av,bearings}$ = 0.339 W, showing that both components have a similar contribution to $P_{av,tot}$, for regular waves, with $P_{av,PTO}$ being larger.

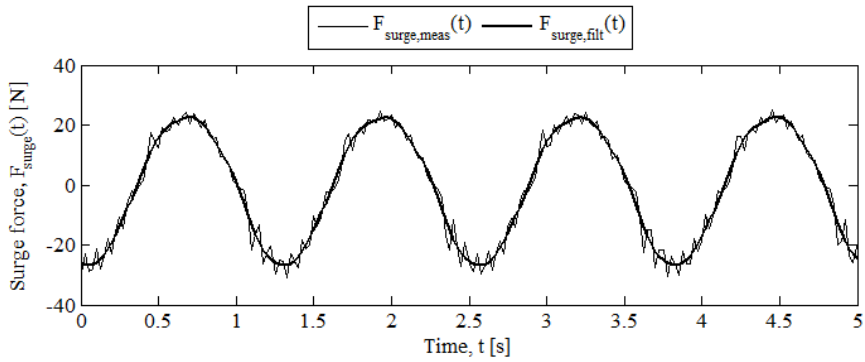

(a)

Figure 4.20. *Cont.*

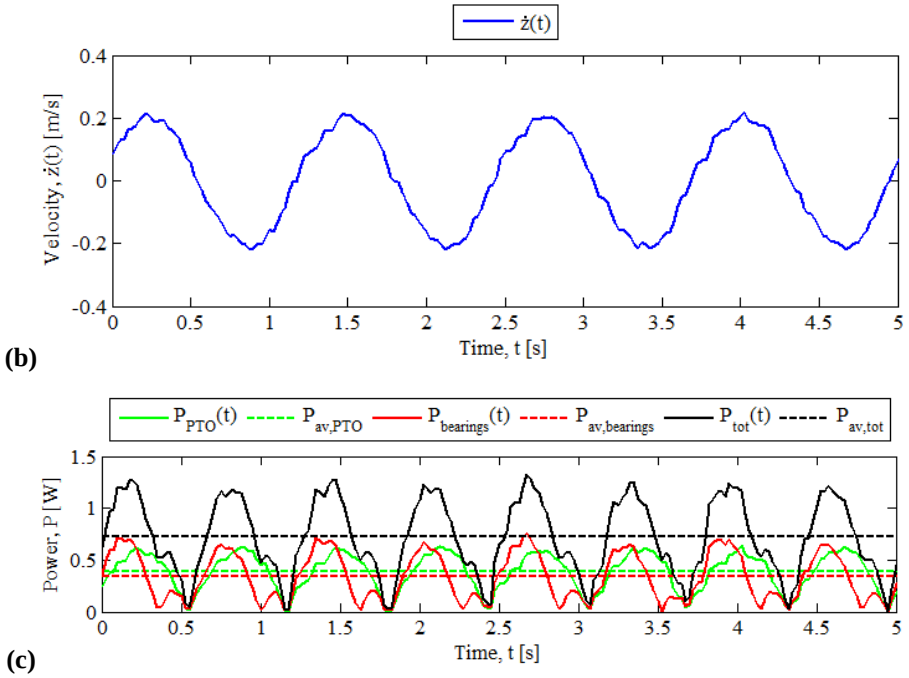

Figure 4.20. Actual values of: (a) the measured surge forge, $F_{surge}(t)$, and the filtered surge force, $F_{surge,filt}(t)$; (b) the heave WEC buoy velocity, $\dot{z}(t)$; and instantaneous absolute values of (c) total power absorption, $P_{tot}(t)$, power absorption of the PTO-system, $P_{PTO}(t)$, and power absorption of the WEC shaft bearings, $P_{bearings}(t)$. The dashed horizontal lines represent time-averaged values. Results are presented for the individual WEC #05 under regular waves (H = 0.074 m, T = 1.260 s, wave angle, θ = 0º).

4.6.2.2. Irregular long-crested waves

All results presented in this section refer to the individual WEC #05 under irregular long-crested waves (H_{m0} = 0.104 m, T_p = 1.260 s).

In Figure 4.21, plot (a) shows the normalized values of filtered surge force, $F_{surge,filt}(t)$, and the heave WEC buoy velocity, $\dot{z}(t)$. $F_{surge,filt}(t)$ is normalized to the maximum absolute value of filtered surge force, $F_{surge,filt,MAX}$, while $\dot{z}(t)$ is normalized to the maximum absolute value of the amplitude of the time derivative of $z(t)$, $\dot{z}_{A,MAX}$. $F_{surge,filt}(t)$ and $\dot{z}(t)$ are not sinusoidal, as for regular waves, due to the irregular sea state.

Figure 4.21(b) shows normalized instantaneous values of total power absorption, $P_{tot}(t)$, and the power absorption of the WEC shaft bearings,

$P_{bearings}(t)$. Figure 4.21(c) shows the power absorption of the PTO-system, $P_{PTO}(t)$. In plots (b) and (c), the dashed horizontal lines represent time-averaged values. $P_{tot}(t)$, $P_{PTO}(t)$ and $P_{bearings}(t)$ are normalized to the maximum value of the instantaneous total power absorption, $P_{tot,MAX}$. The time instants when the peak values of $\dot{z}(t)$ occur, match the time instants when peak values of $P_{tot}(t)$ occur.

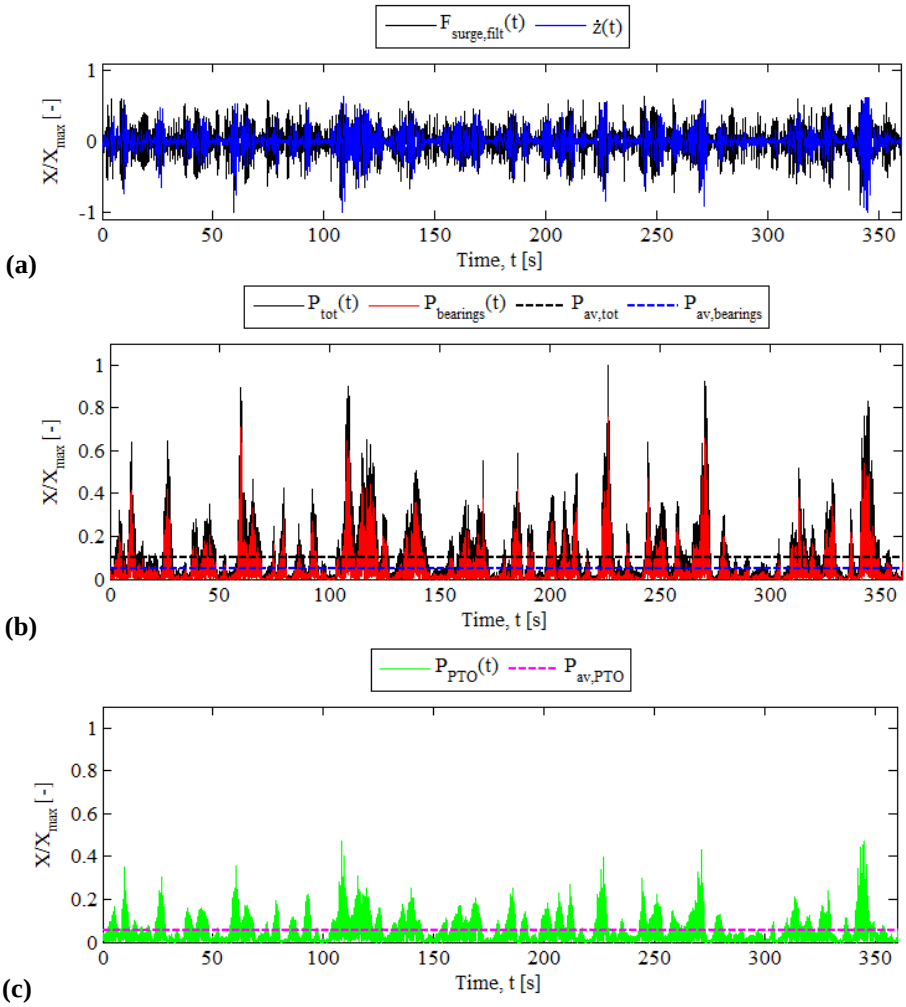

Figure 4.21. Normalized values of: (a) the filtered surge force, $F_{surge,filt}(t)$, and the heave WEC buoy velocity, $\dot{z}(t)$; (b) instantaneous total power absorption, $P_{tot}(t)$, and instantaneous power absorption of the WEC shaft bearings, $P_{bearings}(t)$; and (c) instantaneous power absorption of the PTO-system, $P_{PTO}(t)$. The dashed horizontal lines represent time-averaged values. Results are presented for the individual WEC #05 under irregular long-crested waves (H_{m0} = 0.104 m, T_p=1.260 s).

In Figure 4.22, plot (a) shows the actual values of the filtered surge force, $F_{surge,filt}(t)$, while plot (b) shows $\dot{z}(t)$, the time derivative of $z(t)$. Also, the absolute average values have been calculated for the surge force and the WEC buoy velocity: $F_{av,surge}$ = 14.491 N and $\dot{z}_{av}$ = 0.067 m/s. Figure 4.22(c) shows the instantaneous absolute values of the total power absorption, $P_{tot}(t)$, and the power absorption of the WEC shaft bearings, $P_{bearings}(t)$, while plot (d) shows the power absorption of the PTO-system, $P_{PTO}(t)$. In plots (c) and (d), the dashed horizontal lines represent time-averaged values. The average value of the instantaneous total power absorption, $P_{av,tot}$, of the individual WEC #05 under irregular long-crested waves (H_{m0} = 0.104 m, T_p = 1.260 s) is 0.374 W. Moreover, $P_{av,PTO}$ = 0.195 W and $P_{av,bearings}$ = 0.178 W, showing that both components have a similar contribution to $P_{av,tot}$, for irregular waves, however, with $P_{av,PTO}$ being more significant.

$P_{tot}(t)$ reaches higher absolute peak values when WEC #05 is under long-crested irregular waves (3.747 W) compared to the situation when WEC #05 is tested under regular waves (1.322 W). However, the average instantaneous total power absorption of WEC #05, $P_{av,tot}$, is higher for regular waves compared to that for irregular long-crested waves, which can also be concluded by the higher $F_{av,surge}$ and $\dot{z}_{av}$ found for the WEC buoy under regular waves. These optimal peaks occur when, within the generated wave spectrum, a wave with wave period close or equal to the nominal value of the peak wave period, T_p = 1.26 s, propagates towards WEC #05, as the WEC's PTO-system has been tuned to absorb power optimally from waves under regular waves with T = 1.26 s. Instead, for regular waves, the power output of the WEC unit is optimal, since the wave period is theoretically constant, T = 1.26 s, at d_w = 0.70 m. However, a commercial PTO-system typically is optimally controlled to obtain optimum power absorption over a wider wave spectrum. In this research, no optimal control has been applied, since the objective is not to optimize power absorption of the WEC (array) but to create measurable WEC array effects through the developed PTO-system.

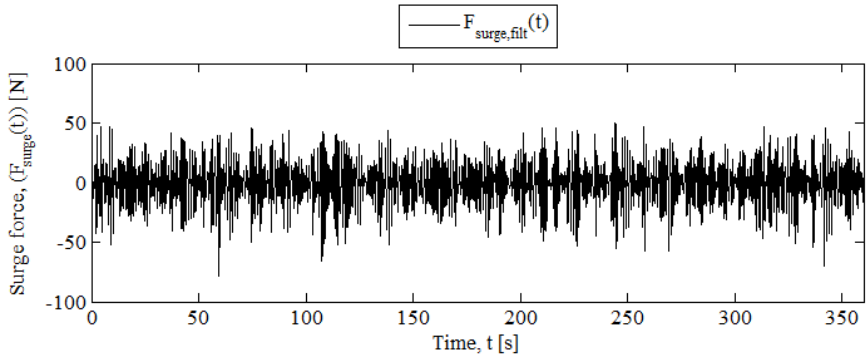

(a)

Figure 4.22. *Cont.*

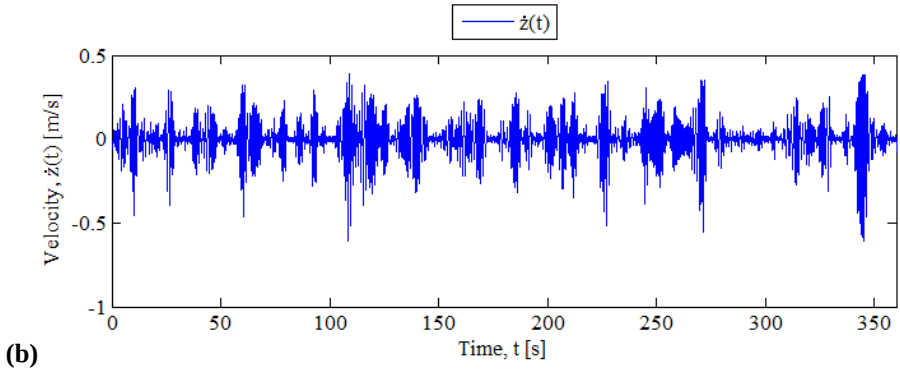

(b)

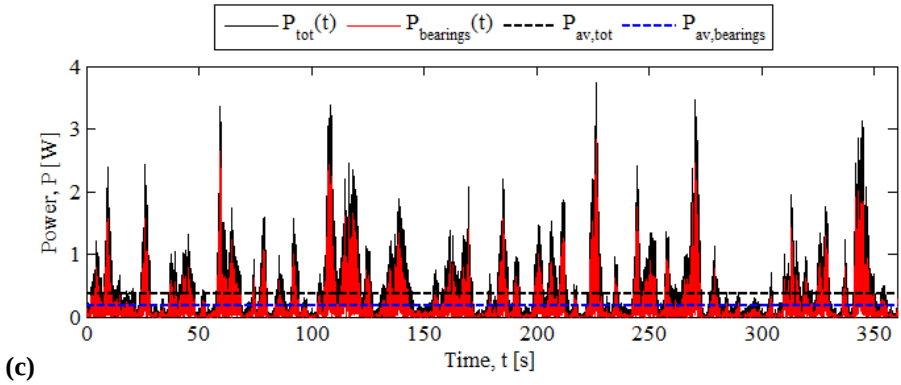

(c)

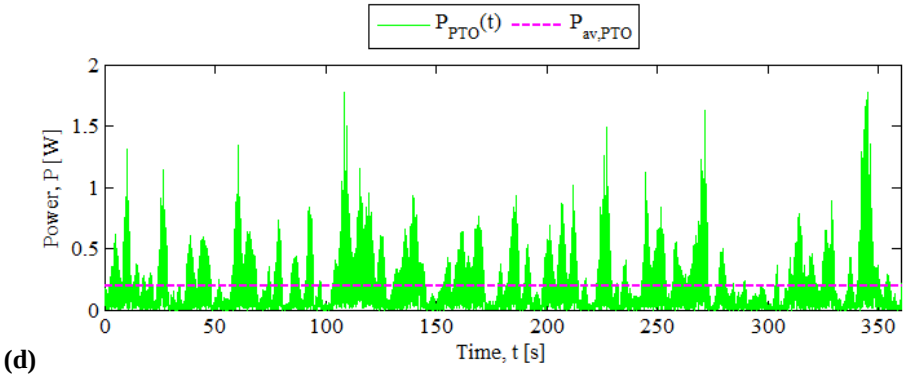

(d)

Figure 4.22. Actual values of: (a) the filtered surge force, $F_{surge,filt}(t)$; (b) the heave WEC buoy velocity, $\dot{z}(t)$; Absolute values of instantaneous: (c) total power absorption, $P_{tot}(t)$, and power absorption of the WEC shaft bearings, $P_{bearings}(t)$; and (d) power absorption of the PTO-system, $P_{PTO}(t)$. The dashed horizontal lines represent time-averaged values. Results are presented for the individual WEC #05 under irregular long-crested waves (H_{m0} = 0.104 m, T_p = 1.260 s).

4.6.2.3. Irregular short-crested waves

All results presented in this section refer to the individual WEC #05 under irregular short-crested waves (H_{m0} = 0.104 m, T_p = 1.260 s, s = 10).

In Figure 4.23, plot (a) shows the normalized values of filtered surge force, $F_{surge,filt}(t)$, and the heave WEC buoy velocity, $\dot{z}(t)$. $F_{surge,filt}(t)$ is normalized to the maximum absolute value of filtered surge force, $F_{surge,filt,MAX}$, while $\dot{z}(t)$ is normalized to the maximum absolute value of the amplitude of the time derivative of $z(t)$, $\dot{z}_{A,MAX}$. $F_{surge,filt}(t)$ and $\dot{z}(t)$ are not sinusoidal, as for regular waves, due to the irregular sea state. Figure 4.23(b) shows the instantaneous normalized values of total power absorption, $P_{tot}(t)$, and the instantaneous power absorption of the WEC shaft bearings, $P_{bearings}(t)$. Figure 4.23(c) shows the instantaneous power absorption of the PTO-system, $P_{PTO}(t)$. $P_{tot}(t)$, $P_{PTO}(t)$ and $P_{bearings}(t)$ are normalized to the maximum value of the instantaneous total power absorption, $P_{tot,MAX}$. In plots (b) and (c), the dashed horizontal lines represent time-averaged values. $P_{tot}(t)$ clearly shows a peak which follows the peak values of $F_{surge,filt}(t)$ and $\dot{z}(t)$ at the same time instant.

In Figure 4.24, plot (a) shows the actual values of the filtered surge force, $F_{surge,filt}(t)$, while plot (b) shows $\dot{z}(t)$, the time derivative of $z(t)$. Also, the absolute average values have been calculated for the surge force and the WEC buoy velocity: $F_{av,surge}$ = 15.607 N and $\dot{z}_{av}$ = 0.095 m/s. Figure 4.24(c) shows the instantaneous absolute values of the total power absorption, $P_{tot}(t)$, and the power absorption of the WEC shaft bearings, $P_{bearings}(t)$, while plot (d) shows the power absorption of the PTO-system, $P_{PTO}(t)$. In plots (c) and (d), the dashed horizontal lines represent time-averaged values. The average value of the instantaneous total power absorption, $P_{av,tot}$, of the individual WEC #05 under irregular short-crested waves (H_{m0} = 0.104 m, T_p = 1.260 s, s = 10) is 0.547 W. Moreover, $P_{av,PTO}$ = 0.274 W and $P_{av,bearings}$ = 0.272 W, showing that both components have a very similar contribution to $P_{av,tot}$, for irregular short-crested waves.

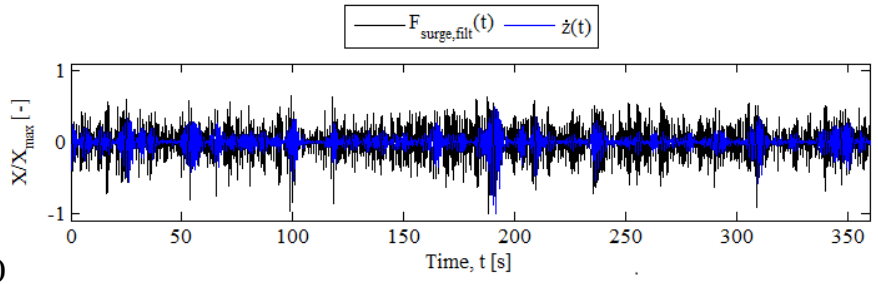

(a)

Figure 4.23. *Cont.*

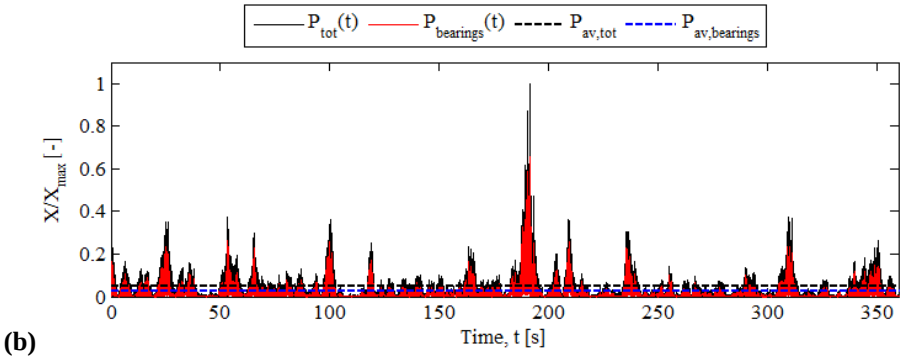

(b)

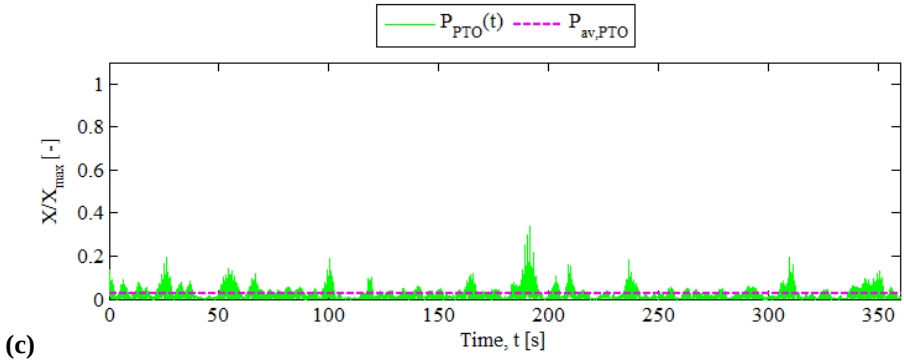

(c)

Figure 4.23. Normalized values of: (a) filtered surge force, $F_{surge,filt}(t)$, and the heave WEC buoy velocity, $\dot{z}(t)$; (b) instantaneous total power absorption, $P_{tot}(t)$, and instantaneous power absorption of the WEC shaft bearings, $P_{bearings}(t)$; (c) instantaneous power absorption of the PTO-system, $P_{PTO}(t)$. The dashed horizontal lines represent time-averaged values. Results are presented for the individual WEC #05 under irregular short-crested waves (H_{m0} = 0.104 m, T_p = 1.260 s, s = 10).

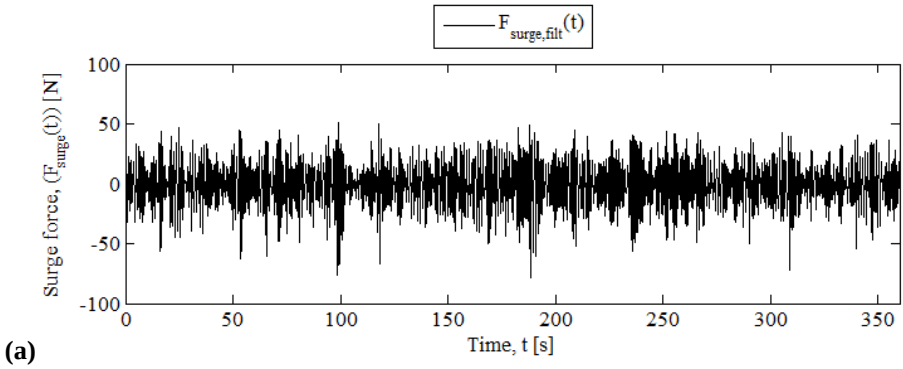

(a)

Figure 4.24. *Cont.*

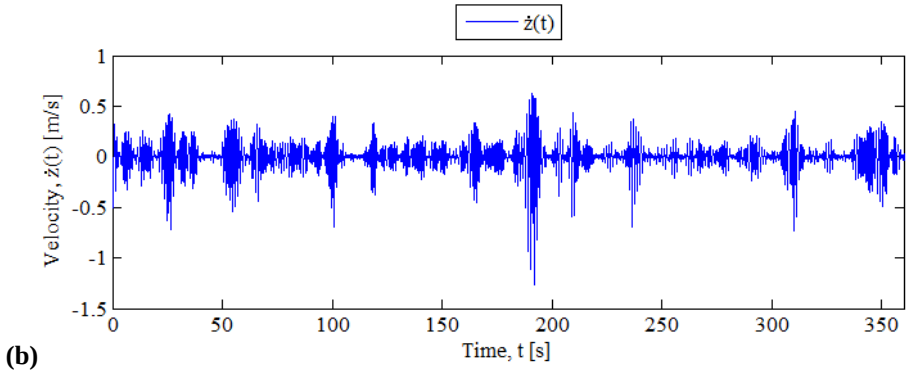

(b)

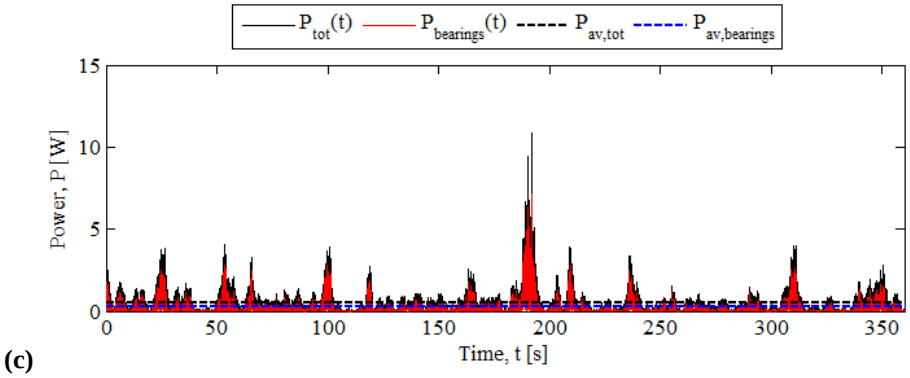

(c)

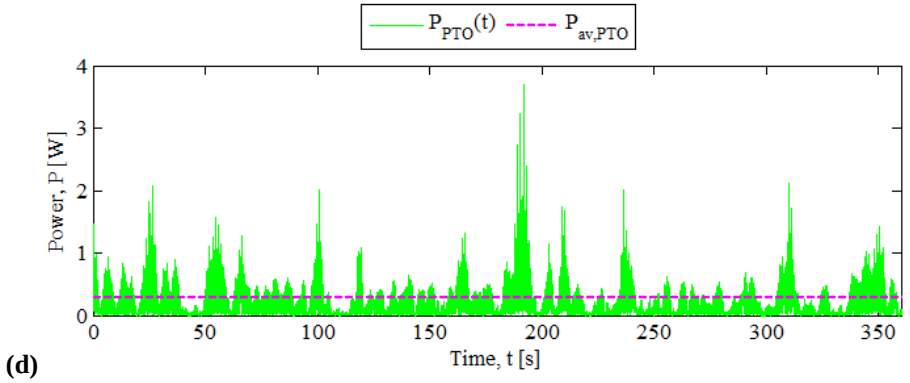

(d)

Figure 4.24. Actual values of: (a) the filtered surge force, $F_{surge,filt}(t)$; (b) the heave WEC buoy velocity, $\dot{z}(t)$; Absolute values of instantaneous (c) total power absorption, $P_{tot}(t)$, and power absorption of the WEC shaft bearings, $P_{bearings}(t)$; and (d) power absorption of the PTO-system, $P_{PTO}(t)$. The dashed horizontal lines represent time-averaged values. Results are presented for the individual WEC #05 under irregular short-crested waves (H_{m0} = 0.104 m, T_p = 1.260 s, s = 10).

The peak values of the instantaneous total power absorption, P_{tot}, are 7.149 W to 10.830 W, which are higher than the peak value obtained both for long-crested irregular (3.747 W) and regular waves (1.322 W). This peak is due to high values of the WEC buoy heave velocity for short-crested waves. Heave excitation is shown to be significant for wind waves, observed also by comparing $\dot{z}_{av}$ for different sea states. The average value of instantaneous total power absorption of WEC #05, $P_{av,tot}$, is higher for irregular short-crested waves (s = 10) (0.547 W) than for irregular long-crested waves (0.374 W), which is attributed, on the one hand to the high heave excitation of the WEC buoy, and on the other hand to the quick wave height recovery in the lee of the WEC (thus limited wave field modification in the far-field for an individual WEC). The latter becomes more obvious in the case of the large WEC array of 25 WEC units, both by results of power output and wave field modification, in Sections 4.6.3.1 - 4.6.3.2 and 4.6.8 - 4.6.9. However the highest $P_{av,tot}$ for the individual WEC #05 is obtained for regular waves (0.727 W), as expected, since the WEC's PTO-system has been tuned optimally to absorb power from the incoming waves, for this sea state.

4.6.3. WEC array interaction factor and results' presentation

The WEC array interaction factor —$\bar{q}$-factor— as described in literature, e.g. in ([32]-[36]), is a measure that quantifies the effect of intra-array interactions on the power absorption of a WEC array. The interaction factor is the ratio of the total power from the entire WEC array to that of the same number of WECs in isolation. If all the WECs are geometrically and operationally identical, as in this PhD research, the WEC array interaction $\bar{q}$-factor is:

$$\bar{q} - factor = \frac{\sum_{i=1}^{N} P_{i,tot}}{N \cdot P_{0,tot}} \tag{4.1}$$

where $P_{0,tot}$ represents the total power absorbed by an individual WEC unit; $P_{i,tot}$ represents the power absorbed by the i WEC in an array, and N the number of WECs in the array. When $\bar{q}$-factor is higher than unity ($\bar{q}$-factor > 1.0), the total WEC array power averaged per WEC unit in the array, is greater than the power of an individual WEC unit (in isolation). In this case, intra-array interactions have a constructive effect on the power absorption of the entire WEC array. When $\bar{q}$-factor is smaller than unity ($\bar{q}$-factor < 1.0), the total WEC array power averaged per WEC unit in the array, is less than the power of an individual WEC unit (in isolation). In this case, intra-array interactions have a destructive effect on the power absorption of the entire WEC array.

The interaction $\bar{q}$-factor has been calculated for selected array geometric configurations from the performed WEC array experiments, using the time averaged values of the instantaneous total power absorption, $P_{av,tot}$, both for the considered WEC array configurations and for the individual WEC unit (WEC #05). Power output results are presented here for the 5x5-WEC rectilinear and staggered array, as well as for the 3x3-WEC rectilinear 5D and 10D arrays.

The instantaneous absolute values of the total power absorption, $P_{tot}(t)$, the power absorption of the PTO-system, $P_{PTO}(t)$, and the power absorption of the WEC shaft bearings, $P_{bearings}(t)$, have been calculated. In addition, the surge force, $F_{surge}(t)$, and WEC buoy heave velocity, $\dot{z}(t)$are presented.

All tests presented in this section, have been performed using a spring compression increment dx = 30.5 mm at the PTO-system and coefficient of friction, μ = 0.17, to estimate the forces applied through the WEC shaft bearings and the PTO-system. However, all $\bar{q}$-factors are independent of the coefficient of friction, μ. Moreover, for the sake of simplicity and since irregular waves represent realistic wave conditions for real wave farm applications, only results for irregular long-crested (H_{m0} = 0.104 m, T_p = 1.260 s) and short-crested (H_{m0} = 0.104 m, T_p = 1.260 s, s = 10) waves are presented for the WEC arrays. The wind directional waves have been selected, instead of the swell waves, as these conditions lead to larger differences compared to the long-crested irregular waves.

The total power absorption, $P_{tot}(t)$, has been estimated for the presented WEC arrays. Surge force, $F_{surge}(t)$, measurements have been acquired along the central WEC column, as seen previously. For calculating $P_{tot}(t)$, the wave induced surge force, $F_{surge}(t)$, on WECs of the same row is considered to be equal to the measured surge force, $F_{surge}(t)$, on the respective WEC unit from the central column. In all 2-D top views of the wave basin, the waves propagate from the bottom to the top of the figures.

First, a detailed description is presented in Sections 4.6.3.1 - 4.6.3.4 of the obtained results on the power absorption by the WEC arrays. A summary of the main observations is given in Section 4.6.4.

4.6.3.1. Power absorption of the 5x5-WEC rectilinear array

4.6.3.1.1. Irregular long-crested waves

In Figure 4.25, plot (a) shows the absolute instantaneous normalized values of total power absorption, $P_{tot}(t)$, and the power absorption of the WEC shaft bearings, $P_{bearings}(t)$. Plot (b) shows the power absorption of the PTO-system, $P_{PTO}(t)$. The dashed horizontal lines represent time-averaged values. $P_{tot}(t)$, $P_{PTO}(t)$ and $P_{bearings}(t)$ are normalized to the maximum value of the instantaneous total power absorption, $P_{tot,MAX}$.

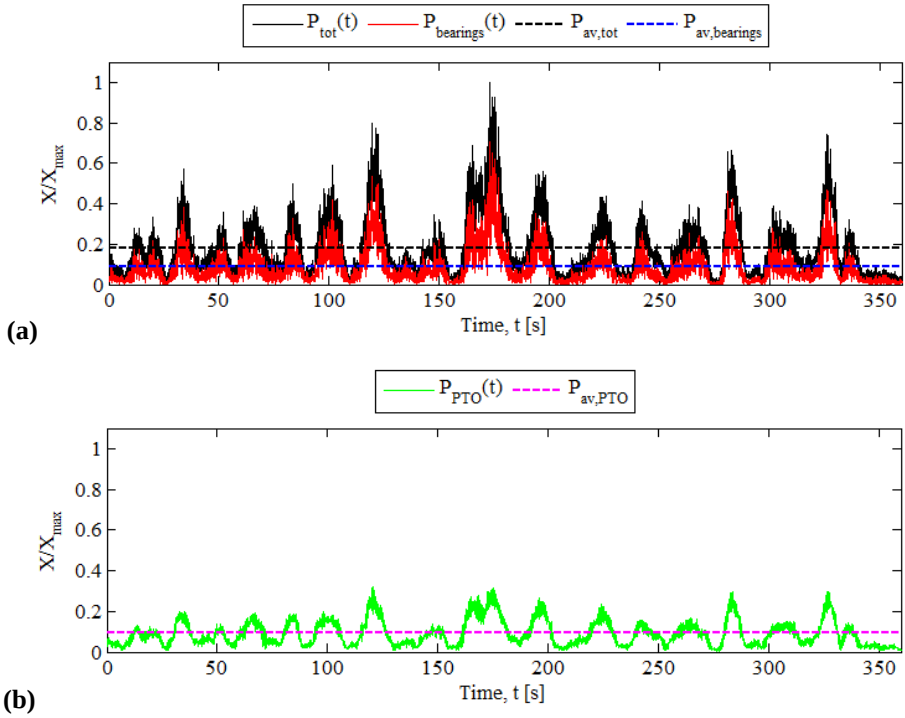

Figure 4.25. Absolute normalized instantaneous values of: (a) total power absorption, $P_{tot}(t)$, and power absorption of the WEC shaft bearings, $P_{bearings}(t)$; and (b) power absorption of the PTO-system, $P_{PTO}(t)$. The dashed horizontal lines represent time-averaged values. Results are presented for the entire 5x5-WEC rectilinear array under irregular long-crested waves (H_{m0} = 0.104 m, T_p = 1.260 s).

Figure 4.26 shows the time-averaged absolute values of the instantaneous total power absorption, $P_{av,tot}$, —in W— for each WEC unit of the 5x5-WEC rectilinear array. The highest values of $P_{av,tot}$ are obtained for the 2nd and 3rd row of WECs and are higher than the $P_{av,tot}$ obtained for the individual isolated WEC #05 (0.374 W) under the same wave conditions. For long-crested irregular waves, there are 12 WEC units within the array (almost 50.0 % of the total number of WECs), for which the intra-array interactions have a constructive effect on their power output. For all WECs of the 2nd and 3rd row (and a couple from the front and 4th row) positive intra-array interactions take place. For all the WECs of the 5th row and 80.0 % of the WECs from the 4th and the front row, destructive intra-array interactions occur. WECs #01 and #02, benefit the least and the most from those intra-array interactions, respectively.

Therefore, $P_{av,tot}$ of each WEC unit is affected by the operation of the WEC array as a whole, since none of them has power output equal to that of the individual WEC #05. Moreover, the WECs of the last two rows clearly experience negative

intra-array interactions, and attenuation of absorbed power is observed in the longitudinal direction of the wave basin towards the wave absorbing beach. Also the WECs of the front row show lower power output.

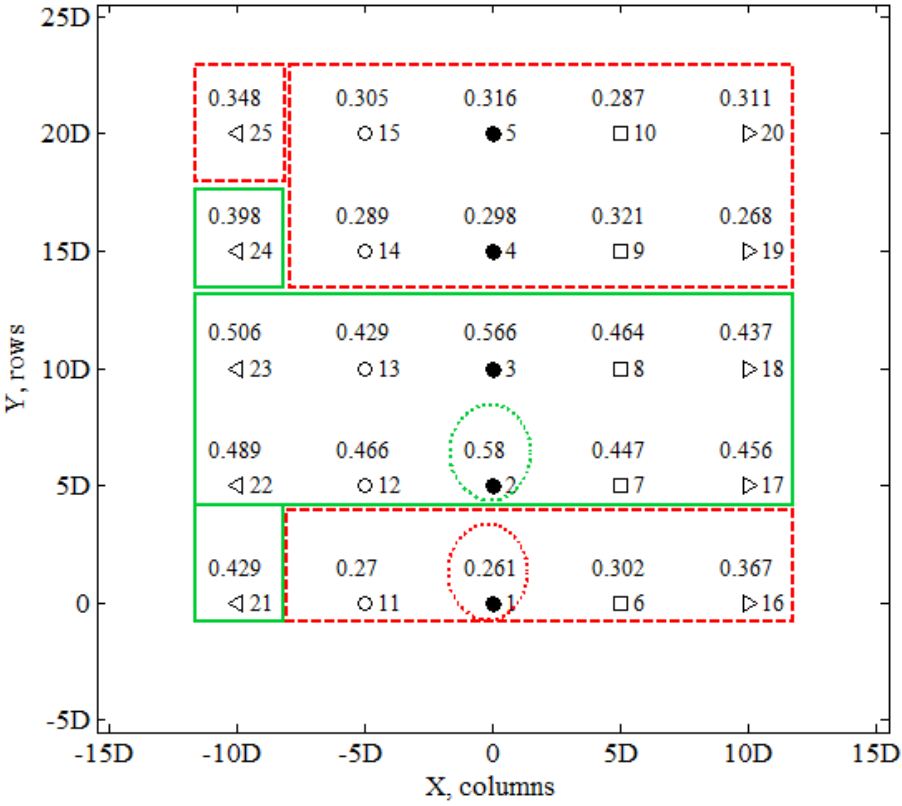

Figure 4.26. Absolute time-averaged instantaneous total power absorption, $P_{av,tot}$, (in W) for each of the 25 WEC units of the 5x5-WEC rectilinear array. Irregular long-crested waves (H_{m0} = 0.104 m, T_p = 1.260 s). The basin width (X, columns) and length (Y, rows) are expressed in number of WEC unit diameters, D = 0.315 m. WECs indicated within: the boxes of continuous line, have greater power output than that of the individual WEC #05 (0.374 W); the boxes of dashed line, have smaller power output than that of the individual isolated WEC #05; the circles of dotted line, are the two WECs with the lowest and the highest power output within the entire array.

Furthermore, Eq. (4.2) has been used to quantify these intra-array interactions between the WECs of the array, relative to the power output from the individual WEC #05 (in isolation):

$$\frac{P_{i,tot} - P_{0,tot}}{P_{0,tot}} \; x \; 100 \; \% \qquad (4.2)$$

where $P_{0,tot}$ represents the total power absorbed by the individual WEC #05 in isolation, and $P_{i,tot}$ represents the total power absorbed by the i WEC in the array (values are used from Figure 4.26). A positive difference indicates, therefore, constructive effect, while negative difference indicates destructive effect, respectively, of the intra-array interactions on the power output of the i WEC in the array. The difference percentages in the measured power output of each WEC unit, $P_{i,tot}$, normalised by $P_{0,tot}$, calculated using Eq. (4.2), are presented in Figure 4.27 by a contour plot of the difference percentages (with the discrete percentage values). In Figure 4.27, the dark shaded areas indicate the areas within the array where destructive (negative) intra-array interactions take place.

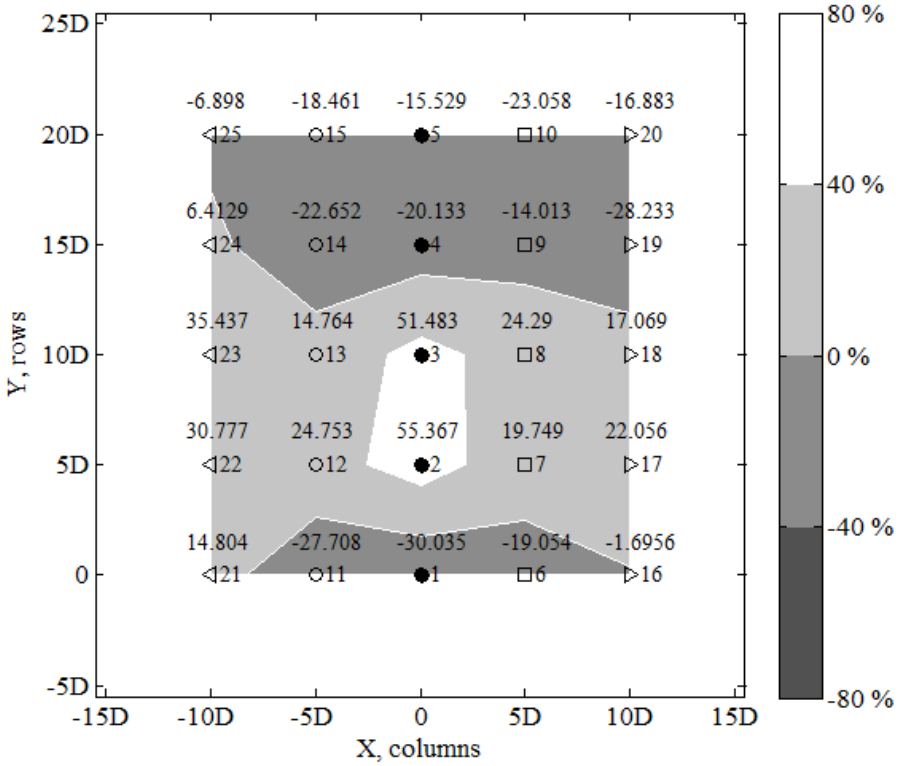

Figure 4.27. Difference percentages in non-dimensional time-averaged total power output ($P_{i,tot}/P_{0,tot}$) calculated using Eq. (4.2) for target conditions of irregular long-crested waves (H_{m0} = 0.104 m and T_p = 1.26 s). Discreet values are shown at the WEC locations within the WEC array. Shading in contour plot denotes non-dimensional difference percentage: 40 to 80 % (white), 0 to 40 % (light gray), 0 to -40 % (gray), -40 to -80 % (dark gray). The basin width (X, columns) and length (Y, rows) are expressed in number of WEC unit diameters, D = 0.315 m.

In Figure 4.28, plot (a) shows the absolute instantaneous values of the total power absorption, $P_{tot}(t)$, and the power absorption of the WEC shaft bearings, $P_{bearings}(t)$, while plot (b) shows the power absorption of the PTO-system, $P_{PTO}(t)$. The time-averaged values (indicated by the dashed horizontal lines) have been estimated for the entire 5x5-WEC rectilinear array; $P_{av,tot}$ = 9.612 W, $P_{av,bearings}$ = 4.711 W and $P_{av,PTO}$ = 4.901 W, showing the similar contribution of both $P_{av,bearings}$ and $P_{av,PTO}$ to $P_{av,tot}$, as found for the individual WEC #05 under long-crested irregular waves.

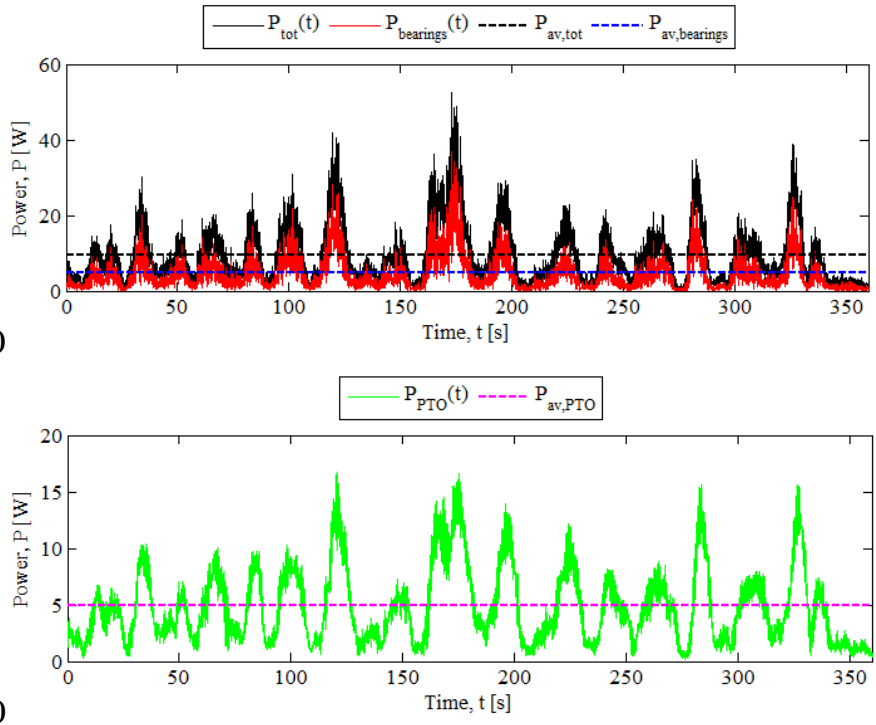

Figure 4.28. Absolute values of the instantaneous: (a) total power absorption, $P_{tot}(t)$, and power absorption of the WEC shaft bearings, $P_{bearings}(t)$; and (b) power absorption of the PTO-system, $P_{PTO}(t)$. The dashed horizontal lines represent time-averaged values. Results are presented for the entire 5x5-WEC rectilinear array under irregular long-crested waves (H_{m0} = 0.104 m, T_p = 1.260 s).

Moreover, the interaction $\bar{q}$-factor, for the 5x5-WEC rectilinear array is obtained by using Eq. (4.1), $P_{av,tot}$ obtained for the entire array (9.612 W) (Figure 4.28(a)) and $P_{av,tot}$ for the individual isolated WEC #05 (0.374 W), for the same wave conditions. The resulting WEC array interaction $\bar{q}$-factor is 1.029. As $\bar{q}$-factor > 1.0, intra-array interactions have a constructive effect on the overall power

absorption of the entire WEC array. WEC #05 absorbs 15.51 % less power when it operates within the 5x5-WEC rectilinear array, compared to the same individual WEC #05 in isolation. In order to provide an idea of the effectiveness of the number of rows and columns within an array, also the $\bar{q}$-factors of each of the five 5-WEC rows and the five 5-WEC columns of the array have been separately calculated (Table 4.6), using Eq. (4.1).

Table 4.6. WEC array interaction factor, $\bar{q}$-factor, calculated both for the entire array and each WEC array column / row (5x5-WEC rectilinear array; irregular long-crested waves: H_{m0} = 0.104 m and T_p = 1.26 s).

	WECs #21-#25	WECs #11-#15	WECs #01-#05	WECs #06-#10	WECs #16-#20	$P_{av,tot}$ of row [W]	$\bar{q}$-factor row [-]
$P_{av,tot}$ of each WEC [W]	column 1	column 2	column 3	column 4	column 5		
row 1	0.429	0.270	0.261	0.302	0.367	1.630	0.873
row 2	0.489	0.466	0.580	0.447	0.456	2.439	1.305
row 3	0.506	0.429	0.566	0.464	0.437	2.403	1.286
row 4	0.398	0.289	0.298	0.321	0.268	1.574	0.843
row 5	0.348	0.305	0.316	0.287	0.311	1.566	0.838
$P_{av,tot}$ of column [W]	2.169	1.759	2.022	1.823	1.839	$P_{av,tot}$ of array [W] 9.612	
$\bar{q}$-factor column [-]	1.161	0.941	1.082	0.976	0.985	$P_{av,tot}$ of individual WEC #05 [W] 0.374	
						$\bar{q}$-factor array [-] 1.029	

The column $\bar{q}$-factors are closer to 1.0 (ranging from about -6.0 % to +16.0 %, compared to $\bar{q}$-factor = 1.0) and globally indicate more positive conditions regarding the power output (per column), for all columns. As a result, there is no indication that specific columns are significantly less effective, and therefore no indication is given for e.g. need for limiting or increasing the number of columns within the array. Moreover, the column $\bar{q}$-factors are closer to the WEC array $\bar{q}$-factor.

On the other hand, the resulting $\bar{q}$-factors per row, show significant variations (ranging from about -16.0 % to +31.0 %, compared to $\bar{q}$-factor = 1.0), showing pronounced negative intra-array interactions for the last two rows. Attenuation of absorbed power is observed, and therefore the last two rows do not operate effectively. This conclusion gives an indication for the need to limit the number of rows within an array. Moreover, the row $\bar{q}$-factors are not representative of the WEC array $\bar{q}$-factor, in contrast to the column $\bar{q}$-factors.

4.6.3.1.2. Irregular short-crested waves

In Figure 4.29, plot (a) shows the absolute instantaneous normalized values of total power absorption, $P_{tot}(t)$, and the power absorption of the WEC shaft bearings, $P_{bearings}(t)$. Plot (b) shows the power absorption of the PTO-system, $P_{PTO}(t)$. The dashed horizontal lines represent time-averaged values. $P_{tot}(t)$, $P_{PTO}(t)$ and $P_{bearings}(t)$ are normalized to the maximum value of the instantaneous total power absorption, $P_{tot,MAX}$. Figure 4.30 shows the time-averaged absolute value of instantaneous total power absorption, $P_{av,tot}$, —in W— for each WEC of the 5x5-WEC rectilinear array.

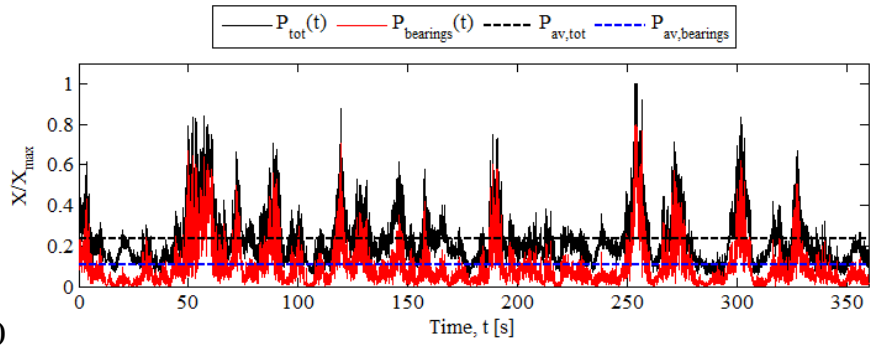

(a)

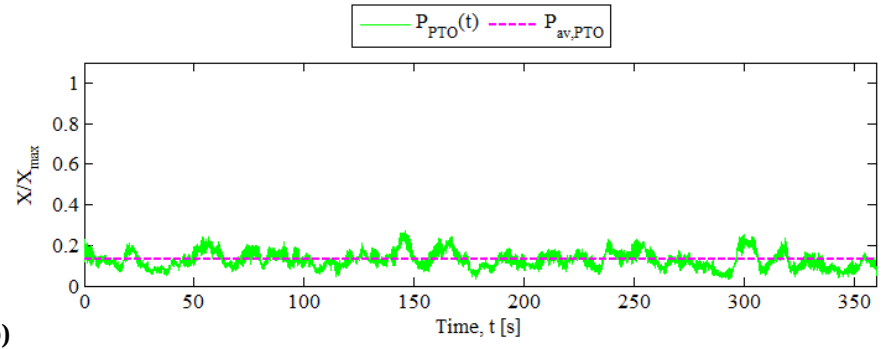

(b)

Figure 4.29. *Cont.*

Figure 4.29. Absolute normalized values of instantaneous: (a) total power absorption, $P_{tot}(t)$, and power absorption of the WEC shaft bearings, $P_{bearings}(t)$; and (b) power absorption of the PTO-system, $P_{PTO}(t)$. The dashed horizontal lines represent time-averaged values. Results are presented for the entire 5x5-WEC rectilinear array under irregular short-crested waves (H_{m0} = 0.104 m, T_p = 1.260 s, s = 10).

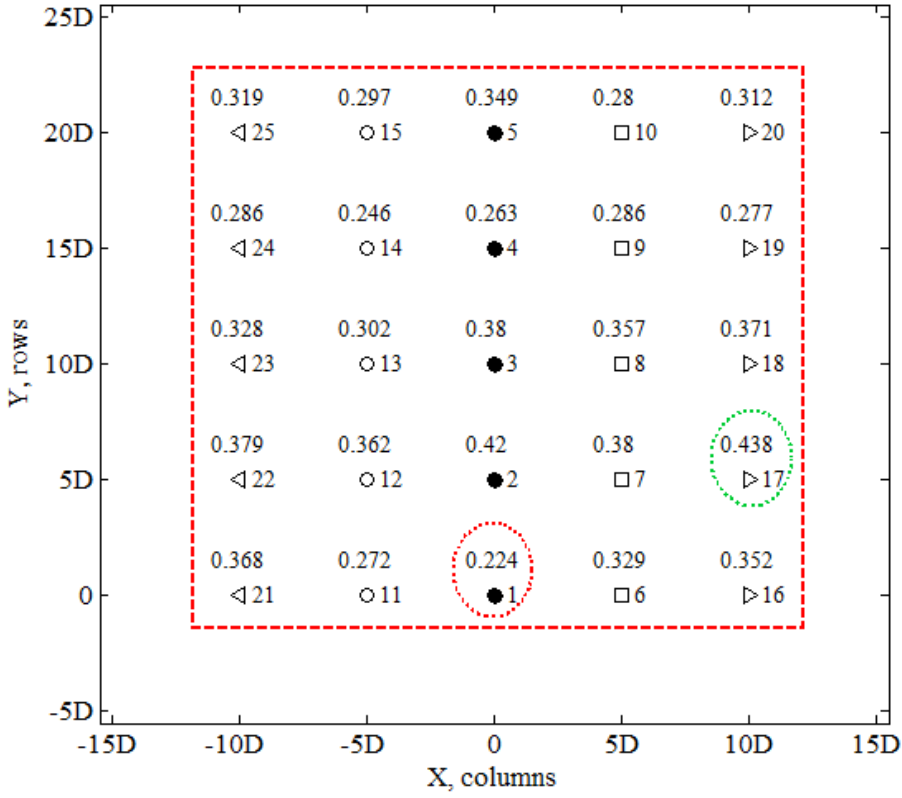

Figure 4.30. Absolute time-averaged instantaneous total power absorption, $P_{av,tot}$, (in W) for each of the 25 WEC units of the 5x5-WEC rectilinear array. Irregular short-crested waves (H_{m0} = 0.104 m, T_p = 1.260 s, s = 10). The basin width (X, columns) and length (Y, rows) are expressed in number of WEC unit diameters, D = 0.315 m. WECs indicated within: the box of dashed line, have smaller power output than that of the individual isolated WEC #05 (0.547 W); the circles of dotted line, are the two WECs with the lowest and the highest power output within the entire array.

The highest values of $P_{av,tot}$ are obtained for the 2nd row, followed by the 3rd and the 5th row of WECs. However, all WECs of the array absorb less wave energy compared to the individual WEC #05 (0.547 W), under the same wave conditions. For short-crested irregular waves, all WEC units experience destructive intra-array interactions, which have negative influence on the overall power absorption of the WEC array. WECs #01 and #02 / #17, suffer the most and the least from negative hydrodynamic intra-array interactions that take place within the WEC array, respectively.

Moreover, similarly to the long-crested irregular waves, attenuation of absorbed power is observed in the longitudinal direction of the wave basin towards the wave absorbing beach, as well as less power absorption by the WECs at the front row. As for long-crested irregular waves, WEC #01 experiences intra-array interactions in the most negative way. Also, WEC #02, for both sea states, has the largest power output (for short-crested waves, WEC #17 has the largest output but differs only by 1.4 % from that of WEC #02, from the same row).

Furthermore, the difference percentages in the measured power output of each WEC unit, $P_{i,tot}$, normalised by $P_{0,tot}$, calculated using Eq. (4.2), are presented in Figure 4.31, by a contour plot of the difference percentages (with the discrete percentage values). In Figure 4.31, the dark shaded areas indicate the areas within the array where the most negative intra-array interactions take place. Also Figure 4.31 shows that there is small variation regarding power output by each WEC unit. This variation is large in the case of long-crested irregular waves.

In Figure 4.32, plot (a) shows the absolute instantaneous values of the total power absorption, $P_{tot}(t)$, and the power absorption of the WEC shaft bearings, $P_{bearings}(t)$, while plot (b) shows the power absorption of the PTO-system, $P_{PTO}(t)$. The time-averaged values (indicated by the dashed horizontal lines) have been estimated for the entire 5x5-WEC rectilinear array; $P_{av,tot}$ = 8.180 W, $P_{av,bearings}$ = 3.746 W and $P_{av,PTO}$ = 4.434 W, showing a similar contribution of both $P_{av,bearings}$ and $P_{av,PTO}$ to $P_{av,tot}$, as found for the individual WEC #05 under irregular directional wind waves, with $P_{av,PTO}$ being higher.

Moreover, the interaction $\bar{q}$-factor for the 5x5-WEC rectilinear is obtained by using Eq. (4.1), $P_{av,tot}$ obtained for the entire array (8.180 W) (Figure 4.32(a)) and $P_{av,tot}$ for the individual WEC #05 (0.547 W), for the same wave conditions. The resulting WEC array interaction $\bar{q}$-factor is 0.599. As $\bar{q}$-factor < 1.0, intra-array interactions have a destructive effect on the overall power absorption of the WEC array. WEC #05 absorbs 36.20 % less power compared to the same individual isolated WEC #05, when it operates within 5x5-WEC rectilinear array.

Also the $\bar{q}$-factors of each of the five 5-WEC rows and the five 5-WEC columns of the array have been separately calculated (Table 4.7), using Eq. (4.1), similarly to the analysis for long-crested irregular waves.

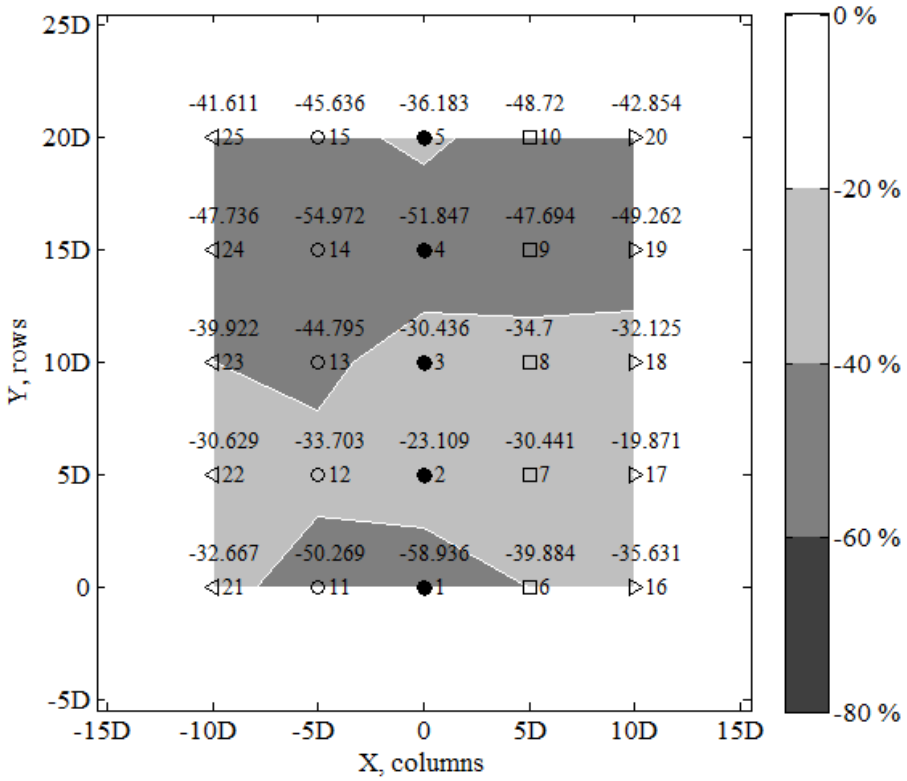

Figure 4.31. Difference percentages in non-dimensional time-averaged total power output ($P_{i,tot}/P_{0,tot}$) calculated using Eq. (4.2), for target conditions of irregular short-crested waves (H_{m0} = 0.104 m, T_p = 1.26 s, s = 10). Discreet values are shown at the WEC locations within the WEC array. Shading in contour plot denotes non-dimensional difference percentage: 0 to -20 % (white), -20 to -40 % (light gray), -40 to -60 % (gray), -60 to -80 % (dark gray). The basin width (X, columns) and length (Y, rows) are expressed in number of WEC unit diameters, D = 0.315 m.

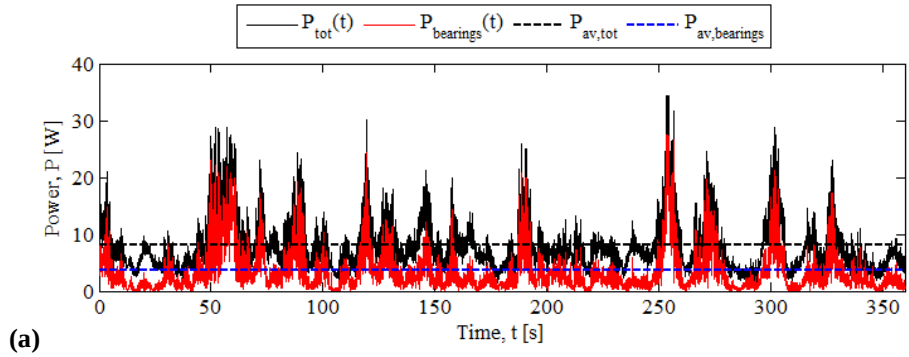

(a)

Figure 4.32. *Cont.Next Page*

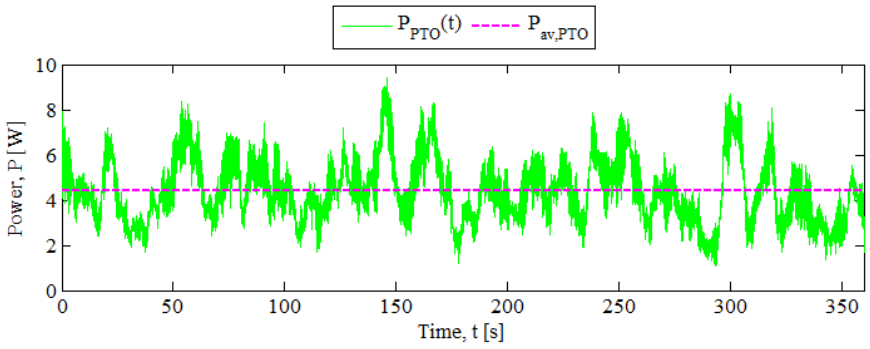

(b)

Figure 4.32. Absolute values of the instantaneous: (a) total power absorption, $P_{tot}(t)$, and power absorption of the WEC shaft bearings, $P_{bearings}(t)$; and (b) power absorption of the PTO-system, $P_{PTO}(t)$. The dashed horizontal lines represent time-averaged values. Results are presented for the entire 5x5-WEC rectilinear array under irregular short-crested waves (H_{m0} = 0.104 m, T_p = 1.260 s, s = 10).

Table 4.7. WEC array interaction factor, $\bar{q}$-factor, calculated both for the entire array and each WEC array column / row (5x5-WEC rectilinear array; irregular short-crested waves: H_{m0} = 0.104 m, T_p = 1.26 s, s = 10).

	WECs #21-#25	WECs #11-#15	WECs #01-#05	WECs #06-#10	WECs #16-#20	$P_{av,tot}$ of row [W]	$\bar{q}$-factor row [-]
$P_{av,tot}$ of each WEC [W]	column 1	column 2	column 3	column 4	column 5		
row 1	0.368	0.272	0.224	0.329	0.352	1.545	0.565
row 2	0.379	0.362	0.420	0.380	0.438	1.980	0.724
row 3	0.328	0.302	0.380	0.357	0.371	1.738	0.636
row 4	0.286	0.246	0.263	0.286	0.277	1.358	0.497
row 5	0.319	0.297	0.349	0.280	0.312	1.558	0.570
$P_{av,tot}$ of column [W]	1.681	1.479	1.637	1.632	1.751	$P_{av,tot}$ of array [W] 8.180	
$\bar{q}$-factor column [-]	0.615	0.541	0.599	0.597	0.641	$P_{av,tot}$ of individual WEC #05 [W] 0.547	
						$\bar{q}$-factor array [-] 0.599	

In Table 4.7, the WEC array column $\bar{q}$-factors range between -45.9 % and -35.9 %, compared to $\bar{q}$-factor = 1.0, while the resulting $\bar{q}$-factors per WEC array row, show very similar variation (ranging from -50.3 % to -27.6 %, compared to $\bar{q}$-factor = 1.0). Therefore, for short-crested irregular wind waves, the effect of the number of rows is not pronounced as for long-crested waves. Attenuation of absorbed wave power is observed towards the longitudinal direction of the WEC array, yet not as clear as for long-crested irregular waves. Also, less clear differences are found between the $\bar{q}$-factors calculated for columns and for rows.

4.6.3.2. Power absorption of the 5x5-WEC staggered array

4.6.3.2.1. Irregular long-crested waves

In Figure 4.33, plot (a) shows the absolute normalized instantaneous values of total power absorption, $P_{tot}(t)$, and the power absorption of the WEC shaft bearings, $P_{bearings}(t)$. Plot (b) shows the power absorption of the PTO-system, $P_{PTO}(t)$. The dashed horizontal lines represent time-averaged values. $P_{tot}(t)$, $P_{PTO}(t)$ and $P_{bearings}(t)$ are normalized to the maximum value of the instantaneous total power absorption, $P_{tot,MAX}$.

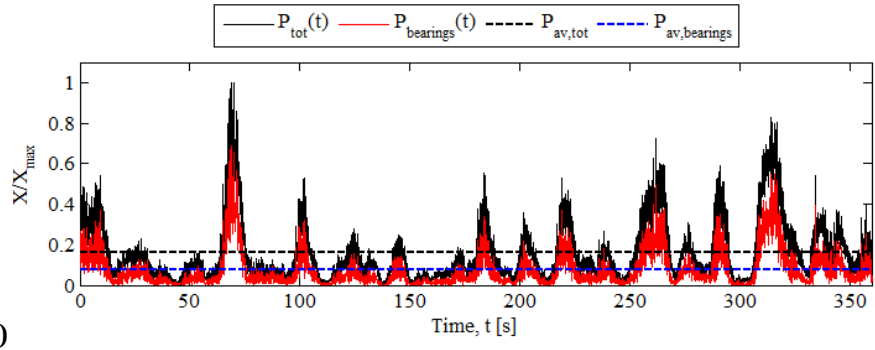

(a)

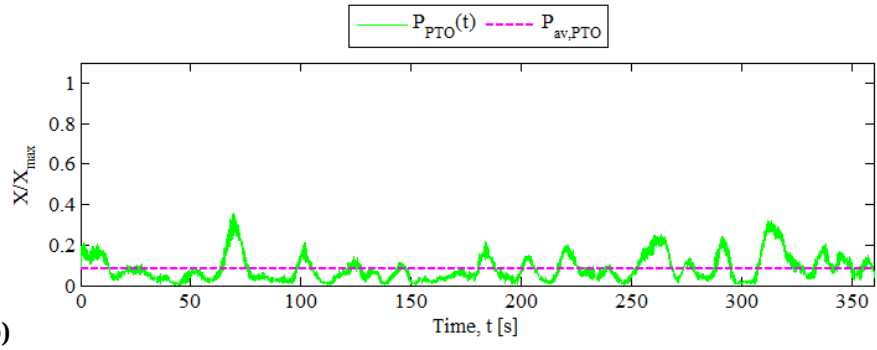

(b)

Figure 4.33. *Cont.*

Figure 4.33. Absolute normalized values of the instantaneous: (a) total power absorption, $P_{tot}(t)$, and power absorption of the WEC shaft bearings, $P_{bearings}(t)$; and (b) power absorption of the PTO-system, $P_{PTO}(t)$. The dashed horizontal lines represent time-averaged values. Results are presented for the entire 5x5-WEC staggered array under irregular long-crested waves (H_{m0} = 0.104 m, T_p = 1.260 s).

Figure 4.34 shows the time-averaged absolute values of instantaneous total power absorption, $P_{av,tot}$, —in W— for each WEC unit of the 5x5-WEC staggered array. The highest values of $P_{av,tot}$ are obtained on the 2nd and 3rd row of WECs, as well as for the 60 % of the WECs from the front and the 4th row, and are higher than the $P_{av,tot}$ obtained for the individual WEC #05 (0.374 W), under the same wave conditions. For long-crested irregular waves, there are 16 WEC units within the array (64.0 % of the total number of WECs), for which the intra-array interactions have a constructive effect on their power output. For 40 % of the WECs of the front and 4th row, as well as for all WECs of the last row, destructive intra-array interactions take place. WECs #10 (at the rear row) and #02 (at the 2nd row), benefit the least and the most from the intra-array interactions that occur within the WEC array, respectively. WEC #02 still has the highest power output, as for the 5x5-WEC rectilinear array. Similarly to the rectilinear array, attenuation of absorbed power is observed in the longitudinal direction of the wave basin towards the wave absorbing beach, and thus parallel to the wave propagation direction. For the staggered array, by shifting two WEC rows to the right, positive effect on the power output of four extra WEC units has been achieved, compared to the rectilinear array. Wider spreading of the constructive intra-array interactions has been achieved, and consequently destructive interactions have been limited. In this way, a more effective WEC array configuration has been identified.

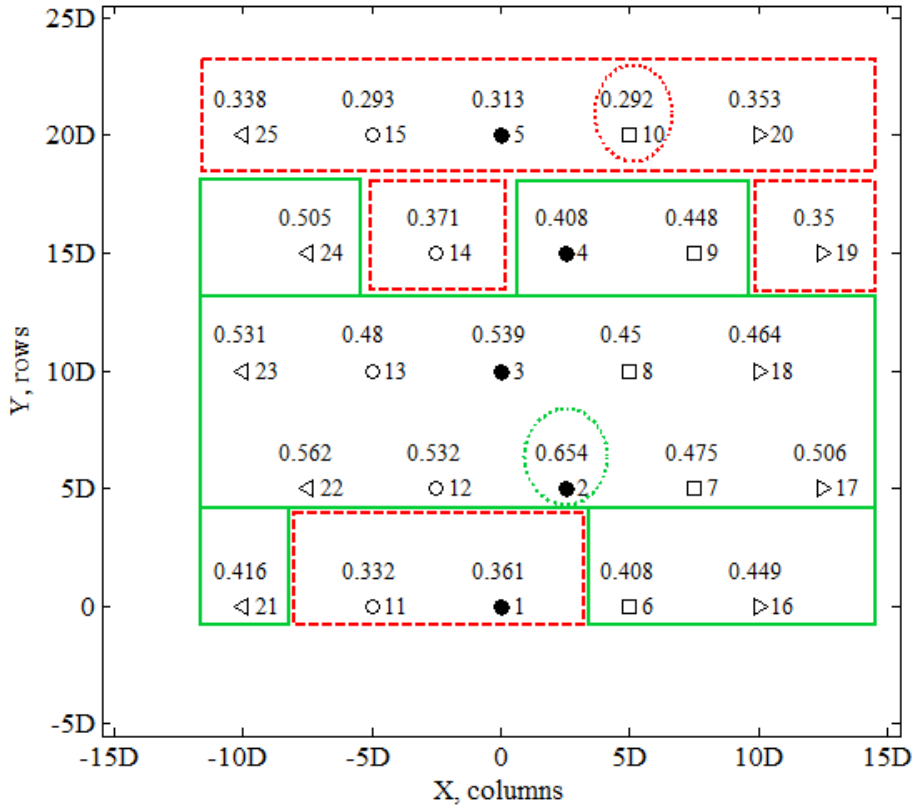

Figure 4.34. Absolute time-averaged instantaneous total power absorption, $P_{av,tot}$, (in W) for each of the 25 WEC units of the 5x5-WEC staggered array. Irregular long-crested waves (H_{m0} = 0.104 m, T_p = 1.260 s). The basin width (X, columns) and length (Y, rows) are expressed in number of WEC unit diameters, D = 0.315 m. WECs indicated within: the boxes of continuous line, have greater power output than that of the individual WEC #05 (0.374 W); the boxes of dashed line, have smaller power output than that of the individual isolated WEC #05; the circles of dotted line, are the two WECs with the lowest and the highest power output within the entire array.

Furthermore, the difference percentages in the measured power output of each WEC unit, $P_{i,tot}$, normalised by $P_{0,tot}$, calculated using Eq. (4.2), are presented in Figure 4.35 by a contour plot of the difference percentages (with the discrete percentage values). In Figure 4.35, the dark shaded areas indicate the areas within the array, where destructive (negative) intra-array interactions take place.

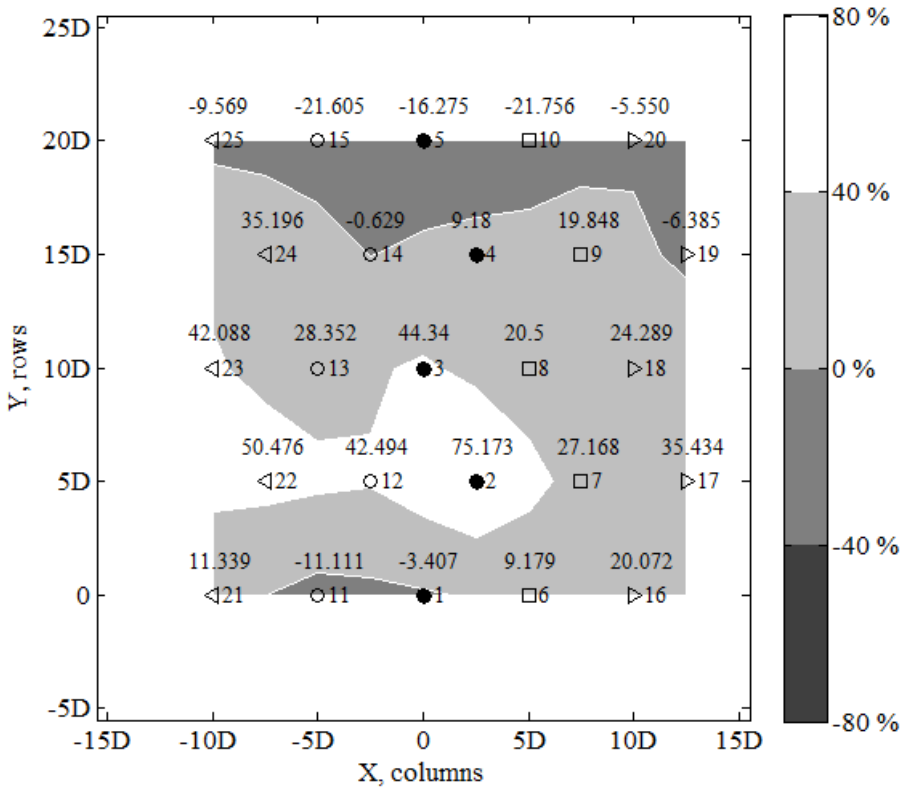

Figure 4.35. Difference percentages in non-dimensional time-averaged total power output ($P_{i,tot}/P_{0,tot}$) between tests with an array and with an individual WEC, for target conditions of irregular long-crested waves (H_{m0} = 0.104 m and T_p = 1.26 s). Discreet values are shown at the WEC locations within the WEC array. Shading in contour plot denotes non-dimensional difference percentage: 40 to 80 % (white), 0 to 40 % (light gray), -0 to -40 % (gray), -40 to -80 % (dark gray). The basin width (X, columns) and length (Y, rows) are expressed in number of WEC unit diameters, D = 0.315 m.

In Figure 4.36, plot (a) shows the absolute instantaneous values of the total power absorption, $P_{tot}(t)$, and the power absorption of the WEC shaft bearings, $P_{bearings}(t)$, plot (b) shows the power absorption of the PTO-system, $P_{PTO}(t)$. The time-averaged values (indicated by the dashed horizontal lines) have been estimated for the entire 5x5-WEC staggered array; $P_{av,tot}$ = 10.831 W, $P_{av,bearings}$ = 5.218 W and $P_{av,PTO}$ = 5.613 W, showing the similar contribution of both $P_{av,bearings}$ and $P_{av,PTO}$ to $P_{av,tot}$, as found for the individual isolated WEC #05 under irregular long-crested waves.

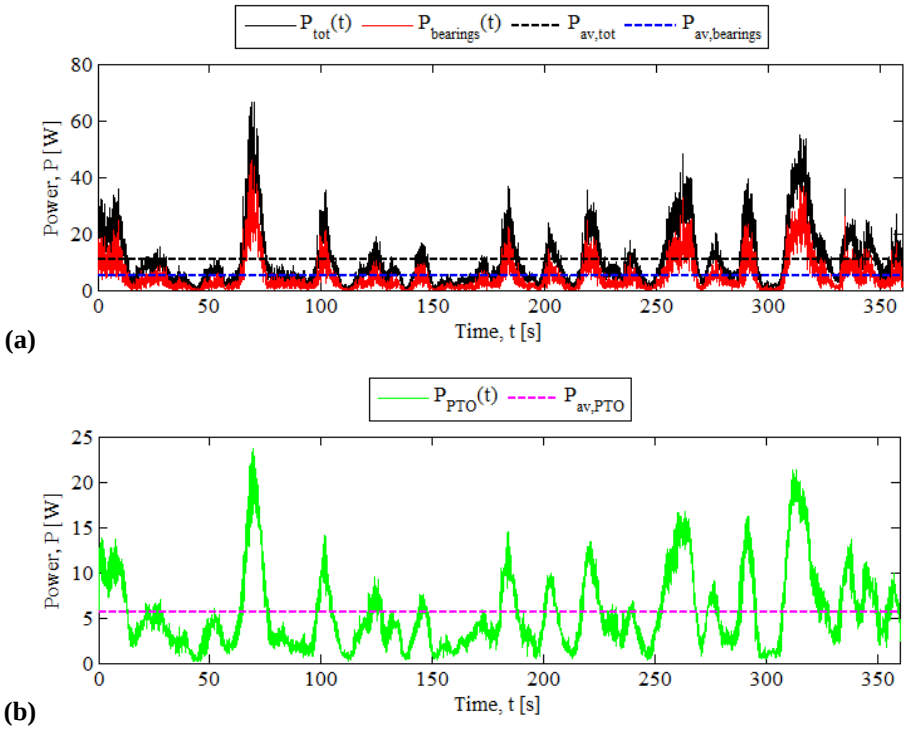

Figure 4.36. Absolute values of the instantaneous: (a) total power absorption, $P_{tot}(t)$, and power absorption of the WEC shaft bearings, $P_{bearings}(t)$; and (b) power absorption of the PTO-system, $P_{PTO}(t)$. The dashed horizontal lines represent time-averaged values. Results are presented for the entire 5x5-WEC staggered array under irregular long-crested waves (H_{m0} = 0.104 m, T_p = 1.260 s).

Moreover, the interaction $\bar{q}$-factor for the 5x5-WEC staggered array is obtained using Eq. (4.1), $P_{av,tot}$ obtained for the entire array (10.831 W) and $P_{av,tot}$ for the individual isolated WEC #05 (0.374 W) for the same wave conditions. The resulting WEC array interaction $\bar{q}$-factor is 1.160. As $\bar{q}$-factor > 1.0, intra-array interactions have a constructive effect on the overall power absorption of the WEC array. Therefore, the staggered array results lead to a more effective WEC array geometric configuration (by 13.10 %, relative to $\bar{q}$-factor = 1.0), compared to the 5x5-WEC rectilinear array. WEC #05 absorbs 16.31 % less power compared to the same individual WEC #05, when it operates within 5x5-WEC staggered array.

Similarly to the rectilinear array, also the $\bar{q}$-factors of each of the five 5-WEC rows and the five 5-WEC columns of the array have been separately calculated (Table 4.8), using Eq. (4.1). All column $\bar{q}$-factors are greater than unity (ranging from +7.5 % to about +26.0 %, compared to $\bar{q}$-factor = 1.0) and globally indicate more positive conditions regarding the power output (per column), for all columns. As a result, intra-array interactions per WEC array column are positive (or less

destructive) and, the same conclusions can be made for the number of columns as for the rectilinear array under long-crested irregular waves. Moreover, the column $\bar{q}$-factors are closer to the WEC array $\bar{q}$-factor.

On the other hand, the resulting $\bar{q}$-factors per row, show significant variations (ranging from about -15.0 % to +46.0 % , compared to $\bar{q}$-factor = 1.0). Similarly to the rectilinear array, pronounced negative intra-array interactions are observed for the last row. Attenuation of absorbed power is observed along the longitudinal direction of the arrays, while the last row does not operate effectively. This conclusion could be an indication for the need to limit the number of rows within the array. Moreover, the row $\bar{q}$-factors are not representative of the WEC array $\bar{q}$-factor, in contrast to the column $\bar{q}$-factors. In addition, by shifting WEC rows 2 and 4 to the right, a significant optimization of the row $\bar{q}$-factors has been achieved for all rows, and in particular for the first four rows. However, for the last (5^{th}) row no significant optimization has been achieved, indicating that there is a limit of WEC row efficiency within the array, thus a limit of number of rows for which an array is efficient, regarding power output.

Compared to the $\bar{q}$-factors obtained by the 5x5-WEC rectilinear array for the same wave conditions, all calculated $\bar{q}$-factors for the staggered array indicate more constructive effect of the intra-array interactions on the WECs' power output.

Table 4.8. WEC array interaction factor, $\bar{q}$-factor, calculated both for the entire array and each WEC array column / row (5x5-WEC staggered array; irregular long-crested waves: H_{m0} = 0.104 m and T_p = 1.26 s).

	WECs #21-#25	WECs #11-#15	WECs #01-#05	WECs #06-#10	WECs #16-#20	$P_{av,tot}$ of row [W]	$\bar{q}$-factor row [-]
$P_{av,tot}$ of each WEC [W]	column 1	column 2	column 3	column 4	column 5		
row 1	0.416	0.332	0.361	0.408	0.449	1.966	1.052
row 2	0.562	0.532	0.654	0.475	0.506	2.730	1.461
row 3	0.531	0.480	0.539	0.450	0.464	2.464	1.319
row 4	0.505	0.371	0.408	0.448	0.350	2.082	1.114
row 5	0.338	0.293	0.313	0.292	0.353	1.589	0.850
$P_{av,tot}$ of column [W]	2.352	2.008	2.275	2.073	2.122	$P_{av,tot}$ of array [W] 10.831	
$\bar{q}$-factor column [-]	1.259	1.075	1.218	1.110	1.136	$P_{av,tot}$ of individual WEC #05 [W] 0.374	
						$\bar{q}$-factor array [-] 1.160	

4.6.3.2.2. Irregular short-crested waves

In Figure 4.37, plot (a) shows the absolute instantaneous normalized values of total power absorption, $P_{tot}(t)$, and the power absorption of the WEC shaft bearings, $P_{bearings}(t)$. Plot (b) shows the power absorption of the PTO-system, $P_{PTO}(t)$. The dashed horizontal lines represent time-averaged values. $P_{tot}(t)$, $P_{PTO}(t)$ and $P_{bearings}(t)$ are normalized to the maximum value of the instantaneous total power absorption, $P_{tot,MAX}$.

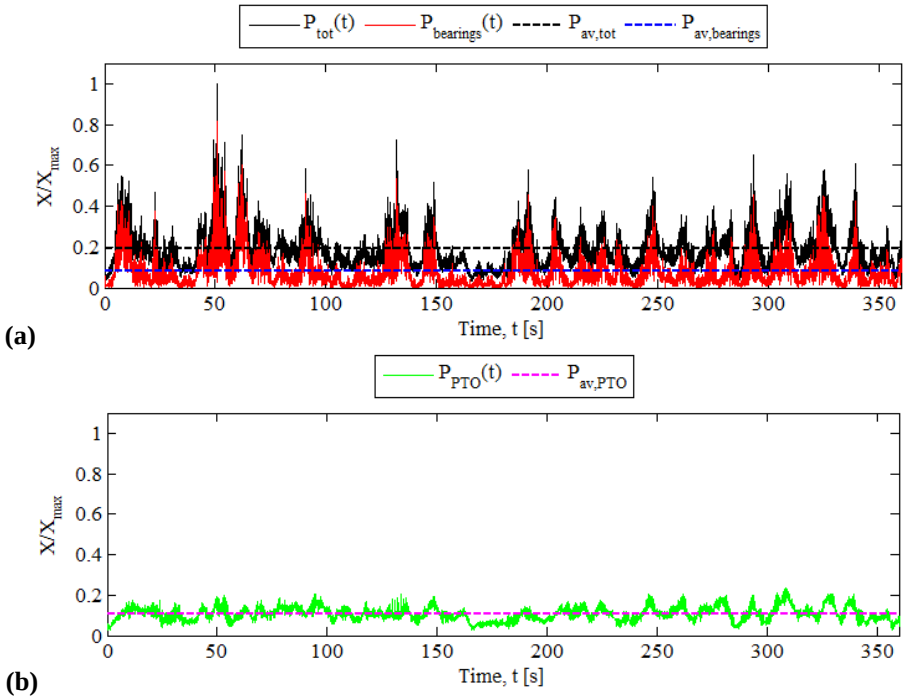

Figure 4.37. Absolute normalized values of the instantaneous: (a) total power absorption, $P_{tot}(t)$, and power absorption of the WEC shaft bearings, $P_{bearings}(t)$; and (b) power absorption of the PTO-system, $P_{PTO}(t)$. The dashed horizontal lines represent time-averaged values. Results are presented for the entire 5x5-WEC staggered array under irregular short-crested waves (H_{m0} = 0.104 m, T_p = 1.260 s, s = 10).

Figure 4.38 shows the time-averaged absolute values of instantaneous total power absorption, $P_{av,tot}$, —in W— for each WEC unit of the 5x5-WEC staggered array. The highest values of $P_{av,tot}$ are obtained on the 2nd row, followed by the 3rd and the front row of WECs, which differs from the rectilinear array due to change of the array geometric configuration. However, all WECs of the array absorb less wave energy compared to the individual WEC #05 (0.547 W) under the same wave

conditions. For short-crested irregular waves, all WEC units experience destructive intra-array interactions which have a significant negative influence on the overall power absorption of the WEC array. WECs #04 and #02, suffer the most and the least, respectively, from the hydrodynamic intra-array interactions that take place within the WEC array.

Moreover, similarly to the long-crested irregular waves, attenuation of absorbed power is observed in the longitudinal direction of the wave basin towards the wave absorbing beach, as less power is absorbed by the WECs of the last two rows. As for long-crested irregular waves, WEC #02 has the largest power output, being at a central location of the WEC array.

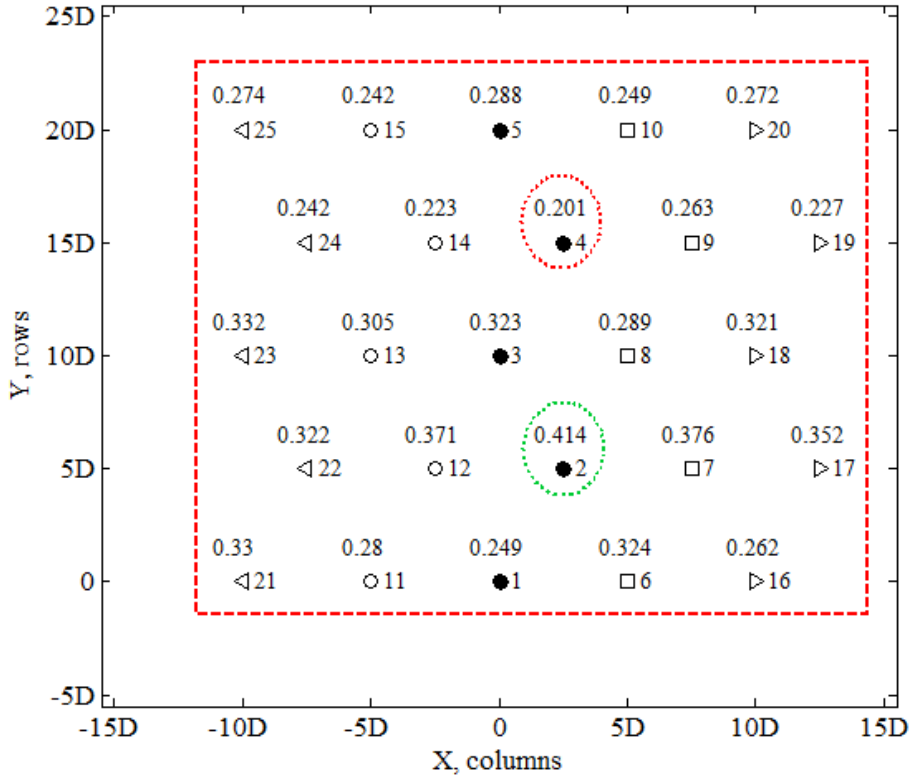

Figure 4.38. Absolute time-averaged instantaneous total power absorption, $P_{av,tot}$, (in W) for each of the 25 WEC units of the 5x5-WEC rectilinear array. Irregular short-crested waves (H_{m0} = 0.104 m, T_p = 1.260 s, s = 10). The basin width (X, columns) and length (Y, rows) are expressed in number of WEC unit diameters, D = 0.315 m. WECs indicated within: the box of dashed line, have smaller power output than that of the individual isolated WEC #05 (0.547 W); the circles of dotted line, are the two WECs with the lowest and the highest power output within the entire array.

Furthermore, the difference percentages in the measured power output of each WEC unit, $P_{i,tot}$, normalised by $P_{0,tot}$, calculated using Eq. (4.2), are presented in Figure 4.39, by a contour plot of the difference percentages (with the discrete percentage values). In Figure 4.39, the dark shaded areas indicate the areas within the array where the largest negative intra-array interactions take place. Figure 4.39 shows that there is very small variation regarding power output by each WEC unit, similarly to the rectilinear array under the same wave conditions. This variation is clearly present in the case of long-crested irregular waves.

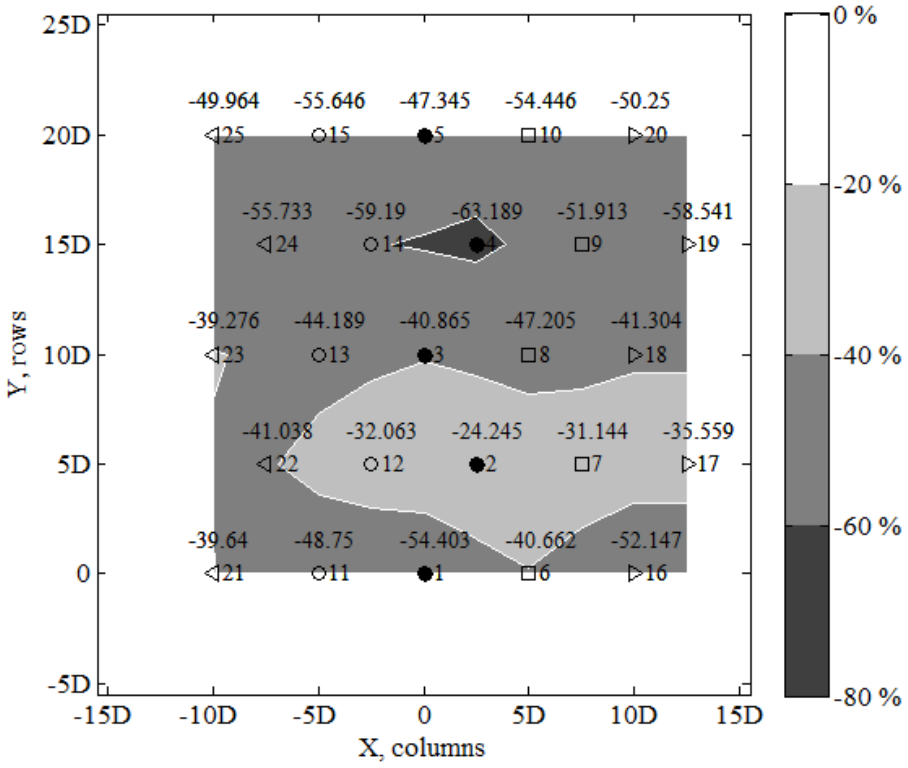

Figure 4.39. Difference percentages in non-dimensional time-averaged total power output ($P_{i,tot}/P_{0,tot}$) between tests with an array and with an individual WEC, for target conditions of irregular short-crested waves (H_{m0} = 0.104 m, T_p = 1.26 s, s = 10). Discreet values are shown at the WEC locations within the WEC array. Shading in contour plot denotes non-dimensional difference percentage: 0 to -20 % (white), -20 to -40 % (light gray), -40 to -60 % (gray), -60 to -80 % (dark gray). The basin width (X, columns) and length (Y, rows) are expressed in number of WEC unit diameters, D = 0.315 m.

In Figure 4.40, plot (a) shows the absolute instantaneous values of the total power absorption, $P_{tot}(t)$, and the power absorption of the WEC shaft bearings, $P_{bearings}(t)$, while plot (b) shows the power absorption of the PTO-system, $P_{PTO}(t)$. The time-averaged values (indicated by the dashed horizontal lines) have been estimated for the entire 5x5-WEC staggered array; $P_{av,tot}$, = 7.332 W, $P_{av,bearings}$ = 3.226 W and $P_{av,PTO}$= 4.106 W. In this case, a clear difference in the contribution of $P_{av,bearings}$ and $P_{av,PTO}$ to $P_{av,tot}$ is found, with $P_{av,PTO}$ being almost 28.0 % higher than $P_{av,bearings}$.

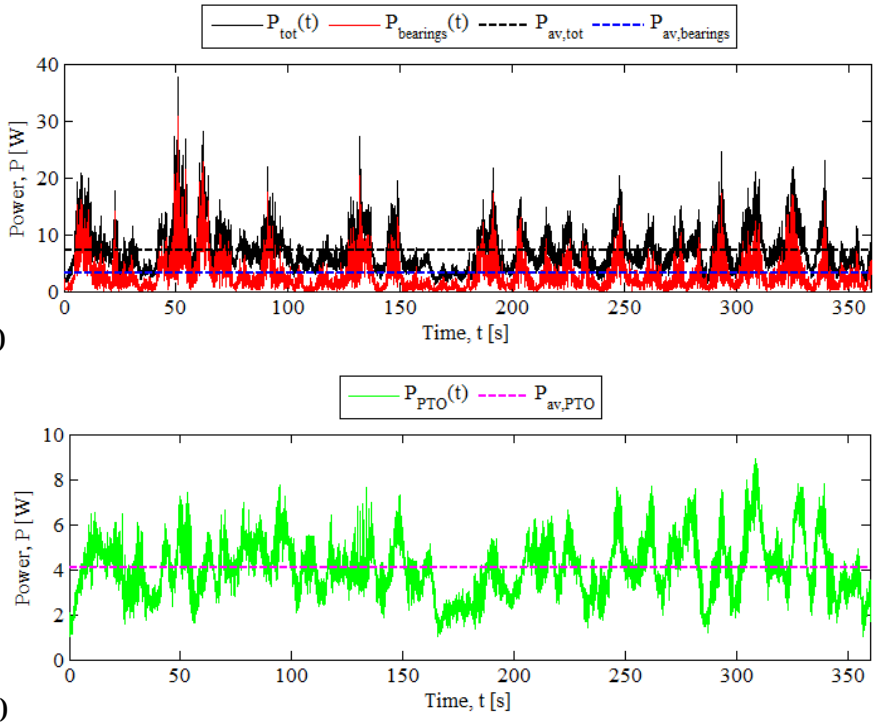

Figure 4.40. Absolute values of the instantaneous: (a) total power absorption, $P_{tot}(t)$, and power absorption of the WEC shaft bearings, $P_{bearings}(t)$; and (b) power absorption of the PTO-system, $P_{PTO}(t)$. The dashed horizontal lines represent time-averaged values. Results are presented for the entire 5x5-WEC staggered array under irregular short-crested waves (H_{m0} = 0.104 m, T_p = 1.260 s, s = 10).

Moreover, the interaction $\bar{q}$-factor for the 5x5-WEC staggered array is obtained using Eq. (4.1), the $P_{av,tot}$ of the entire array (7.332 W) (from Figure 4.40(a)) and $P_{av,tot}$ for the individual WEC #05 (0.547 W) for the same wave conditions. The resulting WEC array interaction $\bar{q}$-factor is 0.537. As $\bar{q}$-factor < 1.0, intra-array interactions have a significant destructive effect on the overall power absorption of

the WEC (more than 50.0 % of the WEC array effectiveness has been removed due to intra-array interactions, compared to the long-crested irregular waves). Most importantly, even though the change in geometric configuration (from rectilinear to staggered array) is significantly beneficial for the long-crested irregular waves (around 13.1 %), for directional wind waves the opposite is observed. For short-crested irregular waves, the change from rectilinear to staggered geometric configuration results in a reduction of the WEC array $\bar{q}$-factor by 10.4 %. WEC #05 absorbs 47.40 % less power compared to the same individual isolated WEC #05, when it operates within 5x5-WEC staggered array.

Also the $\bar{q}$-factors of each of the five 5-WEC rows and the five 5-WEC columns of the array have been separately calculated (Table 4.9), using Eq. (4.1).

Table 4.9. WEC array interaction factor, $\bar{q}$-factor, calculated both for the entire array and each WEC array column / row (5x5-WEC staggered array; irregular short-crested waves: H_{m0} = 0.104 m, T_p = 1.26 s, s = 10).

	WECs #21-#25	WECs #11-#15	WECs #01-#05	WECs #06-#10	WECs #16-#20	$P_{av,tot}$ of row [W]	$\bar{q}$-factor row [-]
$P_{av,tot}$ of each WEC [W]	column 1	column 2	column 3	column 4	column 5		
row 1	0.330	0.280	0.249	0.324	0.262	1.445	0.529
row 2	0.322	0.371	0.414	0.376	0.352	1.836	0.672
row 3	0.332	0.305	0.323	0.289	0.321	1.570	0.574
row 4	0.242	0.223	0.201	0.263	0.227	1.156	0.423
row 5	0.274	0.242	0.288	0.249	0.272	1.325	0.485
$P_{av,tot}$ of column [W]	1.500	1.422	1.476	1.501	1.433	$P_{av,tot}$ of array [W] 7.332	
$\bar{q}$-factor column [-]	0.549	0.520	0.540	0.549	0.524	$P_{av,tot}$ of individual WEC #05 [W] 0.547	
						$\bar{q}$-factor array [-] 0.537	

The WEC array column $\bar{q}$-factors are ranging from -48.0 % to -45.1 %, compared to $\bar{q}$-factor = 1.0, while the resulting $\bar{q}$-factors per row, show very similar

variation (ranging between -57.7 % and -32.8 %, compared to $\bar{q}$-factor = 1.0). For short-crested irregular wind waves, the effect of the number of rows is less pronounced as for long-crested waves. In this case clear attenuation of absorbed wave power is observed towards the longitudinal direction of the WEC array (as for long-crested waves, but not for the same wave conditions for the rectilinear array). Differences are found between the $\bar{q}$-factors calculated for columns and for rows, yet not particularly significant.

4.6.3.3. Power absorption of the 3x3-WEC rectilinear 5D array

For the 3x3-WEC rectilinear 5D array configuration, no results for short-crested waves are presented since the objective is to compare power output results with the 3x3-WEC rectilinear 10D array, which has twice as large WEC spacing. Moreover, results are compared to those from the 5x5-WEC rectilinear array with the same spacing, to show the effect of larger number of columns and rows. Therefore, only long-crested waves are presented, since this sea state results in clearer power output differences (as seen for the 5x5-WEC arrays) throughout the array.

4.6.3.3.1. Irregular long-crested waves

Figure 4.41 shows the time-averaged absolute values of the instantaneous total power absorption, $P_{av,tot}$, —in W— for each WEC unit of the 3x3-WEC rectilinear 5D array. The highest values of $P_{av,tot}$ are obtained at 67.0 % of the middle row of WECs, and are higher than the $P_{av,tot}$ obtained by the individual isolated WEC #05 (0.374 W) under the same wave conditions. For long-crested irregular waves, there are 2 WEC units within the array (22.2 % of the total number of WECs), for which the intra-array interactions have a constructive effect on their power output. For all WECs of the front and the last row, as well as for 1 WEC of the middle row, destructive intra-array interactions take place. WECs #01 (at the front row) and #02 (at the middle row), benefit the least and the most from the intra-array interactions that occur within the WEC array, respectively. WEC #02 still has the highest power output, as for the 5x5-WEC rectilinear array. Similarly to the rectilinear array, attenuation of absorbed power is observed in the longitudinal direction of the wave basin towards the wave absorbing beach and thus parallel to the wave propagation direction. The 3x3-WEC rectilinear 5D array has not enough WEC units (especially columns) to allow the occurrence of significantly positive intra-array interactions.

The time-averaged, $P_{av,tot}$, estimated for the entire 3x3-WEC rectilinear 5D array, is 2.697 W (smaller by a factor of around 3.6 compared to the 5x5-WEC rectilinear array, which is, though, composed of 16 extra WEC units).

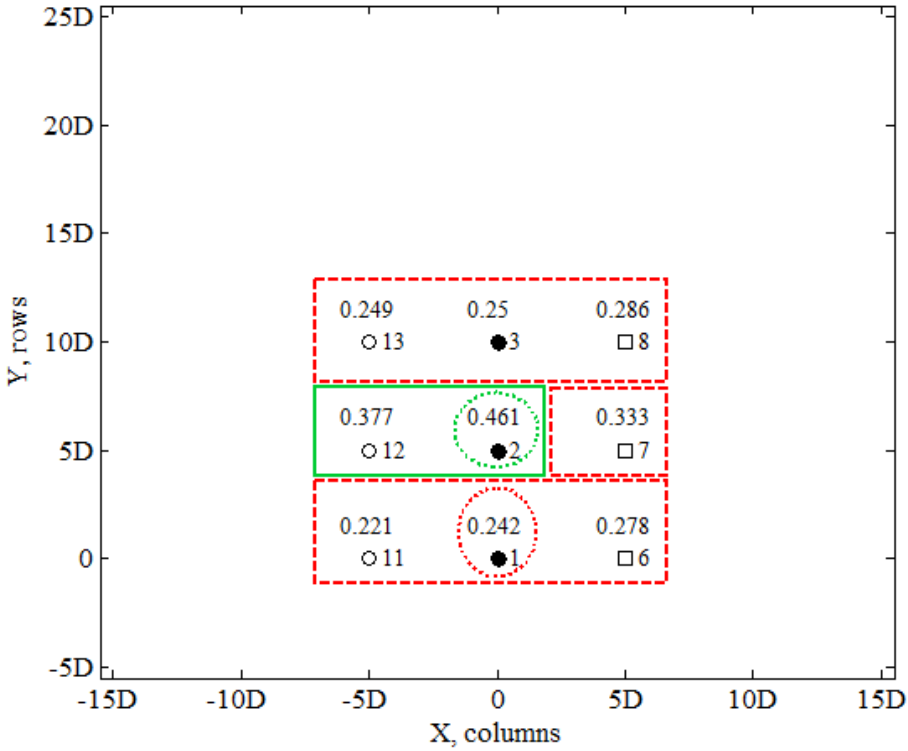

Figure 4.41. Absolute time-averaged instantaneous total power absorption, $P_{av,tot}$, (in W) for each of the 9 WEC units of the 3x3-WEC rectilinear 5D array. Irregular long-crested waves (H_{m0} = 0.104 m, T_p = 1.260 s). The basin width (X, columns) and length (Y, rows) are expressed in number of WEC unit diameters, D = 0.315 m. WECs indicated within: the boxes of continuous line, have greater power output than that of the individual WEC #05 (0.374 W); the boxes of dashed line, have smaller power output than that of the individual WEC #05; the circles of dotted line, are the two WECs with the lowest and the highest power output within the entire array.

Moreover, the interaction $\bar{q}$-factor for the 3x3-WEC rectilinear 5D array has been obtained by using Eq. (4.1), $P_{av,tot}$ obtained for the entire array (2.697 W) and $P_{av,tot}$ for the individual WEC #05 (0.374 W) for the same wave conditions. The resulting WEC array interaction $\bar{q}$-factor is 0.802. As $\bar{q}$-factor < 1.0, intra-array interactions have a destructive effect on the overall power absorption of the WEC array. However, even though the array has only 9 WECs, the WEC array $\bar{q}$-factor is larger than that found for short-crested waves for the large 5x5-WEC arrays.

Similarly to the 5x5-WEC arrays, also the $\bar{q}$-factors of each of the three 3-WEC rows and the three 3-WEC columns of the array have been separately calculated (Table 4.10), using Eq. (4.1). All column $\bar{q}$-factors are smaller than unity (ranging from -24.4 % to -15.0 %, compared to $\bar{q}$-factor = 1.0) and globally indicate negative conditions regarding the power output (per column), for all columns. As a result, intra-array interactions per WEC array column are negative. Moreover, the column $\bar{q}$-factors are closer to the WEC array $\bar{q}$-factor. The 5x5-WEC rectilinear array under long-crested irregular waves, results in column $\bar{q}$-factors larger or close to unity, though. This is a result of the larger number of columns, which appear to contribute positively in the development of constructive intra-array interactions.

Table 4.10. WEC array interaction factor, $\bar{q}$-factor, calculated both for the entire array and each WEC array column / row (3x3-WEC rectilinear 5D array; irregular long-crested waves: H_{m0} = 0.104 m and T_p = 1.26 s).

	WECs -	WECs #11-#13	WECs #01-#03	WECs #06-#08	WECs -	$P_{av,tot}$ of row [W]	$\bar{q}$-factor row [-]
$P_{av,tot}$ of each WEC [W]	column 1	column 2	column 3	column 4	column 5		
row 1	-	0.221	0.242	0.278	-	0.741	0.661
row 2	-	0.377	0.461	0.333	-	1.171	1.045
row 3	-	0.249	0.250	0.286	-	0.785	0.700
row 4	-	-	-	-	-	-	-
row 5	-	-	-	-	-	-	-
$P_{av,tot}$ of column [W]	-	0.847	0.953	0.897	-	$P_{av,tot}$ of array [W] 2.697	
$\bar{q}$-factor column [-]	-	0.756	0.850	0.800	-	$P_{av,tot}$ of individual WEC #05 [W] 0.374	
						$\bar{q}$-factor array [-] 0.802	

On the other hand, the resulting $\bar{q}$-factors per row, show significant variations (ranging between -33.9 % and +0.45 %, compared to $\bar{q}$-factor = 1.0). Similarly to the 5x5-WEC arrays, pronounced negative intra-array interactions are observed for

the last row. Attenuation of absorbed power is observed and therefore the last row does not operate effectively. Moreover, similarly to the 5x5-WEC arrays, the front row also suffers from negative intra-array interactions. Finally, the row $\bar{q}$-factors are not representative of the WEC array $\bar{q}$-factor, in contrast to the column $\bar{q}$-factors.

4.6.3.4. Power absorption of the 3x3-WEC rectilinear 10D array

For the 3x3-WEC rectilinear 10D array configuration, no results for short-crested waves are presented since the objective is to compare power output results with the 3x3-WEC rectilinear 5D array, which half WEC spacing. Therefore, only long-crested waves are presented, since this sea state results in clearer power output differences (as seen for the 5x5-WEC arrays) throughout the array.

4.6.3.4.1. Irregular long-crested waves

Figure 4.42 shows the time-averaged absolute values of the instantaneous total power absorption, $P_{av,tot}$, —in W— for each WEC unit of the 3x3-WEC rectilinear 10D array. The highest values of $P_{av,tot}$ are obtained at the middle row of WECs, and for all WECs the obtained $P_{av,tot}$ values are higher than the $P_{av,tot}$ of the individual WEC #05 (0.374 W) under the same wave conditions. For long-crested irregular waves, intra-array interactions have a constructive effect on the power output of all 9 WEC units. WECs #01 (at the front row) and #03 (at the middle row), benefit the least and the most from the intra-array interactions that occur within the WEC array, respectively. WEC #03 (with the highest power output) is now situated in the centre of the array, such as the centrally located WEC #02 for all previous WEC array configurations, indicating that the middle WEC(s) benefit the most from intra-array interactions. Similarly to the rectilinear arrays, attenuation of absorbed power is observed in the longitudinal direction of the wave basin towards the wave absorbing beach and thus parallel to the wave propagation direction. The spacing between the WEC units of the 3x3-WEC rectilinear 10D array is large enough to allow the occurrence of significantly positive intra-array interactions.

The time-averaged, $P_{av,tot}$, estimated for the entire 3x3-WEC rectilinear 10D array, is 5.662 W (larger by a factor of around 2.1 compared to the 3x3-WEC rectilinear 5D array and smaller by a factor of around 1.7 compared the 5x5-WEC rectilinear array, which is, though, composed of 16 extra WEC units).

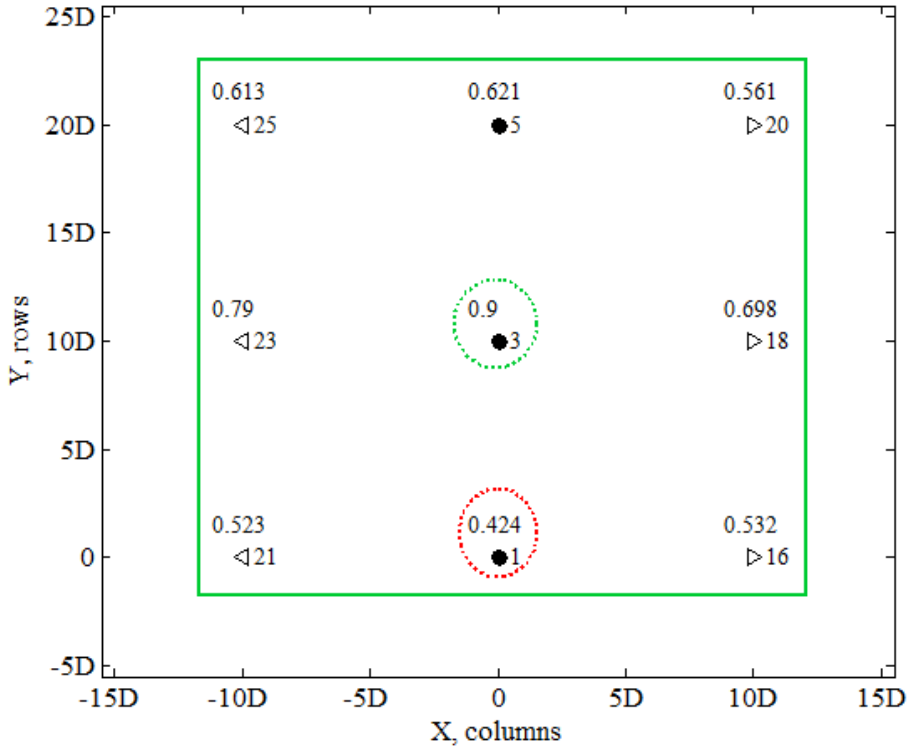

Figure 4.42. Absolute time-averaged instantaneous total power absorption, $P_{av,tot}$, (in W) for each of the 9 WEC units of the 3x3-WEC rectilinear 10D array. Irregular long-crested waves (H_{m0} = 0.104 m, T_p = 1.260 s). The basin width (X, columns) and length (Y, rows) are expressed in number of WEC unit diameters, D = 0.315 m. WECs indicated within: the boxes of continuous line, have greater power output than that of the individual WEC #05 (0.374 W); the circles of dotted line, are the two WECs with the lowest and the highest power output within the entire array.

Moreover, the interaction $\bar{q}$-factor for the 3x3-WEC rectilinear 10D array has been obtained using Eq. (4.1), $P_{av,tot}$ obtained for the entire array (5.662 W) and $P_{av,tot}$ for the individual isolated WEC #05 (0.374 W) for the same wave conditions. The resulting interaction $\bar{q}$-factor is 1.684, much larger compared to that found for all previous array configurations of 5D spacing between the WECs. As $\bar{q}$-factor > 1.0, intra-array interactions have a constructive effect on the overall power absorption of the WEC array. Despite the relatively small number of WECs within the array (only 9 WECs), the WEC array $\bar{q}$-factor is larger than that found for the large 5x5-WEC arrays, under the same wave conditions. This indicates that the spacing is large enough between the WECs, avoiding not only negative intra-array interactions, but also achieving significant constructive intra-array interactions

between the WECs of the array. Most importantly, none of the WECs (and especially the reference WEC #05) has power output equal to that obtained by the individual isolated WEC #05, indicating that intra-array interactions still occur for an array with $10D$ spacing between the devices. In particular, WEC #05 within the array extracts around 1.7 times more power from the waves, compared to the situation when WEC #05 operates as individual device (in isolation). The same WEC #05 absorbs 15.51 % and 16.31 % less power compared to the individual WEC #05, when it operates within the rectilinear and the staggered 5x5-WEC array, respectively.

Consequently, the 3x3-WEC rectilinear $10D$ array results in a significantly more effective (by 88.2 %) WEC array geometric configuration, compared to the 3x3-WEC rectilinear $5D$ array.

Similarly to the 5x5-WEC arrays, also the $\bar{q}$-factors of each of the three 3-WEC rows and the three 3-WEC columns of the array have been separately calculated (Table 4.11), using Eq. (4.1).

Table 4.11. WEC array interaction factor, $\bar{q}$-factor, calculated both for the entire array and each WEC array column / row (3x3-WEC rectilinear $10D$ array; irregular long-crested waves: H_{m0} = 0.104 m and T_p = 1.26 s).

	WECs #21;23;25	WECs -	WECs #01;03;05	WECs -	WECs #16;18;20	$P_{av,tot}$ of row [W]	$\bar{q}$-factor row [-]
$P_{av,tot}$ of each WEC [W]	column 1	column 2	column 3	column 4	column 5		
row 1	0.523	-	0.424	-	0.532	1.479	1.320
row 2	-	-	-	-	-	-	-
row 3	0.790	-	0.900	-	0.698	2.388	2.131
row 4	-	-	-	-	-	-	-
row 5	0.613	-	0.621	-	0.561	1.795	1.601
$P_{av,tot}$ of column [W]	1.926	-	1.945	-	1.791	$P_{av,tot}$ of array [W] 5.662	
$\bar{q}$-factor column [-]	1.718	-	1.735	-	1.598	$P_{av,tot}$ of individual WEC #05 [W] 0.374	
						$\bar{q}$-factor array [-] 1.684	

All column $\bar{q}$-factors are greater than unity (ranging from +59.8 % to +73.5 %, compared to $\bar{q}$-factor = 1.0) and globally show positive conditions regarding the power output (per column), for all columns. As a result, the effect of intra-array interactions per WEC array column is positive. The column $\bar{q}$-factors are closer to the $\bar{q}$-factor of the entire array. Also the 5x5-WEC rectilinear (and the staggered) array under long-crested irregular waves, results in column $\bar{q}$-factors larger or close to unity. This is a result of the larger number of columns which appear to contribute positively in the constructive intra-array interactions.

The resulting $\bar{q}$-factors per row, show significant variations (ranging from +32.0 % to +113.10 %, compared to $\bar{q}$-factor = 1.0). Similarly to the 5x5-WEC arrays, less constructive intra-array interactions are observed for the front and the last row, and attenuation of absorbed power is observed. The row $\bar{q}$-factors are not representative of the WEC array $\bar{q}$-factor, in contrast to the column $\bar{q}$-factors. In addition, by making the WEC spacing twice as large, a significant optimization of all $\bar{q}$-factors has been achieved (especially for the rows).

4.6.4. Main observations on the power absorption by the WEC (arrays)

Firstly, the absolute instantaneous total power absorption, $P_{tot}(t)$, has been calculated for WEC #05, situated at the central column and the last row of WECs. WEC #05 has been selected, based on a comparative analysis between the five WECs of the central column, for which also surge force measurements are available. All tests presented here, have been performed using a spring compression increment dx = 30.5 mm at the PTO-system, which corresponds to optimal power absorption of an individual WEC unit under regular waves of H = 0.074 m and T = 1.260 s. Moreover for the calculation of all power values a coefficient of friction, μ = 0.17, has been used for the PTO-system and the WEC-shaft bearings.

The power output of the individual WEC #05 (in isolation), the 5x5-WEC rectilinear array, the 5x5-WEC staggered array, the 3x3-WEC rectilinear 5D array and the 3x3-WEC rectilinear 10D array, has been estimated for irregular (H_{m0} = 0.104 m, T_p = 1.260 s) long- and short crested (s = 10) waves. The latter two wave farm configurations are shown only for long-crested irregular waves, while WEC #05 is presented also for regular waves with H = 0.074 m and T_p = 1.260 s.

The absolute values of the instantaneous and time-averaged, total power absorption, P_{tot}, the power absorption of the PTO-system, P_{PTO}, and the power absorption of the WEC shaft bearings, $P_{bearings}(t)$, have been obtained. All results of the two components of P_{tot}, for all sea states and WEC (array) configurations, indicate that both the force applied through the PTO-system and the WEC shaft bearings have a similar contribution to P_{tot}, with P_{PTO}, always being larger.

For the WEC arrays, also the interaction $\bar{q}$-factor, has been estimated, as the ratio of the total time-averaged power from the entire WEC array to that of the same number of WEC #05 in isolation. For all WEC array configurations, none of the WEC units absorb equal power to the individual isolated WEC #05, and therefore intra-array interactions are present for all shown WEC array results. In order to provide an idea of the effectiveness of the number of rows and columns within an array, also the $\bar{q}$-factors of each of the WEC rows and columns have been separately calculated.

o **Power absorption of an individual WEC unit:**

A time domain numerical model based on a state-space formulation of the hydrodynamic damping force and accounting for non-linear mechanical constraints has been shown to provide a reasonable prediction of response and power output from an individual float. These predictions depend on the magnitude of friction coefficient for the PTO-system and the WEC shaft bearings and to-date have been conducted with an idealisation of the WEC buoy geometry, as presented in [21]

The absolute average values for the surge force and the WEC buoy velocity have been calculated: $F_{av,surge}$ = 16.075 N and $\dot{z}_{av}$ = 0.134 m/s (regular waves), $F_{av,surge}$ = 14.491 N and $\dot{z}_{av}$ = 0.067 m/s (irregular long-crested waves), and $F_{av,surge}$ = 15.607 N and $\dot{z}_{av}$ = 0.095 m/s (irregular short-crested waves).

Also the time-averaged value of the instantaneous total power absorption, $P_{av,tot}$, of the individual WEC #05 has been estimated: 0.727 W (regular waves), 0.374 W (irregular long-crested waves) and 0.547 W (irregular short-crested waves). $P_{av,tot}$ for regular waves is larger, as expected, since the WEC's PTO-system has been tuned, to absorb optimally power from waves, for these wave conditions. Moreover, $P_{av,tot}$ for irregular short-crested waves is larger than that obtained for irregular long-crested waves, due to larger wave induced surge force and WEC buoy velocity for this sea state (42.0 % larger velocity which has effect on both components of $P_{av,tot}$).

o **Power absorption of the 5x5-WEC rectilinear array:**

Irregular long-crested waves:

- The highest values of $P_{av,tot}$ are obtained for the 2nd and 3rd row of WECs and are higher than the $P_{av,tot}$ obtained by the individual isolated WEC #05.
- There are 12 WEC units within the array (almost 50.0 % of the total number of WECs), for which the intra-array interactions have a constructive effect on their power output.

- For all WECs of the 2nd and 3rd row (and a couple from the front and 4th row) constructive intra-array interactions take place.
- For all the WECs of the 5th row and 80.0 % of the WECs from the 4th and the front row, destructive intra-array interactions occur.
- WECs #01 and #02, benefit the least and the most from those intra-array interactions, respectively. The largest power output is found at a central location in the array (WEC #02).
- Attenuation of absorbed power is observed in the longitudinal direction of the wave basin, as well as less absorption by the WECs at the front row, comparable to that of the last rows.
- The resulting interaction $\bar{q}$-factor is 1.029. As $\bar{q}$-factor > 1.0, intra-array interactions have a limited constructive effect on the overall power absorption of the entire WEC array. In this case, intra-array interactions are definitely present, since none of the WECs absorbs power equal to that absorbed by an individual isolated WEC, but constructive interactions appear to compensate for the destructive interactions that take place within the array.
- WEC #05 absorbs 15.51 % less power when it operates within the 5x5-WEC rectilinear array, compared to the same individual WEC #05.
- The column $\bar{q}$-factors range between -6.0 % and +16.0 %, compared to $\bar{q}$-factor = 1.0, and globally indicate more positive conditions regarding the power output (per column), for all columns. There is no indication that specific columns are significantly less effective, and thus, also no indication for need for limiting the number of columns within the array. Moreover, the column $\bar{q}$-factors are closer to the WEC array $\bar{q}$-factor.
- The row $\bar{q}$-factors vary significantly, between -16.0 % and +31.0 % compared to $\bar{q}$-factor = 1.0. Pronounced negative intra-array interactions are shown for the last two rows.
- Attenuation of absorbed power is observed parallel to the wave propagation direction, and therefore the last two rows do not operate effectively. This conclusion gives an indication for the need to limit the number of rows within the array.
- The row $\bar{q}$-factors are not representative of the WEC array $\bar{q}$-factor, in contrast to the column $\bar{q}$-factors.

Irregular short-crested waves:

- The highest values of $P_{av,tot}$ are obtained for the 2nd row, followed by the 3rd and the front row of WECs. All WECs of the array absorb less wave energy compared to the individual isolated WEC #05.
- For all WECs units, destructive intra-array interactions occur.
- WECs #01 and #02 / #17, suffer the most and the least from negative hydrodynamic intra-array interactions that take place within the WEC array, respectively. As for long-crested irregular waves, the largest power output is found (almost) at a central location in the array (WEC #02).
- No large variation of the power output by each of the WECs is found, clearly observed for long-crested irregular waves.
- The resulting interaction $\bar{q}$-factor is 0.599. As $\bar{q}$-factor < 1.0, intra-array interactions have a destructive effect on the overall power absorption of the entire WEC array.
- WEC #05 absorbs 36.20 % less power when it operates within the 5x5-WEC rectilinear array, compared to the same individual WEC #05.
- The column and row $\bar{q}$-factors range between -45.9 % and -35.9 % and between -50.3 % and -27.6 %, respectively, compared to $\bar{q}$-factor = 1.0, showing very similar variation.
- For short-crested waves, the effect of the number of rows is not as pronounced as for long-crested waves.
- Attenuation of absorbed wave power is observed towards the longitudinal direction of the WEC array, yet, not as clear as for long-crested waves.

o **Power absorption of the 5x5-WEC staggered array:**

The results obtained for the 5x5-WEC staggered array are directly compared to those obtained for the 5x5-WEC rectilinear array. The objective is to investigate the effect of changing the WEC array configuration by shifting rows, on the intra-array interactions and thus on the power absorption.

Irregular long-crested waves:

- The highest values of $P_{av,tot}$ are obtained on the 2nd and 3rd row of WECs, as well as for 60 % of the WECs from the front and the 4th row, and are higher than the $P_{av,tot}$ obtained for the individual isolated WEC #05.
- There are 16 WEC units within the array (64.0 % of the total number of WECs), for which the intra-array interactions have a constructive effect on their power output.
- For 40 % of the WECs of front and 4th row, as well as for all WECs of the last row, destructive intra-array interactions take place.
- WECs #10 (at the rear row) and #02 (at the 2nd row), benefit the least and the most from the intra-array interactions that occur within the WEC array, respectively.
- WEC #02 still has the highest power output, as for the 5x5-WEC rectilinear array, installed at a central location within the WEC array.
- Attenuation of absorbed power is observed in the longitudinal direction of the wave basin, similarly to the rectilinear array.
- For the staggered array, by shifting two WEC rows to the right, positive effect on the power output of four extra WEC units has been achieved, compared to the rectilinear array. Wider spreading of the constructive intra-array interactions has been achieved, and consequently destructive interactions have been limited. A more effective WEC array configuration has been identified.
- The resulting interaction $\bar{q}$-factor is 1.160. As $\bar{q}$-factor > 1.0, intra-array interactions have a constructive effect on the overall power absorption of the entire WEC array.
- The staggered array results in a WEC array geometric configuration, 13.10 % more effective, compared to the 5x5-WEC rectilinear array.
- WEC #05 absorbs 16.31 % less power when it operates within the 5x5-WEC staggered array, compared to the same individual isolated WEC #05.
- The column $\bar{q}$-factors range from +7.5 % to +26.0 %, compared to $\bar{q}$-factor = 1.0, and globally indicate more positive conditions regarding the power output (per column), for all columns. There is no indication that specific columns are significantly less effective, and thus also no indication for need to limit the number of columns within the array. Moreover, the column $\bar{q}$-factors are closer to the WEC array $\bar{q}$-factor.

- The row $\bar{q}$-factors vary significantly, from -15.0 % to +46.0 % compared to $\bar{q}$-factor = 1.0. Pronounced negative intra-array interactions are shown for the last row.
- Attenuation of absorbed power is observed parallel to the wave propagation direction, and therefore the last row does not operate effectively. This conclusion gives an indication for the need to limit the number of rows within the array.
- The row $\bar{q}$-factors are not representative of the WEC array $\bar{q}$-factor, in contrast to the column $\bar{q}$-factors.
- By shifting WEC rows 2 and 4 to the right, a significant optimization of the row $\bar{q}$-factors has been achieved for all rows, and in particular for the first four ones. However, for the last (5^{th}) row no significant optimization has been achieved, indicating that there is a limit of WEC row efficiency within the array, thus a limit of number of rows for which the array is efficient regarding power absorption.
- Compared to the $\bar{q}$-factors obtained by the 5x5-WEC rectilinear array for the same wave conditions, all calculated $\bar{q}$-factors for the staggered array indicate more constructive effect of the intra-array interactions on the WECs' power output.

Irregular short-crested waves:

- The highest values of $P_{av,tot}$ are obtained for the 2^{nd} row, followed by the 3^{rd} and the front row of WECs, which differs from the rectilinear array due to change of the array geometric configuration. All WECs of the array absorb less wave energy compared to the individual isolated WEC #05.
- For all WECs units, destructive intra-array interactions occur.
- WECs #04 and #02, suffer the most and the least from negative hydrodynamic intra-array interactions that take place within the WEC array, respectively. As for long-crested irregular waves and for the rectilinear array, the largest power output is found at a central location in the array (WEC #02).
- Attenuation of absorbed wave power is observed towards the longitudinal direction of the WEC array (yet, not as clear as for long-crested waves).
- A clear difference in the contribution of $P_{av,bearings}$ and $P_{av,PTO}$ to $P_{av,tot}$ (unlike the rest of the cases) is found, with $P_{av,PTO}$ being almost 28.0 % higher than $P_{av,bearings}$. Since the WEC buoy velocity is used for calculation of both

components of $P_{av,tot}$, this larger difference between $P_{av,PTO}$ and $P_{av,bearings}$, can be due to lower wave induced surge force on the WEC buoys. This lower F_{surge}, can be result of the combination of wind waves with a closely-spaced staggered configuration. As a result, incoming waves come from various directions and thus horizontal forces on the buoys that eliminate each other, as well as less waves travel in-between the WECs due to the staggered lay-out.

- The resulting interaction $\bar{q}$-factor is 0.537. As $\bar{q}$-factor < 1.0, intra-array interactions have a destructive effect on the overall power absorption of the entire WEC array (more than 50.0 % of the WEC array effectiveness has been removed due to intra-array interactions, compared to the array under irregular long-crested waves).
- Even though the change in geometric configuration (from rectilinear to staggered array) is significantly beneficial for the long-crested irregular waves (around 13.1 %), for directional waves the opposite is observed with a reduction of the WEC array $\bar{q}$-factor by 10.4 % (for wind waves).
- WEC #05 absorbs 47.40 % less power when it operates within the 5x5-WEC rectilinear array, compared to the same individual isolated WEC #05.
- The column and row $\bar{q}$-factors range from -48.0 % to -45.1 %, and from -57.7 % to -32.8 %, respectively, compared to $\bar{q}$-factor = 1.0, showing very similar variation.
- For short-crested waves, the effect of the number of rows is not as clear as for long-crested waves, yet visible.
- Clear attenuation of absorbed wave power is observed towards the longitudinal direction of the WEC array (as for long-crested waves, but not for the same wave conditions for the rectilinear array).

o **Power absorption of the 3x3-WEC rectilinear 5*D* array:**

Results obtained for this WEC array configuration, are compared to power output results by the 3x3-WEC rectilinear 10*D* array, with twice as large WEC spacing. It is also compared to the large 5x5-WEC rectilinear array, to show the effect of e.g. larger number of columns and rows. Therefore, only long-crested waves are presented, since this sea state results in clearer power output differences (as seen for the 5x5-WEC arrays).

Irregular long-crested waves:

- The highest values of $P_{av,tot}$ are obtained on 67.0 % of the middle row of WECs, and are higher than the $P_{av,tot}$ obtained for the individual isolated WEC #05.
- Only for 22.2 % of the total number of WECs within the array, the intra-array interactions have a constructive effect on their power output.
- For all WECs of the front and the last row, as well as for 1 WEC of the middle row, destructive intra-array interactions take place.
- WECs #01 (at the front row) and #02 (at the middle row), benefit the least and the most from the intra-array interactions that occur within the WEC array, respectively. The largest power output is found at a central location in the array (WEC #02), as for all previous WEC array configurations.
- Attenuation of absorbed power is observed in the longitudinal direction of the wave basin, similarly to the 5x5-WEC rectilinear (and staggered) array.
- The 3x3-WEC rectilinear $5D$ array has not enough WEC units (especially columns) to allow the occurrence of significantly positive intra-array interactions, compared to the 5x5-WEC rectilinear array.
- $P_{av,tot}$ of the entire 3x3-WEC rectilinear $5D$ array, is smaller by a factor of 3.6 compared to the 5x5-WEC rectilinear array, which is, though, composed of 16 extra WEC units.
- The resulting interaction $\bar{q}$-factor is 0.802. As $\bar{q}$-factor < 1.0, intra-array interactions have a destructive effect on the overall power absorption of the entire WEC array. However, even though the array has only 9 WECs the WEC array $\bar{q}$-factor is larger than that found for short-crested waves for both large 5x5-WEC arrays.
- The column $\bar{q}$-factors range between -24.4 % and -15.0 %, compared to $\bar{q}$-factor = 1.0, and globally indicate negative conditions regarding the power output (per column), for all columns.
- The fact that the 5x5-WEC rectilinear array results in column $\bar{q}$-factors larger or close to unity, indicates that a larger number of columns can compensate for the less absorbed power achieved by arrays of less columns. As such, increasing the columns of an array, appears to contribute positively in the constructive intra-array interactions. Increasing the number of rows, is not expected to contribute, though, according to the obtained results from the large 5x5-WEC arrays.
- The column $\bar{q}$-factors are closer to the WEC array $\bar{q}$-factor.

- The row $\bar{q}$-factors vary significantly, between -33.9 % and +0.45 % compared to $\bar{q}$-factor = 1.0. Pronounced negative intra-array interactions are shown for the last row.
- Attenuation of absorbed power is observed in the direction parallel to the wave propagation and therefore the last row does not operate effectively.
- Similarly to the 5x5-WEC arrays, the front row also suffers from negative intra-array interactions.
- The row $\bar{q}$-factors are not representative of the WEC array $\bar{q}$-factor, in contrast to the column $\bar{q}$-factors.

o **Power absorption of the 3x3-WEC rectilinear 10D array:**

Results obtained for this WEC array configuration, are compared to power output results by the 3x3-WEC rectilinear 5D array, with smaller WEC spacing. Therefore, only long-crested waves are presented, since this sea state results in clearer power output differences (as seen for the 5x5-WEC arrays).

Irregular long-crested waves:

- The highest values of $P_{av,tot}$ are obtained on the middle row of WECs, and for all WECs the obtained $P_{av,tot}$ values are higher than the $P_{av,tot}$ of the individual isolated WEC #05.
- WECs #01 (at the front row) and #03 (at the center of the array), benefit the least and the most from the intra-array interactions that occur within the WEC array, respectively. The largest power output is found at a central location in the array (WEC #03), as for all previous WEC array configurations (WEC #02), indicating that the middle WEC(s) benefit the most from intra-array interactions.
- Attenuation of absorbed power is observed in the longitudinal direction of the wave basin, similarly to both previous rectilinear arrays.
- The spacing between the WEC units of the 3x3-WEC rectilinear 10D array is large enough to allow the occurrence of significantly positive intra-array interactions.
- $P_{av,tot}$ of the entire 3x3-WEC rectilinear 10D array, is larger by a factor of 2.1 compared to the 3x3-WEC rectilinear 5D array and smaller by a factor of 1.7

compared the 5x5-WEC rectilinear array, which is, though, composed of 16 extra WEC units.

- The resulting interaction $\bar{q}$-factor is 1.684, much larger compared to that found for all previous array configurations of 5D spacing between the WECs. As $\bar{q}$-factor > 1.0, intra-array interactions have a constructive effect on the overall power absorption of the entire WEC array.
- Even though the array has only 9 WECs, the WEC array $\bar{q}$-factor is larger than that found for the large 5x5-WEC arrays, for the same wave conditions. This indicates that the spacing is large enough between the WECs, avoiding not only negative intra-array interactions, but also achieving significant constructive intra-array interactions between the WECs of the array.
- None of the WECs (and especially the reference WEC #05) has power output equal to that by the individual isolated WEC #05, indicating that intra-array interactions still occur for an array with 10D spacing between the devices.
- WEC #05 within the array extracts 1.7 times more power from the waves, compared to the situation when WEC #05 operates as individual device (in isolation). The same WEC #05 absorbs 15.51 % and 16.31 % less power compared to the individual WEC #05, when it operates within the rectilinear and the staggered 5x5-WEC array, respectively.
- The 3x3-WEC rectilinear 10D array results in a significantly more (by 88.2 %) effective WEC array geometric configuration, compared to the 3x3-WEC rectilinear 5D array.
- The column $\bar{q}$-factors range between +59.8 % and +73.5 % %, compared to $\bar{q}$-factor = 1.0, and globally indicate very positive conditions regarding the power output (per column), for all columns.
- The fact that the 5x5-WEC rectilinear array results in column $\bar{q}$-factors larger or close to unity, indicates that a larger number of columns can compensate the less absorbed power achieved by smaller spacing between the WECs. Increasing the columns of an array can offer an alternative solution, when limited area is available for the installation of a WEC array.
- Moreover, the column $\bar{q}$-factors are closer to the WEC array $\bar{q}$-factor.
- The row $\bar{q}$-factors vary significantly, from +32.0 % to +113.10 % compared to $\bar{q}$-factor = 1.0.
- Similarly to the 5x5-WEC arrays, less constructive intra-array interactions are observed for the front and the last row, and attenuation of absorbed power is observed.

- The row $\bar{q}$-factors are not representative of the WEC array $\bar{q}$-factor, in contrast to the column $\bar{q}$-factors.
- By making the WEC spacing twice as large, a significant optimization of all $\bar{q}$-factors has been achieved (especially for the rows).

An overview of the absolute values of the time-averaged instantaneous total power absorption, $P_{av,tot}$, and of the resulting interaction $\bar{q}$-factors for the presented WEC array geometric configurations, is presented in Table 4.12.

Table 4.12. Overview of the time-averaged instantaneous total power absorption $P_{av,tot}$ and interaction $\bar{q}$-factors for different WEC array geometric configurations and for irregular sea states (LCW: abbreviation for long-crested irregular waves; SCW: abbreviation for short-crested irregular waves). Values from Tables 4.6 - 4.11.

	Individual WEC unit		**5x5-WEC rectilinear array**		**5x5-WEC staggered array**		**3x3-WEC rectilinear 5*D* array**		**3x3-WEC rectilinear 10*D* array**	
	$P_{av,tot}$ [W]	$\bar{q}$-factor [-]	$P_{av,tot}$ [W]	$\bar{q}$-factor [-]	$P_{av,tot}$ [W]	$\bar{q}$-factor [-]	$P_{av,tot}$ [W]	$\bar{q}$-factor [-]	$P_{av,tot}$ [W]	$\bar{q}$-factor [-]
LCW	0.374	N/A	9.612	1.029	10.831	1.160	2.697	0.802	5.662	1.684
SCW s = 10	0.547	N/A	8.180	0.599	7.332	0.537	-		-	

4.6.5. Recorded incident wave conditions

To determine the incident undisturbed (i.e. no WECs present) wave field conditions, each sea state has been recorded for three wave basin arrangements:

1. at the wave gauge locations of *WG plan 1* (Figure 4.9) used during the WEC (array) tests for both *WEC shafts stencils 1* and *2* (WEC units are held stationary above the water surface; WEC shafts are present);

2. at the wave gauge locations of *WG plan 1* (Figure 4.9) used during the WEC (array) tests in an empty wave basin (i.e. no WEC support structures are present);

3. at the wave gauge locations of *WG plan* 2 (Figure 4.10) in an empty wave basin (i.e. no WEC support structures are present).

In this section, wave field results for long- and short crested (with spreading parameter, s = 10) irregular waves are presented. Moreover, for all data reported here, the wave generator has been operated in absorption mode, with activated AWACS. The data have been analysed using Wavelab [37]. In all 2-D plan views of the wave basin presented here, the basin width (X, columns) and length (Y, rows) are expressed in number of WEC unit diameters, D = 0.315 m, with the start of the axes set at the centre on WEC unit #01.

For regular waves with target wave height, H_{0r} = 0.074 m, and wave period T = 1.26 s, there is only 3.0 % deviation of the measured wave height, $\overline{H_m}/H_{0r}$, between repetition of the same regular wave conditions (Figure 4.43). The subscripts "*m*" and "*0r*" denote "*measured value*" and "*target value*" of regular wave, respectively.

In Figure 4.43, a contour plot is presented of the standard deviation, s_n, of the non-dimensional mean of the recorded wave height, $\overline{H_m}/H_{0r}$ over eight different measurements of the mean wave height, $\overline{H_m}$.

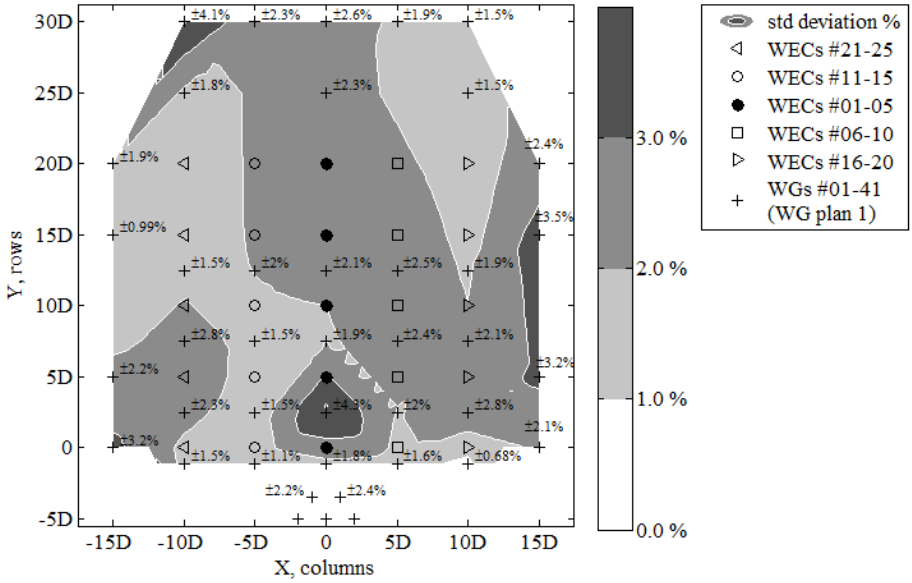

Figure 4.43. Standard deviation, s_n, of the non-dimensional mean of the wave height, $[\overline{H_m}/\ H_{0r}]$, over eight measurements of the mean wave height, $\overline{H_m}$, of regular waves with target wave height H_{0r} = 0.074 m and wave period T = 1.26 s. Measurements are taken at the wave gauge locations within and around the WEC array (*WG plan 1*). Shading in contour plot denotes s_n less than 1.0 % (white), 1.0-2.0% (light gray), 2.0-3.0% (gray), >3.0% (dark gray). The basin width (X, columns) and length (Y, rows) are expressed in number of WEC unit diameters, D = 0.315 m. Results from [21].

The wave gauge locations, where s_n exceeds 3.0 % (yet, s_n remains less than 4.3 %) are limited (at five out of 41 WGs) and are observed at X= ±15D, at Y = 30D and at a location between WECs #01 and #02 (X = 0, Y = 2.5D).

For regular waves, the non-dimensional measured mean wave height at each wave gauge location over eight test repetitions, varies with position within the basin (Figure 4.44). In Figure 4.44, the discrete mean values of $[\overline{H_m} / H_{0r}]$ are shown throughout the wave basin. Moreover, a contour plot is presented of the absolute values of the mean differences calculated using Equation (4.3):

$$\frac{'target\ undisturbed\ wave\ field' - 'mean\ recorded\ undisturbed\ wave\ field\ over\ 8\ repetitions'}{'target\ undisturbed\ wave\ field'} x100\% = \left| \frac{H_{0r} - \overline{H_m}}{H_{0r}} \right| x\ 100\ \% \quad (4.3)$$

In Figure 4.44, in the largest part of the wave basin, the absolute differences remain smaller than 10 %. Differences greater than 15 % are limited and localized.

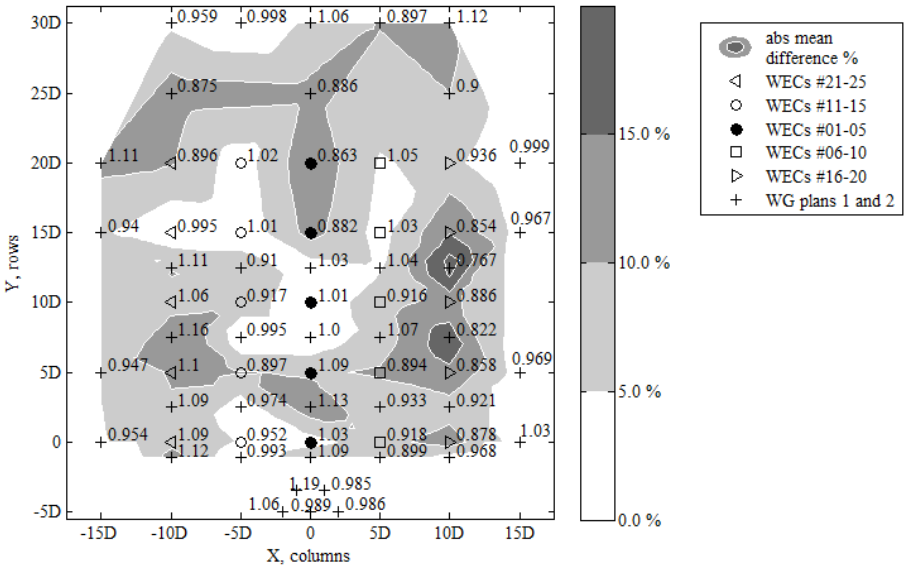

Figure 4.44. Variation of measured regular non-dimensional mean wave height $[\overline{H_m}/H_{0r}]$ over 8 test repetitions, across the test region for target wave height H_{0r} = 0.074 m and wave period T = 1.26 s. Discrete measurements are shown at the wave gauge locations within and around the WEC array (*WG plan 1*) and at the WEC centrelines (*WG plan 2*). Data at *WG plan 1* recorded with WEC support structures in position. Shading in contour plot denotes non-dimensional absolute difference percentage between H_{0r} and $\overline{H_m}$ less than 5% (white), 5-10% (light gray), 10-15% (gray), >15% (dark gray). The basin width (X, columns) and length (Y, rows) are expressed in number of WEC unit diameters, D = 0.315 m. Results from [21].

For irregular waves, the measured wave height based on the spectral density, H_{m0}, also varies with position within the basin, although the spatial variation is less than for regular waves, across the width of the wave basin. This spatial variation of the measured H_{m0} is presented in (Figure 4.45(a)) for irregular long-crested waves and Figure (4.45(b)) for irregular short-crested waves with s = 10. The subscripts "$m0$" and "$0i$" denote "*measured value*" and "*target value*" of irregular waves, respectively. In Figure 4.45(a-b), the discrete values of the non-dimensional measured wave height at each wave gauge location, (H_{m0} / H_{0i}), are shown throughout the wave basin. Moreover, contour plots are presented of the absolute values of the differences calculated using Equation (4.4):

$$\frac{'target\ undisturbed\ wave\ field' - 'recorded\ undisturbed\ wave\ field'}{'target\ undisturbed\ wave\ field'} x100\% = \left|\frac{H_{0i} - H_{m0}}{H_{0i}}\right| x\ 100\ \% \quad (4.4)$$

In Figure 4.45(a-b), the differences remain in the largest part of the wave basin within the range 0.0 – 10.0%, with limited wave gauge locations exceeding 15.0%.

The cause of this spatial variation of wave height is attributed to small differences of wave generation across the wave basin width, and to development of slightly varying reflection from the wave absorbing beach. The profile of the wave absorbing beach has been constructed manually, using gravel material. Change in the geometry of the beach profile has been observed, between the first and the last day of the experiments, after exposure to varying wave conditions with varying wave attack angles. Therefore, the beach profile does not have completely identical characteristics along the basin width, which can be responsible for different reflection characteristics and the above variation in the measured wave height, H_{m0}, along the wave basin width.

Moreover, repetitive data variation, e.g. the peak of absolute difference larger than 15.0 % found at a specific wave gauge location of *WG plan 2* between WECs #22 and #12, shown in Figure 4.45(a-b), may indicate a localized laboratory effect related to the operation of this specific wave gauge during the experiments shown in Figure 4.45(a-b).

As a conclusion, the accuracy of the generated waves for the irregular wave conditions presented here, is described by differences of 5.0 % and 10.0 % for long- and short-crested waves, respectively, in the largest part of the wave basin, and remains below 10.0 % and 15.0 % (besides at two WG locations), respectively, in the entire basin.

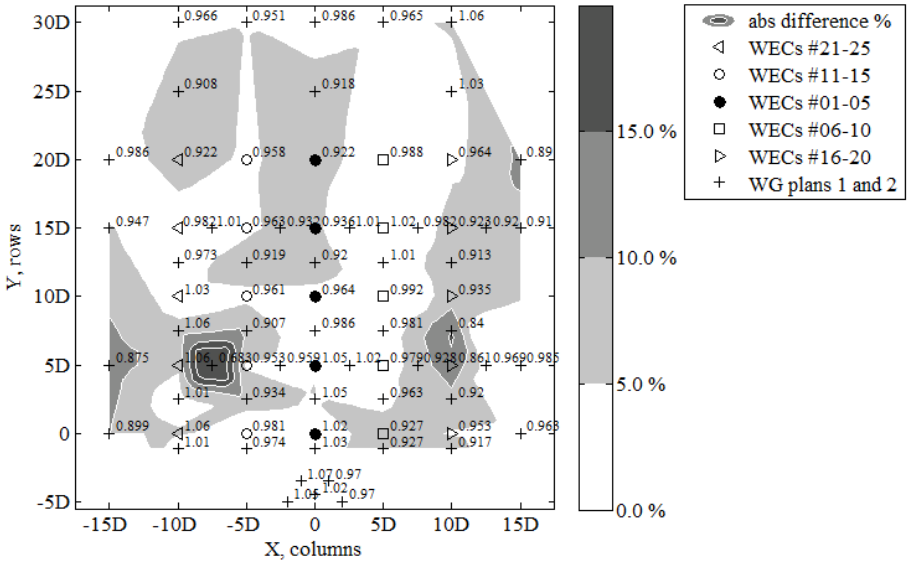

(a) long-crested irregular waves.

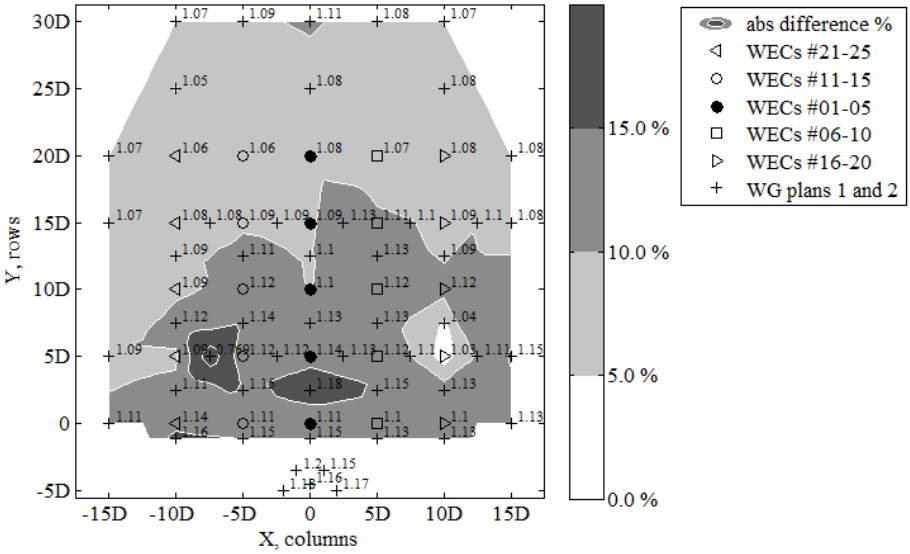

(b) short-crested irregular waves with spreading parameter, s = 10.

Figure 4.45. Variation of non-dimensional wave height (H_{m0} / H_{0i}) across the test region for target conditions of irregular waves defined by JONSWAP spectra with H_{m0} = 0.104 m and T_p = 1.26 s: (a) long-crested waves; (b) short-crested waves with s = 10. Discrete measurements are shown at the wave gauge locations within and around the WEC array (*WG plan 1* with WEC support structures in position) and at the WEC centrelines (*WG plan 2*). Shading in contour plot denotes non-dimensional absolute difference percentage between H_{0i} and H_{m0} (calculated using Equation (4.4)) less than 5 % (white), 5-10% (light gray), 10-15% (gray), >15% (dark gray).

4.6.6. Influence of the WEC support structures on the incident wave field

The measured wave heights, H_m and H_{m0}, for regular and irregular waves respectively, from the tests with and without the presence of the WEC support structures have been compared, in order to quantify the influence of the WEC shafts and metal bases on the incident wave field.

The difference percentages in the recorded wave height, H_{m0}, normalised to the target wave height, H_{0r} or H_{0i} respectively, between the tests with the presence of WEC support structures and tests in an empty wave basin, are given in Figures 4.46 and 4.47(a-b). Figure 4.46 presents results for regular waves with wave period, T = 1.26 s, and target wave height H_{0r} = 0.074 m. Figures 4.47(a) and 4.47(a) show results for irregular long-crested and short-crested (for s = 10) waves, respectively, with wave period, T_p = 1.26 s and target significant wave height H_{0i} = 0.104 m.

The discrete values of the difference percentages shown in Figures 4.46 and 4.47(a-b) are calculated by subtracting the non-dimensional wave heights measured in an empty wave basin, from the wave heights at the same wave gauge locations with the presence of the WEC support structures. The wave heights are made non-dimensional by dividing by the wave heights measured in an empty wave basin. A positive value thus indicates an increase in wave height, H_{m0}, while a negative value indicates wave height decrease, due to the presence of the WEC support structures. Moreover, shading contour plots of the absolute values of the calculated differences, are presented.

In Figure 4.46 for regular waves, a variation of up to 5.0 % is found for the largest part of the test region. The area where the variation is ranging between 5.0 % and 10.0 % is limited, while only two measurements exceed 10.0 % (+11.3 %).

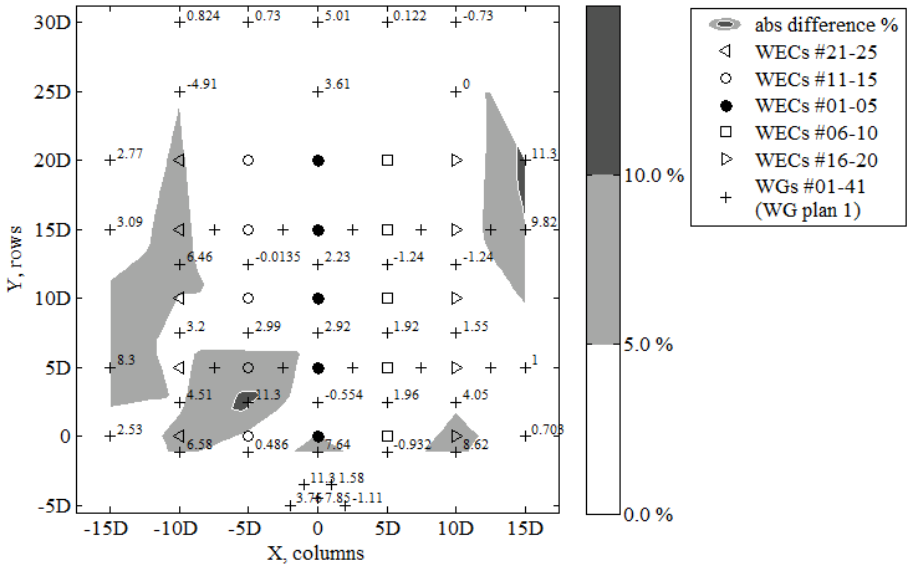

Figure 4.46. Difference percentages in non-dimensional wave height (H_m / H_{0r}) between tests without and with the presence of the WEC support structures across the test region of the basin, for target regular wave height H_{0r} = 0.074 m and wave period T = 1.26 s. Discreet values are shown at the wave gauge locations within and around the WEC array (*WG plan 1*). Shading in contour plot denotes non-dimensional absolute difference percentage less than 5 % (white), 5-10% (light gray), >10% (dark gray). The basin width (X, columns) and length (Y, rows) are expressed in number of WEC unit diameters, D = 0.315 m.

In both Figures 4.47(a) and 4.47(b) for irregular waves, the variations are found up to 5.0 % for the largest part of the test region. For long-crested waves (Figure 4.47(a)), the area where the variation is ranging between 5.0 % and 10.0 % is limited, with only 9 measurements out of 41, found for variation larger than 5.5 % and a maximum value of -8.96 %. For short-crested waves (Figure 4.47(b)), the area where the variation is ranging between 5.0 % and 10.0 % is even smaller, with just 2 measurements out of 41, found for variation larger than 5.5 % and a maximum value of 15.8 %.

However, the variations do not appear at the same locations and are randomly distributed across the test region: there is an increase at specific locations and a decrease at other nearby locations, without a noticeable trend. The variations shown in Figures 4.46 and 4.47(a-b) using two different tests (without and with WEC support structures) are similar to the spatial variations described in Section 4.6.5, and even smaller. Therefore, the effect of the presence of the WEC support structures on the wave height, H_{m0}, is confirmed to be small.

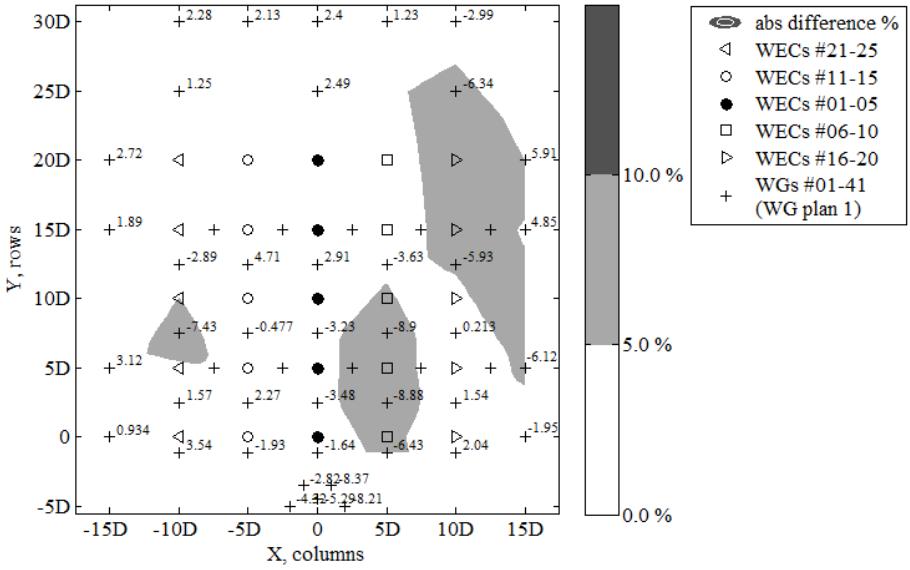

(a) long-crested irregular waves.

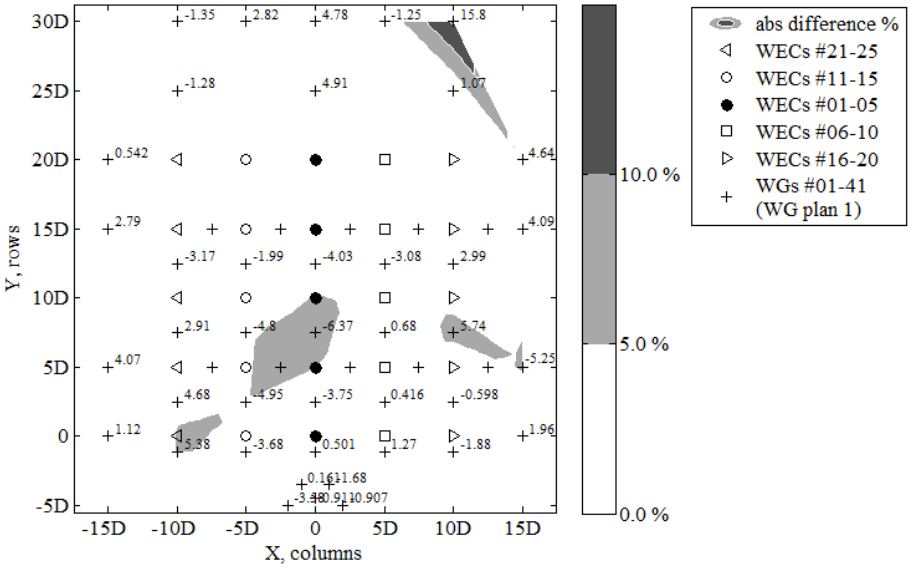

(b) short-crested irregular waves with spreading parameter, s = 10.

Figure 4.47. Difference percentages in non-dimensional wave height (H_{m0} / H_{0i}) between tests without and with the presence of the WEC support structures across the test region of the basin, for target conditions of irregular waves defined by JONSWAP spectra with target wave height H_{m0} = 0.104 m and T_p = 1.26 s: (a) long-crested waves; (b) short-crested waves with s = 10. Discreet values are shown at the wave gauge locations within and around the WEC array (*WG plan 1*). Shading in contour plot denotes non-dimensional absolute difference percentage less than 5 % (white), 5-10% (light gray), >10% (dark gray).

4.6.7. Presentation methodology of wave field modifications around the WEC arrays

One of the main research objectives is to study the effect of WEC arrays on the wave field. In the following sections, the wave field modifications due to wave energy extraction and the WECs' motion have been quantified, around various WEC arrays. Extra-array effects have been investigated by modifying the WEC array geometric configurations. All wave field results are presented in terms of the radiated, diffracted and perturbed wave fields, described in detail in Chapter 3.

First, a detailed description is presented in Sections 4.6.8 - 4.6.12 of the obtained results on wave field alteration induced by the WEC arrays. At the end of each section, a summary of the main observations is given. A detailed discussion and conclusions on the obtained results on wave field modifications by the arrays is provided in Chapter 5. In the latter chapter, also based on the existing literature, guidelines for design of WEC arrays have been derived.

Irregular long-crested and short-crested waves (s = 10, wind waves and s = 75, swell waves with long decay distance), defined by JONSWAP spectra with target wave height based on the spectral density H_{m0} = 0.104 m and T_p = 1.26 s are analysed, for investigating the effect of wave directionality on WEC array effects. The following contributing wave field components are separately presented: (i) the diffracted wave field due to stationary WEC units, and (ii) the radiated wave field due to oscillation of the WEC units under incident wave field. Moreover, irregular long-crested waves with T_p = 1.18 s are presented, representing the effect on the resulting wave fields, of incoming waves with peak period equal to the resonance period of an individual WEC unit, T_n (see Chapter 2).

To measure the combined incident and diffracted wave field, all 25 WEC units are held stationary at mean draft, d_{buoy} = 0.315 m. To measure the combined incident-diffracted-radiated wave field (or else the "perturbed" wave field) due to the response of the WECs, damping has been applied through the PTO-system and through the WEC shaft bearings. For all wave field results presented in this chapter, dx = 30.5 mm spring compression increment has been applied on each WEC unit. The diffracted wave field is then calculated as the difference between the wave field measured around stationary WEC units and the incident wave field. The radiated wave field is calculated as the difference between the measured perturbed wave field and the diffracted wave field. The radiated wave field includes radiated waves that are subsequently diffracted, and it also accounts for the absorption effects at the WEC units.

The following difference percentage terms are defined and plotted in all contour plots shown for the wave fields around the WEC arrays presented in this chapter:

(a) wave diffraction around stationary WEC units. For quantifying the diffraction effect, the recorded undisturbed wave field when no WECs or shafts are

present is used to exclude the wave basin effects that develop in the empty wave basin:

$$\frac{'\text{diffracted wave field}'-'\text{recorded undisturbed wave field}'}{'\text{recorded undisturbed wave field}'}\ x\ 100\ \% \qquad (4.5)$$

(b) a variant of Equation (4.5) showing the difference percentage used for quantifying the effect of the wave diffraction around stationary WEC units relative to the target undisturbed wave field. This variant shows the differences between the recorded and the target undisturbed wave field when no WECs or shafts are present:

$$\frac{'\text{diffracted wave field}'-'\text{recorded undisturbed wave field}'}{'\text{target undisturbed wave field}'}\ x\ 100\ \% \qquad (4.6)$$

(c) difference percentage used for quantifying the effect of radiation on the perturbed wave field due to damped response of the WEC units:

$$\frac{'\text{perturbed wave field}'-'\text{diffracted wave field}'}{'\text{recorded undisturbed wave field}'}\ x\ 100\ \% \qquad (4.7)$$

(d) difference percentage used for quantifying the effect of the heaving WECs under wave action (causing the perturbed wave field), on the recorded undisturbed wave field:

$$\frac{'\text{perturbed wave field}'-'\text{recorded undisturbed wave field}'}{'\text{recorded undisturbed wave field}'}\ x\ 100\ \% \qquad (4.8)$$

Note that in the figures where the terms of Equations 4.5 and 4.6 are plotted, the difference percentages are positive, when diffraction effects around the stationary WEC units increase the incident wave field heights compared to the undisturbed incident wave field when no WECs are present. Also in the figures where the term of Equation 4.7 is plotted, the difference percentages are positive, when radiation effects due to the WECs' response, increase the perturbed wave field heights compared to the combined incident and diffracted wave field. Moreover, in the figures where the term of Equation 4.8 is plotted, the difference percentages are positive, when the effect of the heaving WECs under wave action causes increase of the perturbed wave field heights, compared to the undisturbed incident wave field.

On the other hand, negative difference percentages indicate a decrease of the diffracted wave field component (figures where the terms of Equations 4.5 and 4.6 are plotted) compared to the undisturbed incident wave field. Also negative difference percentages show that radiation effects (figures where the term of Equation 4.7 is plotted) reduce the perturbed wave field heights, compared to the combined incident and diffracted wave field. In the figures where the term of

Equation 4.8 is plotted, negative difference percentages indicate wave height attenuation caused by the heaving WECs under wave action, compared to the undisturbed incident wave field. These negative differences in the latter figures, therefore, refer to wave height decrease due to wave power extraction by the WEC units.

4.6.8. Wave field modification around a 5x5-WEC rectilinear array

In this section, the wave field modifications due to wave energy extraction and the WECs' motion have been quantified, around a 5x5-WEC rectilinear array, illustrated in Figure 4.48. The measured change of the wave field for unidirectional irregular waves, is presented separately for the diffracted (Figures 4.49(a-b) and 4.52(a-b)), the radiated (Figures 4.49(c) and 4.52(c)) and the perturbed (Figures 4.49(d) and 4.52(d)) wave field, for T_p = 1.26 s and T_p = 1.18 s, respectively. Similarly, Figures 4.50(a-d) and 4.51(a-d) present the wave fields for the short-crested waves with spreading parameter, s = 10 and s = 75, respectively.

(a)

(b)

Figure 4.48. The 5x5-WEC rectilinear array in the DHI Shallow Water wave basin**,** (a) after construction and before filling of the wave basin with water. View from behind the wave absorbing beach. (b) under irregular long-crested waves with θ = 0°. View from behind the wave generator.

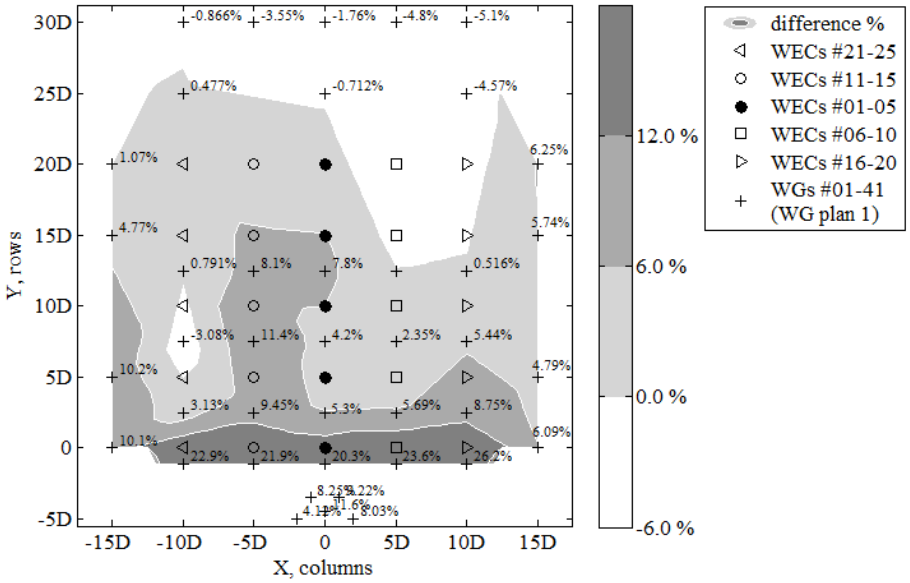

(a) Diffracted wave field normalized by recorded undisturbed wave field.

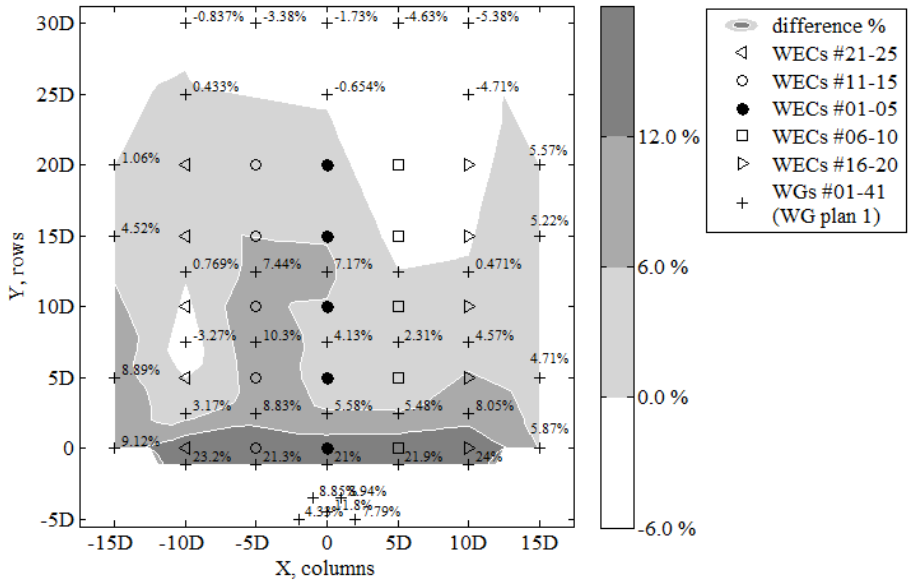

(b) Diffracted wave field normalized by target undisturbed wave field.

Figure 4.49. *Cont. Next Page*

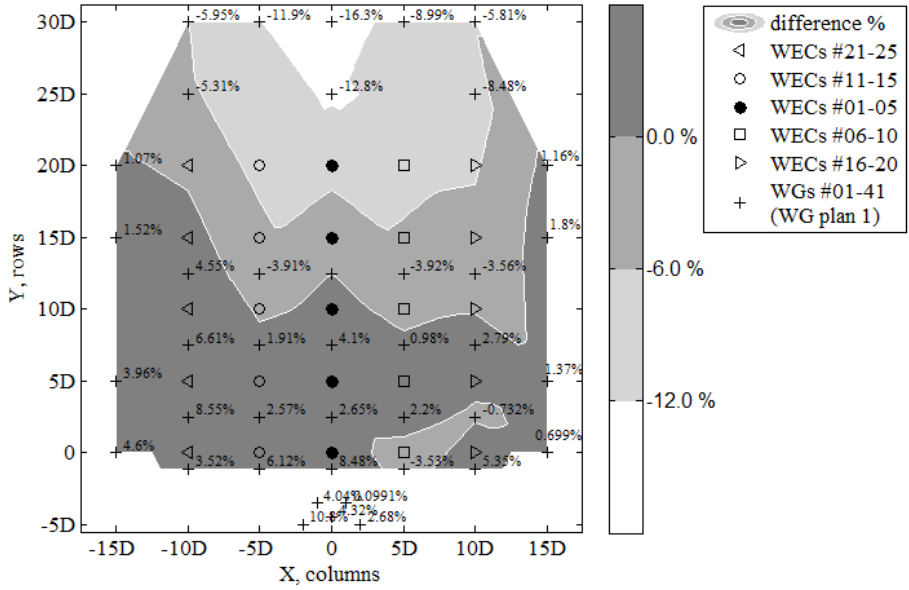

(c) Radiated wave field normalized by recorded undisturbed wave field.

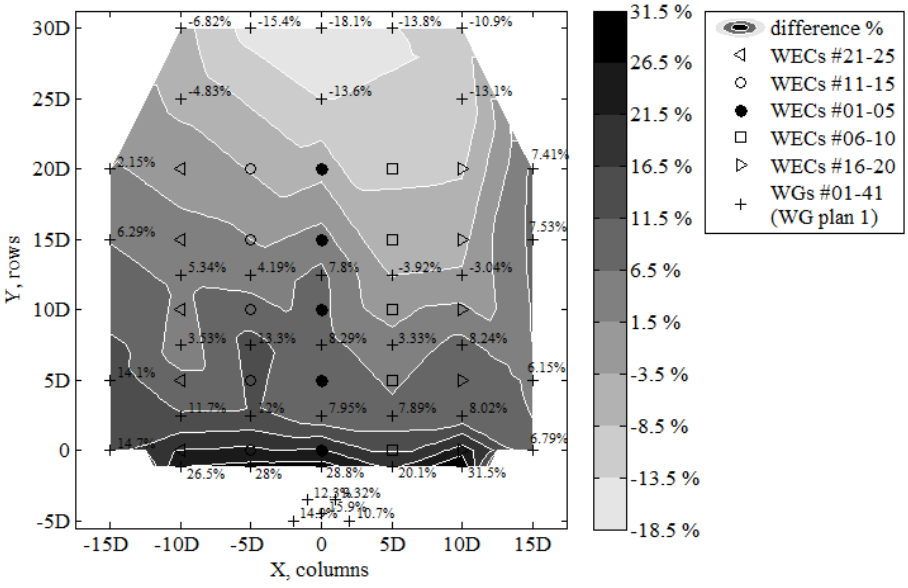

(d) Perturbed wave field normalized by recorded undisturbed wave field.

Figure 4.49. Non-dimensional percentage of change of H_{m0} at locations within and around the 5x5-WEC rectilinear array due to diffracted (stationary WECs), radiated (heaving WECs with damping applied) and perturbed wave field (heaving WECs with damping applied). Unidirectional irregular waves of T_p = 1.26 s and H_{m0} = 0.104 m. The basin width (X, columns) and length (Y, rows) are expressed in number of WEC unit diameters, D = 0.315 m.

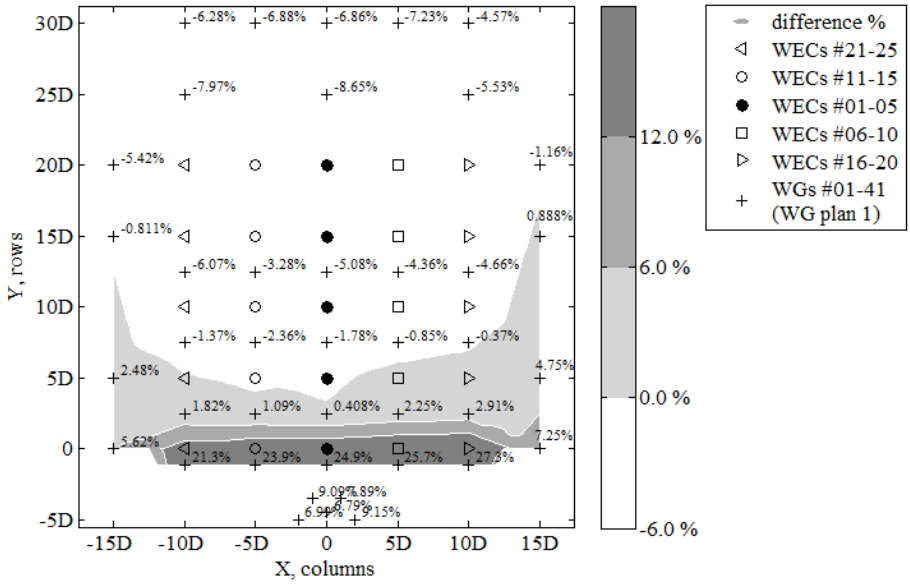

(a) Diffracted wave field normalized by recorded undisturbed wave field.

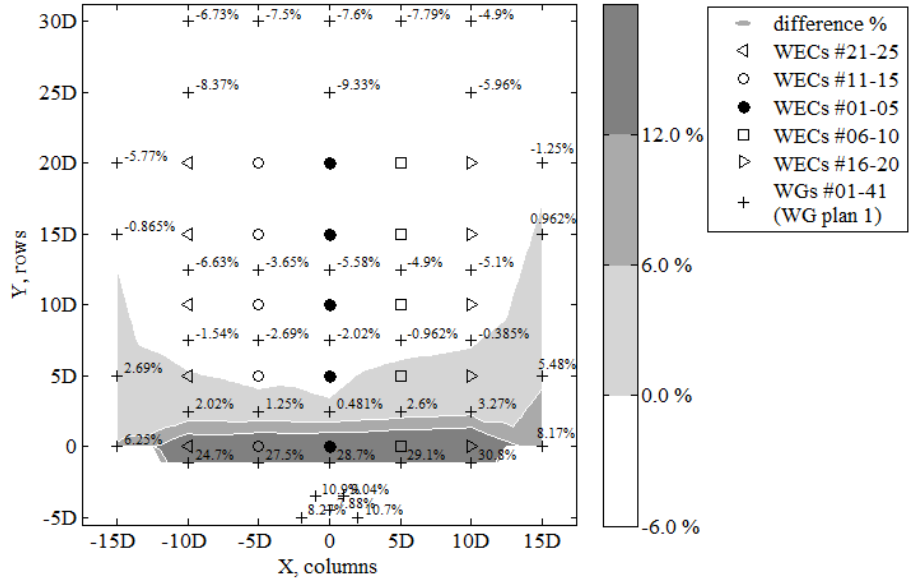

(b) Diffracted wave field normalized by target undisturbed wave field.

Figure 4.50. *Cont. Next Page*

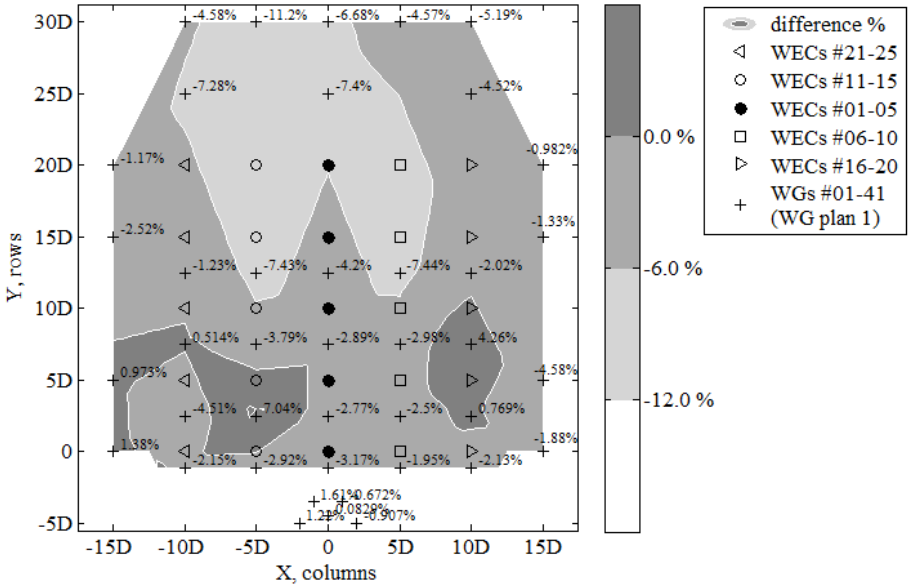

(c) Radiated wave field normalized by recorded undisturbed wave field.

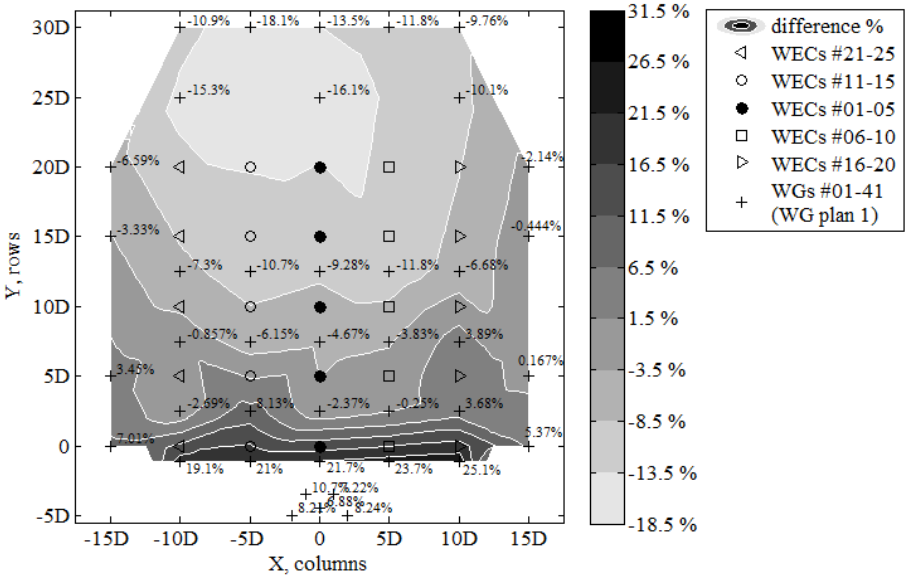

(d) Perturbed wave field normalized by recorded undisturbed wave field.

Figure 4.50. Non-dimensional percentage of change of H_{m0} at locations within and around the 5x5-WEC rectilinear array due to diffracted (stationary WECs), radiated (heaving WECs with damping applied) and perturbed wave field (heaving WECs with damping applied). Short-crested irregular waves of T_p = 1.26 s, H_{m0} = 0.104 m and spreading parameter, s =10. The basin width (X, columns) and length (Y, rows) are expressed in number of WEC unit diameters, D = 0.315 m.

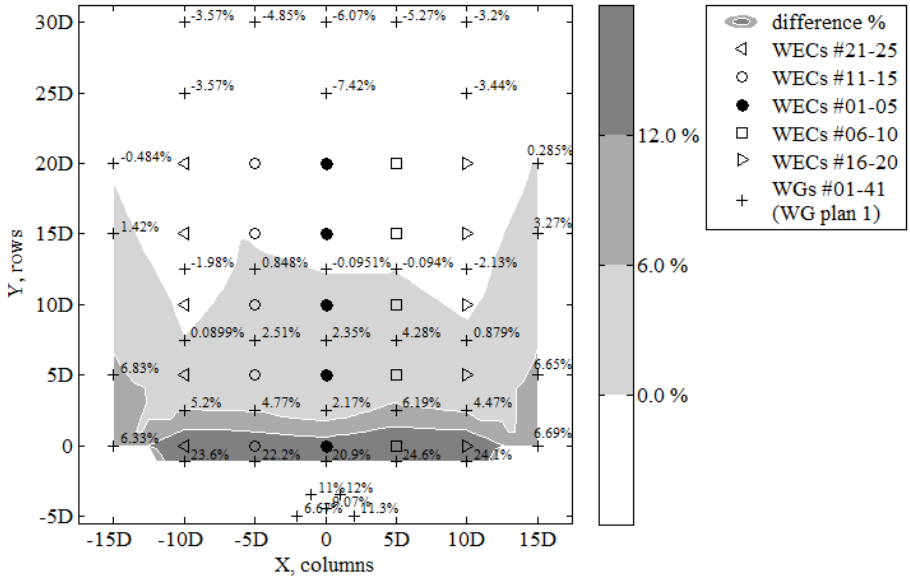

(a) Diffracted wave field normalized by recorded undisturbed wave field.

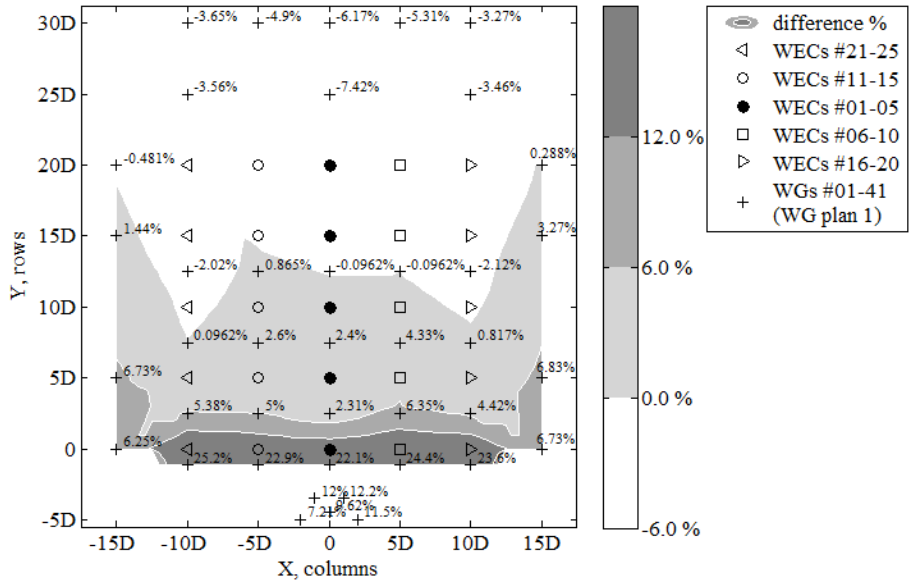

(b) Diffracted wave field normalized by target undisturbed wave field.

Figure 4.51. *Cont. Next Page*

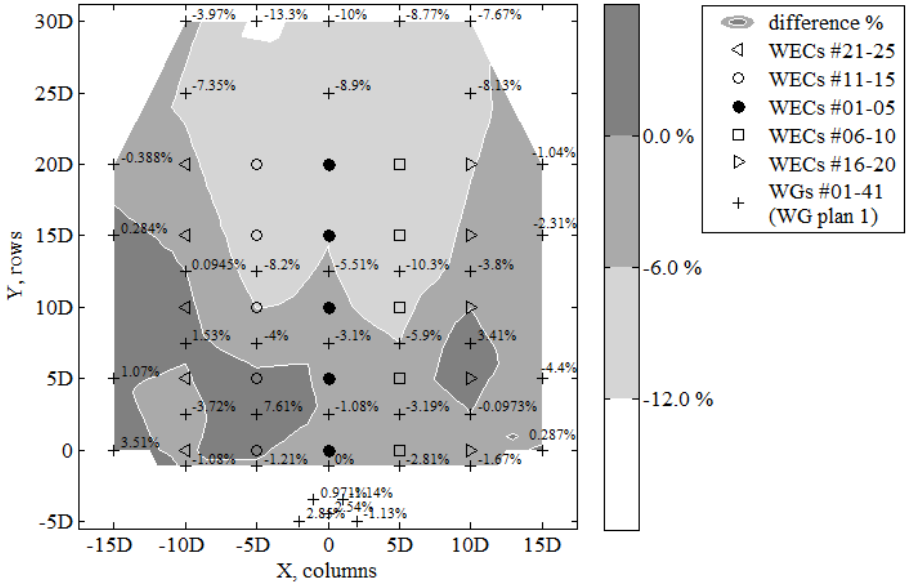

(c) Radiated wave field normalized by recorded undisturbed wave field.

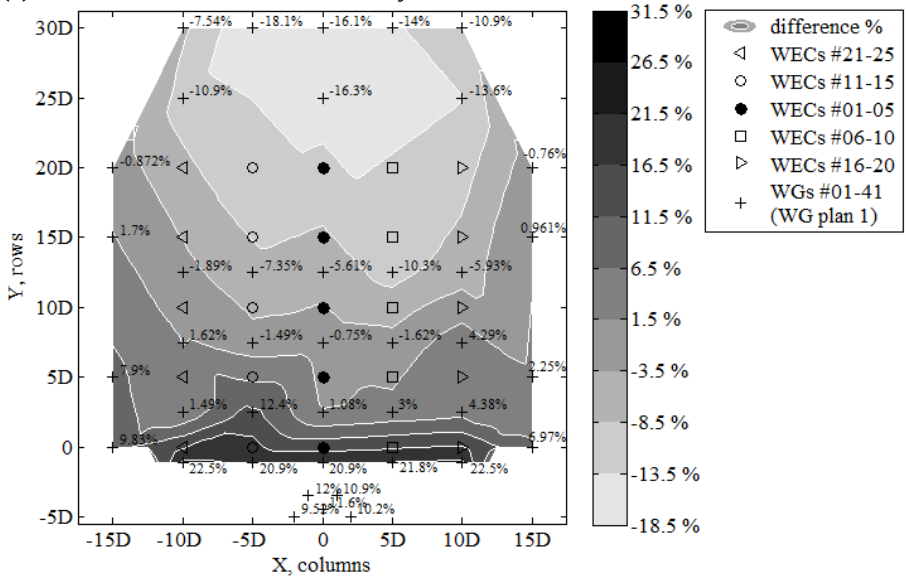

(d) Perturbed wave field normalized by recorded undisturbed wave field.

Figure 4.51. Non-dimensional percentage of change of H_{m0} at locations within and around the 5x5-WEC rectilinear array due to diffracted (stationary WECs), radiated (heaving WECs with damping applied) and perturbed wave field (heaving WECs with damping applied). Short-crested irregular waves of T_p = 1.26 s, H_{m0} = 0.104 m and spreading parameter, s = 75. The basin width (X, columns) and length (Y, rows) are expressed in number of WEC unit diameters, D = 0.315 m.

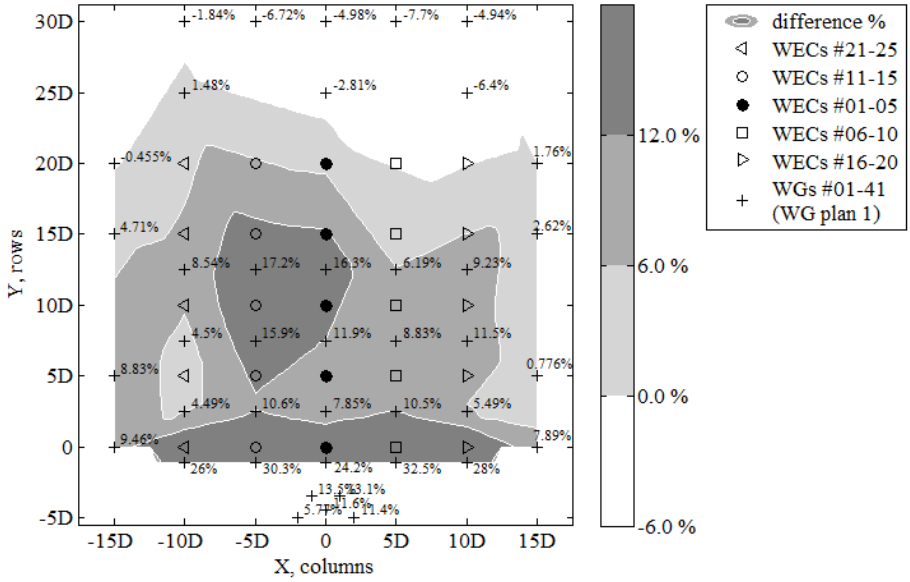

(a) Diffracted wave field normalized by recorded undisturbed wave field.

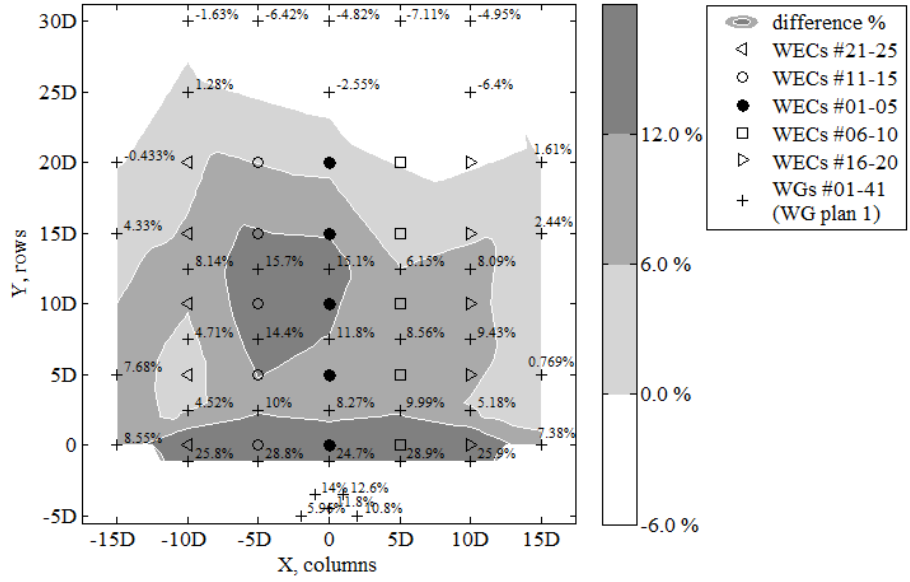

(b) Diffracted wave field normalized by target undisturbed wave field.

Figure 4.52. *Cont. Next Page*

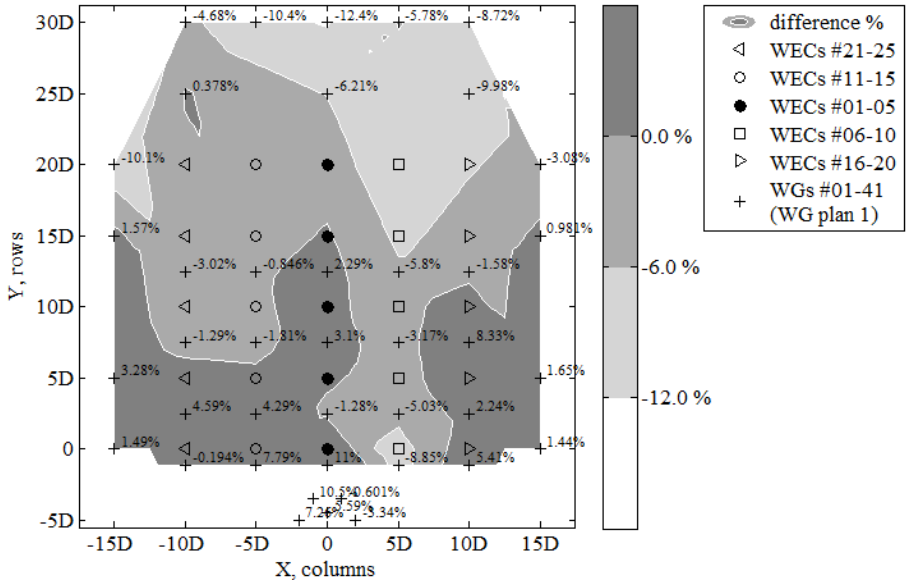

(c) Radiated wave field normalized by recorded undisturbed wave field.

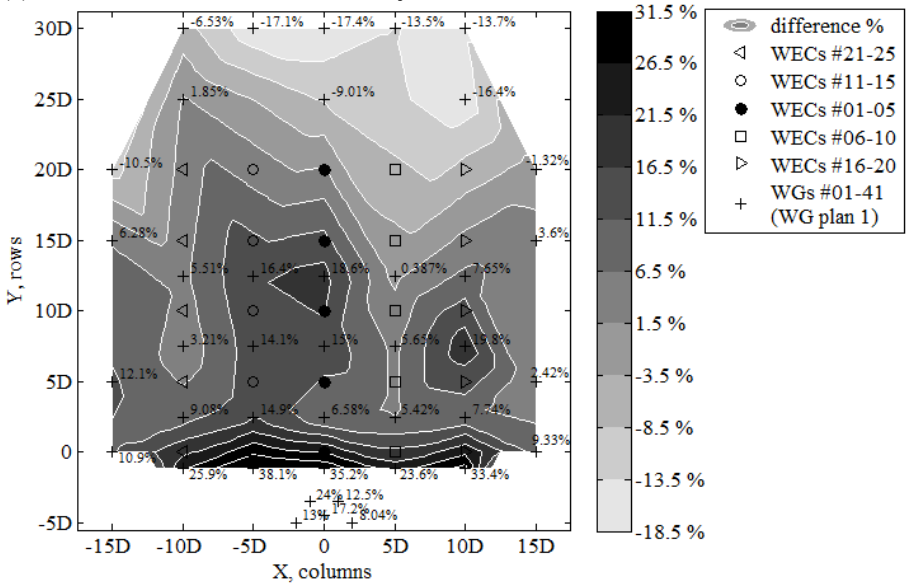

(d) Perturbed wave field normalized by recorded undisturbed wave field.

Figure 4.52. Non-dimensional percentage of change of H_{m0} at locations within and around the 5x5-WEC rectilinear array due to diffracted (stationary WECs), radiated (heaving WECs with damping applied) and perturbed wave field (heaving WECs with damping applied). Unidirectional irregular waves of T_p = 1.18 s and H_{m0} = 0.104 m. The basin width (X, columns) and length (Y, rows) are expressed in number of WEC unit diameters, D = 0.315 m.

Quantifying the effect of the wave directionality on WEC array effects

Firstly, sea states of the same peak period T_p = 1.26 s are discussed, to investigate the effect of the wave directionality on the resulting wave fields, due to the WECs motion and power extraction.

o Diffracted wave field

For unidirectional waves, up to 5.10 % of wave height decrease downwave and 26.20 % wave height increase upwave is observed when the 25 WEC units are held stationary at mean draft, d_{buoy} (Figure 4.49(a)). For wind short-crested waves (s = 10), wave height decrease downwave ranges between 7.23 % and 8.65 % and the increase upwave reaches 27.30 % (Figure 4.50(a)). For swell short-crested waves (s = 75), wave height decrease downwave ranges between 6.07 % and 7.42 % and the increase upwave reaches 24.60 % (Figure 4.50(a)). These percentages differ slightly in Figure 4.49(b) where the recorded wave heights are normalized by the target wave height H_{0i} (at the same WG locations, 5.38 % of wave height decrease downwave and 24.00 % wave height increase upwave, respectively). Also for short-crested waves, these percentages show small variation, with the wave height decrease downwave ranging between 7.79 % and 9.33 % and the increase upwave reaching 30.80 % for s = 10 (Figure 4.50(b)), as well as wave height decrease downwave ranging between 6.17 % and 7.42 % and increase upwave reaching 25.2 % for s = 75 (Figure 4.51(b)).

o Radiated wave field

When looking at the effect of the WECs on the wave field due to radiation only, for long-crested waves (Figure 4.49(c)) approximately 16.30 % wave height decrease is observed downwave of the WEC array and 8.48-10.80 % increase upwave. For short-crested waves with s = 10 (Figure 4.50(c)), the effect of radiation is similar, but more limited downwave of the array, where up to 11.20 % wave height decrease is observed. Upwave, the situation is different compared to long-crested waves, as the wave heights decrease by 1.95 - 3.17 % directly upwave of the front row of five WECs. Closer to the wave paddles, again, wave height increase is observed as for the long-crested waves, but very limited (up to 1.61 %). Moreover, for short-crested swell waves with s = 75 (Figure 4.51(c)), the effect of radiation represents an intermediate situation between long-crested and wind irregular waves, with a wave height decrease of 13.30 % downwave of the array. Upwave, again an intermediate situation is observed; yet this time, the results are closer to those for wind waves as the wave heights decrease by 1.08-2.81 % directly upwave of the front row of five WECs. Closer to the wave paddles, again, a limited wave height increase is observed (up to 2.85 %).

o Perturbed wave field

As presented in Figures 4.49(d) - 4.51(d) for the perturbed wave field, there is clearly wave height attenuation in the lee of the WEC array due to the operation of the heaving WEC units. Up to 18.10 % of wave height decrease is observed downwave (and 31.50 % very localised wave height increase upwave of the front row of five WECs) when the 25 WECs are operating under long-crested waves. For short-crested wind waves, the same order of magnitude of wave height decrease is found downwave of the array (up to 18.10 %). Upwave of the front row of five WECs, 25.10 % very localised wave height increase is observed similarly to the unidirectional waves but 6.0 % smaller. For short-crested swell waves, wave height decrease downwave of the array is found to be in the same magnitude but smaller (up to 16.1-16.3 %). Upwave of the front row of five WECs, 22.50 % very localised wave height increase is observed, and indicates an intermediate situation compared to long-crested and wind waves.

Quantifying the effect of different wave periods on WEC array effects

o Diffracted, radiated and perturbed wave field

Concerning the results from two different wave periods for irregular unidirectional waves, T_p = 1.18 s results in 7.70 % (5.10 % for T_p = 1.26 s) of wave height decrease downwave, while 32.5 % (26.20 % for T_p = 1.26 s) wave height increase upwave is observed when the 25 WEC units are held stationary at mean draft, d_{buoy} (Figure 4.52(a)). These percentages differ slightly in Figure 4.52(b) where the recorded wave heights are normalized by the target wave height H_{0i} (at the same WG locations, 7.11 % of wave height decrease downwave and 28.90 % wave height increase upwave, respectively). When looking at the effect of the WECs on the wave field due to radiation only, in Figure 4.52(c) approximately 12.4 % (16.30 % for T_p = 1.26 s) wave height decrease is observed downwave of the WEC array, and up to 11.00 % (8.48 - 10.80 % for T_p = 1.26 s) increase upwave. For the perturbed wave field, Figure 4.52(d) shows slightly reduced wave height attenuation in the lee of the WEC array compared to the waves of T_p = 1.26 s (18.10 %), found to be 17.40 %. Therefore, regarding the presented percentages, no significant difference is observed between long-crested waves of T_p = 1.26 s and T_p = 1.18 s. However, as discussed in the following, the wave field patterns are different.

Extents of WEC array effects for varying wave directionality

When comparing long- to short-crested waves, with regard to the extents of WEC array effects, the following observations can be made.

o Diffracted wave field

Regarding the diffraction effect on the recorded undisturbed wave field (Figures 4.49a-4.51a), the zone where wave height increase is observed for short-crested wind waves, is very limited compared to the long-crested waves (of the same T_p), so that increase stops after the second row of five WECs for directional waves. For long-crested waves, wave height increase is observed even at locations downwave of the WEC array. For s = 75, an intermediate situation is found where wave height increase stops more or less after the third WEC row. Consequently, wave height decrease is observed already after the second row of five WECs for short-crested wind waves (for swell directional waves after the third to fourth row), while for long-crested waves this decrease occurs only after a distance of $5D$ downwave of the last row of 5 WECs. The order of magnitudes of the maximum percentages found for wave height decrease and increase when looking at the same locations/distances upwave or downwave of the array, are, nevertheless, very similar for all sea states; i.e. in front of the first row of WECs or within the *CERC 5 WG array* and at locations with coordinates $((10D, 25D); (10D, 30D))$, respectively. Moreover, for all tests, wave height increase higher than 6.0 % is observed within a zone with similar extents, i.e. this zone is limited within the WGs surrounding the front row of five WECs, which are the first WECs facing the incoming waves. As conclusion from the above observations for Figures 4.49(a) - 4.51(a), the largest wave field variations between long- and short-crested wind waves are found between the zone downwave of the second row of WECs and at a distance $5D$ downwave of the last row of WECs. This zone of variations between short- and long-crested waves has the same length as the length of the WEC array ($20D$). The swell directional waves result in an intermediate situation with more similarities to the long-crested waves. The same conclusions can be made when comparing Figures 4.49(b)-4.51(b). Also, note that the differences presented in Figures 4.49(a-b)-4.51(a-b) are progressing from positive (wave height increase) to negative (wave height decrease), almost "parallel" to the WEC rows towards the opposite end of the wave basin (landwards).

o Radiated wave field

Regarding the radiation effect on the perturbed wave field due to damped response of the WEC units, for the same peak wave period (Figures 4.49(c)-4.51(c)), the zone where wave height increase is observed for short-crested waves of both directionalities, is very limited compared to the long-crested irregular waves. For unidirectional waves this increase is still observed until the WECs of the third row, while wave height decrease starts clearly after the third row of WECs. For both long- and short crested waves, this decrease is smaller at the outermost sides of the array. The order of magnitudes of the maximum percentages found for wave height decrease when looking at the same distances downwave of the array, are similar for

both wave types; e.g. at the location with coordinates (-5D, 30D). Moreover, after the last row of WECs, the patterns of wave height decrease are similar for the all sea states where variations become higher than -6.00 %. As conclusion from the above observations for Figures 4.49(c) - 4.51(c), the largest wave field variations between long- and short-crested waves are found for the zone upwave of the third row of WECs. The short-crested waves result in rather symmetric wave fields around the WECs. Also, note that the differences presented in Figures 4.49(c) - 4.51(c) are progressing from positive (wave height increase) to negative (wave height decrease) towards the opposite end of the wave basin (landwards), with a diagonal pattern towards the WEC columns located at the sides of the WEC array.

o Perturbed wave field

Regarding the effect on the recorded undisturbed wave field caused by the perturbed wave field around the WEC array (Figures 4.49(d) - 4.51(d)), the zone where wave height increase is observed for short-crested wind waves, is very limited compared to the long-crested and directional swell irregular waves, so that increase stops downwave of the front row of 5 WECs for wind waves. Consequently, wave height decrease is observed already after the front row of WECs for short-crested waves, while for long-crested and directional swell waves this decrease starts to take place only after the third row of 5 WECs. The order of magnitudes of the maximum percentages found for wave height decrease and increase when looking at the same locations/distances upwave or downwave of the array, are, nevertheless, very similar for all sea states; i.e. in front of the first row of WECs or within the *CERC 5 WG array* and at locations with coordinates ((-5D, 5D); (10D, 30D)), respectively. Moreover, for both wave types, wave height increase higher than 12.10 % is observed within a zone with similar extents, i.e. this zone is limited to the WGs upwave of the front row of 5 WECs (the first WECs facing the incoming waves), due to diffraction effects. As conclusion from the above observations for Figures 4.49(d) - 4.51(d), the largest wave field variations between long- and short-crested waves (with s = 10) are found between the zone downwave of the front row of WECs and at a distance 5D downwave of the last row of WECs. This zone of variations between wind and long-crested waves has a length of 25D. Also, note that the differences presented in Figures 4.49(d) - 4.51(d) for wave height increase between 8.00 % and 31.50 % are progressing, almost "parallel" to the front WEC row towards the opposite end of the wave basin (landwards). When wave height attenuation starts to take over, the pattern of the differences for both sea states becomes diagonal towards the WEC columns located at the sides of the WEC array. This wave pattern is a result of the increased wave height at the sides of the array, reaching up to the fifth row for long-crested irregular waves and up to the fourth row for swell directional waves. For wind waves, increased wave height is found only at

the sides of the front row. However, downwave of the front row, wave height decrease is less at the sides compared to the central area of the array. Most importantly, for all sea states, the highest wave height dissipation is observed at locations, at least at distance $10D$ downwave of the WEC array, and within a zone of width $-5D < X < +5D$.

Extents of WEC array effects for different wave periods

By comparing long-crested waves of different peak wave periods, T_p, with regard to the extent of WEC array effects, the following are observed.

o Diffracted wave field

Regarding the diffraction effect on the recorded undisturbed wave field (Figures 4.49(a-b) and 4.52(a-b), the zone where wave height increase is observed for T_p = 1.18 s, is wider compared to that for T_p = 1.26 s due to different wave reflection characteristics and due to change of wavelength compared to the WEC array spacings. Peak period T_p = 1.18 s results in higher wave heights (at least 8.0 % increase) within the area of the WECs, while the area around the devices shows very similar wave field characteristics for both wave periods. Downwave of the array, T_p = 1.18 s is responsible for higher wave attenuation (by 2.0 % to 3.0 %), starting for both sea states after a distance of $5D$ downwave of the last row of 5 WECs. The order of magnitudes of the maximum percentages found for wave height decrease and increase when looking at the same locations/distances upwave or downwave of the array, are, nevertheless, very similar for both wave periods. As conclusion from the above observations for Figures 4.49(a-b) - 4.52(a-b), the largest wave field variations between long-crested waves of T_p = 1.26 s and T_p = 1.18 s are found within the extents of the WEC array.

o Radiated wave field

Regarding the radiation effect on the perturbed wave field due to damped response of the WEC units for different peak wave periods (Figures 4.49(c) and 4.52(c)), large differences are observed in the resulting wave patterns. The most pronounced difference is the lack of wave field symmetry for long-crested waves of T_p = 1.18 s, compared to long-crested waves of T_p = 1.26 s. A peak wave period equal to the resonance period of an individual WEC unit results in the non-symmetric wave field of Figure 4.52(c), while the zone where wave height increase is observed for this period, is more limited compared to waves of T_p = 1.26 s. As conclusion from the observations for Figures 4.49(c) and 4.52(c), large wave field variations between long-crested waves of T_p = 1.26 s and T_p = 1.18 s, are found

throughout the entire domain as no symmetry and clear wave pattern is observed for peak wave period close to the resonance period of an individual WEC unit. Also T_p = 1.18 s results in less wave height attenuation along the central WEC column (up to 6.0 %), as well as to less wave height increase across the first three WEC rows.

o Perturbed wave field

Concerning the effect on the recorded undisturbed wave field caused by the perturbed wave field around the WEC array due to different peak wave periods (Figures 4.49(d) and 4.52(d)), in the zone around the front row of WECs similar percentages of wave height increase are observed for both wave periods, yet higher for T_p = 1.18 s. Also downwave of the array, within - 5D < X < 5D and for Y=30D, wave height dissipation is very similar. However, the wave patterns are again different, with a clear lack of symmetry for T_p = 1.18 s. Moreover, wave height increase successes wave height decrease with repetition, in the lateral direction of the wave basin for T_p = 1.18 s, which is not observed for T_p = 1.26 s. Finally, also for T_p = 1.18 s, the wave height is increased at the sides of the array (yet no symmetry is observed).

Wave spectra at various locations around the WEC array

Furthermore, in Figure 4.53 for long-crested waves of T_p = 1.26 s, and Figure 4.54 for short-crested wind waves, the wave spectra are plotted for various locations around the WEC array for the recorded undisturbed wave field (no WECs are present), the diffracted wave field around stationary WEC units, the perturbed wave field due to responding WEC units and for the target undisturbed wave field, respectively. These two sea states have been selected since they result in significant wave field variations when compared to each other and to the undisturbed wave field. The locations considered are: (0,-5D) upwave of the WEC array at WG #03, (0, 7.5D) at the centre of the WEC array at WG #08, (0, 25D) downwave of the WEC array at WG #10, and (15D, 5D) at the side of the WEC array at WG #24. The change of H_{m0} at these locations is as shown in Figures 4.49 and 4.50.

Therefore, spectra of the target (or else the "theoretical") wave field, $S_T(f)$, the recorded undisturbed wave field, $S_U(f)$, the diffracted wave field only, $S_D(f)$, and the perturbed wave field, $S_P(f)$, are presented. $S_D(f)$ is very similar to $S_P(f)$, showing low impact of the radiated wave field on the resulting perturbed wave spectra upwave (Figures 4.53(a) and 4.54(a)), especially for short-crested waves. The same conclusion can be drawn for the location given at the centre of the WEC array in Figures 4.53(b) and 4.54(a). Downwave of the WEC array (Figures 4.53(c) and 4.54(c)), diffracted and undisturbed wave spectra are similar, especially for long-crested waves, so nearly all of the transmitted wave change is due to radiation

at this specific location. At the side of the WEC array, the recorded undisturbed wave field and the perturbed wave field spectra do not show large variations, showing limited effect of the WEC units on the resulting perturbed wave field at that location.

Moreover, downwave of the WEC array (at WG #10) a clear wave spectrum attenuation is observed when comparing the perturbed to the recorded undisturbed wave field spectrum, for both sea states.

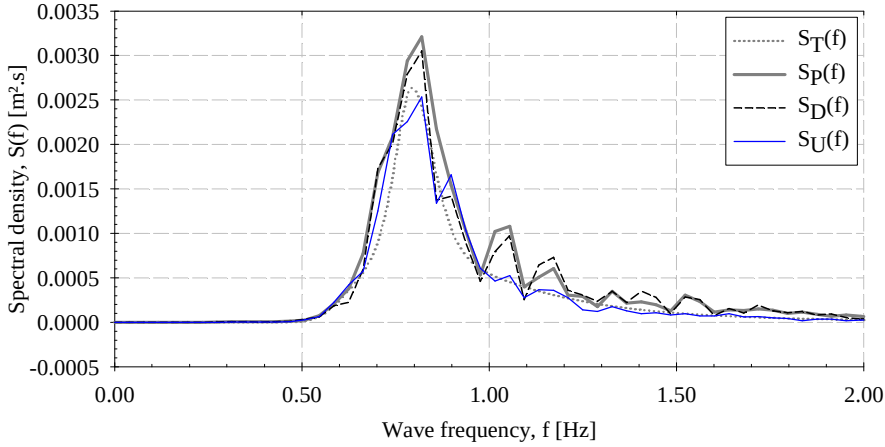

(a) Location (0, -5D): upwave of the WEC array at WG #03

(representing frequency dependent reflection $K_R(\omega)$).

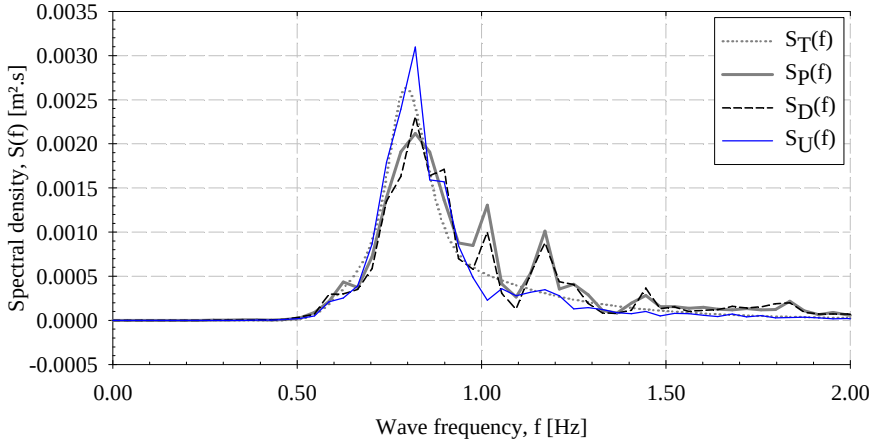

(b) Location (0,7.5D): centre of the WEC array at WG #08.

Figure 4.53. *Cont.*

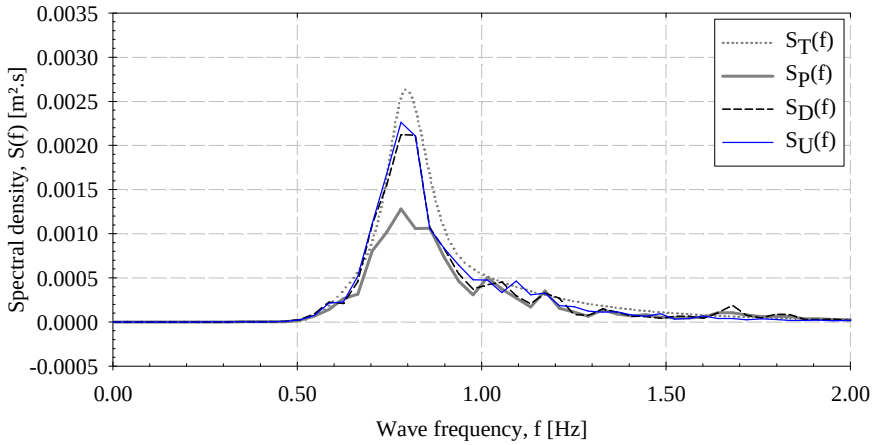

(c) Location (0, 25D): downwave of the WEC array at WG #10

(representing frequency dependent transmission $K_T(\omega)$).

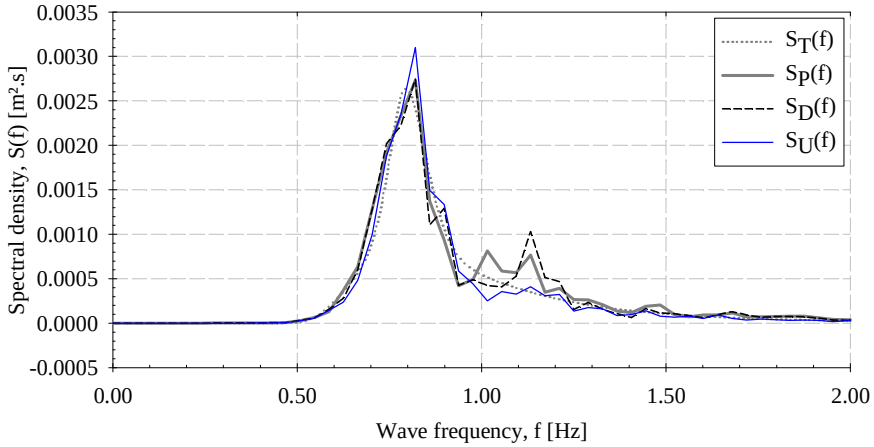

(d) Location (15D, 5D): at the side of the WEC array at WG #24.

Figure 4.53. Spectra of target undisturbed wave field (dotted line), $S_T(f)$, recorded undisturbed wave field (thin solid line), $S_U(f)$, diffracted wave field only (dashed line), $S_D(f)$, and perturbed wave field (thick line), $S_P(f)$, at locations within and around array (*WG plan 1*) of the 5x5-WEC rectilinear array with WECs at lateral and longitudinal spacing, $w = l = 5D$. Unidirectional irregular wave as in Figure 4.49.

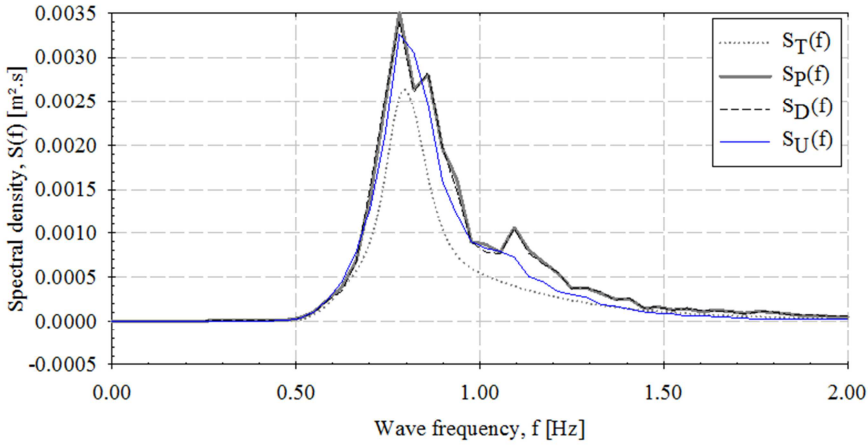

(a) Location (0, -5D): upwave of the WEC array at WG #03 (representing frequency dependent reflection $K_R(\omega)$).

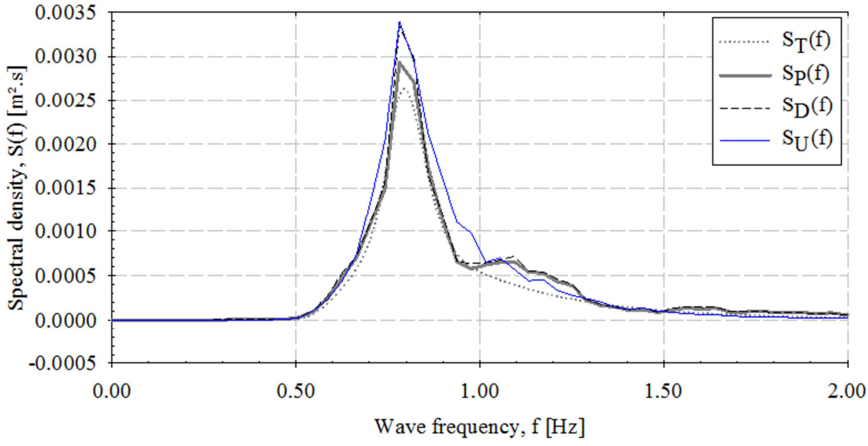

(b) Location (0, 7.5D): centre of the WEC array at WG #08.

Figure 4.54. *Cont.*

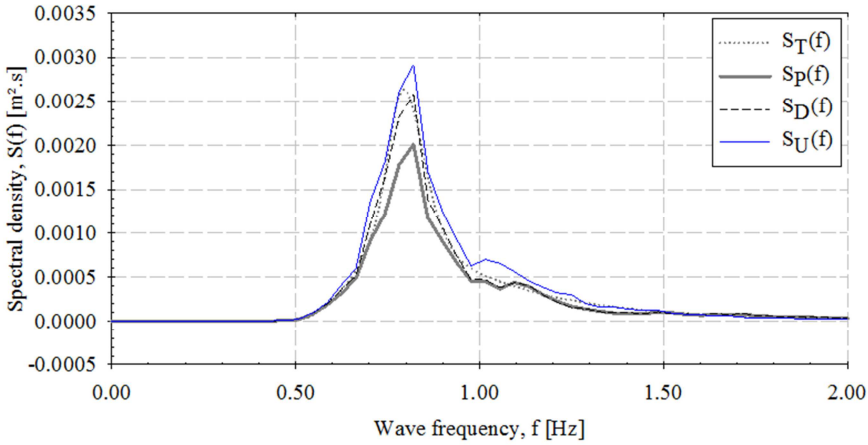

(c) Location (0, 25D): downwave of the WEC array at WG #10

(representing frequency dependent transmission $K_T(\omega)$).

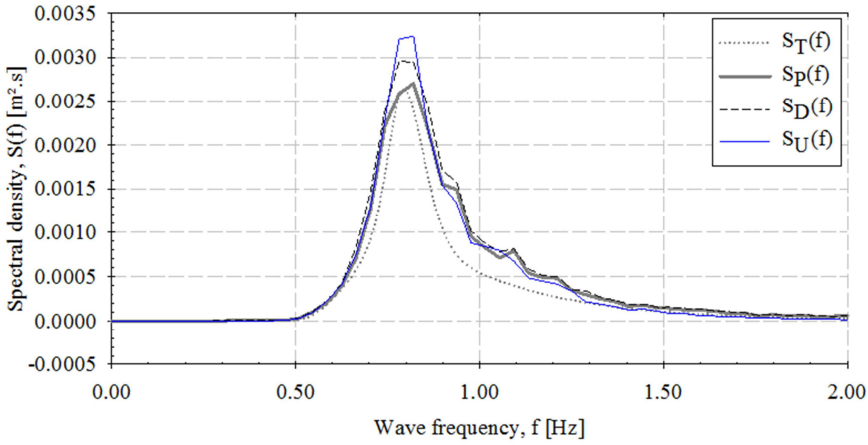

(d) Location (15, 5D): at the side of the WEC array at WG #24.

Figure 4.54. Spectra of target undisturbed wave field (dotted line), $S_T(f)$, recorded undisturbed wave field (thin solid line), $S_U(f)$, diffracted wave field only (dashed line), $S_D(f)$, and perturbed wave field (thick line), $S_P(f)$, at locations within and around array (*WG plan 1*) of the 5x5-WEC rectilinear array with WECs at lateral and longitudinal spacing, $w = l = 5D$. Short-crested irregular waves as in Figure 4.50.

4.6.8.1. Main observations on wave field modification around a 5x5-WEC rectilinear array

The wave field modifications due to wave energy extraction and the WECs' motion have been quantified for a 5x5-WEC rectilinear array, in terms of the non-dimensional percentage of change of H_{m0} at locations within and around the array due to the diffracted, radiated and perturbed wave field. The tested sea states have been also analysed in terms of spatial variation of the resulting wave height increase/reduction, and thus with regard to the extents of WEC array effects. The accuracy of generating the target wave fields has been evaluated. For all presented results, the difference between recorded and target undisturbed wave field is shown not to be significant.

o **Diffracted wave field:**

When considering only the calculated difference percentages, up to 5.10 %, 8.65 %, 7.42 % and 7.70 % of wave height decrease downwave, is found for irregular unidirectional waves of T_p = 1.26 s, short-crested wind waves, directional swell and unidirectional waves of T_p = 1.18 s, respectively. Waves of longer wavelength result in lower wave height dissipation downwave. Larger differences are found between wind and long-crested irregular waves, while swell directional waves represent an intermediate situation. Upwave of the front WEC row, local wave height increase is observed for all sea states.

With regard to the extents of WEC array effects:

- Wave height decrease is observed already after the second row of five WECs for wind waves (for swell directional waves after the third to fourth row), while for long-crested waves this decrease occurs only after a distance of $5\,D$ downwave of the last row of 5 WECs.
- For all tests, the highest wave height increase is observed within the front row of five WECs, facing as first, the incoming waves.
- The largest wave field variations between long- and short-crested wind waves are found between the zone downwave of the second row of WECs and at a distance $5D$ downwave of the last row of WECs (zone width = $20D$).
- The swell directional waves result in an intermediate situation with more similarities to long-crested irregular waves.

- The wave field evolution shows change from wave height increase to wave height decrease, almost "parallel" to the WEC rows, towards the opposite end of the wave basin (landwards).
- The largest wave field variations between long-crested waves of T_p = 1.26 s and T_p = 1.18 s are found within the extents of the WEC array.

o **Radiated wave field:**

When considering only the calculated difference percentages, up to 16.30 %, 11.20 %, 13.30 % and 12.40 % of wave height decrease downwave, is observed for unidirectional waves of T_p = 1.26 s, short-crested wind waves, directional swell and unidirectional waves of T_p = 1.18 s, respectively. The effect of varying the wave directionality parameter is rather limited, but when comparing irregular long-crested to wind waves, larger differences are found. Moreover, as a result of T_p = 1.18 s being equal to the resonance period of a WEC unit, wave height attenuation downwave is smaller than for longer waves.

With regard to the dimensions of WEC array effects:

- The largest wave field variations between long- and short-crested waves are found for the zone upwave of the third row of WECs. Short-crested waves result in rather symmetric wave fields around the WECs.
- The wave field evolution shows change from wave height increase to wave height decrease, with a diagonal pattern towards the WEC columns located at the sides of the WEC array.
- Large wave field variations between long-crested waves of T_p = 1.26 s and T_p = 1.18 s, are found throughout the entire domain as no symmetry and clear wave pattern is observed for peak wave period close to the resonance period of a WEC unit.

o **Perturbed wave field:**

When considering only the calculated difference percentages, up to 18.10 %, 18.10 %, 16.30 % and 17.40 % of wave height dissipation downwave, is observed for irregular unidirectional waves of T_p = 1.26 s, short-crested wind waves, directional swell and unidirectional waves of T_p = 1.18 s, respectively. A large, very localised wave height increase, ranging between 22.50 % and 38.10 % for all sea states, is

found upwave of the front row of five WECs. For all tests, the same order of magnitude of wave height reduction is found downwave of the array.

Regarding the dimensions of WEC array effects:

- Wave height decrease is observed already after the front row of WECs for irregular short-crested waves, while for irregular long-crested and directional swell waves, this decrease starts to take place only after the third row of 5 WECs.
- For all sea states, the highest wave height increase is found upwave of the front row of 5 WECs (the first ones facing the incoming waves), as a result of significant diffraction effects.
- The largest wave field variations between irregular long- and short-crested waves (with s = 10) are found between the zone downwave of the front row of WECs and at a distance $5D$ downwave of the last row of WECs (zone width = $25D$).
- For all irregular long-crested and swell waves, wave height increase has a "parallel" pattern to the front WEC row. This pattern becomes diagonal towards the WEC columns located at the sides of the WEC array, and is result of increased wave height at the sides of the array. For wind waves, increased wave height is found only at the sides of the front row (yet, wave height reduction is smaller at the sides of the entire array).
- For all sea states, the highest wave height dissipation is observed at locations, at least at distance $10D$ downwave of the WEC array, and within a zone of width $-5D < X < +5D$.
- In the results from wave spectra at a location downwave of the WEC array, a clear wave spectrum attenuation is observed, for both irregular long-crested and wind waves of T_p = 1.26 s.

4.6.9. Wave field modification around a 5x5-WEC staggered array

In this section, the wave field modifications due to wave energy extraction and the WECs' motion have been quantified, around a 5x5-WEC staggered array, illustrated in Figure 4.55, during experiments in the DHI wave basin.

The wave field difference percentage terms have been calculated, using Equations 4.9 – 4.12, and plotted in Figures 4.56 - 4.59, as for the 5x5-WEC rectilinear array. The measured change of the wave field for unidirectional irregular

waves, is presented separately for the diffracted (Figures 4.56(a-b) and 4.59(a-b)), the radiated (Figures 4.56(c) and 4.59(c)) and the perturbed (Figures 4.56(d) and 4.59(d)) wave field, for T_p = 1.26 s and T_p = 1.18 s, respectively. In addition, Figures 4.57(a-d) and 4.58(a-d) present wave fields for the short-crested irregular waves with spreading parameter, s = 10 and s = 75, respectively.

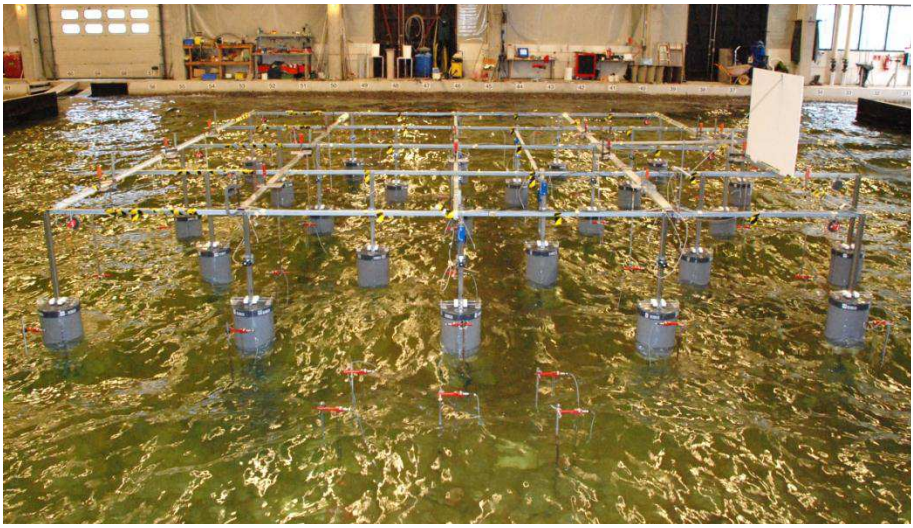

Figure 4.55. The 5x5-WEC staggered array in the DHI Shallow Water wave basin under irregular long-crested waves with θ = 0°. View from behind the wave generator.

Quantifying the effect of the wave directionality on WEC array effects

Firstly, sea states of the same peak period T_p = 1.26 s are discussed, to investigate the effect of the wave directionality on the resulting wave fields, due to the WECs' motion and power extraction. Moreover, the results obtained for the 5x5-WEC staggered array are compared to results obtained for the 5x5-WEC rectilinear array from the previous section; the aim is to quantify the effect of changing the WEC array geometric configuration on the resulting wave fields.

o Diffracted wave field

For irregular unidirectional waves of T_p = 1.26 s, up to 5.83 % (5.10 % for the rectilinear array) of wave height decrease downwave and 34.20 % (26.20 % for the rectilinear array) wave height increase upwave is observed when the 25 WEC units are held stationary at mean draft, d_{buoy} (Figure 4.56(a)). For wind short-crested

waves (s = 10), wave height decrease downwave does not become larger than 3.93 % (for the rectilinear array reduction up to 8.65 %) and the increase upwave reaches 29.40 % (27.30 % for the rectilinear array) (Figure 4.57(a)). For swell short-crested waves (s = 75), wave height decrease downwave reaches 4.69 % (6.07 % and 7.42 % for the rectilinear array) and the increase upwave reaches 29.00 % (24.60 % for the rectilinear array) (Figure 4.58(a)), very similar to the wind waves. These percentages differ slightly in Figure 4.56(b) where the recorded wave heights are normalized by the target wave height H_{0i} (at the same WG locations, 5.63 % of wave height decrease downwave and 34.50 % wave height increase upwave, respectively). Also for short-crested irregular waves, these percentages show small variation, with the wave height decrease downwave ranging between 2.12 % and 4.23 % and the increase upwave reaching 33.80 % for s = 10 (Figure 4.57(b)). Wave height decrease downwave ranges between 0.39 % and 3.75 % and the increase upwave reaches 29.9 % for s = 75 (Figure 4.58(b)).

- Radiated wave field

When looking at the effect of the WECs on the wave field due to radiation only, for irregular long-crested waves of T_p = 1.26 s (Figure 4.56(c)) approximately 15.10 % wave height decrease is observed downwave of the WEC array (16.30 % for the rectilinear array) and up to 5.70 % increase upwave (8.48 - 10.80 % for the rectilinear array). For short-crested irregular waves with s = 10 (Figure 4.57(c)), the effect of radiation is similar downwave of the array, where up to 11.10 % wave height decrease is observed (11.20 % for the rectilinear array). Upwave, the situation is different compared to long-crested waves, as the wave heights decrease by 4.52-6.69 % (1.95-3.17 % for the rectilinear array) directly upwave of the front row of five WECs. Closer to the wave paddles, again, up to 4.87 % wave height decrease is observed, similarly to the long-crested waves (up to 3.95 %). For the rectilinear array, though, a small wave height increase is observed within the *CERC 5 WG array* (up to 1.61 %). Moreover, for short-crested swell waves with s = 75 (Figure 4.58(c)), the effect of radiation represents an intermediate situation between long-crested and wind irregular waves, with wave height decrease of 11.70 % (13.30 % for the rectilinear array) downwave of the array. Upwave, again an intermediate situation is observed, yet this time the results are closer to those for wind waves, as the wave heights decrease by 4.66 % (1.08-2.81 % for the rectilinear array) directly upwave of the front row of five WECs. Closer to the wave paddles, a limited wave height increase of 4.24 % is observed (up to 2.85 % for the rectilinear array).

- Perturbed wave field

As presented in Figures 4.56(d) - 4.58(d) for the perturbed wave field, there is clearly wave height attenuation in the lee of the WEC array due to the operation of

the heaving WEC units. A large wave height decrease of up to 20.80 % is found downwave (up to 18.10 % for the rectilinear array), and 28.60 % very localised wave height increase upwave of the front row of five WECs (31.50 % for the rectilinear array) when the 25 WECs are operating under irregular long-crested waves of T_p = 1.26 s. This larger wave height dissipation compared to that caused by the rectilinear arrays, is also explained by the results for power output of the 5x5-WEC staggered array. The staggered array results in higher absolute time-averaged power output and higher WEC array interaction factor compared to the rectilinear array under the same wave conditions (see Section 4.6.3.2.1). For short-crested wind waves, wave height decrease ranges between 13.70 % and 15.00 % and is much smaller compared to that found for the long-crested waves (20.80 %), as well as to that found for the rectilinear array (18.10 %). This lower wave height attenuation is also explained by the power output of the 5x5-WEC staggered array for wind waves, which results in lower absolute time-averaged power absorption and lower WEC array interaction factor compared to: (i) the long-crested waves for the staggered array, and (ii) the rectilinear array under the same wave conditions (see Sections 4.6.3.2.1 and 4.6.3.1.2, respectively). Upwave of the front row of five WECs, 23.10 % (25.10 % for the rectilinear array) very localised wave height increase is observed, which is lower compared to the unidirectional waves. For short-crested swell waves, wave height decrease downwave of the array is found to be in the same magnitude of wind waves, but smaller (up to 15.0-15.4 %). Upwave of the front row of five WECs, 24.30 % very localised wave height increase is observed similarly to the wind waves. As for the rectilinear array, swell directional waves show slightly an intermediate situation between long-crested and wind waves of the same peak period for the perturbed wave field around the WECs.

Quantifying the effect of different wave periods on WEC array effects

- Diffracted, radiated and perturbed wave field

Regarding the results from two different peak wave periods for unidirectional irregular waves, T_p = 1.18 s results in 5.15 % of wave height decrease downwave (5.83 % for T_p = 1.26 s, and 7.70 % for the rectilinear array with T_p = 1.18 s). Moreover, 40.2 % wave height increase upwave is observed (34.2 % for T_p = 1.26 s, and 32.5 % for T_p = 1.18 s for the rectilinear array) when the 25 WEC units are held stationary at mean draft, d_{buoy} (Figure 4.59(a)). These percentages differ slightly in Figure 4.59(b) where the recorded wave heights are normalized by the target wave height H_{0i} (at the same WG locations, 4.75 % of wave height decrease downwave and 38.20 % wave height increase upwave, respectively). When looking at the effect of the WECs on the wave field due to radiation only, in Figure 4.59(c) approximately 13.8 % wave height decrease is observed downwave of the WEC

array (15.10 % for T_p = 1.26 s, and 12.4 % for T_p = 1.18 s for the rectilinear array), as well as a decrease of up to 5.56 % upwave (5.70 % for T_p = 1.26 s, but 11.00 % increase for T_p = 1.18 s for the rectilinear array). The perturbed wave field of Figure 4.59(d), shows reduced wave height attenuation in the lee of the WEC array compared to the waves of T_p = 1.26 s (20.80 %) and is found to be 16.10 % (17.40 % for the rectilinear array). Therefore, regarding the presented percentages, a significant difference is observed between long-crested waves of T_p = 1.26 s and T_p = 1.18 s, as well as regarding the resulting wave field patterns, discussed in the following. This is not observed, though, when similar percentages of T_p = 1.26 s and T_p = 1.18 s are compared for the 5x5-WEC rectilinear array, as seen Section 4.6.8. This observation supports the aspect that wave period has effect on the WEC array effects, related to the WEC array geometric layout.

Extents of WEC array effects for varying wave directionality

When comparing long- to short-crested waves, with regard to the extent of WEC array effects, several observations can be made.

- Diffracted wave field

Regarding the diffraction effect on the recorded undisturbed wave field (Figures 4.56(a)-4.58(a)), the zone where wave height increase is observed for short-crested wind waves, is very limited compared to the long-crested waves (of the same T_p); increase stops after the third row of five WECs for directional waves (after the second WEC row for the rectilinear array). For long-crested irregular waves, wave height increase is observed even at locations downwave of the WEC array, similar to the rectilinear array.

For waves of s = 75, the situation is very similar to the wind waves, with slightly wider areas of wave height increase at the WEC array sides (yet, for the rectilinear array, waves of s = 75 lead to an intermediate situation between irregular long-crested and wind waves). Consequently, wave height decrease is observed already after the third row of five WECs for short-crested waves, while for irregular long-crested waves this decrease occurs only after a distance of 5D downwave of the last row of 5 WECs. The order of magnitudes of the maximum percentages found for wave height decrease and increase, when looking at the same locations/distances upwave or downwave of the array, are, nevertheless, very similar for all sea states; i.e. in front of the first row of WECs or within the *CERC 5 WG array* and at locations with coordinates ((10D, 25D); (0, 30D)), respectively. Moreover, for all tests, wave height increase higher than 12.0 % is observed within a zone with similar extents, i.e. this zone surrounds the front row of five WECs, thus the first WECs facing the incoming waves. As conclusion from the above observations for Figures

4.56(a)-4.58(a), the largest wave field variations between long- and short-crested irregular waves are found between the zone downwave of the third row of WECs and at a distance 5D downwave of the last row of WECs. This zone of variations between short- and long-crested waves has a width of 15D. The swell directional waves do not result in a clear intermediate situation, as for the rectilinear array, and show more similarities to the wind waves. The same conclusions can be made when comparing Figures 4.56(b) - 4.58(b). Also, note that the differences presented in Figures 4.56(a-b) - 4.58(a-b) are progressing from positive (wave height increase) to negative (wave height decrease), almost "parallel" to the WEC rows towards the opposite end of the wave basin (landwards). The same observation is made for the diffracted wave field by the 5x5-WEC rectilinear array.

o Radiated wave field

Regarding the radiation effect on the perturbed wave field due to damped response of the WEC units, for the same peak wave period (Figures 4.56(c)-4.59(c)), no wave height increase is observed for all sea states. For the rectilinear array, this zone is limited for short-crested waves and quite wide (around 50.0 % of the array area) for long-crested waves, reaching 8.55 % wave height increase. For both long- and short crested waves, at the outermost sides of the array this decrease is smaller, similar to the findings for the rectilinear array. The order of magnitudes of the maximum percentages found for wave height decrease when looking at the same distances downwave of the array, are very similar for both types of directional waves and not far from the decrease found for the long-crested irregular waves (difference of around 4.0 % in wave height decrease). The same result is obtained for the area downwave of the rectilinear array. As conclusion from the above observations for Figures 4.56(c) - 4.59(c), the largest wave field variations between long- and short-crested waves are found for the zone between WEC rows 2 and 3, as well as within a distance of 10D after the last WEC row and especially downwave of the middle WEC column. The short-crested waves result in less symmetric wave fields around the WECs, while the opposite is found for the rectilinear array. Also, note that the differences presented in Figures 4.56(c) - 4.58(c) are progressing from smaller to higher wave height decrease towards the opposite end of the wave basin (landwards), with a diagonal pattern towards the WEC columns located at the sides of the WEC array.

o Perturbed wave field

Regarding the effect on the recorded undisturbed wave field caused by the perturbed wave field around the WEC array (Figures 4.56(d) - 4.59(d)), the zone where wave height increase is observed for short-crested waves, is very limited, compared to the irregular long-crested waves, so that increase stops downwave of

the front row of 5 WECs. Here, directional swell and wind waves result in similar wave fields; this is not observed for the rectilinear array, where swell waves lead to a situation similar to that for long-crested waves. Consequently, wave height decrease is observed already after the front row of WECs for short-crested waves, while for long-crested waves this decrease occurs only after the third row of 5 WECs. The maximum percentages found for wave height decrease and increase when looking at the same locations/distances upwave or downwave of the array, differ by at least 5.80 % for long- and short-crested waves. In the case of the rectilinear array, however, the magnitude of wave height decrease/increase at the same locations is very similar for all sea states. Responsible for these large differences between extra-array effects caused by long- and short-crested waves, is the large difference in the power output for these sea states, as seen in Section 4.6.3.2. As conclusion from the above observations for Figures 4.56(d) - 4.59(d), the largest wave field variations between long- and short-crested waves are found between the zone downwave of the front row of WECs and the last row of WECs, as well as at a distance greater than $5D$ downwave of the WEC array. This zone of variations between wind and long-crested waves has a length of $25D$. Also, note that the differences presented in Figures 4.56(d) - 4.59(d) for wave height increase between 8.00 % and 31.50 % are progressing, almost "parallel" to the front WEC row towards the opposite end of the wave basin (landwards). When wave height attenuation starts to take over, this pattern becomes diagonal towards the WEC columns located at the sides of the WEC array for both sea states. This wave pattern, similar to that caused by the rectilinear WEC array, is a result of the increased wave height at the sides of the array, reaching up to the fifth row for long-crested irregular waves. For directional waves, increased wave height is found only at the sides of the front row (yet, for the rectilinear array, wave height increase is found up to the fourth row for swell directional waves). However, after the front row, wave height decrease is less at the sides compared to the central area of the array, as for the rectilinear array. Most importantly, for all sea states, the highest wave height dissipation is observed at locations, at least at distance $10D$ downwave of the WEC array, and within a zone of width $-5D < X < +5D$, observed also for the rectilinear array.

Extents of WEC array effects for different wave periods

When comparing long-crested waves of different peak wave periods, with regard to the extent of WEC array effects, several observations can be made.

o Diffracted wave field

Regarding the diffraction effect on the recorded undisturbed wave field (Figures 4.56(a-b) and 4.59(a-b)), the zone where wave height increase is observed for T_p =

1.26 s, is slightly wider compared to that for T_p = 1.18 s due to different wave reflection characteristics and due to change of wavelength compared to the WEC array spacing. For the rectilinear array, the opposite is observed (peak period T_p = 1.18 s results in at least 8.0 % higher wave height increase within the area of the WECs). As a conclusion from Figures 4.56(a-b) - 4.59(a-b), no large wave field variations between long-crested waves of T_p = 1.26 s and T_p = 1.18 s are observed. However, this is not confirmed for the rectilinear array, for which larger differences are found within the extents of the WEC array, indicating again a relationship between the wave period and the WEC array geometric layout.

o Radiated wave field

Concerning the radiation effect on the perturbed wave field due to damped response of the WEC units for different peak wave periods (Figures 4.56(c) and 4.59(c)), no large differences are observed in the resulting wave patterns. For the rectilinear array, however, large differences are observed; a clear lack of wave field symmetry for irregular long-crested waves of T_p = 1.18 s is found, compared to long-crested waves of T_p = 1.26 s. In the case of the staggered array, the effect of a peak wave period equal to the resonance period of the individual WEC units is smoothened due the array configuration. As conclusion from the above observations for Figures 4.56(c) and 4.59(c), no large wave field variations between long-crested waves of T_p = 1.26 s and T_p = 1.18 s, are found while the wave field symmetry is not significantly affected by a peak wave period close to the resonance period of a WEC unit. Also both wave periods result in similar wave height decrease (13.8 % – 15.1 %) along the central WEC column, while for the rectilinear array this wave height attenuation is limited to 6.0 %.

o Perturbed wave field

Concerning the effect on the recorded undisturbed wave field caused by the perturbed wave field around the WEC array due to different peak wave periods (Figures 4.56(d) and 4.59(d)), in the zone around the front row of WECs similar percentages of wave height increase are observed for both wave periods (slightly higher for T_p = 1.18 s). Also the wave patterns are similar, which though is not observed for the rectilinear array; there, a clear lack of symmetry for T_p = 1.18 s is found due to pronounced resonance effects. Moreover, increased wave height at the sides of the array is found, reaching up to the fourth row for long-crested irregular waves of T_p = 1.18 s (up to the fifth row for T_p = 1.26 s). Finally, downwave of the array wave height dissipation is observed within a similar area (within a zone of width - $5D$ < X < + $5D$ and at least $10D$ downwave of the array) with T_p = 1.26 s resulting to 4.7 % higher wave height dissipation.

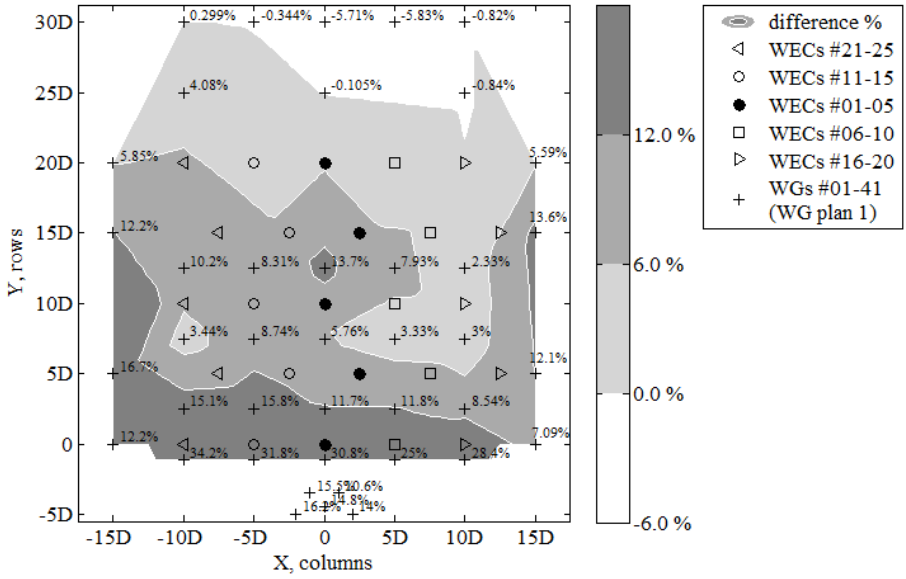

(a) Diffracted wave field normalized by recorded undisturbed wave field.

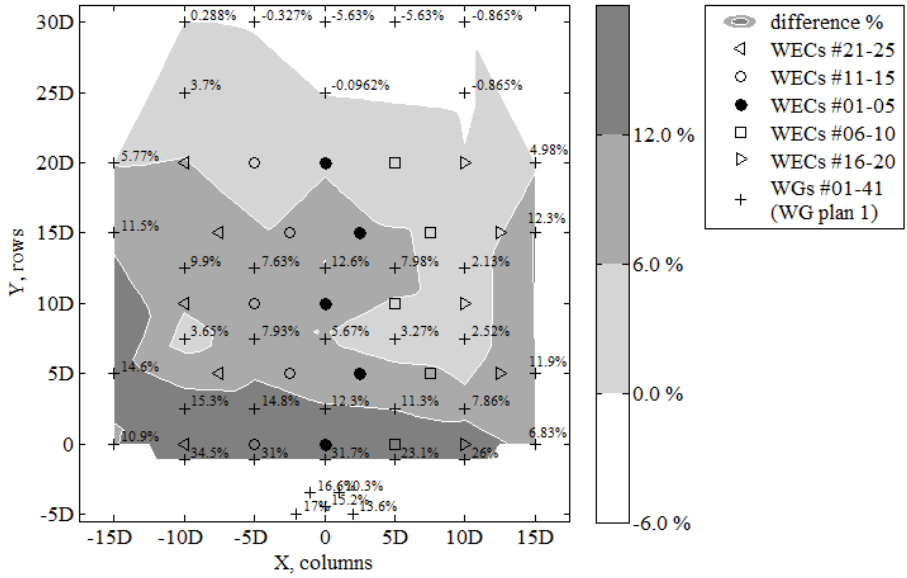

(b) Diffracted wave field normalized by target undisturbed wave field.

Figure 4.56. *Cont. Next Page*

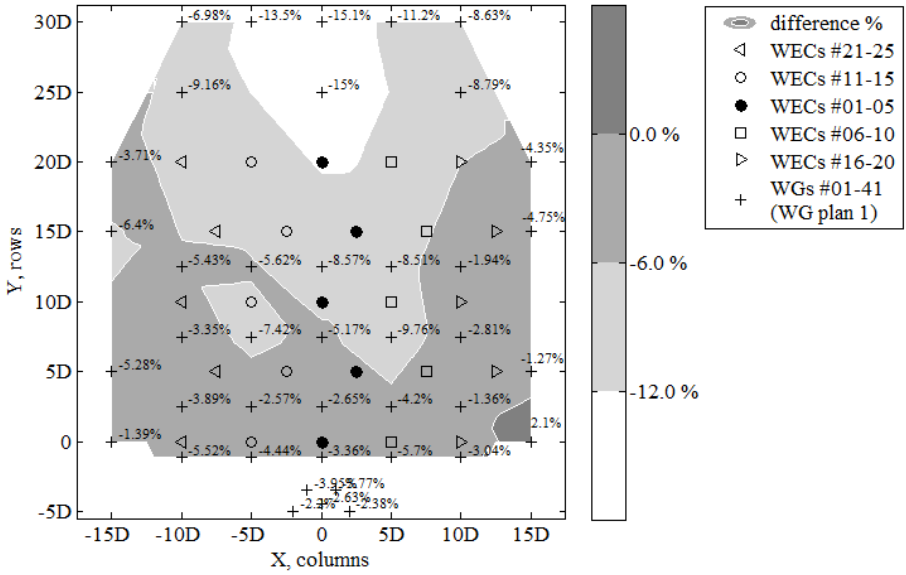

(c) Radiated wave field normalized by recorded undisturbed wave field.

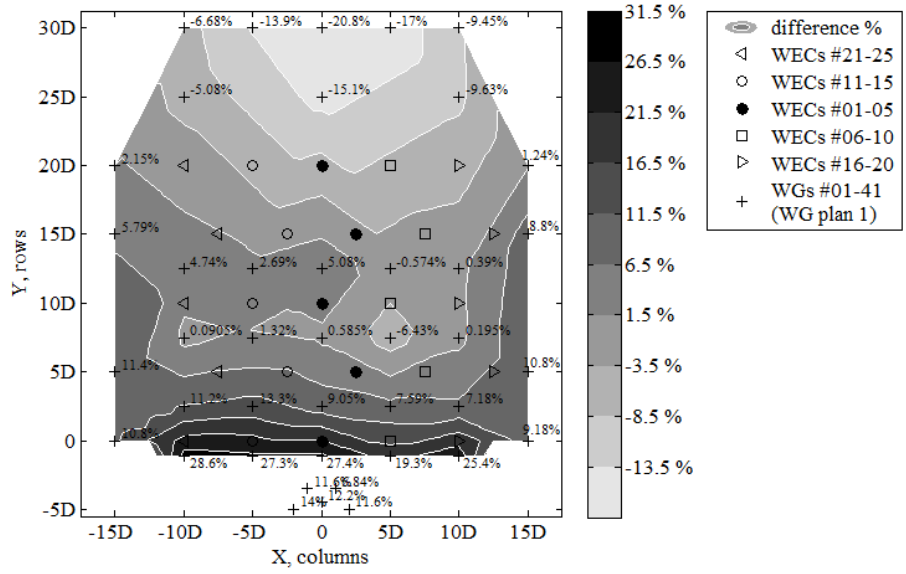

(d) Perturbed wave field normalized by recorded undisturbed wave field.

Figure 4.56. Non-dimensional percentage of change of H_{m0} at locations within and around the 5x5-WEC staggered array due to diffracted (stationary WECs), radiated (heaving WECs with damping applied) and perturbed wave field (heaving WECs with damping applied). Unidirectional irregular waves of T_p = 1.26 s and H_{m0} = 0.104 m. The basin width (X, columns) and length (Y, rows) are expressed in number of WEC unit diameters, D = 0.315 m.

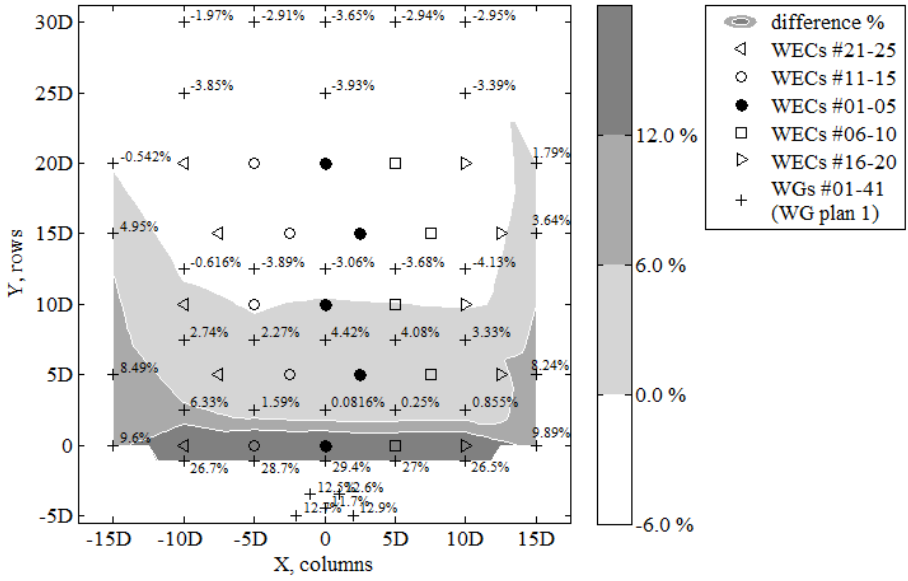

(a) Diffracted wave field normalized by recorded undisturbed wave field.

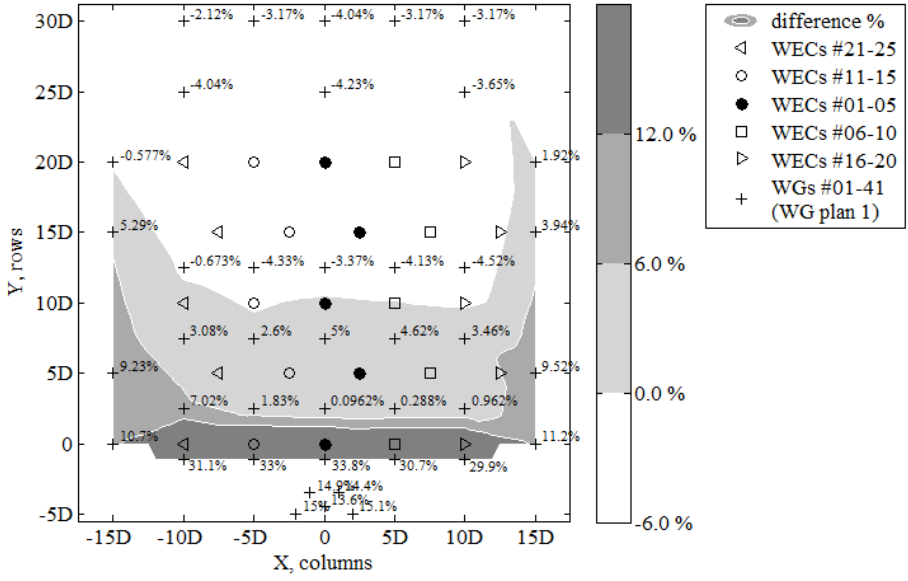

(b) Diffracted wave field normalized by target undisturbed wave field.

Figure 4.57. *Cont. Next Page*

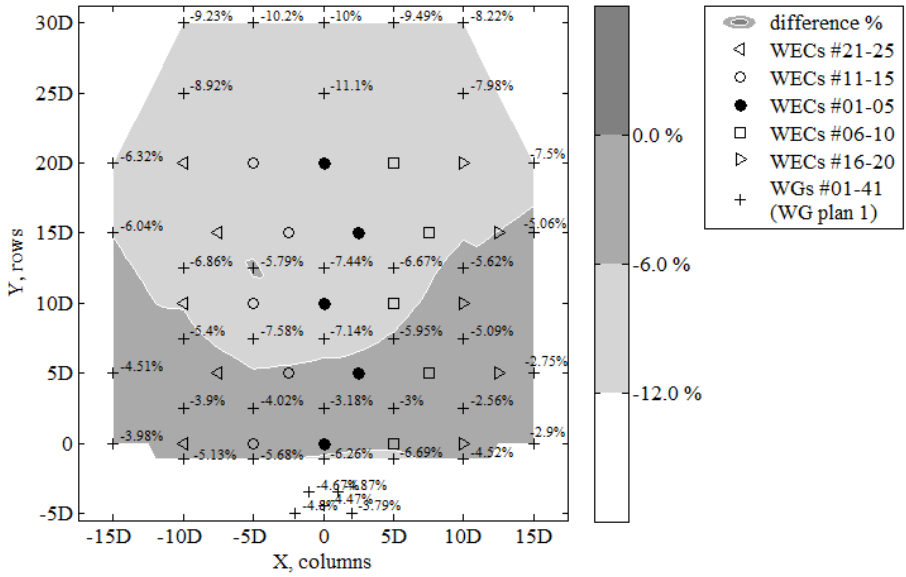

(c) Radiated wave field normalized by recorded undisturbed wave field.

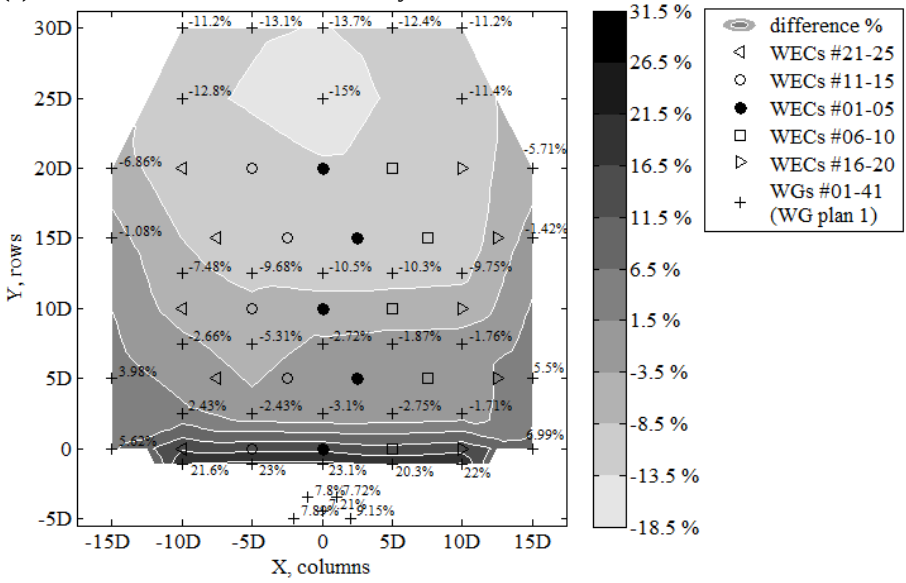

(d) Perturbed wave field normalized by recorded undisturbed wave field.

Figure 4.57. Non-dimensional percentage of change of H_{m0} at locations within and around the 5x5-WEC staggered array due to diffracted (stationary WECs), radiated (heaving WECs with damping applied) and perturbed wave field (heaving WECs with damping applied). Short-crested irregular waves of T_p = 1.26 s, H_{m0} = 0.104 m and spreading parameter, s =10. The basin width (X, columns) and length (Y, rows) are expressed in number of WEC unit diameters, D = 0.315 m.

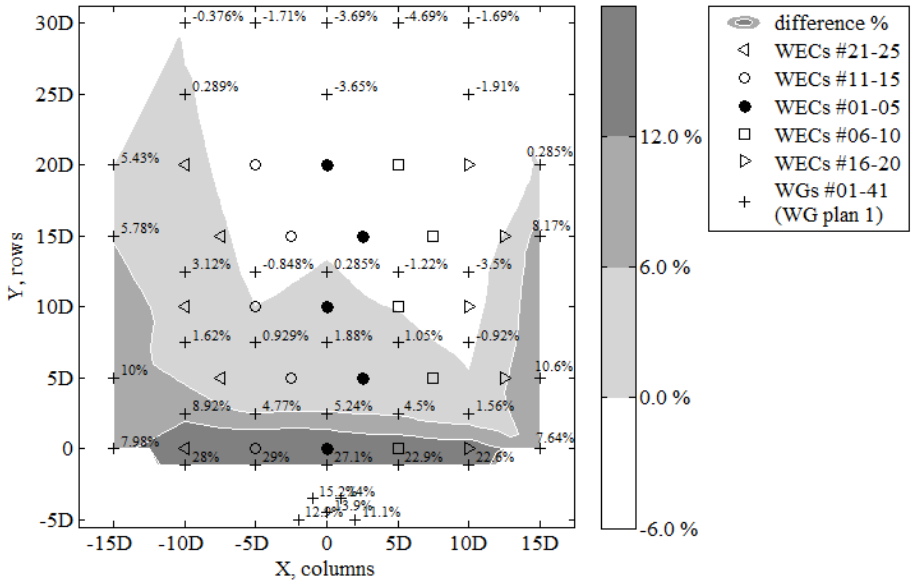

(a) Diffracted wave field normalized by recorded undisturbed wave field.

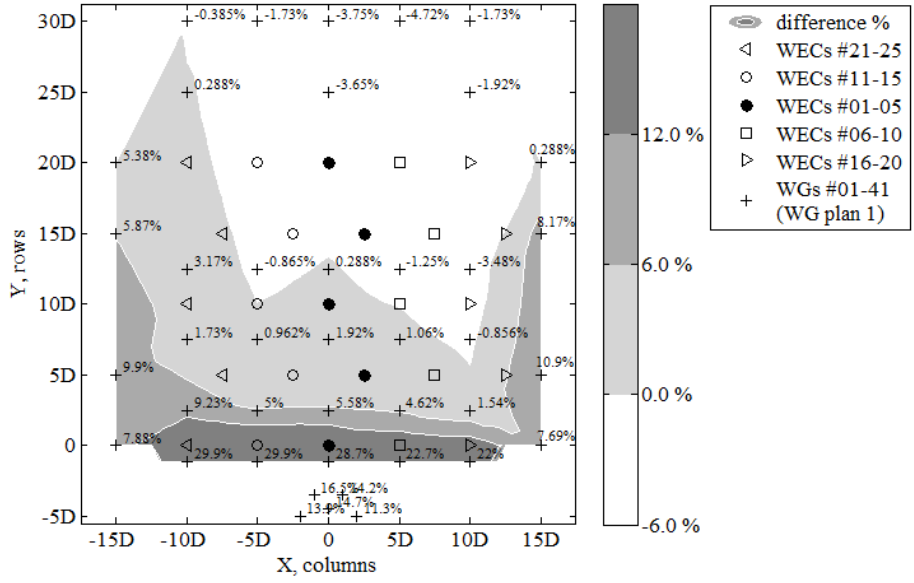

(b) Diffracted wave field normalized by target undisturbed wave field.

Figure 4.58. *Cont. Next Page*

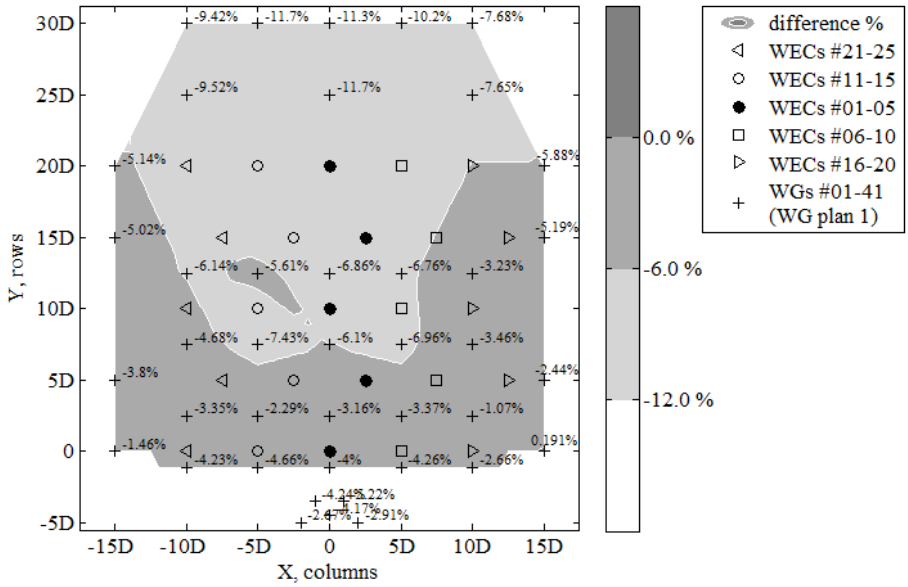

(c) Radiated wave field normalized by recorded undisturbed wave field.

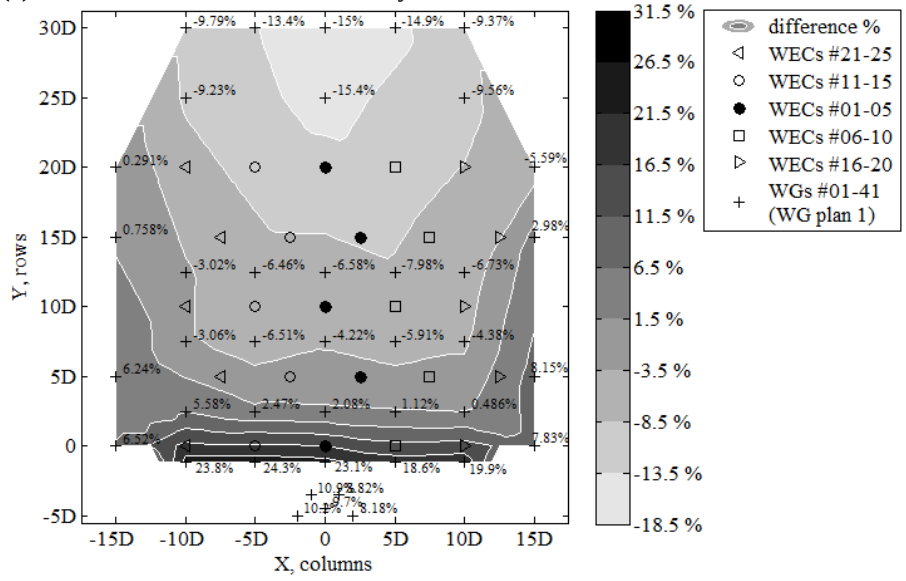

(d) Perturbed wave field normalized by recorded undisturbed wave field.

Figure 4.58. Non-dimensional percentage of change of H_{m0} at locations within and around the 5x5-WEC rectilinear array due to diffracted (stationary WECs), radiated (heaving WECs with damping applied) and perturbed wave field (heaving WECs with damping applied). Short-crested irregular waves of T_p = 1.26 s, H_{m0} = 0.104 m and spreading parameter, s = 75. The basin width (X, columns) and length (Y, rows) are expressed in number of WEC unit diameters, D = 0.315 m.

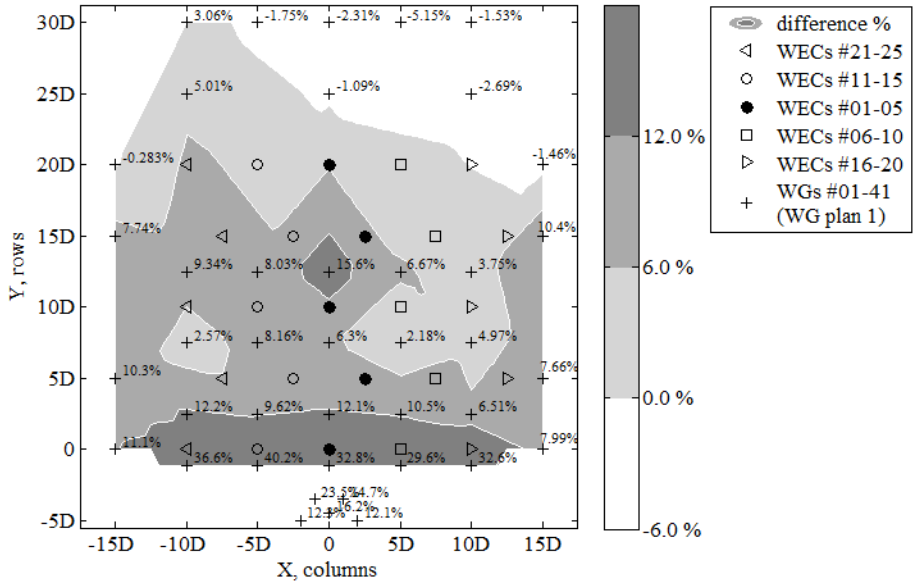

(a) Diffracted wave field normalized by recorded undisturbed wave field.

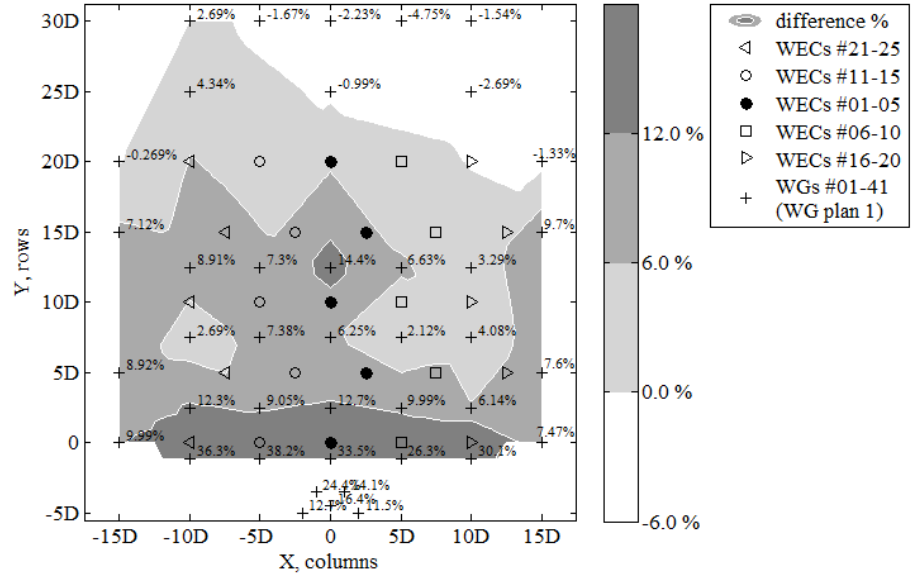

(b) Diffracted wave field normalized by target undisturbed wave field.

Figure 4.59. *Cont. Next Page*

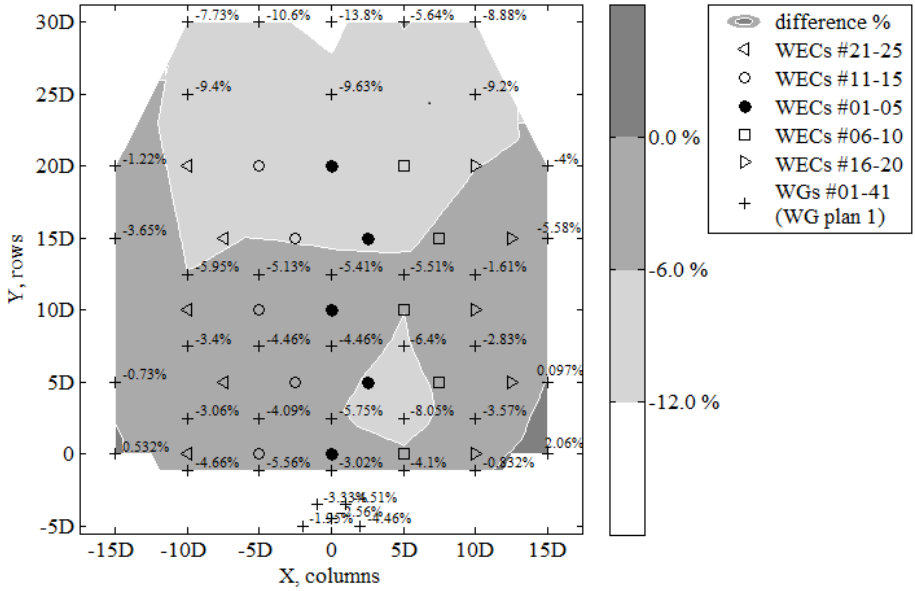

(c) Radiated wave field normalized by recorded undisturbed wave field.

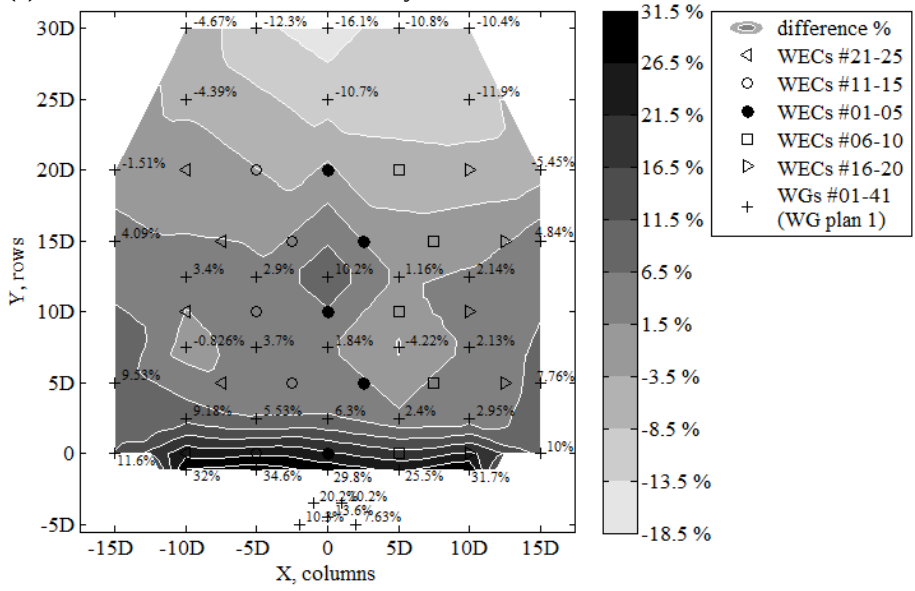

(d) Perturbed wave field normalized by recorded undisturbed wave field.

Figure 4.59. Non-dimensional percentage of change of H_{m0} at locations within and around the 5x5-WEC staggered array due to diffracted (stationary WECs), radiated (heaving WECs with damping applied) and perturbed wave field (heaving WECs with damping applied). Unidirectional irregular waves of T_p = 1.18 s and H_{m0} = 0.104 m. The basin width (X, columns) and length (Y, rows) are expressed in number of WEC unit diameters, D = 0.315 m.

4.6.9.1. Main observations on wave field modification around a 5x5-WEC staggered array

The wave field modifications due to wave energy extraction and the WECs' motion have been quantified for a 5x5-WEC staggered array, in terms of the non-dimensional percentage of change of H_{m0}, at locations within and around the array due to diffracted, radiated and perturbed wave field. The tested sea states have been also analysed in terms of spatial variation of the resulting wave height increase/reduction, and thus with regard to the extents of WEC array effects.

The accuracy of generating the target wave fields has been evaluated. For all presented results, the difference between recorded and target undisturbed wave field is shown not to be significant.

A comparison to the 5x5-WEC rectilinear array has been conducted, to investigate the effect of changing the WEC array geometric configuration, on the resulting wave fields and the WEC array effects.

o **Diffracted wave field:**

When considering only the calculated difference percentages, up to 5.83 %, 3.93 %, 4.69 % and 5.15 % of wave height decrease downwave, is found for irregular unidirectional waves of T_p = 1.26 s, short-crested wind waves, directional swell and unidirectional waves of T_p = 1.18 s, respectively. Due to the staggered rows, almost no significant difference in wave height reduction is found for the two tested wave periods. Larger differences are found between wind and long-crested irregular waves. Upwave of the front WEC row, local wave height increase is observed for all sea states. At downwave locations, when comparing the two considered WEC array configurations, wind waves result in the largest differences. Thus downwave of the 5x5-WEC staggered array, the effect of diffraction on the wave heights is not affected significantly for the long-crested waves, while for wind waves is reduced by a factor of 2.2 compared to the 5x5-WEC rectilinear array.

With regard to the extents of WEC array effects:

- Wave height decrease is observed already after the third row for short-crested waves, while for long-crested waves this decrease occurs only after a distance of $5D$ downwave of the last row of 5 WECs. For the 5x5-WEC rectilinear array, this decrease occurs earlier for short-crested waves (second row, and third to fourth row, for wind and swell directional waves, respectively).
- For all tests, the highest wave height increase is observed within the front row of five WECs, facing as first the incoming waves.

- The largest wave field variations between long- and short-crested wind waves are found between the zone downwave of the third row of WECs and at a distance $5D$ downwave of the last row of WECs (zone width = $15D$). For the 5x5-WEC rectilinear array, this zone width is $20D$, starting downwave of the second row of WECs.
- The swell directional waves do not result in a clearly intermediate situation with more similarities to the wind waves.
- The wave field evolution shows change from wave height increase to wave height decrease, almost "parallel" to the WEC rows, towards the opposite end of the wave basin (landwards). This observation is also made for the 5x5-WEC rectilinear array.
- No large wave field variations between irregular long-crested waves of T_p = 1.26 s and T_p = 1.18 s are observed. However, this is not confirmed for the rectilinear array, for which larger differences are found within the extents of the WEC array. This result indicates a relationship between the wave period and the WEC array geometric layout.

o **Radiated wave field:**

When considering only the calculated difference percentages, up to 15.10 %, 11.10 %, 11.70 % and 13.80 % of wave height decrease downwave, is observed for irregular unidirectional waves of T_p = 1.26 s, short-crested wind waves, directional swell and unidirectional waves of T_p = 1.18 s, respectively. The effect of varying the wave directionality parameter is rather limited, but when comparing long-crested to wind waves, larger differences are found. Moreover, as a result of T_p = 1.18 s being equal to the resonance period of a WEC unit, wave height attenuation downwave is smaller than for longer waves. At downwave locations, when comparing the two considered WEC array configurations, no significant differences are found for the majority of the sea states (only T_p = 1.18 s results in the largest differences).

With regard to the dimensions of WEC array effects:

- The largest wave field variations between irregular long- and short-crested waves are found for the zone between WEC rows 2 and 3, as well as within a distance of $10D$ downwave of the array.
- Short-crested waves result in less symmetric wave fields around the WECs, while the opposite is found for the rectilinear array.

- The wave field evolution shows change from wave height increase to wave height decrease, with a diagonal pattern towards the WEC columns located at the sides of the WEC array.
- No large wave field variations between long-crested waves of T_p = 1.26 s and T_p = 1.18 s are found, while the wave field symmetry is not significantly affected by a peak wave period close to the resonance period of a WEC unit; this effect is smoothened due the array configuration. For the rectilinear array, however, large differences are observed while a clear lack of wave field symmetry for long-crested waves of T_p = 1.18 s is found.

o **Perturbed wave field:**

When considering only the calculated difference percentages, up to 20.80 %, 15.00 %, 15.40 % and 16.10 % of wave height dissipation downwave, is observed for irregular unidirectional waves of T_p = 1.26 s, short-crested wind waves, directional swell and unidirectional waves of T_p = 1.18 s, respectively. Thus, this configuration results in around 15.0 % higher wave height attenuation downwave of the staggered WEC array for long-crested irregular waves, compared to the rectilinear array. A large, very localised wave height increase, ranging between 23.10 % and 34.60 % for all sea states, is found upwave of the front row of five WECs. Unlike for the 5x5-WEC rectilinear array, wave height reduction varies downwave of the array, for different sea states.

This larger wave height dissipation, compared to that caused by the rectilinear array, is also explained by the results for power output of the 5x5-WEC staggered array for irregular long-crested waves. Higher time-averaged power absorption and higher WEC array interaction factor, by almost 13.00 % is achieved by the staggered array compared to the rectilinear array, under the same wave conditions (see Section 4.6.3.2.1). For short-crested wind waves, wave height decrease is much smaller compared to that found for the long-crested waves, as well as to that found for wind waves for the rectilinear array (reduced by 21.0 %). This lower wave height attenuation is also explained by the power output analysis, resulting to lower time-averaged power absorption and lower WEC array interaction factor compared to: (i) the long-crested waves for the staggered array, and (ii) the rectilinear array under the same wave conditions, reduced by 11.54 % (see Sections 4.6.3.2.1 and 4.6.3.1.2, respectively). A larger difference is observed between long-crested waves of T_p = 1.26 s and T_p = 1.18 s for this WEC array configuration, which is not observed for the 5x5-WEC rectilinear array. This outcome supports the aspect that wave period influences the WEC array effects, related to the WEC array geometric layout.

Regarding the dimensions of WEC array effects:

- Wave height decrease is observed already after the front row of WECs for irregular short-crested waves, while for long-crested waves this decrease starts to take place only after the third row of 5 WECs. For the rectilinear array, swell directional waves result in similar wave pattern as for the long-crested irregular waves, also with regard to wave height increase at the sides of the array.
- For all sea states, the highest wave height increase is found upwave of the front row of 5 WECs (the first ones facing the incoming waves), as a result of significant diffraction effects.
- The largest wave field variations between irregular long- and short-crested waves (with s = 10) are found between the zone downwave of the front row and the last row of WECs and at a distance greater than 5D downwave of the WEC array (zone width = 25D), similar to the rectilinear array.
- For long-crested waves, wave height increase has a "parallel" pattern to the front WEC row. This pattern becomes diagonal towards the WEC columns located at the sides of the WEC array, and is result of increased wave height at the sides of the array. For short-crested waves, increased wave height is found only at the sides of the front row (yet, wave height reduction is smaller at the sides of the entire array).
- For all sea states, the highest wave height dissipation is observed at locations, at least at distance 10D downwave of the WEC array, and within a zone of width - 5D < X < + 5D, similarity to the rectilinear array.
- Wave patterns are similar for both studied peak wave periods. This is not observed for the rectilinear array where a clear lack of symmetry for T_p = 1.18s is found, due to pronounced resonance effects for this WEC array configuration.

4.6.10. Wave field modification around a 13-WEC staggered array

In this section, the wave field modifications due to wave energy extraction and the WECs' motion have been quantified, around a 13-WEC staggered array, illustrated in Figure 4.60.

For the 13-WEC staggered array, both the lateral, w, and the longitudinal, l, spacing between the WECs, respectively, is twice as large as for the staggered and rectilinear 5x5-WEC arrays; thus $w = 10D$ between the WEC units of the same row, and $l = 10D$ between the WEC units of the same column. The results obtained from the 13-WEC staggered array are compared to the results obtained for the 5x5-WEC staggered array, as both arrays have the same number of rows (5) and columns (5). The objective of this comparison is to quantify the effect of modifying the spacing between the WECs (and the WEC number within an array) on the resulting WEC array effects for a staggered WEC array geometric configuration.

The difference percentage terms have been calculated and plotted in Figures 4.61-4.64 for the WEC array, using Equations 4.5 – 4.8. The measured change of the wave field for unidirectional irregular waves, is presented separately for the diffracted (Figures 4.61(a-b) and 4.64(a-b)), the radiated (Figures 4.61(c) and 4.64(c)) and the perturbed (Figures 4.61(d) and 4.64(d)) wave field, for T_p = 1.26 s and T_p = 1.18 s, respectively. Similarly, Figures 4.62(a-d) and 4.63(a-d) present the wave fields for the short-crested waves with spreading parameter, s = 10 and s = 75, respectively.

Figure 4.60. The 13-WEC staggered array under irregular short-crested waves. 13 WECs are interacting with the waves, while the rest 12 WEC units are held stationary above the water surface. View from the control platform location.

Quantifying the effect of the wave directionality on WEC array effects

Firstly, sea states of the same peak period (T_p = 1.26 s) are discussed, to investigate the effect of the wave directionality on the resulting wave fields, due to the WECs' motion and power extraction. Moreover, the results obtained for the 13-WEC staggered array are compared to results obtained for the 5x5-WEC staggered array from the previous section, in order to quantify the effect of changing the spacing between the WECs in a geometric configuration (and the WEC number).

o Diffracted wave field

For unidirectional waves of T_p = 1.26 s, a wave height decrease ranging between 5.34 % and 5.90 % is found downwave, very similar to the 5x5-WEC staggered array (up to 5.83 %). Also 29.90 % wave height increase upwave is observed (34.20 % for the 5x5-WEC staggered array) when the 13 WEC units are held stationary at mean draft, d_{buoy} (Figure 4.61(a)). However, this wave height increase remains very localised (in front of the WECs) and does not extend in-between them (there, this increase reduces to maximum 9.23 %), in contrast to the previous arrays of $w = l = 5D$. For wind short-crested waves (s = 10), wave height decrease at downwave locations does not become larger than 4.95 % (for the 5x5-WEC staggered array up to 3.93 %). The increase upwave reaches locally in front of the WECs 23.20 % (29.40 % for the 5x5-WEC staggered array) (Figure 4.62(a)), reducing to maximum 4.49 % in-between the devices, similarly to the long-crested waves. For swell short-crested waves (s = 75), wave height decrease downwave, reaches 5.45 % (4.69 % for the 5x5-WEC staggered array), while the increase upwave of the WEC units reaches 24.00 % (29.00 % for the 5x5-WEC staggered array) (Figure 4.63(a)), very similar to the wind waves. These percentages differ slightly in Figure 4.61(b) where the recorded wave heights are normalized by the target wave height H_{0i} (at the same WG locations, 6.15 % of wave height decrease downwave, and 27.40 % wave height increase upwave, respectively). Also for short-crested waves, these percentages show small variation, with a wave height decrease downwave up to 5.38 % and an increase upwave reaching 26.20 % for s = 10 (Figure 4.62(b)). Wave height decrease downwave reaches 5.45 % (no change for s = 75) and the increase upwave reaches 23.5 % for s = 75 (Figure 4.63(b)).

o Radiated wave field

When looking at the effect of the WECs on the wave field due to radiation only, for long-crested waves of T_p = 1.26 s (Figure 4.61(c)) approximately 5.65 % to 7.77 % wave height decrease is observed downwave of the WEC array (15.10 % for the 5x5-WEC staggered array). Up to 5.31 % increase is found upwave (5.70 % for the 5x5-WEC staggered array). For short-crested waves with s = 10 (Figure 4.62(c)), the

effect of radiation is very small downwave of the array, where maximum 1.52 % wave height decrease is observed (11.10 % for the 5x5-WEC staggered array). Upwave, the situation is different compared to long-crested waves, as the wave heights show only increase of up to 5.17 % directly upwave of the front row of three WECs (however, decrease of 4.52-6.69 % is found for the 5x5-WEC staggered array). For the long-crested waves, a mixed situation of both wave height increase and decrease is found upwave of the front WEC row (+5.31 % and -4.05 %, respectively). Closer to the wave paddles, similar wave height increase is observed for both sea states (long-crested and wind waves) with up to 5.81 % and 8.31 % increase, for wind and long-crested waves, respectively. However, for the 5x5-WEC staggered array these wave field changes result in 4.87 % (wind waves) and 3.95 % (long-crested waves) wave height decrease, closer to the wave paddles. Moreover, for short-crested swell waves with $s = 75$ (Figure 4.63(c)), the effect of radiation represents an intermediate situation between irregular long-crested and wind waves, with wave height decrease of 3.55 % downwave of the array (11.70 % for the 5x5-WEC staggered array). Directional swell waves result in a not significantly wider area of wave height increase, compared to wind waves. The wave heights increase by 6.28 % directly upwave of the front row of three WECs (however, decrease of 4.66 % is found for the 5x5-WEC staggered array). Closer to the wave paddles, again, a limited wave height increase of 7.68 % is observed (up to 4.24 % for the 5x5-WEC staggered array). For wind waves, no large differences are observed between the wave field recorded by a WG in the vicinity of a WEC unit and by a WG in an in-between distance, i.e. at a $5D$ distance from the WEC unit. However, for irregular long-crested and swell waves such differences are present; these are, yet, less pronounced compared to those found for the diffracted wave field.

o Perturbed wave field

As presented in Figures 4.61(d) - 4.63(d) for the perturbed wave field, there is wave height attenuation in the lee of the WEC array due to the operation of the heaving WEC units. This attenuation is not as significant as for the 5x5-WEC staggered array with $w = l = 5D$ spacing between the WECs. For the 5x5-WEC staggered array a large wave height decrease of up to 20.80 % is found downwave, while for the 13-WEC staggered array, wave height attenuation is found to be at least by a factor of two smaller (between 7.56 % and 11.6 %) (Figure 4.61(d)). Furthermore, up to 30.3 % wave height increase upwave of each of the three front WECs (up to 28.60 % along the entire front WEC row of the 5x5-WEC staggered array). This wave height increase is very localised, in front of the WECs, and does not extend in-between them (there, this increase reduces to maximum 7.33 %), in contrast to the previous arrays of $w = l = 5D$. For short-crested wind waves, wave height decrease ranges between 3.25 % and 5.99 % and is by a factor of two smaller,

compared to that found for the irregular long-crested waves. Compared to the wave height dissipation found for the 5x5-WEC staggered array (ranging between 13.70 % and 15.00 %), wave height reduction found for the 13-WEC staggered array is 2.5 times lower. Most importantly, wave height recovery is observed already after a distance of 5D downwave of the last WEC row, which is half of the spacing between the WECs, $w = l = 10D$. As a result, the wave heights at a distance 10D downwave of the WEC array, start to become higher, as recorded along the entire row of WGs with X= -10D to +10D and Y= 30D. Upwave of the front row of three WECs, 24.90 % very localised wave height increase is observed (23.10 % for the 5x5-WEC staggered array), lower compared to the unidirectional waves. This wave height increase reduces to maximum 7.29 % in-between the WECs. For short-crested swell waves, wave height decrease downwave of the array is found to be in the same magnitude of irregular long-crested waves, but smaller (up to 7.72 %). Similarly to wind waves, wave directionality results also for short-crested swell waves, in wave height recovery at the same distances downwave of the WEC array. Upwave of the front row of three WECs, 27.40 % very localised wave height increase is observed similarly to the wind waves (24.30 % for the 5x5-WEC staggered array). Unlike for the 5x5-WEC staggered array, here swell directional waves represent a clear intermediate situation between long-crested and wind waves (of the same peak wave period) for the perturbed wave field around the WECs. Consequently, a large spacing between the WECs limits extra-array effects, especially when the waves are directional.

Quantifying the effect of different wave periods on WEC array effects

- Diffracted, radiated and perturbed wave field

Regarding the results from two different peak wave periods for irregular unidirectional waves, T_p = 1.18 s results in 6.6 % of wave height decrease downwave (5.83 % for T_p = 1.26 s, and 5.15 % for T_p = 1.18 s for the 5x5-WEC staggered array). Up to 32.6 % wave height increase upwave is observed (29.9 % for T_p = 1.26 s, and 40.2 % for T_p = 1.18 s for the 5x5-WEC staggered array) when the 13 WEC units are held stationary at mean draft, d_{buoy} (Figure 4.64(a)). In-between the WECs of the front row, this wave height increase reduces to maximum 15.00 % (9.23 % for T_p = 1.26 s). This difference in wave height reduction between the WECs indicates a relationship between wave period and spacing between the WECs, influencing the intra-array interactions. Moreover, when waves of shorter wavelength (for T_p = 1.18 s) propagate through the WEC array, wave height recovery is observed already after a distance of 5D downwave of the last WEC row, similarly to irregular short-crested waves of T_p = 1.26 s.

These percentages differ slightly in Figure 4.64(b) where the recorded wave heights are normalized by the target wave height H_{0i} (at the same WG locations, 6.61 % of wave height decrease downwave, and 32.20 % wave height increase upwave, respectively). When looking at the effect of the WECs on the wave field due to radiation only, in Figure 4.64(c) approximately a range of 1.29 % to 5.72 % wave height decrease is observed downwave of the WEC array (5.65 % to 7.77 % for T_p = 1.26 s, and 13.8 % for T_p = 1.18 s for the 5x5-WEC staggered array). Upwave, a decrease of up to 14.30 % is found (5.31 % for T_p = 1.26 s, but 5.56 % increase for the 5x5-WEC staggered array). However, both wave height increase and decrease patterns alternate for the case of T_p = 1.18 s, as this peak wave period is equal to the natural period of a WEC unit. The perturbed wave field of Figure 4.64(d) shows similar wave height attenuation in the lee of the WEC array, compared to the waves of T_p = 1.26 s (ranging between 5.44 % to 11.6 %) and is found to be widely ranging between 2.51 % and 13.40 % (16.10 % for the 5x5-WEC staggered array), again due to "close to" resonance conditions. Therefore, regarding the presented percentages, no significant difference is observed between irregular long-crested waves of T_p = 1.26 s and T_p = 1.18 s. With regard to the resulting wave field patterns, the effect of resonance conditions is visible. This is not confirmed, though, for waves of T_p = 1.18 s, propagating through the 5x5-WEC staggered array.

Extents of WEC array effects for varying wave directionality

When comparing long- to short-crested waves, with regard to the extent of WEC array effects, the following findings are described.

o Diffracted wave field

Regarding the diffraction effect on the recorded undisturbed wave field (Figures 4.61(a) - 4.63(a)), the zone where wave height increase larger than 12.0 % is observed, is for all sea states very localized (only in front of the first WEC row). For the 5x5-WEC staggered array this zone is much wider and extends from the entire front WEC row to almost the second row, for long-crested waves, while includes the entire front row for short-crested waves (of the same T_p). For short-crested waves, also wave height increase 6.0 - 12.0 % is found to be a local effect around the front WECs, both for the 5x5- and the 13-WEC staggered arrays. However, for the long-crested waves, 6.0 - 12.0 % wave height increase is found in a larger area within the array; for the 5x5-WEC staggered array it extends up to the fifth WEC row (and up to 6.0 % extending at 10D downwave of the array), and for the 5x5- and the 13-WEC staggered arrays up to the fourth row (and up to 6.0 % by the fifth row).

Consequently, wave height decrease is observed already after the front row of three WECs for short-crested waves (after the third row of five WECs for the 5x5-

WEC staggered array). For long-crested waves this decrease occurs only after the fourth to the fifth row of WECs (after a distance of 5*D* downwave of the last row of 5 WECs for the 5x5-WEC staggered array). The order of magnitudes of the maximum percentages found for wave height decrease and increase when looking at the same locations/distances upwave or downwave of the array, are, nevertheless, very similar for all sea states. As conclusion from the above observations for Figures 4.61(a)-4.63(a), the largest wave field variations between long- and short-crested waves are found within the zone downwave of the front row of WECs and upwave of the fifth row of WECs (within the zone downwave of the third row of WECs and at a distance 5*D* downwave of the last row of WECs, for the 5x5-WEC staggered array). Therefore, compared to the 5x5-WEC staggered array, this zone of variations has been moved upwave. Also, this zone of variations between short- and long-crested waves has a length shorter than the length of the WEC array (20*D*). The swell directional waves result in an intermediate situation similar to the rectilinear array, which is not confirmed for the 5x5-WEC staggered array. The same conclusions can be made when comparing Figures 4.61(b) - 4.63(b). Also, note that the differences presented in Figures 4.61(a-b) - 4.63(a-b) are progressing from positive (wave height increase) to negative (wave height decrease), towards the opposite end of the wave basin (landwards). The same observation is made for the diffracted wave field by 5x5-WEC arrays, but in these cases, the wave field evolution has a "parallel" pattern to the WEC rows, which is not found when the WEC spacing becomes twice as large.

- Radiated wave field

Regarding the radiation effect on the perturbed wave field due to damped response of the WEC units for the same peak wave period (Figures 4.61(c) - 4.63(c)), wave height increase is observed for all sea states. However, for the 5x5-WEC staggered array, no wave height increase is observed for all sea states. The order of magnitudes of the maximum percentages found for wave height decrease when looking at the same distances downwave of the array, are very similar for all wave types. As conclusion from the above observations for Figures 4.61(c) - 4.63(c), the largest wave field variations between long- and short-crested waves are found for the area within the WEC array (for the 5x5-WEC staggered array, for the zone between WEC rows 2 and 3, as well as within a distance of 10*D* after the last WEC row and especially downwave of the middle WEC column). The long-crested waves result in less symmetric wave fields around the WECs, similar to the 5x5-WEC rectilinear array, while the opposite is found for the 5x5-WEC staggered array. Also, note that the differences presented in Figures 4.61(c) - 4.63(c) are progressing from smaller to higher wave height decrease, towards the opposite end of the wave basin

(landwards). The wave field pattern is diagonal towards the WEC columns located at the sides of the WEC array, similarly to both 5x5-WEC arrays.

o Perturbed wave field

Regarding the effect on the recorded undisturbed wave field caused by the perturbed wave field around the WEC array (Figures 4.61(d) - 4.63(d)), the zone where wave height increase is observed for short-crested waves, is limited (it stops before the end of the WEC array) and is comparable to that for irregular long-crested waves. On the contrary, for the 5x5-WEC staggered array there is a clear difference between short- and long-crested waves. Consequently, wave height decrease is observed only after the third row of WECs for short-crested waves (already after the front row of WECs for the 5x5-WEC staggered array), while for long-crested waves this decrease occurs after the fourth row of three WECs (after the third row of 5 WECs for the 5x5-WEC staggered array). In the case of the 13-WEC staggered array, the magnitude of wave height decrease/increase at the same locations is very similar for all sea states, as for the rectilinear array. However, for the 5x5-WEC staggered array, the maximum percentages found for wave height decrease and increase when looking at the same locations/distances upwave or downwave of the array, differ by at least 5.80 %, between long- and short-crested waves. Responsible for these small differences between extra-array effects caused by irregular long- and short-crested waves for the 13-WEC staggered array, is the large spacing between the WECs. As conclusion from the above observations for Figures 4.61(d) - 4.63(d), the largest wave field variations between irregular long- and short-crested waves are found between the zone downwave of the front row of WECs and the last row of WECs, but not much at a distance greater than $5D$ downwave of the WEC array, as found for 5x5-WEC staggered array. Most importantly, the wave field in the distances in-between the WECs shows large variations and indicates wave height recovery between the WECs. This wave recovery is observed both in the lateral and longitudinal direction of the wave basin. Also, the wave height dissipation is mostly observed at a distance of about $5D$ downwave of the WEC array, and is not maintained at a distance of $10D$ downwave of the array. For the 13-WEC staggered array wave recovery is observed at a distance of $10D$ downwave of the last row of WECs. Also, note that the differences presented in Figures 4.61(d) - 4.63(d) for wave height increase between 8.00 % and 31.50 %, are not progressing "parallel" to the front WEC row towards the opposite end of the wave basin (landwards), as it occurs for the 5x5-WEC staggered array. This increase is local and is not maintained between the WECs due to the large spacing. When wave height attenuation starts to take over, the pattern of the differences for both sea states becomes diagonal towards the WEC columns located at the sides of the WEC array. This wave pattern is a result of the increased wave height at the sides of the array, reaching up to the fourth

row for long-crested irregular waves (up to the fifth for the 5x5-WEC staggered array), up to the third row for swell directional waves and up to the second row for wind waves. Note that for the 5x5-WEC staggered array and for both directional sea states, wave height increase at the sides is observed only for the front row, due to the smaller spacing between the WECs. Moreover, in particular for irregular long-crested waves, this wave height increase at the sides of the rows is not symmetric due to the shifted layout of the array (also found for the 5x5-WEC staggered array). Most importantly, for all sea states, the highest wave height dissipation is observed within a zone of width - $5D$ < X < + $5D$, at distance $5D$ downwave of the WEC array (at $10D$ for the 5x5-WEC staggered array), wave height recovery is observed for all sea states at locations at distance $10D$ downwave of the WEC array. In addition, wave height increase successes wave height decrease with repetition, in the lateral direction of the wave basin for long-crested irregular waves of T_p = 1.26 s, which leads to the conclusion that wave recovery occurs at both directions within these large distances in-between the WECs.

Extents of WEC array effects for different wave periods

When comparing long-crested waves of different peak wave periods, with regard to the extent of WEC array effects, the following observations can be made.

- Diffracted wave field

Regarding the diffraction effect on the recorded undisturbed wave field (Figures 4.61(a-b) and 4.64(a-b)), the zone where wave height increase is observed for T_p = 1.26 s is slightly smaller. This is observed especially for wave height increase larger than 12.0 % around the front WECs facing the incoming waves, compared to that for T_p = 1.18 s (similar to the 5x5-WEC rectilinear array). This is due to different wave reflection characteristics and due to change of wavelength compared to the WEC array spacings, while for the 5x5-WEC staggered array the opposite is observed. As conclusion from the above on Figures 4.61(a-b) - 4.64(a-b), no large wave field variations between irregular long-crested waves of T_p = 1.26 s and T_p = 1.18 s are found, besides in the area around the front WECs (this is also found for the 5x5-WEC staggered array).

- Radiated wave field

Regarding the radiation effect on the perturbed wave field due to damped response of the WEC units for different peak wave periods (Figures 4.61(c) and 4.64(c)), again no large differences are observed in the resulting wave patterns, similarly to the 5x5-WEC staggered array. As conclusion from Figures 4.61(c) and

4.64(c), no large wave field variations occur between irregular long-crested waves of T_p = 1.26 s and T_p = 1.18 s. However, no wave field symmetry is observed, affected by a peak wave period equal to the resonance period of a WEC unit. Also both wave periods result in similar levels of wave height decrease downwave (average around 7.0 %).

o Perturbed wave field

Concerning the effect on the recorded undisturbed wave field caused by the perturbed wave field around the WEC array due to different peak wave periods (Figures 4.61(d) and 4.64(d)), in the zone around the front row of WECs, higher wave height increase is observed for T_p = 1.18 s (also the 5x5-WEC staggered array resulted in (slightly) higher increase for T_p = 1.18 s). Downwave of the array, wave height dissipation is observed within an area of similar extents, while the wave patterns for both wave periods are similar. Moreover, wave height increase successes wave height decrease with repetition, in the lateral direction of the wave basin for T_p = 1.18 s, which is observed also for T_p = 1.26 s; this leads to the conclusion that wave recovery occurs at both directions within the in-between distances of the WECs. Finally, also for T_p = 1.18 s, the wave height is increased at the sides of the array (yet, no symmetry is observed).

As a result, for a twice as large spacing between the WECs no significant differences are observed between the two tested peak periods. This finding indicates that a large enough spacing leads to a geometric configuration, less dependent on the wavelength of the incoming waves.

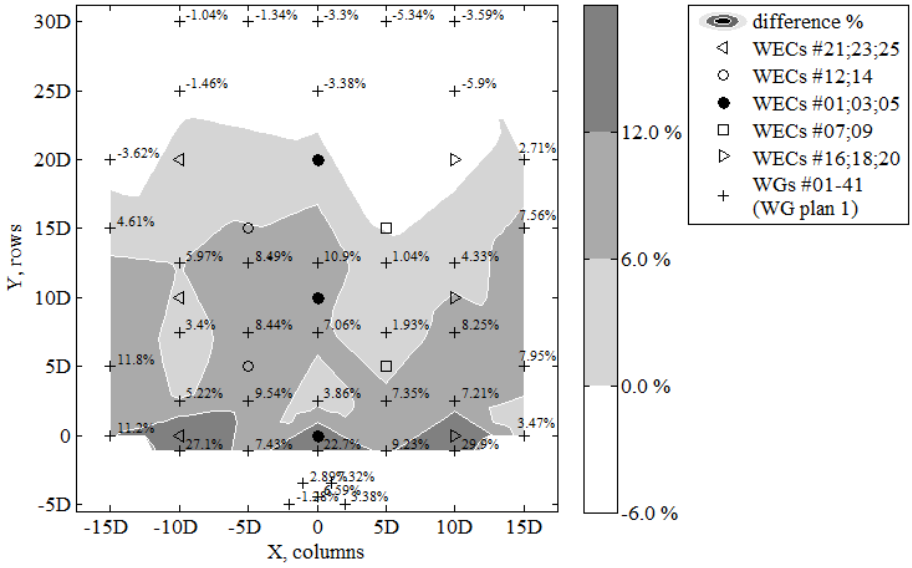

(a) Diffracted wave field normalized by recorded undisturbed wave field.

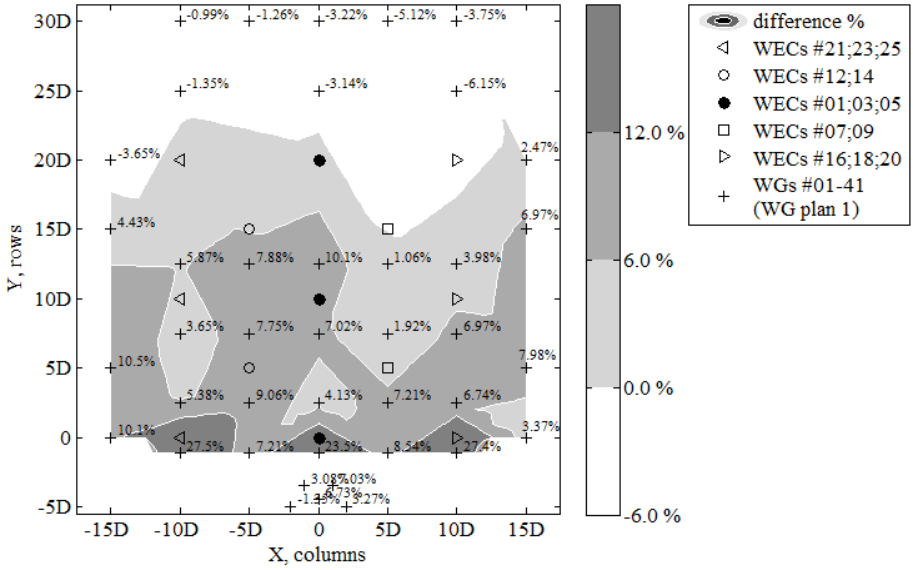

(b) Diffracted wave field normalized by target undisturbed wave field.

Figure 4.61. *Cont. Next Page*

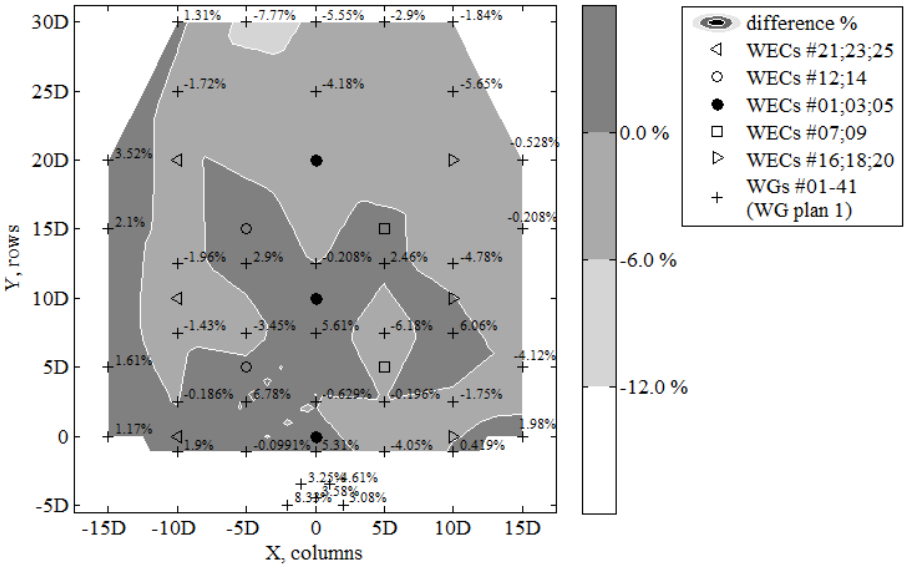

(c) Radiated wave field normalized by recorded undisturbed wave field.

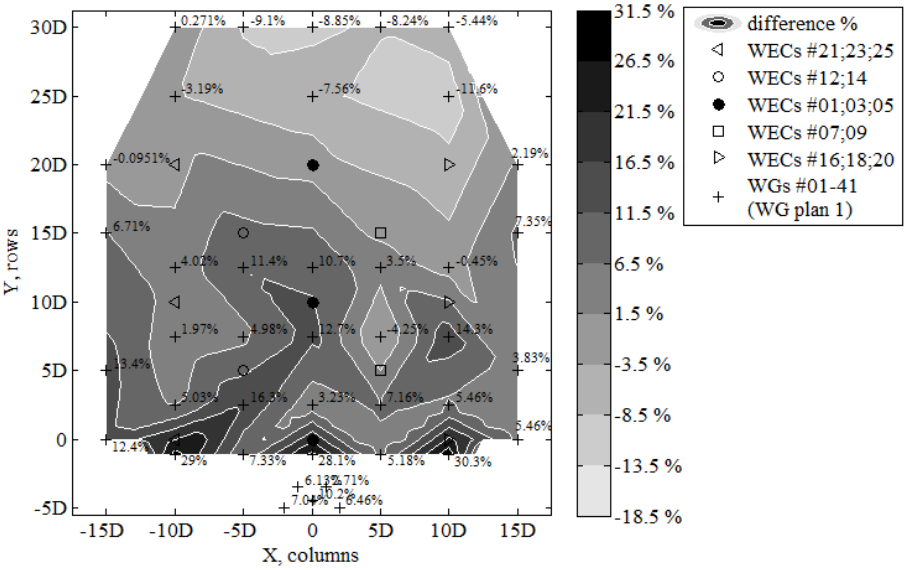

(d) Perturbed wave field normalized by recorded undisturbed wave field.

Figure 4.61. Non-dimensional percentage of change of H_{m0} at locations within and around the 13-WEC staggered array due to diffracted (stationary WECs), radiated (heaving WECs with damping applied) and perturbed wave field (heaving WECs with damping applied). Unidirectional irregular waves of T_p = 1.26 s and H_{m0} = 0.104 m. The basin width (X, columns) and length (Y, rows) are expressed in number of WEC unit diameters, D = 0.315 m.

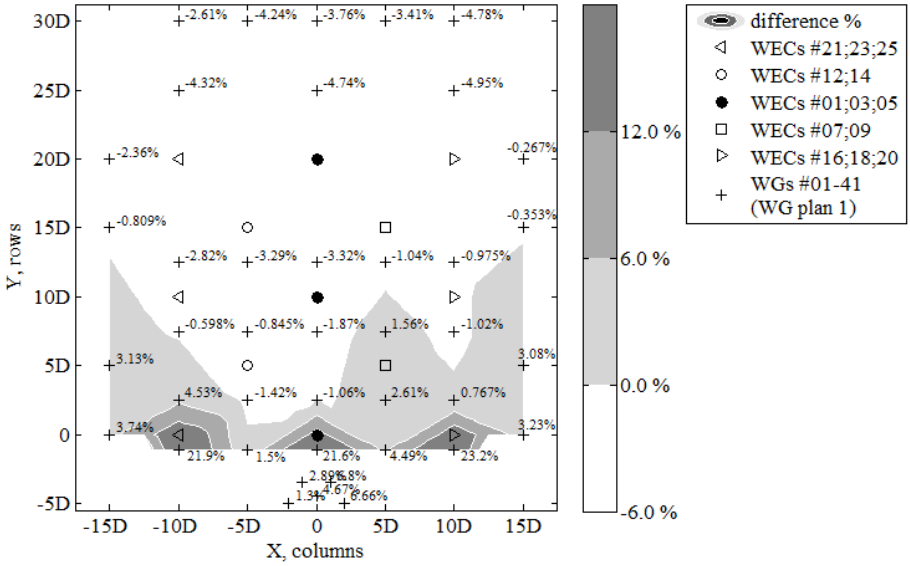

(a) Diffracted wave field normalized by recorded undisturbed wave field.

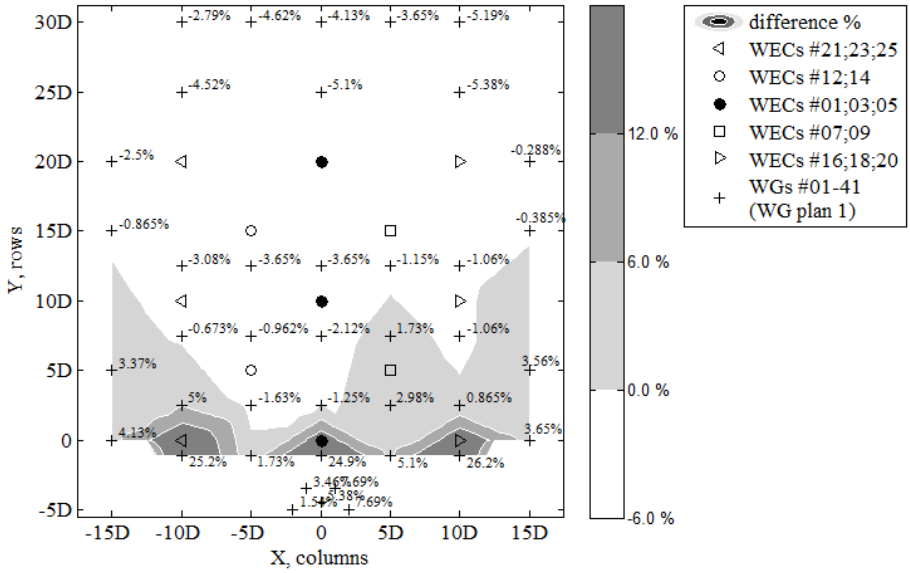

(b) Diffracted wave field normalized by target undisturbed wave field.

Figure 4.62. *Cont. Next Page*

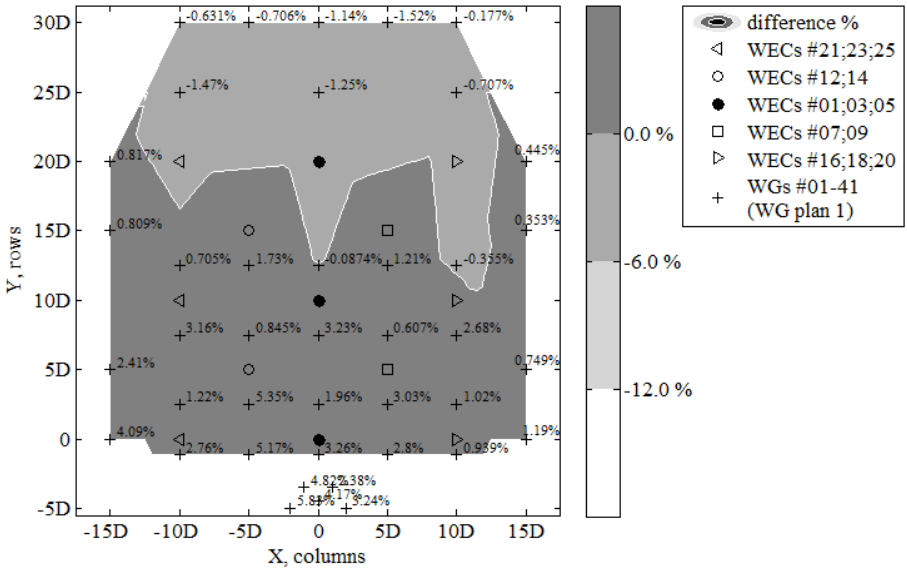

(c) Radiated wave field normalized by recorded undisturbed wave field.

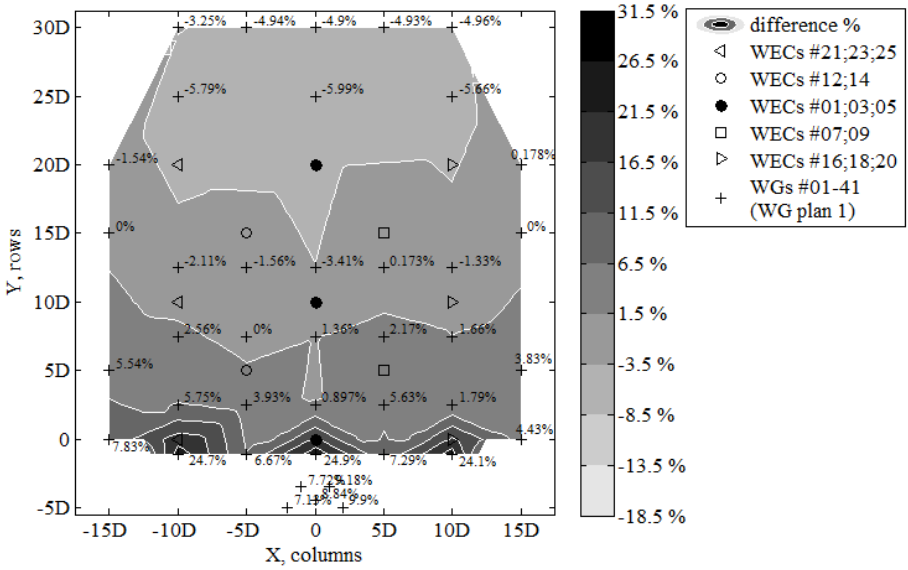

(d) Perturbed wave field normalized by recorded undisturbed wave field.

Figure 4.62. Non-dimensional percentage of change of H_{m0} at locations within and around the 13-WEC staggered array due to diffracted (stationary WECs), radiated (heaving WECs with damping applied) and perturbed wave field (heaving WECs with damping applied). Short-crested irregular waves of T_p = 1.26 s, H_{m0} = 0.104 m and spreading parameter, s =10. The basin width (X, columns) and length (Y, rows) are expressed in number of WEC unit diameters, D = 0.315 m.

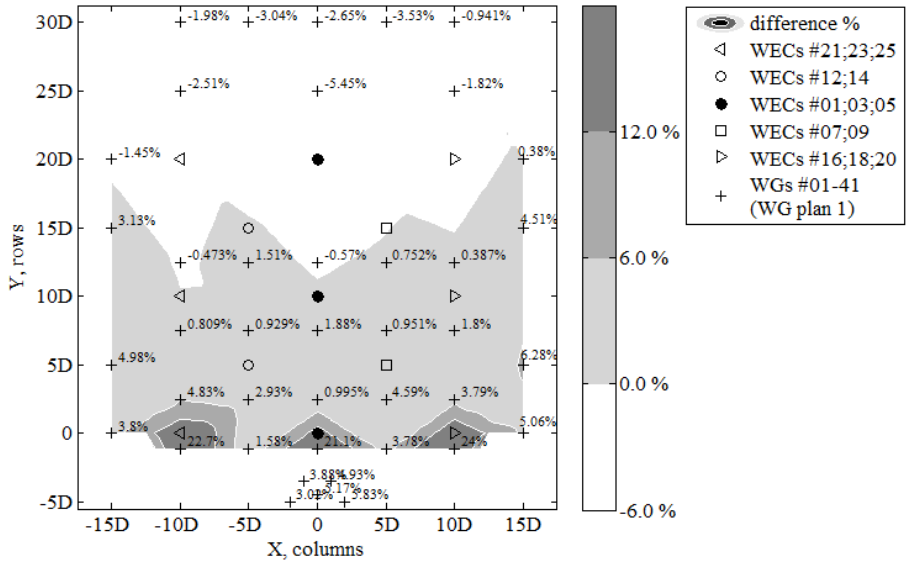

(a) Diffracted wave field normalized by recorded undisturbed wave field.

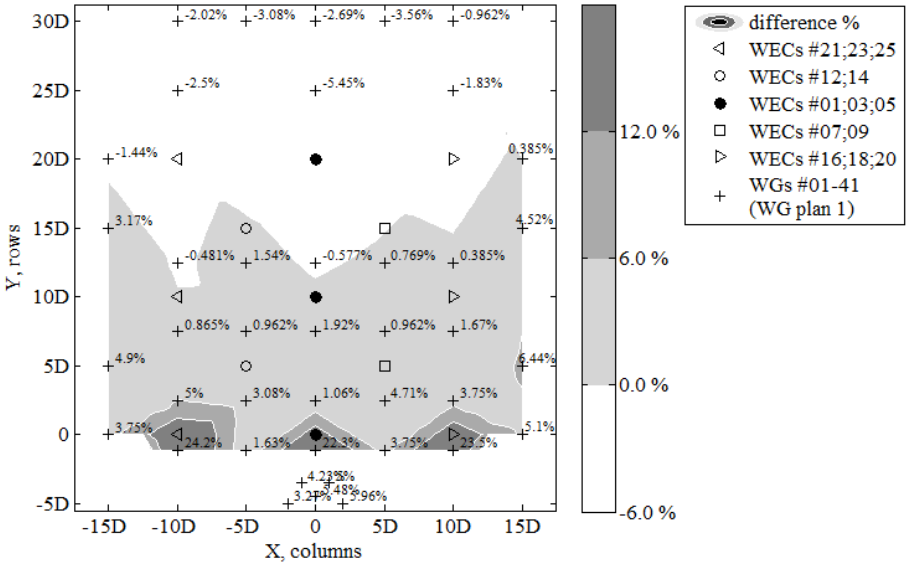

(b) Diffracted wave field normalized by target undisturbed wave field.

Figure 4.63. *Cont. Next Page*

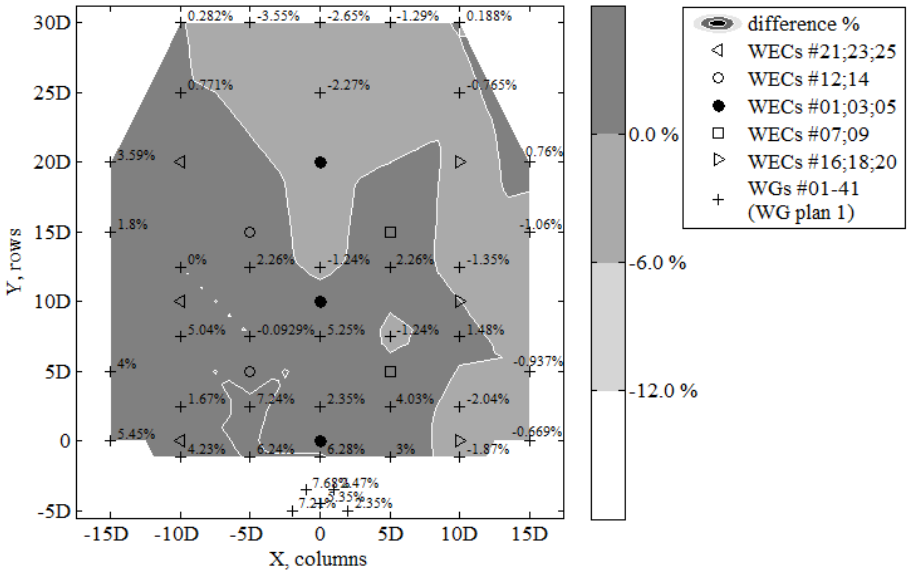

(c) Radiated wave field normalized by recorded undisturbed wave field.

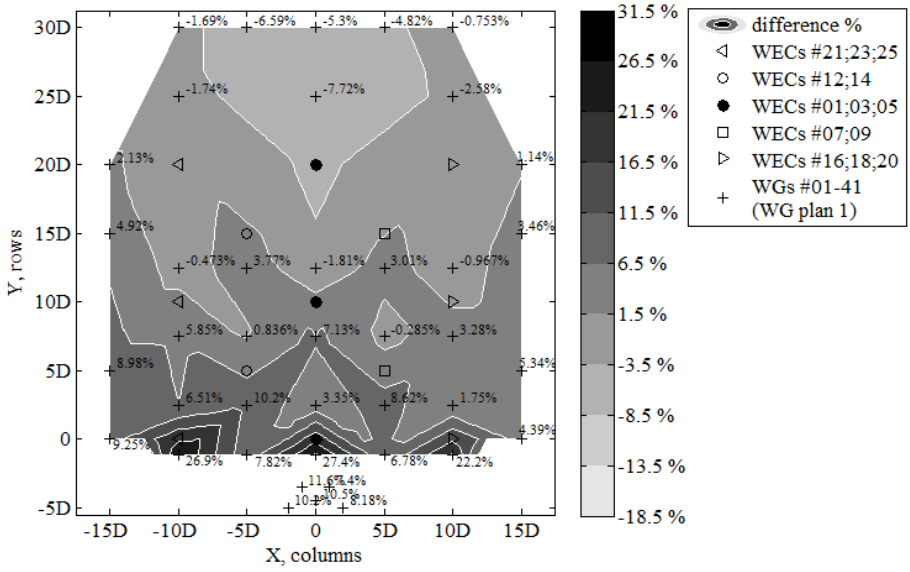

(d) Perturbed wave field normalized by recorded undisturbed wave field.

Figure 4.63. Non-dimensional percentage of change of H_{m0} at locations within and around the 13-WEC staggered array due to diffracted (stationary WECs), radiated (heaving WECs with damping applied) and perturbed wave field (heaving WECs with damping applied). Short-crested irregular waves of T_p = 1.26 s, H_{m0} = 0.104 m and spreading parameter, s = 75. The basin width (X, columns) and length (Y, rows) are expressed in number of WEC unit diameters, D = 0.315 m.

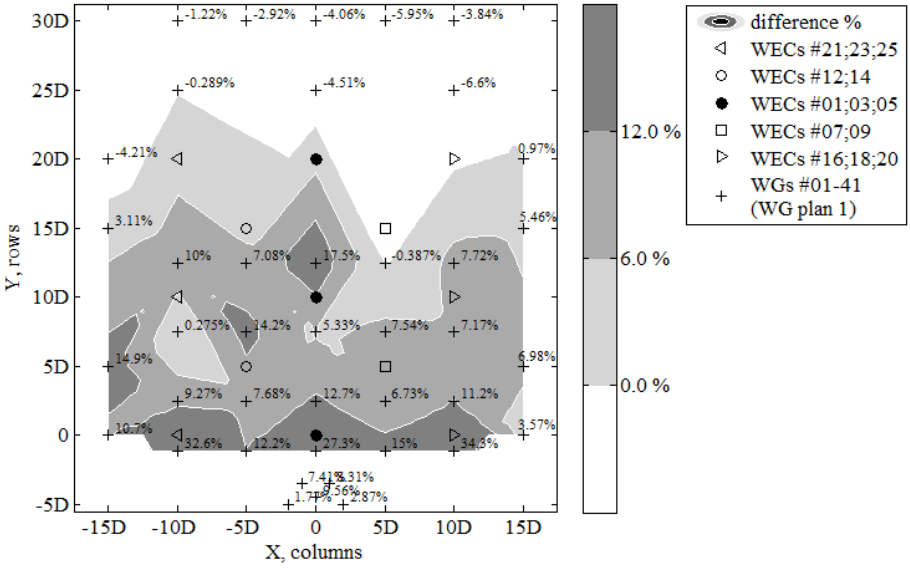

(a) Diffracted wave field normalized by recorded undisturbed wave field.

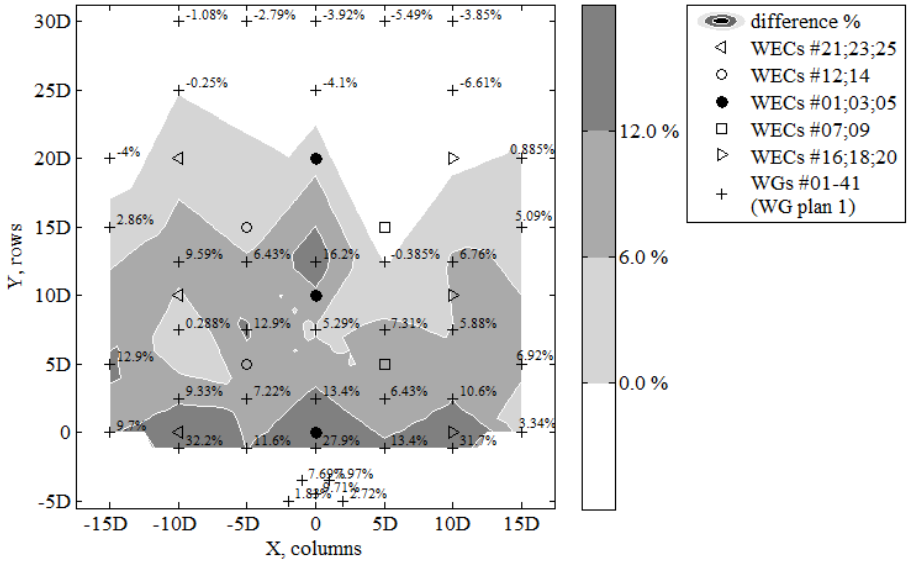

(b) Diffracted wave field normalized by target undisturbed wave field.

Figure 4.64. *Cont. Next Page*

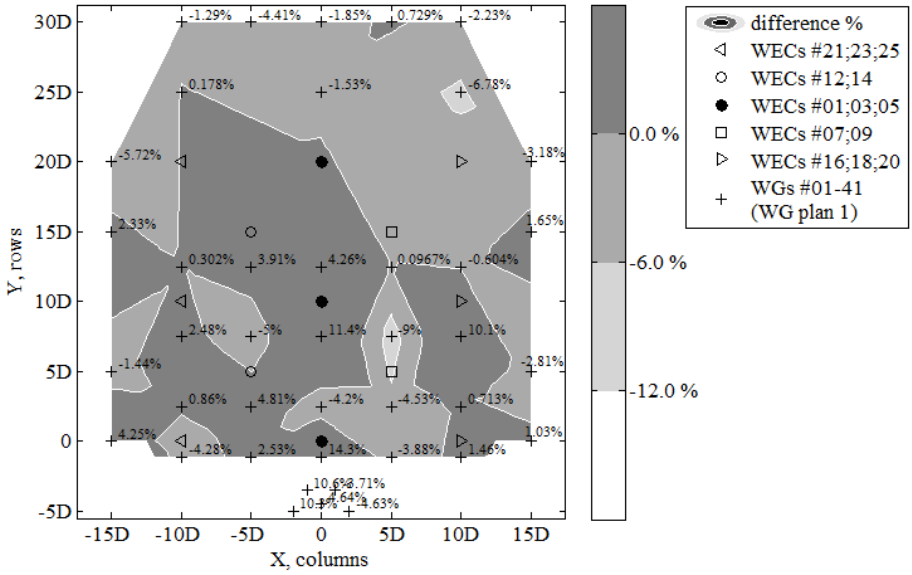

(c) Radiated wave field normalized by recorded undisturbed wave field.

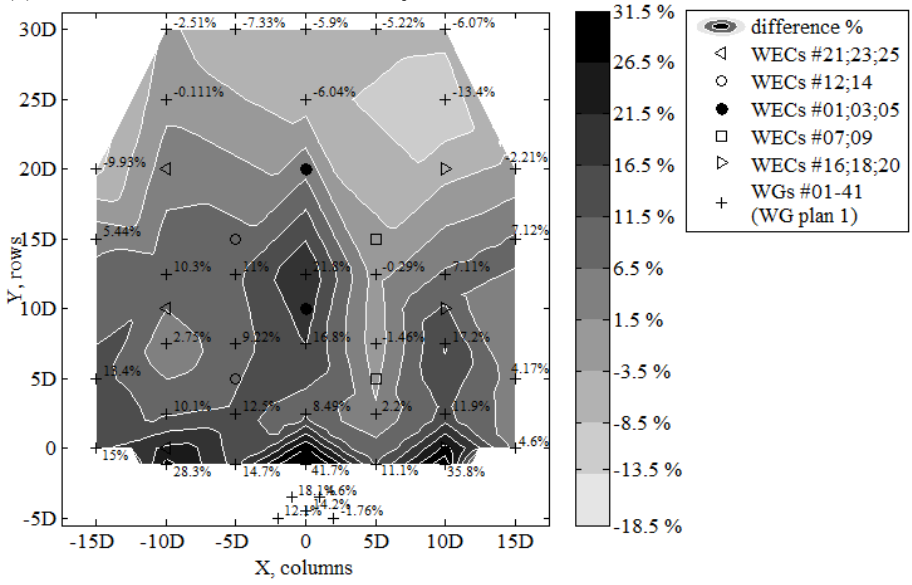

(d) Perturbed wave field normalized by recorded undisturbed wave field.

Figure 4.64. Non-dimensional percentage of change of H_{m0} at locations within and around the 13-WEC staggered array due to diffracted (stationary WECs), radiated (heaving WECs with damping applied) and perturbed wave field (heaving WECs with damping applied). Unidirectional irregular waves of T_p = 1.18 s and H_{m0} = 0.104 m. The basin width (X, columns) and length (Y, rows) are expressed in number of WEC unit diameters, D = 0.315 m.

4.6.10.1. Main observations on wave field modification around a 13-WEC staggered array

The wave field modifications due to wave energy extraction and the WECs' motion have been quantified for a 13-WEC staggered array, in terms of the non-dimensional percentage of change of H_{m0}, at locations within and around the array due to diffracted, radiated and perturbed wave field. The tested sea states have been also analysed in terms of spatial variation of the resulting wave height increase/reduction, and thus with regard to the extents of WEC array effects.

The accuracy of generating the target wave fields has been evaluated. For all presented results, the difference between recorded and target undisturbed wave field is shown not to be significant.

A comparison to the 5x5-WEC staggered array, as both arrays have the same number of rows and columns, has been conducted to investigate the effect of changing the WEC array geometric configuration (twice as large spacing between the WECs), on the resulting wave fields and the WEC array effects.

o **Diffracted wave field:**

When considering only the calculated difference percentages, up to 5.90 %, 4.95 %, 5.45 % and 6.60 % of wave height decrease downwave, is found for irregular unidirectional waves of T_p = 1.26 s, short-crested wind waves, directional swell and unidirectional waves of T_p = 1.18 s, respectively. Due to the staggered rows, almost no significant difference in wave height reduction is found for two different wave periods. No significant differences are found between short-crested and long-crested irregular waves, with swell directional waves representing an intermediate situation. Upwave of the front WEC row, local wave height increase is observed for all sea states. However, this wave height increase remains very localised (in front of the WECs only) and does not extend in-between the WECs, in contrast to the previous arrays of $w = l = 5D$. For T_p = 1.18 s the wave heights are reduced the least in-between the WECs of the front row, indicating a relationship between wave period and WEC spacing. Moreover, when waves of shorter wavelength (for T_p = 1.18 s) propagate through the WEC array, wave height recovery is observed already after a distance of $5D$ downwave of the last WEC row, similarly to short-crested waves of T_p = 1.26 s. Thus downwave of the 13-WEC staggered array, the effect of diffraction on the wave heights is not affected significantly when looking at waves of the two different tested wavelengths, compared to the 5x5-WEC staggered array.

With regard to the extents of WEC array effects:

- Wave height decrease is observed already after the front row for short-crested waves (third row for the 5x5-WEC staggered array), while for irregular long-crested waves this decrease occurs after the fourth to the fifth row (only after a distance of 5D downwave of the last row of 5 WECs the 5x5-WEC staggered array).
- For all tests, the highest wave height increase is observed locally upwave of the front three WECs, facing as first the incoming waves. However, this increase is not maintained in-between the devices.
- The largest wave field variations between long- and short-crested wind waves are found within the zone (width = 20D) downwave of the front row of WECs and upwave of the fifth row of WECs (within the zone downwave of the third row of WECs and at a distance 5D downwave of the last row of WECs, for the 5x5-WEC staggered array). Therefore, compared to the 5x5-WEC staggered array, this zone of variations has been moved upwave.
- The swell directional waves result in an intermediate situation.
- The wave field evolution shows change from wave height increase to wave height decrease towards the opposite end of the wave basin (landwards), similar to the 5x5-WEC rectilinear array. The same observation is made for the diffracted wave field by the 5x5-WEC arrays, but in these cases the wave field evolution has a "parallel" pattern to the WEC rows, which is not found when the WEC spacing becomes twice as large.
- No large wave field variations between long-crested waves of T_p = 1.26 s and T_p = 1.18 s are found, besides in the area around the front WECs, similarly to the 5x5-WEC staggered array.

o **Radiated wave field:**

When considering only the calculated difference percentages, up to 7.77 %, 1.52 %, 3.55 % and 6.60 % of wave height decrease downwave, is observed for irregular unidirectional waves of T_p = 1.26 s, short-crested wind waves, directional swell and unidirectional waves of T_p = 1.18 s, respectively. The effect of varying the wave directionality parameter is rather limited, but when comparing long-crested to wind waves, larger differences are found. Moreover, as a result of T_p = 1.18 s being equal to the resonance period of a WEC unit, wave height attenuation downwave is lower than for longer waves, with transverse wave height variations present. At downwave locations, when comparing the two considered WEC array configurations,

significant differences are found for most of the sea states, while wind waves result in the largest differences. Thus downwave of the 13-WEC staggered array, the effect of radiation on the wave heights, is reduced by at least a factor of 2.0 for long-crested waves, and by a factor of 7.0 for wind waves, compared to the 5x5-WEC staggered array.

With regard to the dimensions of WEC array effects:

- the largest wave field variations between long- and short-crested waves, are found for the area within the WEC array (for the 5x5-WEC staggered array, for the zone between WEC rows 2 and 3, as well as within a distance of $10D$ after the last WEC row and especially downwave of the middle WEC column).
- The long-crested waves result in less symmetric wave fields around the WECs, similar to the 5x5-WEC rectilinear array, while the opposite is found for the 5x5-WEC staggered array.
- The wave field evolution shows change from wave height increase to wave height decrease. This increase has a diagonal pattern towards the WEC columns located at the sides of the WEC array, similarly to the 5x5-WEC arrays.
- No large wave field variations between long-crested waves of T_p = 1.26 s and T_p = 1.18 s are found. The wave field symmetry is affected by a peak wave period equal to the resonance period of a WEC unit; this effect is smoothened for the 5x5-WEC staggered array.

o **Perturbed wave field:**

When considering only the calculated difference percentages, up to 11.60 %, 5.99 %, 7.72 % and 13.40 % of wave height dissipation downwave, is observed for irregular unidirectional waves of T_p = 1.26 s, short-crested wind waves, directional swell and unidirectional waves of T_p = 1.18 s, respectively. Thus, this configuration results in lower wave height attenuation downwave of the staggered WEC array, by a factor of 2.0 for long-crested irregular waves, and by a factor of 2.5 for wind waves. A large, very localised wave height increase, ranging between 24.30 % and 32.60 % for all sea states, is found upwave of each of the three front WECs. This wave height increase is very localised, in front of the WECs and does not extend in-between them, in contrast to the previous arrays of $w = l = 5D$. No significant difference is observed between long-crested waves of T_p = 1.26 s and T_p = 1.18 s for this WEC array configuration, which is not confirmed for the 5x5-WEC staggered array.

Regarding the dimensions of WEC array effects:

- Wave height decrease is observed only after the third row of WECs for short-crested waves (already after the front row of WECs for the 5x5-WEC staggered array), while for irregular long-crested waves this decrease occurs after the fourth row of three WECs (after the third row of 5 WECs for the 5x5-WEC staggered array).
- The magnitude of wave height decrease/increase at the same locations is very similar for all sea states, as for the rectilinear array, while the opposite is observed for the 5x5-WEC staggered array. Responsible for these small differences between extra-array effects caused by long- and short-crested waves for the 13-WEC staggered array, is the large spacing between the WECs.
- The largest differences between long- and short-crested waves are found between the zone downwave of the front row of WECs and the last row of WECs, but not particularly at a distance greater than $5D$ downwave of the WEC array, as found for 5x5-WEC staggered array.
- The wave field in the distances in-between the WECs shows large variations and indicates wave height recovery between the devices. This wave recovery is observed both in the lateral and longitudinal direction of the wave basin.
- Wave height dissipation is mostly observed at a distance of about $5D$ downwave of the WEC array, and is not maintained at a distance of $10D$ downwave of the array. For the 13-WEC staggered array wave recovery is observed at a distance of $10D$ downwave of the last row of WECs.
- For all sea states, the highest wave height dissipation is observed within a zone of width $-5D < X < +5D$, at distance $5D$ downwave of the WEC array (at $10D$ for the 5x5-WEC staggered array), as wave height recovery is observed for all sea states at locations at distance $10D$ downwave of the WEC array.
- The wave field evolution shows change from wave height increase to wave height decrease towards the opposite end of the wave basin (landwards). For all sea states increase or (smaller reduction) of wave height is found at the sides of the array.
- For all tests, the highest wave height increase is observed locally upwave of the front three WECs, facing as first, the incoming waves, but not maintained in-between the devices.

  For a twice as large spacing between the WECs, no significant differences are observed between the two tested peak wave periods. This observation indicates that a large enough spacing, leads to a geometric configuration less dependent on the wavelength of the incoming waves.

4.6.11. Wave field modification around a 3x3-WEC rectilinear 10D array

In this section, the wave field modifications due to wave energy extraction and the WECs' motion have been quantified, around a 3x3-WEC rectilinear 10D array, illustrated in Figure 4.65. Both the lateral, w, and the longitudinal, l, spacing between WECs, respectively, is twice as large as for the rectilinear 5x5-WEC rectilinear array; thus w = 10D between the WEC units of the same row, and l = 10D between the WEC units of the same column. The results obtained from the 3x3-WEC rectilinear 10D array are, firstly, compared to the results obtained for the 5x5-WEC rectilinear array, as both arrays have the same extents (20D x 20D). However, these two arrays do not have the same number of rows and columns. The objective of this comparison is to quantify the effect of modifying the spacing between the WECs (and the WEC number within an array) on the resulting WEC array effects for a rectilinear WEC array geometric configuration.

All wave field results are presented in terms of the perturbed wave fields. No data are available for the diffracted (and therefore for the radiated only) wave field for this WEC array configuration.

Figure 4.65. The 3x3-WEC rectilinear 10D array under irregular short-crested waves. 9 WECs are interacting with the waves, while the rest 16 WEC units are held stationary above the water surface. View from the control platform location.

Difference percentage terms have been calculated for the WEC array, using Equation 4.8, and plotted in Figure 4.66. The measured change of the perturbed wave field is presented for unidirectional irregular waves of T_p = 1.26 s (Figure 4.66(a)), short-crested waves with spreading parameter, s = 10 (Figure 4.66(b)) and

s = 75 (Figure 4.66(c)), respectively, and for unidirectional irregular waves of T_p = 1.18 s (Figure 4.66(d)).

Quantifying the effect of the wave directionality on WEC array effects

Firstly, sea states of the same peak wave period (T_p = 1.26 s) are discussed, to investigate the effect of the wave directionality on the resulting wave fields, due to the WECs motion and power extraction.

o Perturbed wave field

For unidirectional waves, up to 8.87 % of wave height decrease downwave and 28.20 % wave height increase upwave is observed when the 9 WEC units are operating (Figure 4.66(a)). This wave height increase upwave of the front 3 WECs is very local, while in-between the WECs, the maximum wave height increase reduces to 5.35 %. A very similar situation of localized wave height increase is observed also for the 13-WEC staggered array of the same WEC spacing, which is not confirmed for the 5x5-WEC rectilinear array (31.50 % very localised wave height increase upwave of the entire front row of five WECs). However, for the 5x5-WEC rectilinear array, clear wave height attenuation in the lee of the WEC array is observed, reaching 18.10 % (larger by a factor of 2.0).

For short-crested wind waves Figure 4.66(b), the same order of magnitude of wave height decrease is found downwave of the array as for irregular long-crested waves (up to 7.26 %) (18.10 % for the 5x5-WEC rectilinear array). Upwave of the front three WECs, very localised wave height increase is observed up to 21.3 % (25.10 % in front of the entire row of five WECs for the 5x5-WEC rectilinear array) similarly to the unidirectional waves, but 7.5 % smaller increase. For short-crested swell waves (Figure 4.66(c)), wave height decrease downwave of the array is found to be in the same magnitude, up to 8.73 % (for the 5x5-WEC rectilinear array, up to 16.1-16.3 %). Upwave of the first row of three WECs, 23.50 % very localised wave height increase is observed (22.50 % for the front row of five WECs of the 5x5-WEC rectilinear array), a percentage lying between these found for long- and short-crested wind waves.

Quantifying the effect of different wave periods on WEC array effects

o Perturbed wave field

Figure 4.66(d), for unidirectional waves of T_p = 1.18 s, shows slightly higher wave height attenuation in the lee of the WEC array, compared to the waves of T_p = 1.26 s (8.87 %) and is found to be up to 11.40 %. For the 5x5-WEC rectilinear array, though, the opposite is observed. However, regarding the presented percentages, no

significant difference is observed between irregular long-crested waves of T_p = 1.26 s and T_p = 1.18 s.

Extents of WEC array effects for varying wave directionality

When comparing irregular long- to short-crested waves, with regard to the extent of WEC array effects, several observations can be made.

- Perturbed wave field

Regarding the effect on the recorded undisturbed wave field caused by the perturbed wave field around the WEC array, the zone where wave height increase is observed for short-crested waves, is very limited compared to long-crested waves, so that increase stops downwave of the front row of 3 WECs. This observation is similar to that made for the 5x5-WEC rectilinear array, besides that for that WEC array configuration directional swell waves show more similarities with the long-crested waves. Consequently, wave height decrease is observed already after the first row of WECs for short-crested waves, while for long-crested waves this decrease occurs slightly upwave of the third row of three WECs. The order of magnitudes of the maximum percentages found for wave height decrease and increase when looking at the same locations/distances upwave or downwave of the array, are, nevertheless, very similar for all sea states. Moreover, for all wave types, wave height increase higher than 12.00 % is observed within a zone with similar extents, i.e. this zone is limited upwave of the front three WECs, the first devices facing the incoming waves. A similar result is found for the front row of the 5x5-WEC rectilinear array. However, as observed for all WEC arrays with large spacing between the WECs (= 10D) this wave height increase is not maintained in-between the WECs, as it occurs for WEC arrays of 5D spacing. As conclusion from the above observations for Figures 4.66(a-c), the largest wave field variations between irregular long- and short-crested waves are found within the extents of the entire WEC array (for the 5x5-WEC rectilinear array the largest differences are found between the zone downwave of the front WEC row and at a distance 5D downwave of the last WEC row). This zone of variations between wind and long-crested waves has a length of 20D (25D for the 5x5-WEC rectilinear array). Moreover, wave height increase is found at the sides of the array, reaching up to the third row for long-crested irregular and swell directional waves (up to the fifth and fourth, for long-crested and swell directional waves, respectively, for the 5x5-WEC rectilinear array). For wind waves, increased wave height is found only at the sides of the front row, similar to the 5x5-WEC rectilinear array. However, after the front row, wave height decrease is less at the sides compared to the central area of the array. For all sea states, the highest wave height dissipation is observed locally at locations 5D - 10D downwave of the WEC array; this wave height increase successes wave height

decrease with repetition in the lateral direction of the wave basin, indicating wave height recovery in the lateral direction of the wave basin.

Extents of WEC array effects for different wave periods

- Perturbed wave field

When comparing long-crested waves of different peak wave periods, with regard to the extent of WEC array effects, the following are observed. The effect on the recorded undisturbed wave field caused by the perturbed wave field around the WEC array due to different peak wave periods (Figures 4.66(a) and 4.66(d)), in the zone around the front row of WECs higher wave height increase is observed for T_p = 1.18 s. Also downwave of the array, within X = -5D to 5D and for Y=30D, wave height dissipation is very similar (yet, higher for T_p = 1.18 s). The wave patterns are very similar, which is not observed for the 5x5-WEC rectilinear array. Moreover, wave height increase successes wave height decrease with repetition, in the lateral direction of the wave basin for T_p = 1.18 s, also observed for T_p = 1.26 s, indicating recovery of the wave height in the lateral direction of the wave basin. Finally, also for T_p = 1.18 s, the wave height is increased at the sides of the array (yet, no symmetry is observed).

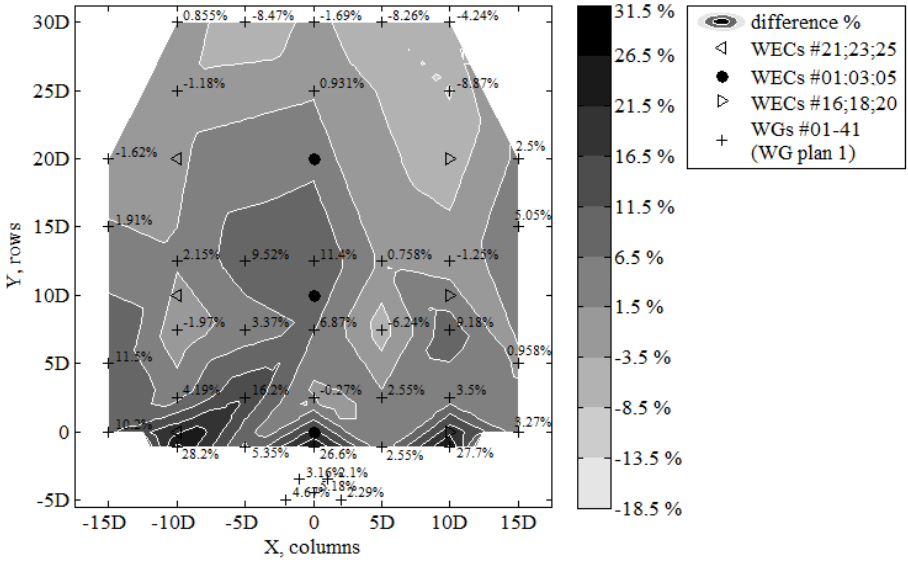

(a) Perturbed wave field normalized by recorded undisturbed wave field for unidirectional irregular waves with T_p = 1.26 s.

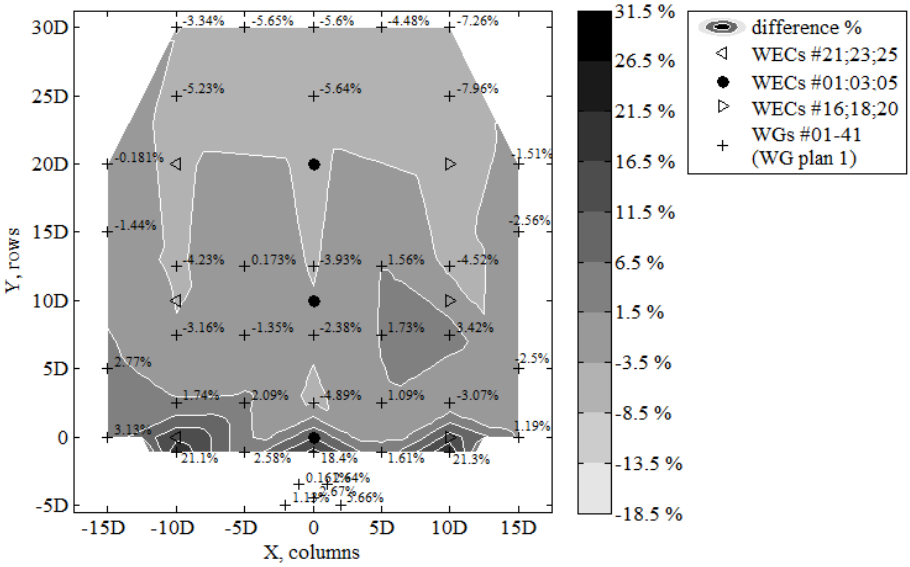

(b) Perturbed wave field normalized by recorded undisturbed wave field for short-crested irregular waves (s = 10) with T_p = 1.26 s.

Figure 4.66. *Cont. Next Page*

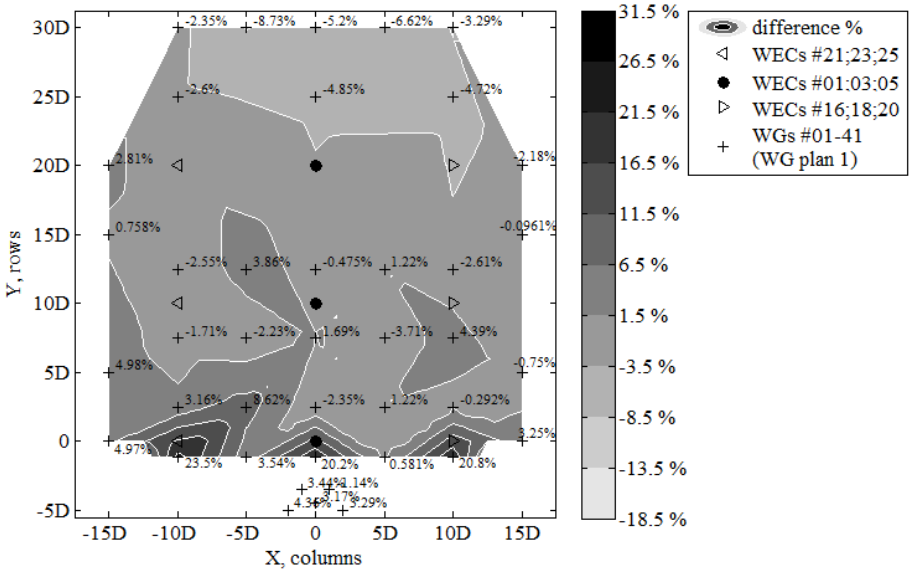

(c) Perturbed wave field normalized by recorded undisturbed wave field for short-crested irregular waves (s = 75) with T_p = 1.26 s.

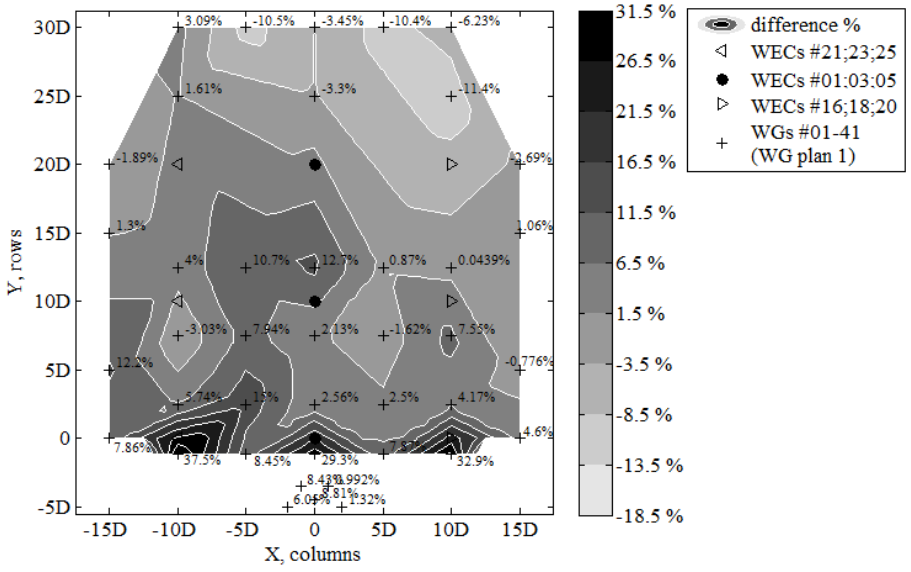

(d) Perturbed wave field normalized by recorded undisturbed wave field for unidirectional irregular waves with T_p = 1.18 s.

Figure 4.66. Non-dimensional percentage of change of H_{m0} at locations within and around the 3x3-WEC rectilinear 10D array due to the perturbed wave field (heaving WECs with damping applied). (a) Unidirectional irregular waves of T_p = 1.26 s and H_{m0} = 0.104 m. (b) Short-crested irregular waves of T_p = 1.26 s, H_{m0} = 0.104 m and

Figure 4.66. *Cont.*

spreading parameter, s =10. (c) Short-crested irregular waves of T_p = 1.26 s, H_{m0} = 0.104 m and spreading parameter, s =75. (d) Unidirectional irregular waves of T_p = 1.18 s and H_{m0} = 0.104 m. The basin width (X, columns) and length (Y, rows) are expressed in number of WEC unit diameters, D = 0.315 m.

4.6.11.1. Main conclusions on wave field modification around a 3x3-WEC rectilinear 10D array

The wave field modifications due to wave energy extraction and the WECs' motion have been quantified for a 3x3-WEC rectilinear 10D array, in terms of the non-dimensional percentage of change of H_{m0}, at locations within and around the array due to the perturbed wave field. No diffracted (and thus no radiated) wave field data is available for this WEC array configuration. The tested sea states have been also analysed in terms of spatial variation of the resulting wave height increase/reduction, and thus with regard to the extents of WEC array effects.

Both the lateral, w = 10D, and the longitudinal, l = 10D, spacing between WECs of the same row and the same column, respectively, is twice as large as for the 5x5-WEC rectilinear array. A comparison to the 5x5-WEC rectilinear array has been conducted to investigate the effect of changing the spacing between the WECs of an array, on the resulting wave fields and the WEC array effects, as both arrays have the same extents (20D x 20D) (however, different number of rows and columns). Also comparison to the 13-WEC staggered array is made, as this array has the same spacing between the WECs and same extents (20D x 20D).

- **Perturbed wave field:**

When considering only the calculated difference percentages, up to 8.87 %, 7.26 %, 8.73 % and 11.40 % of wave height dissipation downwave, is observed for unidirectional waves of T_p = 1.26 s, short-crested wind waves, directional swell and unidirectional waves of T_p = 1.18 s, respectively. A large, very localised wave height increase, ranging between 21.30 % and 37.50 % for all sea states, is found upwave of the front three WECs, which reduces significantly in-between the WECs. This increase pattern is observed also for the 13-WEC staggered array of the same WEC spacing, but not for the 5x5-WEC rectilinear array. Similarly to the 5x5-WEC rectilinear array and for all sea states, the same order of magnitude of wave height reduction is found downwave of the array. Unidirectional waves of T_p = 1.18 s show slightly higher wave height attenuation in the lee of the WEC array compared to the

waves of T_p = 1.26 s (for the 5x5-WEC rectilinear array, though, the opposite is observed).

Regarding the dimensions of WEC array effects:

- wave height decrease is observed already after the front row of WECs for short-crested waves, while for irregular long-crested waves this decrease starts to take place only after the third row of 3 WECs (for the 5x5-WEC rectilinear array, directional swell waves show similar results to long-crested waves).
- For all tests, the highest wave height increase is observed locally upwave of the front three WECs, facing as first, the incoming waves. This increase is not maintained in-between the devices.
- The largest wave field variations between long- and short-crested waves are found within the extents of the entire WEC array (for the 5x5-WEC rectilinear array the largest differences are found between the zone downwave of the front WEC row and at a distance $5D$ downwave of the last WEC row). This zone of variations between wind and long-crested waves has a length of $20D$ ($25D$ for the 5x5-WEC rectilinear array).
- The wave field evolution shows change from wave height increase to wave height decrease towards the opposite end of the wave basin (landwards).
- For all sea states, increase of wave height is found at the sides of the array. For wind waves, increased wave height is found only at the sides of the front row (yet, wave height reduction is smaller at the sides of the entire array).
- For all sea states, the highest wave height dissipation is observed locally at locations $5D$ - $10D$ downwave of the WEC array. Wave height increase successes wave height decrease with repetition in the lateral direction of the wave basin, indicating recovery of the wave height in the lateral direction of the wave basin.
- No clear wave height recovery is observed down wave the array, as seen for the 13-WEC staggered array of the same spacing.
- For as twice as large spacing between the WECs, no significant differences are observed between the two tested peak wave periods, which is not confirmed for the 5x5-WEC rectilinear array. This observation indicates that a large enough spacing leads to a geometric configuration, less dependent on the wavelength of the incoming waves.

4.6.12. Wave field modification around a 3x3-WEC rectilinear 5D array

In this section, the wave field modifications due to wave energy extraction and the WECs' motion have been quantified, around a 3x3-WEC rectilinear 5D array. Both the lateral, w, and the longitudinal, l, spacing between WECs, respectively, is half of those for the 3x3-WEC rectilinear 10D array; thus w = 5D between the WEC units of the same row, and l = 5D between the WEC units of the same column. The results obtained from the 3x3-WEC rectilinear 5D array are directly compared to the results obtained for 3x3-WEC rectilinear 10D array, as both arrays have the same number of rows, columns and WEC units. The objective of this comparison is to quantify the effect of modifying the spacing between the WECs (by keeping the same WEC number within an array) on the resulting WEC array effects for a rectilinear WEC array geometric configuration. Moreover, the effect of reducing the number of columns and rows is presented by comparing to the 5x5-WEC rectilinear array.

All wave field results are presented in terms of the perturbed wave fields. No data are available for the diffracted (and therefore for the radiated, only) wave field for this WEC array configuration.

Difference percentage terms have been calculated for this WEC array, using Equation 4.8, and plotted in Figure 4.67. The measured change of the perturbed wave field is presented for unidirectional irregular waves of T_p = 1.26 s (Figure 4.67(a)), short-crested waves with spreading parameter, s = 10 (Figure 4.67(b)) and s = 75 (Figure 4.67(c)), respectively, and for unidirectional irregular waves of T_p = 1.18 s (Figure 4.67(d)).

Quantifying the effect of the wave directionality on WEC array effects

Firstly, sea states of the same peak wave period T_p = 1.26 s are discussed, to investigate the effect of the wave directionality on the resulting wave fields, due to the WECs' motion and power extraction.

- Perturbed wave field

For unidirectional waves, up to 8.72 % of wave height decrease downwave (8.87 % for the 3x3-WEC rectilinear 10D array), and 27.80 % wave height increase upwave (28.20 % for the 3x3-WEC rectilinear 10D array) is observed when the 9 WEC units are operating (Figure 4.67(a)). Wave height increase upwave of the front 3 WECs is found along the entire WEC row (for the 3x3-WEC rectilinear 10D array increase is very local, while in-between the WECs the maximum wave height increase reduces to 5.35 %). A similar situation is observed for the 5x5-WEC rectilinear array (31.50 % very localised wave height increase upwave of the entire

front row of five WECs). For the 5x5-WEC rectilinear array, however, up to 18.1 % wave height dissipation is observed at the same locations (larger by a factor of 2.07).

For short-crested wind waves (Figure 4.67(b)), up to 10.2 % wave height decrease is found downwave of the array (up to 7.26 % for the 3x3-WEC rectilinear 10D array, and 18.10 % for the 5x5-WEC rectilinear array). Wave recovery is also clearly observed downwave of the 3x3-WEC rectilinear 5D array, which occurs at a distance of 20D downwave of the WEC array. Upwave of the front three WECs, wave height increase is observed up to 30.1 % (21.3 %, locally upwave of each WEC of the 3x3-WEC rectilinear 10D array, and 25.10 % in front of the entire row of five WECs for the 5x5-WEC rectilinear array), similarly to the unidirectional waves. For short-crested swell waves (Figure 4.67(c)), wave height decrease downwave of the array is found to be in the same magnitude, up to 11.5 % – 12.0 % (8.73 % for the 3x3-WEC rectilinear 10D array, and up to 16.1 % - 16.3 % for the 5x5-WEC rectilinear array). However, similar to the case of wind waves, wave recovery is observed at a distance of 20D downwave of the WEC array. For wind waves, this wave recovery is more pronounced; at distance 20D downwave of the array, wave height dissipation is no longer observed for s = 10, while for s = 75 wave height attenuation of 9.16 % is still present at the same downwave location. Moreover, along the front row of three WECs, 27.5 % localised wave height increase is observed (23.50 % for the 3x3-WEC rectilinear 10D array, and 22.50 % for the first row of five WECs, for the 5x5-WEC rectilinear array).

Quantifying the effect of different wave periods on WEC array effects

- Perturbed wave field

Figure 4.67(d), for unidirectional waves of T_p = 1.18 s, shows the same level of wave height attenuation in the lee of the WEC array (8.43 %) compared to the waves of T_p = 1.26 s (8.87 %). For the 5x5-WEC rectilinear array, though, the opposite is observed which indicates that the geometric configuration, in combination with the wave period, affect the extra-array effects of the WEC array. Regarding the presented percentages, no significant difference is observed between long-crested waves of T_p = 1.26 s and T_p = 1.18 s, as well as between the resulting wave field patterns.

Extents of WEC array effects for varying wave directionality

When comparing long- to short-crested waves, with regard to the extent of WEC array effects, several observations can be made.

o Perturbed wave field

With regard to the effect on the recorded undisturbed wave field caused by the perturbed wave field around the WEC array, the zone where wave height increase is observed for short-crested waves, is very limited compared to the irregular long-crested, so that increase stops downwave of the front row of 3 WECs. This observation is similar to that made, both for the 3x3-WEC rectilinear 10D array and the 5x5-WEC rectilinear array, besides that, for the latter array configuration, directional swell waves show more similarities with the long-crested waves. Consequently, wave height decrease is observed already after the front row of WECs for short-crested waves, while for long-crested waves this decrease occurs downwave of the WEC array (slightly upwave of the third row of three WECs for the 3x3-WEC rectilinear 10D array). The order of magnitudes of the maximum percentages found for wave height decrease and increase, are, nevertheless, very similar for all sea states, but the locations/distances upwave or downwave of the array differ (which is not confirmed for the 3x3-WEC rectilinear 10D array). Moreover, for all wave types, wave height increase higher than 12.00 % is observed within a zone with similar extents, i.e. this zone is limited upwave of the front three WECs, the first devices facing the incoming waves. A similar result is found for the front row both of the 3x3-WEC rectilinear 10D and the 5x5-WEC rectilinear arrays. As conclusion from the above observations for Figures 4.67(a) - 4.67(c), the largest wave field variations between long- and short-crested irregular waves, are found within the extents of the WEC array and downwave of the array (for the 3x3-WEC rectilinear 10D array, the largest differences are found within the array). This zone of variations between wind and long-crested irregular waves has a length of 30D (20D for the 3x3-WEC rectilinear 10D array and 25D for the 5x5-WEC rectilinear array). When wave height attenuation starts to take over, the pattern of the differences for both sea states, becomes diagonal towards the WEC columns located at the sides of the WEC array. This wave pattern is a result of the increased wave height at the sides of the array, reaching up to the fifth row for long-crested irregular and swell directional waves (up to the third row for the 3x3-WEC rectilinear 10D array; and for the 5x5-WEC rectilinear array up to the fifth and fourth row, for long-crested and swell directional waves, respectively). For wind waves, increased wave height is found only at the sides of the front row, similar to both the 3x3-WEC rectilinear 10D and the 5x5-WEC rectilinear arrays. However, after the front row, wave height decrease is less at the sides compared to the central area of the array. Most importantly, for long-crested and directional waves, the highest wave height dissipation is observed at locations, at least at distance 15D - 20D downwave of the WEC array (for swell directional waves, wave recovery is observed at 20D distance), and within a zone of width - 5D < X < + 5D. For wind waves, though, wave height dissipation is observed only up to 2.5D downwave of the array, while wave height is fully recovered at 20D downwave of the WEC array.

Extents of WEC array effects for different wave periods

o Perturbed wave field

When comparing long-crested waves of different peak wave periods, with regard to the extent of WEC array effects, a number of observations can be made, regarding the effect on the recorded undisturbed wave field caused by the perturbed wave field around the WEC array (Figures 4.67(a) and 4.67(d)). In the zone around the front row of WECs higher wave height increase is observed for T_p = 1.18 s, similar to the observations for the 3x3-WEC rectilinear 10D array. Also downwave of the array, within X = -5D to 5D and for Y=30D, wave height dissipation is very similar (observed also for the 3x3-WEC rectilinear 10D array). The wave patterns are very similar as also seen for the 3x3-WEC rectilinear 10D array, which is not observed for the 5x5-WEC rectilinear array. Finally, also for T_p = 1.18 s, the wave height is increased at the sides of the array.

o General

Through the above comparisons it is clear that the 3x3-WEC rectilinear 5D array due to its limited extents (10D x 10D) does not cause the large wave height dissipation found for the larger arrays (the 5x5-WEC rectilinear array with extents 20D x 20D). However, due to small spacing, it causes wave attenuation which, for long-crested waves, is maintained for long distances downwave of the array. This effect, however, is not caused by the array of the same number of WECs but with larger spacing (the 3x3-WEC rectilinear 10D array).

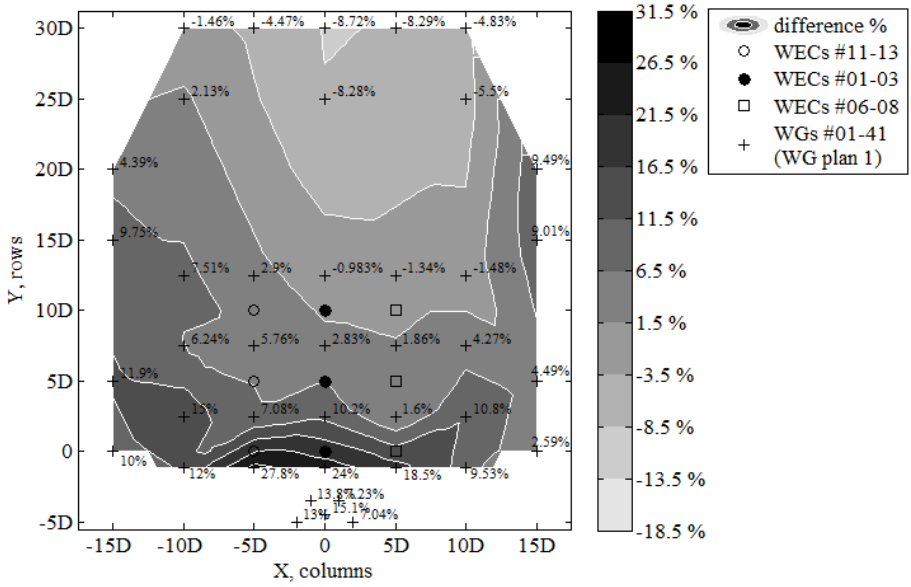

(a) Perturbed wave field normalized by recorded undisturbed wave field for unidirectional irregular waves with T_p = 1.26 s.

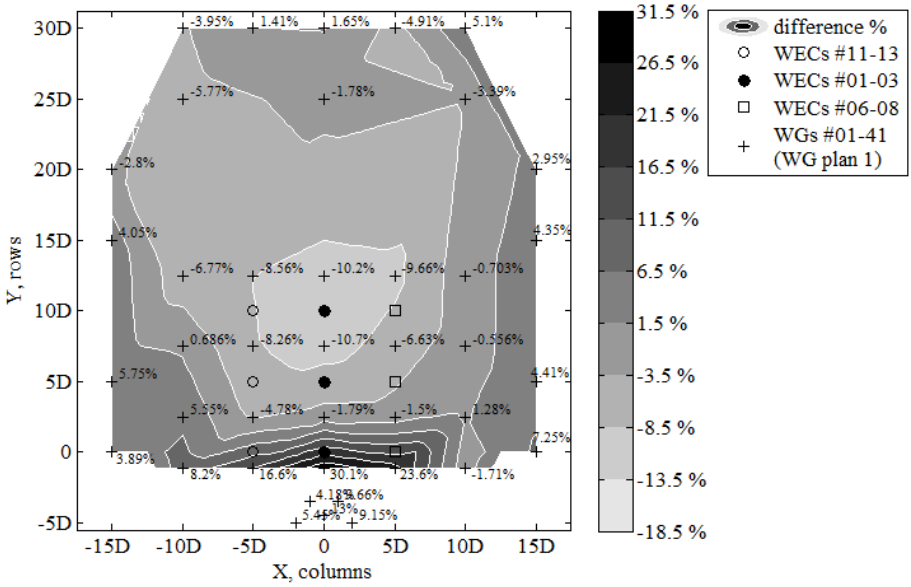

(b) Perturbed wave field normalized by recorded undisturbed wave field for short-crested irregular waves (s = 10) with T_p = 1.26 s.

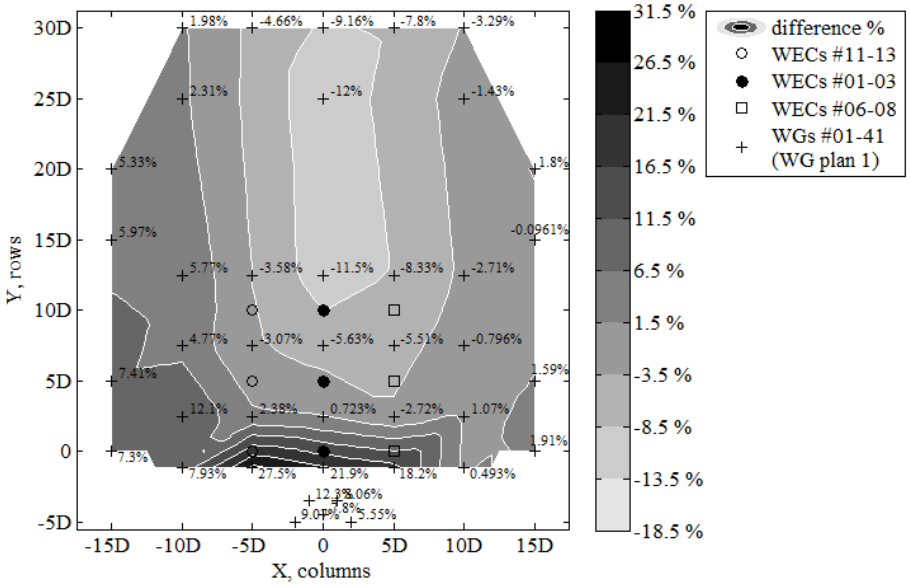

(c) Perturbed wave field normalized by recorded undisturbed wave field for short-crested irregular waves (s = 75) with T_p = 1.26 s.

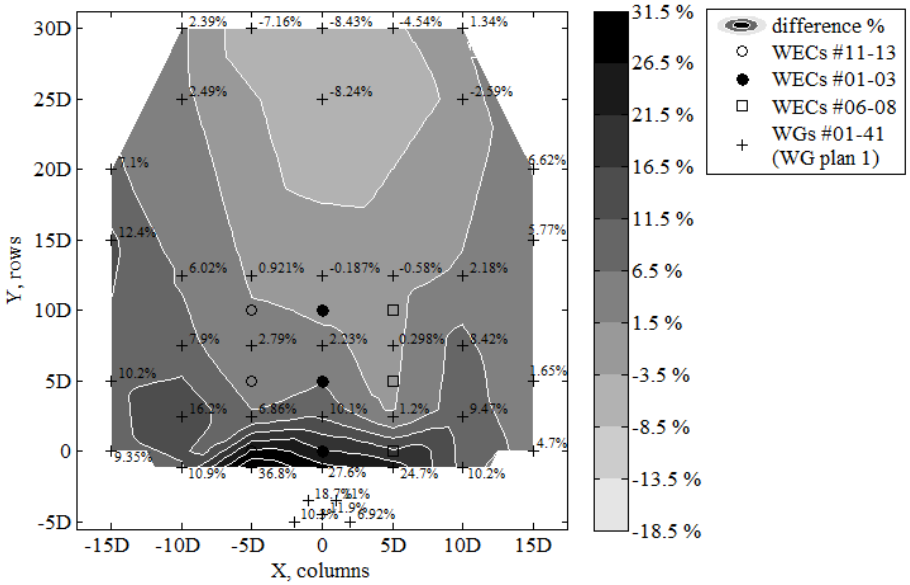

(d) Perturbed wave field normalized by recorded undisturbed wave field for long-crested irregular waves with T_p = 1.18 s.

Figure 4.67. Non-dimensional percentage of change of H_{m0} at locations within and around the 3x3-WEC rectilear 5D array due to the perturbed wave field (heaving WECs with damping applied). (a) Unidirectional irregular waves of T_p = 1.26 s and H_{m0} = 0.104 m. (b) Short-crested irregular waves of T_p = 1.26 s, H_{m0} = 0.104 m and

Figure 4.67. *Cont.*

spreading parameter, s =10. (c) Short-crested irregular waves of T_p = 1.26 s, H_{m0} = 0.104 m and spreading parameter, s = 75. (d) Unidirectional irregular waves of T_p = 1.18 s and H_{m0} = 0.104 m. The basin width (X, columns) and length (Y, rows) are expressed in number of WEC unit diameters, D = 0.315 m.

4.6.12.1. Main conclusions on wave field modification around a 3x3-WEC rectilinear 5D array

The wave field modifications due to wave energy extraction and the WECs' motion have been quantified for a 3x3-WEC rectilinear 5D array, in terms of the non-dimensional percentage of change of H_{m0}, at locations within and around the array due to the perturbed wave field. No diffracted (and thus no radiated) wave field data is available for this WEC array configuration. The tested sea states have been also analysed in terms of spatial variation of the resulting wave height increase/reduction, and thus with regard to the extents of WEC array effects.

Both the lateral, w = 5D, and the longitudinal, l = 5D, spacing between WECs of the same row and the same column, respectively, are half of the spacing of the 3x3-WEC rectilinear 10D array and equal to that of the 5x5-WEC rectilinear array. A comparison to the 3x3-WEC rectilinear 10 D array has been conducted to investigate the effect of changing the spacing between the WECs of an array, on the resulting wave fields and the WEC array effects, as both arrays have the same number of rows and columns. Also comparison to the 5x5-WEC rectilinear array is made, to investigate the effect of reducing the number of rows at the rear, and columns at the sides of the array.

- **Perturbed wave field:**

When considering only the calculated difference percentages, up to 8.72 %, 10.20 %, 12.00 % and 8.43 % of wave height dissipation downwave, is observed for unidirectional waves of T_p = 1.26 s, short-crested wind waves, directional swell and unidirectional waves of T_p = 1.18 s, respectively. A large, wave height increase, ranging between 27.50 % and 36.80 % for all sea states, is found upwave of the entire front row of three WECs, unlike for the 3x3-WEC rectilinear 10D array and similarly to the 5x5-WEC rectilinear array. In general, larger wave height dissipation is found, compared to the 3x3-WEC rectilinear 10D array. Compared to the 5x5-WEC rectilinear array, however, wave height dissipation is smaller by a factor of 2.07. For both types of short-crested waves, wave height recovery at a distance of

20D downwave of the WEC array, is observed (very pronounced for wind waves). No significant differences in wave attenuation is observed between irregular long-crested waves of T_p = 1.26 s and T_p = 1.18 s.

Regarding the dimensions of WEC array effects:

- wave height decrease is observed already after the front row of WECs for short-crested waves, while for long-crested irregular waves this decrease occurs downwave of the WEC array (slightly upwave of the third row of three WECs for the 3x3-WEC rectilinear 10D array).

- For all tests, the highest wave height increase is observed locally upwave of the entire front row of three WECs, facing as first, the incoming waves. This increase is maintained in-between the devices, similarly to the 5x5-WEC rectilinear array and unlike for the 3x3-WEC rectilinear 10D array.

- The largest wave field variations between long- and short-crested waves are found within the extents of the WEC array and downwave of the array (for the 3x3-WEC rectilinear 10D array, the largest differences are found within the array). This zone of variations between wind and long-crested irregular waves has a length of 30D (20D for the 3x3-WEC rectilinear 10D array, and 25D for the 5x5-WEC rectilinear array).

- The wave field evolution shows change from wave height increase to wave height decrease towards the opposite end of the wave basin (landwards). Wave height increase has a "parallel" pattern to the front WEC row, which becomes diagonal as wave attenuation starts to take over.

- For all sea states, increase of wave height is found at the sides of the array. For wind waves, increased wave height is found only at the sides of the front row (yet, wave height reduction is smaller at the sides of the entire array).

- For long-crested and directional swell waves, the highest wave height dissipation is observed at locations, at least at distance 15D - 20D downwave of the WEC array, and within a zone of width - 5D < X < + 5D.

- Clear wave height recovery is observed downwave of the array (not found for neither the 3x3-WEC rectilinear 10D array, nor for the 5x5-WEC rectilinear array). For wind waves, wave height is fully recovered at 20D downwave of the WEC array.

- No significant differences are found between the two tested peak wave periods.

- It is clear that the 3x3-WEC rectilinear 5D array due to its limited extents (10D x 10D) does not cause the large wave height dissipation found for the larger arrays (the 5x5-WEC rectilinear array with extents 20D x 20D). However, due to small spacing, it causes wave attenuation which, for long-crested irregular waves, is

maintained for long distances downwave of the array. This effect, however, is not achieved by the array of the same number of WECs but with larger spacing (the 3x3-WEC rectilinear 10D array) and thus, by the array of larger extents.

4.7. Conclusions

Experiments have been performed in a large wave basin with wave energy converter arrays of different geometric configurations and for varying wave conditions. Wave elevations, the WECs' heave displacement and wave induced surge forces on the WECs have been simultaneously measured.

The results presented in this chapter, concern a set of long- and short crested wave conditions and show power absorption by selected WEC array configurations, wave field variation of the generated waves in an empty wave basin, the effect of the structures used for supporting the WECs in the incoming waves, and finally wave field modifications caused by WEC arrays of various geometric configurations and WEC numbers. The accuracy of the generated wave fields is evaluated and the effect of the support structures is confirmed to be small. A detailed discussion and conclusions on the obtained results on power absorption and wave field modifications by the arrays is provided in Chapter 5, where, also based on the existing literature, guidelines for design of WEC arrays have been derived.

The power output is presented of an individual WEC, of the 5x5-WEC rectilinear, the 5x5-WEC staggered, the 3x3-WEC rectilinear 5D and the 3x3-WEC rectilinear 10D arrays, in terms of the WEC array interaction factor using the isolated WEC #05 as reference. The objective is to investigate the effect of changing the WEC array configuration and the wave conditions, on the intra-array interactions, and in particular on the power absorption of the array.

Two sea states have been analysed: irregular long- and short-crested wind waves (s = 10). For irregular long-crested waves and for the large 5x5-WEC arrays, the staggered geometric configuration results in larger WEC array interaction factor compared to the rectilinear arrangement of the WECs. For both 5x5-WEC arrays, constructive intra-array interactions occur for the WECs under long-crested waves, while the opposite is observed for wind waves. In directional wind waves, no large variations of power output between the WECs of the array are observed, while the rectilinear array results in higher WEC array interaction factor. By investigating the 3x3-WEC arrays under irregular long-crested waves, the array of 10D spacing results in significantly higher WEC array interaction factor, compared to all presented arrays. Large constructive intra-array interactions occur, therefore, when the spacing between the WECs becomes large. The 3x3-WEC rectilinear array of 5D spacing results in negative interactions between the WECs regarding power output.

The wave field modifications due to wave energy extraction and the WECs' motion have been quantified for several WEC arrays, in terms of the non-dimensional percentage of change of H_{m0}, at locations within and around the array due to diffracted, radiated and perturbed wave field. The tested sea states have been also analysed in terms of spatial variation of the resulting wave height increase/reduction, and thus with regard to the extents of WEC array effects. The 5x5-WEC rectilinear, the 5x5-WEC staggered, the 13-WEC staggered, the 3x3-WEC rectilinear $5D$ and the 3x3-WEC rectilinear $10D$ arrays are presented. This data analysis aims to investigate the effect of changing the WEC array configuration and sea state conditions, on the WEC array effects and especially on wave height dissipation downwave (representing extra-array effects).

Four sea states have been analysed: irregular long-crested waves of two different peak wave periods, as well as short-crested waves (s = 10, wind waves; and s = 75, swell waves). The accuracy of generating the target wave fields has been evaluated. For the presented results, the difference between recorded and target undisturbed wave field is shown to be small.

There is clearly wave height attenuation in the lee of the WEC arrays due to the heaving WECs which extract energy from the waves. For long-crested irregular waves, up to 18.10 % of wave height decrease is observed downwave of 25 WECs arranged in rectilinear geometric configuration (with spacing between the WECs equal to $5D$). Wave height attenuation increases, reaching 20.80 %, when the same 25 WECs are arranged in staggered geometric configuration using the same spacing, $5D$. However, wave height reduction is expected to be larger, since the WEC units used for the experiments presented in this PhD research are not optimally controlled under irregular seas, and, thus, extract less power from the incoming waves in irregular wave conditions. In real wave farm applications, though, WECs are designed to be optimally controlled to extract a great amount of power from the waves, and therefore will cause larger wave height dissipation downwave.

The 5x5-WEC arrays under wind seas result also in large wave height attenuation but smaller than that caused under irregular long-crested waves. Also the zone of wave height attenuation downwave is shorter in length for wind seas.

WEC arrays of larger spacing between the WECs (i.e. $10D$) cause less wave height attenuation downwave, for all sea states, while for wind waves wave height recovery is observed in rather short distances downwave of such arrays.

The patterns of wave height attenuation within the WEC arrays differ for different sea states. For short-crested wind waves (spreading parameter s = 10), wave height decrease is observed already after the front row of WECs, while for long-crested waves this decrease occurs only after the third row of WECs.

The results for wave height attenuation found downwave of WEC arrays can be further used for estimating the coastline evolution due to the presence of a WEC array, i.e. by applying traditional formulae predicting the long-shore sediment

transport and erosion or accretion, based on wave height parameters, e.g. as performed in ([38]; [39]).

The data obtained from these experimental tests will be very useful to validate and extend a large range of numerical models used to model response, power absorption and wave field modifications due to oscillating WECs. Validation of such models will enable optimization of the geometrical layout of WEC arrays for real applications and will therefore enable reduction of the cost of energy from wave energy systems.

Most importantly, the obtained WEC array database within this PhD research is comprehensive, and is applicable not only to WEC arrays but also to floating structures/platforms, stationary cylinders under wave action, etc., for understanding of e.g. wave impact on the cylinders and wave field modifications around them.

Within this chapter, the third part of this PhD research (as part of the WECwakes project) has been introduced and it has been shown that: **(i)** large-scale experiments have been performed with large WEC arrays composed of up to 25 WECs, **(ii)** a comprehensive WEC array database for heaving WECs has been created in which wave elevations, WEC response and wave induced surge forces on the WECs have been simultaneously measured. The created WEC array database comprises a wide range of parameter variations such as: the array geometric configuration, the WEC number, the lateral and longitudinal (centre-to-centre) spacing between the WECs, the WECs' motion (decay motion, stationary WECs, "free" response or damped motion of WECs with varying damping), wave conditions (varying wave period, wave heights, wave attack angles) and wave types (regular, polychromatic, irregular long- and short-crested with varying spreading parameters), **(iii)** constructive or destructive intra-array interactions affect the power absorption of the entire WEC array, and **(iv)** large arrays of 25 WECs are shown to have significant effect on the resulting wave field downwave of the WEC array, which can influence neighbouring activities in the sea, coastal eco-systems and even the coastline and the coastal defence conditions and parameters, for real wave energy applications.

4.8. References

[1] Beels, C.; Troch, P.; Kofoed, J.P.; Frigaard, P.; Vindahl Kringelum, J.; Carsten Kromann, P.; Heyman Donovan, M.; De Rouck, J.; De Backer, G. *A methodology for production and cost assessment of a farm of wave energy converters.* Renewable Energy, **2010**; 36(12), 3402-3416.

[2] Troch, P.; Beels, C.; De Rouck, J.; De Backer, G. *Wake effects behind a farm of wave energy converters for irregular long-crested and short-crested waves.* In the Proceedings of the International Conference on Coastal Engineering, No. 32(**2010**), Shanghai, China.

[3] Child, B.F.M. *On the configuration of arrays of floating wave energy converters.* Ph.D Thesis, Edingburgh University, **2011**.

[4] Borgarino, B.; Babarit, A.; Ferrant, P. *Impact of wave interactions effects on energy absorption in large arrays of wave energy converters.* Ocean Engineering, **2012**; 41, 79 88.

[5] Babarit, A. *On the park effect in arrays of oscillating wave energy converters.* Renewable Energy, **2013**; 58, 68–78.

[6] Folley, M., Babarit, A.; O' Boyle, L.; Child, B.; Forehand, D.; Silverthorne, K.; Spinneken, J.; Stratigaki, V.; Troch, P. *A review of numerical modelling of wave energy converter arrays*. In the Proceedings of the 31st International Conference on Offshore Mechanics & Arctic Engineering; Rio de Janeiro, Brazil, **2012.**

[7] Li, Y.; Yu, Y.-H. *A synthesis of numerical methods for modelling wave energy converter-point absorbers.* Renewable & Sustainable Energy Reviews, **2012**; 16.6:4352-4364.

[8] Troch, P. *MILDwave – A numerical model for propagation and transformation of linear water waves.* Internal Report, Department of Civil Engineering, Ghent University, **1998**.

[9] Vantorre, M.; Banasiak, R.; Verhoeven, R. *Modelling of hydraulic performance and wave energy extraction by a point absorber in heave.* Applied Ocean Research; **2004**; 26:61–72.

[10] De Backer, G. *Hydrodynamic Design Optimization of wave energy converters consisting of heaving point absorbers.* PhD thesis. Department of Civil Engineering, Ghent University, Belgium, **2009**.

[11] Zanuttigh, B; Angelelli, E.; Kofoed, J.P. *Effects of mooring systems on the performance of a wave activated body energy converter.* Renewable Energy, **2013**; 57, 422-431.

[12] Budal, K.; Falnes, J.; Kyllingstad, A.; Oltedal, G. *Experiments with point absorbers in regular waves.* In the Proceedings of the 1st Symposium on Wave Energy Utilization, **1979**; pp. 253–282, Gothenburg.Sweden.

[13] Vantorre M. *Third-order potential theory for determining the hydrodynamic forces on axisymmetric floating and submerged bodies in a forced periodic heave motion.* PhD thesis, Ghent University, **1985**.

[14] Marquis, L.; Kramer, M.; Frigaard, P. *First Power Production figures from the Wave Star Roshage Wave Energy Converter*. In the Proceedings of the 3rd International Conference on Ocean Energy (ICOE-**2010**), Bilbao.

[15] Thomas, S.; Weller, S.; Stallard, T.J. *Float response within an array: Numerical and experimental comparison.* In the Proceedings of the 2nd International Conference on Ocean Energy (ICOE), Brest, France, October **2008**.

[16] Weller, S.D.; Stallard, T.J.; Stansby, P.K. *Interaction factors for a rectangular array of heaving floats in irregular waves.* IET Renewable Power Generation. **2010**; 4(6), 628–637.

[17] Alexandre, A.; Stallard, T.; Stansby, P.K. *Transformation of Wave Spectra across a Line of Wave Devices.* In the Proceedings of the 8th European Wave and Tidal Energy Conference, **2009**; Uppsala, Sweden

[18] Ashton, I., Johanning, L.; Linfoot, B. *Measurement of the Effect of Power Absorption in the Lee of a Wave Energy Converter.* In the Proceedings of the 28th International Conference on Offshore Mechanics & Arctic Engineering, Honolulu, Hawaii, OMAE **2009**, vol. OMAE2009-79793.

[19] Folley, M.; Whittaker, T. *Preliminary cross-validation of wave energy converter array interactions.* In the Proceedings of the OMAE2013 Conference, **2013**; Nantes, France.

[20] Stratigaki, V.; Troch, P.; Stallard, T.; Forehand, D.; Kofoed, J.P.; Folley, M.; Benoit, M.; Babarit, A.; Kirkegaard, J. *Wave Basin Experiments with Large Wave Energy Converter Arrays to Study Interactions between the Converters and Effects on Other Users in the Sea and the Coastal Area.* Energies **2014**, *7*, 701-734.

[21] Troch, P.; Stratigaki, V.; Stallard, T.; Kofoed, J.P.; Forehand, D.; Folley, M.; Benoit, M.; Babarit, A.; Gallach Sánchez, D.; De Bosscher, L.; Rauwoens, P.; Elsässer, B.; Lamont-Kane, P.; McCallum, P.; McNatt, C.; Angelelli, E.; Percher, A.; Carpentero Moreno, E.; Bellew, S.; Dombre, E.; Charrayre, F.; Vantorre, M.; Kirkegaard, J.; Carstensen, S. *Large scale physical modelling of an array of 25 wave energy converters in the WECwakes project.* In the Proceedings of the 10th European Wave and Tidal Energy Conference Series (EWTEC), Aalborg, Denmark, 2-5 September **2013**.

[22] Borgman, L. E.; Panicker, N. N. *Design study for a suggested wave gage array off point mugu*, California. Tech. Rep. 1-14, Hydraulic Eng. Lab., Univ. Calif., Berkeley, California, **1970**.

[23] Stratigaki, V. and Troch, P.. *Large scale experiments on wave energy converter farms to study the near-field effects between the converters and the far-field effects on other users in the coastal area: the WECwakes research project.* EU FP7 HYDRALAB IV programme (contract no. 261520), Research report, Ghent University, Ghent, 28 August **2013**.

[24] O'Boyle, L. *Wave Fields around Wave Energy Converter Arrays*, PhD Thesis, Queen's University, Belfast, **2013**

[25] Longuet-Higgins, M.S.; Cartwright, D.E.; Smith, N.D. *Observations of the directional spectrum of sea waves using motions of a floating buoy.* In Ocean Wave Spectra, Prentice Hall, New York, **1963**; pages 111–136.

[26] Goda, Y.; Suzuki, Y. *Computation of refraction and diffraction of sea waves with Mitsuyasu's directional spectrum.* Tech. Note of Port and Harbour Res. Inst., **1975**; 230.

[27] Beels, C.; Troch, P.; De Backer, G.; Vantorre, M.; De Rouck, J. *Numerical implementation and sensitivity analysis of a wave energy converter in a time-dependent mild-slope equation model.* Coastal Engineering, **2010**; 57(5), 471-492.

[28] Beels, C.; Troch, P.; De Visch, K.; Kofoed, J.P.; De Backer, G. *Application of the time-dependent mild-slope equations for the simulation of wake effects in the lee of a farm of Wave Dragon wave energy converters.* Renewable Energy, **2010**; 35, 1644-1661.

[29] D. I. M. Forehand, A. P. McCabe, and A. R. Wallace. *A hydrodynamic, time-domain, wave energy converter array model using state-space techniques*. To be submitted to Ocean Engineering, **2013**.

[30] WAMIT version 7.0 user manual. [Online]. Available: http://www.wamit.com/. Accessed March **2013**.

[31] Weller, S., Stallard, T. & Stansby, P.K.. *Experimental measurements of irregular wave interaction factors in closely spaced arrays.* Proceedings of the 8th European Wave & Tidal Energy Conference, Sweden, **2009**.

[32] Budal K. *Theory of absorption of wave power by a system of interacting bodies.* Journal of Ship Research **1977**;vol. 21:248-53.

[33] Evans DV. *Some theoretical aspects of three dimensional wave energy absorbers.* In the Proceedings of the 1st symposium on wave energy utilization, Gothenburg, Sweden; **1979**.

[34] Falnes J. *Radiation impedance matrix and optimum power absorption for interacting oscillators in surface waves.* Applied Ocean Research **1980**;vol. 2:75-80.

[35] Child B, Venugopal V. *Interaction of waves with an array of floating wave energy devices.* In the Proceedings of the 7th European wave and tidal energy conference, Porto, Portugal; **2007**.

[36] Babarit, A.. *On the park effect in arrays of oscillating wave energy converters.* Renewable Energy. 58, 68-78, **2013**.

[37] Aalborg University: WaveLab 3.33 Manual. **2007**; homepage: http://www.hydrosoft.civil.auc.dk/

[38] Mendoza, E.; Silva, R.; Zanuttigh, B.; Angelelli, E.; Lykke Andersen, T.; Martinelli, L.; Nørgaard, J.Q.H.; Ruol, P. *Beach response to wave energy converter farms acting as coastal defense.* Coastal Engineering, Available online 12 November; ISSN 0378-3839, http://dx.doi.org/10.1016/j.coastaleng.2013.10.018, **2013.**

[39] Nørgaard, J.H., Lykke Andersen, T.. *Experimental and numerical investigation of wave transmission from a floating Wave Dragon wave energy converter*. International Ocean and Polar Engineering Conference, Rhodes (ISOPE), **2012**.

5

Guidelines for design of WEC arrays

Abstract: *In this chapter, a detailed overview is provided of the main conclusions obtained from the experimental testing of the large WEC arrays presented in Chapter 4, within the third part of this PhD dissertation. Furthermore, based both on the conclusions of the experiments and on results found in the literature regarding power absorption and wave field modifications by WEC arrays, guidelines are presented for the design of WEC arrays. These guidelines concern intra-array interactions and extra-array effects and can be used for optimal design of WEC arrays by wave farm developers. Such guidelines, based both on large WEC array experiments, and the to-date state of the art, are not available in the literature.*

5.1. Introduction

In this chapter, guidelines for design of WEC arrays are presented. These guidelines are based on results for both power output and wave field modifications from the experiments with large WEC arrays performed within this PhD research. The experimental arrangement and the obtained results and analysis are presented in detail in Chapter 4. Such guidelines are not available in literature for large WEC arrays, except for recommendations based on numerical results, only [1].

5.2. Conclusions from experiments with large WEC arrays

5.2.1. Power output

General

The time-averaged power output of the individual WEC #05 (in isolation), of the 5x5-WEC rectilinear array ($w = l = 5D$), of the 5x5-WEC staggered array ($w = l = 5D$), of the 3x3-WEC rectilinear $5D$ array ($w = l = 5D$) and the 3x3-WEC rectilinear $10D$ array ($w = l = 10D$), has been estimated for irregular long- and short crested waves (w and l are the lateral and longitudinal spacing between the WECs, respectively). These sea states have been selected, as being representative for realistic wave conditions.

For the WEC arrays, the interaction $\bar{q}$-factor, has been estimated, as the ratio of the total time-averaged power from the entire WEC array to that of the same number of the reference WEC #05 in isolation. For all of the presented WEC array configurations, none of the WEC units absorb equal power to that by the individual WEC #05 (in isolation). Therefore intra-array interactions (destructive or constructive) are present for all shown WEC arrays, even for the arrays of larger spacing between the devices.

Long-crested irregular waves

- For all WEC arrays, the highest time-averaged power absorption per WEC is obtained by WECs in the second row, followed by the third and the front row. The time-averaged power absorption of those WECs is higher than that obtained by the individual WEC #05 (in isolation).

- Only for the 3x3-WEC rectilinear $10D$ array, intra-array interactions have constructive effect on the power output of all WEC units of the array. The 5x5-WEC staggered array follows, regarding positive intra-array interactions, and then the 5x5-WEC rectilinear array. Consequently, the highest WEC array interaction $\bar{q}$-factor, is obtained for the 3x3-WEC rectilinear $10D$ array, followed by the 5x5-WEC staggered array and finally by the 5x5-WEC rectilinear array. For the 3x3-WEC rectilinear $5D$ array, destructive intra-array interactions take place. However, as seen by the total time-averaged power output results for the entire 3x3-WEC rectilinear $10D$ array, large spacing is not sufficient to reach the power output obtained by the 5x5-WEC arrays, and therefore larger number of WECs is necessary.

- The same WEC unit absorbs up to 16.31 % less power compared to the individual WEC #05 (in isolation), when it operates within the rectilinear and the staggered 5x5-WEC array. For the same WEC unit, though, significant positive effect of the intra-array interactions is achieved, when it operates within the 3x3-WEC rectilinear $10D$ array. As a conclusion, for the array of the large $10D$ spacing, and certainly for the arrays of smaller spacing, intra-array interactions still occur. These interactions are significant and cannot be neglected due to the large spacing between the WECs. This is in agreement with numerical studies by [2] for 2 heaving WEC cylinders.

- The WECs of the front row, facing as first the incoming waves, experience destructive intra-array interactions, besides for the 3x3-WEC rectilinear $10D$ array where the spacing between the WECs is large enough to prevent negative effect of these hydrodynamic interactions. The WECs of the front row experience larger surge force, as measured, but have smaller response amplitudes and therefore velocities. As a consequence, the resulting power output of the front WECs is smaller compared to other rows and for these WEC units negative intra-array interactions are observed. A similar observation has been made in [3] for a 3x1-WEC array (floats). In [3], also a 9x9-WEC array has been tested; there, the largest power output has been found at the front row. However, only regular waves have been studied in [3].

- Moreover, WEC units located at central locations within the presented arrays, benefit the most from the intra-array interactions, compared to the rest of the WECs within the array. This is due to the perturbed wave field sent back by the surrounding WECs. The largest power output is found, thus, at central locations in the array. In [3] similar conclusions have been made for the centrally located WECs, of the tested WEC array configurations.

- The column $\bar{q}$-factors indicate generally more positive results, compared to the row $\bar{q}$-factors. There is no indication that specific columns are significantly

less effective, and thus, also no indication for need to limit the number of columns within the tested arrays. Moreover, the column $\bar{q}$-factors are closer to the WEC array $\bar{q}$-factor.

- On the other hand, the row $\bar{q}$-factors of the last (and the front) rows of the arrays, indicate pronounce negative (or less constructive for the 3x3-WEC rectilinear $10D$ array) intra-array interactions. Attenuation of absorbed power is observed in the longitudinal direction of the wave basin, and therefore the last rows do not operate effectively. This conclusion gives an indication for need to limit the number of rows within an array. Moreover, this conclusion is in agreement with [4] who simulated numerically a 5x5-WEC array of OSWCs (Oscillating Surge Wave Energy Converters) and made a similar analysis of the average absorbed power per row. Also in [5], where a 3x4-WEC array (of floats with $4D$ spacing) has been experimentally tested, similar conclusions have been made, as well as in [6] where a 5x1-WEC array has been tested under regular seas.

- The 3x3-WEC rectilinear $10D$ array is a small array composed of just 9 WEC units. Nevertheless, the WEC array $\bar{q}$-factor is larger than that found for the large 5x5-WEC arrays, for the same wave conditions. This indicates that the spacing is large enough between the WECs, avoiding not only negative intra-array interactions, but also achieving significant constructive intra-array interactions between the WECs of the array. The 3x3-WEC rectilinear $10D$ array results in a significantly more (by 88.2 %) effective WEC array geometric configuration, compared to the 3x3-WEC rectilinear $5D$ array. Compared to all WEC arrays, by making the WEC spacing twice as large, a significant optimization of all $\bar{q}$-factors is achieved (especially for the rows).

- The 3x3-WEC rectilinear $5D$ array has not sufficient WEC units (only a few columns) to allow the occurrence of positive intra-array interactions, compared to the 5x5-WEC rectilinear array. Intra-array interactions have a destructive effect on the overall power absorption of the entire WEC array. However, even though the array is composed of just 9 WECs, the WEC array $\bar{q}$-factor for a long-crested sea is larger than that found for the large 5x5-WEC arrays under short-crested irregular waves.

- For the staggered array, by shifting two WEC rows, positive effect on the power output of four extra WEC units has been achieved as well as higher total power absorption, compared to the rectilinear array. Wider spreading of the constructive intra-array interactions has been achieved, and consequently destructive interactions have been limited. This WEC array configuration is the most effective (13.10 % better performance compared to the 5x5-WEC rectilinear array) for both long-crested waves and small spacing between the

WECs. However, it performs by 10.22 % less good, compared to the 5x5-WEC rectilinear array, under wind waves.

- By changing the geometric configuration of the 5x5-WEC array from rectilinear to staggered, a significant optimization of the row $\bar{q}$-factors has been achieved for all rows, and in particular for the first four ones. However, for the last (5^{th}) row no significant optimization has been achieved, indicating that there is a limit of WEC row efficiency within an array, thus a limit of number of rows for which a row (or even the entire array) performs efficiently. This conclusion is in agreement with the guidelines reported in [1] based on numerical simulations.
- The 5x5-WEC rectilinear array (spacing $5D$) results in WEC array $\bar{q}$-factor larger than unity, while the 3x3-WEC rectilinear $5D$ array (spacing $5D$) has $\bar{q}$-factor lower than unity. Therefore, a larger number of columns can compensate for the less absorbed power per WEC unit, found for small arrays.
- The 5x5-WEC arrays (spacing $5D$) result in column $\bar{q}$-factors larger or close to unity. This indicates that a larger number of columns (compared to the 3x3-WEC rectilinear $10\,D$ array) can compensate for the less absorbed power achieved by WEC arrays of small spacing. Consequently, increasing the number of the array columns can offer an alternative option for achieving constructive intra-array interactions within an array, without having to use large spacing between the WECs. This is particularly useful when the area available for the installation of a WEC array is limited.

Short-crested irregular wind waves

- For both analysed WEC arrays, the highest time-averaged power absorption per WEC is obtained at the second row, followed by the third and the front row of WECs, which differs from the rectilinear array due to change of the array geometric configuration.
- All WECs of the array absorb less wave energy compared to the individual WEC #05 (in isolation). Directional wind waves cause for both WEC array geometric configurations significant destructive intra-array interactions.
- Similarly to long-crested waves, the WEC units centrally situated within the array benefit the most from intra-array interactions. Therefore, as for long-crested irregular waves, the largest power output is found at central locations within the arrays, in accordance to findings from [3].

- WEC units located at the front or the last two rows suffer the most from negative intra-array interactions.
- Attenuation of absorbed wave power is observed in the longitudinal direction of the WEC array, towards the wave absorbing beach. However, this attenuation is not as clear as for long-crested waves, due to the wave directionality. This is also shown by the small differences between the variation ranges, both of the column and the row $\bar{q}$-factors.
- Even though the change in geometric configuration (from rectilinear to staggered array) is significantly beneficial for the long-crested irregular waves (around 13.10 %), for directional wind waves the opposite is observed, with a reduction of the WEC array $\bar{q}$-factor by 10.22 %.
- For short-crested waves, the effect of the number of rows is not as pronounced as for long-crested waves. However this attenuation is observed, which indicates the need to limit the number of the rows of the WEC array. Attenuation of absorbed wave power is observed towards the longitudinal direction of the WEC array, as for long-crested waves.
- The effectiveness of the 5x5-WEC staggered array has been reduced by almost 53.0 % due to intra-array interactions that take place within the WECs of the array, induced by wind waves.

5.2.2. Wave field modification

The wave field modifications due to wave energy extraction and the WECs' motion have been analysed for various WEC array configurations in Chapter 4, in terms of (i) the diffracted, (ii) the radiated and (iii) the perturbed wave field, as well as (iv) the dimensions of WEC array effects. Wave height dissipation is of particular interest, representing extra-array effects. Also wave height increase is discussed, as a result of intra-array interactions between the WEC units, as well as, a result of wave-WEC interactions.

Several sea states have been analysed: irregular long-crested and short-crested waves (s = 10, wind waves and s = 75, swell waves), for investigating the effect of wave directionality on WEC array effects. In addition, irregular long-crested waves with peak wave period $T_p = T_n$, the resonance period of an individual WEC unit have been analysed. Only irregular waves are discussed, since real wave farm applications will only experience irregular waves in the installation site.

Wave field results obtained for the 5x5-WEC rectilinear, the 5x5-WEC staggered, the 13-WEC staggered, the 3x3-WEC rectilinear 5D and the 3x3-WEC

rectilinear $10D$ arrays, are compared in terms of changing the WEC array geometric configuration (i.e. shifting rows to create staggered layouts, making the spacing between the WECs larger or smaller, removing / adding rows or columns, removing / adding WEC units).

5.2.2.1. Diffracted wave field

General:

- The highest wave height reduction is observed in the lee of the 5x5-WEC rectilinear array, as a result of the small WEC spacing, the large number of rows and columns, the large number of WEC units, and the large spatial extents of this array.
- However, no large differences downwave of the arrays are observed for all analysed WEC arrays and all sea states.
- Larger differences are found between wind and long-crested irregular waves, while swell directional waves (mainly) represent an intermediate situation.
- The wave field evolution shows change from wave height increase to wave height decrease towards the opposite end of the wave basin (landwards). For the WEC arrays of $5D$ spacing between the devices, the wave field evolution has a "parallel" pattern to the WEC rows, which is not found when the WEC spacing becomes twice as large.
- For all sea states and WEC arrays, the highest wave height increase is observed within the front row of WECs, facing as first, the incoming waves. However, for WEC arrays of the larger spacing ($w = 10D$), this wave height increase remains very localised (in front of the WECs only) and does not extend in-between the devices, in contrast to the arrays of $w = l = 5D$.

Long-crested irregular waves

- No large wave field variations between irregular long-crested waves of two different peak wave periods are found, besides in the area around the front WECs. This is a result of the rather small difference between the tested wave periods (yet one of them represents situation of $T_p = T_n$).
- Waves of longer wavelength result in lower wave height dissipation downwave. For the staggered arrays, due to the shifted rows, almost no

significant difference in wave height reduction is found for the two different peak wave periods. However, this is not confirmed for the rectilinear array, for which larger differences are found within the extents of the WEC array. This result indicates a relationship between the wave period and the WEC array geometric layout.

- For long-crested waves of shorter wavelength, propagating through the largely-spaced arrays, wave heights are reduced the least in-between the WECs of the front row, indicating a relationship between wave period and WEC spacing.

Short-crested irregular waves

- Wave height decrease is observed already at the first three rows for wind waves.

5.2.2.2. Radiated wave field

General:

- For the WEC arrays of $5D$ spacing between the devices, radiation has a significant (and very similar for all arrays) effect on wave height reduction, downwave. For the WEC arrays of $10D$ spacing between the devices, the effect of radiation downwave is small, and in the same order of magnitude as that caused by diffraction effects. This is a result of the large spacing between the WECs, which limits the interaction between the radiated wave fields from neighbouring WEC units.
- The wave field evolution shows change from wave height increase to wave height decrease, with a diagonal pattern towards the WEC columns located at the sides of the WEC arrays.

Long-crested irregular waves:

- For long-crested waves of shorter T_p (in this case also equal to the resonance period of an individual WEC unit), wave height reduction downwave is smaller.

- For the 5x5-WEC staggered arrays, no large wave field variations between long-crested irregular waves of two different peak wave periods are found, while the wave field symmetry is not significantly affected by a peak wave period close to the resonance period of a WEC unit. Effects appear to be smoothened due the shifted rows. For the 5x5-WEC rectilinear and the 13-WEC staggered arrays, however, large differences are observed while a clear lack of wave field symmetry for long-crested waves of $T_p = T_n$ is found.
- For the WEC array of larger ($10D$) spacing, also transverse wave height variations are found for long-crested irregular wave conditions of $T_p = T_n$.

Short-crested irregular waves:

- The effect of varying the wave directionality parameter is rather limited, but when comparing wind to long-crested irregular waves, larger differences are observed.
- Short-crested waves result in rather symmetric wave fields around the WECs, besides for the array of spacing $10D$.

5.2.2.3. Perturbed wave field

General:

- Downwave of all WEC arrays, wave height dissipation is observed for the perturbed wave field. Similarly, in [7], a 5x1- and a 5x2-WEC array have been tested under irregular waves. For the latter array, up to 14.0 % wave height dissipation downwave has been found.
- For all tests and WEC array configurations, the highest wave height increase is observed locally upwave of the entire front row of WECs, facing as first, the incoming waves. This increase is maintained in-between the devices for the arrays of $5D$ spacing, but not for the arrays of $10D$ spacing. This is also shown in [8] where wave farms of increasing spacing have been numerically investigated.
- The wave field evolution shows change from wave height increase to wave height decrease towards the opposite end of the wave basin (landwards).

- For all sea states, increase of wave height is found at the sides of the array (as shown e.g. in [8], [9], [10]). For wind waves, increased wave height is found only at the sides of the front row (yet, wave height reduction is smaller at the sides of the entire array), also shown numerically in [10].
- For all sea states and all WEC arrays, the highest wave height dissipation is observed within a zone of $-5D < X < +5D$ (zone width < $10D$) downwave of the arrays. This result agrees with numerical studies of e.g. 9 generic WECs both for short-crested waves [10] and for long-crested irregular waves [11].
- For both 5x5-WEC arrays and all sea states (WEC spacing $5D$), the highest wave height dissipation is observed at locations at least $10D$ downwave of the WEC array ([10], [11]).
- For the 13-WEC staggered array (WEC spacing $10D$ between WECs of the same columns and the same rows) and all sea states, the highest wave height dissipation is observed at distance $5D$ downwave of the WEC array; wave height recovery is observed for all sea states at locations at a distance of $10D$ downwave of the WEC array. Therefore, the larger WEC spacing results in shorter wave height dissipation area downwave of the array.
- For the 3x3-WEC rectilinear $10D$ array (WEC spacing $10D$) and all sea states, the highest wave height dissipation is observed locally at locations $5D$ - $10D$ downwave of the WEC array. No clear wave height recovery is observed downwave of the array, as seen for the 13-WEC staggered array of the same spacing. Therefore, the larger WEC spacing results in shorter wave height dissipation area downwave of the array.
- For the 3x3-WEC rectilinear $5D$ array and long-crested / swell irregular waves, the highest wave height dissipation is observed at locations, at least at distance $15D$ - $20D$ downwave of the WEC array. For swell directional waves, wave height recovery is observed downwave of the array, while wave height is fully recovered at $20D$ downwave of the WEC array for short-crested wind waves.
- For the arrays of $10D$ spacing, the largest wave field variations between irregular long- and short-crested wind waves (with $s = 10$) are found within the extents of the array (zone width = $10D$ to $20D$).
- For the arrays of $5D$ spacing, the largest wave field variations between long- and short-crested wind waves are found between the zone downwave of the front row of WECs and at a distance $5D$ downwave of the last row of WECs (zone width = $25D$ to $30D$).
- For the arrays of $10D$ spacing, the wave field in the distances in-between the WECs, shows large variations and indicates wave recovery between the WECs.

This wave recovery is observed both in the lateral and in the longitudinal direction of the wave basin and remains visible within the extents of the arrays.

Long-crested irregular waves

- For arrays of $5\,D$ spacing between the devices, the largest wave height dissipation is found for the 5x5-WEC staggered array, followed by the 5x5-WEC rectilinear array, then for the 13-WEC staggered array and finally for the 3x3-WEC rectilinear $5D$ array.
- Staggered geometric configurations of large arrays result in larger wave height dissipation downwave of the array, and therefore to more significant extra-array effects; this conclusion is in agreement with numerical studies in [11].
- This larger wave height dissipation (15.0 % higher than the rectilinear array) found for the 5x5-WEC staggered array, is also shown by the results for power output of this array configuration for long-crested waves. Higher average power and higher WEC array interaction factor, by almost 13.00 % is achieved by the staggered array compared to the 5x5-WEC rectilinear array, under the same wave conditions. Also, unlike for the 5x5-WEC rectilinear array, wave height reduction varies downwave of the array for different sea states, as a result of the small spacing and the staggered layout.
- The 3x3-WEC rectilinear $5D$ and the 3x3-WEC rectilinear $10D$ arrays, result in similar level of wave height attenuation in their lee. Two targets are achieved by the 3x3-WEC rectilinear $10D$ array geometric configuration, due to the large spacing between the devices: (i) the most limited extra-array effects compared to all WEC arrays of $5D$ spacing between the devices; and (ii) the largest WEC array interaction $\bar{q}$-factor.
- It is clear that the 3x3-WEC rectilinear $5D$ array due to its limited extents ($10D$ x $10D$) does not cause the large wave height dissipation found for larger arrays (the 5x5-WEC rectilinear array with extents $20D$ x $20D$). However, due to small spacing, it causes wave attenuation which, for long-crested irregular waves, is maintained for long distances downwave of the array.

Wind short-crested irregular waves

- For arrays of $5D$ spacing between the devices and for wind waves, the largest wave height dissipation is found for the 5x5-WEC rectilinear array, followed

by the 5x5-WEC staggered array, the 3x3-WEC rectilinear $5D$ array, the 3x3-WEC rectilinear $10D$ array, and finally the 13-WEC staggered array.

- For short-crested wind waves, wave height decrease in the lee of the 5x5-WEC staggered array is much smaller compared to that found for the long-crested irregular waves, as well as to that found for wind waves for the rectilinear array (reduced by 11.54 %). This lower wave height attenuation is also explained by the power output, resulting to the lowest time-averaged absorbed power and WEC array lower interaction factor compared to: (i) the long-crested irregular waves for the staggered array, and (ii) the rectilinear array under the same wave conditions.
- For both 5x5-WEC array configurations and for short-crested wind waves, wave height decrease is equal or much smaller compared to that found for the long-crested waves.
- For all WEC arrays, wave height dissipation is observed already after the front row of WECs for short-crested waves for wind waves.
- For the 3x3-WEC rectilinear $5D$ array, waves are fully recovered at $20D$ downwave of the WEC array for short-crested wind waves, while wave height recovery starts shortly downwave of the array. This shorter length of wave height recovery downwave of directional waves has been found also numerically for 9 generic WECs in [10] and for 18 OSWCs in [9].

Swell short-crested irregular waves

- For swell directional waves and for all presented WEC arrays, an intermediate situation is obtained regarding wave height modifications.
- Wave height decrease starts to take place only after the third row of WECs, for all arrays.
- Wave height recovery at a distance of $20D$ downwave of the WEC array, is observed for the small 3x3-WEC rectilinear $5D$ array.

Different peak wave periods

- For all WEC array configurations, no significant differences are found between the two tested peak wave periods: the 5x5-WEC staggered array results in smoothened wave field modifications due to the shifted rows, both the 13-WEC staggered array and the 3x3-WEC rectilinear $10D$ array have large

enough spacing, and the 3x3-WEC rectilinear $5D$ array has very limited extents. Only for the 5x5-WEC rectilinear array, difference is found in the resulting wave patterns for the two studied wave periods.

- However, the staggered arrays result in slightly larger differences between the two wave periods. This observation supports the aspect that wave period has effect on the WEC array effects, related to the WEC array geometric layout.
- Larger wave height attenuation is observed for the longer wave period, with the shorter one corresponding to the resonance period of an individual WEC unit.

5.3. Guidelines for design of WEC arrays

Based on the analysis presented in Chapter 4 and the conclusions presented in Sections 5.2 and 5.3, guidelines for the design of WEC arrays are proposed in this section.

These guidelines for design of WEC arrays are based both on the first physical modelling of large WEC arrays, compared to findings from the literature, by numerical studies of similar WEC arrays as well as experiments of small WEC arrays (see Section 5.2 and 5.3).

The distances mentioned in the guidelines are presented in terms of the characteristic dimension of a WEC (thus for a WEC buoy, the diameter, D). *Width* and *length* refer to dimensions in the lateral (perpendicular to the wave propagation direction, $\theta = 0°$) and the longitudinal (parallel to the wave propagation direction, $\theta = 0°$) direction of the WEC array. Conventionally, here a *row* and a *column* of WECs, refers to a number of devices oriented perpendicular and parallel, respectively, to the wave propagation direction, $\theta = 0°$. Moreover, the terms "*front row*" and "*last row*" refer to the rows facing the incoming waves, as first and as last, respectively. The guidelines are also presented in terms of the lateral, w, and longitudinal, l, spacing between the WECs. In addition, the WEC array interaction $\bar{q}$-factor is used to quantify the efficiency of an array regarding power absorption, and is the ratio of the total power from the entire WEC array to that of the same number of WECs in isolation. When $\bar{q}$-factor > 1.0, intra-array interactions have a constructive effect on the power absorption of the entire WEC array, while their effect is destructive when $\bar{q}$-factor < 1.0.

Moreover, the guidelines are distinguished between those referring to intra-array interactions and those referring to extra-array effects of WEC arrays. Furthermore, the proposed guidelines are distinguished between guidelines for small WEC arrays (number of WEC units < 9), for large WEC arrays (number of WEC units > 9) and guidelines proposed for WEC arrays of any size. A last classification of the proposed guidelines is based on the sea state, and is indicated using the

abbreviation "LCW", when a guideline applies to long-crested irregular waves and the abbreviation "SCW" when it applies to short-crested wind waves, since those two sea states can result in significantly different WEC array effects.

5.3.1. Small WEC arrays

5.3.1.1. Intra-array interactions

- The spacing between the WECs should be as large as possible (at least $10D$) in order to achieve constructive or less destructive intra-array interactions within an array.

5.3.1.2. Extra-array effects

- Small spacing ($w = l = 5D$) between the WECs results in limited wave height dissipation downwave of the array.
- Installation of more smaller WEC arrays of large spacing ($w = l = 10D$), instead of one very large array with small WEC spacing, is preferable, as smaller arrays cause limited extra-array effects.
- (SCW). For wind directional waves and small arrays of small spacing ($w = l = 5D$), waves are fully recovered at a distance $20D$ downwave of the WEC array, while the wave height recovery starts shortly downwave of the array.

5.3.2. Large WEC arrays

5.3.2.1. Intra-array interactions

- (LCW). For long-crested irregular waves, staggered WEC array geometric configurations of small spacing ($w = l = 5D$) result in higher WEC array interaction $\bar{q}$-factor compared to rectilinear arrays of equal WEC spacing and number of WECs.
- (SCW). For wind directional waves, staggered WEC array configurations of small spacing ($w = l = 5D$) result in lower WEC array interaction $\bar{q}$-factor compared to rectilinear arrays of equal WEC spacing and number of WECs. When the WEC spacing is small, less wind waves propagate in-between the

WECs compared to long-crested irregular waves. As a result, less wave power is absorbed by the WEC array.

- (SCW). The effectiveness of a large WEC array of small spacing ($w = l = 5D$) can reduce significantly under short-crested wind waves.
- (SCW). When large wave directionality is characteristic of the WEC array installation site, larger spacing (at least $w = l = 10D$) should be used between the WECs.
- In case sufficiently large surface area is available at the installation site, the spacing between the WECs should be as large as possible (at least $w = l = 10D$).

5.3.2.2. Extra-array effects

- (LCW). For long-crested waves, staggered WEC array geometric configurations of small spacing ($w = l = 5D$) result in higher wave height dissipation in the lee of the array, compared to rectilinear arrays of equal WEC spacing and number of WECs.
- (SCW). For short-crested wind waves, staggered WEC array geometric configurations of small spacing ($w = l = 5D$) result in lower wave height dissipation in the lee of the array, compared to rectilinear arrays of equal WEC spacing and number of WECs.
- The installation of large WEC arrays very close to other activities in the sea or other marine (energy) projects, or close to the coastline, should be avoided if the dominating local wave conditions indicate large wave height dissipation, and given that these activities, coastal eco-systems or coastal defence projects, are sensitive to wave height dissipation.

5.3.3. All WEC arrays

5.3.3.1. Intra-array interactions

- None of the WECs of an array, with spacing between the WECs at least $w = l = 5D$ - $10D$, absorbs power equal to that absorbed by an individual WEC in isolation. The power absorbed by each of the WEC units of an array, can be higher or lower than that absorbed by an individual WEC in isolation.

- Intra-array interactions take place within an array even at WEC spacing $w = l = 10D$, which are not negligible.
- By increasing the spacing between the WECs of an array, negative effects of the intra-array interactions can be turned into positive. However, a large spacing only, is not sufficient to extract significant amount of power from the waves. Therefore, the use of large spacing should be accompanied by the increase of the WEC number within an array and by keeping the spacing large.
- In case, both increasing the WEC number within an array and keeping the spacing large is not possible, i.e. due to lack of sufficient ocean surface area, the number of WECs should be increased by adding columns and not rows.
- The WECs situated centrally within an array, seem to benefit the most or suffer the least from intra-array interactions, when these are constructive or destructive, respectively. This occurs due to superposition of the diffracted and the radiated waves by the neighbouring WECs.
- The last rows benefit the least or suffer the most from intra-array interactions, when these are constructive or destructive, respectively.
- Larger ($w = l = 10D$) spacing between the WECs results in higher WEC array interaction $\bar{q}$ -factor and to more positive (or less negative) intra-array interactions.
- There is no indication for need to limit the number of columns within an array.
- The number of rows should be as limited as possible. Attenuation of absorbed power occurs through the rows. For wind directional waves, wave height attenuation takes place already after the front row of WECs, which results in even more negative power extraction conditions for the following rows.
- When there is a need to increase the absorbed power of the WEC array, this should be realized by adding columns and not rows of WECs.
- Large spacing (at least $w = l = 10D$) leads to wave height recovery within the extents of the array, both in the lateral and the longitudinal direction.

5.3.3.2. Extra-array effects

- Wave height dissipation downwave of an array occurs within a zone of width at least equal to the width of the array. The highest wave height dissipation is observed within a zone of width $10D$ downwave of arrays of width $10D$ - $20D$. This zone is gradually filled up with increasing distance from the array.

- At the sides of the array, the wave height is increased (or less decreased for wind waves) due to diffraction effects.
- The larger the spacing between the WECs, the shorter the length of the zone of wave height dissipation and the sooner wave height recovery occurs downwave of the WEC array.
- For large ($10D$) spacing between the WECs, wave height recovery occurs at a distance larger than $10D$ downwave of the array.
- For small ($5D$) spacing between the WECs, wave height dissipation is still present at least at a distance $20D$ downwave of the array.

5.3.3.3. Intra-array interactions and extra-array effects

- By using a large ($10D$) spacing between the WECs, the following tasks are achieved leading to high WEC array efficiency:

  (i) limited wave height dissipation downwave of the array (thus limited extra-array effects for other users in the sea);

  (ii) wave height recovery within the extents of the array, both in the lateral and the longitudinal direction (leads to constructive intra-array interactions);

  (iii) a large WEC array interaction $\bar{q}$-factor (due to constructive intra-array interactions).

  The WEC array efficiency can be maximized by using staggered lay-outs, combined with large spacing.

- Usually research is focused on the performance of a WEC concept, by conducting numerical and / or experimental research with an individual device. However, this should be only the first phase for a wave energy project. Therefore it is absolutely necessary to move to the phase of studying large arrays of a WEC concept, numerically and / or experimentally. This phase cannot be lacking from the design of a WEC array, especially when limited ocean surface areas are available for the installation of such marine energy projects, and in particular, when this project is expected to influence its environment.

5.3.3.4. Sea states and variation in wave directionality

- Very commonly, WEC concepts are tuned in detail to extract optimally wave power from the waves, under controlled (laboratory) conditions and under monochromatic waves. However, these conditions do not represent a realistic situation.
- Both irregular long- and short-crested waves should be investigated, in order to study WEC array effects and power absorption numerically and experimentally, since the proposed sea states represent realistic wave conditions in the installation site of a wave farm. Most importantly, the proposed sea states represent worst-case and best-case conditions, as seen in the analysis presented in this PhD work, which is advised to use for dimensioning of any offshore or coastal project. In particular for experimental research, since it is not straightforward to construct models of large WEC arrays and laboratory time is expensive, priority should be given to long-crested and wind directional waves.
- Variation between wave directionality should be investigated only when this is an important characteristic of the installation site. Swell directional waves result in intermediate situations regarding wave height modifications, between irregular long-crested and short-crested wind waves. It is expected that similar results will be obtained also for power output.

5.4. References

[1] Babarit, A.. *On the park effect in arrays of oscillating wave energy converters*. Renewable Energy. 58, 68-78, **2013**.

[2] Babarit A. *Impact of long separating distances on the energy production of two interacting wave energy converters*. Ocean Engineering **2010**;vol. 37:718-29.

[3] T.J. Stallard, P.K. Stansby, A. Williamson. *An experimental study of closely spaced point absorber arrays*. Proceedings of the 18th International Offshore & Polar Engineering Conference (**2008**), Canada.

[4] Borgarino B, Babarit A, Ferrant P. *Impact of wave interactions effect on energy absorption in large arrays of wave energy converters*. Ocean Engineering **2011**;vol. 41:79-88.

[5] S.D. Weller, T.J. Stallard, P.K. Stansby. *Interaction factors for a rectangular array of heaving floats in irregular waves*. IET Renewable Power Generation. 4(6), (**2010**), 628–637.

[6] S. Thomas, S. Weller, T.J. Stallard. *Float response within an array: Numerical and experimental comparison.* Proceedings of the 2nd International Conference on Ocean Energy (ICOE-**2008**), Brest, France.

[7] Alexandre, A., Stallard, T.J., Stansby, P.K.. *Transformation of wave spectra across a line of wave devices.* Proceedings of the 8th European Wave & Tidal Energy Conference (EWTEC), Uppsala, Sweden, **2009**.

[8] Beels, C., P. Troch, G. De Backer, M. Vantorre, and J. De Rouck. *Numerical implementation and sensitivity analysis of a wave energy converter in a time-dependent mild-slope equation model.* Coastal Engineering, Vol. 57(5), pp. 471-492, **2010**.

[9] Borgarino B, Babarit A, Ferrant P.. *Impact of the separating distance between interacting wave energy converters on the overall energy extraction of an array*. Proc. of 9th European wave and tidal energy conference, Southampton, UK, **2011**.

[10] Beels, C. *Optimization of the lay-out of a farm of wave energy converters in the North Sea: analysis of wave power resources, wake effects, production and cost.* PhD dissertation, Ghent University, **2009**.

[11] P. Troch, C. Beels, J. De Rouck, G. De Backer. *Wake effects behind a farm of wave energy converters for irregular long-crested and short-crested waves*. Proceedings of the International Conference on Coastal Engineering, No. 32 (**2010**), Shanghai, China. Paper #: waves.22. Retrieved from http://journals.tdl.org/ICCE/.

6

Conclusions

Abstract: *In this chapter, the general conclusions of this PhD research are presented, as well as recommendations for further research.*

6.1. General

Ocean wave energy is one of the intensively developing renewable energy resources with great potential. Energy from ocean waves can be utilized by installing Wave Energy Converters (abbreviated as *WECs*) in the sea, which are devices that convert the kinetic and/or potential energy of waves into electricity.

In order to extract a considerable amount of energy at a specific site location, and to make the commercial exploitation of wave energy possible, installation of large numbers of WECs will be required, arranged in an array (or a *farm* or *park*) and using a particular geometric layout. The power production of the array may be smaller or larger than the sum of the power produced by the equivalent number of individual WECs, due to hydrodynamic interactions between the WECs within an array (so-called *intra-array interactions* or *park effect*). Moreover, as a result of the large number of WECs within an array, usually wave height attenuation is observed numerically and in scale model experiments with small WEC arrays (so-called *extra-array effects*). These wave field modifications can influence neighbouring activities in the sea, other marine (energy) projects, coastal eco-systems and even the coastline and the coastal defence conditions and parameters.

Therefore, an accurate understanding is required of the *WEC array effects*, consisting of the *intra-array interactions* between WECs in a wave farm and the *extra-array effects* on the environment.

Numerical studies on WEC arrays have provided a first insight into the magnitude and extent of *WEC array effects*. However, there has been very limited validation of these numerical models using physical scale models of WEC arrays; only a few are reported in the literature using typically less than 12 WECs. There is a clear knowledge gap in the literature and need for experiments on large WEC arrays. Such experimental data are essential for the evaluation of the accuracy of the employed numerical tools, their verification, as well as for their further development and improvement.

The large number of different WEC concepts, developed during the past decades, becomes prohibitive for WEC array testing, as, very often, WEC concepts are based on complex operating and structural principles or geometries. WEC developers tend to focus on the optimization of single prototype devices, and, thus, WEC concepts do not reach the stage of WEC array testing within a normal research funding period. Therefore a simple WEC device is necessary, easy to construct and to operate, specially developed for performing experiments with large WEC arrays. The obtained results can be extrapolated to WEC concepts based on similar operating principles.

WEC array effects are intensively numerically modeled by employing several numerical methods: (i) for investigating wave-WEC interactions, wave energy absorption and intra-array interactions (e.g. models based on the Boundary Element

Methods (BEMs) or the Navier-Stokes equations); and (ii) for investigating extra-array effects of WEC arrays in large areas (wave propagation models). However, these models suffer from a common problem; they cannot be used to model simultaneously, both intra-array interactions and extra-array effects, due to limitations such as insufficient accuracy or high computational cost. Therefore a coupling methodology is necessary for the efficient and accurate numerical combined modelling of WEC array effects.

This PhD research has focused on experimental testing of WEC arrays taking into account the above mentioned shortcomings, which are dealt with in three parts of the manuscript.

6.2. First part: design, development and evaluation of a WEC for array testing

Before performing experiments with large WEC arrays, the development of a simple WEC unit has been achieved, specially designed for WEC array testing. The developed WEC unit has been experimentally and numerically modeled in detail, in advance, to ensure high performance. The objective of developing this WEC was not to introduce a new WEC concept in the wave energy sector, but to create a WEC that efficiently supports and facilitates experimental and numerical modelling of large WEC arrays. The WEC unit is also representative of a wide range of WEC concepts and has a generic geometry based on the point absorber type, currently dominating in the wave energy sector.

The developed WEC unit aimed at a number of key requirements, necessary for its reproduction in large numbers, and for the easy repositioning of the WECs within the wave basin/flume to allow testing of alternative WEC array geometric configurations. Firstly, the developed WEC is robust; it is easy to operate and, economically and practically, straightforward and feasible to manufacture, since it facilitates low cost construction of identical WEC units. Secondly, the WEC unit is sufficiently large to develop measurable response and energy extraction for the tested incident wave conditions. The WEC has been designed to simulate the real impact of WECs on the wave climate, by using a simple concept of energy extraction from the incoming waves. This characteristic results in measurable changes to the wave field and, therefore, facilitates the quantification of extra-array effects. Thirdly, the WEC is straightforward to be modelled analytically and numerically in a response model, since the number of degrees of freedom of the entire WEC array is limited (equal to the number of WEC units within an array). This has been achieved by designing a single-degree-of-freedom (DOF) WEC unit, and e.g. not a 6-DOF (or less) WEC unit, which would result in high complexity of

the numerical and analytical treatment of the entire WEC array, proportional to the total number of DOFs of all WECs. In addition, the WEC has an idealised and simple WEC buoy geometry with vertical sides at the water plane.

The developed WEC unit has been first thoroughly tested in two wave flumes and a wave basin, to satisfy the necessary requirements. Due to its simple design, the developed WEC unit allowed experiments of 36 different WEC (array) configurations, in total. Linear analysis of the WEC response using WAMIT, as well as experimental testing have been conducted, with the aim to evaluate the performance of the WEC unit. Four series of experiments have been performed, including mechanical testing of the WEC shaft bearings, evaluation of the WEC support system, response of an individual WEC unit under incident waves and response of up to four WEC units forming a small array. Experimental evaluation of the WEC units is conducted using the tensile test machine and the wave flume at Ghent University, in Belgium, the wave basin of the Queen's Marine Laboratory of the Queen's University of Belfast (UK), and the wave flume (large-scale facility) of Flanders Hydraulics Research, in Belgium. The proposed WEC unit has been shown to satisfy the performance requirements for large array experiments, as well as the feasibility requirements for the reproduction of identical WEC units in large numbers.

6.3. Second part: numerical modelling of WEC (array) effects by heaving wave energy converters

A methodology has been developed for the numerical modelling of wave field modifications as a result of energy extraction from incoming waves by WECs. A coupled numerical modelling has been developed for the combined simulation of intra-array interactions and extra-array effects of WEC (arrays). This generic coupling methodology combines the approach of wave-structure interaction solvers used for investigating intra-array effects, which model physically correct wave energy absorption and the resulting wave fields induced by oscillating WECs or WEC arrays, and approach of wave propagation models used for predicting extra-array effects, which can model the effect of WEC arrays on the wave field over large areas and the shoreline. In addition, a wave generation technique has been developed, for generating the perturbed wave field induced by an oscillating WEC, in a wave propagation model. A wave generation circle is used, surrounding the WEC, on which prescribed internal boundary wave conditions are inserted as input, provided by a wave-structure interaction solver. Most importantly, both, the presented coupling methodology and wave generation technique are generic: (i) the coupling can be realized between any wave-structure solver and wave propagation

model, and (ii) they apply to any oscillating/floating structure, e.g. oscillating water columns/WECs, floating breakwaters, platforms, etc. The coupling methodology has been verified, by employing the heaving WEC developed within the first part of this PhD research. In this test case, coupling between the wave-structure interaction solver, WAMIT, and the time domain wave propagation model, MILDwave, has been realized. The results obtained for the diffracted, radiated and perturbed wave field around the WEC under incident waves, using the presented coupling methodology are verified against the results obtained from the wave-structure model, showing very good agreement. Therefore, the coupling methodology implemented in the wave propagation model MILDwave is suitable for modelling extra-array effects of the simulated WEC.

Within the second part of this PhD work, it has been shown that the numerical coupling methodology for predicting WEC array effects can combine (i) the advantages of wave-structure interaction solvers, and (ii) the benefits of wave propagation models, yielding a cost-effective and accurate tool/methodology.

6.4. Third part: experiments with large WEC arrays

The main deliverable was to perform experiments with large wave energy converter arrays, in order to create a comprehensive database for the detailed investigation of WEC array effects. Through the analysis of the obtained measurements, WEC array effects have been quantified for a range of array geometric configurations. Most importantly, guidelines for the design of WEC arrays have been generated, based both on the performed experiments and the existing state of the art.

These experiments have been prepared and carried out within this PhD research and are part of the research project "WECwakes", funded by the EU FP7 HYDRALAB IV programme. Firstly, a testing programme has been designed based on literature study on research with WEC arrays. In this way, the important varying parameters have been identified for WEC array testing, e.g. array geometric configurations, spacing between the WECs, sea states characteristics. Secondly, the experimental testing has been carried out in the Shallow Water Wave Basin of DHI (Hørsholm, Denmark) with WEC arrays composed of up to 25 identical WEC units, developed during the first part of this PhD research.

This experimental set-up of 25 individual WEC units in an array layout, placed in a large wave basin, is at present the largest set-up of its kind, worldwide, studying the important impacts of WEC array effects on power absorption and wave conditions.

A comprehensive database for point absorber type WEC arrays has been created. Firstly, data from large WEC arrays concerning the physical modelling of intra-array interactions and extra-array effects have been obtained, for the first time. Secondly, the obtained database comprises a wide range of parameter variations such as: the array geometric configuration, the WEC number, the lateral and longitudinal (centre-to-centre) spacing between the WECs, the WECs' motion (decay motion, stationary WECs, "free" response or damped motion of WECs with varying damping), wave conditions (varying wave period, wave heights, wave attack angles) and wave types (regular, polychromatic, irregular long- and short-crested with varying spreading parameters). Thirdly, this database is applicable not only to WEC arrays but also to floating structures/platforms, stationary cylinders under wave action, etc.; the obtained measurements can be used for investigating e.g. wave impact on the cylinders and wave field modifications around them. A fourth advantage of the obtained database, is its non-confidentiality. The data is accessible to the research community as specified under the HYDRALAB rules.

Another achievement based on the acquired WEC array database, is the data analysis performed in this PhD research. Both the obtained results by the WEC array experiments and a literature research, have resulted in a first set of generic guidelines for WEC array design. These guidelines can be used by wave energy project developers for optimal design of WEC arrays regarding their power absorption, as well as their impact on the environment. These guidelines are based on results concerning constructive or destructive influence of intra-array interactions on the overall power absorption of the tested WEC array configurations. Moreover, these guidelines are based on the obtained results for wave height dissipation downwave of the tested WEC arrays (thus, extra-array effects), as e.g. the large arrays of 25 WECs, both in rectilinear and staggered lay-out, are shown to have significant effect on the resulting wave field downwave of the WEC array.

6.5. Recommendations for further research

From the previous, the key results of this PhD research are: (a) the first large WEC array database; (b) quantification of WEC array effects for a range of WEC array geometric configurations and sea state characteristics, (c) guidelines for design of WEC arrays; (d) the development and reproduction in large numbers of a WEC for array testing, representative of point absorber type WEC concepts; (e) a numerical methodology to tackle both intra-array interactions and extra-array effects of WECs.

However, due to the large applicability of the obtained database, still significant research in a number of topics should be performed:

- The measurements obtained from the WEC array experimental tests will be very useful to validate and extend a large range of numerical models used to simulate response, power absorption and wave field modifications due to oscillating WECs. One of these models is MILDwave, with the coupling methodology implemented, by which e.g. the resulting diffracted, radiated and perturbed wave fields around the tested WEC arrays can be simulated.

- The test case used to verify the presented coupling methodology, illustrates the coupling of the BEM approach of linearized flow theory and the approach of a time domain wave propagation model. A shortcoming of the BEM theory is its poor description of viscous effects, incorporated in a parameterized way. Essential physics which are not captured by BEM solvers are e.g. the vortex shedding (viscous effect) downwave of a heaving buoy, wave overtopping, and the re-entering impact of an out-of-water body.

  Because of its better description of the physics, the use of a Navier-Stokes solver for modelling WEC behavior would be more appropriate. This aspect is particularly interesting especially when non-linear effects occur; a Navier-Stokes solver allows intrinsically a fully non-linear approach and has the potential to simulate WECs even in storm seas, as well as to model overtopping WECs using a free surface treatment (e.g. a Volume-of-Fluid approach).

  Validation of this coupling can be performed using the here obtained WEC array database.

- Further analysis of the obtained database for WEC array configurations which are not analysed yet, i.e. wave field and power output results for a number of WEC array configurations and sea states.

- Extension of the obtained database using the 25 (or more) WEC models for wider ranges of the tested parameters, i.e. the array geometric configuration, the WEC number, the lateral and longitudinal (centre-to-centre) spacing between the WECs, wave conditions (varying wave period, wave heights, wave attack angles).

  For instance, the obtained database mainly includes moderate wave conditions. To fully cover the validation of e.g. a Navier-Stokes solver and the coupling methodology, the data set can be extended to regimes where non-linear effects occur, i.e. larger wave heights and smaller spacings between the WECs. As such, issues regarding survivability of WEC farms can be addressed.

- With the aid of an efficient coupling numerical modelling tool, a sensitivity analysis on the essential parameters governing the WEC array layout and dimensions can be performed for various wave climates. As a result, a tool for WEC array performance analysis can be developed based on the coupling

methodology, which can deliver case-specific recommendations and guidelines in order to:

- optimize the array geometrical configuration to achieve intra-array interactions that positively affect the overall WEC array power production;

- mitigate or regulate the influence of WEC arrays on neighboring ocean energy projects, other users in the sea or the coastline.

- The most important challenge faced by the wave energy industry is the reduction of the cost of energy, which, at the moment, hinders the real application of WEC arrays. Therefore, attention should be given to:

  - the development of generic techno-economic optimization methodologies for wave energy at the WEC array level. The geometrical layout of arrays can be optimized to achieve reduction of cost of energy and increase of the array economic performance and technical efficiency, based on development of numerical methods;

  - a proof-of-concept application of this techno-economic optimization to generic and specific close-to-market WECs.

A

The wave propagation model MILDwave

Abstract: *In this appendix, a short overview is provided on the solution scheme of the mild-slope wave propagation model, MILDwave, as well as information on the model's applications. The theoretical equations and the wave generation techniques used in MILDwave are presented in Chapter 3. Moreover, the implementation of wave growth by wind in MILDwave is presented realized within this PhD work, as well as its validation and application for wave farm design.*

A.1 Short description of the wave propagation model MILDwave

A.1.1 Introduction

The numerical model MILDwave is a mild-slope wave propagation model based on the equations of Radder and Dingemans [1] and developed by Troch [2]. The phase-resolving model MILDwave is able to simulate linear water waves over a mildly varying bathymetry by calculating instantaneous surface elevations throughout the domain. Wave transformation processes such as refraction, shoaling, reflection, transmission, diffraction and wave breaking are simulated intrinsically. MILDwave can generate regular and irregular long- and short-crested waves, as well as radiated waves. Furthermore, wind effect can be simulated in MILDwave simulations.

Typical application of the model is the study of wave penetration in harbours, e.g. Zeebrugge and Ostend in Belgium (e.g. in [3] - [7]) and Hanstholm in Denmark ([8] - [11]). The behaviour of wave energy converters (e.g. in [12] - [19]), is being studied using a "sponge layer" technique. Moreover, several wave transformation studies have been carried out using MILDwave, e.g. along the Norwegian coast [20] and along the Belgian coast for the Thorntonbank, Flanders Bays ([21] - [23]).

Bathymetries can be modelled accurately in MILDwave since the model has mostly been applied using small grid cell sizes, providing, however, results in a time efficient way even for large fine grids. MILDwave is also used in the coastal engineering research group at Ghent University for several research and educational purposes within the frame of PhD research and Master theses. Moreover, MILDwave is used by the Flemish government for calculating and modelling wave penetration into several Belgian coastal harbours, within the project of Integrated Flood Risk Management of the Belgian coast.

A.1.2 The solution scheme of MILDwave

Equations (A.1) and (A.2) (presented in Chapter 3, in detail) are discretized and solved using the finite difference scheme, shown in Figure A.1. The finite scheme consists of a two-step space-centred, time-staggered computational grid. The numerical domain is divided in grid cells with dimensions Δx and Δy and central differences are used for spatial and time derivates. The water surface elevation, η, and velocity potential ϕ are calculated in the centre of each grid cell at different time levels, $(n+\frac{1}{2})\Delta t$ and $(n+1)\Delta t$ using the discretized Equations (A.5) and (A.6):

$$\frac{\partial \eta}{\partial t} = B\phi - \nabla \cdot (A \nabla \phi) \tag{A.1}$$

$$\frac{\partial \phi}{\partial t} = -g\eta \tag{A.2}$$

with

$$B = \frac{\overline{\omega}^2 - \overline{k}^2 \overline{C C_g}}{g} \tag{A.3}$$

$$A = \frac{\overline{C C_g}}{g} \tag{A.4}$$

$$\begin{aligned} \eta_{i,j}^{n+\frac{1}{2}} \cong \eta_{i,j}^{n-\frac{1}{2}} + B_{i,j}\phi_{i,j}^{n}\Delta t - \frac{A_{i+1,j} - A_{i-1,j}}{2\Delta x}\frac{\phi_{i+1,j}^{n} - \phi_{i-1,j}^{n}}{2\Delta x}\Delta t \\ - A_{i,j}\frac{\phi_{i-1,j}^{n} - 2\phi_{i,j}^{n} + \phi_{i+1,j}^{n}}{(\Delta x)^2}\Delta t \\ - \frac{A_{i,j+1} - A_{i,j-1}}{2\Delta y}\frac{\phi_{i,j+1}^{n} - \phi_{i,j-1}^{n}}{2\Delta y}\Delta t \\ - A_{i,j}\frac{\phi_{i,j-1}^{n} - 2\phi_{i,j}^{n} + \phi_{i,j+1}^{n}}{(\Delta y)^2}\Delta t \end{aligned} \tag{A.5}$$

$$\phi_{i,j}^{n+1} \cong \phi_{i,j}^{n} - g\eta_{i,j}^{n+\frac{1}{2}}\Delta \mathrm{t} \tag{A.6}$$

Terms A en B are computed using Equations (A.3) and (A.4). Lower index, i,j, defines the spatial grid cell at position $i\Delta x$ and $j\Delta y$, respectively, while upper index, n, signifies the time step $n\Delta t$. Wave generation starts from quiescent water conditions at t = 0. Each time step, first $\eta_{i,j}^{n+\frac{1}{2}}$ and then $\phi_{i,j}^{n+1}$ is calculated in the centre of each grid cell. The grid cell size is selected so that (L_{min} / 20) ≤ Δx = Δy ≤ (L_{min} / 10) (L_{min} = shortest wavelength for irregular waves, corresponding to maximum wave frequency). The time step, Δt, meets the Courant-Friedrichs-Lewy

criterion $\Delta t \leq (\Delta x / C)$, thus Δt must be selected so small that the displacement of the wave front in a time interval does not exceed the grid size Δx (where C is the phase velocity). When wave breaking occurs, finer grid cell sizes should be used.

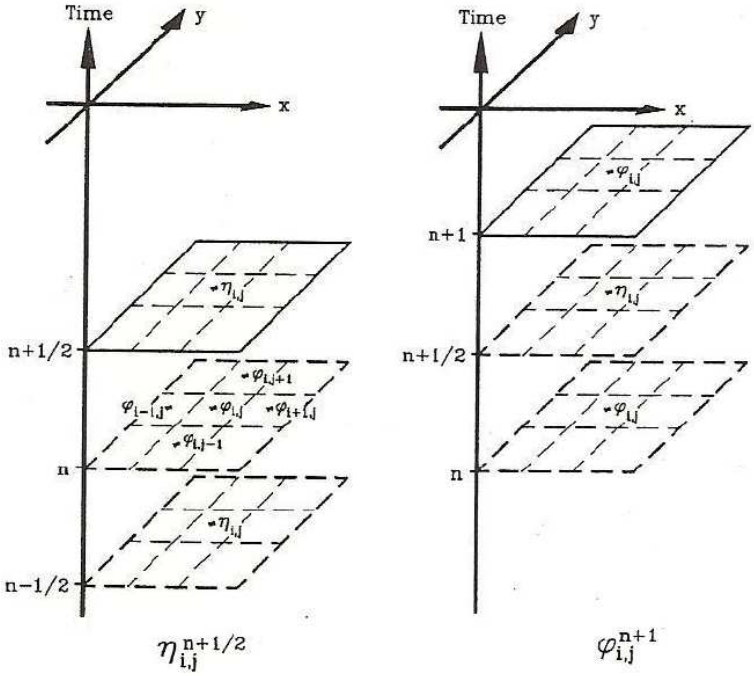

Figure A.1. Finite difference scheme (computational space-centred, time-staggered grid) used by MILDwave [24].

A.1.3 The MILDwave user interface

MILDwave is easily operated using two executable files in a user friendly interface: the Preprocessor (Figure A.2) for the preparation of the input files and the Calculator (Figure A.3) for the performance of the calculations. Several types of output files are available; electronic wave gauges can be installed in the simulation domain to measure the surface elevations on predefined locations, the surface elevations in the simulation domain (3-D output) on multiple time instants can be provided, as well as the disturbance coefficient K_d and the vector field of the wave power P throughout the simulation domain. The disturbance coefficient K_d is given by the ratio $H_{(m0)}/H_{(m0)_{GB}}$, where $H_{(m0)}$ is the local wave height for regular waves or for irregular waves based on the spectral density,respectively, and $H_{(m0)_{GB}}$ is the incident wave height at the wave generation boundary, for regular waves or for irregular waves based on the spectral density, respectively.

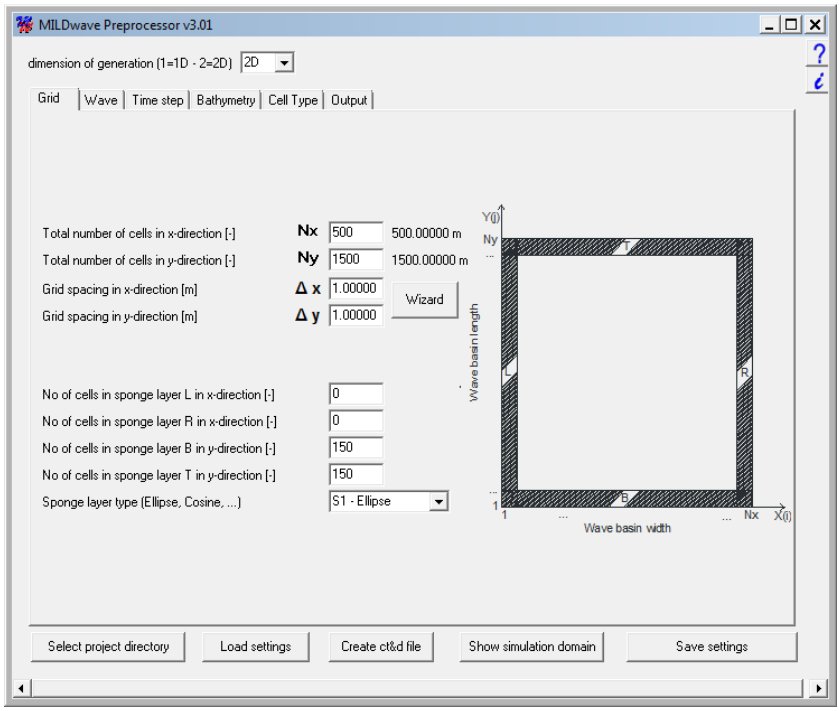

Figure A.2. First tab of the MILDwave Pre-processor, used to prepare the input files and to preview the numerical domain.

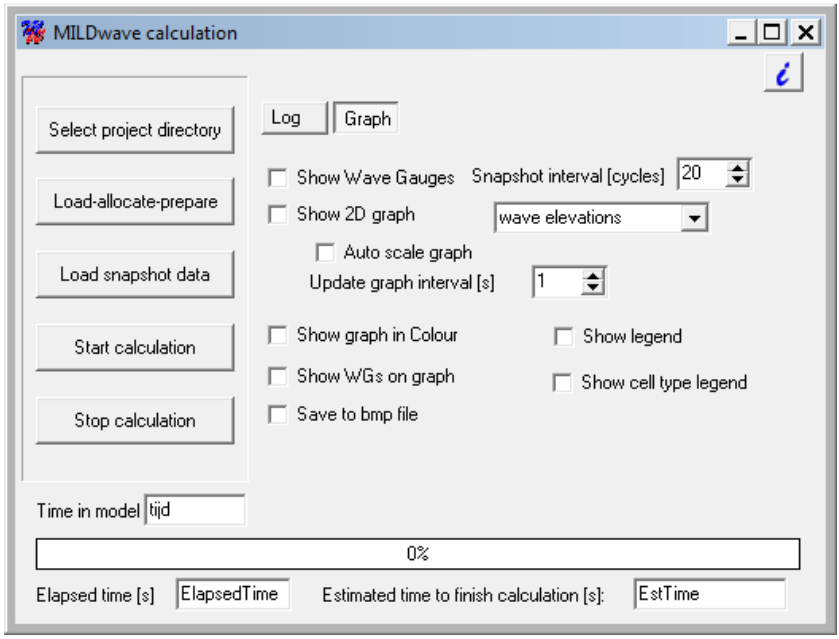

Figure A.3. The MILDwave Calculator, used to perform calculations.

A.2 Wave breaking and wave regeneration by wind in MILDwave

A.2.1 Wave breaking in MILDwave

In Equations A.1 and A.2 an energy dissipation term (D_B/E) accounting for depth-induced wave breaking in MILDwave has been implemented based on [25] for regular and on [26] for irregular waves as given by Equation A.7:

$$\begin{cases} \dfrac{\partial \eta}{\partial t} = \dfrac{\omega^2 - k^2 CC_g}{g}\phi - \nabla \cdot \left(\dfrac{CC_g}{g} \nabla \phi \right) - \left(\dfrac{D_B}{E} \right) \eta \\ \dfrac{\partial \phi}{\partial t} = -g\eta \end{cases} \tag{A.7}$$

A.2.2 Wave growth by wind in MILDwave

Due to the purpose of phase-resolving models (i.e. the investigation of nearshore wave behaviour), wind was not considered to be a major contributor to the wave evolution over the relatively small distances of such applications. Moreover, wind input is a frequency-dependent phenomenon and therefore, implementing wind contribution in this type of models is not straightforward. As a result, the effect of wind on wave growth is not taken into account in the majority of the time-domain models, which was a generally accepted approach.

On the other hand, wind effects are commonly described in spectral models. The dependency of the wave frequency on wind effects can rather easily be expressed in the action balance equations used by spectral models. Also, the areas investigated are much larger, allowing wave evolution due to wind which represents an important influence in spectral models. Nevertheless, studies carried out using phase-averaging models have shown that wind can also be significant over small distances, which has led to growing interest for incorporation of the wind influence also in time-domain models.

In this appendix the implementation of an appropriate expression for the description of wave regeneration by wind in MILDwave is presented based on [17]. Several theories describing the wind effect, based on both phase-averaging and phase-resolving models have been considered and implemented in MILDwave, after being appropriate adjusted to fit in the mild-slope equations. Finally, the theory which introduces wave growth by wind and which results in the most satisfactory

description of this effect in the wave propagation model MILDwave, is selected for investigating wake effects by WEC farms.

Here, results are presented based on the expression of wave growth by wind which has been used for the CREDIZ model by Vogel et al. [27]. Vogel et al. [27] postulated a theory for the implementation of wind energy in the phase-resolving wave model CREDIZ, which is based on the parabolic approximation of the mild-slope equation.

The negative energy dissipation term W_g [27] of Eq. (A.8), which expresses energy contribution and describes the net effect of wave growth by wind, is implemented into the hyperbolic mild-slope equations and is used for both regular and long-crested irregular waves:

$$W_g = -\frac{2C_g}{H_S}\frac{dH_S}{dy} \tag{A.8}$$

To compute the gradient dH_s/dy, the growth curve of Wilson-Krylov ([28]; [29]) is used, as given in Eq. (A.9):

$$\frac{gH_S}{V_y^2} = \beta_v \left[1 - \left(1 + \alpha_v \sqrt{gy/V_y^2} \right)^{-2} \right] \tag{A.9}$$

The hyperbolic mild-slope equations used in MILDwave (Eq. (A.7)) for the calculation of the surface elevation, η, and the velocity potential, ϕ, result in Eq. (A.10) by including both the dissipation effect of depth-induced breaking (D_B/E) and the energy contribution effect of wind (W_g, (Eq. (A.8)):

$$\begin{cases} \dfrac{\partial \eta}{\partial t} = \dfrac{\omega^2 - k^2 C C_g}{g}\phi - \nabla \cdot \left(\dfrac{C C_g}{g} \nabla \phi \right) - \left(\dfrac{D_B}{E} + W_g \right)\eta \\ \dfrac{\partial \phi}{\partial t} = -g\eta \end{cases} \tag{A.10}$$

A.2.2.1 Validation of wave growth by wind in MILDwave

The validation of the extra term, W_g, of Eq. (A.10), which describes the wind input, is carried out by comparison of numerical results with the theoretical growth curves of Wilson-Krylov ((Wilson, 1965); (Krylov et al., 1976)), both for regular and long-crested irregular waves.

In Table A.1 the characteristics of a small sample of the performed test cases are presented. In the first column the name of the test case is given, in columns 2-4 the wave and wind characteristics of the tests are provided and in the last column the type of the generated waves by MILDwave is given.

In Figure A.4 (A-C), the evolution of wave growth by wind along a longitudinal cross section of the numerical basin in MILDwave, parallel to the wave propagation direction, is shown for the wave and wind conditions of Table A.1. Moreover, the simulation results are plotted against theoretical results for wave growth using Wilson-Krylov growth curves. The numerical results from the applied wind module in MILDwave show very good agreement with the theoretical values of the growth curve of Wilson-Krylov for regular waves generated in "Test case 4-6" as shown in Figure A.4(A). The same observations can be made for the rest of the conducted test cases of Table A.1 for irregular long-crested waves (Figures A.4(B) and A.4 (C)). As a conclusion, the wind module results in an adequate description of the wave growth by wind, for regular and long-crested irregular waves.

Table A.1. Wave characteristics of the test cases presented in Figure A.4 (A, B and C).

Test case	$H_{(s)}$**[m]**	$T_{(p)}$ **[s]**	U_{10} **[m/s]**	**Type of wave generation**
A: 4-6	2.0	5	20	Regular
B: J-4	1.0	5.2	12.0	Long-crested irregular JONSWAP (γ =3.3)
C: PM-4	3.0	7.6	25.0	Long-crested irregular Pierson-Moskowitz

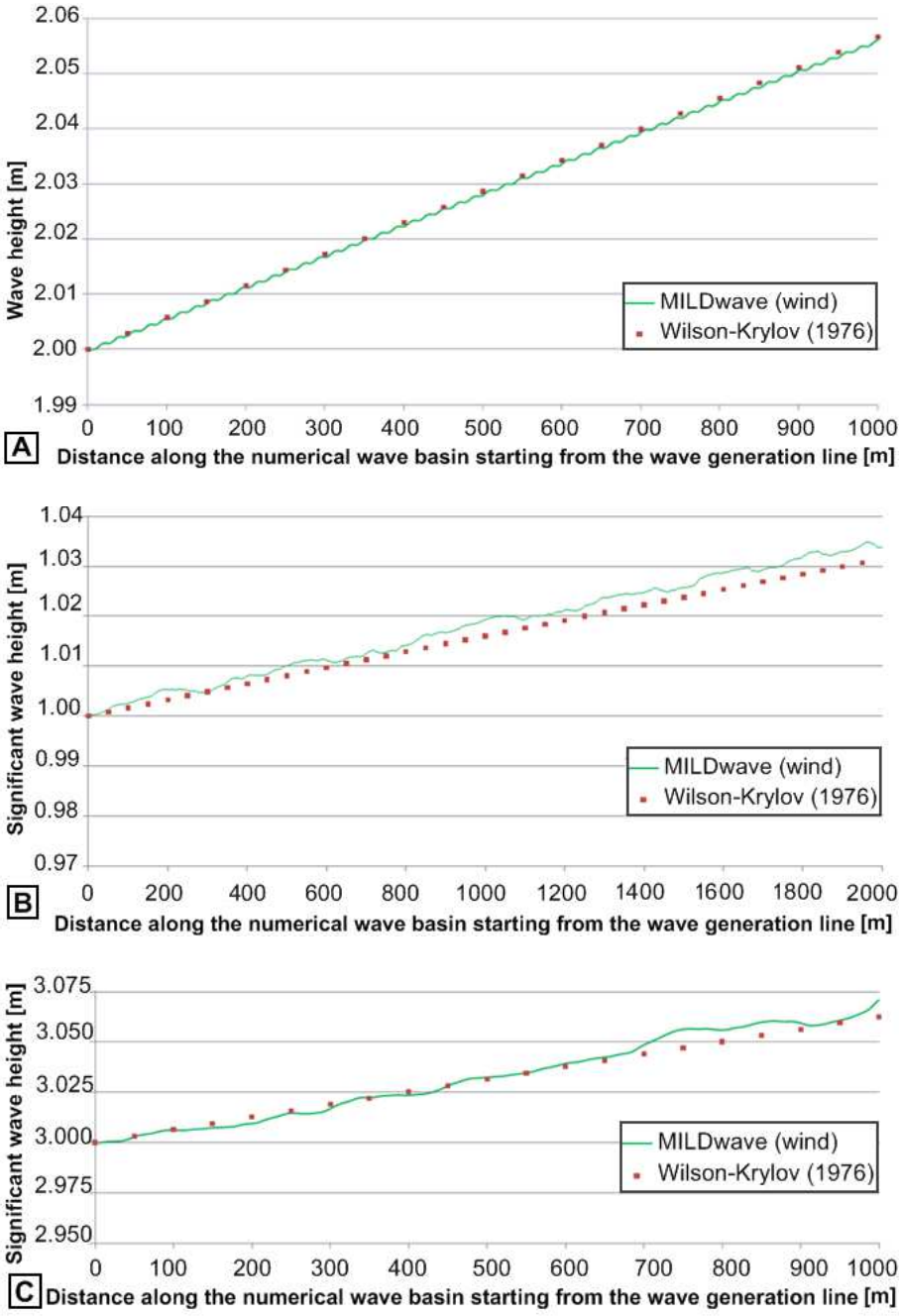

Figure A.4. Evolution of wave growth along a longitudinal section of the numerical wave basin for the test cases of Table A.1: MILDwave results (continuous line), Wilson-Krylov growth curve (dotted line). A) Test case 4-6; B) Test-case J-4, and C) Test-case PM-4 [17].

A.2.2.2 Extra-array effects in the lee of WECs

The modified model MILDwave has been also applied to investigate the influence of the wind on extra-array effects in the lee of, first, an individual WEC and secondly, arrays of WECs. The evolved technique has been applied on WEC arrays composed by "hypothetical" WECs with basic dimensions 36 m x 36 m exhibiting a certain amount of absorption and on Wave Dragon WECs [30].

The extra-array effects behind WEC arrays are investigated for various wave conditions under the effect of wind. Results are presented in terms of the disturbance coefficient, K_d . When the wind effect is incorporated, the values of the K_d coefficients are increased, which also results in increased available wave power in the lee of the WECs (Figures A.5(A-B)).

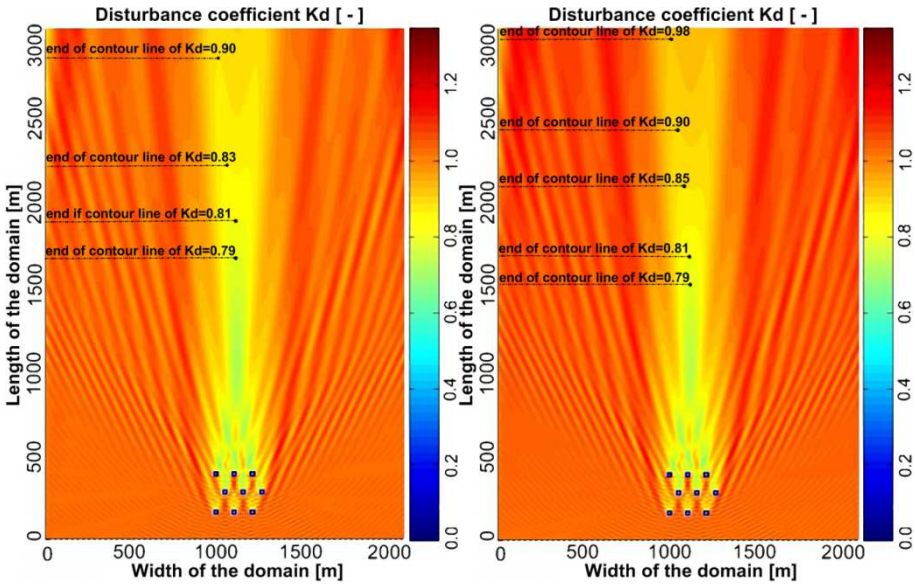

Figure A.5. MILDwave results for extra-array effects downwave of a WEC array of "hypothetical" devices for regular incident waves (H = 1.0 m, T = 5.2 s). Contour plots of $K_d$coefficients for a staggered WEC array layout. Left (A): no wind effect is simulated; Right (B): wind effect is simulated (U_{10} = 10.0 m/s) [17].

Within the computational domains shown in Figures A.5(A-B), the extra-array effects downwave of an array composed of 9 "hypothetical" WECs can be visualized, thus devices with a specific amount of reflection and absorption. The waves propagate from the bottom to the top of the figures. On Figures A.5(A-B), the

K_d values of several contour lines are indicated, showing the differences between the two simulations regarding the calculated K_d values.

Also in the plot of K_d values of Figure A.6 the same observations can be made. In Figure A.6 numerical results are presented along a longitudinal section of a numerical wave basin in MILDwave, parallel to the wave propagation direction. At the wave generation boundary regular incident waves of wave height, H = 1.0 m and wave period, T = 5.2 s are generated. The K_d coefficients calculated using MILDwave with and without a wind input term are plotted against a distance that starts right behind the last WEC of the WEC array towards the downwave direction. An increasing difference between the values of the K_d coefficients with an increasing distance downwave of the WEC farm is observed.

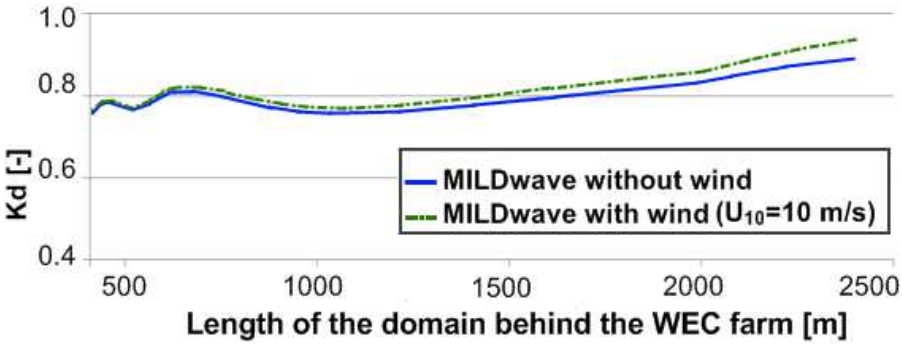

Figure A.6. MILDwave results for extra-array effects downwave of a WEC array of "hypothetical" devices for regular incident waves (H = 1.0 m and T = 5.2 s) without and with the effect of wind (U_{10} = 10.0 m/s). Longitudinal cross section of the calculated K_d coefficients downwave of the WEC array [17].

Besides "hypothetical" WECs with basic dimensions 36 m x 36 m, also farms of Wave Dragon WECs [30] are investigated (Figure A.7). It is observed that the influence of wind just behind a WEC or a WEC array is very small and increases with an increasing distance after the WECs. This is illustrated by a test case with a row of three Wave Dragon WECs (in-between spacing equal to two times the width of one Wave Dragon WEC). The imposed wave characteristics are: significant wave height H_s equal to 3.0 m, peak wave period T_p equal to 8.4 s and wind velocity U_{10} equal to 15.0 m/s.

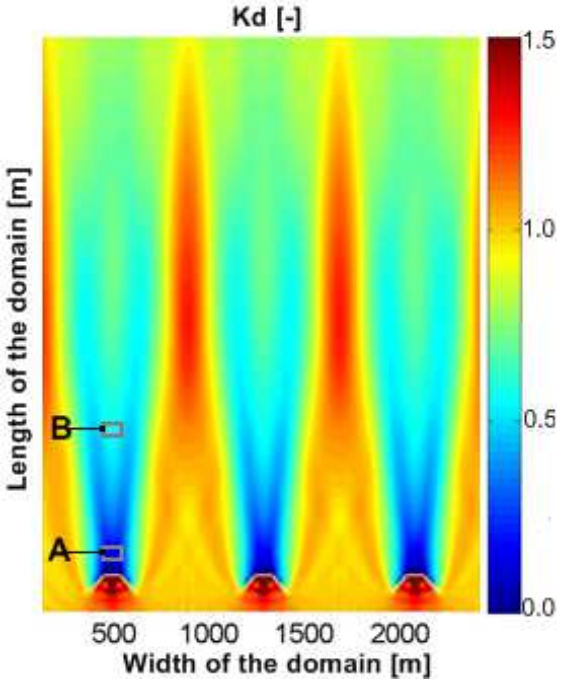

Figure A.7. MILDwave results for extra-array effects downwave of a row of Wave Dragon WECs for irregular incident waves (H_s = 3.0 m, T_p = 8.4 s and U_{10} = 15.0 m/s). Contour plots of the calculated K_d coefficients [17].

At a distance of 100 m behind a WEC situated at the outer position of the row (location A, Figure A.7), the available wave power is equal to 1.44 MW, when no wind is applied. If the wind effect is incorporated a wave power equal to 1.46 MW is found, calculated over an area of 2100 m², indicating an increase of about 1.4 % of the available power. At a distance of 500 m behind the WEC (location B, Figure A.7), where a second row of WECs could be placed, these values of the available wave power increase to 5.49 MW and 5.74 MW for conditions without the effect of wind and with the wind effect, respectively. Therefore, at location B an increase of about 4.6 % of the available power is observed indicating the rather small effect of wind within relatively short distances, for the presented location and type of WEC (use of absorption coefficients and geometry of the Wave Dragon WEC). At larger distances (more than 500 m) the effect of wind significantly increases (also shown in Figures A.6(A-B) for the "hypothetical" WECs).

A.3 References

[1] Radder, A.C., and M.W. Dingemans. *Canonical equations for almost periodic, weakly nonlinear gravity waves.* Wave Motion, 7, 473-485, **1985**.

[2] Troch, P.. *MILDwave – A numerical model for propagation and transformation of linear water waves.* Internal Report, Dept. of Civil Engineering, Ghent University, **1998**.

[3] Stratigaki, V., and Troch, P.. *Design of Ostend harbour: numerical simulation of wave diffraction through the gap at Montgomery dock using the 'mild slope' wave propagation model, MILDwave.* Report for Flemish Government, Brussels, Belgium, **2010**.

[4] Stratigaki, V., Vanneste, D., Troch, P., Gysens, S., and Willems, M.. *Numerical modelling of wave penetration in Ostend Harbour.* Proceedings of the International Conference on Coastal Engineering, No. 32(2010), Shanghai, China. Paper #790: waves.42. Retrieved from http://journals.tdl.org/ICCE/ , **2010**.

[5] Stratigaki, V., and Troch, P.. *Zeebrugge Harbour: Numerical Simulation of Wave diffraction through the gap of the breakwaters using the 'mild slope' wave propagation model, MILDwave,* Internal report, Dept. of Civil Engineering, Ghent University, **2011**.

[6] Gruwez, V., Bolle, A., Verwaest, T., Hassan, W.. *Numerical and physical modelling of wave penetration in Oostende harbour during severe storm conditions.* 5th SCACR International Short Conference on Applied Coastal Research: proceedings, 6th-9th June, 2011 - RWTH Aachen University, Germany. Mitteilungen des Lehrstuhls und Instituts für Wasserbau und Wasserwirtschaft der Rheinisch-Westfälischen Technischen Hochschule Aachen, 165: pp. 198-205, **2012**.

[7] Gruwez, V., Bolle, A., and Verwaest, T. (2012). *Numerical Modelling of Wave Penetration, Comparison with Physical Model and Field Measurements in Zeebrugge Harbour*. Proceedings of the 4th International Conference on the Application of Physical Modelling to Port and Coastal Protection – Coastlab12, 17th-20th September, 2012 – Ghent University - Ghent, Belgium, **2012**.

[8] Margheritini, L., Kofoed, J.P., Stratigaki, V., and Troch, P.. *Estimation of Wave Conditions for SSG Breakwater at Hanstholm Location.* Aalborg University, Department of Civil Engineering. 78 pp. (DCE Contract Reports; 90) , **2010**.

[9] Margheritini, L., Frigaard, P., and Stratigaki, V.. *Characterization of Wave Climate at Hanstholm Location with Focus on the Ratio between Average and Extreme Waves Heights.* 9th EWTEC2011, 5-9 September **2011**, Southampton, UK.

[10] Margheritini, L., Stratigaki, V., and Troch, P.. *Geometry optimization of an Overtopping Wave Energy Device implemented into the new breakwater of the Hanstholm Port Expansion.* Proceedings of the 22nd International Offshore and Polar Engineering Conference - ISOPE **2012**, Rhodes, Greece.

[11] Stratigaki, V., Troch, P., Margheritini, L., and Kofoed, J.P.. *Estimation of wave conditions along a new breakwater for the Hanstholm harbour, using the numerical model MILDwave.* Proceedings of the 22nd International Offshore and Polar Engineering Conference - ISOPE **2012**, Rhodes, Greece.

[12] Beels, C., P. Troch, G. De Backer, M. Vantorre, and J. De Rouck.. *Numerical implementation and sensitivity analysis of a wave energy converter in a time-dependent mild-slope equation model.* Coastal Engin. Vol. 57(5), pp. 471-492, **2010**.

[13] Beels, C., P. Troch, K. De Visch, J.P. Kofoed, and G. De Backer. *Application of the time-dependent mild-slope equations for the simulation of wake effects in the lee of a farm of Wave Dragon wave energy converters.* Renewable Energy, 35, pp.1644-1661, **2010**.

[14] Beels C., P. Troch, J.P. Kofoed, P. Frigaard, J. Vindahl Kringelum, P. Carsten Kromann, M. Heyman Donovan, J. De Rouck and G. De Backer. *A methodology for production and cost assessment of a farm of wave energy converters.* Accepted for Renewable Energy, **2010**.

[15] Troch, P., Beels, C., De Rouck, J., and De Backer, G.. *Wake effects behind a farm of wave energy converters for irregular long-crested and short-crested waves*. Proceedings of the International Conference on Coastal Engineering, No. 32(**2010**), Shanghai, China. Paper #: waves.22. Retrieved from http://journals.tdl.org/ICCE/.

[16] Troch, P. and Stratigaki, V.. *Optimalisatie van de lay-out van een park golfenergieconvertoren via numerieke modellering van de zogeffecten. Thema "Energie"*, Het Ingenieursblad – Koninklijke Vlaamse Ingenieursvereniging (KVIV) (October 2011, Belgium), Issue: JG80 - 5/2011, pages: 53-58 (in Dutch), **2011**.

[17] Stratigaki, V., Troch, P., Baelus, L., and Keppens, Y.. *Introducing wave regeneration by wind in a mild-slope wave propagation model, MILDwave, to investigate the wake effects in the lee of a farm of wave energy converters.* Proc. of 30th OMAE 2011, Rotterdam. http://dx.doi.org/10.1115/OMAE2011-49347, **2011**.

[18] Stratigaki, V., Troch, P., and Degroote, J.. *Numerical modelling of wake effects of a farm of Wave Energy Converters: computational performance evaluation,* Proceedings of the 5th International Conference on Advanced COmputational Methods in Engineering (ACOMEN), 14-17 November 2011, Liège, Belgium, **2011**.

[19] Folley, M., Babarit, A., O' Boyle, L., Child, B., Forehand, D., Silverthorne, K., Spinneken, J., Stratigaki, V., Troch, P.. *A review of numerical modelling of wave energy converter arrays*. Proc. of the 31st OMAE 2012, Rio de Janeiro, Brazil, **2012**.

[20] Kofoed, J.P., L., Margheritini, V. Stratigaki, and P. Troch. *Estimation of Wave Conditions for SSG Breakwater at Svåheia SSG pilot site.* Aalborg University, Department of Civil Engineering. 154 pp. (DCE Contract Reports; 52), **2008**.

[21] Stratigaki, V., and Troch, P.. *Wave Propagation over the Thornton bank (Belgium) using the 'Mild Slope' Wave Propagation Model, MILDwave.* Internal Report, Department of Civil Engineering, Ghent University, Ghent, **2010**.

[22] Stratigaki, V., and Troch, P.. *MILDwave simulatie van golfvoortplanting langsheen de Vlaamse baaien m.b.v. de 'mild-slope' golfvoortplantingsmodel, MILDwave.* Internal Report, Department of Civil Engineering, Ghent University, Ghent, in Dutch, **2012**.

[23] Stratigaki, V., Troch, P., Malherbe, B., and Fordeyn, J.. *Vlaamse Baaien Development Plan: Estimation of the wave climate for Flanders Bays using the numerical model MILDwave.* Proceedings of the 4th International Conference on the Application of Physical Modelling to Port and Coastal Protection – Coastlab12, 17th-20th September, 2012 – Ghent University - Ghent, Belgium, **2012**.

[24] Andersen, S., and T. Klindt. *Random wave propagation-based on the mildslope equation.* Master's thesis, Dept. of Civil Engineering, Aalborg University, **1994**.

[25] Deigaard, R., Justesen, P., and Fredsoe, J.. *Modelling of Undertow by a One-Equation Turbulence Model*, Coastal Engineering, **15**, pp. 431-458, **1991**.

[26] Baldock, T.E., Holmes, P., Bunker, S., Van Weert, P.. *Cross-shore Hydrodynamics within an Unsaturated Surf Zone.* Coastal Engineering, 34, pp. 173-196, **1998**.

[27] Vogel, J.A., Radder, A.C., and De Reus, J.H.. *Verification of Numerical Wave Propagation Models in Tidal Inlets*, Proceedings of the 23rd International Conference on Coastal Engineering, Malaga, Spain, ASCE, pp. 433-447, **1988**.

[28] Wilson, B.W.. *Numerical Prediction of Ocean Waves in the North Atlantic for December*. Deutsche Hydrographische Zeitschrift, **18** (3), pp. 114-130, 1965.

[29] Krylov, Y.M., Strekalov, S.S., and Tsyplukhin, V.F.. *Vetrovye Volug i ich Vozdejstvie na Sooruzewija (Wind Waves and Their Impact on Structures)*, Hydrometeoizdat, Leningrad, **1976**.

[30] Tedd, J., Kofoed, J.P., Friis-Madsen, E., and Christensen, L.. *"Section 7.5.5. Wave Dragon". In J. Cruz, editor, Ocean Wave Energy, Current Status and Perspectives*, Springer, pp. 371–382, **2008**.

B

WEC array experiments: Database composition, force gauges and CERC 5 wave gauge array lay-out

Abstract: *In this appendix, first an example of the acquired data from one test (list of recorded parameters) showing the composition of the created database within this PhD research is presented. In addition, a plan view of the locations of the force gauges and of the CERC 5 wave gauge array in the Shallow Water Wave basin of DHI is shown. The force gauges are mounted on the WECs during the large WEC array experiments. These force gauges have been used to measure wave induced surge force on the WEC buoys. The numbering and the locations are indicated in the plan view. On each of the WEC units of the central column, two force gauges are installed at the top and at the bottom of the WEC shaft, as described / illustrated in Chapter 4. Finally, the CERC 5 wave gauge array is used upwave of the WEC arrays for estimating wave directionality and wave reflection.*

o Description of Table B.1

In Table B.1, an example of the acquired data from one test (list of recorded parameters) showing the **composition of the created database** within this PhD research is presented.

The example of Table B.1 refers to the experimental set-up of Figure 4.7 (Chapter 4), for which 25 WECs have been tested under waves. The WEC numbering (WEC #01 – WEC #25) shown in Table B.1 is presented in Figure 4.7 (Chapter 4), while the wave gauges numbering (WG #01 – WG #41) is presented in Figure 4.9 (Chapter 4). For the numbering of the potentiometers mounted on each of the WECs (Pot #01 – Pot #25), the numbering of the WECs is used (shown in Figure 4.7, Chapter 4), while the origin of the instrumentation is also mentioned (UGent or DHI). The numbering and location of force gauges (FG #01 - #10) is presented in Figure B.1 (Appendix B).

The first column of Table B.1 provides the number of the *acquisition channel*. The second column provides the *channel name*, as used in the data acquisition system. The third column provides a short *description of the channel content* and therefore of the recorded parameter. In the fourth column, the *units* of the recorded parameter are provided. In column 5, the type of the employed instrument is provided. Details on the employed measurement methods are found in Chapters 2 and 4. Except for time series of wave elevations, WEC heave displacement and wave induced surge forces on the WEC buoys, also temperature and the wave paddle displacement measurements have been taken .

The parameters of Table B.1 have been recorded for all combinations of performed tests with the experimental set-ups of Table 4.5 (Chapter 4 / Appendix D), for the sea-states presented in Tables 4.1 – 4.4 (Chapter 4 / Appendix C) and for the PTO-system characteristics presented in Table E.1 (Appendix E). The above combinations have led to the acquisition of the parameters listed in Table B.1 for 590 tests.

Table B.1. List of acquired data, acquisition channels and employed instrumentation (Table page 1/3).

Ch. #	Channel name	Channel content description	Units	Type of instrument employed
1	Time	Time with step 0.025 s	seconds [s]	-
2	WG #01	Wave elevations at WG #01	meters [m]	DHI type resistive wave gauge
3	WG #02	Wave elevations at WG #02	meters [m]	DHI type resistive wave gauge
4	WG #03	Wave elevations at WG #03	meters [m]	DHI type resistive wave gauge
5	WG #04	Wave elevations at WG #04	meters [m]	DHI type resistive wave gauge
6	WG #05	Wave elevations at WG #05	meters [m]	DHI type resistive wave gauge
7	WG #06	Wave elevations at WG #06	meters [m]	DHI type resistive wave gauge
8	WG #07	Wave elevations at WG #07	meters [m]	DHI type resistive wave gauge
9	WG #08	Wave elevations at WG #08	meters [m]	DHI type resistive wave gauge
10	WG #09	Wave elevations at WG #09	meters [m]	DHI type resistive wave gauge
11	WG #10	Wave elevations at WG #10	meters [m]	DHI type resistive wave gauge
12	WG #11	Wave elevations at WG #11	meters [m]	DHI type resistive wave gauge
13	WG #12	Wave elevations at WG #12	meters [m]	DHI type resistive wave gauge
14	WG #13	Wave elevations at WG #13	meters [m]	DHI type resistive wave gauge
15	WG #14	Wave elevations at WG #14	meters [m]	DHI type resistive wave gauge
16	WG #15	Wave elevations at WG #15	meters [m]	DHI type resistive wave gauge
17	WG #16	Wave elevations at WG #16	meters [m]	DHI type resistive wave gauge
18	WG #17	Wave elevations at WG #17	meters [m]	DHI type resistive wave gauge
19	WG #18	Wave elevations at WG #18	meters [m]	DHI type resistive wave gauge
20	WG #19	Wave elevations at WG #19	meters [m]	DHI type resistive wave gauge
21	WG #20	Wave elevations at WG #20	meters [m]	DHI type resistive wave gauge
22	WG #21	Wave elevations at WG #21	meters [m]	DHI type resistive wave gauge
23	WG #22	Wave elevations at WG #22	meters [m]	DHI type resistive wave gauge
24	WG #23	Wave elevations at WG #23	meters [m]	DHI type resistive wave gauge
25	WG #24	Wave elevations at WG #24	meters [m]	DHI type resistive wave gauge
26	WG #25	Wave elevations at WG #25	meters [m]	DHI type resistive wave gauge
27	WG #26	Wave elevations at WG #26	meters [m]	DHI type resistive wave gauge
28	WG #27	Wave elevations at WG #27	meters [m]	DHI type resistive wave gauge
29	WG #28	Wave elevations at WG #28	meters [m]	DHI type resistive wave gauge
30	WG #29	Wave elevations at WG #29	meters [m]	DHI type resistive wave gauge
31	WG #30	Wave elevations at WG #30	meters [m]	DHI type resistive wave gauge
32	WG #31	Wave elevations at WG #31	meters [m]	DHI type resistive wave gauge
33	WG #32	Wave elevations at WG #32	meters [m]	DHI type resistive wave gauge

Table B.1. *Cont.* List of acquired data, acquisition channels and employed instrumentation (Table page 2/3).

Ch. #	Channel name	Channel content description	Units	Type of instrument employed
34	WG #33	Wave elevations at WG #33	meters [m]	DHI type resistive wave gauge
35	WG #34	Wave elevations at WG #34	meters [m]	DHI type resistive wave gauge
36	WG #35	Wave elevations at WG #35	meters [m]	DHI type resistive wave gauge
37	WG #36	Wave elevations at WG #36	meters [m]	DHI type resistive wave gauge
38	WG #37	Wave elevations at WG #37	meters [m]	DHI type resistive wave gauge
39	WG #38	Wave elevations at WG #38	meters [m]	DHI type resistive wave gauge
40	WG #39	Wave elevations at WG #39	meters [m]	DHI type resistive wave gauge
41	WG #40	Wave elevations at WG #40	meters [m]	DHI type resistive wave gauge
42	WG #41	Wave elevations at WG #41	meters [m]	DHI type resistive wave gauge
43	D 1	Wave paddle displacement	meters [m]	Laser measurements of paddle 1 positions
44	Thermo-meter	Temperature	Celsius degrees [C°]	Thermometer
45	FG #01	Surge force at WEC #01 (top)	Newtons [N]	Load Cell-Model 614-Tedea-Huntleigh
46	FG #02	Forces at WEC #01 (bottom)	Newtons [N]	Load Cell-Model 614-Tedea-Huntleigh
47	FG #03	Forces at WEC #02 (top)	Newtons [N]	Load Cell-Model 614-Tedea-Huntleigh
48	FG #04	Forces at WEC #02 (bottom)	Newtons [N]	Load Cell-Model 614-Tedea-Huntleigh
49	FG #05	Forces at WEC #03 (top)	Newtons [N]	Load Cell-Model 614-Tedea-Huntleigh
50	FG #06	Forces at WEC #03 (bottom)	Newtons [N]	Load Cell-Model 614-Tedea-Huntleigh
51	FG #07	Forces at WEC #04 (top)	Newtons [N]	Load Cell-Model 614-Tedea-Huntleigh
52	FG #08	Forces at WEC #04 (bottom)	Newtons [N]	Load Cell-Model 614-Tedea-Huntleigh
53	FG #09	Forces at WEC #05 (top)	Newtons [N]	Load Cell-Model 614-Tedea-Huntleigh
54	FG #10	Forces at WEC #05 (bottom)	Newtons [N]	Load Cell-Model 614-Tedea-Huntleigh
55	FWG	(spare channel used for testing)	-	-
56	Pot #16 (DHI)	Heave displacement: WEC #16	meters [m]	DHI Ship Movement Meter
57	Pot #17 (DHI)	Heave displacement: WEC #17	meters [m]	DHI Ship Movement Meter
58	Pot #18 (DHI)	Heave displacement: WEC #18	meters [m]	DHI Ship Movement Meter
59	Pot #19 (DHI)	Heave displacement: WEC #19	meters [m]	DHI Ship Movement Meter
60	Pot #20 (DHI)	Heave displacement: WEC #20	meters [m]	DHI Ship Movement Meter
61	Pot #21 (DHI)	Heave displacement: WEC #21	meters [m]	DHI Ship Movement Meter
62	Pot #22 (DHI)	Heave displacement: WEC #22	meters [m]	DHI Ship Movement Meter
63	Pot #23 (DHI)	Heave displacement: WEC #23	meters [m]	DHI Ship Movement Meter

Table B.1. *Cont.* List of acquired data, acquisition channels and employed instrumentation (Table page 3/3).

Ch. #	Channel name	Channel content description	Units	Type of instrument employed
64	Pot #24 (DHI)	Heave displacement: WEC #24	meters [m]	DHI Ship Movement Meter
65	Pot #25 (DHI)	Heave displacement: WEC #25	meters [m]	DHI Ship Movement Meter
66	Pot #01 (GENT)	Heave displacement: WEC #01	meters [m]	Draw-wire sensor model FD60; ALTHERIS
67	Pot #02 (GENT)	Heave displacement: WEC #02	meters [m]	Draw-wire sensor model FD60; ALTHERIS
68	Pot #03 (GENT)	Heave displacement: WEC #03	meters [m]	Draw-wire sensor model FD60; ALTHERIS
69	Pot #04 (GENT)	Heave displacement: WEC #04	meters [m]	Draw-wire sensor model FD60; ALTHERIS
70	Pot #05 (GENT)	Heave displacement: WEC #05	meters [m]	Draw-wire sensor model FD60; ALTHERIS
71	Pot #06 (GENT)	Heave displacement: WEC #06	meters [m]	Draw-wire sensor model FD60; ALTHERIS
72	Pot #07 (GENT)	Heave displacement: WEC #07	meters [m]	Draw-wire sensor model FD60; ALTHERIS
73	Pot #08 (GENT)	Heave displacement: WEC #08	meters [m]	Draw-wire sensor model FD60; ALTHERIS
74	Pot #09 (GENT)	Heave displacement: WEC #09	meters [m]	Draw-wire sensor model FD60; ALTHERIS
75	Pot #10 (GENT)	Heave displacement: WEC #10	meters [m]	Draw-wire sensor model FD60; ALTHERIS
76	Pot #11 (GENT)	Heave displacement: WEC #11	meters [m]	Draw-wire sensor model FD60; ALTHERIS
77	Pot #12 (GENT)	Heave displacement: WEC #12	meters [m]	Draw-wire sensor model FD60; ALTHERIS
78	Pot #13 (GENT)	Heave displacement: WEC #13	meters [m]	Draw-wire sensor model FD60; ALTHERIS
79	Pot #14 (GENT)	Heave displacement: WEC #14	meters [m]	Draw-wire sensor model FD60; ALTHERIS
80	Pot #15 (GENT)	Heave displacement: WEC #15	meters [m]	Draw-wire sensor model AD160; ALTHERIS

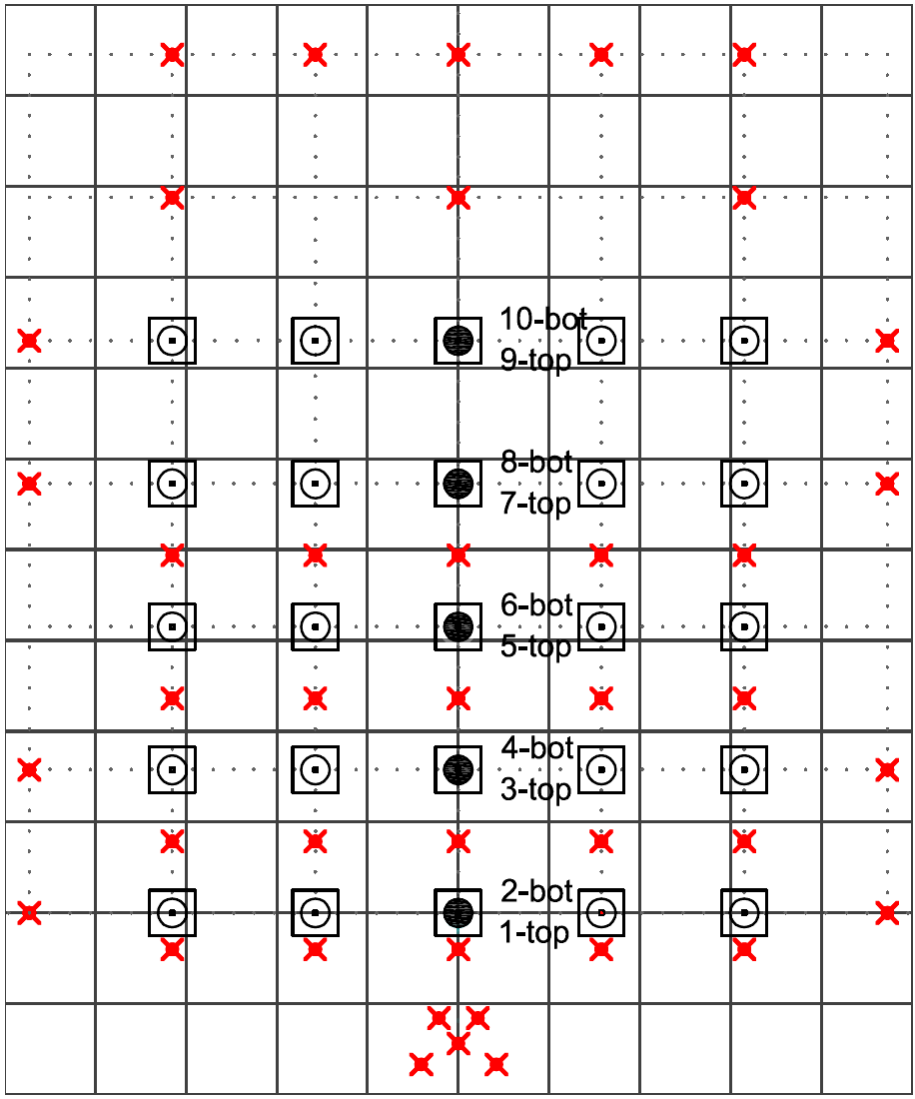

Figure B.1. Plan view of the locations of the force gauges in the Shallow Water Wave basin of DHI, where the numbering and the location are shown. On each of the WEC units of the central column, two force gauges are installed at each WEC unit; one at the top (indicated as "*top*" in Figure B.1), and another one at the bottom (indicated as "*bot*" in Figure B.1) of the WEC shaft, as described / illustrated in Chapter 4.

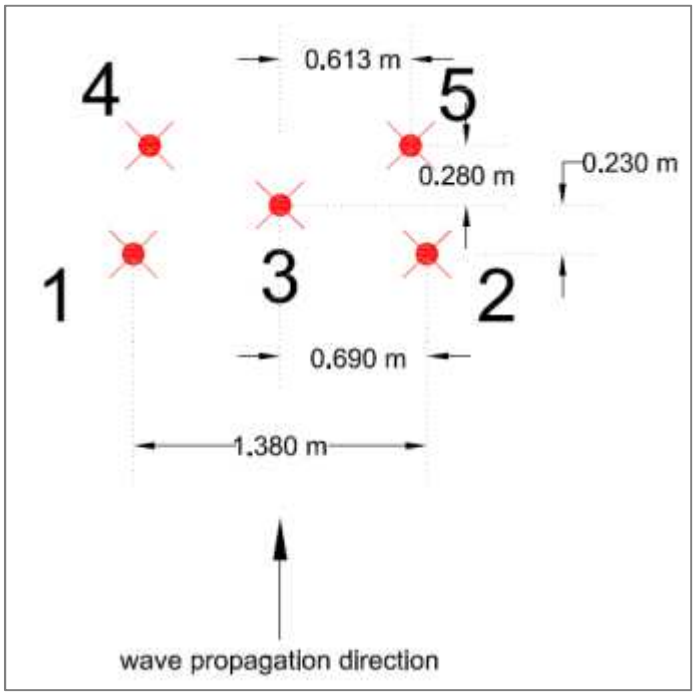

Figure B.2. Detail of the *CERC 5 wave gauge array* and separating distances, used in front of the WEC arrays for estimating wave directionality and wave reflection

C

Summary of sea states tested during the WEC array experiments in the Shallow Water Wave basin of DHI

Abstract: *In this appendix, a summary is presented of all target sea states generated during the WEC array experiments in the Shallow Water Wave basin of DHI. These sea states include varying wave types (regular, polychromatic, irregular long- and short-crested with varying spreading parameters), with varying wave period, wave height and wave attack angles.*

Table C.1. Summary of target sea states tested in the wave basin of DHI.

Sea state	Wave type	H [m]	T [s]	s [-]	Angle [°]
1	Regular waves	0.074	1.18	long-crested	0
2	Regular waves	0.074	1.26	long-crested	0
3	Regular waves	0.074	1.18	long-crested	20
4	Regular waves	0.074	1.26	long-crested	20
5	Regular waves	0.074	1.18	long-crested	10
6	Regular waves	0.074	1.26	long-crested	10
7	Irregular long-crested	0.104	1.18	long-crested	0
8	Irregular long-crested	0.104	1.26	long-crested	0
9	Irregular short-crested	0.104	1.26	75 (short-crested)	0
10	Irregular short-crested	0.104	1.26	10 (short-crested)	0
11	Polychromatic	varies	varies	long-crested	0
12	Regular-AWACS OFF	0.074	1.18	long-crested	0
13	Regular- AWACS OFF	0.074	1.26	long-crested	0
14	Regular- AWACS OFF	0.074	1.18	long-crested	20
15	Regular- AWACS OFF	0.074	1.26	long-crested	20
16	Regular- AWACS OFF	0.074	1.18	long-crested	10
17	Regular- AWACS OFF	0.074	1.26	long-crested	10
18	Irregular long-crested	0.0749	1.05	long-crested	0
19	Irregular long-crested	0.0816	1.10	long-crested	0
20	Irregular long-crested	0.104	1.35	long-crested	0
21	Irregular long-crested	0.104	1.50	long-crested	0

D

Geometric WEC (array) and wave gauges' configurations, tested in the Shallow Water Wave basin of DHI

Abstract: *In this appendix, detailed plan views of all WEC (array) and wave gauges' configurations are presented, tested during the WEC array experiments in the Shallow Water Wave basin of DHI.*

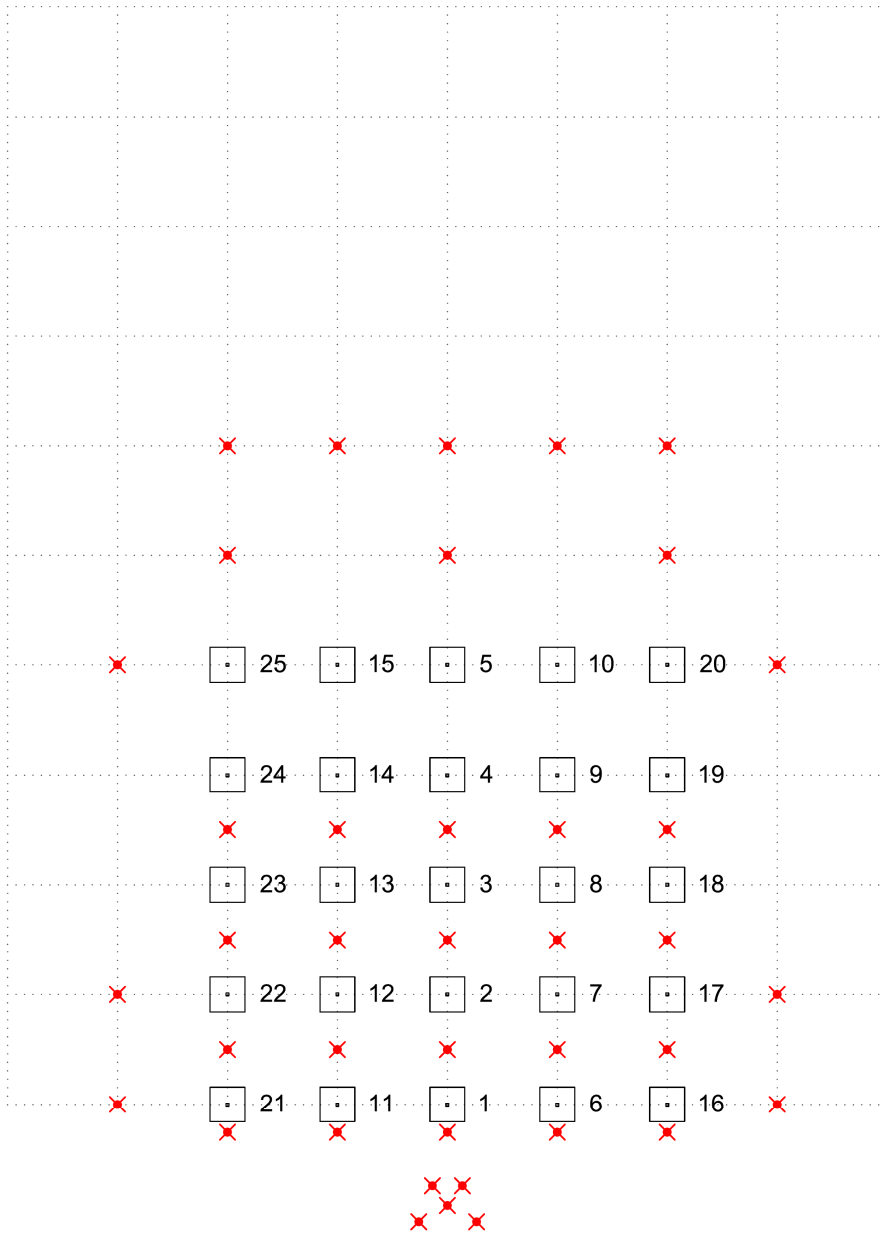

Figure D.1. Plan view of the experimental arrangement with no WECs present. 25 axes are present with an in-between distance equal to 5D (where D is the buoy diameter = 0.315 m). The squares represent the metal bases of the WECs. The numbering of the WECs is shown. The "**x**"-symbols represent the wave gauges. *WG plan 1* and *WEC shafts stencil 1* are used.

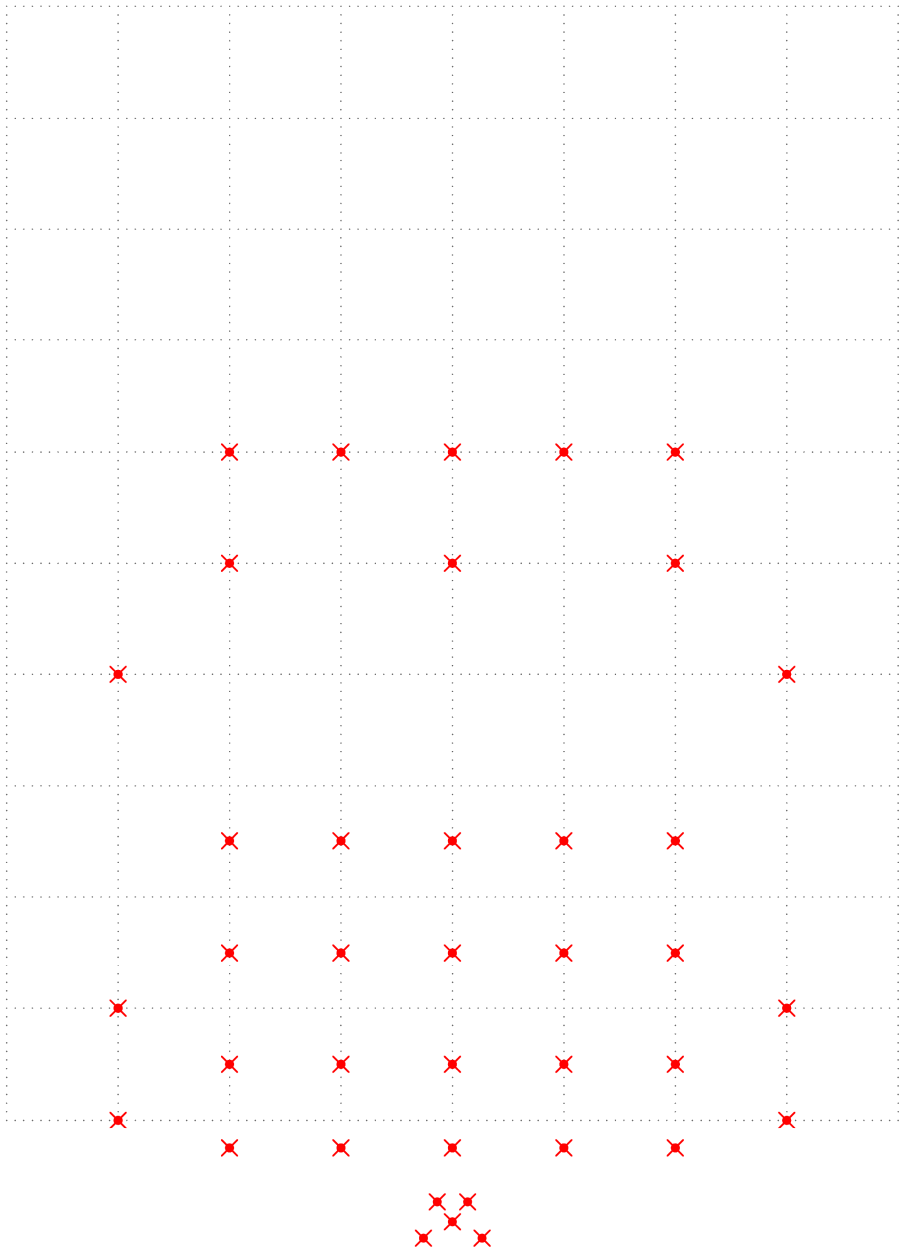

Figure D.2. Plan view of the experimental arrangement with no WECs and no axes present. The "**x**"-symbols represent the wave gauges. *WG plan 1* is used.

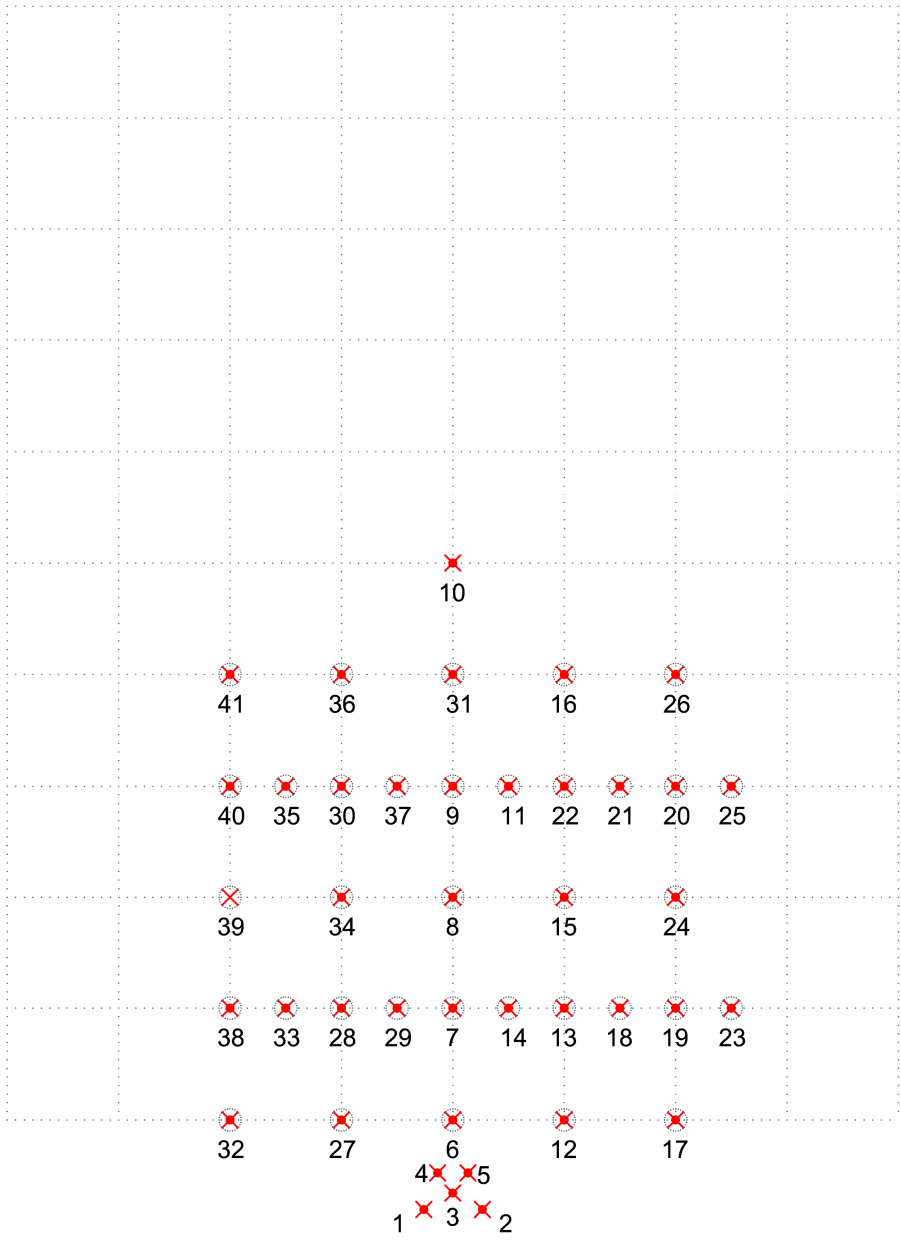

Figure D.3. Plan view of the experimental arrangement with no WECs and no axes present. The "**x**"-symbols represent the wave gauges. *WG plan 2* is used (numbering of WGs is shown), with the wave gauges moved to the locations (WEC buoy center points) where WECs have stand, for both staggered and rectilinear 5x5-WEC arrays.

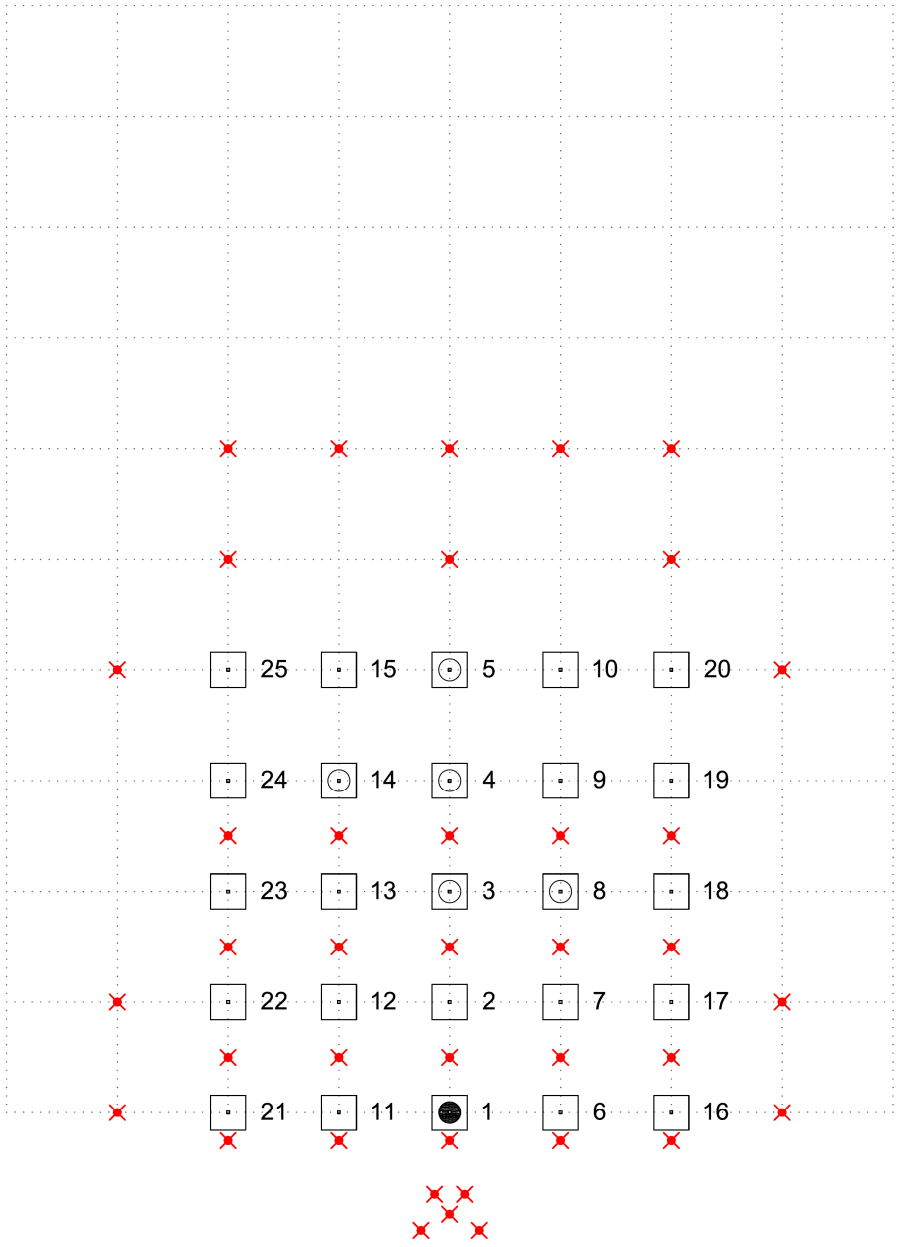

Figure D.4. Plan view of the experimental arrangement with 1 WEC present, each time. 25 axes are continuously present, with an in-between distance equal to 5*D* (where *D* is the buoy diameter = 0.315 m). The "**x**"-symbols represent the wave gauges. *WG plan 1* and *WEC shafts stencil 1* are used. The squares represent the metal bases of the WECs.

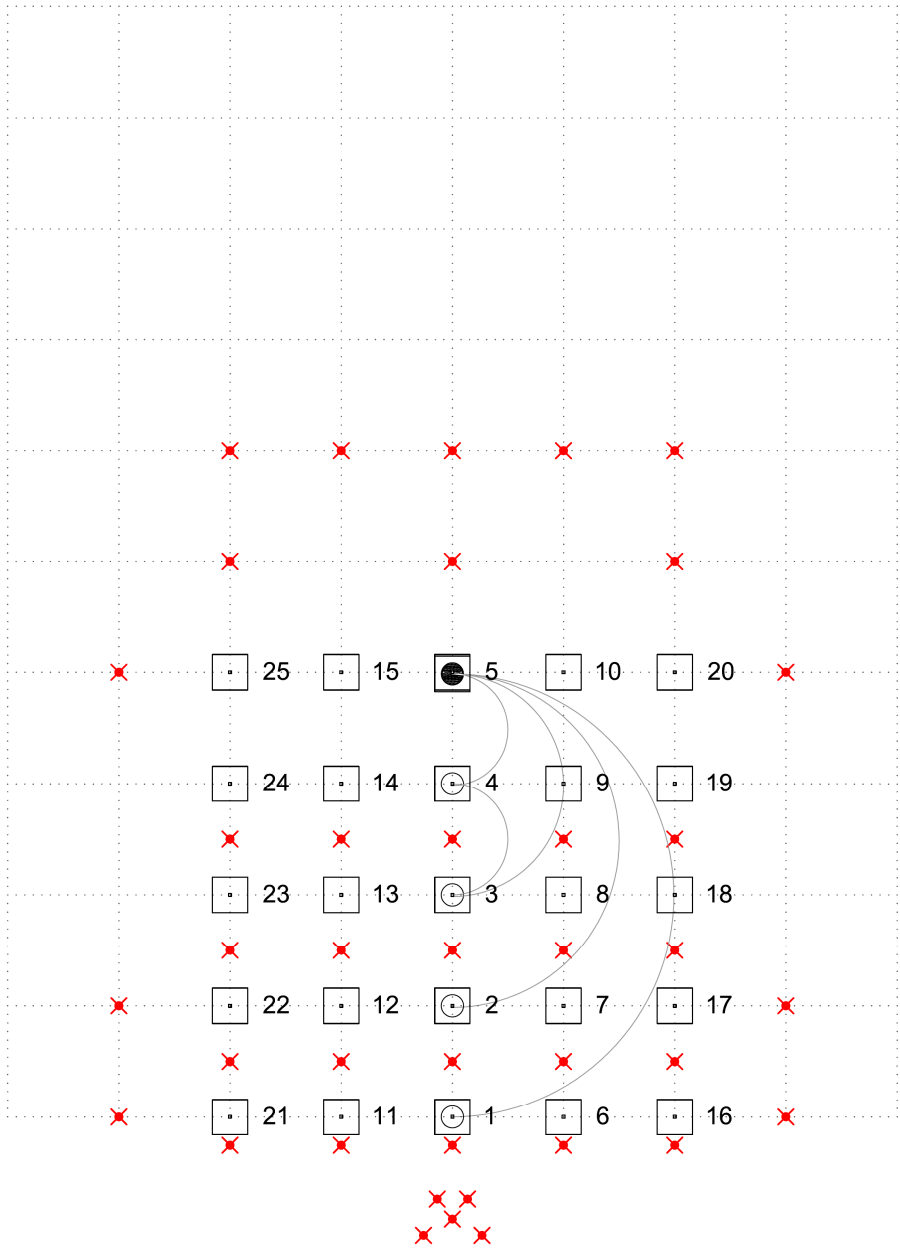

Figure D.5. Plan view of the experimental arrangement with 2 WECs present in a column, each time. 25 axes are continuously present, with an in-between distance equal to 5*D*. The "**x**"-symbols represent the wave gauges. The WEC spacing for the second WEC, changes gradually from 5*D* to 20*D* with a step of 5*D*. The squares represent the metal bases of the WECs. The numbering of the WECs is shown. *WG plan 1* and *WEC shafts stencil 1* are used. The circles represent the locations of the tested pairs of WECs. The semicircular lines indicate the pair combinations tested.

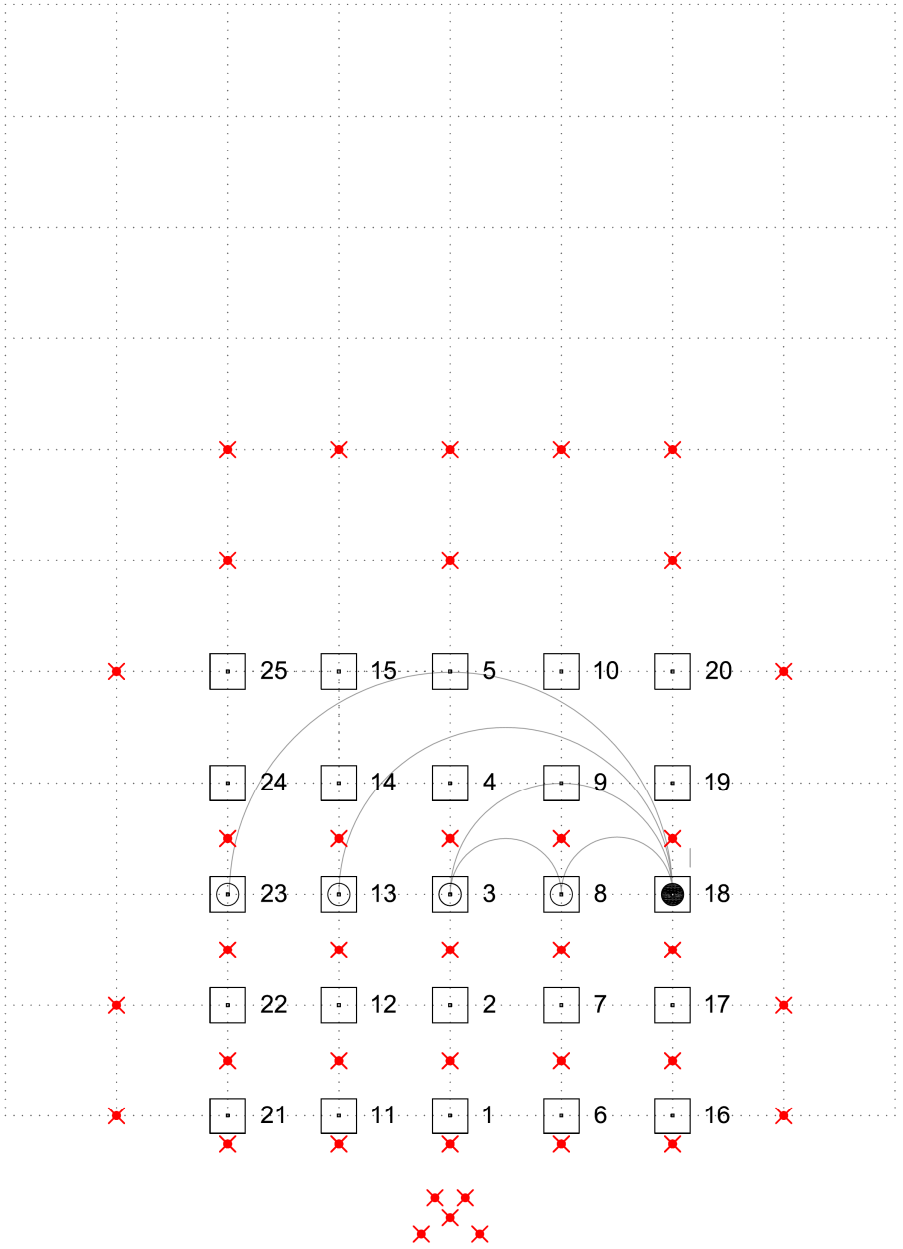

Figure D.6. Plan view of the experimental arrangement with 2 WECs present in a row, each time. 25 axes are continuously present, with an in-between distance equal to $5D$. The "**x**"-symbols represent the wave gauges. The WEC spacing for the second WEC, changes gradually from $5D$ to $20D$ with a step of $5D$. The squares represent the metal bases of the WECs. *WG plan 1* and *WEC shafts stencil 1* are used. The circles represent the WEC locations tested during this configuration, using each time 2 WECs. The semicircular lines indicate the pair combinations tested.

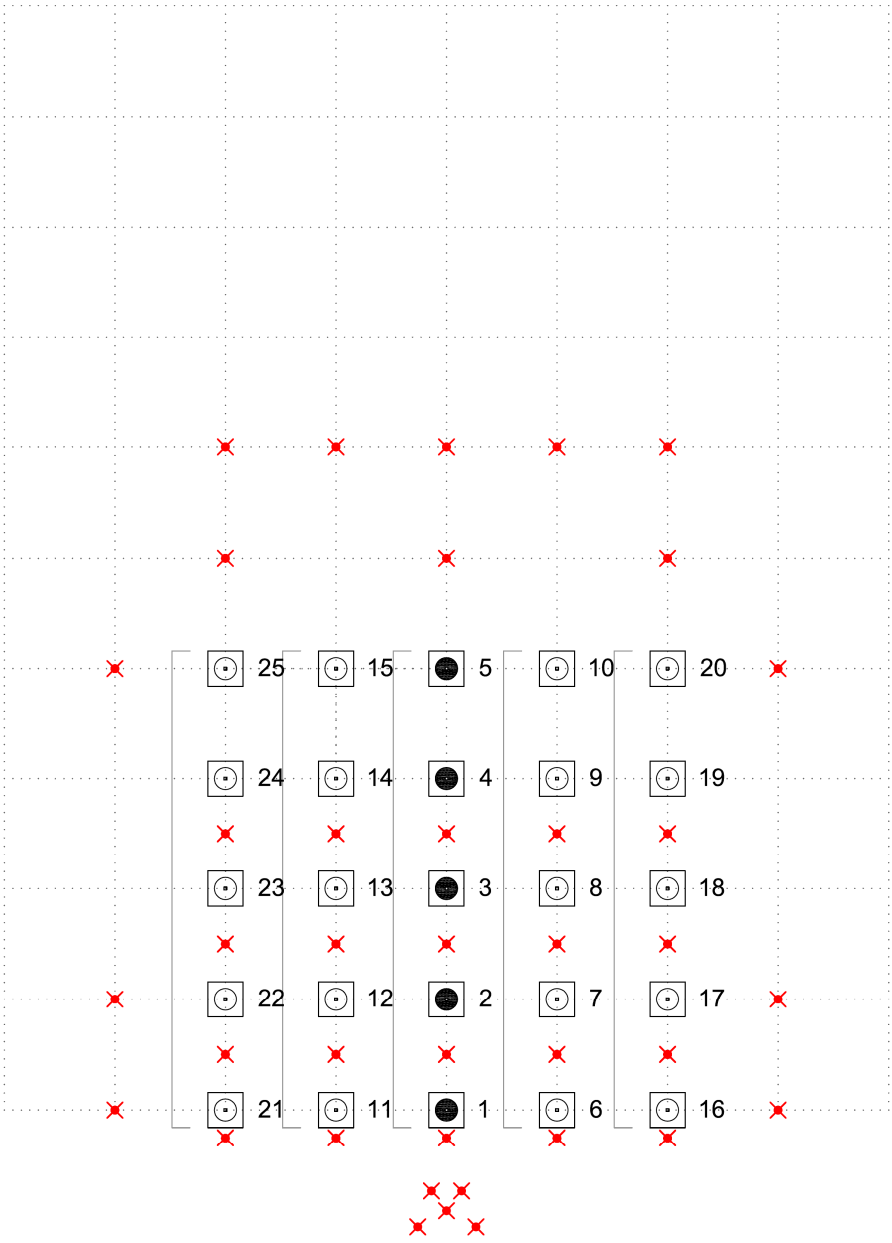

Figure D.7. Plan view of the experimental arrangement with 5 WECs present in a column, each time. 25 axes are continuously present, with an in-between distance equal to 5*D*. The "**x**"-symbols represent the wave gauges. The squares represent the metal bases of the WECs. *WG plan 1* and *WEC shafts stencil 1* are used. The circles represent the WEC locations tested during this configuration, using each time 5 WECs. The light grey lines indicate the WEC array combinations tested.

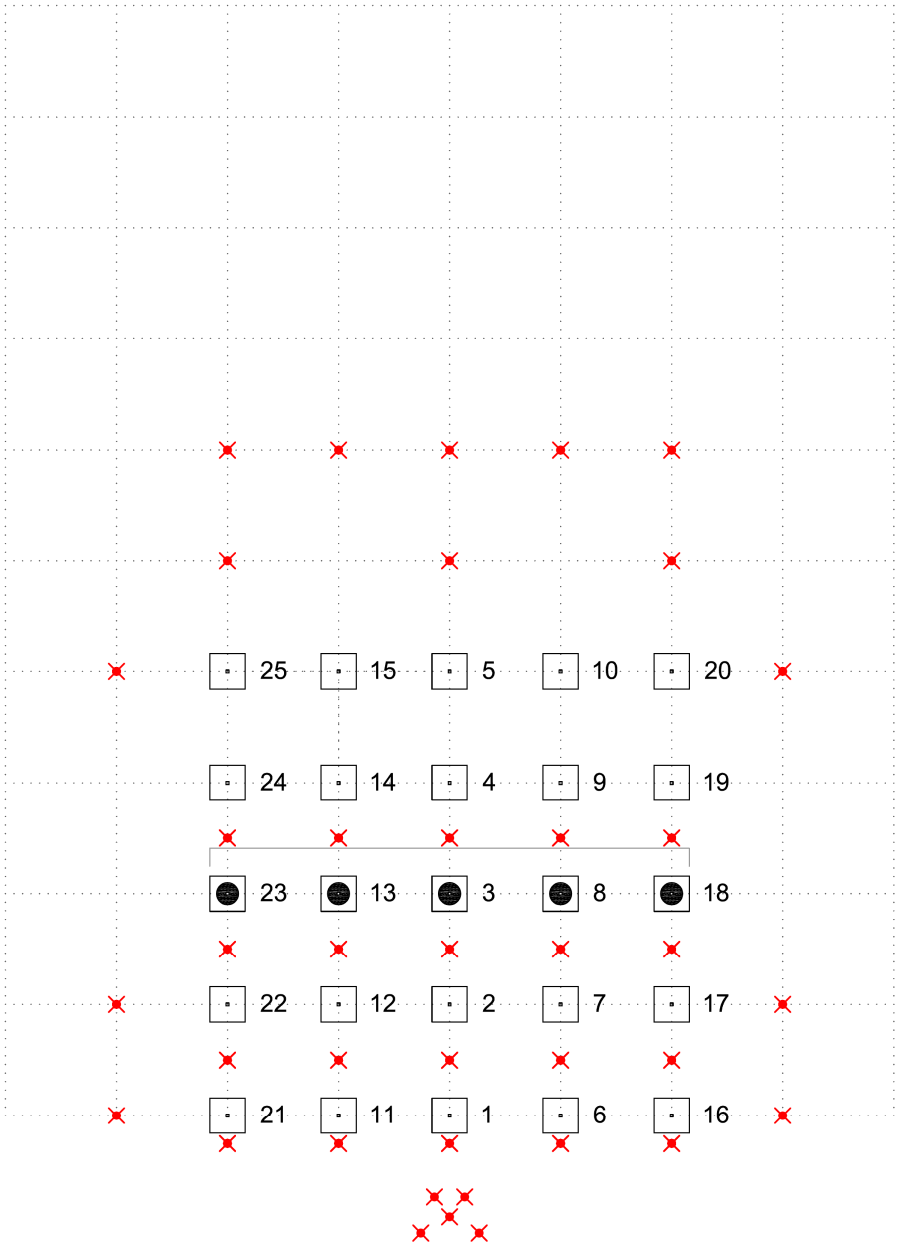

Figure D.8. Plan view of the experimental arrangement with 5 WECs present in a row, each time. 25 axes are continuously present, with an in-between distance equal to 5*D*. The "**x**"-symbols represent the wave gauges. *WG plan 1* and *WEC shafts stencil 1* are used. The numbering of the WECs is shown. The circles represent the WEC locations tested during this configuration, using 5 WECs. The light grey line indicates the WEC array combination tested.

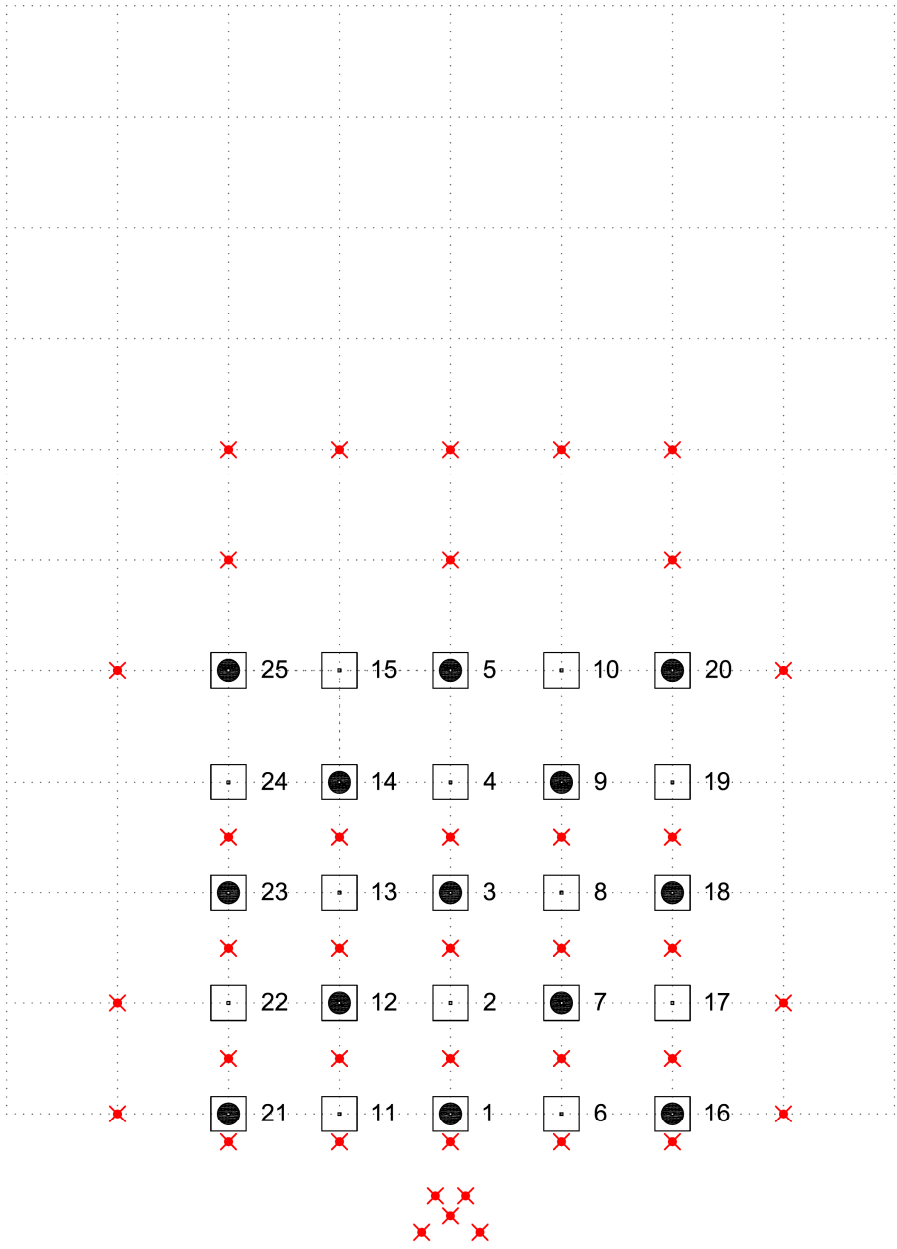

Figure D.9. Plan view of the experimental arrangement with the 13-WEC staggered array. 25 axes are continuously present, with an in-between distance equal to 5*D*. The WEC spacing is 10*D* for WECs of the same row and column. The "**x**"-symbols represent the wave gauges. *WG plan 1* and *WEC shafts stencil 1* are used. The numbering of the WECs is shown. The circles represent the WEC locations tested during this configuration, using 13 WECs.

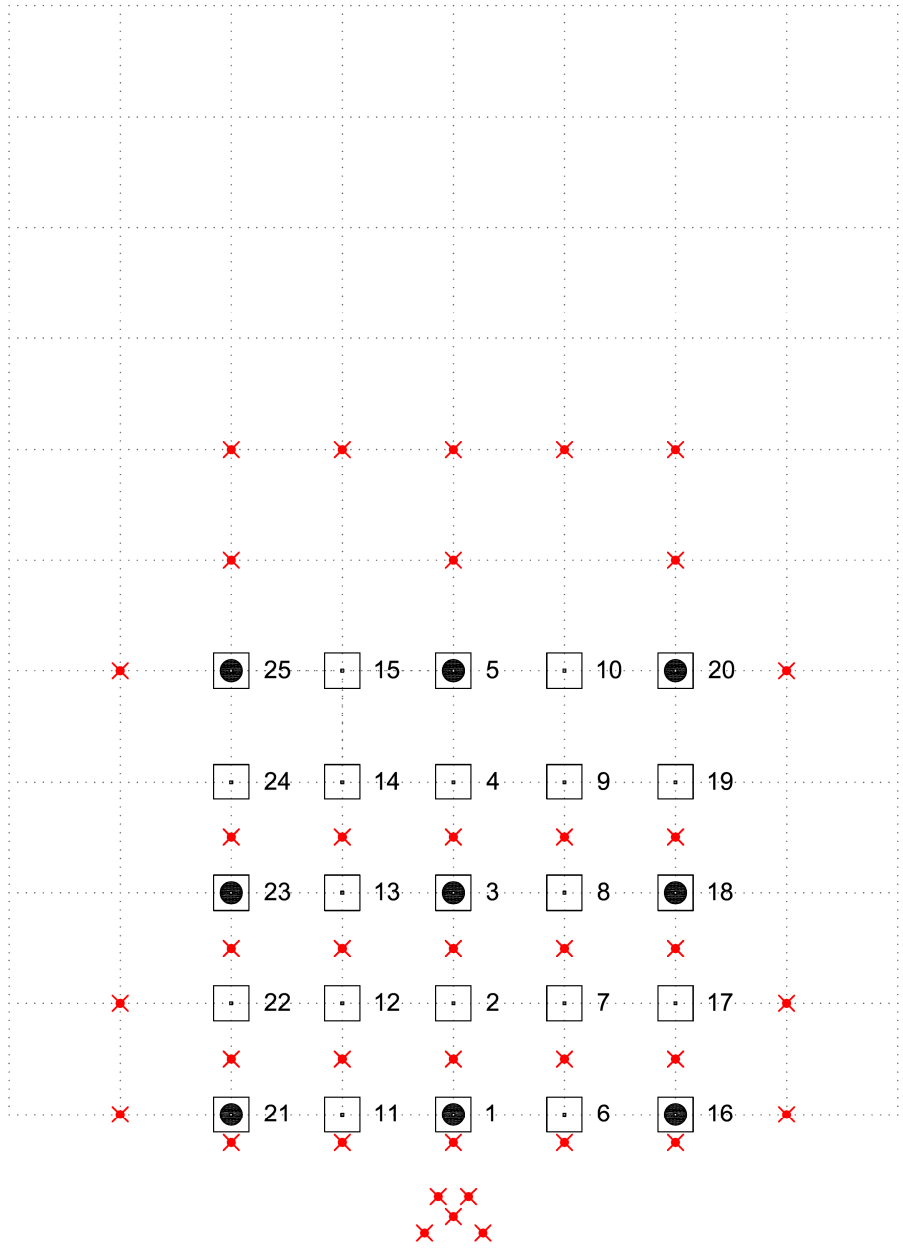

Figure D.10. Plan view of the experimental arrangement with the 3x3-WEC rectilinear 10*D* array (where *D* is the buoy diameter = 0.315 m). 25 axes are continuously present, with an in-between distance equal to 5*D*. The "**x**"-symbols represent the wave gauges. *WG plan 1* and *WEC shafts stencil 1* are used. The squares represent the metal bases of the WECs. The numbering of the WECs is shown. The circles represent the WEC locations tested during this configuration, using 9 WECs.

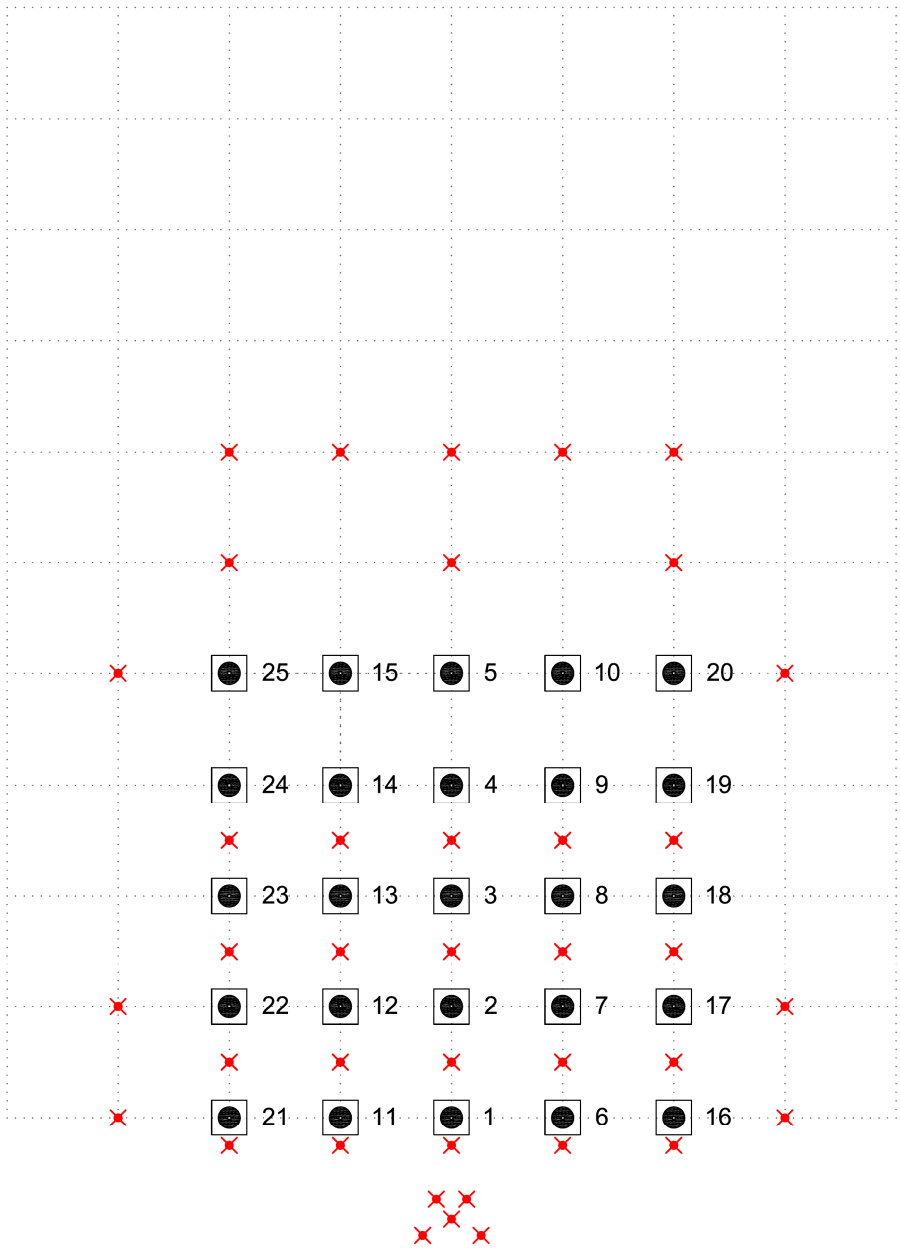

Figure D.11. Plan view of the experimental arrangement with the 5x5-WEC rectilinear array. 25 WECs are present in aligned configuration with a spacing of 5*D*. 25 axes are present, with an in-between distance equal to 5*D*. The "**x**"-symbols represent the wave gauges. *WG plan 1* and *WEC shafts stencil* 1 are used. The numbering of the WECs is shown. The circles represent the WEC locations tested during this configuration, using 25 WECs.

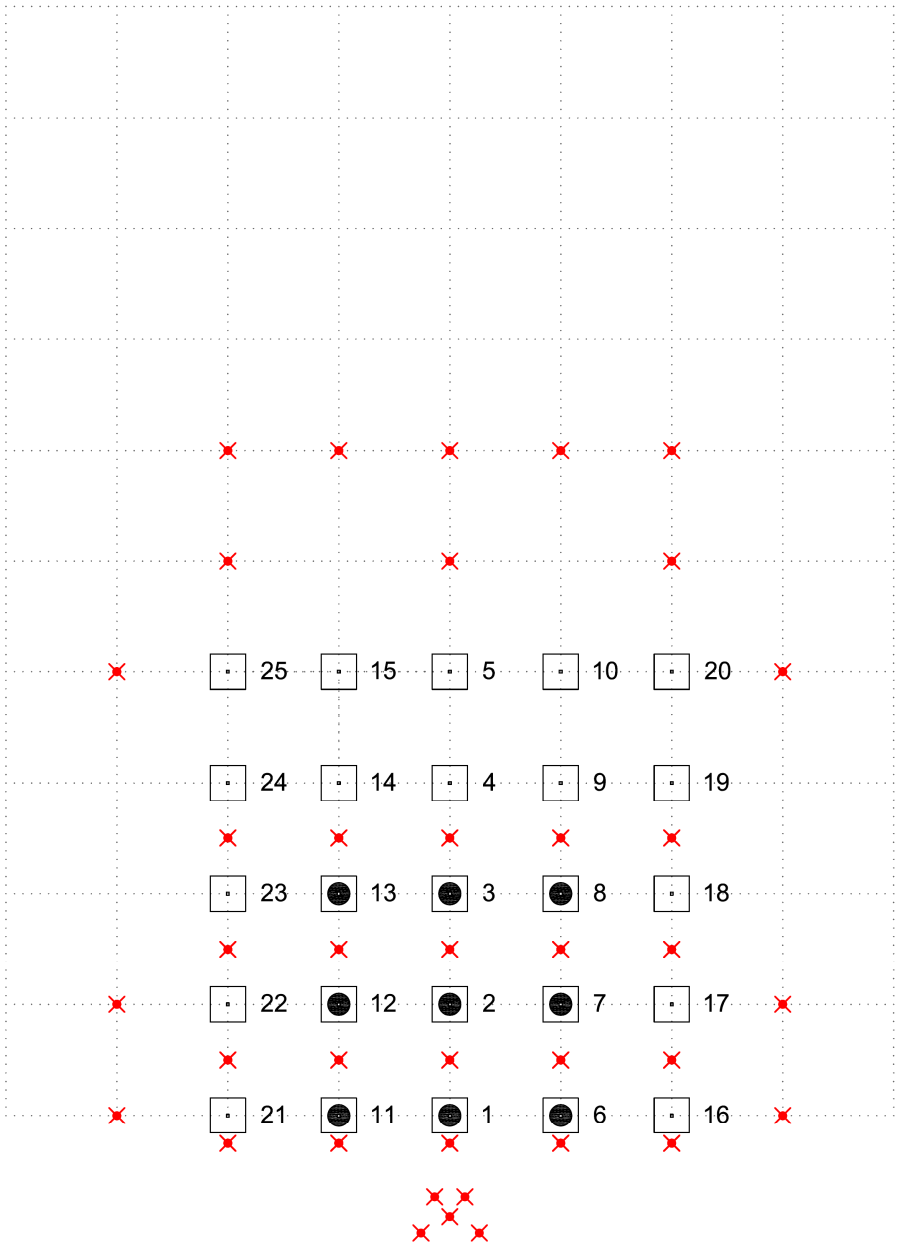

Figure D.12. Plan view of the experimental arrangement with the 3x3-WEC rectilinear 5 *D* array (where *D* is the buoy diameter = 0.315 m). 25 axes are continuously present, with an in-between distance equal to 5*D*. The "**x**"-symbols represent the wave gauges. *WG plan 1* and *WEC shafts stencil 1* are used. The squares represent the metal bases of the WECs. The numbering of the WECs is shown. The circles represent the WEC locations tested during this configuration, using 9 WECs.

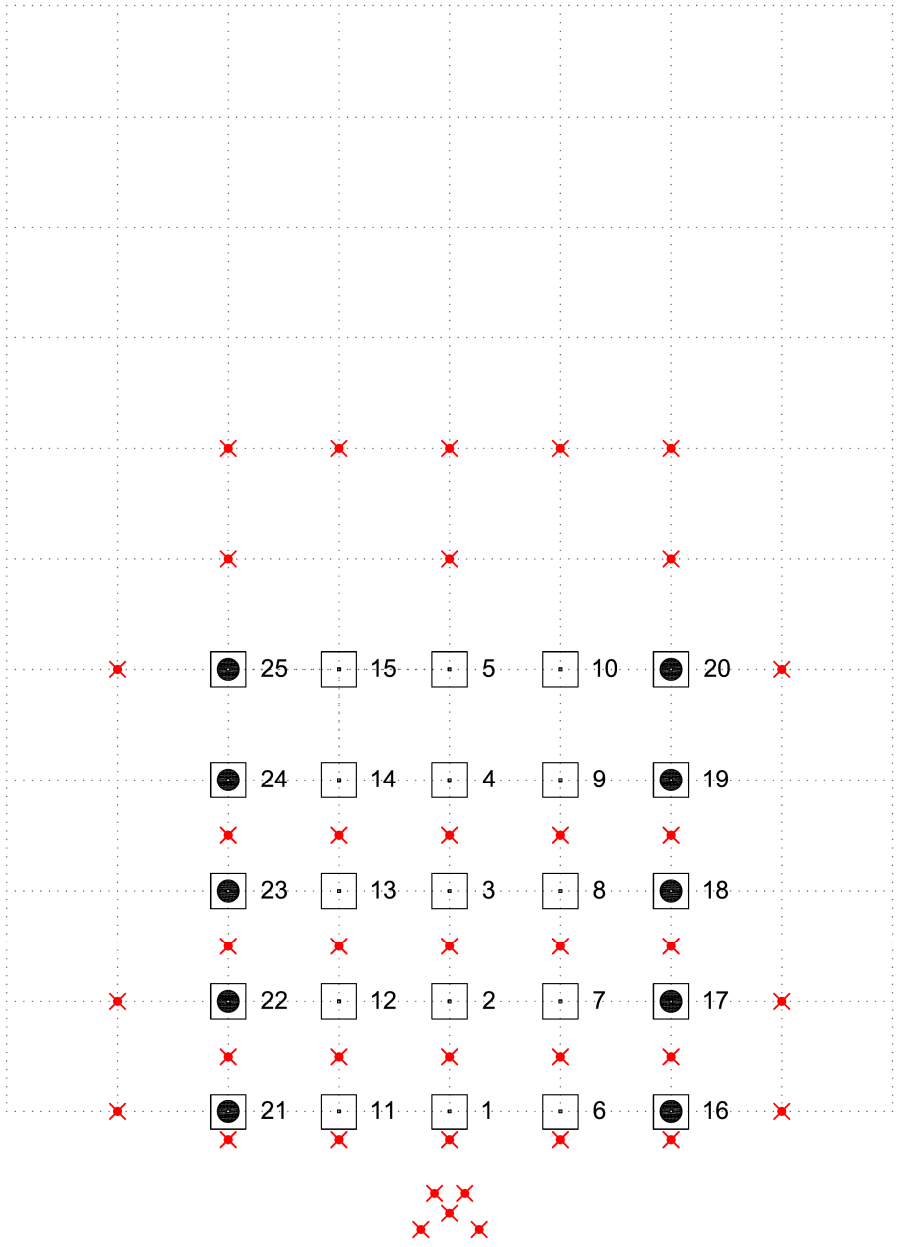

Figure D.13. Plan view of the experimental arrangement with the 10-WEC 2-Columns array. 25 axes are continuously present, with an in-between distance equal to 5*D* (where *D* is the buoy diameter = 0.315 m). The "**x**"-symbols represent the wave gauges. *WG plan 1* and *WEC shafts stencil 1* are used. The squares represent the metal bases of the WECs. The numbering of the WECs is shown. The circles represent the WEC locations tested during this configuration, using 10 WECs.

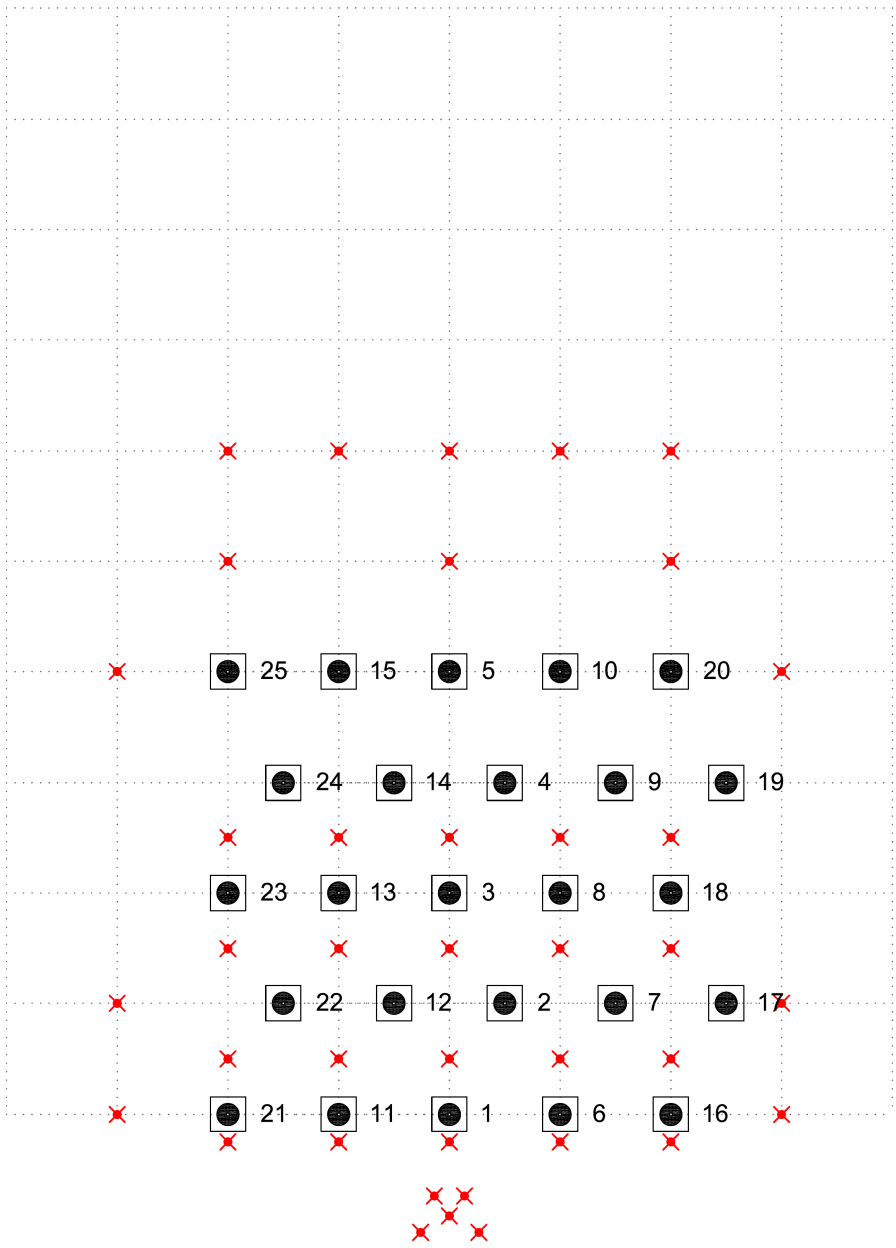

Figure D.14. Plan view of the experimental arrangement with the 5x5-WEC staggered array with WEC spacing 5*D*. Rows 2 and 4 of the configuration shown in Figure D.11 are shifted to the right by 2.5*D*. 25 axes are present with an in-between distance equal to 5*D*. The "**x**"-symbols represent the wave gauges. *WG plan* 1 and *WEC shafts stencil 2* are used. The numbering of the WECs is shown. The circles represent the WEC locations tested during this configuration, using 25 WECs.

E

Summary of PTO settings tested during the WEC array experiments

Abstract: *In this appendix, a summary of the PTO characteristics is provided, tested during the WEC array experiments. The WEC array description is given in the first column of Table E.1. In columns 2-8 the types of tests for various PTO-system and WEC motion characteristics are listed, for each WEC (array) geometric configuration. In columns 2-6 (for WECs under wave action) and in columns 7-8 (tests for WEC decay motion) of Table E.1, the damping settings of the PTO-system are given. Columns 2-5 and 7-8 refer to responding (heaving) WECs, while column 6 refers to tests with stationary WECs. For the tests of column 6 the WECs are held stationary at the equilibrium position (where the WEC buoy draft* d_{buoy} *= 31.5 m) and therefore the WECs behave as "obstacle cylinders" under wave action.*

Note that the damping settings of the PTO-system are expressed in terms of the spring compression increment (dx) *of each of the four springs of the PTO-system (see Chapter 2), with* dx *= 30.5 mm corresponding to optimum damping of the WEC motion. The selection of the used* dx *values is described in Chapter 2 and briefly mentioned in Chapter 4. Further, in the tests listed in columns 5 and 8, no damping is applied ("free" WEC response) on the WECs' motion through the PTO-system and therefore* dx *= 0.0 mm, and thus* F_{PTO} *= 0.*

Table E.1. Summary of WEC (array) geometric configurations and types of tests studied (Table page 1/4).

WEC (array) geometric configuration	Types of tests for various PTO-system and WEC motion characteristics						
	Damped WEC response (*dx*=30.5 mm)	**Damped WEC response (*dx*=35.5 mm)**	**Damped response – varying damping, *dx* [mm]**	**Undamped WEC(s) response (*dx* = 0.0 mm)**	**Stationary WEC(s) (*dx* setting N/A)**	**Damped WEC decay motion (*dx*=30.5 mm)**	**Undamped WEC decay motion (*dx* = 0.0 mm)**
Individual WEC							
Individual WEC # 1	√	√	10.5; 20.5; 40.5; 45.5; 50.5	√	-	√	√
Individual WEC # 3	√	-	10.5; 20.5; 40.5	√	-	-	-
Individual WEC # 4	√	√	20.5; 40.5; 50.5	√	-	-	-
Individual WEC # 5	√	-	10.5; 20.5; 40.5	√	-	√	√
Individual WEC # 8	√	-	-	-	-	-	-
Individual WEC # 14	-	-	40.5; 50.5	-	-	-	-

Table E.1. *Cont.* Summary of WEC (array) geometric configurations and types of tests studied (Table page 2/4).

WEC (array) geometric configuration	Types of tests for various PTO-system and WEC motion characteristics						
	Damped WEC response (*dx*=30.5 mm)	**Damped WEC response (*dx*=35.5 mm)**	**Damped response – varying damping, *dx* [mm]**	**Undamped WEC(s) response (*dx* = 0.0 mm)**	**Stationary WEC(s) (*dx* setting N/A)**	**Damped WEC decay motion (*dx*=30.5 mm)**	**Undamped WEC decay motion (*dx* = 0.0 mm)**
2-WEC arrays; Columns							
WECs # 4 and # 5 (longitudinal spacing, $l = 5D$)	√	-	-	-	√	√: WEC #5	√: WEC #5
WECs # 3 and # 5 (longitudinal spacing, $l = 10D$)	√	-	-	-	-	√: WEC #5	√: WEC #5
WECs # 2 and # 5 (longitudinal spacing, $l = 15D$)	√	-	-	-	-	-	√: WEC #5
WECs # 1 and # 5 (longitudinal spacing, $l = 20D$)	√	-	-	-	-	-	√: WEC #5
WECs # 3 and # 4 (longitudinal spacing, $l = 5D$)	√	-	-	-	-	-	-
2-WEC arrays; Rows							
WECs # 18 and # 8 (lateral spacing, $w = 5D$)	√	-	-	-	√	-	-
WECs # 18 and # 3 (lateral spacing, $w = 10D$)	√	-	-	-	-	-	-
WECs # 18 and # 13 (lateral spacing, $w = 15D$)	√	-	-	-	-	-	-
WECs # 18 and # 23 (lateral spacing, $w = 20D$)	√	-	-	-	-	-	-
WECs # 8 and # 3 (lateral spacing, $w = 5D$)	√	-	-	-	-	-	-

Table E.1. *Cont.* Summary of WEC (array) geometric configurations and types of tests studied (Table page 3/4).

WEC (array) geometric configuration	Types of tests for various PTO-system and WEC motion characteristics						
	Damped WEC response (*dx*=30.5 mm)	**Damped WEC response (*dx*=35.5 mm)**	**Damped response – varying damping, *dx* [mm]**	**Undamped WEC(s) response (*dx* = 0.0 mm)**	**Stationary WEC(s) (*dx* setting N/A)**	**Damped WEC decay motion (*dx*=30.5 mm)**	**Undamped WEC decay motion (*dx* = 0.0 mm)**
5-WEC arrays; Columns (*l* = 5*D*)							
WECs # 1, # 2, # 3, # 4, # 5 (column 3)	√	√	-	-	√	-	√: WEC #3
WECs # 11, # 12, # 13, # 14, # 15 (column 2)	√	-	-	-	-	-	-
WECs # 6, # 7, # 8 , # 9, # 10 (column 4)	√	√	-	-	-	-	-
WECs # 21, # 22, # 23, # 24, # 25 (column 1)	√	-	-	-	-	-	-
WECs # 16, # 17, # 18, # 19, # 20 (column 5)	√	√	-	-	-	-	-
10-WEC arrays; 2 Columns (*w* = 20*D*, *l* = 5*D*)							
WECs # 16, # 17, # 18, # 19, # 20, # 21, # 22, # 23, # 24, # 25 (columns 1 and 5)	√	-	-	-	-	-	-
5-WEC arrays; Rows (*w* = 5*D*)							
WECs # 18, # 8, # 3, # 13, # 23 (row 3)	√	-	-	-	-	-	-
5x5-WEC rectilinear array; 5 Rows x 5 Columns (*w* = 5*D*, *l* = 5*D*)							
WECs # 1 - 25	√	-	-	-	√	-	-

Table E.1. *Cont.* Summary of WEC (array) geometric configurations and types of tests studied (Table page 4/4).

WEC (array) geometric configuration	Types of tests for various PTO-system and WEC motion characteristics						
	Damped WEC response (*dx*=30.5 mm)	**Damped WEC response (*dx*=35.5 mm)**	**Damped response – varying damping, *dx* [mm]**	**Undamped WEC(s) response (*dx* = 0.0 mm)**	**Stationary WEC(s) (*dx* setting N/A)**	**Damped WEC decay motion (*dx*=30.5 mm)**	**Undamped WEC decay motion (*dx* = 0.0 mm)**
3x3-WEC rectilinear array; 3 Rows x 3 Columns (*w* = 10*D*, *l* = 10*D*)							
WECs # 1, # 3, # 5, # 16, # 18, # 20, # 21, # 23, # 25	√	-	-	-	-	-	-
3x3-WEC rectilinear array; 3 Rows x 3 Columns (*w* = 5*D*, *l* = 5*D*)							
WECs # 1, # 2, # 3, # 6, # 7, # 8, # 11, # 12, # 13	√	-	-	-	-	-	-
13-WEC staggered array; 5 Rows x 5 Columns (*w* = 10*D*, *l* = 5*D*)							
WECs # 1, # 3, # 5, # 7, # 9, # 12, # 14, # 16, # 18, # 20, # 21, # 23, # 25	√	-	-	-	√	-	-
5x5-WEC staggered array; 5 Rows x 5 Columns (*w* = 5*D*, *l* = 5*D*)							
WECs # 1 - 25	√	-	-	-	√	-	-

F

Experimental setup in the Shallow Water Wave basin of DHI

Abstract: *In this appendix, a plan view of the experimental arrangement used in the Shallow Water Wave basin of DHI is shown. The standard locations of the wave gauges (WG plan 1), the standard WEC shafts' stencil (WEC shafts' stencil 1) are presented. The location of the control platform is shown, as well as the length of the wave generator and the guide walls used at the sides of the wave basin.*

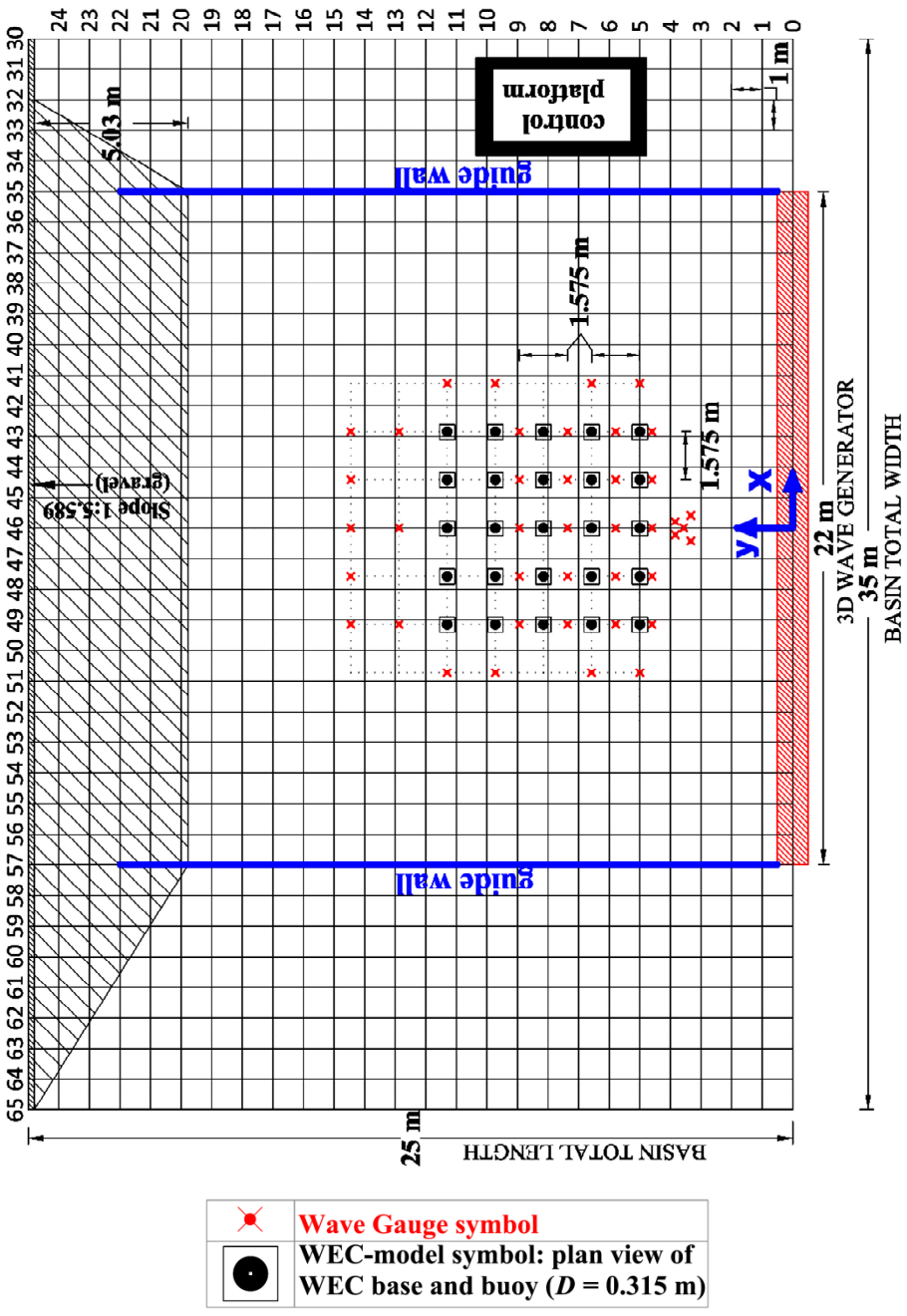

Figure F.1. Experimental arrangement employed the Shallow Water Wave basin of DHI to test large WEC arrays.